FLINDERS
UNIVERSITY
ADELAIDE
AUSTRALIA

Control of Highly Manoeuvrable Autonomous Underwater Vehicles in Full 6 Degrees-of-Freedom

by

Mr Matthew Kokegei, *B.Eng. (Computer Systems)*
School of Computer Science, Engineering and Mathematics
Faculty of Science and Engineering

August, 2014

A thesis presented to the
Flinders University of South Australia
in total fulfilment of the requirements for the degree of
Doctor of Philosophy (Engineering)

Adelaide, South Australia, 2014

Contents

Abstract

Both the scientific and commercial communities are increasingly utilising autonomous underwater vehicles (AUVs) for progressively challenging tasks. In order to improve the level of autonomy in these vehicles, a controller capable of accurately controlling such a complex system within a highly dynamic environment is required.

The mathematical model of an underwater vehicle is highly complex and nonlinear. This is due to hydrodynamic forces such as lift, drag, buoyancy and added mass effects. The addition of sensory equipment to the vehicle, especially those that protrude outside of the hull of the vehicle, can have a significant influence on one, or all, of these hydrodynamics. Furthermore, the complexity of the vehicle model increases significantly when highly dynamic and unknown water currents are acknowledged.

As the methods used to obtain this vehicle model are prone to error, a control strategy that is robust to modelling uncertainty and unknown water current disturbances is required. Furthermore, both computational and manoeuvring efficiency is desirable as both these factors contribute to the overall endurance of the vehicle. Current state of the art control strategies place various assumptions on the vehicle model such that a stable and realisable control law can be obtained. However, due to the nature of these assumptions, highly manoeuvrable underwater vehicles may not be utilised to their full potential, as they cannot safely operate outside the regions where some of these assumptions are violated. Minimising the use of these assumptions when designing a control system will ultimately lead to a more stable

control algorithm that is capable of controlling a vehicle over a much wider range of operation.

The goal of this thesis is to propose and analyse the performance of various control algorithms that are robust to both modelling uncertainty and unknown disturbances, while also improving the computational and manoeuvring efficiency of highly manoeuvrable AUVs. The results presented here are produced using a high fidelity simulation environment such that accurate and reliable behaviour of an AUV is realised without the need for a physical vehicle.

These goals are achieved by presenting a thorough analysis of the mathematical model that determines the dynamic nature of an underwater vehicle. Using a rigorous and systematic mathematical approach, this thesis then derives several simplified models for control design purposes, based on assumptions commonly employed for underwater vehicles. The behaviour of each simplified model is then validated against the behaviour of the model representing the real vehicle under control to verify the integrity of each simplified model.

Based on one of these simplified models, this thesis proposes a novel nonlinear controller utilising the body frame of the vehicle, as opposed to the navigation frame, which is widely adopted in the literature. This control strategy, namely the body frame coupled sliding mode controller (BFCSMC), offers several advantages compared to its existing navigation frame counterpart, namely the navigation frame coupled sliding mode controller (NFCSMC). In particular, the BFCSMC reduces the computational demand, and hence shortens the control execution time, of the vehicle along the desired trajectory. This is achieved while preserving, or improving in some cases, the manoeuvring ability of the vehicle. As part of the control algorithm development, a new uncoupled control strategy based on the literature, namely the body frame uncoupled sliding mode controller (BFUSMC), is also proposed to demonstrate the importance of incorporating the inherent coupling of the vehicle into the design of the control law.

The aim of this thesis is to present control strategies that can be applied to any underwater vehicle. The three control strategies, the BFUSMC, the NFCSMC, and

the BFCSMC, are then implemented, and simulation studies are conducted covering a wide range of manoeuvring complexity. The REMUS 100 AUV is chosen specifically for case study purposes. In particular, the hydrodynamic coefficients that are used by previously presented research for this vehicle are adopted by this thesis to avoid the need for estimating the coefficients.

These simulation studies demonstrate the superior performance of the BFCSMC over the NFCSMC, while the comparison of performance against the BFUSMC demonstrates the importance of including the inherent coupling of the vehicle within the control law.

Following is an analysis of common actuators utilised for AUV manoeuvring, and a novel control allocation scheme is proposed such that the manoeuvring ability of these vehicles is maintained while the manoeuvring efficiency is improved. Simulation studies conducted with this allocation scheme demonstrate that the manoeuvring ability of the vehicle is maintained while utilising this allocation scheme.

Overall, this thesis demonstrates the superior performance of the proposed controller utilising minimal assumptions for the vehicle model, while also demonstrating an allocation scheme that improves the manoeuvring efficiency of an AUV without sacrificing the manoeuvring ability.

Statement of Originality

I certify that this thesis does not incorporate without acknowledgment any material previously submitted for a degree or diploma in any university; and that to the best of my knowledge and belief it does not contain any material previously published or written by another person except where due reference is made in the text.

As specified under Clause 16 of Appendix E of the Flinders University Research Higher Degree Policies and Procedures, I hereby request that access to this thesis be restricted for a period of 18 months from the acceptance of the award of the degree.

Adelaide, August, 2014

Matthew Kokegei

Acknowledgments

Firstly, I would like to offer my sincerest gratitude to my supervisors, Associate Prof. Fangpo He and Associate Prof. Karl Sammut. Your invaluable guidance and support was a constant source of motivation throughout this entire journey.

Within the Intelligent Systems Research Group, I would like to thank Dr. Andrew Lammas and Dr. Tae Hwan Joung, as well as fellow postgraduates Mr. Zheng Zeng and Mr. Jonathan Wheare. Not only was your friendship welcomed, but ongoing group discussions, be it formal or informal, provided both beneficial feedback and a chance to gain a better understanding of how all our respective research areas integrate.

I would like to acknowledge the CSIRO who, via the Wealth from Oceans Flagship program through the Subsea Pipelines Cluster project, provided invaluable support in generating this thesis.

I would like to thank all the staff within the School of Computer Science, Engineering and Mathematics for assisting with paperwork, computer issues, and even the casual chats over coffee.

To my family, my heartfelt thanks for your love and support throughout my life and especially during my time as a postgraduate student. Mum and Dad, David and Michele, Wade and Amie, this would not have been possible without you.

Finally, I would like to say thank you to Cathy. Words cannot describe how much emotional support you have provided me in the time I have known you. I will be

forever grateful for your love, strength, understanding, and assistance, especially during the preparation of this thesis.

Matthew Kokegei

August, 2014

Adelaide

Nomenclature

	Description	Defined in Section
Upper Case		
$\mathbf{A}$	System Matrix	**2.3.5**
$\mathbf{B}$	Input Matrix	**2.3.5**
B	Vehicle Buoyancy	**2.2.2**
$\mathbf{C}$	Output Matrix	**2.3.5**
$\mathbf{C}\left(\dot{\mathbf{q}}_{\mathbf{r}}(t)\right)$	NFCSMC Coriolis and Centripetal Forces Matrix	**3.4.2**
$\mathbf{C}\left(\mathbf{v}_{\mathbf{b}}(t)\right)$	Body Frame Coriolis and Centripetal Forces Matrix	**2.3.1**
$\hat{\mathbf{C}}\left(\dot{\mathbf{q}}_{\mathbf{r}}(t)\right)$	NFCSMC Coriolis and Centripetal Forces Matrix Estimate	**3.4.2**
$\hat{\mathbf{C}}\left(\mathbf{v}_{\mathbf{b}}(t)\right)$	BFCSMC Coriolis and Centripetal Forces Matrix Estimate	**3.6.3**
$\tilde{\mathbf{C}}\left(\dot{\mathbf{q}}_{\mathbf{r}}(t)\right)$	NFCSMC Coriolis and Centripetal Forces Matrix Error	**3.4.2**
$\tilde{\mathbf{C}}\left(\mathbf{v}_{\mathbf{b}}(t)\right)$	BFCSMC Coriolis and Centripetal Forces Matrix Error	**3.6.3**
$\mathbf{C}_{\mathbf{A}}\left(\mathbf{v}_{\mathbf{r}}(t)\right)$	Body Frame Added Mass Coriolis and Centripetal Forces Matrix	**2.2.2**
$\mathbf{C}_{\mathbf{A}_{\eta}}\left(\mathbf{v}_{\mathbf{r}}(t), \boldsymbol{\eta}_{\mathbf{n}}(t)\right)$	Navigation Frame Added Mass Coriolis and Centripetal Forces Matrix	**2.2.2**
$\mathbf{C}_{\mathbf{RB}}\left(\mathbf{v}_{\mathbf{b}}(t)\right)$	Body Frame Rigid Body Coriolis and Centripetal Forces Matrix	**2.2.2**
$\mathbf{C}_{\mathbf{RB}_{\eta}}\left(\mathbf{v}_{\mathbf{b}}(t), \boldsymbol{\eta}_{\mathbf{n}}(t)\right)$	Navigation Frame Rigid Body Coriolis and Centripetal Forces Matrix	**2.2.2**

	Description	**Defined in Section**
$\mathbf{C}_{\boldsymbol{\eta}}\left(\boldsymbol{\nu}_{\mathbf{b}}(t), \boldsymbol{\eta}_{\mathbf{n}}(t)\right)$	Navigation Frame Coriolis and Centripetal Forces Matrix	**2.3.1**
$\mathbf{D}$	Direct Transmission Matrix	**2.3.5**
$\mathbf{D}\left(\dot{\mathbf{q}}_{\mathbf{r}}(t)\right)$	NFCSMC Hydrodynamic Damping Matrix	**3.4.2**
$\mathbf{D}\left(\boldsymbol{\nu}_{\mathbf{b}}(t)\right)$	Body Frame Hydrodynamic Damping Matrix, Assuming No Water Current	**2.3.1**
$\mathbf{D}\left(\boldsymbol{\nu}_{\mathbf{r}}(t)\right)$	Body Frame Hydrodynamic Damping Matrix	**2.2.2**
$\hat{\mathbf{D}}\left(\dot{\mathbf{q}}_{\mathbf{r}}(t)\right)$	NFCSMC Hydrodynamic Damping Matrix Estimate	**3.4.2**
$\hat{\mathbf{D}}\left(\boldsymbol{\nu}_{\mathbf{b}}(t)\right)$	BFCSMC Hydrodynamic Damping Matrix Estimate	**3.6.3**
$\tilde{\mathbf{D}}\left(\dot{\mathbf{q}}_{\mathbf{r}}(t)\right)$	NFCSMC Hydrodynamic Damping Matrix Error	**3.4.2**
$\tilde{\mathbf{D}}\left(\boldsymbol{\nu}_{\mathbf{b}}(t)\right)$	BFCSMC Hydrodynamic Damping Matrix Error	**3.6.3**
$\mathbf{D}_{\mathbf{l}}$	Linear Hydrodynamic Damping Matrix	**2.2.2**
$\mathbf{D}_{\mathbf{n}}\left(\boldsymbol{\nu}_{\mathbf{r}}(t)\right)$	Nonlinear Hydrodynamic Damping Matrix	**2.2.2**
$\mathbf{D}_{\boldsymbol{\eta}}\left(\boldsymbol{\nu}_{\mathbf{b}}(t), \boldsymbol{\eta}_{\mathbf{n}}(t)\right)$	Navigation Frame Hydrodynamic Damping Matrix, Assuming No Water Current	**2.3.1**
$\mathbf{D}_{\boldsymbol{\eta}}\left(\boldsymbol{\nu}_{\mathbf{r}}(t), \boldsymbol{\eta}_{\mathbf{n}}(t)\right)$	Navigation Frame Hydrodynamic Damping Matrix	**2.2.2**
$\mathbf{I}_{\mathbf{o}}$	Inertia Tensor	**2.2.2**
I_x	Moment of Inertia About *x*-axis	**2.2.2**
I_{xy}	Product of Inertia Between *x*-axis and *y*-axis	**2.2.2**
I_{xz}	Product of Inertia Between *x*-axis and *z*-axis	**2.2.2**
I_y	Moment of Inertia About *y*-axis	**2.2.2**
I_{yz}	Product of Inertia Between *y*-axis and *z*-axis	**2.2.2**
I_z	Moment of Inertia About *z*-axis	**2.2.2**
$\mathbf{J}\left(\boldsymbol{\eta}_{\mathbf{n}}(t)\right)$	Body Frame to Navigation Frame Transformation Matrix	**2.2.1**
$\mathbf{K}\left(u_r(t)\right)$	Force Coefficient Matrix	**5.2**

	Description	**Defined in Section**
$K(t)$	Roll Rotational Moment	**2.2.2**
K_{MT}	Main Thruster Torque Reaction Coefficient	**5.2.1**
$K_{RB}(t)$	Rigid Body Roll Rotational Moment	**2.2.2**
$\mathbf{K}_{\mathbf{S_{BC}}}$	BFCSMC Switching Gain Matrix	**3.6.3**
$\mathbf{K}_{\mathbf{S_{BU}}}$	BFUSMC Switching Gain Matrix	**3.5.3**
$\mathbf{K}_{\mathbf{S_{NC}}}$	NFCSMC Switching Gain Vector	**3.4.2**
$K_{S_{U_i}}$	Single DoF Switching Gain	**3.4.1**
$\mathbf{K}_{\mathbf{T_{BC}}}$	BFCSMC Tracking Error Gain Matrix	**3.6.3**
$\mathbf{K}_{\mathbf{T_{BU}}}$	BFUSMC Tracking Error Gain Matrix	**3.5.3**
$\mathbf{K}_{\mathbf{T_{NC}}}$	NFCSMC Tracking Error Gain Matrix	**3.4.2**
$K_{T_{U_i}}$	Single DoF Tracking Error Gain	**3.4.1**
$K_h(t)$	Hydrodynamic Roll Rotational Moment	**2.2.2**
$\hat{\mathbf{K}}_{\mathbf{1}}(u_r(t))$	Stage 1 Force Coefficient Matrix	**5.3.2**
$\hat{\mathbf{K}}_{\mathbf{2}}$	Stage 2 Force Coefficient Matrix	**5.3.2**
$\mathbf{L}(\mathbf{v_r}(t))$	Body Frame Hydrodynamic Lift Matrix	**2.2.2**
$\mathbf{L}_{\boldsymbol{\eta}}(\mathbf{v_r}(t))$	Navigation Frame Hydrodynamic Lift Matrix	**2.2.2**
$\mathbf{M}$	Body Frame System Inertia Matrix	**2.3.1**
$\hat{\mathbf{M}}$	Body Frame System Inertia Matrix Estimate	**3.4.2**
$\tilde{\mathbf{M}}$	Body Frame System Inertia Matrix Error	**3.4.2**
$M(t)$	Pitch Rotational Moment	**2.2.2**
$\mathbf{M_A}$	Body Frame Added Mass Matrix	**2.2.2**
$\mathbf{M}_{\mathbf{A}_{\boldsymbol{\eta}}}(\boldsymbol{\eta}_{\mathbf{n}}(t))$	Navigation Frame Added Mass Matrix	**2.2.2**
M_{HT}	Horizontal Thruster Torque Reaction Coefficient	**5.2.3**
$\mathbf{M_{RB}}$	Body Frame Rigid Body System Inertia Matrix	**2.2.2**

	Description	**Defined in Section**
$M_{RB}(t)$	Rigid Body Pitch Rotational Moment	**2.2.2**
$\mathbf{M}_{\mathbf{RB}_{\boldsymbol{\eta}}}(\boldsymbol{\eta}_{\mathbf{n}}(t))$	Navigation Frame Rigid Body System Inertia Matrix	**2.2.2**
$M_h(t)$	Hydrodynamic Pitch Rotational Moment	**2.2.2**
$\mathbf{M}_{\boldsymbol{\eta}}(\boldsymbol{\eta}_{\mathbf{n}}(t))$	Navigation Frame System Inertia Matrix	**2.3.1**
$N(t)$	Yaw Rotational Moment	**2.2.2**
$N_{RB}(t)$	Rigid Body Yaw Rotational Moment	**2.2.2**
N_{VT}	Vertical Thruster Torque Reaction Coefficient	**5.2.3**
$N_h(t)$	Hydrodynamic Yaw Rotational Moment	**2.2.2**
$\mathbf{R}_{\mathbf{b}}^{\mathbf{n}}(\boldsymbol{\Theta}_{\mathbf{n}}(t))$	Translational Velocities Transformation Matrix	**2.2.1**
$\mathbf{T}$	Actuator Configuration Matrix	**5.2**
$\mathbf{T}_i$	Actuator Configuration Matrix Column	**5.2.1**
$\mathbf{T}_{\boldsymbol{\Theta}}(\boldsymbol{\Theta}_{\mathbf{n}}(t))$	Angular Velocities Transformation Matrix	**2.2.1**
$\hat{\mathbf{T}}_{\mathbf{1}}$	Stage 1 Actuator Configuration Matrix	**5.3.2**
$\hat{\mathbf{T}}_{\mathbf{2}}$	Stage 2 Actuator Configuration Matrix	**5.3.2**
$V(t)$	Scalar Lyapunov-Like Function Candidate	**3.4.1**
$\mathbf{V}_{\mathbf{b}}(t)$	Translational Velocity Components Vector	**2.2.1**
$\mathbf{V}_{\mathbf{r}}(t)$	Relative Translational Velocity Components Vector	**2.2.2**
W	Vehicle Weight	**2.2.2**
$\mathbf{X}(t)$	State Vector	**1.6.1**
$X(t)$	Surge Translational Force	**2.2.2**
$X_{RB}(t)$	Rigid Body Surge Translational Force	**2.2.2**
$X_h(t)$	Hydrodynamic Surge Translational Force	**2.2.2**
$Y(t)$	Sway Translational Force	**2.2.2**

	Description	**Defined in Section**
$Y_{RB}(t)$	Rigid Body Sway Translational Force	**2.2.2**
$Y_h(t)$	Hydrodynamic Sway Translational Force	**2.2.2**
$Z(t)$	Heave Translational Force	**2.2.2**
$Z_{RB}(t)$	Rigid Body Heave Translational Force	**2.2.2**
$Z_h(t)$	Hydrodynamic Heave Translational Force	**2.2.2**

Lower Case

d_{ii}	Single DoF Hydrodynamic Damping	**3.4.1**
$\hat{d}_{ii}$	Single DoF Hydrodynamic Damping Estimate	**3.4.1**
$\tilde{d}_{ii}$	Single DoF Hydrodynamic Damping Error	**3.4.1**
g	Acceleration due to Gravity	**2.2.2**
$\mathbf{g}(\boldsymbol{\eta}_\mathbf{n}(t))$	Body Frame Gravitational and Buoyancy Forces Vector	**2.2.2**
$\hat{\mathbf{g}}(\boldsymbol{\eta}_\mathbf{n}(t))$	Body Frame Gravitational and Buoyancy Forces Vector Estimate	**3.4.2**
$\tilde{\mathbf{g}}(\boldsymbol{\eta}_\mathbf{n}(t))$	Body Frame Gravitational and Buoyancy Forces Vector Error	**3.4.2**
$\mathbf{g}_\boldsymbol{\eta}(\boldsymbol{\eta}_\mathbf{n}(t))$	Navigation Frame Gravitational and Buoyancy Forces Vector	**2.2.2**
l_x	*x*-Axis Actuator Displacement	**5.2**
l_y	*y*-Axis Actuator Displacement	**5.2**
l_z	*z*-Axis Actuator Displacement	**5.2**
m	Vehicle Mass	**2.2.2**
m_{ii}	Single DoF Vehicle Mass/Inertia	**3.4.1**
$\hat{m}_{ii}$	Single DoF Vehicle Mass/Inertia Estimate	**3.4.1**
$\tilde{m}_{ii}$	Single DoF Vehicle Mass/Inertia Error	**3.4.1**
$p_b(t)$	Roll Velocity	**2.2.1**

	Description	**Defined in Section**
$p_c(t)$	Roll Component of Water Velocity, Decomposed in the Body Frame	**2.2.2**
$\mathbf{p_n}(t)$	Position Components Vector	**2.2.1**
$p_r(t)$	Relative Roll Velocity	**2.2.2**
$q_b(t)$	Pitch Velocity	**2.2.1**
$q_c(t)$	Pitch Component of Water Velocity, Decomposed in the Body Frame	**2.2.2**
$q_r(t)$	Relative Pitch Velocity	**2.2.2**
$r_b(t)$	Yaw Velocity	**2.2.1**
$\mathbf{r_b^b}$	Offset Between Centre of Buoyancy and Origin of Body Frame	**2.2.2**
$r_c(t)$	Yaw Component of Water Velocity, Decomposed in the Body Frame	**2.2.2**
$\mathbf{r_g^b}$	Offset Between Centre of Gravity and Origin of Body Frame	**2.2.2**
$r_r(t)$	Relative Yaw Velocity	**2.2.2**
$\mathbf{s}(t)$	Six DoF Measure of Tracking Performance	**3.4.2**
$s_i(t)$	Single DoF Measure of Tracking Performance	**3.4.1**
$\mathbf{u_{CS}}(t)$	Control Surfaces Control Input Vector	**5.3.2**
$u_{\mathrm{MT}}(t)$	Main Thruster Control Input	**5.3.2**
$\mathbf{u_{TT}}(t)$	Tunnel Thrusters Control Input Vector	**5.3.2**
$\mathbf{u}(t)$	Control Input Vector	**5.2**
$u_b(t)$	Surge Velocity	**2.2.1**
$u_c(t)$	Surge Component of Water Velocity, Decomposed in the Body Frame	**2.2.2**
$u_r(t)$	Relative Surge Velocity	**2.2.2**
$\mathbf{u_1}(t)$	Stage 1 Control Input Vector	**5.3.2**
$\mathbf{u_2}(t)$	Stage 2 Control Input Vector	**5.3.2**

	Description	**Defined in Section**
$v_b(t)$	Sway Velocity	**2.2.1**
$v_c(t)$	Sway Component of Water Velocity, Decomposed in the Body Frame	**2.2.2**
$v_r(t)$	Relative Sway Velocity	**2.2.2**
$w_b(t)$	Heave Velocity	**2.2.1**
$w_c(t)$	Heave Component of Water Velocity, Decomposed in the Body Frame	**2.2.2**
$w_r(t)$	Relative Heave Velocity	**2.2.2**
x_b^b	*x*-axis Component of Centre of Buoyancy Vector	**2.2.2**
$x_{d_i}(t)$	Single DoF Desired Position/Orientation	**3.4.1**
x_g^b	*x*-axis Component of Centre of Gravity Vector	**2.2.2**
$x_i(t)$	Single DoF Position/Orientation	**3.4.1**
$\tilde{x}_i(t)$	Single DoF Position/Orientation Tracking Error	**3.4.1**
$x_n(t)$	*x*-axis Component of Position Vector	**2.2.1**
$x_{r_i}(t)$	Single DoF Virtual Reference	**3.4.1**
y_b^b	*y*-axis Component of Centre of Buoyancy Vector	**2.2.2**
y_g^b	*y*-axis Component of Centre of Gravity Vector	**2.2.2**
$y_n(t)$	*y*-axis Component of Position Vector	**2.2.1**
z_b^b	*z*-axis Component of Centre of Buoyancy Vector	**2.2.2**
z_g^b	*z*-axis Component of Centre of Gravity Vector	**2.2.2**
$z_n(t)$	*z*-axis Component of Position Vector	**2.2.1**

Greek Upper Case

$\mathbf{\Theta_n}(t)$	Orientation, or Euler Angles, Vector	**2.2.1**

	Description	Defined in Section
Greek Lower Case		
$\boldsymbol{\alpha}_{\mathbf{BC}}$	BFCSMC Switching Gain Constant Matrix	**3.6.4**
$\boldsymbol{\alpha}_{\mathbf{BU}}$	BFUSMC Switching Gain Constant Matrix	**3.5.4**
$\boldsymbol{\alpha}_{\mathbf{NC}}$	NFCSMC Switching Gain Constant Vector	**3.4.2**
α_i	Single DoF Switching Gain Constant	**3.4.1**
$\dot{\boldsymbol{\eta}}_{\mathbf{c}}(t)$	Six DoF Water Current Velocity Vector, Decomposed in the Navigation Frame	**2.2.2**
$\boldsymbol{\eta}_{\mathbf{d}}(t)$	Six DoF Desired Position and Orientation Vector	**3.4.2**
$\boldsymbol{\eta}_{\mathbf{n}}(t)$	Six DoF Position and Orientation Vector	**2.2.1**
$\dot{\boldsymbol{\eta}}_{\mathbf{n}}(t)$	Six DoF Translational and Angular Velocity Vector, Decomposed in the Navigation Frame	**2.2.1**
$\boldsymbol{\eta}_{\mathbf{n}}^{0}$	Six DoF Position and Orientation Vector Linearisation Point	**2.3.5**
$\dot{\boldsymbol{\eta}}_{\mathbf{r}}(t)$	Six DoF Vehicle Velocity Vector, Relative to Surrounding Water Current Velocity, Decomposed in the Navigation Frame	**2.2.2**
$\theta_n(t)$	Pitch Euler Angle	**2.2.1**
λ_i	Single DoF Control Bandwidth	**3.4.1**
$\boldsymbol{\lambda}$	Six DoF Control Bandwidth	**3.4.2**
$\boldsymbol{\nu}_{\mathbf{b}}(t)$	Six DoF Translational and Angular Velocity Vector, Decomposed in the Body Frame	**2.2.1**
$\boldsymbol{\nu}_{\mathbf{b}}^{0}$	Six DoF Translational and Angular Velocity Vector Linearisation Point	**2.3.5**
$\boldsymbol{\nu}_{\mathbf{c}}(t)$	Six DoF Water Current Velocity Vector, Decomposed in the Body Frame	**2.2.2**
$\boldsymbol{\nu}_{\mathbf{d}}(t)$	Six DoF Desired Translational and Angular Velocities Vector	**3.5.3**
$\boldsymbol{\nu}_{\mathbf{r}}(t)$	Six DoF Vehicle Velocity Vector, Relative to Surrounding Water Current Velocity, Decomposed in the Body Frame	**2.2.2**
ρ	Water Density	**2.2.2**

	Description	**Defined in Section**
$\boldsymbol{\tau}(t)$	Six DoF Body Frame Forces and Moments Vector	**2.2.2**
$\boldsymbol{\tau}^0$	Six DoF Body Frame Forces and Moments Linearisation Point	**2.3.5**
$\hat{\boldsymbol{\tau}}_1(t)$	Six DoF Control Input Forces and Moments Estimate Vector	**5.3.2**
$\tilde{\boldsymbol{\tau}}_1(t)$	Six DoF Control Input Forces and Moments Error Vector	**5.3.2**
$\boldsymbol{\tau}_{RB}(t)$	Six DoF Rigid Body Forces and Moments Vector	**2.2.2**
$\boldsymbol{\tau}_a(t)$	Six DoF Applied Control Input Forces and Moments Vector	**5.2**
$\boldsymbol{\tau}_d(t)$	Six DoF Desired Control Input Forces and Moments Vector	**3.4.2**
$\tau_{d_i}(t)$	Single DoF Desired Control Input Force or Moment	**3.4.1**
$\boldsymbol{\tau}_h(t)$	Six DoF Hydrodynamic Forces and Moments Vector	**2.2.2**
$\tau_i(t)$	Single DoF Force or Moment	**3.4.1**
$\boldsymbol{\tau}_\eta(\boldsymbol{\eta}_n(t))$	Six DoF Navigation Frame Forces and Moments Vector	**2.2.2**
ϕ	Boundary Layer Thickness	**3.3.1**
$\phi_n(t)$	Roll Euler Angle	**2.2.1**
$\psi_n(t)$	Yaw Euler Angle	**2.2.1**
$\boldsymbol{\omega}_b(t)$	Angular Velocity Components Vector	**2.2.1**
$\boldsymbol{\omega}_r(t)$	Relative Angular Velocity Components Vector	**2.2.2**

Symbol

∇	Total Volume of Water Displaced by Vehicle	**2.2.2**

List of Abbreviations

Abbreviation	Description	Defined in Section
2D	Two Dimensional	**2.4.1**
3D	Three Dimensional	**4.4.2**
AoA	Angle of Attack	**2.2.2**
AUV	Autonomous Underwater Vehicle	**1.1.1**
BFCSMC	Body Frame Coupled Sliding Mode Controller	**1.7.1**
BFUSMC	Body Frame Uncoupled Sliding Mode Controller	**1.7.1**
ECEF	Earth-Centred Earth-Fixed	**2.2.1**
ECI	Earth-Centred Inertial	**2.2.1**
DoF	Degree-of-Freedom	**1.1**
FLC	Fuzzy Logic Controller	**1.4.2**
GPC	Generalised Predictive Control	**1.4.2**
GPS	Global Positioning System	**1.3.2**
IAE	Integrated Absolute Error	**4.4**
LOS	Line-of-Sight	**1.3.1**
LTI	Linear, Time-Invariant	**1.4.1**
MIMO	Multi-Input and Multi-Output	**1.4.1**
MPC	Model Predictive Control	**1.4.2**
NED	North-East-Down	**2.2.1**
NFCSMC	Navigation Frame Coupled Sliding Mode Controller	**1.7.1**
NFS	Neuro-Fuzzy System	**1.4.2**
NN	Neural Network	**1.4.2**
NPS	Naval Postgraduate School	**1.4.2**

Abbreviation	**Description**	**Defined in Section**
NUS	National University of Singapore	**1.4.2**
ODIN	Omni-Directional Intelligent Navigator	**3.6.1**
PID	Proportional-Integral-Derivative	**1.4.1**
PDE	Partial Differential Equation	**2.3.5**
REMUS	Remote Environment Monitoring UnitS	**1.1.1**
ROV	Remotely Operated Vehicle	**1.1.1**
SISO	Single-Input and Single-Output	**1.4.1**
SMC	Sliding Mode Control	**1.4.2**
SSR	State-Space Representation	**2.3.5**
STARFISH	Small Team of Autonomous Robotic "Fish"	**1.4.2**
SVD	Singular Value Decomposition	**5.3.2**
USMC	Uncoupled Sliding Mode Controller	**3.4.1**
UUV	Unmanned Underwater Vehicle	**1.1.1**
VSC	Variable Structure Control	**3.2.3**
WHOI	Woods Hole Oceanographic Institute	**1.1.1**

List of Figures

List of Tables

Chapter 1

Introduction

This chapter will discuss the motivation behind the research presented in the following thesis. It will introduce underwater vehicles and conduct a review of the current literature on underwater vehicle control. Finally, this chapter will conclude with a list of original contributions, along with an outline, of the thesis.

1.1. Motivation

Even though water covers over 70% of the Earth's surface, only about 5% of the oceans worldwide have been explored [1]. In order for underwater environments to be mapped and studied, vehicles are required to transport the appropriate equipment to these desired locations for data collection and analysis. These environments are highly dynamic due to the varied sources that influence ocean currents, and it is therefore an extremely difficult task to traverse these environments accurately, efficiently, and safely. Furthermore, if a vehicle is also required to interact with objects in its surrounding environment, there is an increased potential for damage to occur due to collisions.

Control is one of the most critical factors in determining the operational capability of an underwater vehicle. A high level of control is required for a vehicle to traverse an underwater environment efficiently and safely. For this reason, the simplest method for controlling an underwater vehicle is to include a human operator in the control

loop. This operator maintains control of the vehicle at all times. However, due to various factors, such as the extreme operating conditions that exist in the underwater environment, this approach can be impracticable.

For this reason, this thesis will focus on the more difficult problem of controlling an underwater vehicle without human intervention. To achieve this task satisfactorily, knowledge of the underlying model of the vehicle is required. An appropriate control law can then be designed and implemented based on this model. However, obtaining a highly accurate six degree-of-freedom (DoF) mathematical model of an underwater vehicle is often infeasible due to several reasons:

1. The comprehensive mathematical model for describing the motion of an underwater vehicle is highly nonlinear and coupled [2, 3]. This coupling effect means that any small perturbation in one of these parameters from the actual value has the potential to affect not only its DoF, but also all other DoFs.
2. Any small imperfection on the hull of the vehicle will alter the vehicle model, in particular lift and drag parameters. Causes of this include two outer surfaces not meeting together properly, small protrusions due to external sensors attached to the body of the vehicle, or even due to an object being lodged on the vehicle during mission execution.
3. Any alteration of the mass or mass distribution of the vehicle will affect both the inertia tensor and the centre of gravity. Collection and storage of water or seabed samples, placement of equipment on the sea floor, or redistribution of internal equipment are some examples of behaviours that can alter the mass or mass distribution of an underwater vehicle.
4. Water conditions, such as temperature, salinity levels and density, will affect the buoyancy of the vehicle.

For these reasons, a typical approach is to simplify the model, and use this simplified model in the design of the controller. This does make the design process much easier, yet it also removes higher order dynamics from the model during the simplification process. Therefore, the potential for unwanted and unexpected behaviour from the

controller does exist. This behaviour occurs during highly dynamic manoeuvring, particularly coupled manoeuvres at high speeds, as this type of motion is particularly reliant on the higher order dynamics of the model. Therefore, the best compromise is to retain as many of these parameters as possible during the design process while still being able to design a stable and robust controller.

Given this information, the question is how to design and implement a stable and robust controller such that simplification of the model of the underwater vehicle does not introduce unwanted and unexpected behaviour during highly dynamic and coupled manoeuvring. Seeking the answer to this question is the motivation behind the research described in this thesis.

1.1.1. Unmanned Underwater Vehicles

The underwater environment is particularly hostile for humans, even when a reinforced hull provides protection from extreme pressure. The removal of the human operator from such a dangerous environment can be achieved by the use of an unmanned underwater vehicle (UUV). UUVs do not require a large air-filled cockpit to maintain approximate sea level atmospheric pressure, and nor do they require oxygen tanks to provide clean air while also reducing the accumulation of carbon dioxide. Without these requirements, UUVs can be smaller and lighter, and therefore less expensive to operate compared to manned vehicles.

Two broad classes of UUV exist, with the level of intelligence implemented within the vehicle determining to which class the vehicle belongs. These two classes are the remotely operated vehicle (ROV) and the autonomous underwater vehicle (AUV).

1. Remotely Operated Vehicles

ROVs are highly manoeuvrable vehicles that maintain a connection to a base station within a support vessel via a tether. This tether ensures a human operator resides within the control loop to maintain control of the vehicle at all times. Depending on the exact configuration of the vehicle, this tether can provide the electricity to power the various sensors, systems and actuators within the vehicle, and therefore no on-board energy storage system is required. Typical ROVs are box-shaped with various

thrusters mounted around the frame for propulsion and manoeuvring purposes. To assist in the remote control of these vehicles, some form of imaging sensor provides visual feedback to the operator. Due to the open-frame design of the vehicle, the desired mission outcomes will determine which sensors the vehicle carries.

Figure 1.1 shows the Jason ROV, designed and built by Woods Hole Oceanographic Institute (WHOI). Since its first launch in 1988, Jason has successfully conducted many deep-sea observation missions.

The one major restriction that ROVs have compared to other vehicles is the tether. This tether, which provides control, and possibly power, limits the range of the ROV from the support vessel. In the case of Jason, this tether has a total length of 10 km, which restricts Jason's movements to a space within 10 km of the support vessel. Furthermore, this tether adds mass and drag to the vehicle, while underwater obstacles pose a risk of catching on the tether. This tether also adds a possible point of failure, such as what lead to the loss of the Kaiko ROV [5].

2. Autonomous Underwater Vehicles

AUVs require no such tether to complete missions. No human is required to maintain control of the vehicle, as an on-board computer accomplishes this task. This significantly increases the level of autonomy within the vehicle, as the vehicle can be

Figure 1.1: Jason ROV [4]

pre-programmed with the desired mission outcomes, and once launched, is able to decide for itself how best to accomplish this mission. Once the vehicle completes its mission, the operators can download the data collected during the mission for processing and analysis purposes.

There are several advantages for using an AUV compared to the other previously mentioned technologies:

1. There is no human intervention while the vehicle is executing its mission. There is no exposure by humans to the environment experienced by the AUV, unlike manned vehicles, and no requirement of a human operator to maintain control of the vehicle at all times, unlike manned vehicles or ROVs.
2. There is no need for a tether to maintain connection between the AUV and a base station. The AUV is free to manoeuvre unrestricted by cables, and the only limitation on range is due to the amount of energy stored on-board the vehicle.
3. The relatively smaller size and mass of AUVs, compared to both manned vehicles and ROVs, enables deployment from a much larger range of vessels.

These three reasons give rise to a very flexible platform for underwater surveying and exploration.

Figure 1.2 shows the torpedo shaped REMUS (remote environment monitoring units) 6000 AUV, designed by WHOI in cooperation with the Naval Oceanographic Office and the Office of Naval Research. This vehicle is one of a whole line of REMUS AUVs with a large variety of depth ratings and payload capabilities. All the REMUS vehicles are commercially available through Hydroid, a subsidiary of Kongsberg Maritime, who have also had commercial success with the HUGIN range of AUVs.

There are, however, considerations that must be acknowledged when designing an AUV as opposed to an ROV. This is primarily due to the lack of human intervention while an AUV executes its mission. The required behaviour of an AUV places a high level of importance on the autonomy structure of the vehicle to ensure the reliable performance, and therefore the long-term success, of the vehicle. Of particular interest is the controller that is implemented within such a vehicle. The complexity of

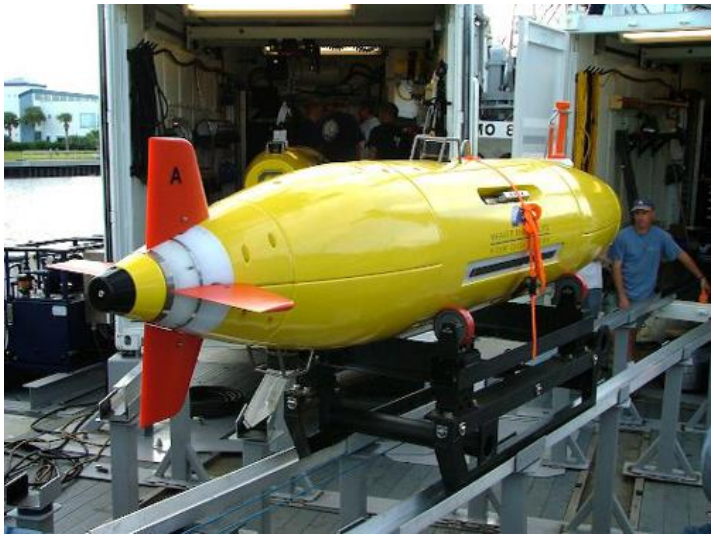

Figure 1.2: REMUS 6000 AUV [6]

the control problem is significantly increased for an AUV due to the autonomous nature of the vehicle. Therefore, the reliability of the controller is much more important for an AUV as opposed to an ROV.

3. Small and Inexpensive AUVs

To this point, the two underwater vehicles seen here have had one specification in common: they both have depth ratings of around 6000 m to 6500 m, with the REMUS 6000 AUV rated to 6000 m and the Jason ROV rated to 6500 m. However, this does not highlight one important aspect that is becoming more and more common in smaller AUVs with lesser depth ratings, and this is modularity. The Gavia AUV is one such vehicle, as seen in Figure 1.3. Gavia, shown in its base form in Figure 1.3(a), can be easily separates into individual modules as seen in Figure 1.3(b), and can be quickly reconfigured from a whole variety of different modules as seen in Figure 1.3(c).

Gavia has a depth rating of 1000 m and a diameter of 0.2 m. The length of the base vehicle seen in Figure 1.3(a) is 1.8 m, yet this length varies depending on the choice of modules seen in Figure 1.3(c). Furthermore, the mass in air of this vehicle in its base configuration is only 49 kg [7], which would increase depending on exact configuration. Taking into consideration that Gavia's depth rating of 1000 m enables the vehicle to operate from the surface to the full depth of the mesopelagic zone,

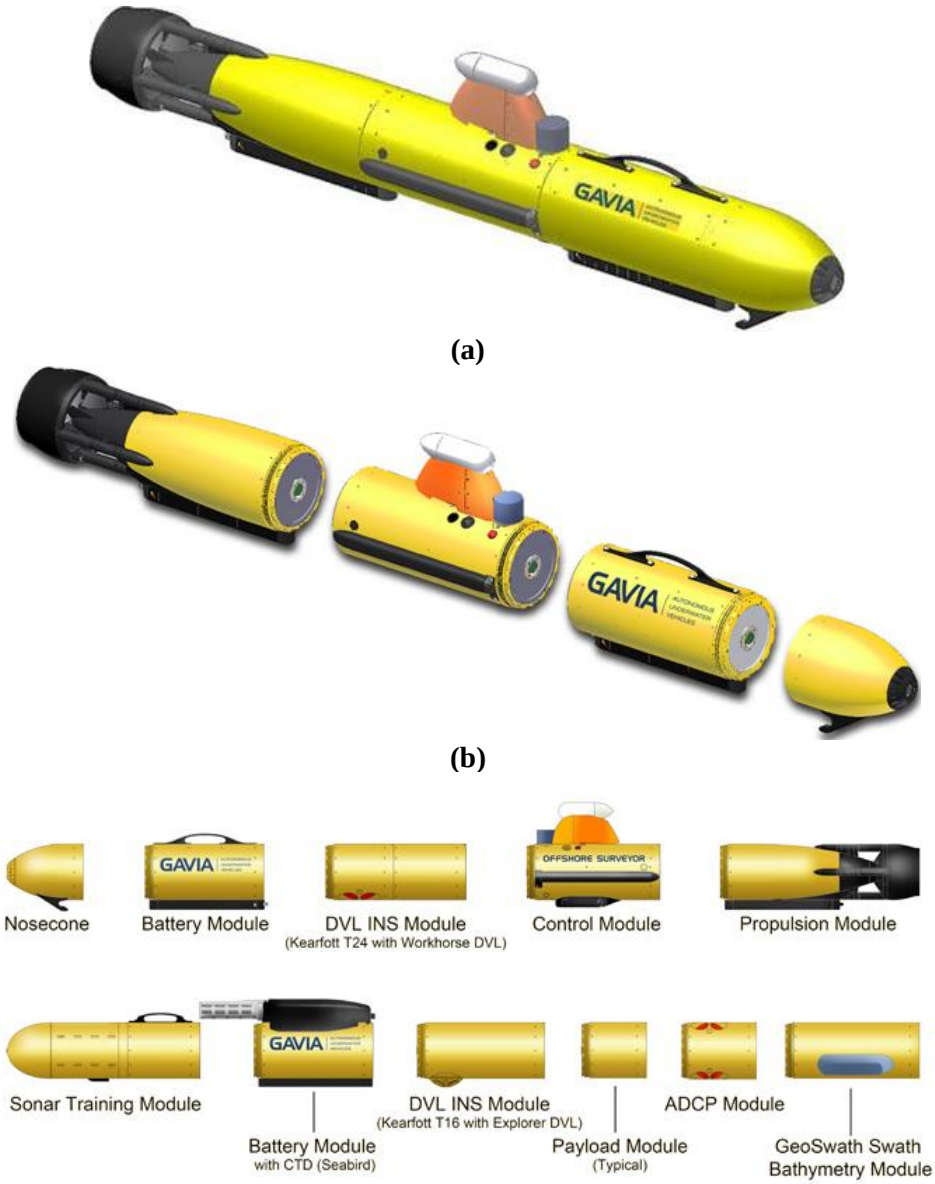

Figure 1.3: (a) Gavia AUV [9], (b) Modular Design [10], Available Modules from Teledyne Gavia [11]

which covers 25% of the total volume of the world's oceans [8], an AUV of this type has almost limitless potential uses. All these factors lead to an underwater vehicle system that is very flexible and relatively inexpensive to operate.

There are, however, limitations associated with a vehicle of this small size and modular nature compared to a larger vehicle of fixed configuration:

1. Less room for internal components, hence the control law must be simpler for implement on less powerful hardware with limited storage capacity, yet still maintain functionality.
2. Less room for energy storage, hence the control law must be computationally efficient, and therefore energy efficient.
3. Variation of the vehicle model when the vehicle is configured with different modules, including imperfections associated with the physical means of connecting these modules together.
4. Likely to be less stable due to decreased distance between centres of gravity and buoyancy.
5. More vulnerable to water current disturbances due to the vehicles reduced size and mass.

Careful design of the control law of an AUV such that it is both energy and computationally efficient can reduce the impact of the first two limitations. In order to address the final three limitations, a control law robust to modelling uncertainty is required such that the impact of modelling error is minimised. Hence, the purpose of this thesis is to propose a strategy for the robust control of an underwater vehicle such that a high level of accuracy in regards to trajectory tracking is maintained while also reducing energy consumption.

1.2. Research Methodology

The previous section detailed the complexities associated with the design and implementation of a controller for a small underwater vehicle. In the absence of a physical vehicle, a simulation study is performed to validate the various controllers developed within this thesis. The following methodology is adopted for the design and simulation study of robust control schemes for such a complex system under the aforementioned demanding circumstances.

1. Develop a plant model to mimic the behaviour of a real vehicle.

   Based on both rigid body dynamics and hydrodynamics, a plant model will be developed to mimic the actual behaviour of a real vehicle. This model will then form the basis for both the control design and the simulation environment.

2. Derive simplified models for the purpose of control design.

   Using a rigid and systematic mathematical approach, various simplified models will be derived based on assumptions commonly employed for underwater vehicles. Following a process of verification and validation, these models will then be used for control design purposes.

3. Verify the validity of these simplified models.

   A verification process will be used to validate the behaviour of the various simplified models against the developed plant model. This process will involve comparing the output of each simplified model with the output of the plant model under identical circumstances such that any instabilities of any simplified model can be easily observed.

4. Develop controllers based on the valid simplified models.

   Following the verification of the simplified models, various controllers will be developed, based on the valid simplified models, to control the plant model within the simulation studies.

5. Perform simulation studies where the developed control schemes are used to control the plant model.

   In order to assess the performance of the developed controllers, a simulation study will be performed, using a high fidelity simulation environment based on the plant model. A diverse range of manoeuvring complexity will be covered such that logical and valid conclusions can be drawn.

1.3. Guidance, Navigation, Control, and Actuation

The control system is just one component within the autonomy structure of an AUV. It is therefore essential to understand how the control system interacts with the other components within this structure. The autonomy structure of an AUV consists of three main subsystems, namely the guidance system, the navigation system, and the control system. Each of these systems is responsible for completing its own individual task, yet all must work cooperatively to allow an underwater vehicle to operate in a truly autonomous nature. Furthermore, actuation is required to apply the appropriate forces and/or moments to the vehicle such that the desired movement is obtained.

Referring to Figure 1.4, the guidance system is responsible for providing information regarding the desired states of the vehicle. The objectives of the overall mission will assist the guidance system in determining what the desired states are, and this system is further responsible for making the vehicle meet these objectives. The navigation system is responsible for analysing the motion of the vehicle, using various sensors and filtering techniques, to obtain an accurate estimate of the current state of the vehicle. It is therefore the responsibility of the control system to determine the appropriate control signals such that the vehicle behaves in a manner defined by the guidance system. These control signals are then applied to the various actuators of the vehicle, which in turn apply the appropriate forces and moments to the vehicle

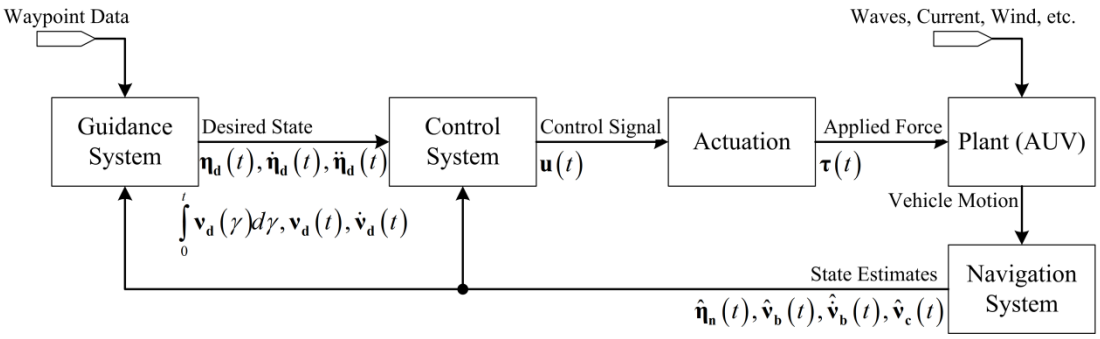

Figure 1.4: Guidance, Navigation, Control, and Actuation Loop

such that the desired motion is produced. This will result in the vehicle meeting the desired objectives, and therefore lead to successful completion of the mission.

1.3.1. Guidance

The guidance system is responsible for generating the desired state of the vehicle, which is then used by the control system to determine the appropriate corrective signal such that this desired state is achieved. With respect to AUVs, the guidance system is essential for providing true autonomy. This system is responsible for the completion of all long-term goals and objectives of the mission.

The guidance system receives information regarding the current state of the vehicle from the navigation system. The guidance system then uses this information to determine what the desired state of the vehicle should be. This desired state is continually updated, based on the current state, such that the overall mission objectives are met. Furthermore, limitations such as manoeuvrability restrictions can be utilised such that the desired state produced by the guidance system is in fact achievable by the vehicle. The control system uses this desired state as the reference input the vehicle is to track.

Due to the limited computational power on board AUVs, the algorithm within the guidance system is normally quite rudimentary, for example a line-of-sight (LOS) guidance system [12]. Appendix B provides an outline of LOS guidance.

In this case, a human mission planner generates a series of waypoints for the vehicle to follow. These waypoints define the overall desired trajectory that the vehicle is required to track. Using this type of system, the human mission planner must take into account, and avoid, all known obstacles within the operational area when defining these waypoints. The LOS guidance system attempts to make the vehicle track the trajectory formed by joining these waypoints, without any allowance for adaptation based on the vehicles perception of the surrounding environment. Due to the simplicity of this technique, it has been previously applied to surface vessels [13, 14] and can easily be extended to submersible vehicles [3, 15].

The control system utilises this desired state information when determining the forces to apply to the vehicle.

1.3.2. Navigation

The navigation system is responsible for estimating the current state of the vehicle, which is then used by the control system to determine the appropriate corrective signal such that the desired state, determined by the guidance system, is achieved. The navigation system is an essential mechanism required for any vehicle to traverse an environment.

Within the context of underwater vehicles, the various states that a navigation system is required to estimate include position, attitude, translational velocity and angular velocity. Furthermore, depending on the availability of processing power and sensory information, the navigation system could potentially estimate various environmental quantities such as water currents.

A suite of sensors provides information regarding aspects of the current state of the vehicle, such as position, attitude, velocity and acceleration. The navigation system uses this information to form an estimated solution of the true current state. The information from these sensors can contain both noise and bias errors, and therefore the navigation algorithm used must attempt to resolve a solution in the presence of these errors. Hence, the output from the navigation system is not necessarily a direct measurement from a particular sensor, but is an estimate of the most likely state of the vehicle based on all measurements received.

Due to the nature of certain sensors, the navigation system can receive information as a constant stream, or intermittently, over the duration of a mission. One of the most common methods for estimating position for ground and aerial vehicles is to use a Global Positioning System (GPS) receiver. However, the propagation of GPS signals through water is very poor. Therefore, GPS is only available to an AUV when it is at, or close to, the surface of the water. When GPS is unavailable, the navigation system must maintain an estimate of the position states using knowledge of the dynamics of the vehicle in conjunction with measurements from other sensors, and update this position estimate when GPS is available to the vehicle.

Various algorithms have been proposed for performing the task of navigation for underwater vehicles, such as simple dead reckoning [16, 17], Kalman filtering [18] and its corresponding derivatives [19], and particle filtering [20, 21].

Overall, the navigation system is responsible for obtaining and maintaining an estimate of the current state of the vehicle. The guidance system uses this estimate to determine the desired state of the vehicle in order to meet the objectives of the mission, while the control system uses this estimate to determine the forces to apply to the vehicle such that the current state moves towards the desired state.

1.3.3. Control

The control system is an essential part of the autonomy architecture of an AUV. This system requires realistic desired state information from the guidance system and accurate current state information from the navigation system. The control system then generates appropriate control signals based on the difference between desired and current states. These control signals are then applied to the various actuators of the vehicle by the actuation system. These actuators then apply a force and/or moment to the vehicle such that, ideally, the current state of the vehicle converges to the desired state of the vehicle.

This control can only be as accurate as the current state estimate from the navigation system, and can only be effective if the desired state provided from the guidance system is realistic and attainable. Therefore, the guidance system, navigation system, and control system must function cooperatively to achieve a truly autonomous vehicle.

Two major components form the control system of an underwater vehicle. The first is the control law, which calculates the overall desired force to apply to the vehicle, and the second is the control allocation, which calculates the control signals to apply to the actuators such that the overall desired force is achieved. As the control law and control allocation are the focus of this thesis, they are both reviewed in more detail in Sections 1.4 and 1.5 respectively.

1.3.4. Actuation

The actuation system receives the control signals from the control system, and applies the appropriate forces and moments to the vehicle such that the desired behaviour determined by the guidance system is achieved. The actuation system consists of the actuators that apply the physical forces and moments to the vehicle.

An overactuated vehicle is a vehicle where multiple actuators are capable of influencing a particular DoF. An example of this is a configuration where control surfaces and tunnel thrusters are both capable of applying a yaw moment to the vehicle. As opposed to underactuated vehicles, where the number of actuators is smaller than the number of controllable DoFs, overactuated vehicles generally possess a higher degree of manoeuvrability. In this case, a control allocation scheme distributes the desired forces and moments amongst the various actuators. This scheme can implement an optimisation algorithm such that a performance metric, typically actuator power consumption, is minimised.

1.4. Underwater Vehicle Control

Control, in a general sense, can be divided into two broad categories, namely classical control and modern control [22]. Control engineers have implemented compensators from both of these categories for AUVs; hence, the following sections will examine both methods. This examination is further extended in Chapter 3 where controllers are designed for AUVs.

1.4.1. Classical Control

Engineers have applied classical control techniques to a wide range of control problems. The most notable compensator from this category is the second order proportional-integral-derivative (PID) compensator. PID control is heavily used in industry today due to its relatively simple structure combined with its straightforward design procedure and proven results.

PID compensators are particularly useful when controlling linear, time-invariant (LTI) systems. However, the mathematical model of an AUV is highly nonlinear and

coupled. Therefore, a process of linearisation is required to obtain a linear model to base the compensator on. This process of linearisation does degrade the quality of the model and therefore affects the accuracy of the compensator. Santhakumar and Asokan [23], Xia *et al* [24], Ferreira *et al* [25], Moreira and Soares [26], and Li and Lee [27] all indicate that linear controllers can yield poor performance when used to compensate nonlinear plant models. As previously stated the mathematical model of an AUV is highly nonlinear and coupled. These nonlinearities and the coupling between DoFs are especially excited when the vehicle undergoes complex coupled manoeuvring, and the process of linearisation removes these nonlinearities from the system model. As this thesis is aimed at controlling highly manoeuvrable AUVs, a linear controller is inadequate when compared to other compensators. Therefore, PID control is not used within this thesis.

1.4.2. Modern Control

Driven by a desire for faster and more accurate robotics, control engineers have been exploring and implementing new design techniques. Modern control is the broad name given to these new techniques in order to differentiate them from the traditional classical control techniques. Modern control methods have not received the same level of acceptance as those of classical control for industrial applications, which can be attributed to a trend of requiring an accurate system model during the design process [22].

Various modern control techniques have been applied to underwater vehicles. Controllers based on neural networks (NNs) have been implemented by, for example, Guo *et al* [28], and Nguyen and Jung [29]. However, limitations have been identified in the use of NNs for underwater vehicles. Yu *et al* [30] acknowledges that the arbitrary determination of both the structure and initial weight of the neural network has a significant impact on the overall performance of the NN controller, while Sun *et al* [31] identifies the computational complexities of both the online learning and offline training procedures used for convergence of neural networks. As the computing power within an AUV is extremely limited, the computational demand of the online learning procedure is a severe implementation limitation. Combining this

fact with the acknowledged performance of the controller being related to arbitrarily chosen initial conditions, neural network controllers are deemed impractical for use in AUVs, particularly low-cost vehicles where computing power and its associated energy consumption are both extremely limited.

Fuzzy logic controllers (FLCs) are controllers that allow for the inclusion of qualitative, not just quantitative, descriptions of the compensated system. DeBitetto [32] used fuzzy logic to control ballast pumps for compensation of both the pitch and depth of a low speed AUV, while Smith *et al* [33] presented the design of a low level flight controller and a high level docking algorithm, both utilising FLCs. Nevertheless, Yu *et al* [30] and Sun *et al* [31] both identify the difficulties in formulating and tuning these controllers. These difficulties, particularly the formulation of the fuzzy rules, will inevitably affect both the performance and the robustness of the controller. Therefore, a more desirable solution is to implement a controller with less dependence on both formulation and tuning.

Considering the documented limitations of both NNs and FLCs, several algorithms have been proposed combining both these techniques, commonly referred to as neuro-fuzzy systems (NFSs), where the limitation of one technique is supposedly overcome by the other technique. Examples of this rationale are presented by Yu *et al* [30], Faruq *et al* [34], Wang and Lee [35], and Wang *et al* [36]. However, in a survey of these techniques conducted by Vieira *et al* [37], a trade-off still exists between the computational complexity and the accuracy of results obtained for such systems, depending on the fuzzy inference model used. Thus, as both the hardware to execute the control algorithm and the energy storage for small AUVs is limited, the desired performance may not be achievable due to a lack of processing power and/or power supply.

Further combinations of NNs with other controllers, such as PID controllers by Xia *et al* [24] and generalised predictive control (GPC), also known as model predictive control (MPC), by Xu and Zhang [38], have also been previously implemented. However, due to the presence of the NN component within the control structure, such schemes will still require large computational demand, which is often infeasible for small AUVs.

An MPC scheme utilising estimated water currents is presented by Medagoda and Williams [39] after acknowledging the compromise between optimality and computational load based on the control horizon associated with MPC schemes. Hence, both the scheme here by Medagoda and Williams [39] and the previous scheme by Xu and Zhang [38] are potentially impractical due to computational load required to generate a reasonable result.

One particular modern control technique that has become quite popular recently is sliding mode control (SMC). This technique enables accurate control of a system, even in the presence of modelling uncertainties and disturbances [31, 40, 41]. Furthermore, this method does not require linearisation of the plant during the design process, unlike classical control techniques, and has been found to be simple to use and implement with minimal tuning [42]. SMC has been applied to a variety of plants, ranging from the thermal control of a space station furnace facility [43], to knee joint angle tracking [44], vehicle active suspension systems [45], and flexible spacecraft attitude manoeuvring [46]. Fossen [2, 3] and Utkin *et al* [47] provide implementation methodologies for controlling a system using sliding modes. Application of SMC to AUVs has been achieved by, for example, Riedel and Healey for the Naval Postgraduate School (NPS) Phoenix AUV [48], Marco and Healey for the NPS Aries AUV [42], and Hong *et al* for the Small Team of Autonomous Robotic "Fish" (STARFISH) AUV at the National University of Singapore (NUS) [40].

Due to the aforementioned qualities of SMC, such as robustness to modelling uncertainty and variation, disturbance rejection, and ease of implementation, the novel compensators presented within this thesis will be based on SMC.

1.5. Control Allocation

Control allocation is the process of utilising the actuators of the vehicle to realise the desired force that is to be applied to the vehicle. The control allocation system receives the desired force from the control law and, using models of the actuators of the vehicle, calculates the control signal to apply to each actuator. Hence, the sum of all forces applied to the vehicle due to each actuator should approximate the desired

force calculated by the control law. Several control allocation schemes have been proposed for use on AUVs. Fossen [3, 49] proposed control allocation systems which ranged from a computational efficient yet inflexible direct inverse method to a highly adaptable yet computationally heavy method.

The direct inverse method requires accurate knowledge of the physical characteristics of each actuator. These characteristics reveal the forces and/or moments that each individual actuator can apply to the vehicle. By solving a series of simultaneous equations, the set of control signals to be applied to each actuator can be obtained from the overall desired force that is to be applied to the vehicle. This process is simple to implement using matrix mathematics, yet requires accurate models of the actuators. Furthermore, this scheme is inflexible to partial or complete actuator failure.

The second method proposed by Fossen [3, 49] formulated the control allocation problem as a quadratic programming optimisation problem. This allowed for such behaviours as biasing towards energy efficient actuators and adaptability to partial or complete actuator failure. The limitation of such a strategy is the computational load required to solve such a problem online. Especially on such a restricted platform as an AUV, the computational resources required for solving an optimisation problem of this type can be infeasible. This is of particular importance when considering a highly manoeuvrable vehicle with multiple actuators acting simultaneously on several DoFs.

1.6. Stability Analysis for AUVs

Proving the stability of a control system is a critically important step in the implementation process. When assessing the stability of underwater vehicle systems, particularly due to the nonlinear nature of these systems, it is common to utilise analysis methods introduced by Lyapunov [50] for time-invariant systems. Lyapunov's methods have further been extended by the use of Barbălat's lemma [51] for application to time-varying systems. It is common to use both these methods when designing and assessing the stability of AUVs controlled by SMC systems, and hence these methods will be introduced here.

1.6.1. Lyapunov Stability

Assessing the stability of nonlinear dynamic systems can be quite difficult, or even impossible, using traditional methods. This depends heavily on the ease of finding a solution to the derivative of the nonlinear system. However, using Lyapunov methods, the stability of a nonlinear system can be assessed without finding an explicit solution to this derivative [50]. Furthermore, the use of Lyapunov methods in the synthesis of the control law guarantees stability and convergence of the nonlinear system.

Nonlinear time-invariant systems can be represented as a system of nonlinear differential equations of the form:

$$\dot{\mathbf{X}}(t) = f\left(\mathbf{X}(t)\right) \tag{1.1}$$

where $\mathbf{X}(t)$ represents the state vector of the system, and $f\left(\mathbf{X}(t)\right)$ does not explicitly depend on time. By using Lyapunov's direct method [52], a Lyapunov function can be formulated to assess the stability of the nonlinear system.

If a Lyapunov function, $V\left(\mathbf{X}(t)\right)$, exists with continuous first-order derivatives such that:

- $V\left(\mathbf{X}(t)\right)$ is positive definite,
- $\dot{V}\left(\mathbf{X}(t)\right)$ is negative definite, and
- $V\left(\mathbf{X}(t)\right) \to \infty$ as $\left\|\mathbf{X}(t)\right\| \to \infty$,

then the equilibrium point $\mathbf{X}^*$ satisfying $f\left(\mathbf{X}^*\right) = 0$ is globally asymptotically stable [53].

1.6.2. Barbălat's Lemma and Lyapunov-Like Stability

The stability of an underwater vehicle can be assessed using Lyapunov's direct method as outlined in Section 1.6.1, yet the stability of a nonlinear control system cannot be performed using the same analysis. This is due to the reference trajectory

that the vehicle being required to follow now being time-varying, and hence the system cannot be represented as Equation (1.1). As the trajectory varies with time, the equivalent system must be formulated as:

$$\dot{\mathbf{X}}(t) = f\left(\mathbf{X}(t), t\right) \tag{1.2}$$

where $f\left(\mathbf{X}(t), t\right)$ is explicitly dependent on time.

Barbălat's lemma states that if the function $g(t)$ has a finite limit as $t \to \infty$, is differentiable and $\dot{g}(t)$ is uniformly continuous (or $\ddot{g}(t)$ is bounded), then $\dot{g}(t) \to 0$ as $t \to \infty$ [51].

Slotine and Li [52] presented a Lyapunov-like version of Barbălat's lemma. This analysis combines Barbălat's lemma with Lyapunov stability analysis such that the stability of time-varying systems in the form of Equation (1.2) can be analysed.

The Lyapunov-like theory of Slotine and Li [52] states that if:

- $V\left(\mathbf{X}(t), t\right)$ is lower bounded,
- $\dot{V}\left(\mathbf{X}(t), t\right)$ is negative semi-definite, and
- $\dot{V}\left(\mathbf{X}(t), t\right)$ is uniformly continuous in time,

then $\dot{V}\left(\mathbf{X}(t), t\right) \to 0$ as $t \to \infty$.

This implies that $V\left(\mathbf{X}(t), t\right)$ approaches a finite limiting value V_∞ where $V_\infty \leq V\left(\mathbf{X}(0), 0\right)$.

As is common for the design and analysis of SMC systems, the control laws presented within this thesis will be designed with the aid of Lyapunov methods while the stability will be assessed using both Lyapunov methods and Barbălat's lemma.

1.7. Contributions and Thesis Organisation

This section will present an outline of the thesis, the original contributions within the thesis, and the publications produced from these contributions.

1.7.1. Outline of the Thesis

This thesis presents the design and simulation results of several controllers, including two novel controllers, for AUVs. An outline of the structure of the thesis is given below.

Chapter 2 presents an overview of the mathematical model of an AUV. This overview begins by presenting the mathematical modelling techniques used to model underwater vehicles. This chapter starts with the kinematic equation, which relates information represented in one frame of reference to another. The matrix representation of the kinetic equation follows, which concerns the motion of the underwater vehicle due to both rigid body dynamics and hydrodynamics. Based on this equation, a model is derived for the plant, to be used in the simulation studies, as well as simplified models, based on common assumptions concerning underwater vehicles, to be used in the control design. This chapter concludes with a verification and validation study of the simplified models, comparing the behaviour of these models against the behaviour of the plant model. From this validation study, several models are identified as being suitable for control design, and these models will be used in Chapter 3 when deriving the compensators within this thesis.

Chapter 3 introduces the core component of this thesis, namely control techniques for underwater vehicles. This chapter begins by comparing different approaches for designing compensators for underwater vehicles, discussing both the advantages and limitations associated with each approach. Following is an analysis of current strategies used for controlling AUVs. This chapter then introduces two novel control approaches, both of which take advantage of performing compensation in the body frame, as opposed to the navigation frame, which is widely adopted in the literature. Firstly, a new uncoupled approach, namely the body frame uncoupled sliding mode controller (BFUSMC), is presented as part of the algorithm development to

demonstrate the importance of including the coupled dynamics within the control law of the compensator. Secondly, a novel coupled approach, namely the body frame coupled sliding mode controller (BFCSMC), is presented and compared with an existing navigation frame counterpart, namely the navigation frame coupled sliding mode controller (NFCSMC).

Chapter 4 presents a simulation study implementing the BFUSMC, the NFCSMC, and the BFCSMC. The plant model developed in Chapter 2 in combination with a LOS guidance system forms the high fidelity simulation environment in which all the control systems are implemented. The input trajectories to this simulation study cover a wide range of manoeuvring complexities such that fair, unbiased, and logical conclusions can be drawn based on the behaviour of each compensator. The results presented show the superior performance of the BFCSMC over the NFCSMC, while the comparative performance of the BFUSMC clearly demonstrates the importance of including the coupling of the model within the control law.

Chapter 5 introduces actuation and allocation for AUVs. This chapter begins with a review of commonly used actuators available to underwater vehicle designers. This includes highlighting their useful characteristics, and well as any possible limitations, that vehicle designers must consider when building such a constrained system. Following this is an overview of control allocation, and a novel control allocation scheme, aimed at decreasing power consumption, is proposed.

Chapter 6 presents a simulation study of the novel control allocation scheme proposed in Chapter 5 in conjunction with the NFCSMC and the BFCSMC as presented in Chapter 3. The BFUSMC is not included within this simulation study, as the nature of this simulation study is unsuitable for such a compensator. The results presented within this chapter demonstrate the maintained manoeuvring capabilities of the vehicle when the novel control allocation scheme is implemented.

Chapter 7 presents a summary of the various control systems and allocation strategies covered in this thesis, and draws generalised conclusions based on the results presented. From these conclusions, an indication of where future work lies within the AUV control area is presented.

1.7.2. Original Contributions to the Thesis

To the author's knowledge, the analysis of the control algorithms and the algorithmic development of the novel BFUSMC and BFCSMC presented in Chapter 3, as well as the novel control allocation scheme presented in Chapter 5, are original. More specifically, the following highlights the original contributions made within this thesis.

1. Two novel controllers, the BFUSMC and the BFCSMC, are proposed, developed and implemented in Chapter 3. The goal of these proposed systems is to address the limitations identified in previously implemented control algorithms by shifting the design of the sliding surface of the SMC from the navigation frame to the body frame. The reasoning for this is because the mathematical model of a body moving through a fluid, represented in the body frame, is only dependent on velocity, whereas this same mathematical model of a body moving through a fluid, represented in the navigation frame, is dependent on both position/attitude and velocity.
2. Chapter 5 contains the novel 2-stage control allocation scheme for overactuated AUVs. This scheme aims to reduce the power consumption of an AUV, while still maintaining full manoeuvrability. The scheme achieves this aim by heavily biasing the allocation of control forces to low power actuators, such as control fins, as opposed to high power actuators, such as thrusters. Moreover, the ability to disable any allocation to high power actuators based on the desired behaviour of the vehicle is achievable. This is particularly useful when, for example, the vehicle is required to cruise from one location to another as power-efficiently as possible without regard for desired attitude.
3. In the context of AUV manoeuvring, Chapter 4 and Chapter 6 present simulation studies and analysis of the BFUSMC and the BFCSMC, along with other controllers considered. This thesis presents a simulation study, as opposed to an experimental study, because the facilities were not available to conduct physical experimentation, i.e., an underwater vehicle and the

associated infrastructure. However, this simulation study did utilise a high fidelity vehicle model as presented in Chapter 2. Based on an experimentally obtained vehicle parameters, such as that presented by Prestero [54], a reliable simulation environment was constructed and used for the purposes of generating results as would be expected from a physical vehicle.

The outcomes of these original contributions provide a basis for further research concerning the development and implementation of algorithms for the autonomous operation of an AUV, with the particular focus on control algorithms.

1.7.3. Publications

The following lists the papers published by the author in the development of this thesis.

1. M. Kokegei, F. He, and K. Sammut, *Fully Coupled 6 Degrees-of-Freedom Control of Autonomous Underwater Vehicles*. Presented at *MTS/IEEE Oceans*. 2008. Quebec City, QC, Canada.

2. M. Kokegei, F. He, and K. Sammut, *Nonlinear Fully-Coupled Control of AUVs*. Presented at *Society of Underwater Technology Annual Conference*. 2009. Perth, Australia.

3. M. Kokegei, F. He, and K. Sammut, *Fully Coupled 6 Degree-of-Freedom Control of an Over-Actuated Autonomous Underwater Vehicle*, in *Autonomous Underwater Vehicles*, N.A. Cruz, Editor 2011, InTech: Rijeka, Croatia. p. 147-170.

Chapter 2

Modelling of Underwater Vehicles

2.1. Introduction

This chapter presents an overview of plant modelling as applied to underwater vehicles. It begins by covering the various matrices that form the full six DoF equations of motion for an underwater vehicle including both the kinematic equation and the kinetic equation that form the complete AUV plant model. As the full six DoF model is highly complex and nonlinear, this chapter presents a discussion of commonly employed simplifications and the resultant simplified models. These simplified models are required for the design and implementation of compensators presented in Chapter 3. The chapter is organised as follows:

- The mathematical equations that govern the motion of an underwater vehicle are presented in Section 2.2. Both the kinematic equation and the kinetic equation are examined in order to obtain a full understanding of the dynamics of an underwater vehicle.
- As the model of an underwater vehicle is highly complex and nonlinear, Section 2.3 presents common simplifications that are employed for the underwater vehicle equations of motion. These simplifications aid in the design and implementation of compensators for these vehicles.

- A comparative study between the plant model outlined in Section 2.2 and the simplified models presented in Section 2.3 is conducted in Section 2.4. From this comparative study, models that are similar in response to the plant are selected for use in the control design presented in Chapter 3.

Fossen [2, 3, 53] has developed a compact and convenient expression for the six DoF nonlinear dynamic equations of motion of an underwater vehicle. This work has been well received [55-57], and as such will form the basis of the plant modelling. As the complexity of this model makes it difficult, if not impossible, for designing compensators, simplified models are obtained using assumptions that are also outlined by Fossen. However, as this thesis is aimed at controlling highly manoeuvrable AUVs, further assumptions are made regarding the effect due to buoyancy and gravity such that the level of manoeuvrability of the vehicle is increased.

2.2. Mathematical Modelling of AUVs

The differential equations that govern the motion of an AUV are highly nonlinear and complex. An analysis of the physical properties of an AUV can reveal the parameters within these equations, yet the complexities will remain. This section will present the development of the equations of motion of an underwater vehicle, and will conclude with the derivation of the plant model that will be used throughout the simulation studies of Chapter 4 and Chapter 6.

To assist in reducing the complexities of the equations of motion of AUVs, certain frames of reference are utilised depending on the properties that each frame of reference possesses. The most common frames of reference used for underwater vehicle control are presented in Section 2.2.1, along with the equation that governs the relationship between these frames.

The kinetic equation, presented in Section 2.2.2, covers both rigid body and hydrodynamic forces in order to realise the model of an underwater vehicle. This section will present the complete underwater vehicle model, along with the various properties that exist for this model. As this is a simulation study of underwater

vehicle motion control, a high fidelity model is required for accurate simulation purposes, hence the need to cover both rigid body dynamics and hydrodynamics in detail.

Based on the kinetic equation developed in Section 2.2.2, the model considered as the plant model within this thesis will be derived in Section 2.2.3. This model is based on a commercially available AUV which has previously been the subject of study to obtain the parameters of the model.

2.2.1. Kinematics

When discussing motion control of AUVs, it is common to utilise several frames of reference. Each frame has its own set of unique properties which makes each useful for representing certain information.

The following section introduces the typical frames of reference used for underwater vehicle control, and therefore will be used within this thesis. These frames are the north-east-down (NED) frame, which is one particular navigation frame, and the body-fixed frame, commonly referred to as the body frame. Directly following these frames of reference will be an introduction and examination of the kinematic equation, focusing on its use for transforming information from the NED frame to the body frame, and vice versa.

1. Frames of Reference

Within the context of control systems for underwater vehicles, the two main reference frames used are the navigation frame and the body frame. Both contain three translational components and three angular components, yet the origin of each frame differs. This difference in origin can lead to useful properties, which contain certain advantages when designing a control system.

(a) Navigation Frame

The navigation frame, as indicated by its name, is a frame in which it is convenient to express navigation information in. Autonomous vehicles have used several different frames for conducting navigation in. Some such frames are the Earth-centred inertial (ECI) frame, the Earth-centred Earth-fixed (ECEF) frame, and the

previously mentioned NED frame. The most common of these navigation frames used within the context of AUV control is the NED frame, and hence will be the frame referred to when mentioning the navigation frame. Figure 2.1 provides a visual comparison of these three different frames.

The NED frame is typically oriented at a tangent to the Earth's surface where the *x*-axis points north, the *y*-axis points east, and the *z*-axis points down. Furthermore, under the assumption that the vehicle is restricted to a small operational space around the origin of this frame, the navigation system can ignore the curvature of the Earth, as the NED frame is generally considered to be a 'flat earth' frame.

(b) Body-Fixed Frame

The body-fixed frame, or body frame, is a reference frame that moves as the vehicle moves. Figure 2.1 illustrates the difference between this frame and the previously mentioned navigation frames.

Various properties exist at different locations within the body of a vehicle. Hence, the choice for the location of the origin of the body frame can take advantage of these properties. One common selection is to place the origin of the body frame at the centre of gravity [2, 3]. As a general rule, the *x*-axis of the body frame points from aft to fore along the longitudinal axis of the vehicle, the *y*-axis points from port to starboard, and the *z*-axis points from top to bottom. It is appropriate to express the velocities of the vehicle in this frame using this orientation.

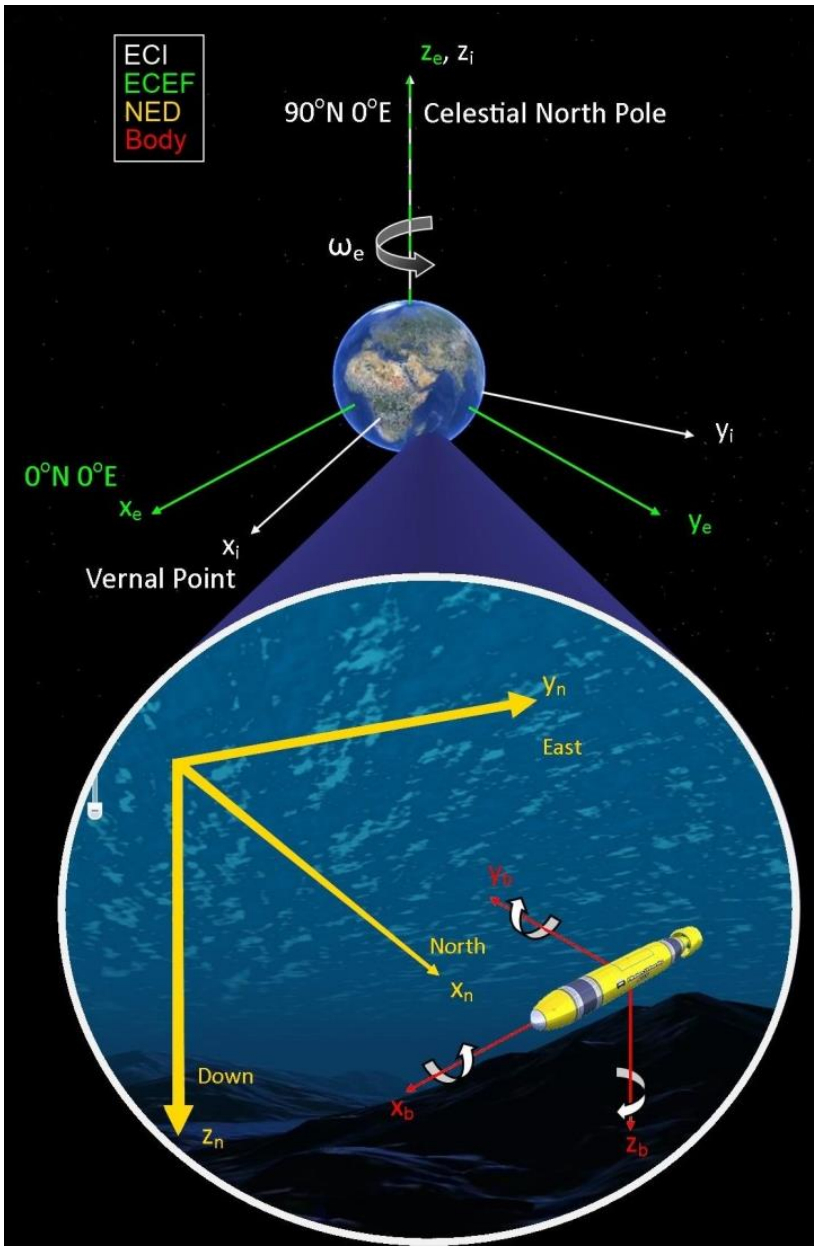

Figure 2.1: Frames of Reference [58]

2. Kinematic Equation

The kinematic equation provides a means of transforming information from the body frame to the navigation frame. It is expressed as:

$$\dot{\boldsymbol{\eta}}_{\mathbf{n}}(t) = \mathbf{J}\left(\boldsymbol{\eta}_{\mathbf{n}}(t)\right)\mathbf{v}_{\mathbf{b}}(t) \tag{2.1}$$

where $\boldsymbol{\eta}_{\mathbf{n}}(t)$ is the six DoF position and orientation vector decomposed in the navigation frame, $\mathbf{v}_{\mathbf{b}}(t)$ is the six DoF translational and angular velocities vector decomposed in the body frame, and $\mathbf{J}\left(\boldsymbol{\eta}_{\mathbf{n}}(t)\right)$ is the transformation matrix used to transform information from the body frame to the navigation frame. This equation is illustrated in Figure 2.2.

The six DoF position and orientation vector, decomposed in navigation frame, is expressed as:

$$\boldsymbol{\eta}_{\mathbf{n}}(t) = \begin{bmatrix} \mathbf{p}_{\mathbf{n}}(t) \\ \boldsymbol{\Theta}_{\mathbf{n}}(t) \end{bmatrix} \tag{2.2}$$

Here, the three position components within $\boldsymbol{\eta}_{\mathbf{n}}(t)$ are given by $\mathbf{p}_{\mathbf{n}}(t)$ and the three orientation or attitude components, also known as Euler angles, are given by $\boldsymbol{\Theta}_{\mathbf{n}}(t)$.

The three position components of $\mathbf{p}_{\mathbf{n}}(t)$ are expressed as:

$$\mathbf{p}_{\mathbf{n}}(t) = \begin{bmatrix} x_n(t) \\ y_n(t) \\ z_n(t) \end{bmatrix} \tag{2.3}$$

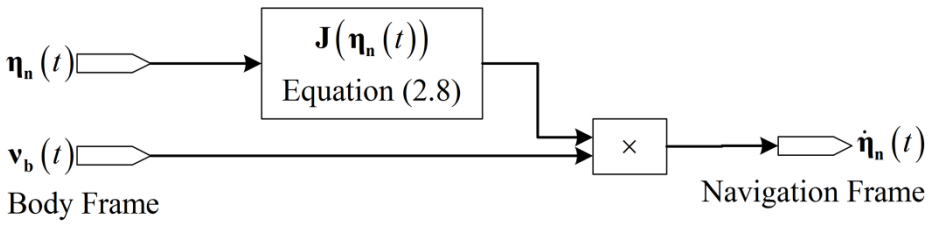

Figure 2.2: The Kinematic Equation

where $x_n(t)$ is the north position, $y_n(t)$ is the east position, and $z_n(t)$ is the down position, or the depth of the vehicle. All three elements of $\mathbf{p_n}(t)$ are with respect to the origin of the NED frame.

The three attitude components of $\mathbf{\Theta_n}(t)$ are expressed as:

$$\mathbf{\Theta_n}(t) = \begin{bmatrix} \phi_n(t) \\ \theta_n(t) \\ \psi_n(t) \end{bmatrix} \tag{2.4}$$

where $\phi_n(t)$ is the roll attitude angle of the vehicle, which is the angular rotation around the *x*-axis, $\theta_n(t)$ is the pitch attitude angle of the vehicle, which is the angular rotation around the *y*-axis, and $\psi_n(t)$ is the yaw attitude angle of the vehicle, which is the angular rotation around the *z*-axis.

The six DoF translational and angular velocity vector of the body frame with respect to the navigation frame, decomposed in the body frame, is expressed as:

$$\mathbf{v_b}(t) = \begin{bmatrix} \mathbf{V_b}(t) \\ \mathbf{\omega_b}(t) \end{bmatrix} \tag{2.5}$$

Here, the three translational velocity components within $\mathbf{v_b}(t)$ are given by $\mathbf{V_b}(t)$ and the three angular velocity components are given by $\mathbf{\omega_b}(t)$.

The three translational velocity components of $\mathbf{V_b}(t)$ are expressed as:

$$\mathbf{V_b}(t) = \begin{bmatrix} u_b(t) \\ v_b(t) \\ w_b(t) \end{bmatrix} \tag{2.6}$$

where $u_b(t)$ is the surge translational velocity of the vehicle, $v_b(t)$ is the sway translational velocity of the vehicle, and $w_b(t)$ is the heave translational velocity of the vehicle.

The three angular velocity components of $\mathbf{\omega_b}(t)$ are expressed as:

$$\boldsymbol{\omega}_{\mathbf{b}}(t)=\begin{bmatrix} p_b(t) \\ q_b(t) \\ r_b(t) \end{bmatrix} \tag{2.7}$$

where $p_b(t)$ is the roll angular velocity of the vehicle, $q_b(t)$ is the pitch angular velocity of the vehicle, and $r_b(t)$ is the yaw angular velocity of the vehicle.

(a) Transformation Matrix

The transformation matrix, used to transform information from the body frame into the navigation frame, is expressed as:

$$\mathbf{J}\left(\boldsymbol{\eta}_{\mathbf{n}}(t)\right)=\begin{bmatrix} \mathbf{R}_{\mathbf{b}}^{\mathbf{n}}\left(\boldsymbol{\Theta}_{\mathbf{n}}(t)\right) & \mathbf{0}_{3\times3} \\ \mathbf{0}_{3\times3} & \mathbf{T}_{\boldsymbol{\Theta}}\left(\boldsymbol{\Theta}_{\mathbf{n}}(t)\right) \end{bmatrix} \tag{2.8}$$

Here, $\mathbf{R}_{\mathbf{b}}^{\mathbf{n}}\left(\boldsymbol{\Theta}_{\mathbf{n}}(t)\right)$ is the translational velocity transformation matrix, and is used for transforming translational velocity components, while $\mathbf{T}_{\boldsymbol{\Theta}}\left(\boldsymbol{\Theta}_{\mathbf{n}}(t)\right)$ is the angular velocity transformation matrix, and is used for transforming angular velocity components.

i. *Translational Velocity Transformation*

The translational velocity transformation matrix, $\mathbf{R}_{\mathbf{b}}^{\mathbf{n}}\left(\boldsymbol{\Theta}_{\mathbf{n}}(t)\right)$, transforms the translational velocities defined in the body frame into the translational velocities defined in the navigation frame. This transformation is based on the angular differences between the two frames represented using the Euler angle notation of Equation (2.4). The matrix used to achieve this transformation is expressed as:

$$\mathbf{R}_{\mathbf{b}}^{\mathbf{n}}\left(\boldsymbol{\Theta}_{\mathbf{n}}(t)\right)=\begin{bmatrix} \cos\psi_n(t)\cos\theta_n(t) & \begin{matrix}-\sin\psi_n(t)\cos\phi_n(t)+\\ \cos\psi_n(t)\sin\theta_n(t)\sin\phi_n(t)\end{matrix} & \begin{matrix}\sin\psi_n(t)\sin\phi_n(t)+\\ \cos\psi_n(t)\cos\phi_n(t)\sin\theta_n(t)\end{matrix} \\ \sin\psi_n(t)\cos\theta_n(t) & \begin{matrix}\cos\psi_n(t)\cos\phi_n(t)+\\ \sin\phi_n(t)\sin\theta_n(t)\sin\psi_n(t)\end{matrix} & \begin{matrix}-\cos\psi_n(t)\sin\phi_n(t)+\\ \sin\theta_n(t)\sin\psi_n(t)\cos\phi_n(t)\end{matrix} \\ -\sin\theta_n(t) & \cos\theta_n(t)\sin\phi_n(t) & \cos\theta_n(t)\cos\phi_n(t) \end{bmatrix} \tag{2.9}$$

ii. *Angular Velocity Transformation*

The angular velocity transformation matrix, $\mathbf{T}_{\Theta}\left(\mathbf{\Theta}_{\mathbf{n}}(t)\right)$, transforms the angular velocities defined in the body frame into the angular velocities defined in the navigation frame. This transformation is also based on the angular differences between the two frames represented using the Euler angle notation of Equation (2.4). The matrix used to achieve this transformation is expressed as:

$$\mathbf{T}_{\Theta}\left(\mathbf{\Theta}_{\mathbf{n}}(t)\right)=\begin{bmatrix}1 & \sin\phi_n(t)\tan\theta_n(t) & \cos\phi_n(t)\tan\theta_n(t)\\ 0 & \cos\phi_n(t) & -\sin\phi_n(t)\\ 0 & \sin\phi_n(t)/\cos\theta_n(t) & \cos\phi_n(t)/\cos\theta_n(t)\end{bmatrix} \tag{2.10}$$

The above-described transformation matrices are used in Equation (2.1) to transform the six DoF body frame velocities into the navigation frame. Furthermore, as $\mathbf{J}\left(\mathbf{\eta}_{\mathbf{n}}(t)\right)$ is invertible with

$$\left|\mathbf{J}\left(\mathbf{\eta}_{\mathbf{n}}(t)\right)\right|=\frac{1}{\cos\theta_n(t)},\ -\tfrac{\pi}{2}<\theta_n(t)<\tfrac{\pi}{2}$$

the six DoF navigation frame velocities can be transformed into the body frame using:

$$\mathbf{v}_{\mathbf{b}}(t)=\mathbf{J}^{-1}\left(\mathbf{\eta}_{\mathbf{n}}(t)\right)\dot{\mathbf{\eta}}_{\mathbf{n}}(t) \tag{2.11}$$

Equation (2.11) is illustrated in Figure 2.3.

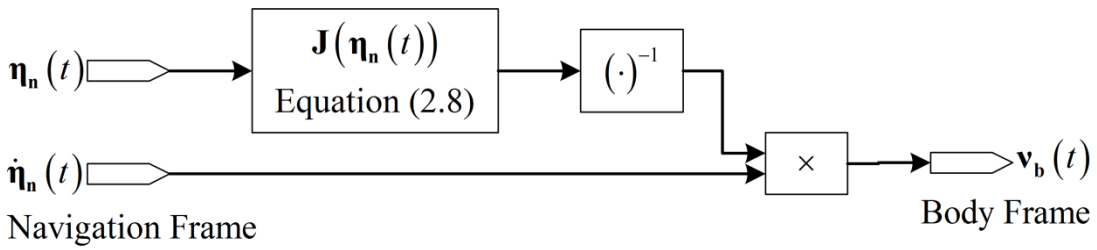

Figure 2.3: The Inverse of the Kinematic Equation

2.2.2. Kinetics

Kinetics is the branch of classical mechanics that studies the causes and effects of motion. The application of various forces and torques, which in turn cause objects to accelerate, is what produces this motion. The physical shape and configuration of a vehicle determines the resultant motion due to an external force or moment. Hence, the parameters within the kinetic equation will be unique to each particular vehicle. A thorough knowledge of the kinetic equation and the role the various parameters play within the kinetic equation is required for the following reasons.

- To establish a model that accurately represents the vehicle to be controlled;
- To develop a simulation model to mimic the behaviour of a physical underwater vehicle;
- To understand the impact of removal of particular terms when simplifying the model for control design purposes.

For these reasons, this section will present the mathematical framework used for describing the motion of an underwater vehicle with the focus being on a torpedo shaped AUV. This framework is presented in the form of a matrix representation of the nonlinear dynamic equations that govern the motion of an underwater vehicle. This equation is then analysed in detail such that a full understanding of the effect each component has on the overall motion of the vehicle. Following this are the complete equations representing the motion of an underwater vehicle decomposed in both the body frame and the navigation frame. Finally, the process for converting a model decomposed in the body frame to the navigation frame, and vice versa, is presented.

1. Matrix Representation

The six DoF nonlinear dynamic equations of motion in matrix form can be expressed as:

$$\begin{aligned}\mathbf{M}_{\mathbf{RB}}\dot{\boldsymbol{\nu}}_{\mathbf{b}}(t)+\mathbf{M}_{\mathbf{A}}\dot{\boldsymbol{\nu}}_{\mathbf{r}}(t)+\mathbf{C}_{\mathbf{RB}}\left(\boldsymbol{\nu}_{\mathbf{b}}(t)\right)\boldsymbol{\nu}_{\mathbf{b}}(t)+\mathbf{C}_{\mathbf{A}}\left(\boldsymbol{\nu}_{\mathbf{r}}(t)\right)\boldsymbol{\nu}_{\mathbf{r}}(t)\\ +\mathbf{D}\left(\boldsymbol{\nu}_{\mathbf{r}}(t)\right)\boldsymbol{\nu}_{\mathbf{r}}(t)+\mathbf{L}\left(\boldsymbol{\nu}_{\mathbf{r}}(t)\right)\boldsymbol{\nu}_{\mathbf{r}}(t)+\mathbf{g}\left(\boldsymbol{\eta}_{\mathbf{n}}(t)\right)=\boldsymbol{\tau}(t)\end{aligned} \tag{2.12}$$

This equation is illustrated in Figure 2.4 where $(\cdot)^{-1}$ indicates matrix inversion. The input to this model is $\boldsymbol{\tau}(t)$, the six DoF forces and moments vector, and $\mathbf{v}_{\mathbf{c}}(t)$, the six DoF water current velocity vector. Both of these vectors are decomposed in the body frame. The outputs are $\mathbf{v}_{\mathbf{b}}(t)$, the six DoF vehicle velocity vector decomposed in the body frame, and $\boldsymbol{\eta}_{\mathbf{n}}(t)$, the vehicle six DoF position and orientation vector decomposed in the navigation frame. The following sections will discuss the details of these and the other various terms contained within Equation (2.12).

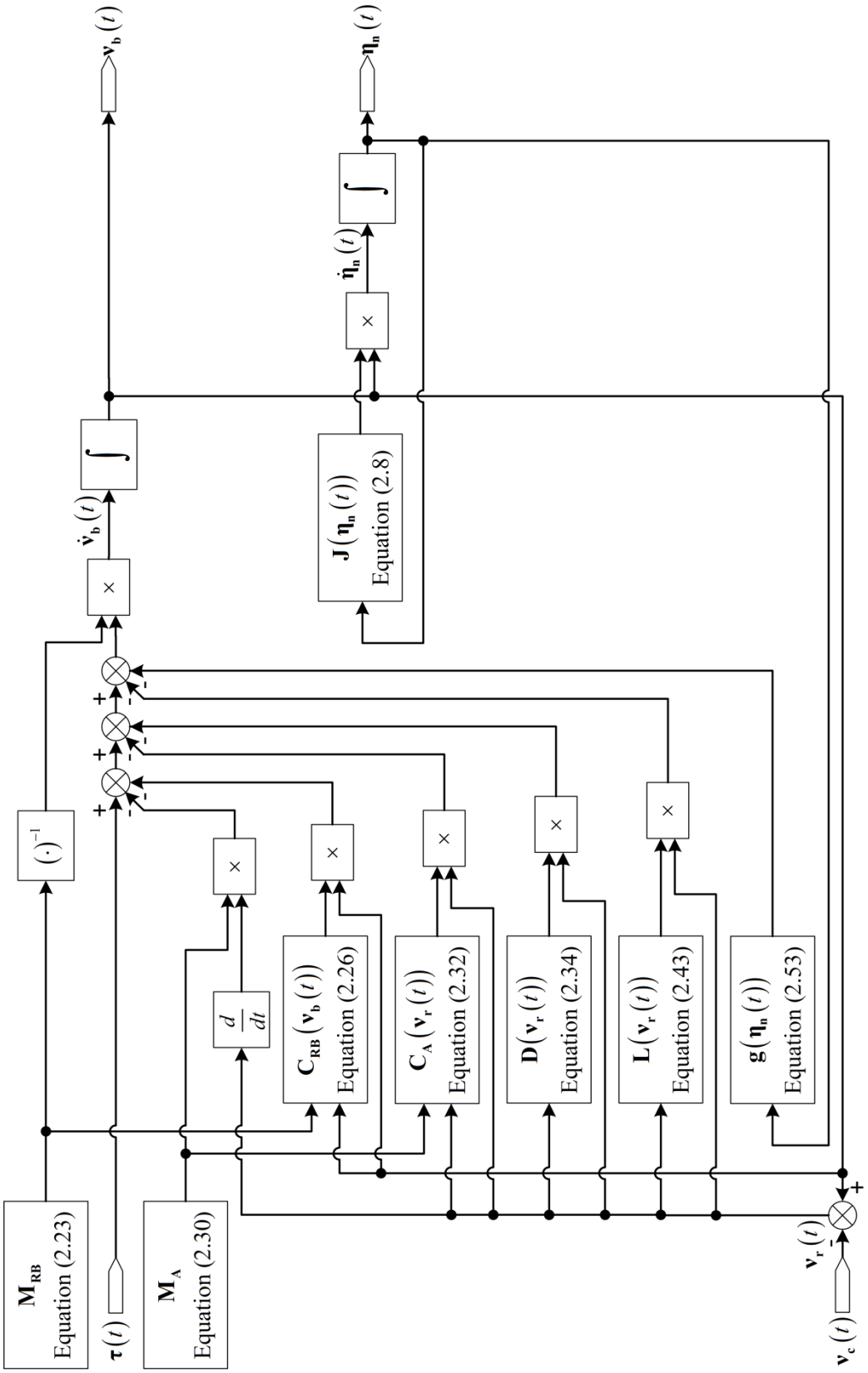

Figure 2.4: AUV Plant Model

The forces and moments vector, $\boldsymbol{\tau}(t)$, is broken down into its three translational and three rotational components using:

$$\boldsymbol{\tau}(t) = \begin{bmatrix} X(t) \\ Y(t) \\ Z(t) \\ K(t) \\ M(t) \\ N(t) \end{bmatrix} \tag{2.13}$$

where $X(t)$ represents the translational force in the surge DoF, $Y(t)$ represents the translational force in the sway DoF, $Z(t)$ represents the translational force in the heave DoF, $K(t)$ represents the rotational moment in the roll DoF, $M(t)$ represents the rotational moment in the pitch DoF, and $N(t)$ represents the rotational moment in the yaw DoF.

Within Equation (2.12), $\mathbf{v_r}(t)$ is the relative velocity of the vehicle with respect to the surrounding water, $\mathbf{v_c}(t)$. $\mathbf{v_r}(t)$ is calculated using:

$$\mathbf{v_r}(t) = \mathbf{v_b}(t) - \mathbf{v_c}(t) \tag{2.14}$$

where

$$\mathbf{v_c}(t) = \begin{bmatrix} u_c(t) \\ v_c(t) \\ w_c(t) \\ p_c(t) \\ q_c(t) \\ r_c(t) \end{bmatrix}$$

The component form of Equation (2.14) can be written as:

$$\mathbf{v}_\mathbf{r}(t)=\begin{bmatrix}\mathbf{V}_\mathbf{r}(t)\\ \boldsymbol{\omega}_\mathbf{r}(t)\end{bmatrix}=\begin{bmatrix}u_r(t)\\ v_r(t)\\ w_r(t)\\ p_r(t)\\ q_r(t)\\ r_r(t)\end{bmatrix}=\begin{bmatrix}u_b(t)-u_c(t)\\ v_b(t)-v_c(t)\\ w_b(t)-w_c(t)\\ p_b(t)-p_c(t)\\ q_b(t)-q_c(t)\\ r_b(t)-r_c(t)\end{bmatrix} \tag{2.15}$$

The analysis of Equation (2.12) is conducted as follows"

1. The cross product operator, which is used extensively in the modelling of underwater vehicles, is introduced. This operation is implemented through the multiplication of the first vector with a skew-symmetric matrix formed from the second vector.
2. Rigid body dynamics, the study of motion of a rigid body due to an external force, is examined. This includes both the rigid body system inertia and the rigid body Coriolis and centripetal forces.
3. The study of the effect on the vehicle due to the surrounding water, hydrodynamics, is then examined. These effects include added mass and its effect on the Coriolis and centripetal forces, hydrodynamic damping or drag forces, lift forces, and gravitational and buoyancy forces.

(a) Cross Product Operator

Throughout the derivation of the plant model, the cross product operator is used. A simple form of implementing the cross product between two vectors is to produce a skew-symmetric matrix from one vector, and multiply this matrix with the other vector.

If the skew-symmetric matrix is defined as:

$$S(\boldsymbol{\beta}):=\begin{bmatrix}0 & -\beta_3 & \beta_2\\ \beta_3 & 0 & -\beta_1\\ -\beta_2 & \beta_1 & 0\end{bmatrix} \tag{2.16}$$

where

$$\boldsymbol{\beta} = \begin{bmatrix} \beta_1 \\ \beta_2 \\ \beta_3 \end{bmatrix},$$

the cross product can be implemented by a simple matrix multiplication as follows:

$$\boldsymbol{\beta} \times \mathbf{x} = S(\boldsymbol{\beta})\mathbf{x} \tag{2.17}$$

(b) Body Frame Rigid Body Dynamics

Rigid body dynamics studies the motion of objects under the influence of external forces. Intrinsic properties of the object determine this motion; with the assumption made here that no bodies experience deformation within the system under study. With respect to underwater vehicles, this means that the vehicle itself is inflexible and there are no effects due to the water surrounding the vehicle. The rigid body dynamic equations for an underwater vehicle can be expressed in the following vectorial form [2].

$$\mathbf{M}_{\mathbf{RB}}\dot{\mathbf{v}}_{\mathbf{b}}(t) + \mathbf{C}_{\mathbf{RB}}\left(\mathbf{v}_{\mathbf{b}}(t)\right)\mathbf{v}_{\mathbf{b}}(t) = \boldsymbol{\tau}_{\mathbf{RB}}(t) \tag{2.18}$$

Here, $\boldsymbol{\tau}_{\mathbf{RB}}(t)$ is the 6×1 rigid body forces and moments vector, $\mathbf{M}_{\mathbf{RB}}$ is the 6×6 rigid body system inertia matrix, and $\mathbf{C}_{\mathbf{RB}}\left(\mathbf{v}_{\mathbf{b}}(t)\right)$ is the 6×6 rigid body Coriolis and centripetal forces matrix. Figure 2.5 highlights the terms responsible for rigid body dynamics within the overall AUV plant model of Figure 2.4, and each of these terms will be discussed in the following sections.

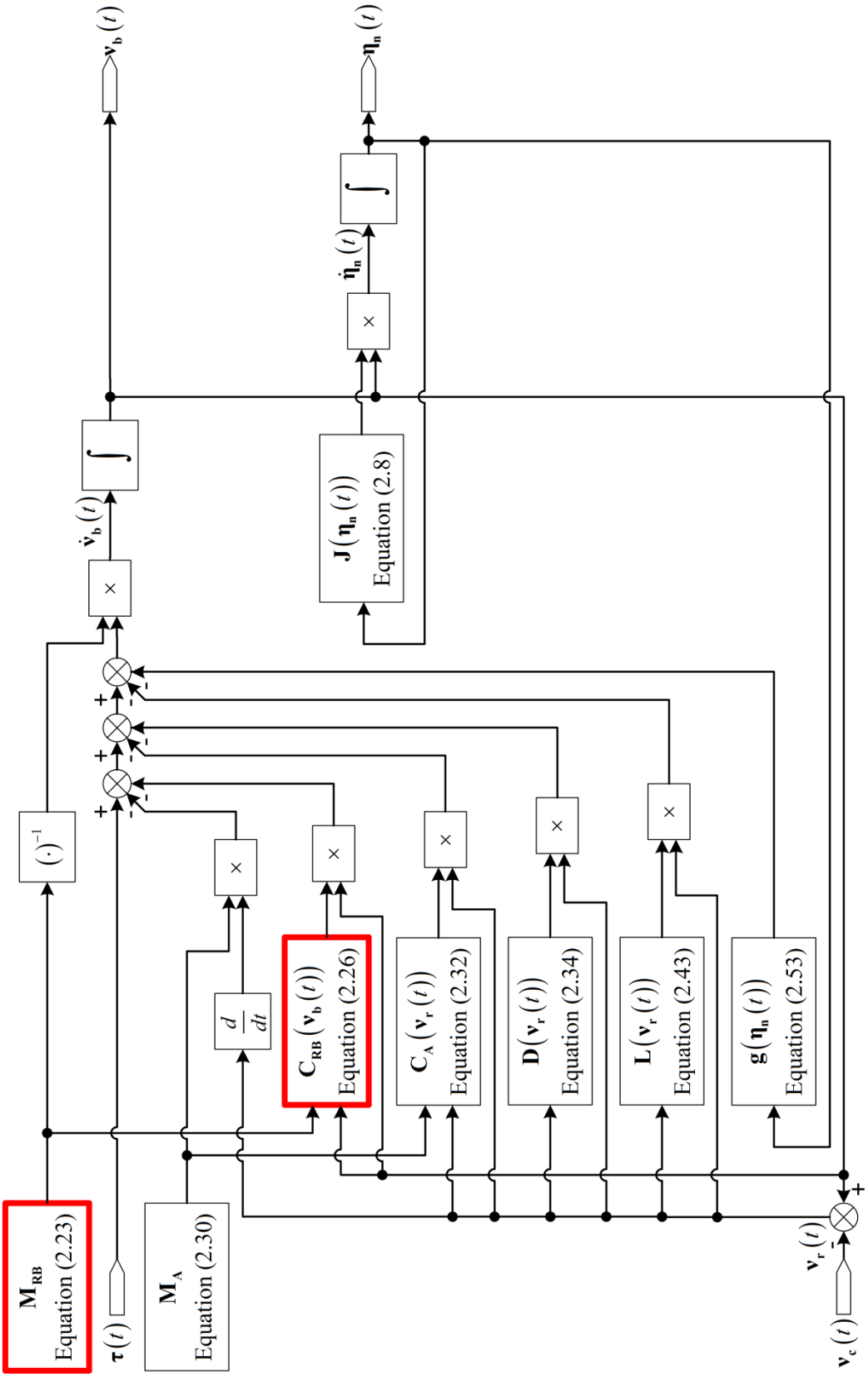

Figure 2.5: AUV Plant Model Highlighting Rigid Body Dynamics

i. *Rigid Body Forces and Moments*

A 6×1 column vector can conveniently represent the forces and moments that produce this rigid body motion. This vector is denoted by $\boldsymbol{\tau}_{\mathbf{RB}}(t)$ and is expressed as:

$$\boldsymbol{\tau}_{\mathbf{RB}}(t)=\begin{bmatrix} X_{RB}(t) \\ Y_{RB}(t) \\ Z_{RB}(t) \\ K_{RB}(t) \\ M_{RB}(t) \\ N_{RB}(t) \end{bmatrix} \tag{2.19}$$

Here, the three translational forces are represented by $X_{RB}(t)$ in the surge DoF, $Y_{RB}(t)$ in the sway DoF, and $Z_{RB}(t)$ in the heave DoF. The three rotational moments are represented by $K_{RB}(t)$ in the roll DoF, $M_{RB}(t)$ in the pitch DoF, and $N_{RB}(t)$ in the yaw DoF.

ii. *Rigid Body System Inertia*

The inertia of an object defines its resistance to a change in its motion, be it translational or rotational. This is a fundamental property that all objects possess, and therefore will be examined here.

Under the assumption of a uniform gravitational field, which ensures that the centre of gravity of an object is coincident with the centre of mass of an object, the mass, *m*, and the 3×3 symmetric inertia tensor $\mathbf{I}_{\mathbf{o}}$, defined as:

$$\mathbf{I}_{\mathbf{o}}=\begin{bmatrix} I_x & -I_{xy} & -I_{xz} \\ -I_{xy} & I_y & -I_{yz} \\ -I_{xz} & -I_{yz} & I_z \end{bmatrix} \tag{2.20}$$

form the 6×6 rigid body system inertia matrix expressed as:

$$\mathbf{M}_{\mathbf{RB}}=\begin{bmatrix} m\mathbf{I}_{3\times3} & -mS\left(\mathbf{r}_{\mathbf{g}}^{\mathbf{b}}\right) \\ -mS\left(\mathbf{r}_{\mathbf{g}}^{\mathbf{b}}\right) & \mathbf{I}_{\mathbf{o}} \end{bmatrix}=\begin{bmatrix} \mathbf{M}_{11} & \mathbf{M}_{12} \\ \mathbf{M}_{21} & \mathbf{M}_{22} \end{bmatrix} \tag{2.21}$$

Within Equation (2.20), I_x, I_y, and I_z are the moments of inertia about the *x*-axis, *y*-axis and *z*-axis respectively, I_{xy}, I_{xz}, and I_{yz} are the products of inertia, and

$$\mathbf{r_g^b} = \begin{bmatrix} x_g^b \\ y_g^b \\ z_g^b \end{bmatrix} \tag{2.22}$$

defines the offset between the centre of gravity and the origin of the body frame. Expanding Equation (2.21) yields:

$$\mathbf{M_{RB}} = \begin{bmatrix} m & 0 & 0 & 0 & mz_g^b & -my_g^b \\ 0 & m & 0 & -mz_g^b & 0 & mx_g^b \\ 0 & 0 & m & my_g^b & -mx_g^b & 0 \\ 0 & -mz_g^b & my_g^b & I_x & -I_{xy} & -I_{xz} \\ mz_g^b & 0 & -mx_g^b & -I_{xy} & I_y & -I_{yz} \\ -my_g^b & mx_g^b & 0 & -I_{xz} & -I_{yz} & I_z \end{bmatrix} \tag{2.23}$$

The rigid body system inertia matrix is symmetric, unique and satisfies the following equation [2]:

$$\mathbf{M_{RB}} = \mathbf{M_{RB}^T} > \mathbf{0} \tag{2.24}$$

Figure 2.6 highlights the term responsible for the rigid body system inertia within the overall AUV plant model of Figure 2.4.

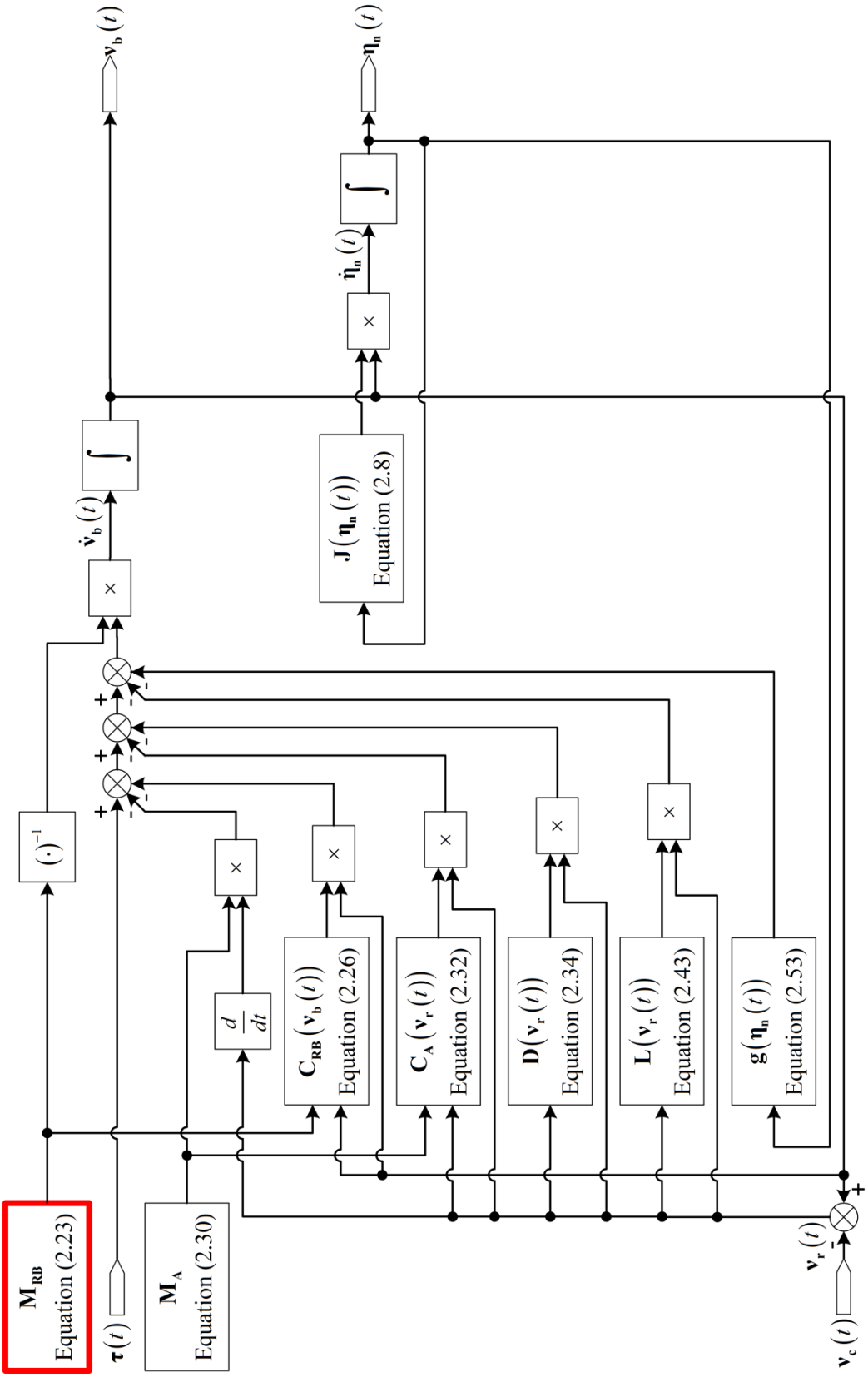

Figure 2.6: AUV Plant Model Highlighting Rigid Body System Inertia

iii. *Rigid Body Coriolis and Centripetal Forces*

Coriolis and centripetal forces are perceived forces due to an object moving within a rotating reference frame. In this case, these forces are due to the vehicle moving within the Earth's reference frame. As these forces are proportional to the mass of the vehicle, they are therefore intrinsically part of the mathematical model of an underwater vehicle. Furthermore, under certain assumptions that will be outlined in Section 2.3, these forces can be ignored due to the structure of the Coriolis and centripetal forces matrix. Therefore, there is a need to examine the structure of this matrix here.

A large number of parameterised representations for the rigid body Coriolis and centripetal forces can be generated using the rigid body system inertia matrix, $\mathbf{M}_{\mathbf{RB}}$ of Equation (2.21), and the previously defined body fixed velocity vector, $\boldsymbol{\nu}_{\mathbf{b}}(t)$ of Equation (2.5). One of these representations is seen in the following equation [3, 59].

$$\mathbf{C}_{\mathbf{RB}}\left(\boldsymbol{\nu}_{\mathbf{b}}(t)\right)=\begin{bmatrix}\mathbf{0}_{3\times 3} & -S\left(\mathbf{M}_{11}\mathbf{V}_{\mathbf{b}}(t)+\mathbf{M}_{12}\boldsymbol{\omega}_{\mathbf{b}}(t)\right)\\ -S\left(\mathbf{M}_{11}\mathbf{V}_{\mathbf{b}}(t)+\mathbf{M}_{12}\boldsymbol{\omega}_{\mathbf{b}}(t)\right) & -S\left(\mathbf{M}_{21}\mathbf{V}_{\mathbf{b}}(t)+\mathbf{M}_{22}\boldsymbol{\omega}_{\mathbf{b}}(t)\right)\end{bmatrix} \quad (2.25)$$

Here $\mathbf{M}_{11}$, $\mathbf{M}_{12}$, $\mathbf{M}_{21}$, and $\mathbf{M}_{22}$ are defined in Equation (2.21). Other representations can be found in Fossen [2, 3].

Expanding Equation (2.25) yields the following structure for $\mathbf{C}_{\mathbf{RB}}\left(\boldsymbol{\nu}(t)\right)$.

$$\mathbf{C}_{\mathbf{RB}}\left(\boldsymbol{\nu}_{\mathbf{b}}(t)\right)=\begin{bmatrix}0 & 0 & 0 & 0 & a_3 & -a_2\\ 0 & 0 & 0 & -a_3 & 0 & a_1\\ 0 & 0 & 0 & a_2 & -a_1 & 0\\ 0 & a_3 & -a_2 & 0 & a_6 & -a_5\\ -a_3 & 0 & a_1 & -a_6 & 0 & a_4\\ a_2 & -a_1 & 0 & a_5 & -a_4 & 0\end{bmatrix} \quad (2.26)$$

where

$$
\begin{aligned}
a_1 &= m\left(u_b(t) + z_g^b q_b(t) - y_g^b r_b(t)\right) \\
a_2 &= m\left(v_b(t) - z_g^b p_b(t) + x_g^b r_b(t)\right) \\
a_3 &= m\left(w_b(t) + y_g^b p_b(t) - x_g^b q_b(t)\right) \\
a_4 &= m\left(-z_g^b v_b(t) + y_g^b w_b(t)\right) + I_x p_b(t) - I_{xy} q_b(t) - I_{xz} r_b(t) \\
a_5 &= m\left(z_g^b u_b(t) - x_g^b w_b(t)\right) - I_{xy} p_b(t) + I_y q_b(t) - I_{yz} r_b(t) \\
a_6 &= m\left(-y_g^b u_b(t) + x_g^b v_b(t)\right) - I_{xz} p_b(t) - I_{yz} q_b(t) + I_z r_b(t)
\end{aligned}
$$

Irrespective of the choice of representation for $\mathbf{C_{RB}}\left(\mathbf{v_b}(t)\right)$, this matrix can always be parameterised such that it is skew-symmetric according to the following equation.

$$\mathbf{C_{RB}}\left(\mathbf{v_b}(t)\right) = -\mathbf{C_{RB}^T}\left(\mathbf{v_b}(t)\right), \forall \mathbf{v_b}(t) \in \mathbb{R}^6 \tag{2.27}$$

Figure 2.7 highlights the term responsible for the rigid body Coriolis and centripetal forces within the overall AUV plant model of Figure 2.4.

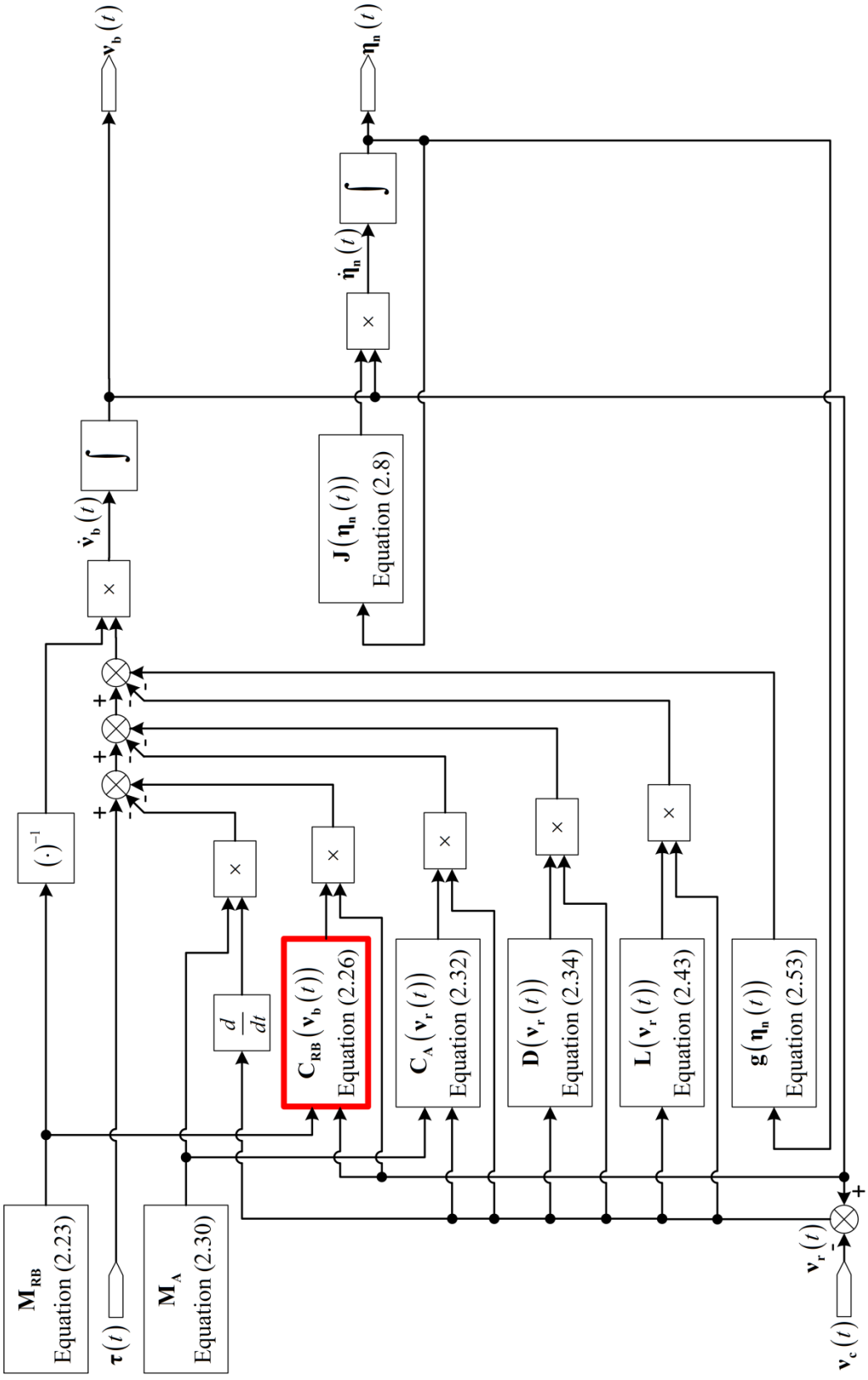

Figure 2.7: AUV Plant Model Highlighting Rigid Body Coriolis and Centripetal Forces

(c) Body Frame Hydrodynamics

The rigid body dynamics of Equation (2.18) ignores any effect due to the water surrounding the vehicle. The study of the effects on the body purely due to the water surrounding the body is called hydrodynamics, and is introduced here.

The generalised hydrodynamic equation for an underwater vehicle is expressed as:

$$\begin{aligned}\mathbf{M}_{\mathbf{A}}\dot{\mathbf{v}}_{\mathbf{r}}(t)+\mathbf{C}_{\mathbf{A}}\left(\mathbf{v}_{\mathbf{r}}(t)\right)\mathbf{v}_{\mathbf{r}}(t)+\mathbf{D}\left(\mathbf{v}_{\mathbf{r}}(t)\right)\mathbf{v}_{\mathbf{r}}(t)\\ +\mathbf{L}\left(\mathbf{v}_{\mathbf{r}}(t)\right)\mathbf{v}_{\mathbf{r}}(t)+\mathbf{g}\left(\boldsymbol{\eta}_{\mathbf{n}}(t)\right)=\boldsymbol{\tau}_{\mathbf{h}}(t)\end{aligned} \tag{2.28}$$

where $\boldsymbol{\tau}_{\mathbf{h}}(t)$ is the 6×1 hydrodynamic forces and moments vector, $\mathbf{M}_{\mathbf{A}}$ is the 6×6 added mass matrix, $\mathbf{C}_{\mathbf{A}}\left(\mathbf{v}_{\mathbf{r}}(t)\right)$ is the 6×6 Coriolis and centripetal forces matrix due to added mass effects, $\mathbf{D}\left(\mathbf{v}_{\mathbf{r}}(t)\right)$ is the 6×6 hydrodynamic damping matrix, $\mathbf{L}\left(\mathbf{v}_{\mathbf{r}}(t)\right)$ is the 6×6 hydrodynamic lift matrix, and $\mathbf{g}\left(\boldsymbol{\eta}_{\mathbf{n}}(t)\right)$ is the 6×1 gravitational and buoyancy forces vector. Figure 2.8 highlights the terms responsible for the hydrodynamics within the overall AUV plant model of Figure 2.4, and each of these terms will be discussed in the following sections.

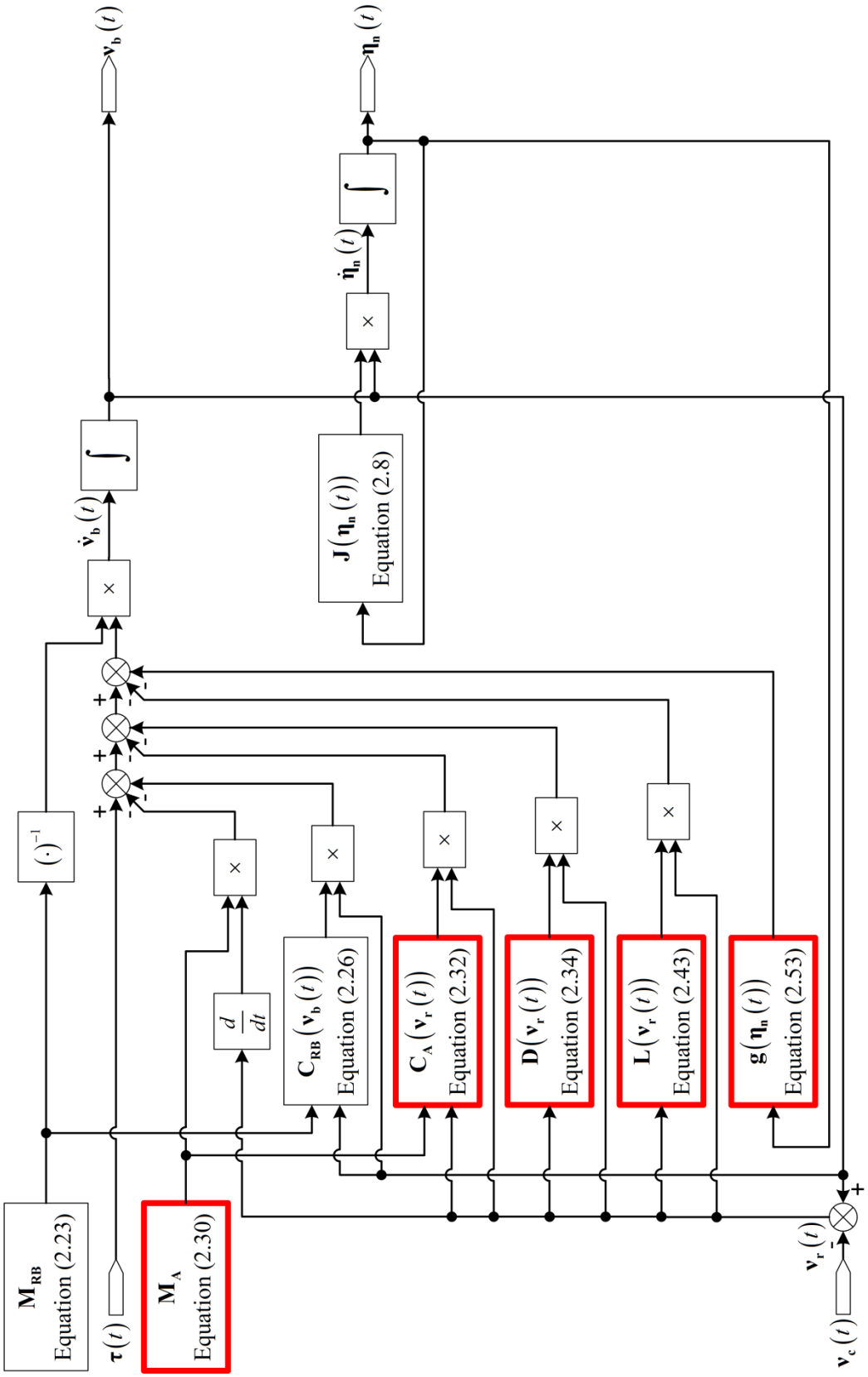

Figure 2.8: AUV Plant Model Highlighting Hydrodynamics

i. *Hydrodynamic Forces and Moments*

A 6×1 column vector can conveniently represent the forces and moments that produce this hydrodynamic motion. This vector is denoted by $\boldsymbol{\tau}_{\mathbf{h}}(t)$ and is expressed as:

$$\boldsymbol{\tau}_{\mathbf{h}}(t)=\begin{bmatrix} X_h(t) \\ Y_h(t) \\ Z_h(t) \\ K_h(t) \\ M_h(t) \\ N_h(t) \end{bmatrix} \tag{2.29}$$

Here, the three translational forces are represented by $X_h(t)$ in the surge DoF, $Y_h(t)$ in the sway DoF, and $Z_h(t)$ in the heave DoF. The three rotational moments are represented by $K_h(t)$ in the roll DoF, $M_h(t)$ in the pitch DoF, and $N_h(t)$ in the yaw DoF.

ii. *Added Mass*

Added mass is a perceived mass added to the vehicle due to it travelling through a fluid. It is a fundamental hydrodynamic force, and hence will be examined here.

As a vehicle travels through a fluid, kinetic energy is imparted on that fluid. This kinetic energy comes from the actuators that are also applying a force to the vehicle. Although it is not the case in reality, this additional kinetic energy can be interpreted as coming from extra mass that the actuators are required to accelerate to make the vehicle move, hence the term added mass.

The added mass matrix, $\mathbf{M}_{\mathbf{A}}$, is a 6×6 matrix of distinct elements and, for the case of a completely submerged underwater vehicle, $\mathbf{M}_{\mathbf{A}}$ is also strictly positive [2]. This added mass matrix is expressed as:

$$\mathbf{M_A} = \begin{bmatrix} X_{\dot{u}} & X_{\dot{v}} & X_{\dot{w}} & X_{\dot{p}} & X_{\dot{q}} & X_{\dot{r}} \\ Y_{\dot{u}} & Y_{\dot{v}} & Y_{\dot{w}} & Y_{\dot{p}} & Y_{\dot{q}} & Y_{\dot{r}} \\ Z_{\dot{u}} & Z_{\dot{v}} & Z_{\dot{w}} & Z_{\dot{p}} & Z_{\dot{q}} & Z_{\dot{r}} \\ K_{\dot{u}} & K_{\dot{v}} & K_{\dot{w}} & K_{\dot{p}} & K_{\dot{q}} & K_{\dot{r}} \\ M_{\dot{u}} & M_{\dot{v}} & M_{\dot{w}} & M_{\dot{p}} & M_{\dot{q}} & M_{\dot{r}} \\ N_{\dot{u}} & N_{\dot{v}} & N_{\dot{w}} & N_{\dot{p}} & N_{\dot{q}} & N_{\dot{r}} \end{bmatrix} \tag{2.30}$$

All the elements contained within $\mathbf{M_A}$ represent partial derivatives in the form of $\frac{\partial \tau_i(t)}{\partial \dot{v}_j(t)}$. For example, $X_{\dot{u}} \triangleq \frac{\partial X(t)}{\partial \dot{u}(t)}$, $Y_{\dot{u}} \triangleq \frac{\partial Y(t)}{\partial \dot{u}(t)}$, and $N_{\dot{p}} \triangleq \frac{\partial N(t)}{\partial \dot{p}(t)}$.

Figure 2.9 highlights the term responsible for the added mass within the overall AUV plant model of Figure 2.4.

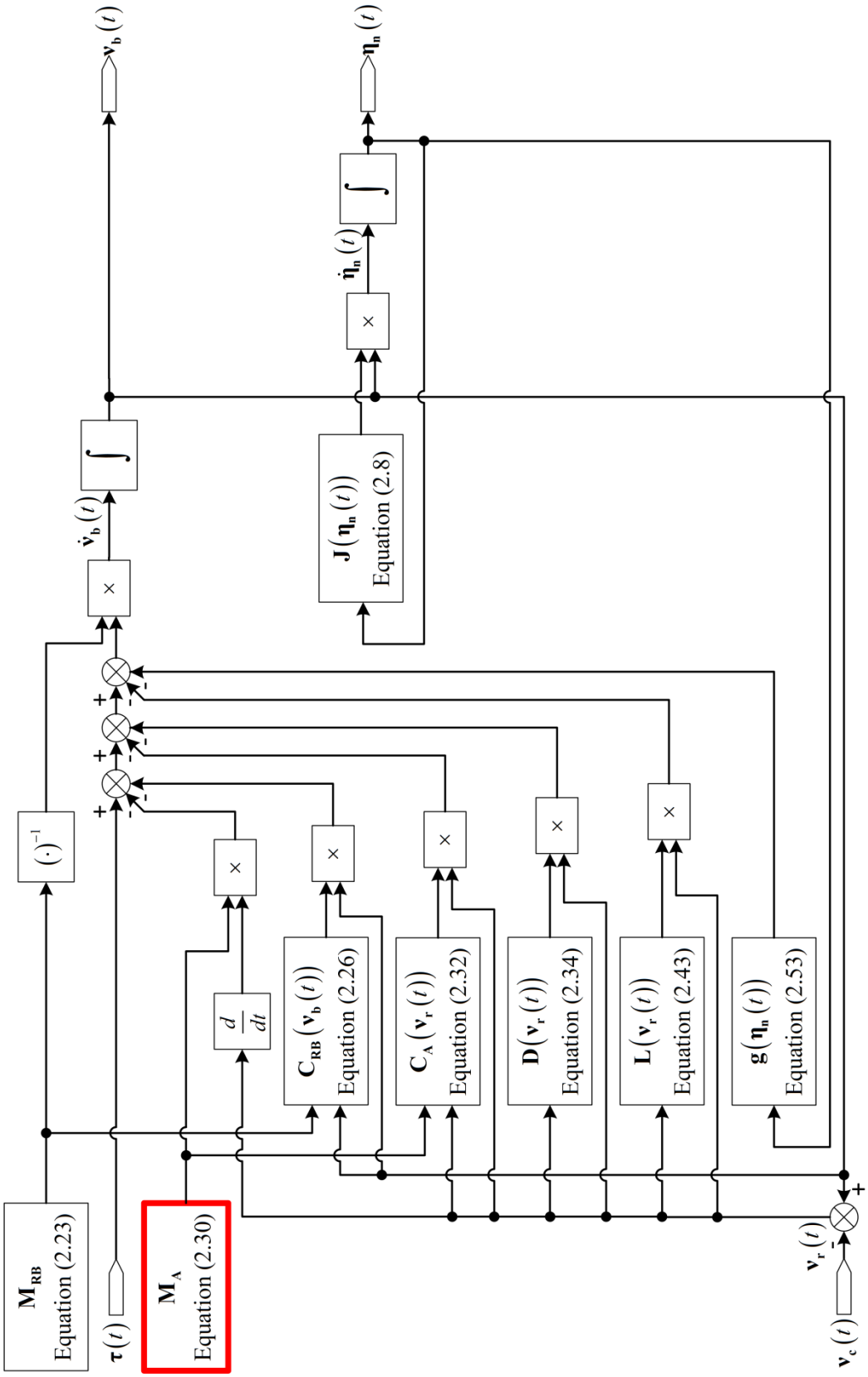

Figure 2.9: AUV Plant Model Highlighting Added Mass

iii. *Added Mass Coriolis and Centripetal Forces*

In a similar fashion to the relationship between the rigid body Coriolis and centripetal forces matrix and the rigid body system inertia matrix, the added mass Coriolis and centripetal forces matrix, $\mathbf{C}_{\mathbf{A}}\left(\mathbf{v}_{\mathbf{r}}(t)\right)$, is dependent on the added mass of an underwater vehicle. As it is identical in structure to $\mathbf{C}_{\mathbf{RB}}\left(\mathbf{v}_{\mathbf{b}}(t)\right)$, it too can be ignored under certain assumptions outlined in Section 2.3. Hence, its structure is examined here.

$\mathbf{C}_{\mathbf{A}}\left(\mathbf{v}_{\mathbf{r}}(t)\right)$ can be calculated from the added mass matrix, as seen in the following equation [3].

$$\mathbf{C}_{\mathbf{A}}\left(\mathbf{v}_{\mathbf{r}}(t)\right)=\begin{bmatrix}\mathbf{0}_{3\times3} & -S\left(\mathbf{A}_{11}\mathbf{V}_{\mathbf{r}}(t)+\mathbf{A}_{12}\boldsymbol{\omega}_{\mathbf{r}}(t)\right)\\ -S\left(\mathbf{A}_{11}\mathbf{V}_{\mathbf{r}}(t)+\mathbf{A}_{12}\boldsymbol{\omega}_{\mathbf{r}}(t)\right) & -S\left(\mathbf{A}_{21}\mathbf{V}_{\mathbf{r}}(t)+\mathbf{A}_{22}\boldsymbol{\omega}_{\mathbf{r}}(t)\right)\end{bmatrix} \quad (2.31)$$

where

$$\mathbf{A}=\tfrac{1}{2}\left(\mathbf{M}_{\mathbf{A}}+\mathbf{M}_{\mathbf{A}}^{T}\right)=\begin{bmatrix}\mathbf{A}_{11} & \mathbf{A}_{12}\\ \mathbf{A}_{21} & \mathbf{A}_{22}\end{bmatrix}$$

Hence,

$$\mathbf{A}_{11}=\begin{bmatrix}X_{\dot{u}} & \tfrac{1}{2}\left(X_{\dot{v}}+Y_{\dot{u}}\right) & \tfrac{1}{2}\left(X_{\dot{w}}+Z_{\dot{u}}\right)\\ \tfrac{1}{2}\left(Y_{\dot{u}}+X_{\dot{v}}\right) & Y_{\dot{v}} & \tfrac{1}{2}\left(Y_{\dot{w}}+Z_{\dot{v}}\right)\\ \tfrac{1}{2}\left(Z_{\dot{u}}+X_{\dot{w}}\right) & \tfrac{1}{2}\left(Z_{\dot{v}}+Y_{\dot{w}}\right) & Z_{\dot{w}}\end{bmatrix}$$

$$\mathbf{A}_{12}=\begin{bmatrix}\tfrac{1}{2}\left(X_{\dot{p}}+K_{\dot{u}}\right) & \tfrac{1}{2}\left(X_{\dot{q}}+M_{\dot{u}}\right) & \tfrac{1}{2}\left(X_{\dot{r}}+N_{\dot{u}}\right)\\ \tfrac{1}{2}\left(Y_{\dot{p}}+K_{\dot{v}}\right) & \tfrac{1}{2}\left(Y_{\dot{q}}+M_{\dot{v}}\right) & \tfrac{1}{2}\left(Y_{\dot{r}}+N_{\dot{v}}\right)\\ \tfrac{1}{2}\left(Z_{\dot{p}}+K_{\dot{w}}\right) & \tfrac{1}{2}\left(Z_{\dot{q}}+M_{\dot{w}}\right) & \tfrac{1}{2}\left(Z_{\dot{r}}+N_{\dot{w}}\right)\end{bmatrix}$$

$$\mathbf{A}_{21}=\begin{bmatrix}\tfrac{1}{2}\left(K_{\dot{u}}+X_{\dot{p}}\right) & \tfrac{1}{2}\left(K_{\dot{v}}+Y_{\dot{p}}\right) & \tfrac{1}{2}\left(K_{\dot{w}}+Z_{\dot{p}}\right)\\ \tfrac{1}{2}\left(M_{\dot{u}}+X_{\dot{q}}\right) & \tfrac{1}{2}\left(M_{\dot{v}}+Y_{\dot{q}}\right) & \tfrac{1}{2}\left(M_{\dot{w}}+Z_{\dot{q}}\right)\\ \tfrac{1}{2}\left(N_{\dot{u}}+X_{\dot{r}}\right) & \tfrac{1}{2}\left(N_{\dot{v}}+Y_{\dot{r}}\right) & \tfrac{1}{2}\left(N_{\dot{w}}+Z_{\dot{r}}\right)\end{bmatrix}$$

$$\mathbf{A}_{22}=\begin{bmatrix}K_{\dot{p}} & \tfrac{1}{2}\left(K_{\dot{q}}+M_{\dot{p}}\right) & \tfrac{1}{2}\left(K_{\dot{r}}+N_{\dot{p}}\right)\\ \tfrac{1}{2}\left(M_{\dot{p}}+K_{\dot{q}}\right) & M_{\dot{q}} & \tfrac{1}{2}\left(M_{\dot{r}}+N_{\dot{q}}\right)\\ \tfrac{1}{2}\left(N_{\dot{p}}+K_{\dot{r}}\right) & \tfrac{1}{2}\left(N_{\dot{q}}+M_{\dot{r}}\right) & N_{\dot{r}}\end{bmatrix}$$

Expanding Equation (2.31) yields the following structure for $\mathbf{C_A}\left(\mathbf{v_r}(t)\right)$:

$$\mathbf{C_A}\left(\mathbf{v_r}(t)\right)=\begin{bmatrix} 0 & 0 & 0 & 0 & b_3 & -b_2 \\ 0 & 0 & 0 & -b_3 & 0 & b_1 \\ 0 & 0 & 0 & b_2 & -b_1 & 0 \\ 0 & b_3 & -b_2 & 0 & b_6 & -b_5 \\ -b_3 & 0 & b_1 & -b_6 & 0 & b_4 \\ b_2 & -b_1 & 0 & b_5 & -b_4 & 0 \end{bmatrix} \tag{2.32}$$

where

$$\begin{aligned}
b_1 &= X_{\dot{u}}u_r(t)+\tfrac{1}{2}\left(X_{\dot{v}}+Y_{\dot{u}}\right)v_r(t)+\tfrac{1}{2}\left(X_{\dot{w}}+Z_{\dot{u}}\right)w_r(t) \\
&\quad +\tfrac{1}{2}\left(X_{\dot{p}}+K_{\dot{u}}\right)p_r(t)+\tfrac{1}{2}\left(X_{\dot{q}}+M_{\dot{u}}\right)q_r(t)+\tfrac{1}{2}\left(X_{\dot{r}}+N_{\dot{u}}\right)r_r(t) \\
b_2 &= \tfrac{1}{2}\left(Y_{\dot{u}}+X_{\dot{v}}\right)u_r(t)+Y_{\dot{v}}v_r(t)+\tfrac{1}{2}\left(Y_{\dot{w}}+Z_{\dot{v}}\right)w_r(t) \\
&\quad +\tfrac{1}{2}\left(Y_{\dot{p}}+K_{\dot{v}}\right)p_r(t)+\tfrac{1}{2}\left(Y_{\dot{q}}+M_{\dot{v}}\right)q_r(t)+\tfrac{1}{2}\left(Y_{\dot{r}}+N_{\dot{v}}\right)r_r(t) \\
b_3 &= \tfrac{1}{2}\left(Z_{\dot{u}}+X_{\dot{w}}\right)u_r(t)+\tfrac{1}{2}\left(Z_{\dot{v}}+Y_{\dot{w}}\right)v_r(t)+Z_{\dot{w}}w_r(t) \\
&\quad +\tfrac{1}{2}\left(Z_{\dot{p}}+K_{\dot{w}}\right)p_r(t)+\tfrac{1}{2}\left(Z_{\dot{q}}+M_{\dot{w}}\right)q_r(t)+\tfrac{1}{2}\left(Z_{\dot{r}}+N_{\dot{w}}\right)r_r(t) \\
b_4 &= \tfrac{1}{2}\left(K_{\dot{u}}+X_{\dot{p}}\right)u_r(t)+\tfrac{1}{2}\left(K_{\dot{v}}+Y_{\dot{p}}\right)v_r(t)+\tfrac{1}{2}\left(K_{\dot{w}}+Z_{\dot{p}}\right)w_r(t) \\
&\quad +K_{\dot{p}}p_r(t)+\tfrac{1}{2}\left(K_{\dot{q}}+M_{\dot{p}}\right)q_r(t)+\tfrac{1}{2}\left(K_{\dot{r}}+N_{\dot{p}}\right)r_r(t) \\
b_5 &= \tfrac{1}{2}\left(M_{\dot{u}}+X_{\dot{q}}\right)u_r(t)+\tfrac{1}{2}\left(M_{\dot{v}}+Y_{\dot{q}}\right)v_r(t)+\tfrac{1}{2}\left(M_{\dot{w}}+Z_{\dot{q}}\right)w_r(t) \\
&\quad +\tfrac{1}{2}\left(M_{\dot{p}}+M_{\dot{q}}\right)p_r(t)+M_{\dot{q}}q_r(t)+\tfrac{1}{2}\left(M_{\dot{r}}+N_{\dot{q}}\right)r_r(t) \\
b_6 &= \tfrac{1}{2}\left(N_{\dot{u}}+X_{\dot{r}}\right)u_r(t)+\tfrac{1}{2}\left(N_{\dot{v}}+Y_{\dot{r}}\right)v_r(t)+\tfrac{1}{2}\left(N_{\dot{w}}+Z_{\dot{r}}\right)w_r(t) \\
&\quad +\tfrac{1}{2}\left(N_{\dot{p}}+K_{\dot{r}}\right)p_r(t)+\tfrac{1}{2}\left(N_{\dot{q}}+M_{\dot{r}}\right)q_r(t)+N_{\dot{r}}r_r(t)
\end{aligned}$$

Similar to $\mathbf{C_{RB}}\left(\mathbf{v}(t)\right)$, $\mathbf{C_A}\left(\mathbf{v_r}(t)\right)$ can also always be parameterised such that it is skew-symmetric, as seen in the following Equation.

$$\mathbf{C_A}\left(\mathbf{v_r}(t)\right)=-\mathbf{C_A}^T\left(\mathbf{v_r}(t)\right),\forall\mathbf{v_r}(t)\in\mathbb{R}^6 \tag{2.33}$$

Figure 2.10 highlights the term responsible for the added mass Coriolis and centripetal forces within the overall AUV plant model of Figure 2.4.

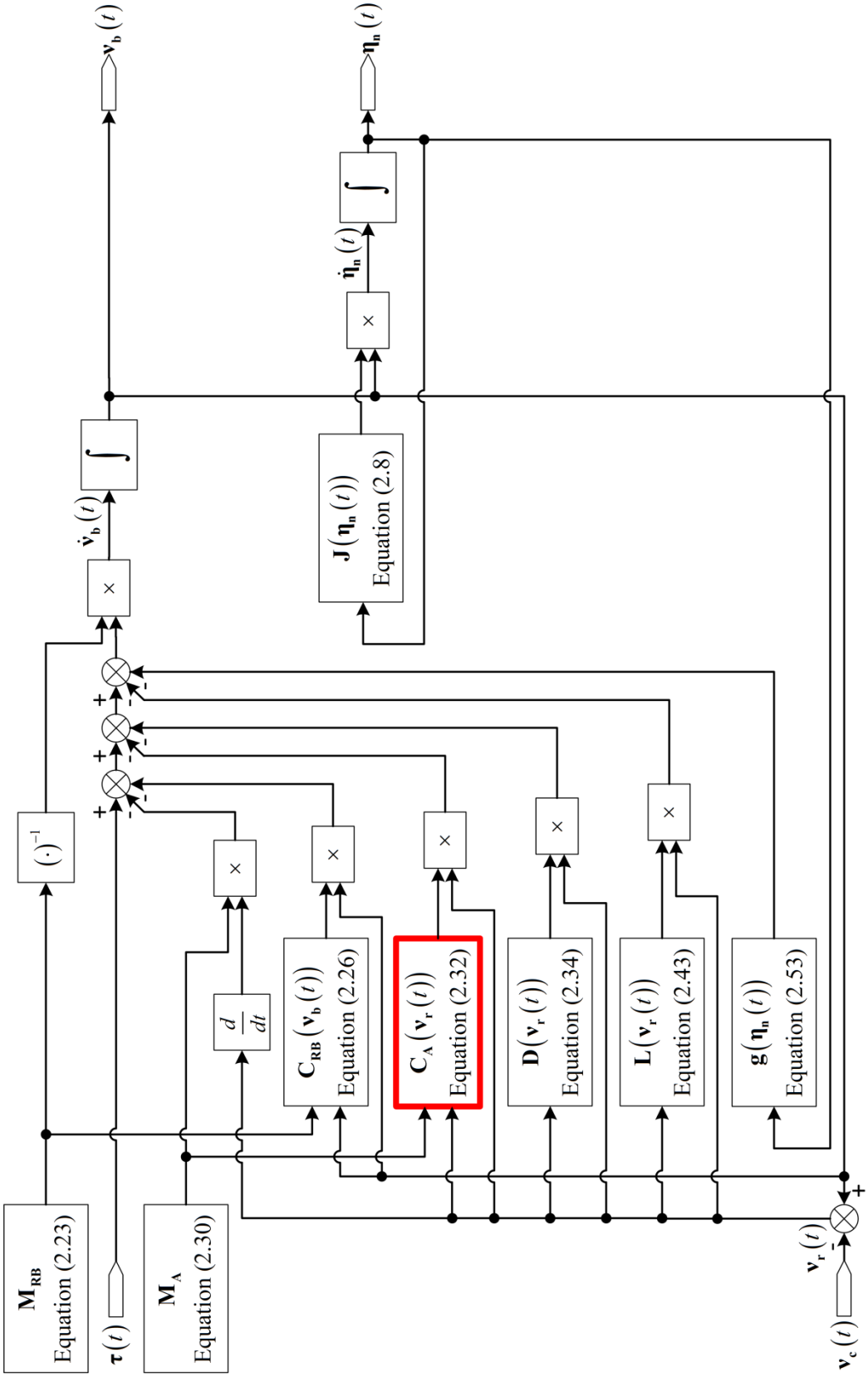

Figure 2.10: AUV Plant Model Highlighting Added Mass Coriolis and Centripetal Forces

iv. *Hydrodynamic Damping Forces*

Hydrodynamic damping forces, also known as drag forces, are the result of a fluid resisting the motion of a vehicle moving through it. These forces are dependent on the shape of the vehicle, and are therefore unique to each vehicle. As properties of the hydrodynamic damping forces matrix are used within the stability proofs of the control algorithms of Chapter 3, this matrix is examined in detail here.

The hydrodynamic damping force is oriented in a direction opposite to the motion of the vehicle and with a magnitude that is related to the velocity of the vehicle along that direction. The hydrodynamic damping forces matrix, $\mathbf{D}(\mathbf{v_r}(t))$, can be considered as a sum of linear damping forces, $\mathbf{D_l}$, and nonlinear damping forces, $\mathbf{D_n}(\mathbf{v_r}(t))$, by:

$$\mathbf{D}(\mathbf{v_r}(t)) = \mathbf{D_l} + \mathbf{D_n}(\mathbf{v_r}(t)) \tag{2.34}$$

Under the assumption that the fluid is ideal, the hydrodynamic damping matrix will be real, nonsymmetric and strictly positive [3].

Figure 2.11 highlights the term responsible for the hydrodynamic damping forces within the overall AUV plant model of Figure 2.4.

v. *Linear Damping*

The linear damping matrix is a full 6×6 matrix representing the parameters associated with the linear damping forces on the vehicle. As indicated by the notation used here, it is seen that the linear damping matrix contains the parameters associated with the resultant force on the vehicle varying linearly with velocity. This linear damping matrix is expressed as:

$$\mathbf{D_l} = \begin{bmatrix} X_u & X_v & X_w & X_p & X_q & X_r \\ Y_u & Y_v & Y_w & Y_p & Y_q & Y_r \\ Z_u & Z_v & Z_w & Z_p & Z_q & Z_r \\ K_u & K_v & K_w & K_p & K_q & K_r \\ M_u & M_v & M_w & M_p & M_q & M_r \\ N_u & N_v & N_w & N_p & N_q & N_r \end{bmatrix} \tag{2.35}$$

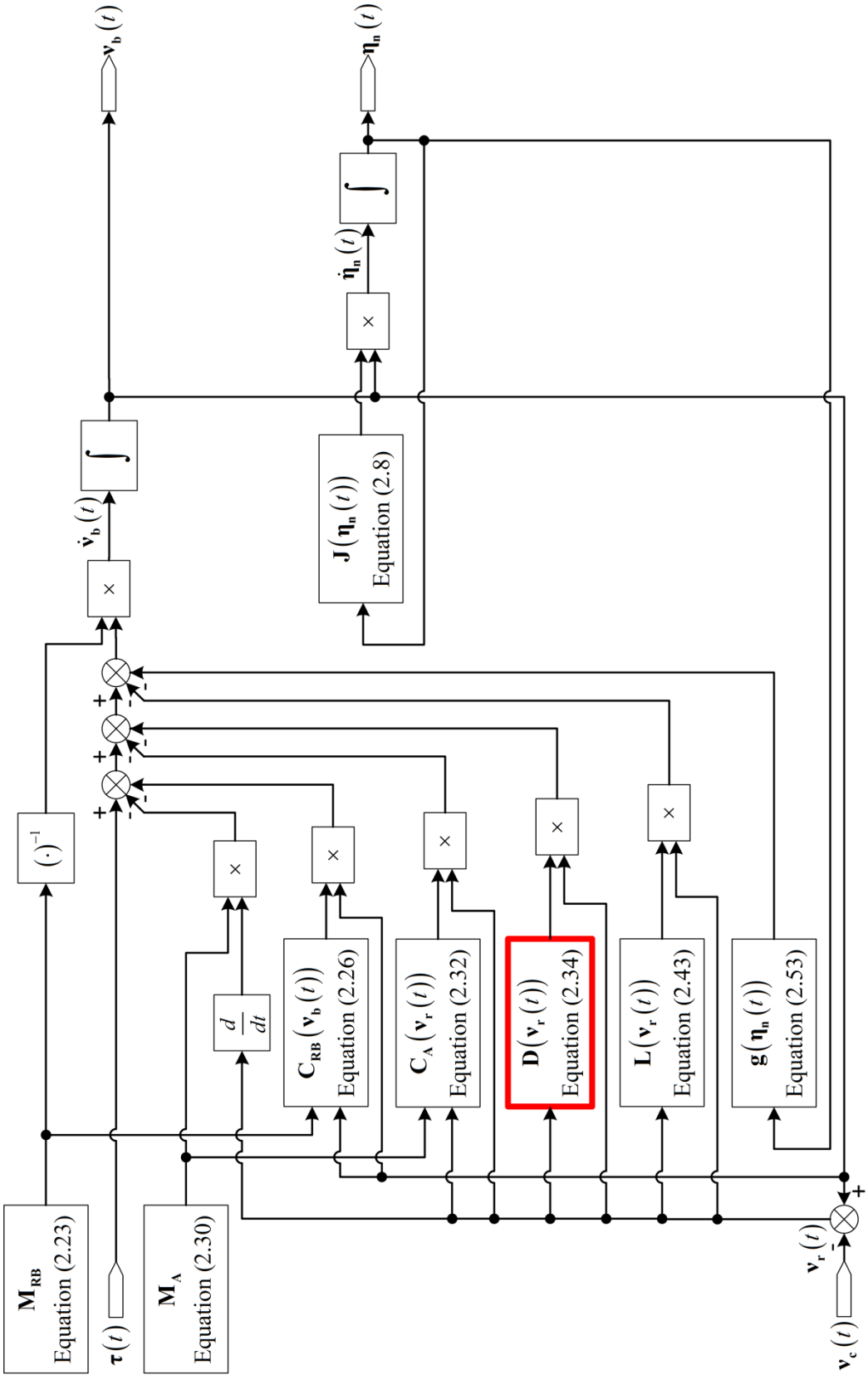

Figure 2.11: AUV Plant Model Highlighting Hydrodynamic Damping Forces

Similar to the added mass matrix of Equation (2.30), the linear damping matrix represents a matrix of partial derivatives, this time in the form of $\frac{\partial \tau_i(t)}{\partial \nu_j(t)}$. For example, $X_u \triangleq \frac{\partial X(t)}{\partial u(t)}$, $Y_u \triangleq \frac{\partial Y(t)}{\partial u(t)}$, and $N_p \triangleq \frac{\partial N(t)}{\partial p(t)}$.

vi. *Nonlinear Damping*

The full nonlinear damping matrix is expressed as:

$$\mathbf{D_n}\left(\mathbf{v_r}(t)\right) = \begin{bmatrix} \left|\mathbf{v_r}(t)\right|^T \mathbf{D_{nX}} \\ \left|\mathbf{v_r}(t)\right|^T \mathbf{D_{nY}} \\ \left|\mathbf{v_r}(t)\right|^T \mathbf{D_{nZ}} \\ \left|\mathbf{v_r}(t)\right|^T \mathbf{D_{nK}} \\ \left|\mathbf{v_r}(t)\right|^T \mathbf{D_{nM}} \\ \left|\mathbf{v_r}(t)\right|^T \mathbf{D_{nN}} \end{bmatrix} \tag{2.36}$$

where $\mathbf{D_{nX}} \cdots \mathbf{D_{nN}}$ are all full 6×6 matrices as seen in the following equations, Equation (2.37) through to Equation (2.42). Therefore, the complete vehicle model will contain 216 parameters associated with nonlinear damping alone. As indicated by the notation used here, the nonlinear damping matrix contains the parameters associated with the resultant force on the vehicle varying in a nonlinear fashion with velocity.

$$\mathbf{D_{nX}} = \begin{bmatrix} X_{|u|u} & X_{|u|v} & X_{|u|w} & X_{|u|p} & X_{|u|q} & X_{|u|r} \\ X_{|v|u} & X_{|v|v} & X_{|v|w} & X_{|v|p} & X_{|v|q} & X_{|v|r} \\ X_{|w|u} & X_{|w|v} & X_{|w|w} & X_{|w|p} & X_{|w|q} & X_{|w|r} \\ X_{|p|u} & X_{|p|v} & X_{|p|w} & X_{|p|p} & X_{|p|q} & X_{|p|r} \\ X_{|q|u} & X_{|q|v} & X_{|q|w} & X_{|q|p} & X_{|q|q} & X_{|q|r} \\ X_{|r|u} & X_{|r|v} & X_{|r|w} & X_{|r|p} & X_{|r|q} & X_{|r|r} \end{bmatrix} \tag{2.37}$$

$$\mathbf{D_{nY}} = \begin{bmatrix} Y_{|u|u} & Y_{|u|v} & Y_{|u|w} & Y_{|u|p} & Y_{|u|q} & Y_{|u|r} \\ Y_{|v|u} & Y_{|v|v} & Y_{|v|w} & Y_{|v|p} & Y_{|v|q} & Y_{|v|r} \\ Y_{|w|u} & Y_{|w|v} & Y_{|w|w} & Y_{|w|p} & Y_{|w|q} & Y_{|w|r} \\ Y_{|p|u} & Y_{|p|v} & Y_{|p|w} & Y_{|p|p} & Y_{|p|q} & Y_{|p|r} \\ Y_{|q|u} & Y_{|q|v} & Y_{|q|w} & Y_{|q|p} & Y_{|q|q} & Y_{|q|r} \\ Y_{|r|u} & Y_{|r|v} & Y_{|r|w} & Y_{|r|p} & Y_{|r|q} & Y_{|r|r} \end{bmatrix} \tag{2.38}$$

$$\mathbf{D_{nZ}} = \begin{bmatrix} Z_{|u|u} & Z_{|u|v} & Z_{|u|w} & Z_{|u|p} & Z_{|u|q} & Z_{|u|r} \\ Z_{|v|u} & Z_{|v|v} & Z_{|v|w} & Z_{|v|p} & Z_{|v|q} & Z_{|v|r} \\ Z_{|w|u} & Z_{|w|v} & Z_{|w|w} & Z_{|w|p} & Z_{|w|q} & Z_{|w|r} \\ Z_{|p|u} & Z_{|p|v} & Z_{|p|w} & Z_{|p|p} & Z_{|p|q} & Z_{|p|r} \\ Z_{|q|u} & Z_{|q|v} & Z_{|q|w} & Z_{|q|p} & Z_{|q|q} & Z_{|q|r} \\ Z_{|r|u} & Z_{|r|v} & Z_{|r|w} & Z_{|r|p} & Z_{|r|q} & Z_{|r|r} \end{bmatrix} \tag{2.39}$$

$$\mathbf{D_{nK}} = \begin{bmatrix} K_{|u|u} & K_{|u|v} & K_{|u|w} & K_{|u|p} & K_{|u|q} & K_{|u|r} \\ K_{|v|u} & K_{|v|v} & K_{|v|w} & K_{|v|p} & K_{|v|q} & K_{|v|r} \\ K_{|w|u} & K_{|w|v} & K_{|w|w} & K_{|w|p} & K_{|w|q} & K_{|w|r} \\ K_{|p|u} & K_{|p|v} & K_{|p|w} & K_{|p|p} & K_{|p|q} & K_{|p|r} \\ K_{|q|u} & K_{|q|v} & K_{|q|w} & K_{|q|p} & K_{|q|q} & K_{|q|r} \\ K_{|r|u} & K_{|r|v} & K_{|r|w} & K_{|r|p} & K_{|r|q} & K_{|r|r} \end{bmatrix} \tag{2.40}$$

$$\mathbf{D_{nM}} = \begin{bmatrix} M_{|u|u} & M_{|u|v} & M_{|u|w} & M_{|u|p} & M_{|u|q} & M_{|u|r} \\ M_{|v|u} & M_{|v|v} & M_{|v|w} & M_{|v|p} & M_{|v|q} & M_{|v|r} \\ M_{|w|u} & M_{|w|v} & M_{|w|w} & M_{|w|p} & M_{|w|q} & M_{|w|r} \\ M_{|p|u} & M_{|p|v} & M_{|p|w} & M_{|p|p} & M_{|p|q} & M_{|p|r} \\ M_{|q|u} & M_{|q|v} & M_{|q|w} & M_{|q|p} & M_{|q|q} & M_{|q|r} \\ M_{|r|u} & M_{|r|v} & M_{|r|w} & M_{|r|p} & M_{|r|q} & M_{|r|r} \end{bmatrix} \tag{2.41}$$

$$\mathbf{D_{nN}} = \begin{bmatrix} N_{|u|u} & N_{|u|v} & N_{|u|w} & N_{|u|p} & N_{|u|q} & N_{|u|r} \\ N_{|v|u} & N_{|v|v} & N_{|v|w} & N_{|v|p} & N_{|v|q} & N_{|v|r} \\ N_{|w|u} & N_{|w|v} & N_{|w|w} & N_{|w|p} & N_{|w|q} & N_{|w|r} \\ N_{|p|u} & N_{|p|v} & N_{|p|w} & N_{|p|p} & N_{|p|q} & N_{|p|r} \\ N_{|q|u} & N_{|q|v} & N_{|q|w} & N_{|q|p} & N_{|q|q} & N_{|q|r} \\ N_{|r|u} & N_{|r|v} & N_{|r|w} & N_{|r|p} & N_{|r|q} & N_{|r|r} \end{bmatrix} \tag{2.42}$$

Similar to the added mass matrix of Equation (2.30) and the linear damping matrix of Equation (2.35), the nonlinear damping matrix represents a matrix of partial derivatives, this time in the form of $\frac{\partial \tau_i(t)}{\partial |\nu_j(t)| \nu_k(t)}$. For example, from Equation (2.37), $X_{|u|u} \triangleq \frac{\partial X(t)}{\partial |u(t)| u(t)}$, from Equation (2.40), $K_{|p|v} \triangleq \frac{\partial K(t)}{\partial |p(t)| v(t)}$, and from Equation (2.42), $N_{|v|r} \triangleq \frac{\partial N(t)}{\partial |v(t)| r(t)}$.

By substituting the expression for $\mathbf{v_r}(t)$ in Equation (2.15), and Equation (2.37) through to Equation (2.42) into the expression for $\mathbf{D_n}(\mathbf{v_r}(t))$ in Equation (2.36), the following column vectors represent each column of the nonlinear damping matrix, $\mathbf{D_n}(\mathbf{v_r}(t))$, of Equation (2.36).

First column of $\mathbf{D_n}(\mathbf{v_r}(t))$:

$$\begin{bmatrix} X_{|u|u}|u_r(t)| + X_{|v|u}|v_r(t)| + X_{|w|u}|w_r(t)| + X_{|p|u}|p_r(t)| + X_{|q|u}|q_r(t)| + X_{|r|u}|r_r(t)| \\ Y_{|u|u}|u_r(t)| + Y_{|v|u}|v_r(t)| + Y_{|w|u}|w_r(t)| + Y_{|p|u}|p_r(t)| + Y_{|q|u}|q_r(t)| + Y_{|r|u}|r_r(t)| \\ Z_{|u|u}|u_r(t)| + Z_{|v|u}|v_r(t)| + Z_{|w|u}|w_r(t)| + Z_{|p|u}|p_r(t)| + Z_{|q|u}|q_r(t)| + Z_{|r|u}|r_r(t)| \\ K_{|u|u}|u_r(t)| + K_{|v|u}|v_r(t)| + K_{|w|u}|w_r(t)| + K_{|p|u}|p_r(t)| + K_{|q|u}|q_r(t)| + K_{|r|u}|r_r(t)| \\ M_{|u|u}|u_r(t)| + M_{|v|u}|v_r(t)| + M_{|w|u}|w_r(t)| + M_{|p|u}|p_r(t)| + M_{|q|u}|q_r(t)| + M_{|r|u}|r_r(t)| \\ N_{|u|u}|u_r(t)| + N_{|v|u}|v_r(t)| + N_{|w|u}|w_r(t)| + N_{|p|u}|p_r(t)| + N_{|q|u}|q_r(t)| + N_{|r|u}|r_r(t)| \end{bmatrix}$$

Second column of $\mathbf{D_n}\left(\mathbf{v_r}(t)\right)$:

$$\begin{bmatrix}
X_{|u|v}|u_r(t)|+X_{|v|v}|v_r(t)|+X_{|w|v}|w_r(t)|+X_{|p|v}|p_r(t)|+X_{|q|v}|q_r(t)|+X_{|r|v}|r_r(t)| \\
Y_{|u|v}|u_r(t)|+Y_{|v|v}|v_r(t)|+Y_{|w|v}|w_r(t)|+Y_{|p|v}|p_r(t)|+Y_{|q|v}|q_r(t)|+Y_{|r|v}|r_r(t)| \\
Z_{|u|v}|u_r(t)|+Z_{|v|v}|v_r(t)|+Z_{|w|v}|w_r(t)|+Z_{|p|v}|p_r(t)|+Z_{|q|v}|q_r(t)|+Z_{|r|v}|r_r(t)| \\
K_{|u|v}|u_r(t)|+K_{|v|v}|v_r(t)|+K_{|w|v}|w_r(t)|+K_{|p|v}|p_r(t)|+K_{|q|v}|q_r(t)|+K_{|r|v}|r_r(t)| \\
M_{|u|v}|u_r(t)|+M_{|v|v}|v_r(t)|+M_{|w|v}|w_r(t)|+M_{|p|v}|p_r(t)|+M_{|q|v}|q_r(t)|+M_{|r|v}|r_r(t)| \\
N_{|u|v}|u_r(t)|+N_{|v|v}|v_r(t)|+N_{|w|v}|w_r(t)|+N_{|p|v}|p_r(t)|+N_{|q|v}|q_r(t)|+N_{|r|v}|r_r(t)|
\end{bmatrix}$$

Third column of $\mathbf{D_n}\left(\mathbf{v_r}(t)\right)$:

$$\begin{bmatrix}
X_{|u|w}|u_r(t)|+X_{|v|w}|v_r(t)|+X_{|w|w}|w_r(t)|+X_{|p|w}|p_r(t)|+X_{|q|w}|q_r(t)|+X_{|r|w}|r_r(t)| \\
Y_{|u|w}|u_r(t)|+Y_{|v|w}|v_r(t)|+Y_{|w|w}|w_r(t)|+Y_{|p|w}|p_r(t)|+Y_{|q|w}|q_r(t)|+Y_{|r|w}|r_r(t)| \\
Z_{|u|w}|u_r(t)|+Z_{|v|w}|v_r(t)|+Z_{|w|w}|w_r(t)|+Z_{|p|w}|p_r(t)|+Z_{|q|w}|q_r(t)|+Z_{|r|w}|r_r(t)| \\
K_{|u|w}|u_r(t)|+K_{|v|w}|v_r(t)|+K_{|w|w}|w_r(t)|+K_{|p|w}|p_r(t)|+K_{|q|w}|q_r(t)|+K_{|r|w}|r_r(t)| \\
M_{|u|w}|u_r(t)|+M_{|v|w}|v_r(t)|+M_{|w|w}|w_r(t)|+M_{|p|w}|p_r(t)|+M_{|q|w}|q_r(t)|+M_{|r|w}|r_r(t)| \\
N_{|u|w}|u_r(t)|+N_{|v|w}|v_r(t)|+N_{|w|w}|w_r(t)|+N_{|p|w}|p_r(t)|+N_{|q|w}|q_r(t)|+N_{|r|w}|r_r(t)|
\end{bmatrix}$$

Fourth column of $\mathbf{D_n}\left(\mathbf{v_r}(t)\right)$:

$$\begin{bmatrix}
X_{|u|p}|u_r(t)|+X_{|v|p}|v_r(t)|+X_{|w|p}|w_r(t)|+X_{|p|p}|p_r(t)|+X_{|q|p}|q_r(t)|+X_{|r|p}|r_r(t)| \\
Y_{|u|p}|u_r(t)|+Y_{|v|p}|v_r(t)|+Y_{|w|p}|w_r(t)|+Y_{|p|p}|p_r(t)|+Y_{|q|p}|q_r(t)|+Y_{|r|p}|r_r(t)| \\
Z_{|u|p}|u_r(t)|+Z_{|v|p}|v_r(t)|+Z_{|w|p}|w_r(t)|+Z_{|p|p}|p_r(t)|+Z_{|q|p}|q_r(t)|+Z_{|r|p}|r_r(t)| \\
K_{|u|p}|u_r(t)|+K_{|v|p}|v_r(t)|+K_{|w|p}|w_r(t)|+K_{|p|p}|p_r(t)|+K_{|q|p}|q_r(t)|+Kp|r_r(t)| \\
M_{|u|p}|u_r(t)|+M_{|v|p}|v_r(t)|+M_{|w|p}|w_r(t)|+M_{|p|p}|p_r(t)|+M_{|q|p}|q_r(t)|+M_{|r|p}|r_r(t)| \\
N_{|u|p}|u_r(t)|+N_{|v|p}|v_r(t)|+N_{|w|p}|w_r(t)|+N_{|p|p}|p_r(t)|+N_{|q|p}|q_r(t)|+N_{|r|p}|r_r(t)|
\end{bmatrix}$$

Fifth column of $\mathbf{D_n}(\mathbf{v_r}(t))$:

$$\begin{bmatrix} X_{|u|q}|u_r(t)|+X_{|v|q}|v_r(t)|+X_{|w|q}|w_r(t)|+X_{|p|q}|p_r(t)|+X_{|q|q}|q_r(t)|+X_{|r|q}|r_r(t)| \\ Y_{|u|q}|u_r(t)|+Y_{|v|q}|v_r(t)|+Y_{|w|q}|w_r(t)|+Y_{|p|q}|p_r(t)|+Y_{|q|q}|q_r(t)|+Y_{|r|q}|r_r(t)| \\ Z_{|u|q}|u_r(t)|+Z_{|v|q}|v_r(t)|+Z_{|w|q}|w_r(t)|+Z_{|p|q}|p_r(t)|+Z_{|q|q}|q_r(t)|+Z_{|r|q}|r_r(t)| \\ K_{|u|q}|u_r(t)|+K_{|v|q}|v_r(t)|+K_{|w|q}|w_r(t)|+K_{|p|q}|p_r(t)|+K_{|q|q}|q_r(t)|+K_{|r|q}|r_r(t)| \\ M_{|u|q}|u_r(t)|+M_{|v|q}|v_r(t)|+M_{|w|q}|w_r(t)|+M_{|p|q}|p_r(t)|+M_{|q|q}|q_r(t)|+M_{|r|q}|r_r(t)| \\ N_{|u|q}|u_r(t)|+N_{|v|q}|v_r(t)|+N_{|w|q}|w_r(t)|+N_{|p|q}|p_r(t)|+N_{|q|q}|q_r(t)|+N_{|r|q}|r_r(t)| \end{bmatrix}$$

Sixth column of $\mathbf{D_n}(\mathbf{v_r}(t))$:

$$\begin{bmatrix} X_{|u|r}|u_r(t)|+X_{|v|r}|v_r(t)|+X_{|w|r}|w_r(t)|+X_{|p|r}|p_r(t)|+X_{|q|r}|q_r(t)|+X_{|r|r}|r_r(t)| \\ Y_{|u|r}|u_r(t)|+Y_{|v|r}|v_r(t)|+Y_{|w|r}|w_r(t)|+Y_{|p|r}|p_r(t)|+Y_{|q|r}|q_r(t)|+Y_{|r|r}|r_r(t)| \\ Z_{|u|r}|u_r(t)|+Z_{|v|r}|v_r(t)|+Z_{|w|r}|w_r(t)|+Z_{|p|r}|p_r(t)|+Z_{|q|r}|q_r(t)|+Z_{|r|r}|r_r(t)| \\ K_{|u|r}|u_r(t)|+K_{|v|r}|v_r(t)|+K_{|w|r}|w_r(t)|+K_{|p|r}|p_r(t)|+K_{|q|r}|q_r(t)|+K_{|r|r}|r_r(t)| \\ M_{|u|r}|u_r(t)|+M_{|v|r}|v_r(t)|+M_{|w|r}|w_r(t)|+M_{|p|r}|p_r(t)|+M_{|q|r}|q_r(t)|+M_{|r|r}|r_r(t)| \\ N_{|u|r}|u_r(t)|+N_{|v|r}|v_r(t)|+N_{|w|r}|w_r(t)|+N_{|p|r}|p_r(t)|+N_{|q|r}|q_r(t)|+N_{|r|r}|r_r(t)| \end{bmatrix}$$

vii. *Hydrodynamic Lift Forces*

When a fluid flows around an object, and a pressure/velocity difference occurs between the fluid flowing on opposite sides of the object, a force is applied to the object perpendicular to this direction of flow. This force is called lift and is caused by a nonzero angle between the direction of flow of the fluid and a reference line, typically the *x*-axis, of the vehicle. This angle is called the angle of attack (AoA). The lift force, which is oriented perpendicular to the direction of flow of the fluid, is in contrast to drag/damping force, which is oriented parallel to the direction of flow of the fluid. Particularly for torpedo shaped underwater vehicles, this lift force is considerably smaller than the hydrodynamic damping force. Therefore, under certain assumptions utilised in Section 2.3, this force is ignored. Hence, there is a need to examine these forces here in order to gain a full understanding of why these forces can be ignored under certain conditions.

Figure 2.12 highlights the term responsible for the hydrodynamic lift forces within the overall AUV plant model of Figure 2.4.

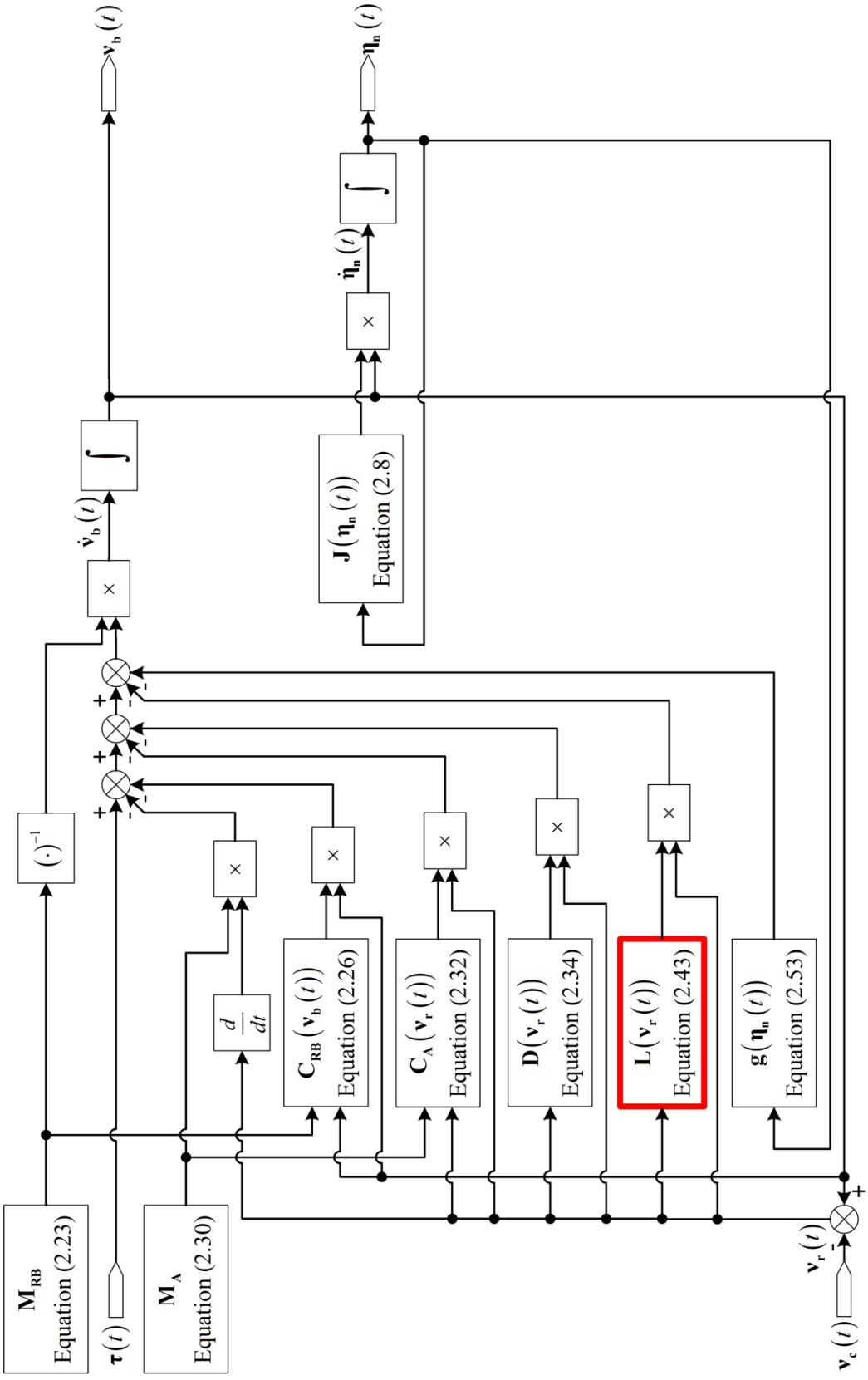

Figure 2.12: AUV Plant Model Highlighting Hydrodynamic Lift Forces

The full lift matrix is expressed as:

$$\mathbf{L}\left(\boldsymbol{\nu}_{\mathbf{r}}(t)\right)=\begin{bmatrix}\boldsymbol{\nu}_{\mathbf{r}}(t)^{T}\,\mathbf{L}_{\mathbf{X}}\\ \boldsymbol{\nu}_{\mathbf{r}}(t)^{T}\,\mathbf{L}_{\mathbf{Y}}\\ \boldsymbol{\nu}_{\mathbf{r}}(t)^{T}\,\mathbf{L}_{\mathbf{Z}}\\ \boldsymbol{\nu}_{\mathbf{r}}(t)^{T}\,\mathbf{L}_{\mathbf{K}}\\ \boldsymbol{\nu}_{\mathbf{r}}(t)^{T}\,\mathbf{L}_{\mathbf{M}}\\ \boldsymbol{\nu}_{\mathbf{r}}(t)^{T}\,\mathbf{L}_{\mathbf{N}}\end{bmatrix} \tag{2.43}$$

where $\mathbf{L}_{\mathbf{X}}\cdots\mathbf{L}_{\mathbf{N}}$ are all full 6×6 matrices, as seen in the following equations, Equation (2.44) through to Equation (2.49)

$$\mathbf{L}_{\mathbf{X}}=\begin{bmatrix}X_{uu} & X_{uv} & X_{uw} & X_{up} & X_{uq} & X_{ur}\\ X_{vu} & X_{vv} & X_{vw} & X_{vp} & X_{vq} & X_{vr}\\ X_{wu} & X_{wv} & X_{ww} & X_{wp} & X_{wq} & X_{wr}\\ X_{pu} & X_{pv} & X_{pw} & X_{pp} & X_{pq} & X_{pr}\\ X_{qu} & X_{qv} & X_{qw} & X_{qp} & X_{qq} & X_{qr}\\ X_{ru} & X_{rv} & X_{rw} & X_{rp} & X_{rq} & X_{rr}\end{bmatrix} \tag{2.44}$$

$$\mathbf{L}_{\mathbf{Y}}=\begin{bmatrix}Y_{uu} & Y_{uv} & Y_{uw} & Y_{up} & Y_{uq} & Y_{ur}\\ Y_{vu} & Y_{vv} & Y_{vw} & Y_{vp} & Y_{vq} & Y_{vr}\\ Y_{wu} & Y_{wv} & Y_{ww} & Y_{wp} & Y_{wq} & Y_{wr}\\ Y_{pu} & Y_{pv} & Y_{pw} & Y_{pp} & Y_{pq} & Y_{pr}\\ Y_{qu} & Y_{qv} & Y_{qw} & Y_{qp} & Y_{qq} & Y_{qr}\\ Y_{ru} & Y_{rv} & Y_{rw} & Y_{rp} & Y_{rq} & Y_{rr}\end{bmatrix} \tag{2.45}$$

$$\mathbf{L}_{\mathbf{Z}}=\begin{bmatrix}Z_{uu} & Z_{uv} & Z_{uw} & Z_{up} & Z_{uq} & Z_{ur}\\ Z_{vu} & Z_{vv} & Z_{vw} & Z_{vp} & Z_{vq} & Z_{vr}\\ Z_{wu} & Z_{wv} & Z_{ww} & Z_{wp} & Z_{wq} & Z_{wr}\\ Z_{pu} & Z_{pv} & Z_{pw} & Z_{pp} & Z_{pq} & Z_{pr}\\ Z_{qu} & Z_{qv} & Z_{qw} & Z_{qp} & Z_{qq} & Z_{qr}\\ Z_{ru} & Z_{rv} & Z_{rw} & Z_{rp} & Z_{rq} & Z_{rr}\end{bmatrix} \tag{2.46}$$

$$\mathbf{L_K} = \begin{bmatrix} K_{uu} & K_{uv} & K_{uw} & K_{up} & K_{uq} & K_{ur} \\ K_{vu} & K_{vv} & K_{vw} & K_{vp} & K_{vq} & K_{vr} \\ K_{wu} & K_{wv} & K_{ww} & K_{wp} & K_{wq} & K_{wr} \\ K_{pu} & K_{pv} & K_{pw} & K_{pp} & K_{pq} & K_{pr} \\ K_{qu} & K_{qv} & K_{qw} & K_{qp} & K_{qq} & K_{qr} \\ K_{ru} & K_{rv} & K_{rw} & K_{rp} & K_{rq} & K_{rr} \end{bmatrix} \tag{2.47}$$

$$\mathbf{L_M} = \begin{bmatrix} M_{uu} & M_{uv} & M_{uw} & M_{up} & M_{uq} & M_{ur} \\ M_{vu} & M_{vv} & M_{vw} & M_{vp} & M_{vq} & M_{vr} \\ M_{wu} & M_{wv} & M_{ww} & M_{wp} & M_{wq} & M_{wr} \\ M_{pu} & M_{pv} & M_{pw} & M_{pp} & M_{pq} & M_{pr} \\ M_{qu} & M_{qv} & M_{qw} & M_{qp} & M_{qq} & M_{qr} \\ M_{ru} & M_{rv} & M_{rw} & M_{rp} & M_{rq} & M_{rr} \end{bmatrix} \tag{2.48}$$

$$\mathbf{L_N} = \begin{bmatrix} N_{uu} & N_{uv} & N_{uw} & N_{up} & N_{uq} & N_{ur} \\ N_{vu} & N_{vv} & N_{vw} & N_{vp} & N_{vq} & N_{vr} \\ N_{wu} & N_{wv} & N_{ww} & N_{wp} & N_{wq} & N_{wr} \\ N_{pu} & N_{pv} & N_{pw} & N_{pp} & N_{pq} & N_{pr} \\ N_{qu} & N_{qv} & N_{qw} & N_{qp} & N_{qq} & N_{qr} \\ N_{ru} & N_{rv} & N_{rw} & N_{rp} & N_{rq} & N_{rr} \end{bmatrix} \tag{2.49}$$

Similar to the added mass matrix of Equation (2.30), the linear damping matrix of Equation (2.35), and the nonlinear damping matrices of Equation (2.37) through to Equation (2.42), the lift matrix represents a matrix of partial derivatives, this time in the form of $\frac{\partial \tau_i(t)}{\partial v_j(t) v_k(t)}$. For example, from Equation (2.44), $X_{uu} \triangleq \frac{\partial X(t)}{\partial u(t) u(t)}$, from Equation (2.47), $K_{pv} \triangleq \frac{\partial K(t)}{\partial p(t) v(t)}$, and from Equation (2.49), $N_{vr} \triangleq \frac{\partial N(t)}{\partial v(t) r(t)}$.

By substituting the expression for $\mathbf{v_r}(t)$ in Equation (2.15), and Equation (2.44) through to Equation (2.49) into the expression for $\mathbf{L}(\mathbf{v_r}(t))$ in Equation (2.43), the following column vectors represent each column of the lift matrix, $\mathbf{L}(\mathbf{v_r}(t))$, of Equation (2.43).

First column of $\mathbf{L}(\mathbf{v}_\mathbf{r}(t))$:

$$\begin{bmatrix} X_{uu}u_r(t)+X_{vu}v_r(t)+X_{wu}w_r(t)+X_{pu}p_r(t)+X_{qu}q_r(t)+X_{ru}r_r(t) \\ Y_{uu}u_r(t)+Y_{vu}v_r(t)+Y_{wu}w_r(t)+Y_{pu}p_r(t)+Y_{qu}q_r(t)+Y_{ru}r_r(t) \\ Z_{uu}u_r(t)+Z_{vu}v_r(t)+Z_{wu}w_r(t)+Z_{pu}p_r(t)+Z_{qu}q_r(t)+Z_{ru}r_r(t) \\ K_{uu}u_r(t)+K_{vu}v_r(t)+K_{wu}w_r(t)+K_{pu}p_r(t)+K_{qu}q_r(t)+K_{ru}r_r(t) \\ M_{uu}u_r(t)+M_{vu}v_r(t)+M_{wu}w_r(t)+M_{pu}p_r(t)+M_{qu}q_r(t)+M_{ru}r_r(t) \\ N_{uu}u_r(t)+N_{vu}v_r(t)+N_{wu}w_r(t)+N_{pu}p_r(t)+N_{qu}q_r(t)+N_{ru}r_r(t) \end{bmatrix}$$

Second column of $\mathbf{L}(\mathbf{v}_\mathbf{r}(t))$:

$$\begin{bmatrix} X_{uv}u_r(t)+X_{vv}v_r(t)+X_{wv}w_r(t)+X_{pv}p_r(t)+X_{qv}q_r(t)+X_{rv}r_r(t) \\ Y_{uv}u_r(t)+Y_{vv}v_r(t)+Y_{wv}w_r(t)+Y_{pv}p_r(t)+Y_{qv}q_r(t)+Y_{rv}r_r(t) \\ Z_{uv}u_r(t)+Z_{vv}v_r(t)+Z_{wv}w_r(t)+Z_{pv}p_r(t)+Z_{qv}q_r(t)+Z_{rv}r_r(t) \\ K_{uv}u_r(t)+K_{vv}v_r(t)+K_{wv}w_r(t)+K_{pv}p_r(t)+K_{qv}q_r(t)+K_{rv}r_r(t) \\ M_{uv}u_r(t)+M_{vv}v_r(t)+M_{wv}w_r(t)+M_{pv}p_r(t)+M_{qv}q_r(t)+M_{rv}r_r(t) \\ N_{uv}u_r(t)+N_{vv}v_r(t)+N_{wv}w_r(t)+N_{pv}p_r(t)+N_{qv}q_r(t)+N_{rv}r_r(t) \end{bmatrix}$$

Third column of $\mathbf{L}(\mathbf{v}_\mathbf{r}(t))$:

$$\begin{bmatrix} X_{uw}u_r(t)+X_{vw}v_r(t)+X_{ww}w_r(t)+X_{pw}p_r(t)+X_{qw}q_r(t)+X_{rw}r_r(t) \\ Y_{uw}u_r(t)+Y_{vw}v_r(t)+Y_{ww}w_r(t)+Y_{pw}p_r(t)+Y_{qw}q_r(t)+Y_{rw}r_r(t) \\ Z_{uw}u_r(t)+Z_{vw}v_r(t)+Z_{ww}w_r(t)+Z_{pw}p_r(t)+Z_{qw}q_r(t)+Z_{rw}r_r(t) \\ K_{uw}u_r(t)+K_{vw}v_r(t)+K_{ww}w_r(t)+K_{pw}p_r(t)+K_{qw}q_r(t)+K_{rw}r_r(t) \\ M_{uw}u_r(t)+M_{vw}v_r(t)+M_{ww}w_r(t)+M_{pw}p_r(t)+M_{qw}q_r(t)+M_{rw}r_r(t) \\ N_{uw}u_r(t)+N_{vw}v_r(t)+N_{ww}w_r(t)+N_{pw}p_r(t)+N_{qw}q_r(t)+N_{rw}r_r(t) \end{bmatrix}$$

Fourth column of $\mathbf{L}(\mathbf{v}_\mathbf{r}(t))$:

$$\begin{bmatrix} X_{up}u_r(t)+X_{vp}v_r(t)+X_{wp}w_r(t)+X_{pp}p_r(t)+X_{qp}q_r(t)+X_{rp}r_r(t) \\ Y_{up}u_r(t)+Y_{vp}v_r(t)+Y_{wp}w_r(t)+Y_{pp}p_r(t)+Y_{qp}q_r(t)+Y_{rp}r_r(t) \\ Z_{up}u_r(t)+Z_{vp}v_r(t)+Z_{wp}w_r(t)+Z_{pp}p_r(t)+Z_{qp}q_r(t)+Z_{rp}r_r(t) \\ K_{up}u_r(t)+K_{vp}v_r(t)+K_{wp}w_r(t)+K_{pp}p_r(t)+K_{qp}q_r(t)+K_{rp}r_r(t) \\ M_{up}u_r(t)+M_{vp}v_r(t)+M_{wp}w_r(t)+M_{pp}p_r(t)+M_{qp}q_r(t)+M_{rp}r_r(t) \\ N_{up}u_r(t)+N_{vp}v_r(t)+N_{wp}w_r(t)+N_{pp}p_r(t)+N_{qp}q_r(t)+N_{rp}r_r(t) \end{bmatrix}$$

Fifth column of $\mathbf{L}(\mathbf{v}_\mathbf{r}(t))$:

$$\begin{bmatrix} X_{uq}u_r(t)+X_{vq}v_r(t)+X_{wq}w_r(t)+X_{pq}p_r(t)+X_{qq}q_r(t)+X_{rq}r_r(t) \\ Y_{uq}u_r(t)+Y_{vq}v_r(t)+Y_{wq}w_r(t)+Y_{pq}p_r(t)+Y_{qq}q_r(t)+Y_{rq}r_r(t) \\ Z_{uq}u_r(t)+Z_{vq}v_r(t)+Z_{wq}w_r(t)+Z_{pq}p_r(t)+Z_{qq}q_r(t)+Z_{rq}r_r(t) \\ K_{uq}u_r(t)+K_{vq}v_r(t)+K_{wq}w_r(t)+K_{pq}p_r(t)+K_{qq}q_r(t)+K_{rq}r_r(t) \\ M_{uq}u_r(t)+M_{vq}v_r(t)+M_{wq}w_r(t)+M_{pq}p_r(t)+M_{qq}q_r(t)+M_{rq}r_r(t) \\ N_{uq}u_r(t)+N_{vq}v_r(t)+N_{wq}w_r(t)+N_{pq}p_r(t)+N_{qq}q_r(t)+N_{rq}r_r(t) \end{bmatrix}$$

Sixth column of $\mathbf{L}(\mathbf{v}_\mathbf{r}(t))$:

$$\begin{bmatrix} X_{ur}u_r(t)+X_{vr}v_r(t)+X_{wr}w_r(t)+X_{pr}p_r(t)+X_{qr}q_r(t)+X_{rr}r_r(t) \\ Y_{ur}u_r(t)+Y_{vr}v_r(t)+Y_{wr}w_r(t)+Y_{pr}p_r(t)+Y_{qr}q_r(t)+Y_{rr}r_r(t) \\ Z_{ur}u_r(t)+Z_{vr}v_r(t)+Z_{wr}w_r(t)+Z_{pr}p_r(t)+Z_{qr}q_r(t)+Z_{rr}r_r(t) \\ K_{ur}u_r(t)+K_{vr}v_r(t)+K_{wr}w_r(t)+K_{pr}p_r(t)+K_{qr}q_r(t)+K_{rr}r_r(t) \\ M_{ur}u_r(t)+M_{vr}v_r(t)+M_{wr}w_r(t)+M_{pr}p_r(t)+M_{qr}q_r(t)+M_{rr}r_r(t) \\ N_{ur}u_r(t)+N_{vr}v_r(t)+N_{wr}w_r(t)+N_{pr}p_r(t)+N_{qr}q_r(t)+N_{rr}r_r(t) \end{bmatrix}$$

viii. *Gravitational and Buoyancy Forces*

Depending on the configuration of an underwater vehicle, the gravitational and buoyancy forces can vary in magnitude from no effect to a considerable effect. This thesis is aimed at controlling highly manoeuvrable underwater vehicles and hence the effect due to gravitational and buoyancy forces will be eliminated from the vehicle model. However, the justification for why this is so needs to be examined. Hence, the requirement of examining the cause and effect of these forces needs to be conducted.

Under the assumption of the vehicle operating in a uniform gravitational field, the force due to gravity, more commonly referred to as weight, *W*, of the vehicle can be calculated using:

$$W = mg \tag{2.50}$$

where *m* is the mass of the vehicle and *g* is the acceleration due to the gravitational field. *W* is directed towards the centre of the Earth.

Buoyancy is a force caused by the amount of fluid displaced by the vehicle. The buoyancy force, *B*, can be calculated using:

$$B = \rho g \nabla \tag{2.51}$$

where ρ is the uniform density of the displaced fluid, g is the acceleration due to the gravitational field, and ∇ is the volume of water displaced. B is directed away from the centre of the Earth.

The position of the centre of gravity with respect to the origin of the body frame has been previously defined as $\mathbf{r_g^b}$ in Equation (2.22). If the position of the centre of buoyancy with respect to the origin of the body frame, $\mathbf{r_b^b}$, is expressed as:

$$\mathbf{r_b^b} = \begin{bmatrix} x_b^b \\ y_b^b \\ z_b^b \end{bmatrix} \tag{2.52}$$

the overall forces due to both gravitational and buoyancy forces can be calculated using:

$$\mathbf{g}\left(\boldsymbol{\eta}_\mathbf{n}(t)\right) = \begin{bmatrix} (W-B)\sin\theta_n(t) \\ -(W-B)\cos\theta_n(t)\sin\phi_n(t) \\ -(W-B)\cos\theta_n(t)\cos\phi_n(t) \\ -\left(y_g^b W - y_b^b B\right)\cos\theta_n(t)\cos\phi_n(t) + \left(z_g^b W - z_b^b B\right)\cos\theta_n(t)\sin\phi_n(t) \\ \left(z_g^b W - z_b^b B\right)\sin\theta_n(t) + \left(x_g^b W - x_b^b B\right)\cos\theta_n(t)\cos\phi_n(t) \\ -\left(x_g^b W - x_b^b B\right)\cos\theta_n(t)\sin\phi_n(t) - \left(y_g^b W - y_b^b B\right)\sin\theta_n(t) \end{bmatrix} \tag{2.53}$$

Figure 2.13 highlights the term responsible for the gravitational and buoyancy forces within the overall AUV plant model of Figure 2.4.

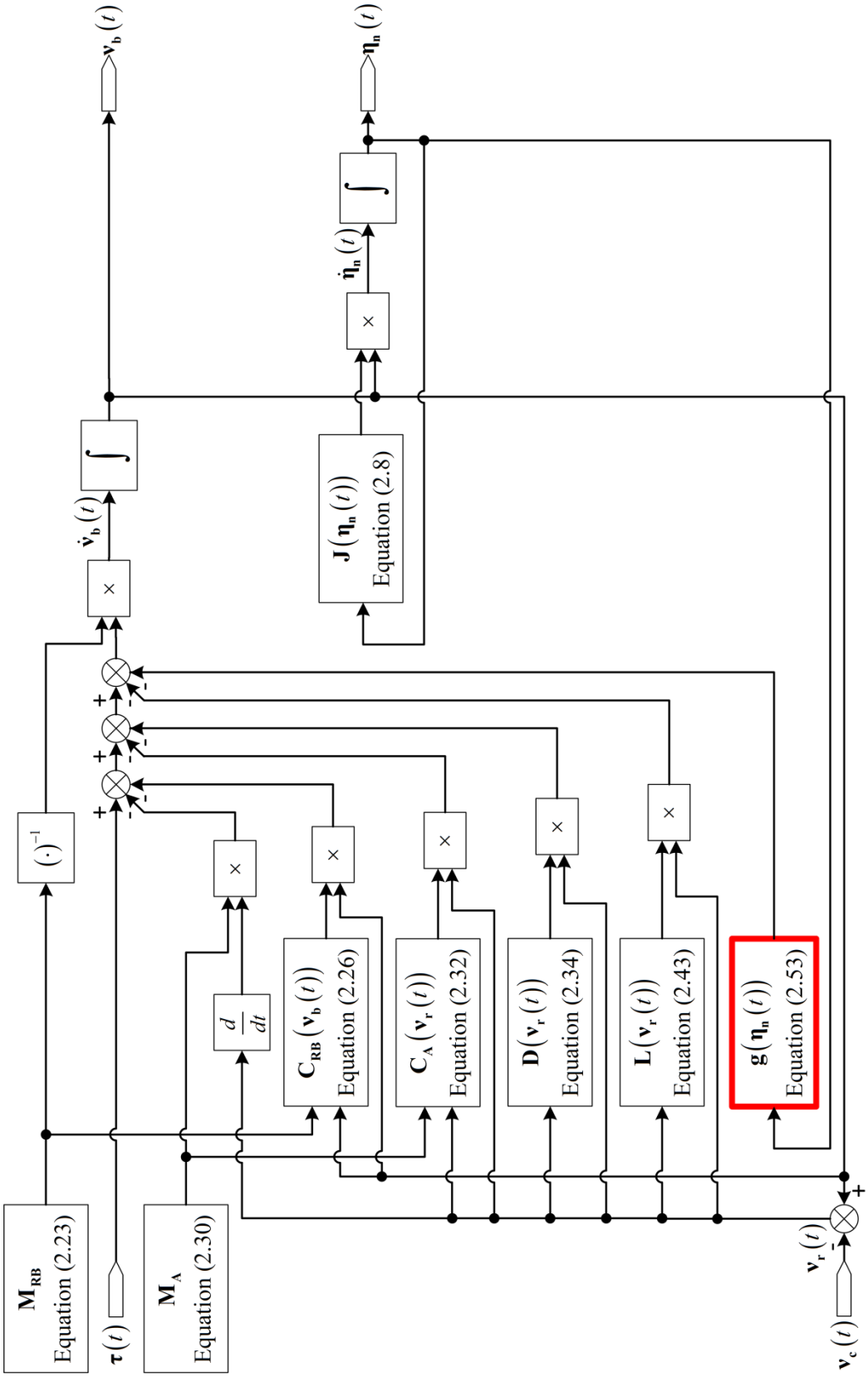

Figure 2.13: AUV Plant Model Highlighting Gravitational and Buoyancy Forces

2. Complete Model

All of the previously described dynamics, be it rigid body dynamics or hydrodynamics, can be combined together to form the equation that represents the complete model of an AUV. This model can be decomposed in either the body frame or the navigation frame. The following sections detail this model decomposed in either frame, as well as the process for transforming models from one frame to the other.

(a) Complete Body Frame Model

Equation (2.12) provides a convenient representation for the model of an underwater vehicle decomposed in the body frame. For convenience, it is shown again here.

$$\begin{aligned}\mathbf{M}_{\mathbf{RB}}\dot{\boldsymbol{\nu}}_{\mathbf{b}}(t)+\mathbf{M}_{\mathbf{A}}\dot{\boldsymbol{\nu}}_{\mathbf{r}}(t)+\mathbf{C}_{\mathbf{RB}}\left(\boldsymbol{\nu}_{\mathbf{b}}(t)\right)\boldsymbol{\nu}_{\mathbf{b}}(t)+\mathbf{C}_{\mathbf{A}}\left(\boldsymbol{\nu}_{\mathbf{r}}(t)\right)\boldsymbol{\nu}_{\mathbf{r}}(t)\\ +\mathbf{D}\left(\boldsymbol{\nu}_{\mathbf{r}}(t)\right)\boldsymbol{\nu}_{\mathbf{r}}(t)+\mathbf{L}\left(\boldsymbol{\nu}_{\mathbf{r}}(t)\right)\boldsymbol{\nu}_{\mathbf{r}}(t)+\mathbf{g}\left(\boldsymbol{\eta}_{\mathbf{n}}(t)\right)=\boldsymbol{\tau}(t)\end{aligned} \tag{2.12}$$

The following properties exist for this body frame model.

$$\mathbf{M}_{\mathbf{RB}}=\mathbf{M}_{\mathbf{RB}}^{T}>\mathbf{0} \tag{2.54}$$

$$\mathbf{C}_{\mathbf{RB}}\left(\boldsymbol{\nu}_{\mathbf{b}}(t)\right)=-\mathbf{C}_{\mathbf{RB}}^{T}\left(\boldsymbol{\nu}_{\mathbf{b}}(t)\right)\forall\boldsymbol{\nu}_{\mathbf{b}}(t)\in\mathbb{R}^{6} \tag{2.55}$$

$$\mathbf{C}_{\mathbf{A}}\left(\boldsymbol{\nu}_{\mathbf{r}}(t)\right)=-\mathbf{C}_{\mathbf{A}}^{T}\left(\boldsymbol{\nu}_{\mathbf{r}}(t)\right)\forall\boldsymbol{\nu}_{\mathbf{r}}(t)\in\mathbb{R}^{6} \tag{2.56}$$

$$\mathbf{D}\left(\boldsymbol{\nu}_{\mathbf{r}}(t)\right)>\mathbf{0}\forall\boldsymbol{\nu}_{\mathbf{r}}(t)\in\mathbb{R}^{6} \tag{2.57}$$

(b) Complete Navigation Frame Model

To obtain water current in the navigation frame, the kinematic equation, Equation (2.1) of Section 2.2.1 is used. Transformation of the water current represented in the body frame to the navigation frame is achieved using:

$$\dot{\boldsymbol{\eta}}_{\mathbf{c}}(t)=\mathbf{J}\left(\boldsymbol{\eta}_{\mathbf{n}}(t)\right)\boldsymbol{\nu}_{\mathbf{c}}(t) \tag{2.58}$$

The relative velocity of the vehicle with respect to the water surrounding it, decomposed in the navigation frame, is expressed as:

$$\dot{\boldsymbol{\eta}}_{\mathbf{r}}(t)=\dot{\boldsymbol{\eta}}_{\mathbf{n}}(t)-\dot{\boldsymbol{\eta}}_{\mathbf{c}}(t)=\mathbf{J}\left(\boldsymbol{\eta}_{\mathbf{n}}(t)\right)\boldsymbol{\nu}_{\mathbf{r}}(t) \tag{2.59}$$

By transforming the various matrices of the body frame model, Equation (2.12), into the navigation frame using the kinematic equation, Equation (2.1), the model of the underwater vehicle is now decomposed in the navigation frame, and is expressed as:

$$\begin{aligned}\mathbf{M}_{\mathbf{RB}_\eta}\left(\boldsymbol{\eta}_\mathbf{n}(t)\right)\ddot{\boldsymbol{\eta}}_\mathbf{n}(t)+\mathbf{M}_{\mathbf{A}_\eta}\left(\boldsymbol{\eta}_\mathbf{n}(t)\right)\ddot{\boldsymbol{\eta}}_\mathbf{r}(t)+\mathbf{C}_{\mathbf{RB}_\eta}\left(\mathbf{v}_\mathbf{b}(t),\boldsymbol{\eta}_\mathbf{n}(t)\right)\dot{\boldsymbol{\eta}}_\mathbf{n}(t)\\+\mathbf{C}_{\mathbf{A}_\eta}\left(\mathbf{v}_\mathbf{r}(t),\boldsymbol{\eta}_\mathbf{n}(t)\right)\dot{\boldsymbol{\eta}}_\mathbf{r}(t)+\mathbf{D}_\eta\left(\mathbf{v}_\mathbf{r}(t),\boldsymbol{\eta}_\mathbf{n}(t)\right)\dot{\boldsymbol{\eta}}_\mathbf{r}(t)\\+\mathbf{L}_\eta\left(\mathbf{v}_\mathbf{r}(t),\boldsymbol{\eta}_\mathbf{n}(t)\right)\dot{\boldsymbol{\eta}}_\mathbf{r}(t)+\mathbf{g}_\eta\left(\boldsymbol{\eta}_\mathbf{n}(t)\right)=\boldsymbol{\tau}_\eta\left(\boldsymbol{\eta}_\mathbf{n}(t)\right)\end{aligned} \tag{2.60}$$

where

$$\begin{aligned}\mathbf{M}_{\mathbf{RB}_\eta}\left(\boldsymbol{\eta}_\mathbf{n}(t)\right)&=\mathbf{J}^{-T}\left(\boldsymbol{\eta}_\mathbf{n}(t)\right)\mathbf{M}_{\mathbf{RB}}\mathbf{J}^{-1}\left(\boldsymbol{\eta}_\mathbf{n}(t)\right)\\
\mathbf{M}_{\mathbf{A}_\eta}\left(\boldsymbol{\eta}_\mathbf{n}(t)\right)&=\mathbf{J}^{-T}\left(\boldsymbol{\eta}_\mathbf{n}(t)\right)\mathbf{M}_{\mathbf{A}}\mathbf{J}^{-1}\left(\boldsymbol{\eta}_\mathbf{n}(t)\right)\\
\mathbf{C}_{\mathbf{RB}_\eta}\left(\mathbf{v}_\mathbf{b}(t),\boldsymbol{\eta}_\mathbf{n}(t)\right)&=\mathbf{J}^{-T}\left(\boldsymbol{\eta}_\mathbf{n}(t)\right)\left[\mathbf{C}_{\mathbf{RB}}\left(\mathbf{v}_\mathbf{b}(t)\right)-\mathbf{M}_{\mathbf{RB}}\mathbf{J}^{-1}\left(\boldsymbol{\eta}_\mathbf{n}(t)\right)\dot{\mathbf{J}}\left(\boldsymbol{\eta}_\mathbf{n}(t)\right)\right]\mathbf{J}^{-1}\left(\boldsymbol{\eta}_\mathbf{n}(t)\right)\\
\mathbf{C}_{\mathbf{A}_\eta}\left(\mathbf{v}_\mathbf{r}(t),\boldsymbol{\eta}_\mathbf{n}(t)\right)&=\mathbf{J}^{-T}\left(\boldsymbol{\eta}_\mathbf{n}(t)\right)\left[\mathbf{C}_{\mathbf{A}}\left(\mathbf{v}_\mathbf{r}(t)\right)-\mathbf{M}_{\mathbf{A}}\mathbf{J}^{-1}\left(\boldsymbol{\eta}_\mathbf{n}(t)\right)\dot{\mathbf{J}}\left(\boldsymbol{\eta}_\mathbf{n}(t)\right)\right]\mathbf{J}^{-1}\left(\boldsymbol{\eta}_\mathbf{n}(t)\right)\\
\mathbf{D}_\eta\left(\mathbf{v}_\mathbf{r}(t),\boldsymbol{\eta}_\mathbf{n}(t)\right)&=\mathbf{J}^{-T}\left(\boldsymbol{\eta}_\mathbf{n}(t)\right)\mathbf{D}\left(\mathbf{v}_\mathbf{r}(t)\right)\mathbf{J}^{-1}\left(\boldsymbol{\eta}_\mathbf{n}(t)\right)\\
\mathbf{L}_\eta\left(\mathbf{v}_\mathbf{r}(t),\boldsymbol{\eta}_\mathbf{n}(t)\right)&=\mathbf{J}^{-T}\left(\boldsymbol{\eta}_\mathbf{n}(t)\right)\mathbf{L}\left(\mathbf{v}_\mathbf{r}(t)\right)\mathbf{J}^{-1}\left(\boldsymbol{\eta}_\mathbf{n}(t)\right)\\
\mathbf{g}_\eta\left(\boldsymbol{\eta}_\mathbf{n}(t)\right)&=\mathbf{J}^{-T}\left(\boldsymbol{\eta}_\mathbf{n}(t)\right)\mathbf{g}\left(\boldsymbol{\eta}_\mathbf{n}(t)\right)\\
\boldsymbol{\tau}_\eta\left(\boldsymbol{\eta}_\mathbf{n}(t)\right)&=\mathbf{J}^{-T}\left(\boldsymbol{\eta}_\mathbf{n}(t)\right)\boldsymbol{\tau}(t)\end{aligned}$$

The following properties exist for this navigation frame model.

$$\mathbf{M}_{\mathbf{RB}_\eta}\left(\boldsymbol{\eta}_\mathbf{n}(t)\right)=\mathbf{M}_{\mathbf{RB}_\eta}^{T}\left(\boldsymbol{\eta}_\mathbf{n}(t)\right)>\mathbf{0}\forall\boldsymbol{\eta}_\mathbf{n}(t)\in\mathbb{R}^6 \tag{2.61}$$

$$\begin{aligned}\mathbf{x}^T(t)\left[\dot{\mathbf{M}}_{\mathbf{RB}_\eta}\left(\boldsymbol{\eta}_\mathbf{n}(t)\right)-2\mathbf{C}_{\mathbf{RB}_\eta}\left(\mathbf{v}_\mathbf{b}(t),\boldsymbol{\eta}_\mathbf{n}(t)\right)\right]\mathbf{x}(t)=\mathbf{0}\\\forall\mathbf{x}(t)\in\mathbb{R}^6,\mathbf{v}_\mathbf{b}(t)\in\mathbb{R}^6,\boldsymbol{\eta}_\mathbf{n}(t)\in\mathbb{R}^6\end{aligned} \tag{2.62}$$

$$\begin{aligned}\mathbf{x}^T(t)\left[\dot{\mathbf{M}}_{\mathbf{A}_\eta}\left(\boldsymbol{\eta}_\mathbf{n}(t)\right)-2\mathbf{C}_{\mathbf{A}_\eta}\left(\mathbf{v}_\mathbf{r}(t),\boldsymbol{\eta}_\mathbf{n}(t)\right)\right]\mathbf{x}(t)=\mathbf{0}\\\forall\mathbf{x}(t)\in\mathbb{R}^6,\mathbf{v}_\mathbf{r}(t)\in\mathbb{R}^6,\boldsymbol{\eta}_\mathbf{n}(t)\in\mathbb{R}^6\end{aligned} \tag{2.63}$$

$$\mathbf{D}_\eta\left(\mathbf{v}_\mathbf{r}(t),\boldsymbol{\eta}_\mathbf{n}(t)\right)>\mathbf{0}\forall\mathbf{v}_\mathbf{r}(t)\in\mathbb{R}^6,\boldsymbol{\eta}_\mathbf{n}(t)\in\mathbb{R}^6 \tag{2.64}$$

The complete navigation frame model, Equation (2.60), is illustrated in Figure 2.14.

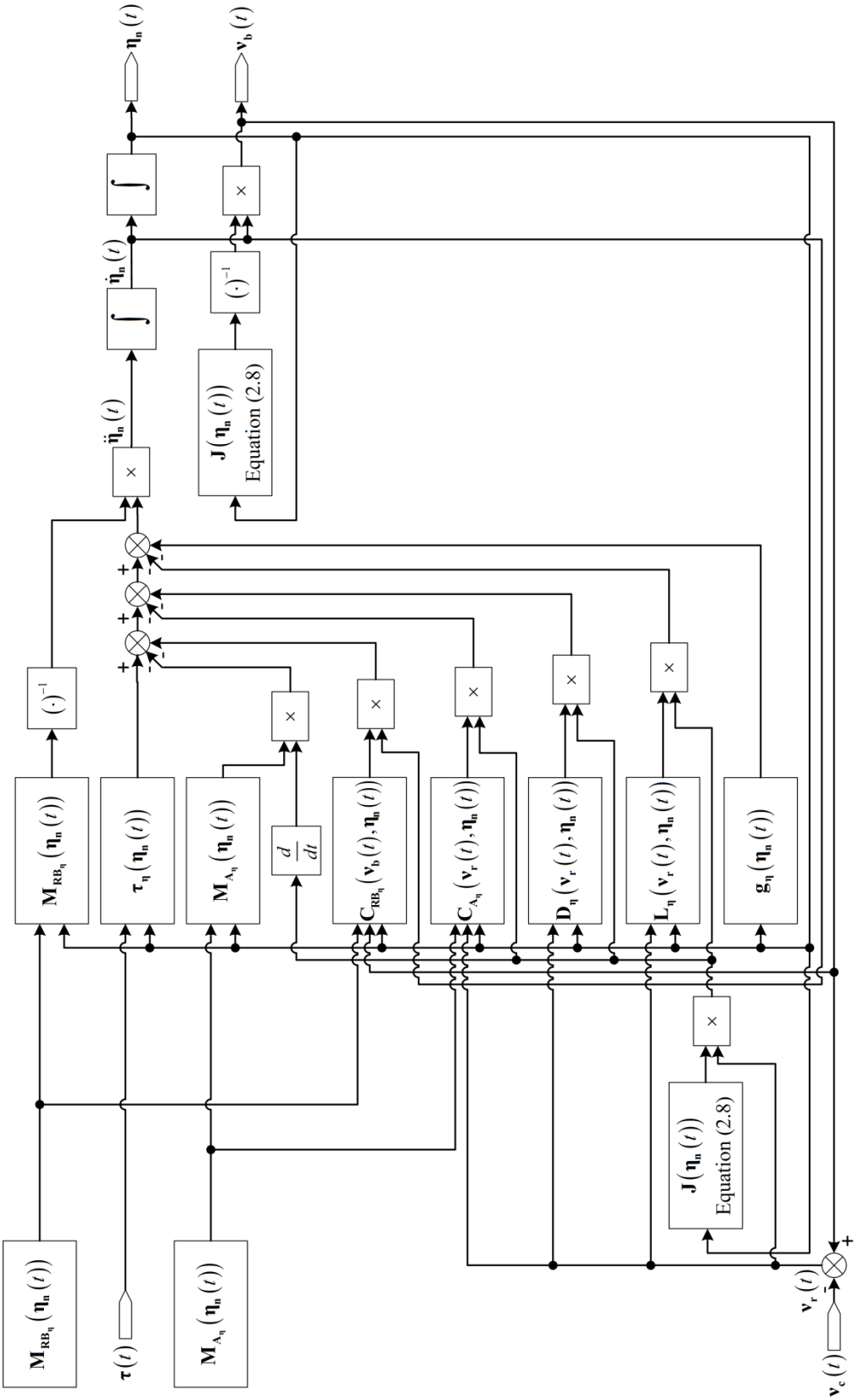

Figure 2.14: Complete Navigation Frame Model

(c) Model Frame Transformation

As can be seen from the previous section, the complete navigation frame model is obtained by transforming the various matrices within the complete body frame model to the navigation frame using the kinematic equation, Equation (2.1). The complete body frame model can also be obtained by transforming the various matrices within the complete navigation frame model using the inverse of the kinematic equation, Equation (2.11). Hence, both of these models are equivalent from a behavioural perspective, and either can be used depending on the particular situation. The transformation of the model from one frame to the other is illustrated in Figure 2.15.

2.2.3. Plant Model

In this thesis, the model used to represent a true AUV for case study purposes is based on the REMUS 100 AUV as outlined in Appendix A. This model has been widely used for simulation purposes. For example, Pan and Xin [60] used this model for the simulation of a robust depth controller, while Lammas *et al* [20, 61] used this model for the simulation of various navigation filters.

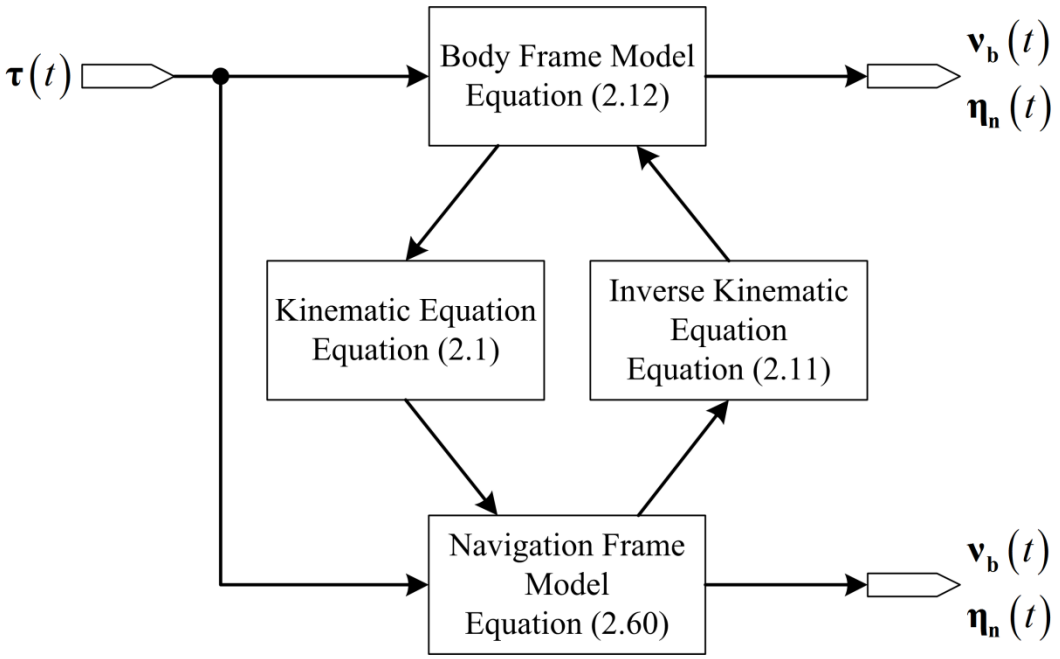

Figure 2.15: Transforming Body Frame Model to Navigation Frame Model, and Vice Versa

A vehicle of this configuration is restricted in its manoeuvring ability primarily due to gravitational and buoyancy forces. It is noted in Appendix A that firstly the weight of the vehicle is 299.0088 N while the buoyancy of the vehicle is 306 N, and secondly the centre of gravity is 0.0196 m below the centre of buoyancy. By observation of the gravitational and buoyancy forces vector of Equation (2.53), this configuration will not only apply significant moments to the vehicle for large roll and pitch angles, the net difference in weight and buoyancy will also apply a constant force of 6.9912 N to the vehicle, directed towards the surface of the water. Under these circumstances, the manoeuvrability and/or efficiency of the vehicle will be considerably restricted as the actuators are continually fighting against these forces and moments.

The aim of this simulation study is the control of highly manoeuvrable underwater vehicles. Therefore, the following modifications are made to the REMUS 100 AUV model used for simulation purposes.

1. The buoyancy of the vehicle is equal to the weight of the vehicle;
2. The centre of buoyancy coincides with the centre of gravity.

By applying these two facts to Equation (2.53), the gravitational and buoyancy forces vector becomes a zero vector, and hence the manoeuvrability of the vehicle is greatly increased. A summary of all the parameters used in the kinetic equation of the plant model, including the modifications made, are contained in Section A.1.1 of Appendix A.

Full Model of the REMUS 100 AUV for Simulation Purposes

Subject to these modifications, the following body frame model is obtained for simulation purposes.

(a) Body Frame Simulation Model – Algorithm 2.1

$$\begin{aligned}\mathbf{M}_{\mathbf{RB}}\dot{\mathbf{v}}_{\mathbf{b}}(t)+\mathbf{M}_{\mathbf{A}}\dot{\mathbf{v}}_{\mathbf{r}}(t)+\mathbf{C}_{\mathbf{RB}}\left(\mathbf{v}_{\mathbf{b}}(t)\right)\mathbf{v}_{\mathbf{b}}(t)+\mathbf{C}_{\mathbf{A}}\left(\mathbf{v}_{\mathbf{r}}(t)\right)\mathbf{v}_{\mathbf{r}}(t)\\ +\mathbf{D}\left(\mathbf{v}_{\mathbf{r}}(t)\right)\mathbf{v}_{\mathbf{r}}(t)+\mathbf{L}\left(\mathbf{v}_{\mathbf{r}}(t)\right)\mathbf{v}_{\mathbf{r}}(t)=\boldsymbol{\tau}(t)\end{aligned} \tag{2.65}$$

This body frame model is illustrated in Figure 2.16.

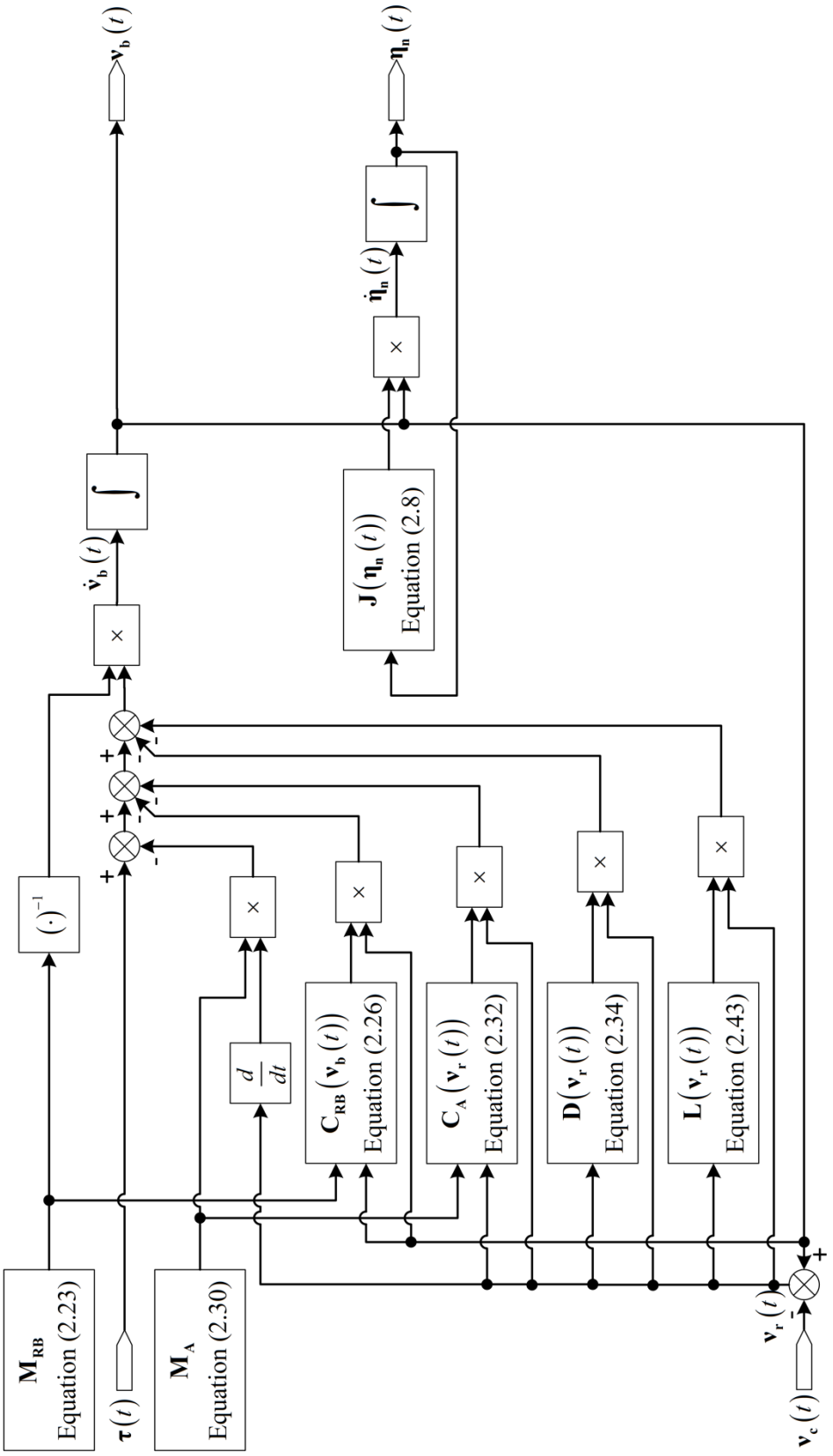

Figure 2.16: Body Frame Simulation Model

2.3. Models for Controller Design

The complete body frame model of Equation (2.12) and the complete navigation frame model of Equation (2.60) both show that the equations representing the mathematical model of an underwater vehicle are highly nonlinear and complex. Therefore, the design of a compensator for such a model would also be complex, or possibly infeasible. To aid in this design process, certain assumptions can be made such that the model is simplified. The design of the compensator is then based on this simplified model instead of the original complex model.

The following sections outline simplifications that are commonly applied to underwater vehicles such that compensators for these vehicles can be realised. The outline of this simplification process is illustrated in Figure 2.17 where the true plant model is first obtained from the physical vehicle. Following, different sets of assumptions are applied to this true plant model such that simplified models are obtained for compensator design purposes.

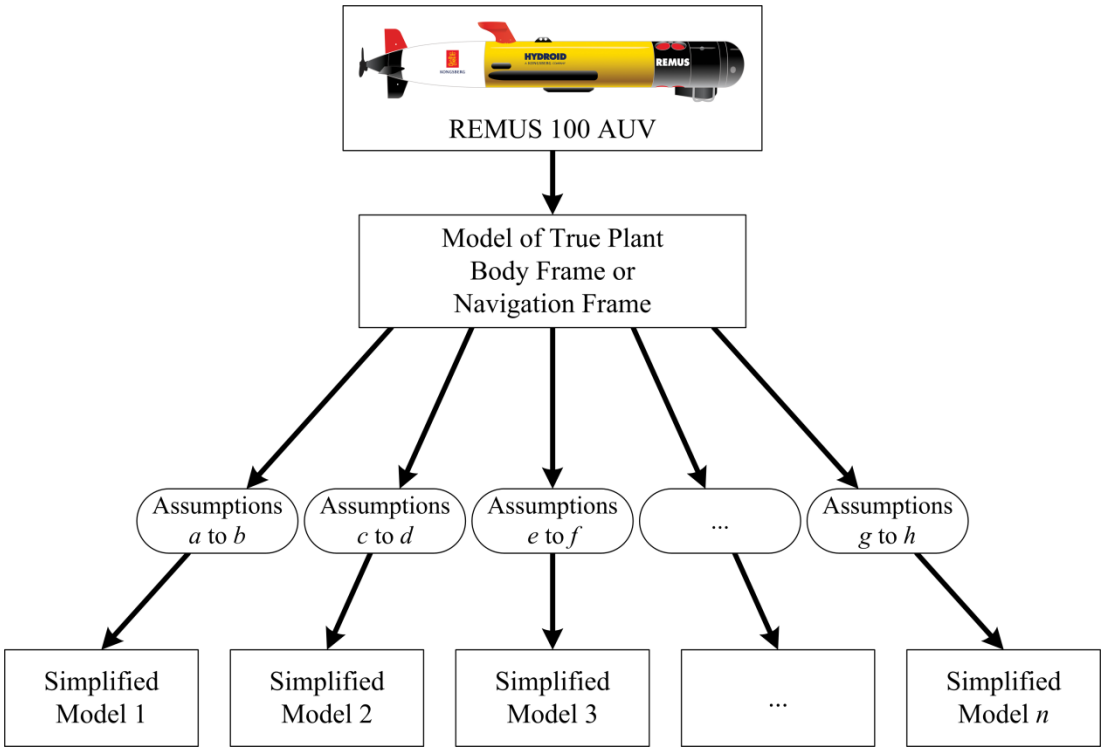

Figure 2.17: Simplified Models

This simplification process will first assume that the fluid the vehicle is moving through is ideal, while also being stationary. This will be followed by assumptions based on maximising the manoeuvrability of the vehicle. Next, assumptions are made regarding the sparsity of the system inertia and hydrodynamic drag matrices, particularly the off-diagonal elements, such that coupling between DoFs are removed. Following is a simplification based on the assumption that the vehicle velocity decomposed in the body frame is the same as the vehicle velocity decomposed in the navigation frame. Finally, a process of linearisation is applied to the model such that a linear model is obtained from the nonlinear model.

2.3.1. Simplified Model 1

As an initial step in deriving a simplified model, assumptions are made regarding certain hydrodynamics. For this simplified model, both lift forces and external current disturbances are ignored, while the added mass matrix is assumed to be positive definite. These three assumptions are detailed as follows:

Assumption 1: $\mathbf{L}\left(\mathbf{v}_{\mathbf{r}}\left(t\right)\right)=\mathbf{0}$

Both hydrodynamic damping forces and hydrodynamic lift forces are due to fluid flow around an object, with damping forces being parallel to this direction of flow and lift forces being perpendicular to this direction of flow. During a typical mission, the underwater vehicle body's angle of attack (AoA) will be zero for the vast majority of manoeuvring, and when this occurs, lift forces will be zero. It has previously been assumed that lift forces on the body of an underwater vehicle are negligible, particularly for the relatively low velocities experienced by AUVs [57], or that the lift forces are assumed to be incorporated into the damping forces matrix [23, 56].

Assumption 2: $\mathbf{v}_{\mathbf{c}}\left(t\right)=\mathbf{0}$

By assuming there are no currents influencing the motion of the vehicle [55, 62], both the body frame model, Equation (2.12), and the navigation frame model, Equation (2.60), can be significantly simplified. This is due to $\mathbf{v}_{\mathbf{r}}\left(t\right)=\mathbf{v}_{\mathbf{b}}\left(t\right)$ and $\dot{\boldsymbol{\eta}}_{\mathbf{r}}\left(t\right)=\dot{\boldsymbol{\eta}}_{\mathbf{n}}\left(t\right)$ when $\mathbf{v}_{\mathbf{c}}\left(t\right)=\mathbf{0}$.

Assumption 3: $\mathbf{M}_{\mathbf{A}} = \mathbf{M}_{\mathbf{A}}^{T} > 0$

Fossen [2, 3] states that the added mass matrix is positive definite under the assumption that the fluid is ideal, there are no waves or currents affecting the vehicle and that the vehicle is at rest. However, Fossen also states that $\mathbf{M}_{\mathbf{A}} = \mathbf{M}_{\mathbf{A}}^{T} > 0$ is a good approximation even if the assumption of an ideal fluid is relaxed. Furthermore, for underwater vehicles operating at sufficient depth, the assumptions of matrix symmetry and frequency independence are reasonable. The assumption of $\mathbf{M}_{\mathbf{A}} = \mathbf{M}_{\mathbf{A}}^{T} > 0$ has previously been used when both analysing the equations of motion of an AUV [59] and in the synthesis of controllers for underwater vehicles [63].

Navigation Frame Simplified Model 1 – Algorithm 2.2

Subject to Assumption 1 through to Assumption 3, the complete navigation frame model of Equation (2.60) can be simplified as follows [2].

$$\begin{aligned}\mathbf{M}_{\boldsymbol{\eta}}\left(\boldsymbol{\eta}_{\mathbf{n}}(t)\right)\ddot{\boldsymbol{\eta}}_{\mathbf{n}}(t) + \mathbf{C}_{\boldsymbol{\eta}}\left(\mathbf{v}_{\mathbf{b}}(t), \boldsymbol{\eta}_{\mathbf{n}}(t)\right)\dot{\boldsymbol{\eta}}_{\mathbf{n}}(t) \\ + \mathbf{D}_{\boldsymbol{\eta}}\left(\mathbf{v}_{\mathbf{b}}(t), \boldsymbol{\eta}_{\mathbf{n}}(t)\right)\dot{\boldsymbol{\eta}}_{\mathbf{n}}(t) + \mathbf{g}_{\boldsymbol{\eta}}\left(\boldsymbol{\eta}_{\mathbf{n}}(t)\right) = \boldsymbol{\tau}_{\boldsymbol{\eta}}\left(\boldsymbol{\eta}_{\mathbf{n}}(t)\right)\end{aligned} \tag{2.66}$$

where

$$\begin{aligned}\mathbf{M}_{\boldsymbol{\eta}}\left(\boldsymbol{\eta}_{\mathbf{n}}(t)\right) &= \mathbf{J}^{-T}\left(\boldsymbol{\eta}_{\mathbf{n}}(t)\right)\mathbf{M}\mathbf{J}^{-1}\left(\boldsymbol{\eta}_{\mathbf{n}}(t)\right) \\ \mathbf{C}_{\boldsymbol{\eta}}\left(\mathbf{v}_{\mathbf{b}}(t), \boldsymbol{\eta}_{\mathbf{n}}(t)\right) &= \mathbf{J}^{-T}\left(\boldsymbol{\eta}_{\mathbf{n}}(t)\right)\left[\mathbf{C}\left(\mathbf{v}_{\mathbf{b}}(t)\right) - \mathbf{M}\mathbf{J}^{-1}\left(\boldsymbol{\eta}_{\mathbf{n}}(t)\right)\dot{\mathbf{J}}\left(\boldsymbol{\eta}_{\mathbf{n}}(t)\right)\right]\mathbf{J}^{-1}\left(\boldsymbol{\eta}_{\mathbf{n}}(t)\right) \\ \mathbf{D}_{\boldsymbol{\eta}}\left(\mathbf{v}_{\mathbf{b}}(t), \boldsymbol{\eta}_{\mathbf{n}}(t)\right) &= \mathbf{J}^{-T}\left(\boldsymbol{\eta}_{\mathbf{n}}(t)\right)\mathbf{D}\left(\mathbf{v}_{\mathbf{b}}(t)\right)\mathbf{J}^{-1}\left(\boldsymbol{\eta}_{\mathbf{n}}(t)\right) \\ \mathbf{g}_{\boldsymbol{\eta}}\left(\boldsymbol{\eta}_{\mathbf{n}}(t)\right) &= \mathbf{J}^{-T}\left(\boldsymbol{\eta}_{\mathbf{n}}(t)\right)\mathbf{g}\left(\boldsymbol{\eta}_{\mathbf{n}}(t)\right) \\ \boldsymbol{\tau}_{\boldsymbol{\eta}}\left(\boldsymbol{\eta}_{\mathbf{n}}(t)\right) &= \mathbf{J}^{-T}\left(\boldsymbol{\eta}_{\mathbf{n}}(t)\right)\boldsymbol{\tau}(t)\end{aligned}$$

The parameters for this model are contained within Appendix A.

The following properties exist for this navigation frame model.

$$\mathbf{M}_{\boldsymbol{\eta}}\left(\boldsymbol{\eta}_{\mathbf{n}}(t)\right) = \mathbf{M}_{\mathbf{RB}_{\boldsymbol{\eta}}}\left(\boldsymbol{\eta}_{\mathbf{n}}(t)\right) + \mathbf{M}_{\mathbf{A}_{\boldsymbol{\eta}}}\left(\boldsymbol{\eta}_{\mathbf{n}}(t)\right) \tag{2.67}$$

$$\mathbf{M}_{\boldsymbol{\eta}}\left(\boldsymbol{\eta}_{\mathbf{n}}(t)\right) = \mathbf{M}_{\boldsymbol{\eta}}^{T}\left(\boldsymbol{\eta}_{\mathbf{n}}(t)\right) > \mathbf{0} \forall \boldsymbol{\eta}_{\mathbf{n}}(t) \in \mathbb{R}^{6} \tag{2.68}$$

$$\mathbf{x}^T(t)\left[\dot{\mathbf{M}}_{\eta}\left(\boldsymbol{\eta}_n(t)\right)-2\mathbf{C}_{\eta}\left(\mathbf{v}_b(t),\boldsymbol{\eta}_n(t)\right)\right]\mathbf{x}(t)=\mathbf{0} \quad \forall \mathbf{x}(t)\in\mathbb{R}^6,\mathbf{v}_b(t)\in\mathbb{R}^6,\boldsymbol{\eta}_n(t)\in\mathbb{R}^6 \tag{2.69}$$

$$\mathbf{D}_{\eta}\left(\mathbf{v}_b(t),\boldsymbol{\eta}_n(t)\right)>\mathbf{0}\forall\mathbf{v}_b(t)\in\mathbb{R}^6,\boldsymbol{\eta}_n(t)\in\mathbb{R}^6 \tag{2.70}$$

Equation (2.66) has been previously used for modelling and control purposes [53, 56].

This simplified model is highlighted in Figure 2.18 and the corresponding navigation frame model, Equation (2.66), is illustrated in Figure 2.19.

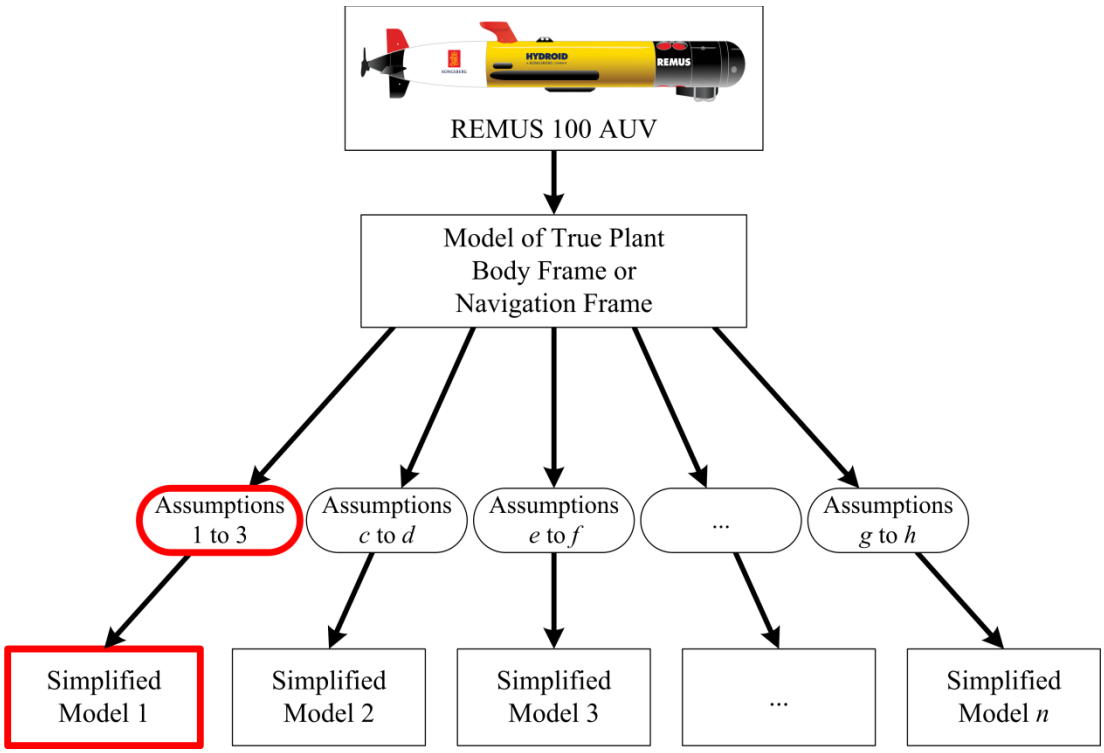

Figure 2.18: Simplified Models, Model 1 Highlighted

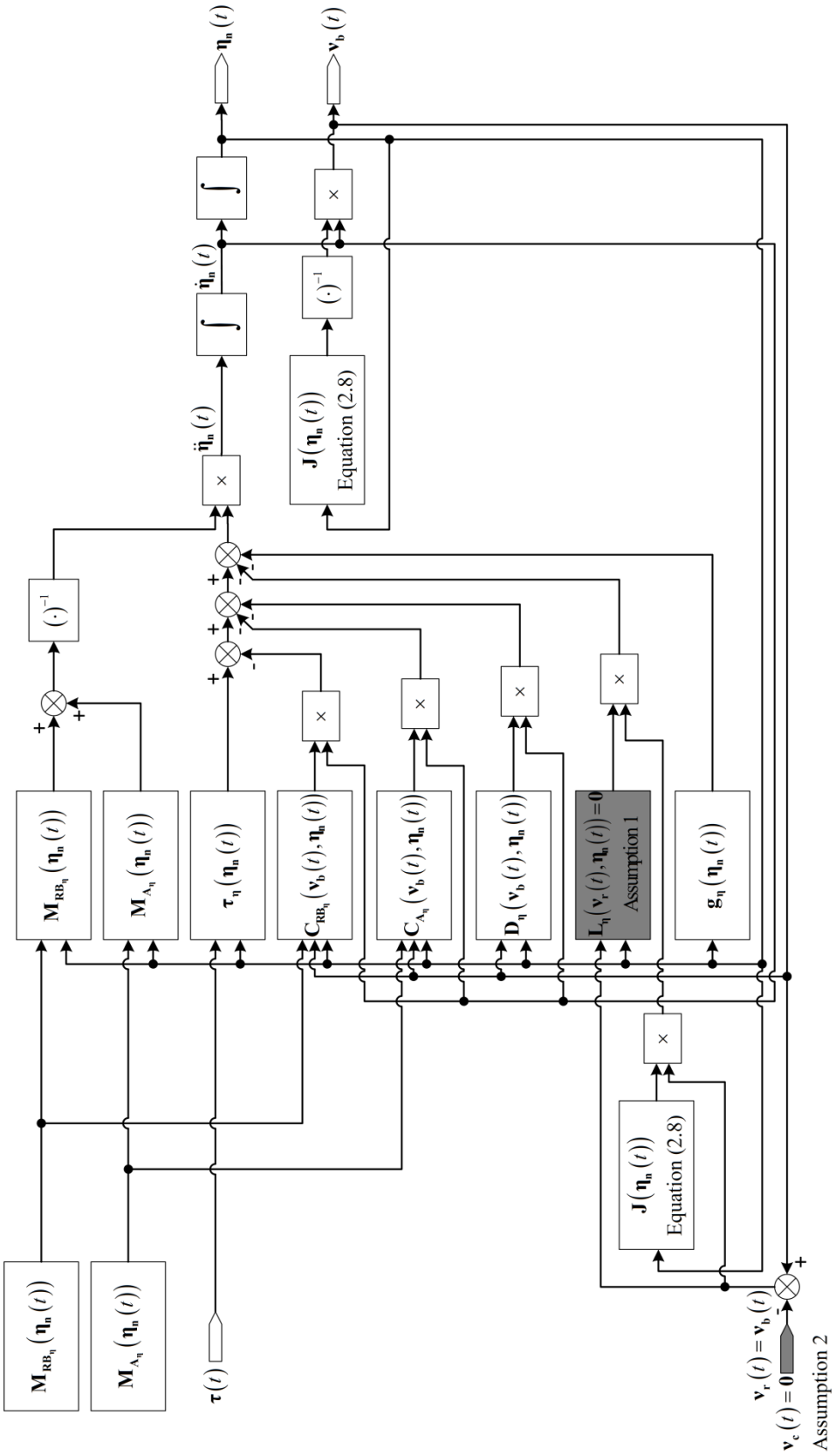

Figure 2.19: Navigation Frame Simplified Model 1

2.3.2. Simplified Model 2

The gravitational and buoyancy forces and moments vector plays a significant role in determining the ease in which large roll and pitch angles of the vehicle are obtained. Therefore, this vector has a substantial impact on the overall manoeuvrability of the vehicle. If the vehicle is designed such that maximum manoeuvrability is desired, it is common to make the following two assumptions.

Assumption 4: $W = B$

By assuming the weight of the vehicle and the buoyancy of the vehicle are equal in magnitude [27, 28, 41, 64-69], there will be no net force on the vehicle either pulling it towards the centre of the Earth, or pushing it away from the centre of the Earth. Instead, there will only be a net moment applied to the attitude of the vehicle such that the centre of gravity is aligned directly below the centre of buoyancy.

Hence,

$$\mathbf{g}\left(\boldsymbol{\eta}_{\mathbf{n}}\left(t\right)\right)=\begin{bmatrix} 0 \\ 0 \\ 0 \\ -W\left(y_g^b-y_b^b\right)\cos\theta_n\left(t\right)\cos\phi_n\left(t\right)+W\left(z_g^b-z_b^b\right)\cos\theta_n\left(t\right)\sin\phi_n\left(t\right) \\ W\left(z_g^b-z_b^b\right)\sin\theta_n\left(t\right)+W\left(x_g^b-x_b^b\right)\cos\theta_n\left(t\right)\cos\phi_n\left(t\right) \\ -W\left(x_g^b-x_b^b\right)\cos\theta_n\left(t\right)\sin\phi_n\left(t\right)-W\left(y_g^b-y_b^b\right)\sin\theta_n\left(t\right) \end{bmatrix}$$

Assumption 5: $\mathbf{r}_{\mathbf{g}}^{\mathbf{b}}=\mathbf{r}_{\mathbf{b}}^{\mathbf{b}}=\mathbf{0}$

If the vehicle's centre of buoyancy and centre of gravity is coincident with the origin of the body frame [63, 64, 69], there will be no moment applied to the vehicle due to the gravitational and buoyancy forces vector. Instead, there will only be a net force either pulling the vehicle towards the centre of the Earth or pushing the vehicle away from the centre of the Earth, depending on if the weight or buoyancy is greater. Hence,

$$\mathbf{g}\left(\boldsymbol{\eta}_{\mathbf{n}}\left(t\right)\right)=\begin{bmatrix}\left(W-B\right)\sin\theta_n\left(t\right)\\ -\left(W-B\right)\cos\theta_n\left(t\right)\sin\phi_n\left(t\right)\\ -\left(W-B\right)\cos\theta_n\left(t\right)\cos\phi_n\left(t\right)\\ 0\\ 0\\ 0\end{bmatrix}$$

Application of both Assumption 4 and Assumption 5 results in the gravitational and buoyancy forces vector of Equation (2.53) simplifying to a zero vector, regardless of the attitude of the vehicle. Therefore,

$$\mathbf{g}\left(\boldsymbol{\eta}_{\mathbf{n}}\left(t\right)\right)=\mathbf{0}\forall\boldsymbol{\eta}_{\mathbf{n}}\left(t\right)\in\mathbb{R}^6$$

This assumption of $\mathbf{g}\left(\boldsymbol{\eta}_{\mathbf{n}}\left(t\right)\right)=\mathbf{0}$ has previously been used when designing controllers for highly manoeuvrable underwater vehicles [41, 64, 66, 68, 70].

Body Frame Simplified Model 2 – Algorithm 2.3

Subject to Assumption 1 through to Assumption 5, the complete body frame model of Equation (2.12) can be simplified as follows.

$$\mathbf{M}\dot{\boldsymbol{\nu}}_{\mathbf{b}}\left(t\right)+\mathbf{C}\left(\boldsymbol{\nu}_{\mathbf{b}}\left(t\right)\right)\boldsymbol{\nu}_{\mathbf{b}}\left(t\right)+\mathbf{D}\left(\boldsymbol{\nu}_{\mathbf{b}}\left(t\right)\right)\boldsymbol{\nu}_{\mathbf{b}}\left(t\right)=\boldsymbol{\tau}\left(t\right)\tag{2.71}$$

The parameters for this model are contained within Appendix A.

Although it is not obvious from Equation (2.71), by taking into account Assumption 3, $\mathbf{M}_{\mathbf{A}}=\mathbf{M}_{\mathbf{A}}^{T}$, the following properties exist for this body frame model.

$$\mathbf{M}=\mathbf{M}_{\mathbf{RB}}+\mathbf{M}_{\mathbf{A}}\tag{2.72}$$

$$\mathbf{M}=\mathbf{M}^{T}>\mathbf{0}\tag{2.73}$$

$$\mathbf{C}\left(\boldsymbol{\nu}_{\mathbf{b}}\left(t\right)\right)=\mathbf{C}_{\mathbf{RB}}\left(\boldsymbol{\nu}_{\mathbf{b}}\left(t\right)\right)+\mathbf{C}_{\mathbf{A}}\left(\boldsymbol{\nu}_{\mathbf{b}}\left(t\right)\right)=-\mathbf{C}^{T}\left(\boldsymbol{\nu}_{\mathbf{b}}\left(t\right)\right)\forall\boldsymbol{\nu}_{\mathbf{b}}\left(t\right)\in\mathbb{R}^6\tag{2.74}$$

$$\mathbf{D}\left(\boldsymbol{\nu}_{\mathbf{b}}\left(t\right)\right)>\mathbf{0}\forall\boldsymbol{\nu}_{\mathbf{b}}\left(t\right)\in\mathbb{R}^6\tag{2.75}$$

Equation (2.71) has been previously used for modelling and control purposes [68].

This simplified model is highlighted in Figure 2.20 and the corresponding body frame model, Equation (2.71), is illustrated in Figure 2.21.

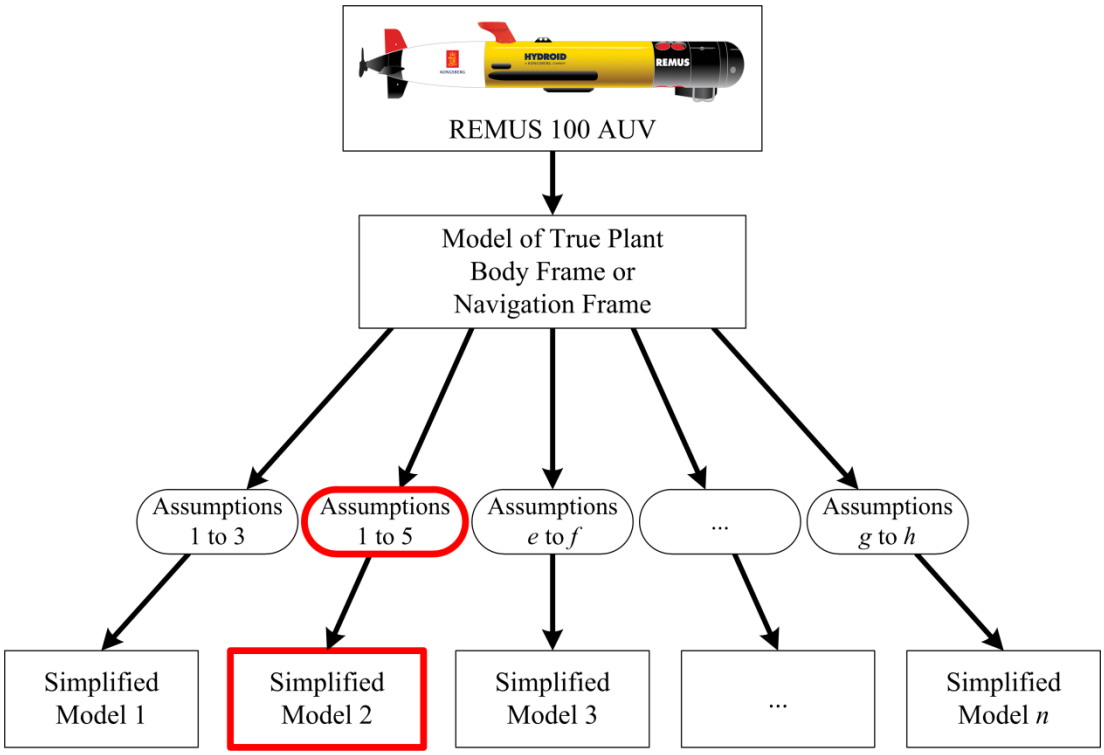

Figure 2.20: Simplified Models, Model 2 Highlighted

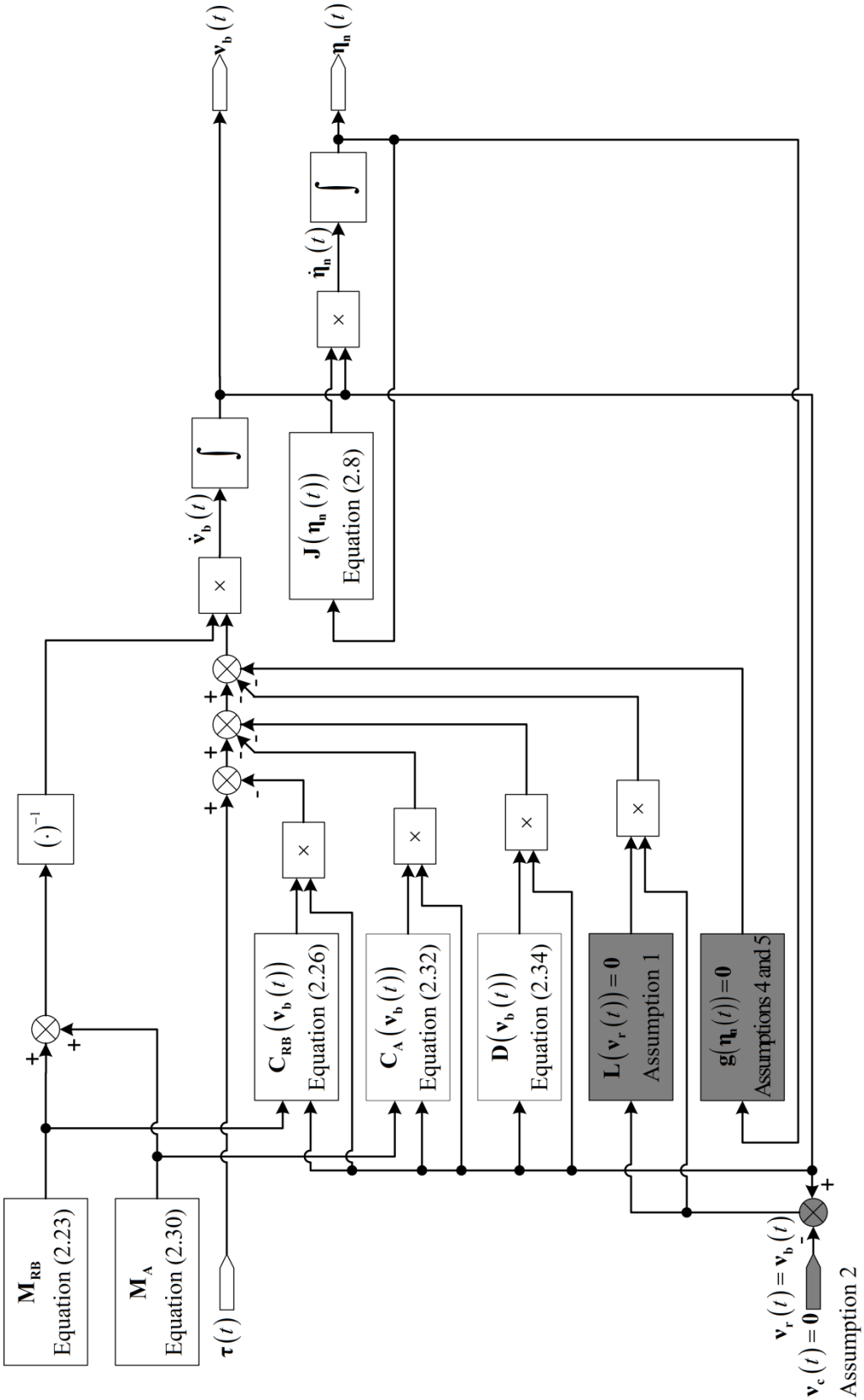

Figure 2.21: Body Frame Simplified Model 2

2.3.3. Simplified Model 3

A further simplification of the model is to decouple the model. This decoupling is achieved by ignoring all elements of the various matrices that are not on the main diagonal. By doing this, all interaction between DoFs is removed, and hence an uncoupled model is produced. Fossen [2, 53] made the following assumptions when designing a sliding mode controller for an underwater vehicle.

Assumption 6: $\mathbf{D}_{\mathbf{l}} = \mathbf{0}$

By assuming there is no linear damping, the hydrodynamic damping forces simplifies by becoming purely nonlinear, i.e., $\mathbf{D}\left(\mathbf{v}_{\mathbf{b}}(t)\right) = \mathbf{D}_{\mathbf{n}}\left(\mathbf{v}_{\mathbf{b}}(t)\right)$.

Assumption 7: $\mathbf{M}$ and $\mathbf{D}\left(\mathbf{v}_{\mathbf{b}}(t)\right)$ are Diagonal

For all matrices of the body frame model of Equation (2.12), all non-zero elements that are not on the main diagonal represent coupling between DoFs. By assuming all the off diagonal elements of the matrices are zero, the system is uncoupled as the matrices of the system are now diagonal matrices. For example, both the system inertia matrix and the damping matrix are reduced to diagonal matrices; hence, no coupling exists within these matrices. Furthermore, the Coriolis and centripetal forces matrix is ignored under this assumption as it is a skew-symmetric matrix, and as such, the main diagonal elements are all zero.

Not only has this assumption been used by Fossen [2, 53], it has also been used by, for example, Evers et al. [57], Jeon et al. [62] and Xu and Zhang [38].

Body Frame Simplified Model 3 – Algorithm 2.4

Subject to Assumption 1 through to Assumption 7, the complete body frame model of Equation (2.12) can be simplified as follows, where both $\mathbf{M}$ and $\mathbf{D}\left(\mathbf{v}_{\mathbf{b}}(t)\right)$ are diagonal matrices.

$$\mathbf{M}\dot{\mathbf{v}}_{\mathbf{b}}(t) + \mathbf{D}\left(\mathbf{v}_{\mathbf{b}}(t)\right)\mathbf{v}_{\mathbf{b}}(t) = \boldsymbol{\tau}(t) \tag{2.76}$$

The parameters for this model are contained within Appendix A.

The following properties exist for this body frame model.

$$\mathbf{M} = \mathbf{M}^T > \mathbf{0} \tag{2.77}$$

$$\mathbf{D}\left(\mathbf{v_b}\left(t\right)\right) = \mathbf{D}^T\left(\mathbf{v_b}\left(t\right)\right) > \mathbf{0} \forall \mathbf{v_b}\left(t\right) \in \mathbb{R}^6 \tag{2.78}$$

This simplified model is highlighted in Figure 2.22 and the corresponding body frame model, Equation (2.76), is illustrated in Figure 2.23.

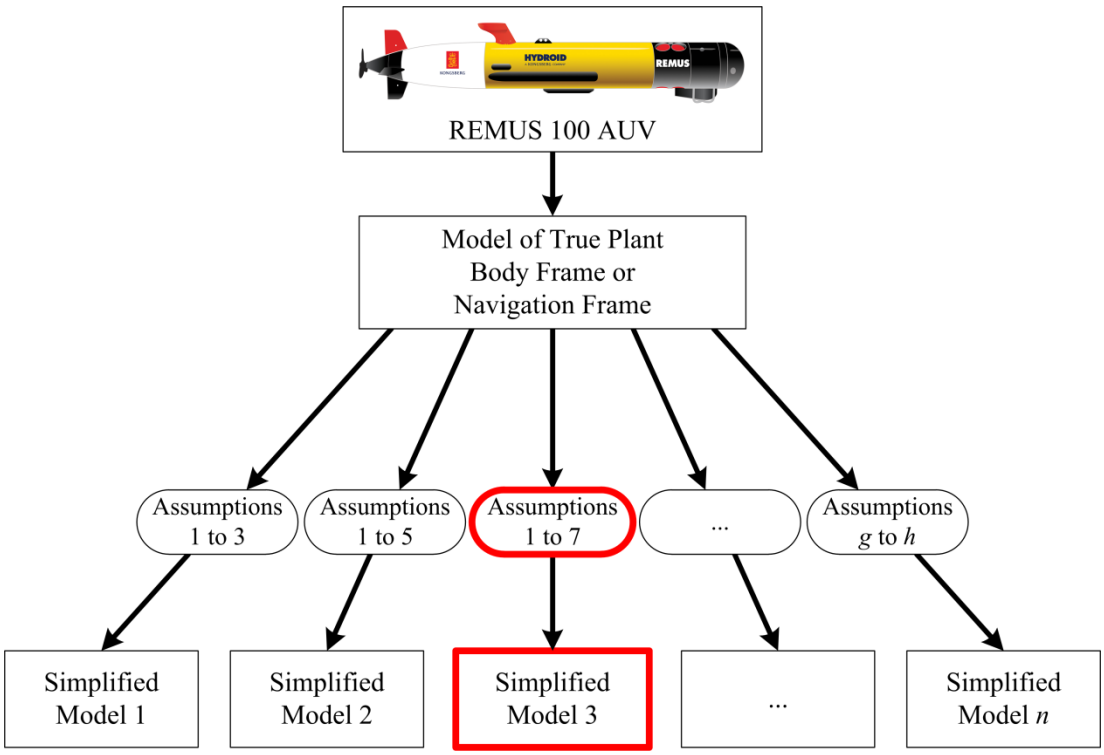

Figure 2.22: Simplified Models, Model 3 Highlighted

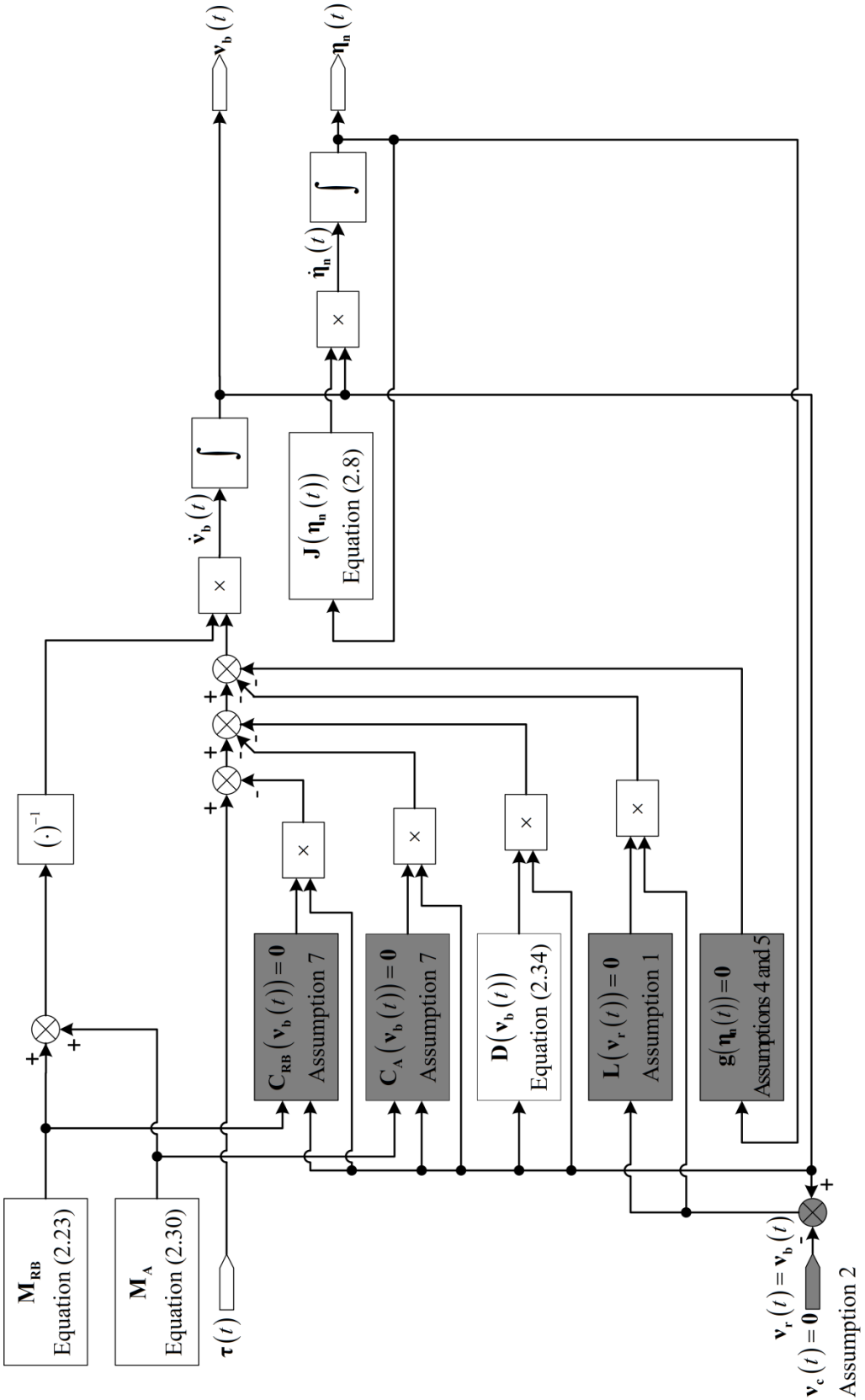

Figure 2.23: Body Frame Simplified Model 3

2.3.4. Simplified Model 4

To this point, all the simplified models retain the behaviour of the body frame rotating within the navigation frame. By removing this behaviour, the vehicle model is significantly simplified, as there is no need to transform information from one frame to another. Fossen [2, 53] made the following assumption when designing a sliding mode controller for an underwater vehicle.

Assumption 8: $\dot{\boldsymbol{\eta}}_{\mathbf{n}}(t) = \mathbf{v}_{\mathbf{b}}(t)$ [2, 53]

If the body frame does not rotate within the navigation frame, and it is initially aligned with the navigation frame, then $\mathbf{J}\left(\boldsymbol{\eta}_{\mathbf{n}}(t)\right) = \mathbf{I} \forall \boldsymbol{\eta}_{\mathbf{n}}(t) \in \mathbb{R}^6$ and hence $\dot{\boldsymbol{\eta}}_{\mathbf{n}}(t) = \mathbf{v}_{\mathbf{b}}(t)$.

Body Frame Simplified Model 4 – Algorithm 2.5

Subject to Assumption 1 through to Assumption 8, the complete body frame model of Equation (2.12) can be simplified as follows.

$$\mathbf{M}\dot{\mathbf{v}}_{\mathbf{b}}(t) + \mathbf{D}\left(\mathbf{v}_{\mathbf{b}}(t)\right)\mathbf{v}_{\mathbf{b}}(t) = \mathbf{M}\ddot{\boldsymbol{\eta}}_{\mathbf{n}}(t) + \mathbf{D}\left(\dot{\boldsymbol{\eta}}_{\mathbf{n}}(t)\right)\dot{\boldsymbol{\eta}}_{\mathbf{n}}(t) = \boldsymbol{\tau}(t) \tag{2.79}$$

The parameters for this model are contained within Appendix A.

Equation (2.79) has previously been used for modelling and control purposes [2, 53].

This simplified model is highlighted in Figure 2.24 and the corresponding body frame model, Equation (2.79), is illustrated in Figure 2.25.

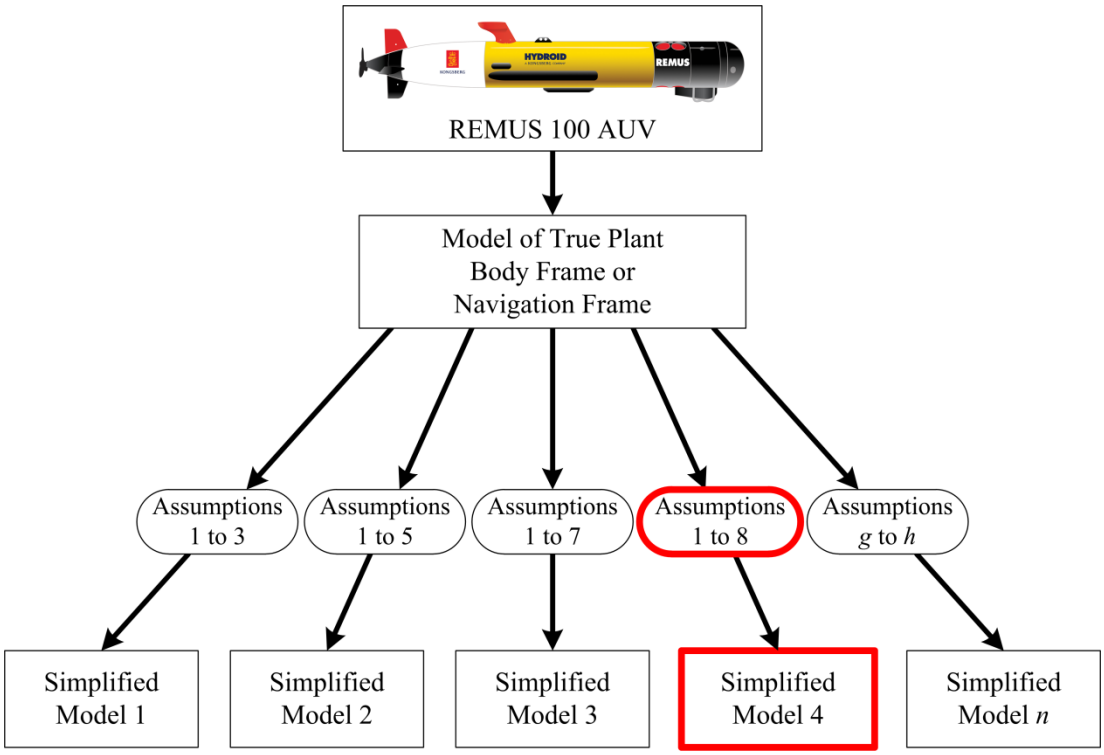

Figure 2.24: Simplified Models, Model 4 Highlighted

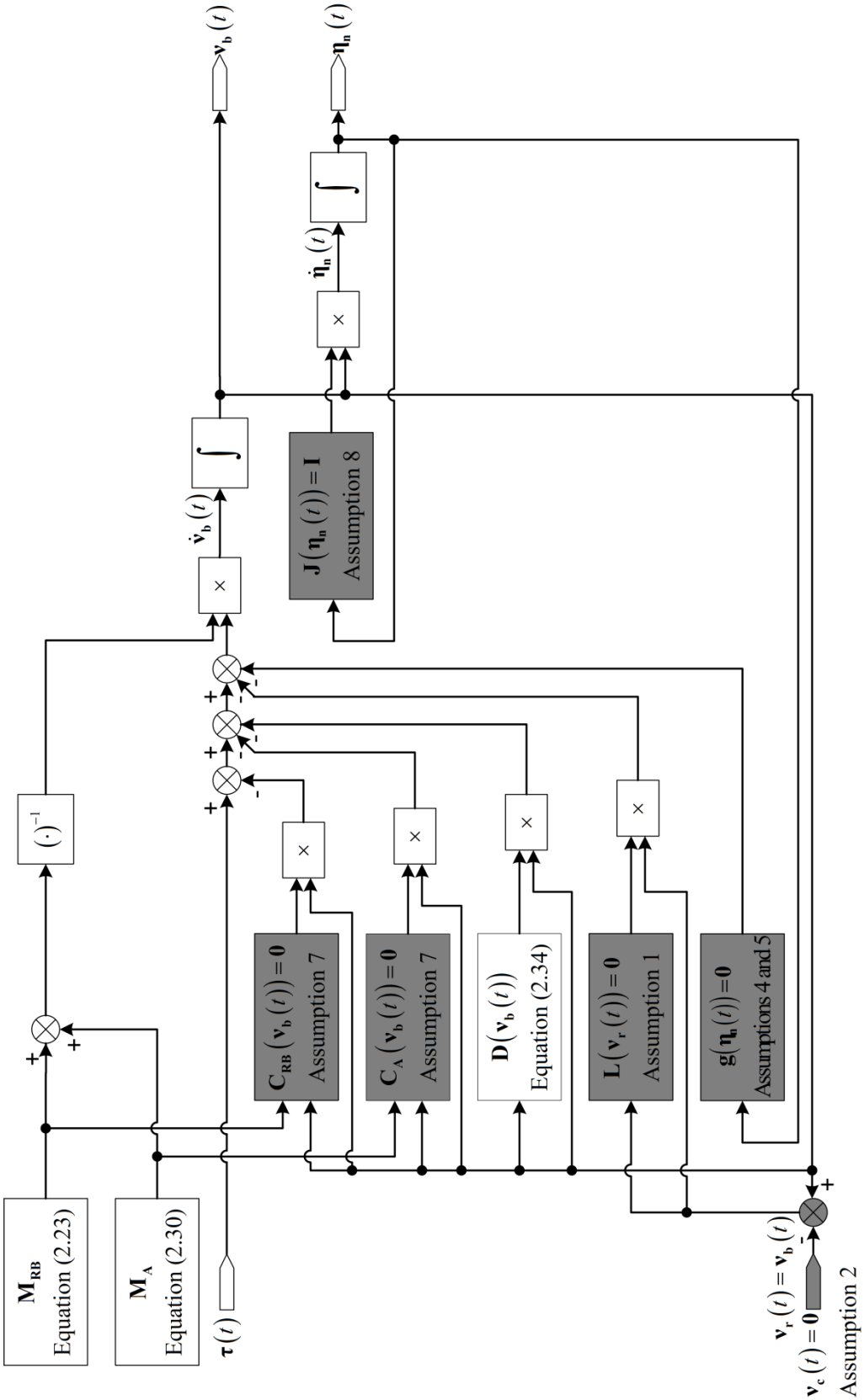

Figure 2.25: Body Frame Model 4

2.3.5. Simplified Model 5

All the simplified models derived to this point retain at least some nonlinearities of the complete model. For the application of a linear controller, such as PID control, to a nonlinear plant, a linearised model is required. In order to obtain a linearised model, a linearisation point consisting of a fixed set of states and a fixed input must be selected. At this linearisation point, the linearised model will be an accurate approximation to the nonlinear model. However, the further away from the linearisation point the linear model is pushed, the worse the approximation becomes.

Simplified Model 5 – Algorithm 2.6

This linearised system is highlighted in Figure 2.26. A state-space representation (SSR) of the linearised model for a nonlinear system, expressed as:

$$\begin{aligned}\dot{\mathbf{X}}(t) &= \mathbf{A}\mathbf{X}(t) + \mathbf{B}\mathbf{u}(t) \\ \mathbf{y}(t) &= \mathbf{C}\mathbf{X}(t) + \mathbf{D}\mathbf{u}(t)\end{aligned} \tag{2.80}$$

and illustrated in Figure 2.27, can be obtained by solving a series of partial

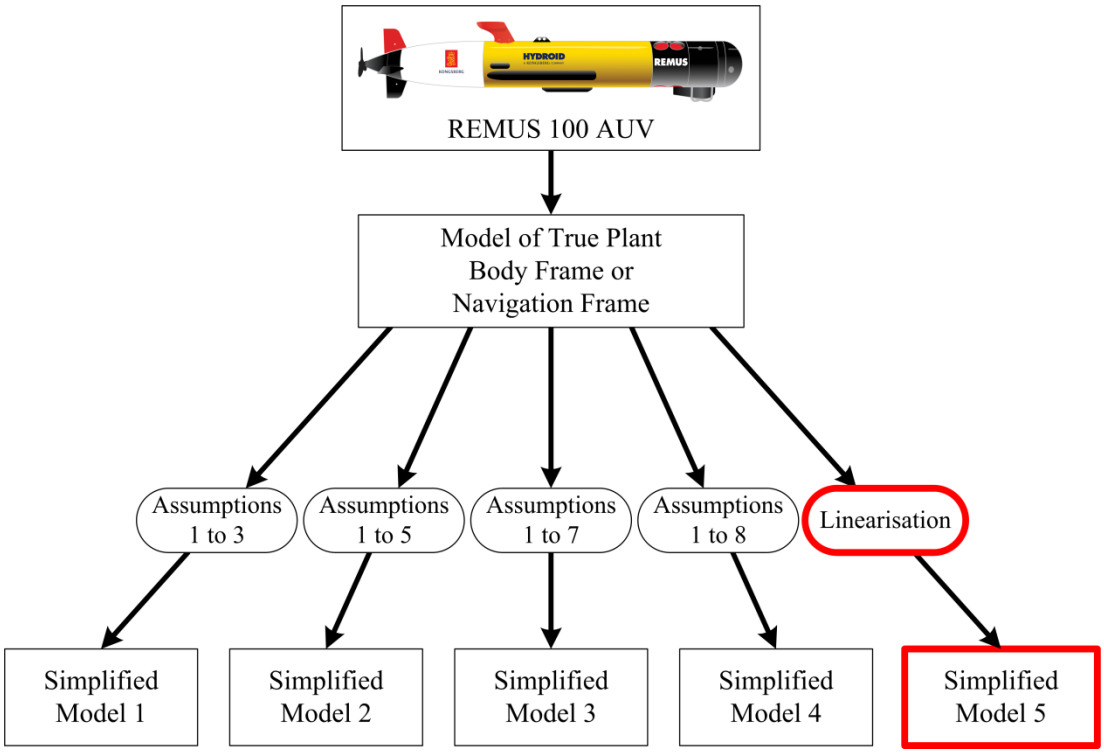

Figure 2.26: Simplified Models, Model 5 Highlighted

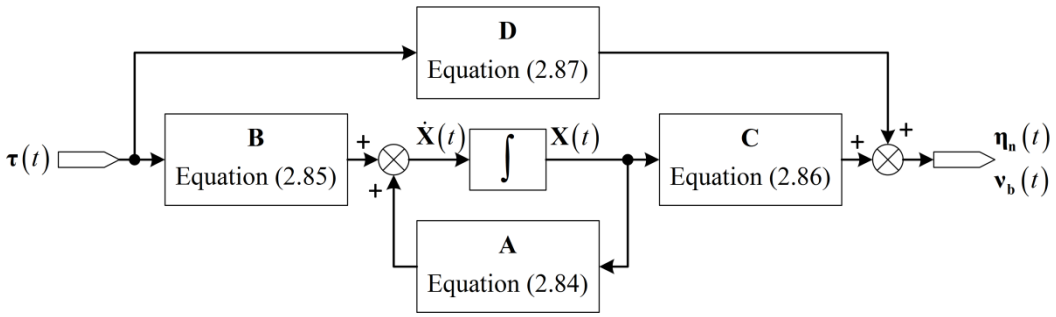

Figure 2.27: Simplified Model 5 (Linearised SSR Model)

differential equations (PDEs) at the linearisation point. As the linearised plant will be less accurate as it is pushed further away from this linearisation point, this point is chosen as a common operating point for the nonlinear plant. This linearisation point occurs at $\boldsymbol{\eta}_{\mathbf{n}}(t)=\boldsymbol{\eta}_{\mathbf{n}}^{0}$, $\mathbf{v}_{\mathbf{b}}(t)=\mathbf{v}_{\mathbf{b}}^{0}$, and $\boldsymbol{\tau}(t)=\boldsymbol{\tau}^{0}$.

Within Equation (2.80),

$$\mathbf{y}(t)=\begin{bmatrix}\mathbf{v}_{\mathbf{b}}(t)\\ \boldsymbol{\eta}_{\mathbf{n}}(t)\end{bmatrix} \tag{2.81}$$

is the output,

$$\mathbf{u}(t)=\boldsymbol{\tau}(t) \tag{2.82}$$

is the input,

$$\mathbf{X}(t)=\begin{bmatrix}\mathbf{v}_{\mathbf{b}}(t)\\ \boldsymbol{\eta}_{\mathbf{n}}(t)\end{bmatrix} \tag{2.83}$$

is the state vector,

$$\mathbf{A}=\begin{bmatrix}\dfrac{\partial\dot{\mathbf{v}}_{\mathbf{b}}(t)}{\partial\mathbf{v}_{\mathbf{b}}(t)} & \dfrac{\partial\dot{\mathbf{v}}_{\mathbf{b}}(t)}{\partial\boldsymbol{\eta}_{\mathbf{n}}(t)}\\ \dfrac{\partial\dot{\boldsymbol{\eta}}_{\mathbf{n}}(t)}{\partial\mathbf{v}_{\mathbf{b}}(t)} & \dfrac{\partial\dot{\boldsymbol{\eta}}_{\mathbf{n}}(t)}{\partial\boldsymbol{\eta}_{\mathbf{n}}(t)}\end{bmatrix}_{\mathbf{v}_{\mathbf{b}}(t)=\mathbf{v}_{\mathbf{b}}^{0},\boldsymbol{\eta}_{\mathbf{n}}(t)=\boldsymbol{\eta}_{\mathbf{n}}^{0}} \tag{2.84}$$

is the system matrix,

$$\mathbf{B} = \left[\begin{array}{c} \dfrac{\partial \dot{\mathbf{v}}_{\mathbf{b}}(t)}{\partial \boldsymbol{\tau}(t)} \\ \dfrac{\partial \dot{\boldsymbol{\eta}}_{\mathbf{n}}(t)}{\partial \boldsymbol{\tau}(t)} \end{array} \right]_{\boldsymbol{\tau}(t)=\boldsymbol{\tau}^0} \tag{2.85}$$

is the input matrix,

$$\mathbf{C} = \mathbf{I}_{12\times 12} \tag{2.86}$$

is the output matrix, and

$$\mathbf{D} = \mathbf{0}_{12\times 6} \tag{2.87}$$

is the direct transmission matrix.

The parameters for this model are contained within Appendix A.

2.4. Model Comparison

With each assumption made in Section 2.3 regarding the simplification of the plant model, the similarities between the simplified model and the plant model are further reduced. If the resulting model is over simplified, it could behave in an entirely different fashion compared to the original model, or even become unstable. If a compensator is designed based on such a model, the resultant compensated system could perform poorly, or become unstable. In order to verify the integrity of a particular simplified model, the behaviour of this simplified model must be compared against the behaviour of the plant model to verify that the key characteristics of the original system are retained. Therefore, a means of comparing the behaviour of these simplified models to the plant model is required.

This section presents a comparison of the response of the different models from Section 2.3. The following models are used in this comparison.

- The plant model is considered as Equation (2.12), outlined in Section 2.2.2;
- Model 1 is considered as the navigation frame model of Equation (2.66), outlined in Section 2.3.1;

- Model 2 is considered as the body frame model of Equation (2.71), outlined in Section 2.3.2;
- Model 3 is considered as the body frame model of Equation (2.76), outlined in Section 2.3.3;
- Model 4 is considered as the model of Equation (2.79), outlined in Section 2.3.4;
- Model 5 is considered as the linear model of Equation (2.80), outlined in Section 2.3.5.

The parameters for all models are contained within Appendix A.

All models, including the plant model, have the same input signals applied, and all comparisons presented here are the differences between the actual plant output and the simplified model output. This is more easily seen in Figure 2.28. Furthermore, all simulation configuration parameters, such as numerical integration method and step size, were kept constant for all simulations to obtain an unbiased response.

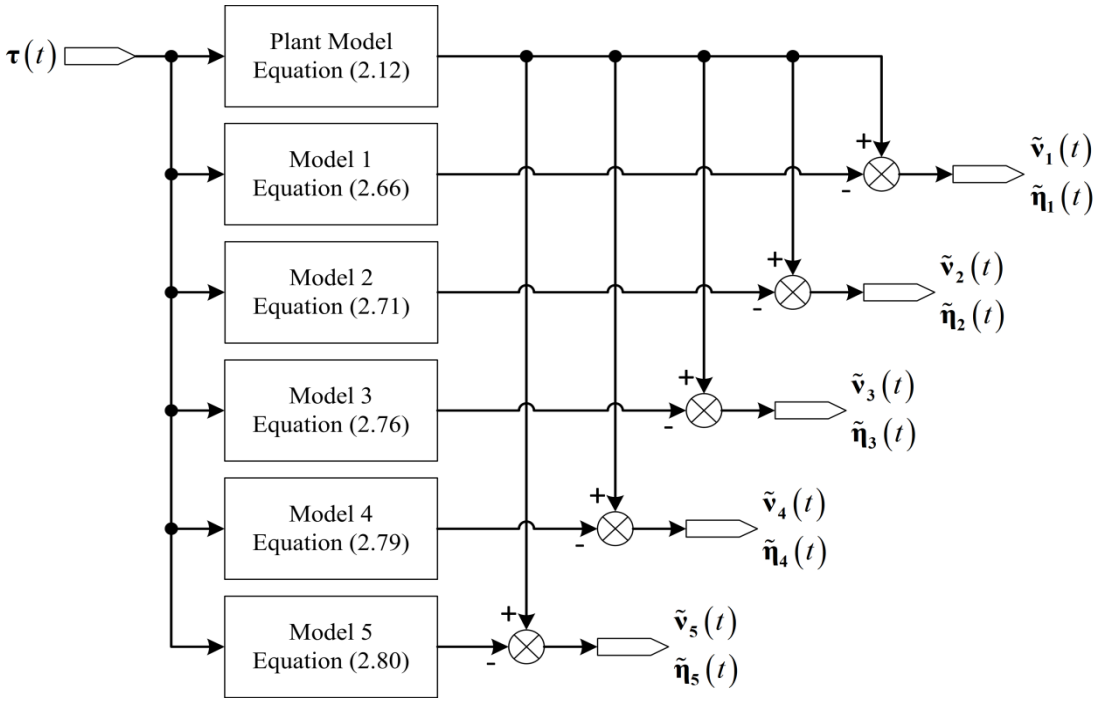

Figure 2.28: Control Model Comparison

2.4.1. Input Signals for Model Comparison

In order to validate the accuracy of the simplified models presented in Section 2.3, a consistent set of input signals is required to excite all the models. The dynamic response of each simplified model is then observed with respect to the plant model presented in Section 2.2.2.

As this is a simulation to validate the accuracy of the simplified models, each response is an open-loop response, i.e., an input force and/or moment is applied to each model and the resulting position, attitude and velocity is observed. A set of input signals were chosen such that a simple, yet typical, manoeuvre for the plant model is performed. The horizontal trajectory of this manoeuvre can be seen in Figure 2.29 where it is obvious that the model is required to follow a circular path.

The desired path for the plant model to follow is to first travel north for approximately 5 m and then travel in a circular path with a radius of approximately 5 m. The desired depth for this manoeuvre is kept constant at 10 m, while the desired surge translational velocity is kept constant at 1 m s^{-1}.

Decomposing this trajectory into its corresponding position and attitude signals is seen in Figure 2.30 and Figure 2.31 respectively.

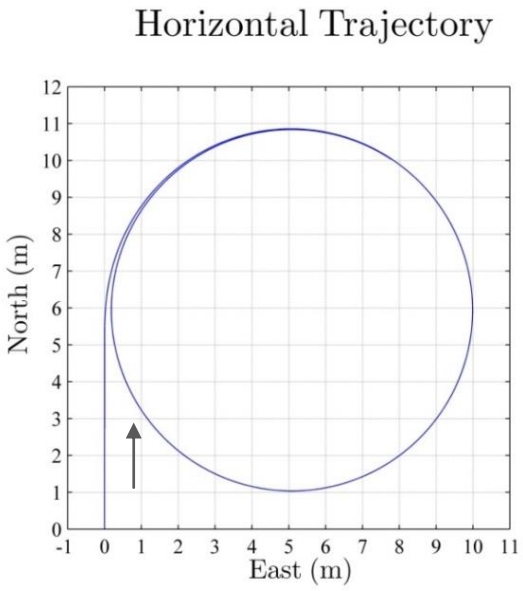

Figure 2.29: Horizontal Trajectory of Plant Model

The desired position of the plant model corresponding to the trajectory of Figure 2.29 is seen in Figure 2.30. Observation of Figure 2.30 indicates that the plant model travels in a straight line for the first 5 s. This is due to the slope of all three positions being constant for this period. After 5 s, the depth remains constant at 10 m, however the north and east positions begin to oscillate. Both the north and east positions need

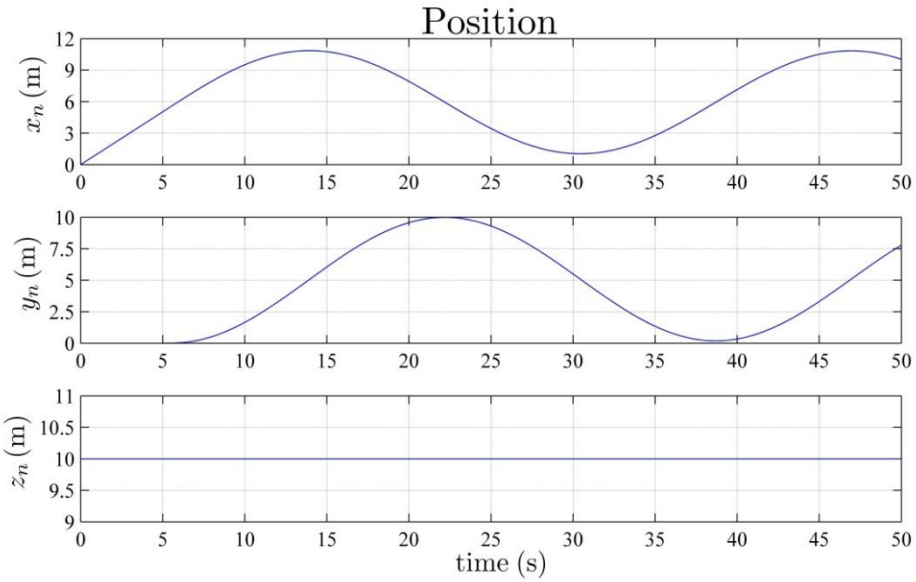

Figure 2.30: Position of Plant Model (Navigation Frame)

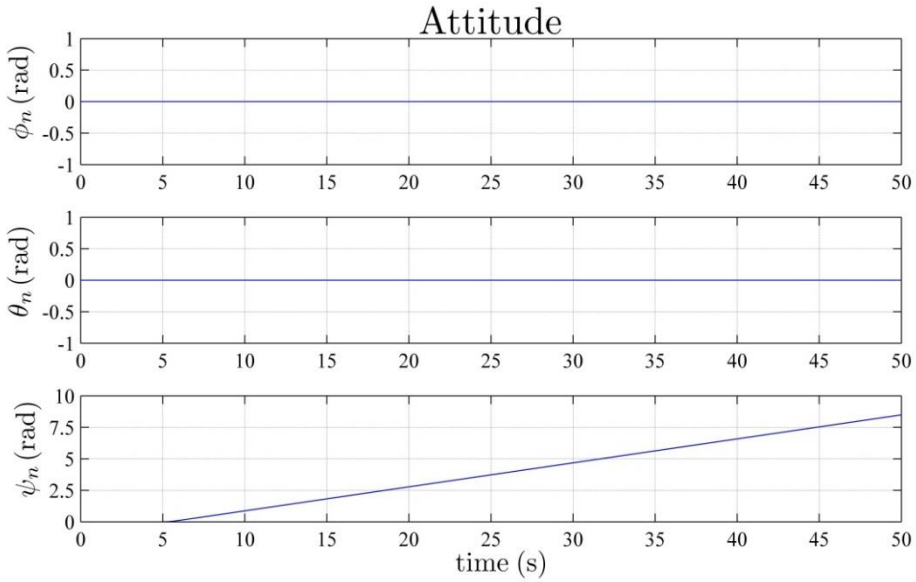

Figure 2.31: Attitude of Plant Model (Navigation Frame)

to behave in a sinusoidal fashion, with a 90° phase difference, to produce the circular motion of the desired path. Hence, the behaviour of the position DoFs are as expected.

The desired attitude of the plant model corresponding to the trajectory of Figure 2.29 is seen in Figure 2.31. Figure 2.31 shows the attitude of the plant being held constant for the first 5 s, which indicates that the vehicle remains facing the same direction for the first 5 s. For the remaining 45 s, the yaw varies in an approximate linear fashion while both roll and pitch are kept constant. In order for the plant model to follow a circular path, the yaw angle will need to change at a constant rate. Hence, the behaviour of the attitude DoFs are as expected.

The input forces and moments, decomposed in the body frame, corresponding to the trajectory of Figure 2.29 are seen in Figure 2.32 and Figure 2.33 respectively.

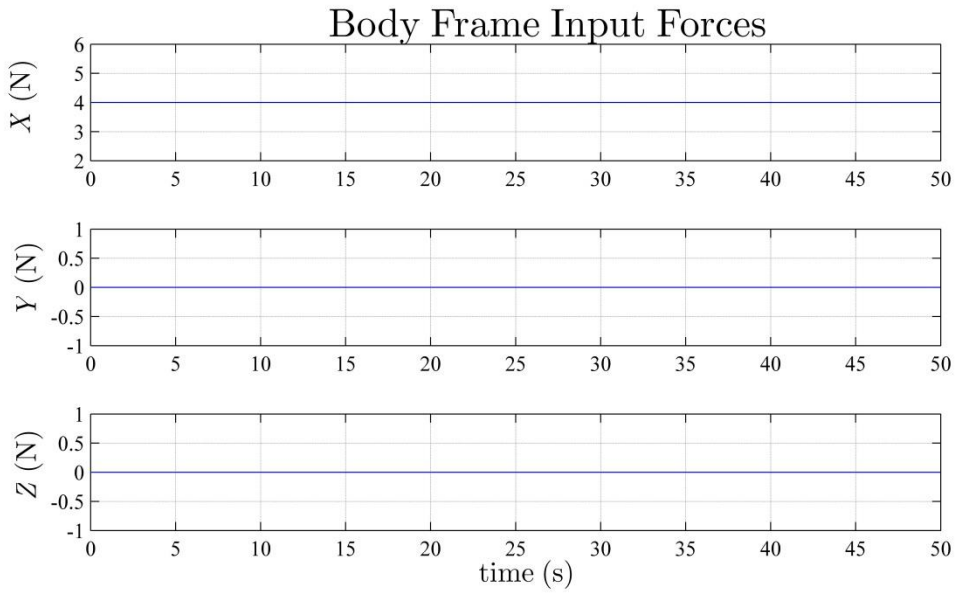

Figure 2.32: Body Frame Input Forces

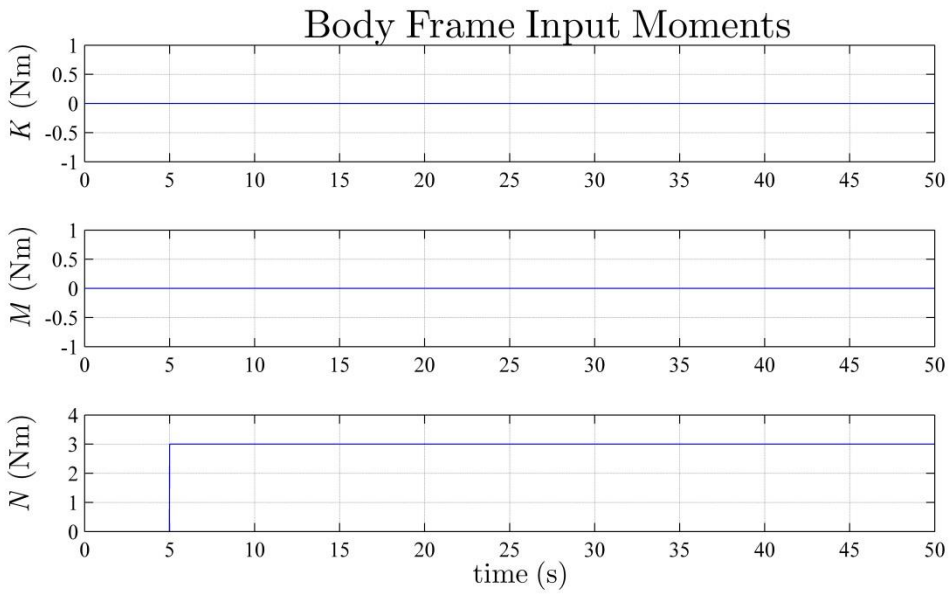

Figure 2.33: Body Frame Input Moments

The input forces for this comparison study, decomposed in the body frame, are seen in Figure 2.32. It is observed from Figure 2.32 that the input forces are held constant throughout the simulation. From Newton's First Law of Motion, this would indicate that the translational motion of the vehicle would be relatively constant. The surge input force, *X*, is constant at 4 N, while both sway and heave input forces, *Y* and *Z* respectively, are constant at 0 N. This indicates that the vehicle should move at a constant forward speed with little sway or heave motion. Hence, the behaviour of the input forces is as expected.

The input moments for this comparison study, also decomposed in the body frame, are seen in Figure 2.33. These input moments are similar to the input forces seen in Figure 2.32, apart from the step change from 0 Nm to 3 Nm in the yaw input moment, *N*, occurring at 5 s. The roll and pitch input moments are held constant at 0 Nm throughout the entire simulation. Again, this would indicate that the rotational velocities of the vehicle are held quite constant, apart from around the step change in the yaw moment. Hence, the behaviour of the input moments is as expected.

2.4.2. Observations for Model Comparison, All Models

This section presents the results of this comparison study. These results are presented in the form of error plots for all position/attitude DoFs decomposed in the navigation frame and all translational/angular velocity DoFs decomposed in the body frame. These errors are calculated as the difference between the output of a particular simplified model and the output of the plant model, as was illustrated in Figure 2.28. To aid in the ease of viewing these results, different thicknesses are used for different curves. This enables easy viewing particularly when multiple curves overlap. Each figure contains three sets of errors with Figure 2.34 presenting position errors, Figure 2.35 presenting attitude errors, Figure 2.36 presenting translational velocity errors, and Figure 2.37 presenting angular velocity errors. Observations regarding these figures will be made immediately following each figure, with concluding remarks concerning the general behaviour of all models to follow all figures.

It is anticipated that, due to the nature of the applied assumptions and the plant model structure, Simplified Model 1 and Simplified Model 2 will behave similarly, while Simplified Model 3 and Simplified Model 4 will also behave similarly. Concerning Simplified Model 1 and Simplified Model 2, the key difference between these models is the assumption that the gravitational and buoyancy forces and moments vector is ignored for Simplified Model 2. However, as the plant model is designed to be highly manoeuvrable, the gravitational and buoyancy forces and moments vector is assumed to be zero, and hence the difference between the models is removed. Concerning Simplified Model 3 and Simplified Model 4, again these two models have very similar assumptions especially regarding hydrodynamics, and therefore it is anticipated that these two models will also behave similarly.

It is also anticipated that Simplified Model 5, the linearised model, will behave poorly compared to the other models. This is due to the process of how a linearised model is derived. Particularly, a linearisation point is selected which corresponds to a specific operating point for the system. For an underwater vehicle, this operating point corresponds to a particular position/attitude, velocity, and input force/moment, all in six DoF, with the resulting linearised model being valid only within the

immediate neighbourhood of this operating point. As the vehicle moves, these quantities determining the operating point will vary, and therefore the operating point of the vehicle will move away from the linearisation point. Hence, the quality of this linearised model will degrade which will result in a larger behavioural difference between the plant model and the linearised model of Simplified Model 5.

1. Simulation of Position Errors

Subject to the input forces and moments outlined in Figure 2.32 and Figure 2.33, the position errors for the five models illustrated in Figure 2.28 are given in Figure 2.34.

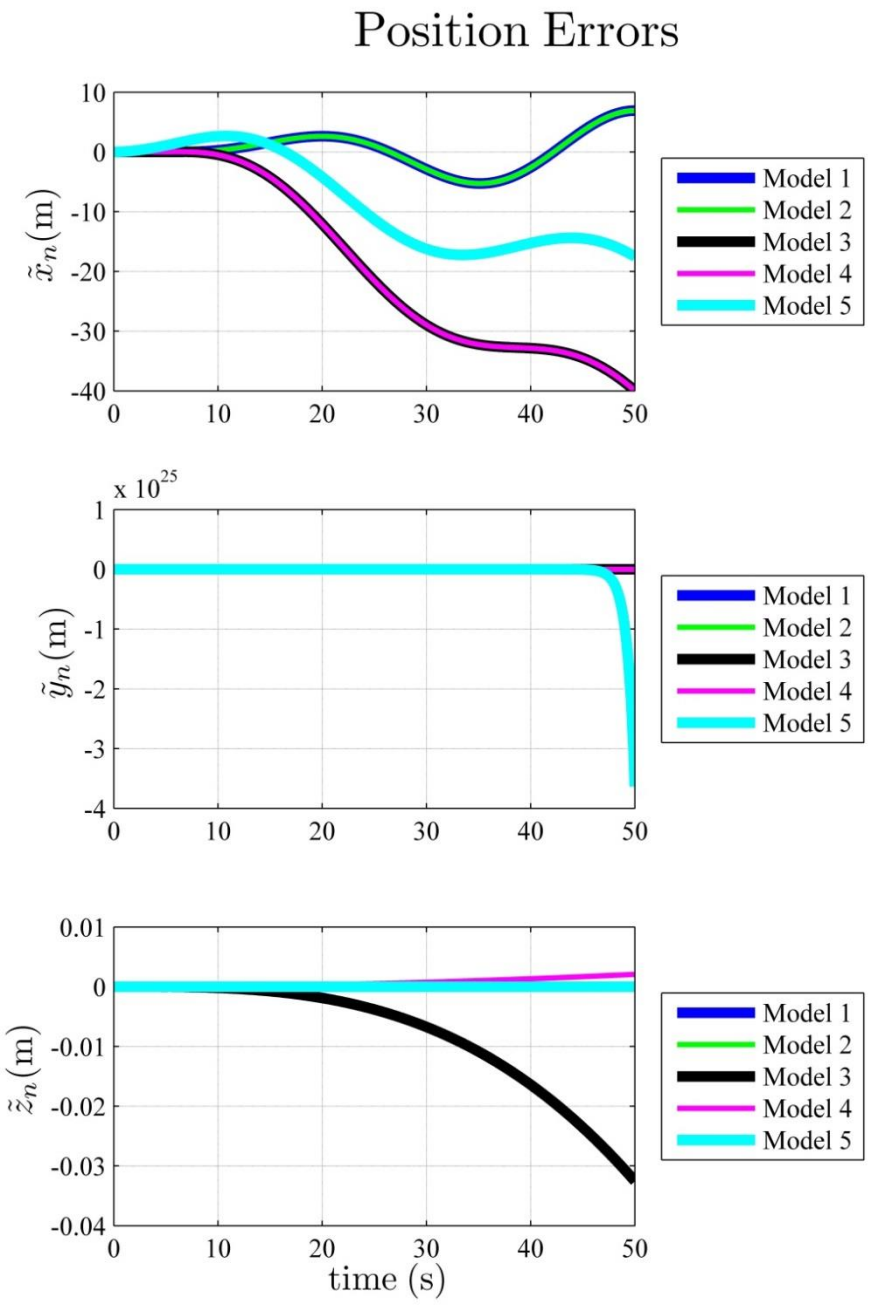

Figure 2.34: Position Errors for Model 1, Model 2, Model 3, Model 4 and Model 5

It is observed from the north position error, $\tilde{x}_n$, that the error for Simplified Model 1 and Simplified Model 2 are similar to each other, while the error of Simplified Model 3 and Simplified Model 4 are also similar. This indicates that similar dynamics are preserved in Simplified Model 1 and Simplified Model 2 from the plant model, while similar dynamics are preserved in Simplified Model 3 and Simplified Model 4 from the plant model.

It is observed from the east position error, $\tilde{y}_n$, that Simplified Model 5 is unstable. This is indicated by the east position error, $\tilde{y}_n$, tending to $-\infty$.

It is observed from the down position error, $\tilde{z}_n$, that there is very little divergence, if any, between the models presented and the plant model. Simplified Model 1, Simplified Model 2, and Simplified Model 5 all behave similarly to the plant, as seen by the error for all three models being zero. Simplified Model 3 has a maximum divergence of approximately 33 mm while Simplified Model 4 has a maximum divergence of approximately 2 mm. Overall, there is very little divergence seen for this error in any model, which is because there is no excitation of this DoF based on the input signals of Figure 2.32 and Figure 2.33.

2. Simulation of Attitude Errors

Subject to the input forces and moments outlined in Figure 2.32 and Figure 2.33, the attitude errors for the five models illustrated in Figure 2.28 are given in Figure 2.35.

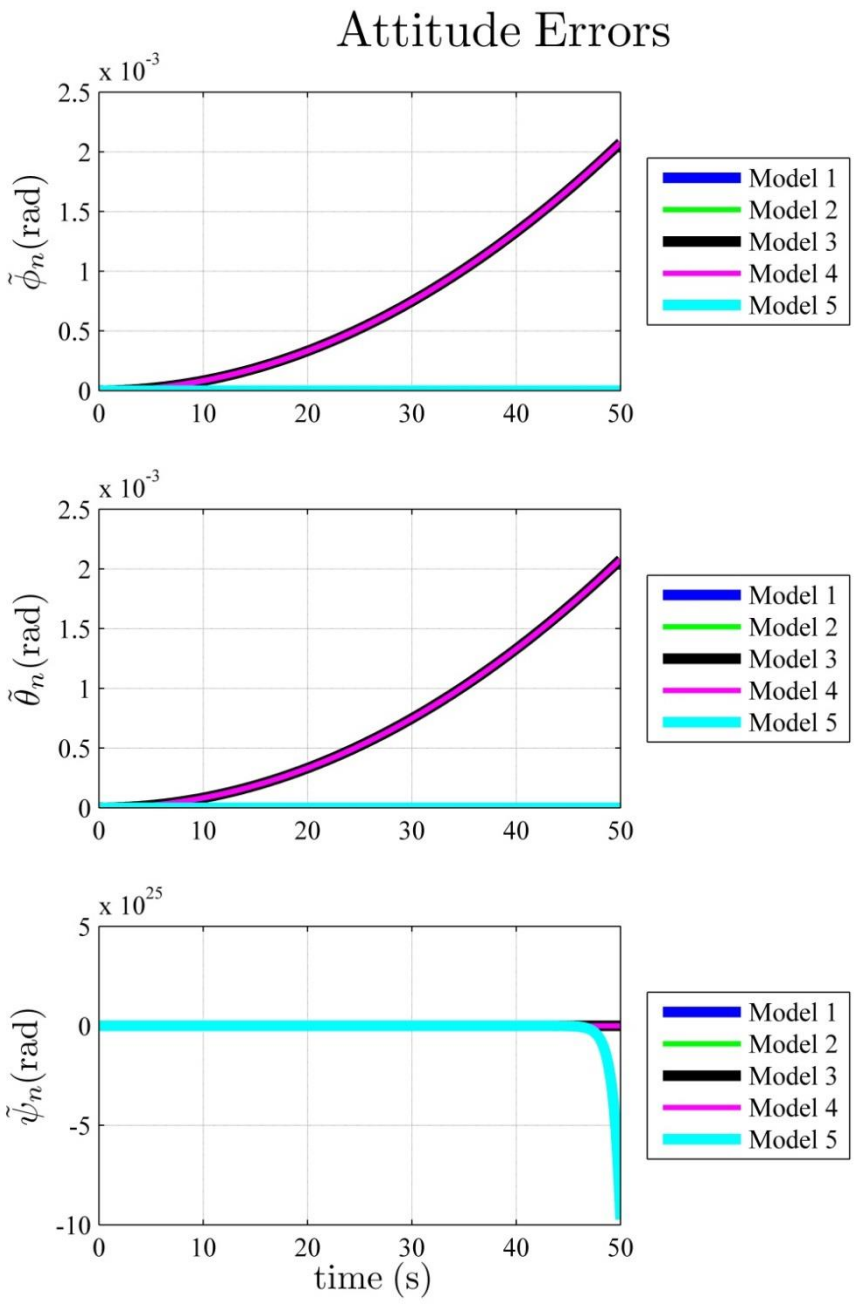

Figure 2.35: Attitude Errors for Model 1, Model 2, Model 3, Model 4 and Model 5

It is observed from both the roll attitude error, $\tilde{\phi}_n$, and the pitch attitude error, $\tilde{\theta}_n$, that again Simplified Model 1 and Simplified Model 2 behave similarly, while Simplified Model 3 and Simplified Model 4 behave similarly. Furthermore, Simplified Model 1, Simplified Model 2, and Simplified Model 5 do not diverge from the plant model, while Simplified Model 3 and Simplified Model 4 have a maximum divergence of approximately $2\text{x}10^{-3}$ rad. This small divergence for all models is because there is no excitation of these DoFs based on the input signals of Figure 2.32 and Figure 2.33.

It is observed from the yaw attitude error, $\tilde{\psi}_n$, that Simplified Model 5 is unstable due to it tending to $-\infty$.

3. Simulation of Translational Velocity Errors

Subject to the input forces and moments outlined in Figure 2.32 and Figure 2.33, the translational velocity errors for the five models illustrated in Figure 2.28 are given in Figure 2.36.

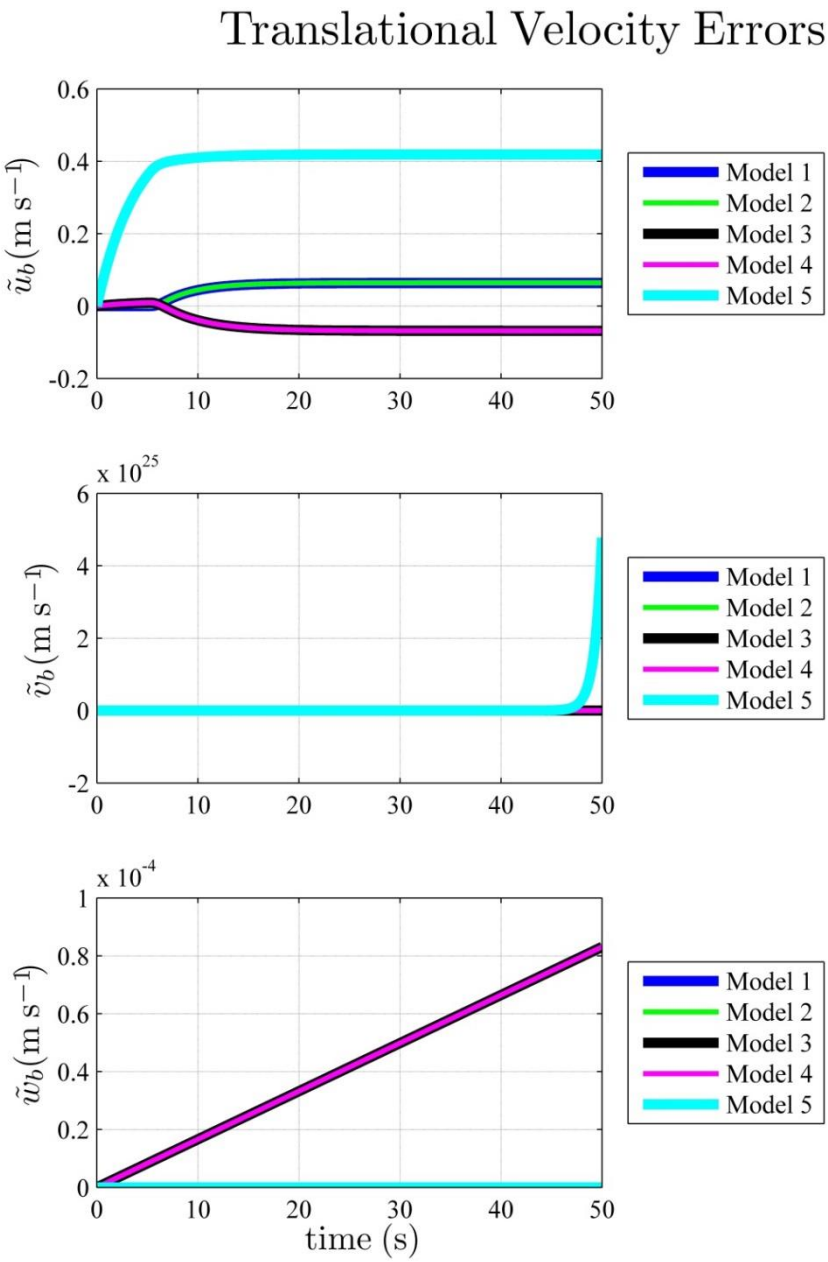

Figure 2.36: Translational Velocity Errors for Model 1, Model 2, Model 3, Model 4 and Model 5

It is observed from the surge translational velocity error, $\tilde{u}_b$, that again Simplified Model 1 and Simplified Model 2 behave similarly with a maximum error divergence of approximately 0.064 m s^{-1}, while Simplified Model 3 and Simplified Model 4 behave similarly with a maximum error divergence of approximately 0.069 m s^{-1}. Simplified Model 5 experiences the largest error divergence of approximately 0.42 m s^{-1}.

It is observed from the sway translational velocity error, $\tilde{v}_b$, that Simplified Model 5 is unstable as the error tends to ∞.

It is observed from the heave translational velocity error, $\tilde{w}_b$, that Simplified Model 1, Simplified Model 2, and Simplified Model 5 experience no error divergence while Simplified Model 3 and Simplified Model 4 experience an error divergence of approximately 8.3×10^{-5} m s^{-1}. These errors are all very small, as this DoF is not excited by the input signals of Figure 2.32 and Figure 2.33.

4. Simulation of Angular Velocity Errors

Subject to the input forces and moments outlined in Figure 2.32 and Figure 2.33, the angular velocity errors for the five models illustrated in Figure 2.28 are given in Figure 2.37.

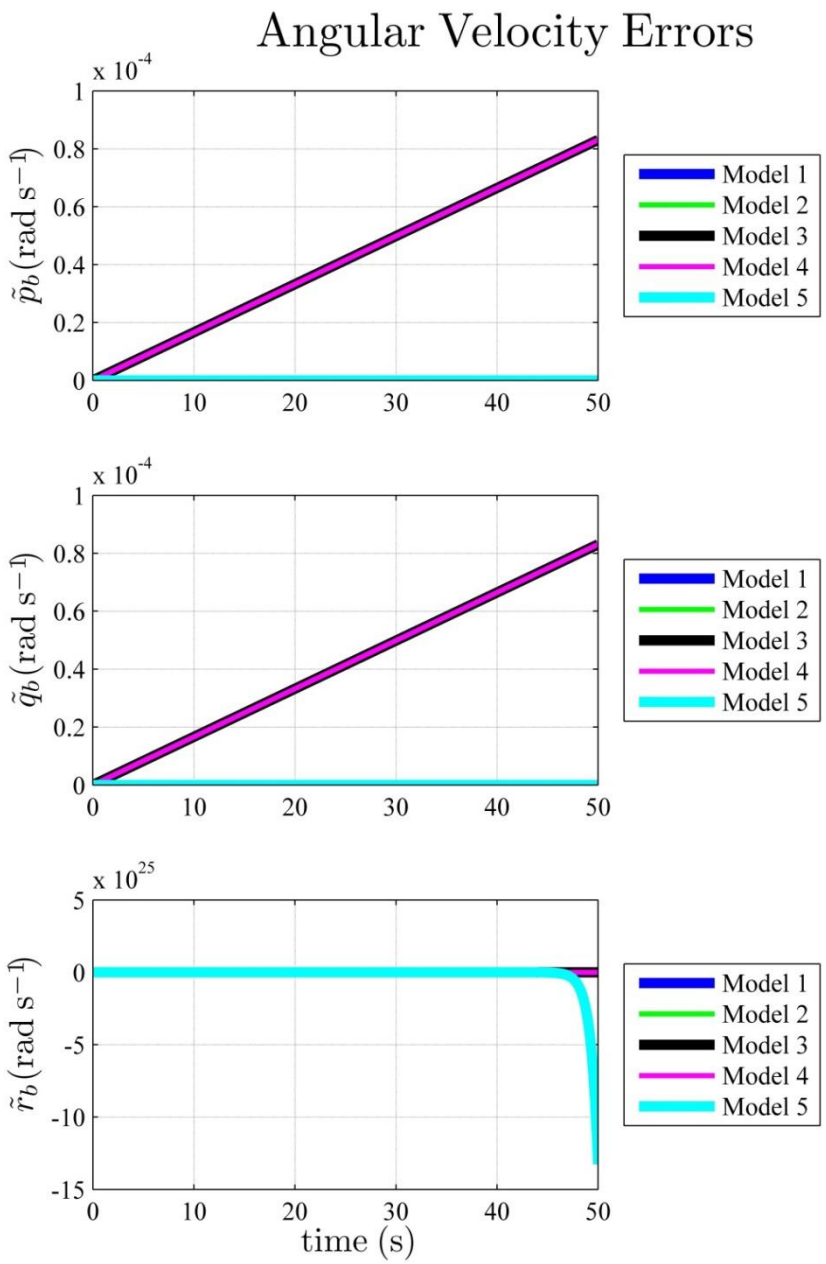

Figure 2.37: Angular Velocity Errors for Model 1, Model 2, Model 3, Model 4 and Model 5

It is observed from both the roll angular velocity error, $\tilde{p}_b$, and the pitch angular velocity error, $\tilde{q}_b$, that again Simplified Model 1 and Simplified Model 2 behave similarly, while Simplified Model 3 and Simplified Model 4 behave similarly. Furthermore, Simplified Model 1, Simplified Model 2, and Simplified Model 5 do not diverge from the plant model, while Simplified Model 3 and Simplified Model 4 have a maximum divergence of approximately $8.3\text{x}10^{-5}$ rad s^{-1}. This small divergence for all models is because there is no excitation of these DoFs based on the input signals of Figure 2.32 and Figure 2.33.

It is observed from the yaw angular velocity error, $\tilde{r}_b$, that Simplified Model 5 is unstable due to it tending to $-\infty$.

5. Concluding Remarks

From the discussion of all 12 error plots presented in Figure 2.34 through to Figure 2.37, there are two main conclusions that can be drawn:

1. With respect to this particular set of inputs, Simplified Model 1 and Simplified Model 2 behave similarly, while Simplified Model 3 and Simplified Model 4 behave similarly.
2. With respect to this particular set of inputs, Simplified Model 5 is unstable.

Firstly, the similar behaviour in models indicates that similar dynamics are preserved during the simplification process for this particular set of inputs. Concerning Simplified Model 1 and Simplified Model 2, the anticipated similar behaviour was demonstrated here. This clearly shows that the extra assumptions made when deriving Simplified Model 2 has no effect on its overall behaviour compared to Simplified Model 1. Concerning Simplified Model 3 and Simplified Model 4, the anticipated similar behaviour was also demonstrated here. Furthermore, the behaviour of Simplified Model 1 and Simplified Model 2 more closely mimicked that of the plant model compared to Simplified Model 3 and Simplified Model 4 as the magnitude of the error curves were either similar or smaller for Simplified Model 1 and Simplified Model 2.

Secondly, the significantly large errors observed for Simplified Model 5 indicate a considerable divergence from the behaviour of the plant model, even for this relatively simple manoeuvre. Again, this is anticipated behaviour as the linearised model is less accurate as the operating point of the model moves further away from the linearisation point.

The performance of Simplified Model 5 is indicative of a lack of ability to represent the plant model accurately, especially compared to the remaining simplified models, which retain at least some of the nonlinearities of the plant model. Hence, due to Simplified Model 5 possessing less credibility compared to the remaining simplified models, the following section will present the same results as seen in this section, yet the behaviour of Simplified Model 5 will be omitted.

2.4.3. Observations for Model Comparison, Nonlinear Models

This section presents a comparative study similar to that of Section 2.4.2, however there is one key difference; the behaviour of Simplified Model 5 is omitted. Simplified Model 5 is obtained by linearising the nonlinear plant model about a particular linearisation point. As the input signals to all the models are time-varying, the system will not be operating within the immediate neighbourhood of this linearisation point throughout the simulation. As seen in Section 2.4.2, instability was observed for this particular set of inputs, which indicates that the operating point is not residing within a close neighbourhood of the linearisation point, and hence the credibility and validity of Simplified Model 5 is severely limited. For this reason, Simplified Model 5 is omitted from the comparative study presented here.

By omitting Simplified Model 5, further insight into the behaviour of the remaining models can be gained, particularly where the instability of Simplified Model 5 was observed. The remaining nonlinear models within this comparative study all possess varying levels of assumptions, and therefore varying degrees of complexity. For a given set of inputs, if similar behaviour is observed between simplified models, then the least complex model will have a distinct advantage when evaluating its convenience for implementation within a constrained system such as an AUV.

1. Simulation of Position Errors

Subject to the input forces and moments outlined in Figure 2.32 and Figure 2.33, the position errors for the four nonlinear simplified models illustrated in Figure 2.28 are given in Figure 2.38.

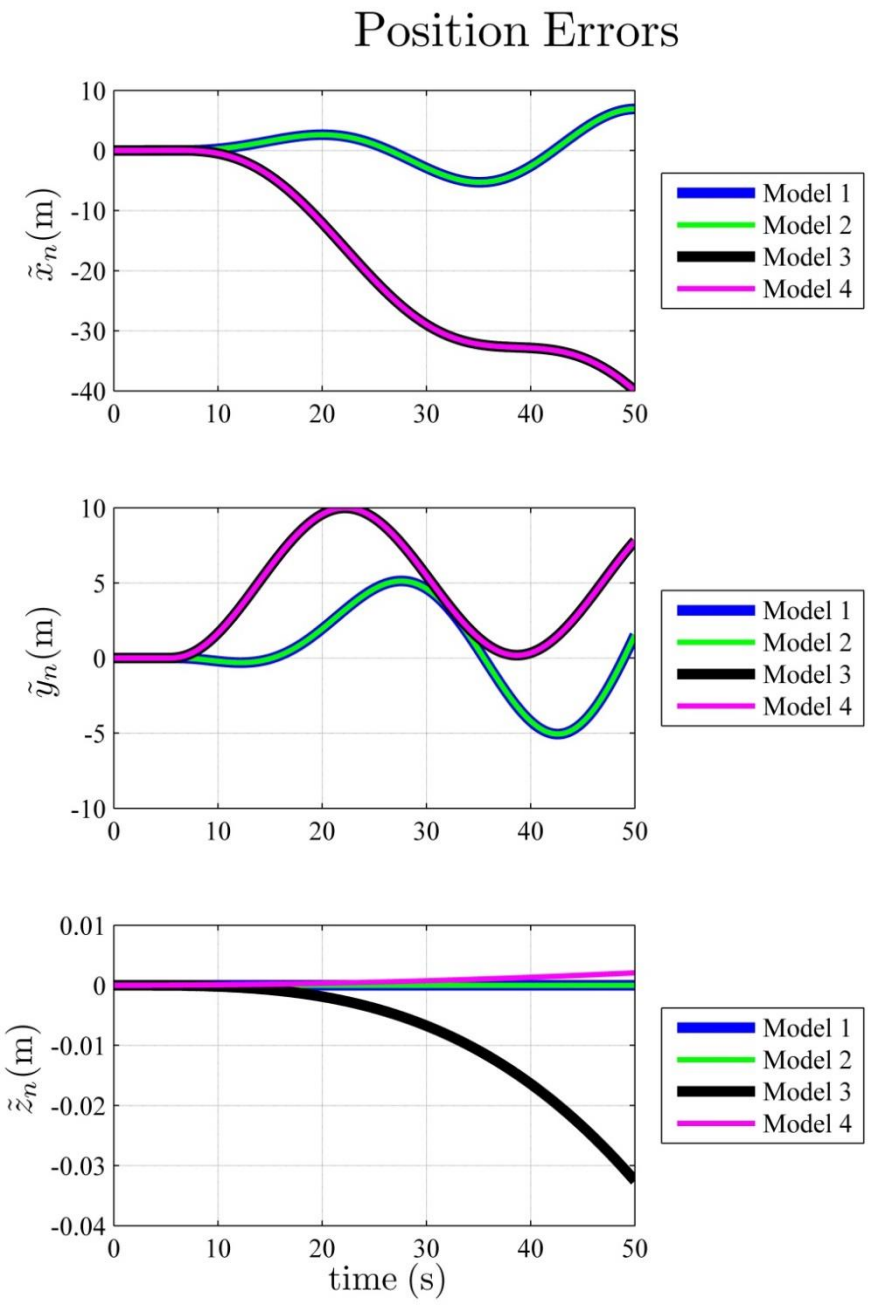

Figure 2.38: Position Errors for Model 1, Model 2, Model 3 and Model 4

As the omission of Simplified Model 5 has little impact on the observations of the north position error, $\tilde{x}_n$, and the down position error, $\tilde{z}_n$, the previous discussion based on Figure 2.34 holds.

With regards to the east position error, $\tilde{y}_n$, the omission of Simplified Model 5 allows for a clearer observation of the behaviour of the remaining four models. This plot reinforces the fact that Simplified Model 1 and Simplified Model 2 behave similarly, while Simplified Model 3 and Simplified Model 4 behave similarly.

2. Simulation of Attitude Errors

Subject to the input forces and moments outlined in Figure 2.32 and Figure 2.33, the attitude errors for the four nonlinear simplified models illustrated in Figure 2.28 are given in Figure 2.39.

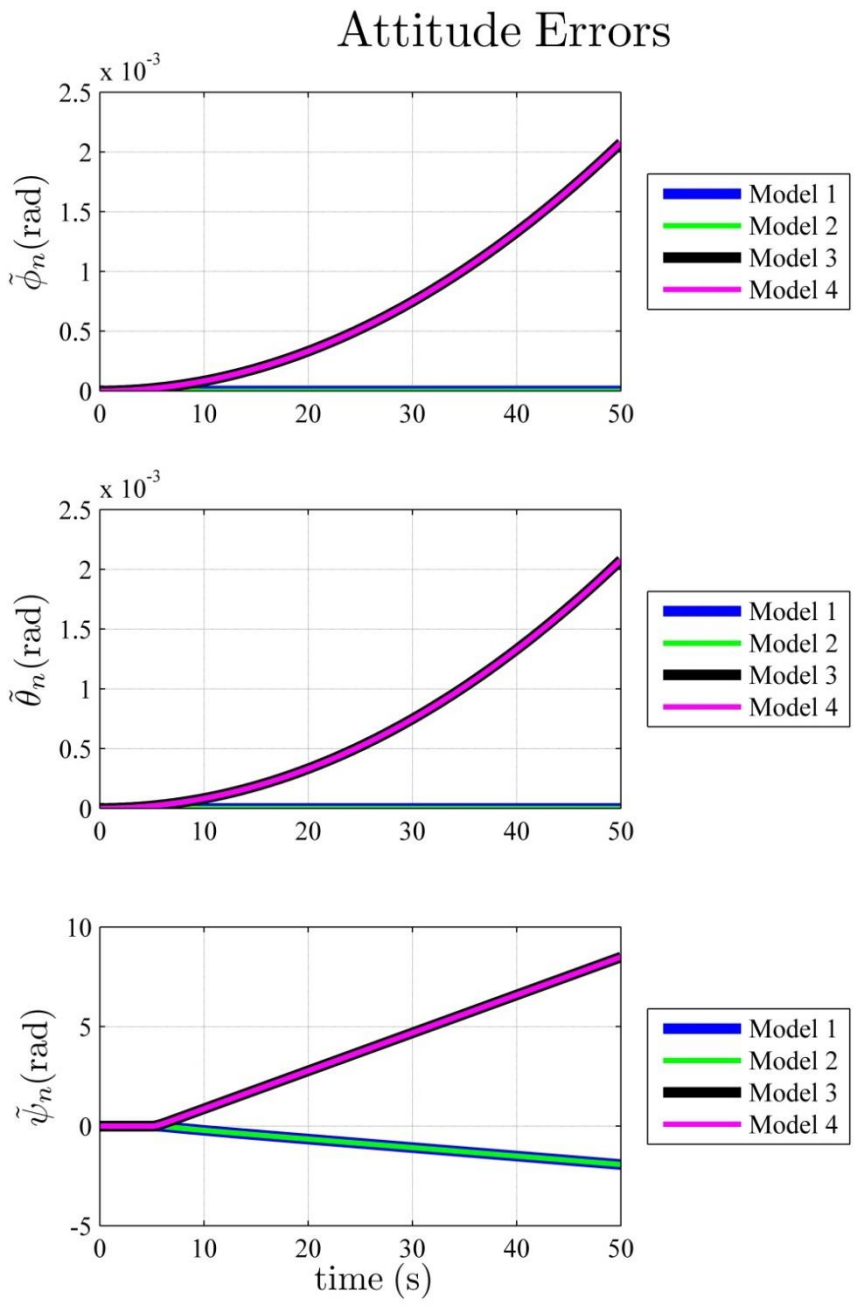

Figure 2.39: Attitude Errors for Model 1, Model 2, Model 3 and Model 4

As the omission of Simplified Model 5 has little impact on the observations of the roll attitude error, $\tilde{\phi}_n$, and the pitch attitude error, $\tilde{\theta}_n$, the previous discussion based on Figure 2.35 holds.

With regards to the yaw attitude error, $\tilde{\psi}_n$, the omission of Simplified Model 5 allows for a clearer observation of the behaviour of the remaining four models. This plot reinforces the fact that Simplified Model 1 and Simplified Model 2 behave similarly, while Simplified Model 3 and Simplified Model 4 behave similarly.

3. Simulation of Translational Velocity Errors

Subject to the input forces and moments outlined in Figure 2.32 and Figure 2.33, the translational velocity errors for the four nonlinear simplified models illustrated in Figure 2.28 are given in Figure 2.40.

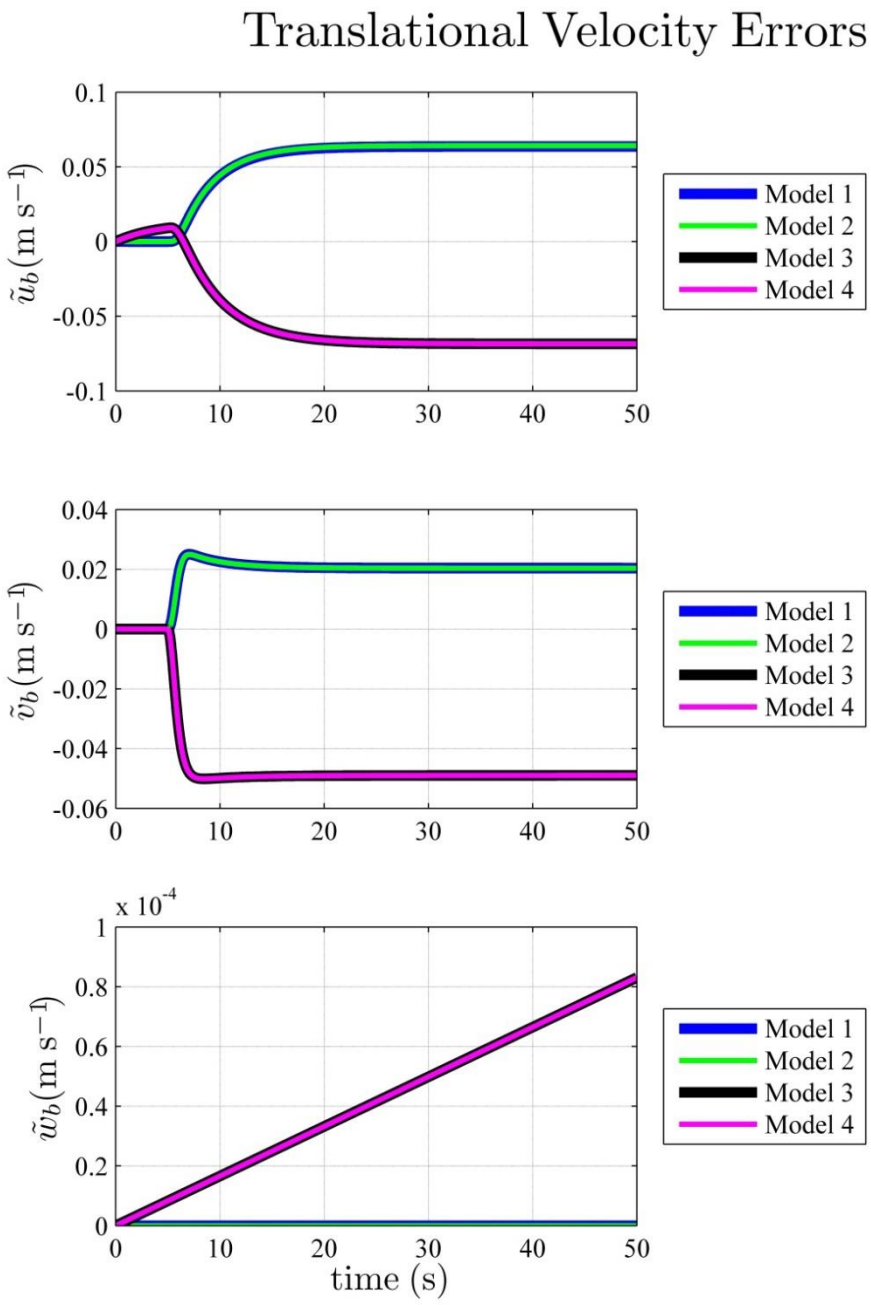

Figure 2.40: Translational Velocity Errors for Model 1, Model 2, Model 3 and Model 4

As the omission of Simplified Model 5 has little impact on the observations of the surge translational velocity error, $\tilde{u}_b$, and the heave translational velocity error, $\tilde{w}_b$, the previous discussion based on Figure 2.36 holds.

With regards to the sway translational velocity error, $\tilde{v}_b$, the omission of Simplified Model 5 allows for a clearer observation of the behaviour of the remaining four models. This plot reinforces the fact that Simplified Model 1 and Simplified Model 2 behave similarly, while Simplified Model 3 and Simplified Model 4 behave similarly.

4. Simulation of Angular Velocity Errors

Subject to the input forces and moments outlined in Figure 2.32 and Figure 2.33, the angular velocity errors for the four nonlinear simplified models illustrated in Figure 2.28 are given in Figure 2.41.

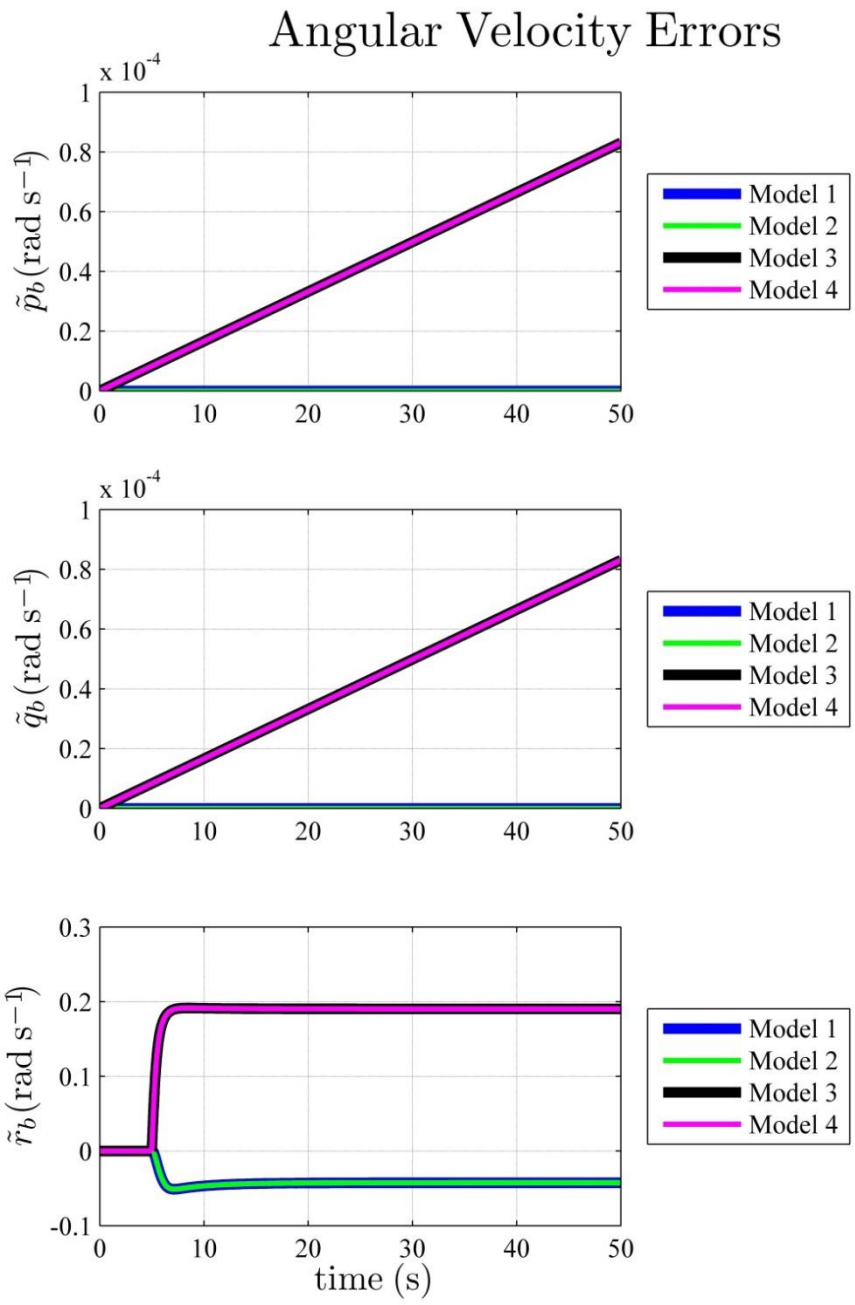

Figure 2.41: Angular Velocity Errors for Model 1, Model 2, Model 3 and Model 4

As the omission of Simplified Model 5 has little impact on the observations of the roll angular velocity error, $\tilde{p}_b$, and the pitch angular velocity error, $\tilde{q}_b$, the previous discussion based on Figure 2.37 holds.

With regards to the yaw angular velocity error, $\tilde{r}_b$, the omission of Simplified Model 5 allows for a clearer observation of the behaviour of the remaining four models. This plot reinforces the fact that Simplified Model 1 and Simplified Model 2 behave similarly, while Simplified Model 3 and Simplified Model 4 behave similarly.

5. Concluding Remarks

Omission of Simplified Model 5 from the comparison study allowed for clear discussions to be made between all four nonlinear models. Observation of all the plots reinforce what was observed previously; Simplified Model 1 and Simplified Model 2 preserve similar dynamics of the plant while Simplified Model 3 and Simplified Model 4 also preserve similar dynamics of the plant. Furthermore, observation of Figure 2.38 through to Figure 2.41 allows conclusions to be drawn with respect to the behaviour of Simplified Model 1 and Simplified Model 2 compared to the behaviour of Simplified Model 3 and Simplified Model 4.

It is observed in Figure 2.38 through to Figure 2.41 that all four models are stable, yet two models, Simplified Model 1 and Simplified Model 2, approximate the behaviour of the plant better than Simplified Model 3 and Simplified Model 4. The majority of plots show this fact, with the only possible exception being the surge translational velocity error, $\tilde{u}_b$ of Figure 2.40. Here the magnitude of error is approximately the same for all four models, yet differing signs of this error is observed.

This is just one observation over a limited simulation time of 50 s. What happens beyond this period cannot be observed from the figures presented here. Furthermore, different input forces and moments will induce different behaviours. What can be observed is that with respect to all error plots, Simplified Model 1 and Simplified Model 2 behave in a much similar fashion to the plant compared to Simplified Model 3 and Simplified Model 4.

Based on these observations, the process of control design presented in Chapter 3 will proceed by utilising Simplified Model 1, Simplified Model 2, Simplified Model 3 and Simplified Model 4. With respect to the particular set of inputs used in this comparative study, Simplified Model 5 is unstable and therefore omitted from the remainder of this thesis.

2.4.4. Conclusions of Model Comparisons

As Simplified Model 1, Equation (2.66), and Simplified Model 2, Equation (2.71), closely mimic the behaviour of the plant, these models are analysed side-by-side here to identify any differences that exist between them. The equations of these models are shown again here for convenience.

$$\begin{aligned}\mathbf{M}_{\boldsymbol{\eta}}\left(\boldsymbol{\eta}_{\mathbf{n}}(t)\right)\ddot{\boldsymbol{\eta}}_{\mathbf{n}}(t)+\mathbf{C}_{\boldsymbol{\eta}}\left(\mathbf{v}_{\mathbf{b}}(t),\boldsymbol{\eta}_{\mathbf{n}}(t)\right)\dot{\boldsymbol{\eta}}_{\mathbf{n}}(t)\\ +\mathbf{D}_{\boldsymbol{\eta}}\left(\mathbf{v}_{\mathbf{b}}(t),\boldsymbol{\eta}_{\mathbf{n}}(t)\right)\dot{\boldsymbol{\eta}}_{\mathbf{n}}(t)+\mathbf{g}_{\boldsymbol{\eta}}\left(\boldsymbol{\eta}_{\mathbf{n}}(t)\right)=\boldsymbol{\tau}_{\boldsymbol{\eta}}\left(\boldsymbol{\eta}_{\mathbf{n}}(t)\right)\end{aligned} \tag{2.66}$$

$$\mathbf{M}\dot{\mathbf{v}}_{\mathbf{b}}(t)+\mathbf{C}\left(\mathbf{v}_{\mathbf{b}}(t)\right)\mathbf{v}_{\mathbf{b}}(t)+\mathbf{D}\left(\mathbf{v}_{\mathbf{b}}(t)\right)\mathbf{v}_{\mathbf{b}}(t)=\boldsymbol{\tau}(t) \tag{2.71}$$

From examination of these models, there are three obvious differences:

1. Equation (2.66) is dependent on $\boldsymbol{\eta}_{\mathbf{n}}(t)$ while Equation (2.71) is not.
2. Equation (2.66) is much more complicated compared to Equation (2.71) due to the extra matrix multiplications present in $\mathbf{M}_{\boldsymbol{\eta}}\left(\boldsymbol{\eta}_{\mathbf{n}}(t)\right)$, $\mathbf{C}_{\boldsymbol{\eta}}\left(\mathbf{v}_{\mathbf{b}}(t),\boldsymbol{\eta}_{\mathbf{n}}(t)\right)$, $\mathbf{D}_{\boldsymbol{\eta}}\left(\mathbf{v}_{\mathbf{b}}(t),\boldsymbol{\eta}_{\mathbf{n}}(t)\right)$, $\mathbf{g}_{\boldsymbol{\eta}}\left(\boldsymbol{\eta}_{\mathbf{n}}(t)\right)$, and $\boldsymbol{\tau}_{\boldsymbol{\eta}}\left(\boldsymbol{\eta}_{\mathbf{n}}(t)\right)$.
3. Equation (2.66) is dependent on gravitational and buoyancy forces, $\mathbf{g}_{\boldsymbol{\eta}}\left(\boldsymbol{\eta}_{\mathbf{n}}(t)\right)$ while Equation (2.71) is not.

Firstly, the impact of $\boldsymbol{\eta}_{\mathbf{n}}(t)$ being present in Equation (2.66) means that this particular model is dependent on the position and attitude of the vehicle, whereas the model represented by Equation (2.71) is not. Hence, any error incurred by estimating $\boldsymbol{\eta}_{\mathbf{n}}(t)$ by a navigation system will have an impact on Simplified Model 1 while this negative impact will be absent in Simplified Model 2.

Secondly, in terms of computational load, any matrix multiplication will affect the processing requirements for evaluating the model. As Simplified Model 1 of

Equation (2.66) has a larger number of matrix multiplications compared to Simplified Model 2 of Equation (2.71), the requirements placed on on-board processing, which is an extremely limited resource for AUVs, will also be significantly larger.

Finally, the presence of $\mathbf{g}_{\eta}\left(\boldsymbol{\eta}_{n}(t)\right)$ in Simplified Model 1 means that this model can reflect the gravitational and buoyancy forces present in the plant, whereas Simplified Model 2 cannot. However, as this simulation study is only concerned with highly manoeuvrable underwater vehicles, Section 2.2.3 outlined the fact that these forces and moments are zero. Therefore, the presence of $\mathbf{g}_{\eta}\left(\boldsymbol{\eta}_{n}(t)\right)$ in Simplified Model 1 will not cause any behavioural difference between Simplified Model 1 and Simplified Model 2.

Overall, the process of control design presented in Chapter 3 will proceed by utilising Simplified Model 1, Simplified Model 2, Simplified Model 3, and Simplified Model 4. With respect to the particular set of inputs used in this comparative study, Simplified Model 5 is unstable and therefore omitted from the remainder of this thesis.

2.5. Chapter Summary

This chapter presented a discussion of the modelling of underwater vehicles for study in this thesis. This discussion facilitates the analysis and design of controllers for this particular plant, and the simulation studies for the evaluation of the controlled system.

Section 2.2 introduced the mathematical equations that govern the motion of an underwater vehicle. More specifically, Section 2.2.1 presented the kinematic equation and Section 2.2.2 presented the kinetic equation, both of which are used when describing the motion of underwater vehicles.

The kinematic equation and the kinetic equation form the basis of the complete model of an AUV. This complete model includes both rigid body dynamics and hydrodynamics. This complete model was developed in such a way as to gain insight into the relevant properties that each component of these dynamics possesses. From

this complete model, the plant model that is to be used in the simulation studies of this thesis was developed in Section 2.2.3. This plant model, based on the REMUS 100 AUV model that has been experimentally validated by Prestero [54], will form part of a high fidelity simulation environment used for simulating the various control strategies presented in this thesis.

The complete model was also used as the basis to derive simplified models for possible use in the design of various control strategies presented in this thesis. Within Section 2.3, a rigid and systematic mathematical approach was used to derive several simplified models, each with its own set of assumptions that were used to derive it. Four of these simplified models retained at least some elements of the nonlinearities of the complete model, while a fifth simplified model was obtained by linearising the complete nonlinear model at a specific linearisation point.

A process of validating the behaviour of these simplified models against the behaviour of the plant model then followed in Section 2.4. This comparative study was used to verify the integrity of the various simplified models and to assess each models potential for use for control design. This study revealed that the linearised model failed to represent the dynamics of the plant model adequately, which was anticipated as the particular set of time-varying inputs used here moved the operating point of the linearised model sufficiently away from the linearisation point such that instabilities were observed. Even though this instability was observed for this particular set of inputs, the very nature of an AUV traversing an underwater environment means that the operating point will be continuously changing, and therefore the occasions where this operating point coincides to the immediate neighbourhood of the linearisation point would be extremely rare. Therefore, the linearised model was omitted from all remaining studies as it was deemed unsuitable to represent the behaviour of the nonlinear plant model accurately.

The four nonlinear simplified models, however, were able to represent the dynamics of the plant model to varying degrees. The two models with the least assumptions imposed on them were better able to mimic the plant model compared to the two models that had the most assumptions imposed on them. Furthermore, there were varying levels in the complexity of these simplified models due to the set of

assumptions being used to derive each model. Especially concerning the models of lower complexity and higher integrity, an accurate controller based on these models is ideally suited to such a constrained computational platform of an AUV. For these reasons, the following chapter will present the derivation of several controllers utilising the four nonlinear simplified models derived in Section 2.3.

Chapter 3

Control Design and Implementation

3.1. Introduction

This chapter introduces the core component of this thesis, namely control techniques for underwater vehicles. These control schemes, utilising four of the simplified models derived in Chapter 2, and will be used in Chapter 4 to control the plant model which was also derived in Chapter 2.

This chapter is organised as follows:

- A comparison of various controller design strategies is given in Section 3.2. Both the level of coupling between DoFs within the control law, and the frame of which the control law is designed in, is examined. Based on these comparisons, an outline of the controllers designed in this chapter is presented.
- An introduction to sliding mode control is presented in Section 3.3. This includes an overview of the concepts of sliding mode control in a general sense. Also included is a discussion of the phenomenon of chattering, its causes, and possible means of reducing the impact of this behaviour on the system.
- Two existing implementations of SMC for underwater vehicles are presented in Section 3.4. The first is a simple controller consisting of six uncoupled

single DoF controllers, one for each DoF. The second is an implementation utilising a vehicle model that retains coupling between DoFs in the design phase. In both of these cases, the sliding surface is designed in the navigation frame.

- The first of the two new compensators is presented in Section 3.5. This design expands upon the previously designed uncoupled SMC by removing the limitation of requiring the body frame of the vehicle remain parallel to the navigation frame.
- The second novel compensator is presented in Section 3.6. This design expands on the previous novel compensator by allowing for coupling between DoFs in the model the compensator is based on. This is similar to the previously designed coupled controller; however, the key difference here is that the sliding surface is defined in the body frame, and therefore results in a more computationally efficient design.

3.2. Comparison of Design Strategies

When designing a compensator for any system, there are usually decisions that need to be made based on, for example, implementation restrictions or desirable properties of the model to be retained. Each of these decisions will dictate the type of control strategy to implement for a particular plant. This section compares some common strategy types employed for underwater vehicles, and concludes with a comparison of the strategies employed within this thesis.

3.2.1. Coupled Strategies vs. Uncoupled Strategies

Control strategies for underwater vehicles can be categorised based on the level of coupling present in the control architecture. Coupling is introduced through the presence of non-zero off-diagonal elements within any of the following matrices.

1. The rigid body system inertia matrix, $\mathbf{M}_{\mathbf{RB}}$ of Equation (2.23);

2. The rigid body Coriolis and centripetal forces matrix, $\mathbf{C}_{\mathbf{RB}}\left(\mathbf{v}_{\mathbf{b}}(t)\right)$ of Equation (2.26);
3. The added mass matrix, $\mathbf{M}_{\mathbf{A}}$ of Equation (2.30);
4. The added mass Coriolis and centripetal forces matrix, $\mathbf{C}_{\mathbf{A}}\left(\mathbf{v}_{\mathbf{r}}(t)\right)$ of Equation (2.32);
5. The hydrodynamic damping matrix, $\mathbf{D}\left(\mathbf{v}_{\mathbf{r}}(t)\right)$ of Equation (2.34);
6. The hydrodynamic lift matrix, $\mathbf{L}\left(\mathbf{v}_{\mathbf{r}}(t)\right)$ of Equation (2.43).

Coupled strategies provide mechanisms that enable coupling between DoFs of the vehicle model to be included and actively compensated for whereas uncoupled strategies generally treat any coupling within the plant model as an unmodelled disturbance.

1. Control Strategies Based on Coupled Vehicle Models

Coupled strategies account for coupling within the model of the underwater vehicle [53]. Hence, there is no need to treat this coupling as an unmodelled disturbance within the system. This means that the model is more accurate over a larger range of operating conditions, particularly when multiple DoFs are excited at the same time. The limitation of this type of strategy is computational demand. In comparison to simple scalar arithmetic, matrix multiplication is more complicated and therefore more computationally demanding.

2. Control Strategies Based on Uncoupled Vehicle Models

Uncoupled strategies are simpler to implement and less computationally expensive than coupled strategies due to the model present containing no interaction between DoFs [2]. Therefore, the application of compensation for each DoF is independent of all other DoFs. This strategy is adequate during simple manoeuvres where a single DoF is excited at a time. However, it is lacking compared to the more complicated coupled strategies during manoeuvres where multiple DoFs are excited at the same time.

3.2.2. Body Frame vs. Navigation Frame

As discussed throughout Chapter 2, the two frames most commonly used within underwater vehicle control are the body frame, with origin fixed in relation to the body of the vehicle, and the navigation frame, with origin fixed in relation to the Earth's surface. Both of these frames have advantages and disadvantages with respect to both modelling and interfacing with other core components of the autonomy structure of an AUV.

1. Control Strategies Based on Body Frame Models

Body frame strategies utilise a model decomposed in the body frame for compensation [57, 68]. As can be seen in the various vehicle models presented in Chapter 2, the body frame models, as compared to their navigation frame counterparts, are simpler as there is no need to transform the various matrices from the body frame to the navigation frame. In this respect, compensators based on body frame models are simpler and more computationally efficient to implement compared to their navigation frame equivalent. However, not all states of the vehicle are measured in the body frame. In general, velocity information is represented in the body frame, yet position and orientation information is represented in the navigation frame. The limitation of using a body frame compensator is that a mechanism of representing this position and orientation information in the body frame is required.

2. Control Strategies Based on Navigation Frame Models

In opposition to body frame strategies, navigation frame strategies require the vehicle model be decomposed in the navigation frame [56]. Therefore, these strategies require the use of more complicated models, as seen in Chapter 2, where there is a need to transform the various matrices within the body frame model into the navigation frame. This increases the computational expense for a navigation frame based strategy that is not required for a body frame based strategy. Furthermore, as mentioned in the previous section, the body frame is a convenient frame for representing velocity information. Therefore, this information must also be transformed from the body frame to the navigation frame in order to be utilised by navigation frame based control strategies.

3.2.3. Sliding Mode Control vs. Other Control

Many different control algorithms have been implemented for controlling underwater vehicles. These range from the classical proportional-integral-derivative (PID) control [15, 71, 72] through to more modern techniques such as neural network (NN) control [28, 29] and model predictive control (MPC) [39], as well as combinations of these techniques such as NN and PID control [24] or NN and MPC [38]. One particular modern control strategy that has received attention recently, particularly for AUVs, is sliding mode control (SMC) [40, 42, 48].

1. Sliding Mode Control

Sliding mode control is a form of variable structure control (VSC) [73] that has properties that make it particularly appealing for application to AUVs. These properties include relatively simple implementation [42] and robustness to both modelling uncertainty and unknown disturbances [31, 40, 41]. Pure SMC has one particular limitation, which is the phenomenon of chattering [74]. Chattering is a high frequency oscillation that is caused by the discontinuous signum function within the control law of SMC. This oscillation can lead to premature wear of actuators [74] and excessive power consumption. However, several methods have been developed with the intention of retaining the desirable properties of SMC while also limiting, or even removing, chattering from the control system [2, 3, 53].

2. Other Control Algorithms

Even though linear controllers, such as PID control [71], has been applied to underwater vehicles, this class of controller is largely unsuitable due to the highly nonlinear nature of the vehicle dynamics combined with the unstructured environment that these vehicles are required to operate in [23-25]. Nonlinear techniques such as NN control and MPC are better suited to AUV control; however, these techniques do have limitations that must also be considered. For example, the teaching and learning cycles for a NN can be vast in terms of both time and resource consumption [31], particularly for a complex vehicle operating in a highly dynamic environment. MPC suffers from similar limitations in terms of resource consumption; the accuracy and optimality of the control solution is proportional to

the horizon used when predicting future control inputs [39], which is also proportional to computational load. Therefore, in order to obtain a high level of accuracy using MPC, large amounts of computational resources are required [38, 39].

3.2.4. Comparison of Strategies

The core component of this thesis is the design of high performance compensators for implementation on AUVs. Based on the comparisons presented in Sections 3.2.1 to 3.2.3, this thesis proposes two novel control strategies. These control strategies are detailed as follows.

The first new strategy to be presented, namely the body frame uncoupled sliding mode controller (BFUSMC), will be based on an uncoupled model. The reduced complexity of utilising an uncoupled model is beneficial particularly for a vehicle with minimal computational capabilities to execute the control algorithm. Under highly constrained circumstances, a control algorithm of this nature can be acceptable, particularly if the coupled dynamics of the vehicle are not excited. However, the limitation of such a strategy is exposed when these coupled dynamics are excited, which can lead to potentially limited performance. Therefore, the development of this strategy is to highlight the importance of including coupling within the control structure.

The second strategy to be presented, namely the body frame coupled sliding mode controller (BFCSMC), is a novel controller based on a coupled model decomposed in the body frame. The performance of the BFCSMC will be compared with that of the BFUSMC to demonstrate the performance benefits of explicitly including coupling within the control strategy. The BFCSMC will also be compared to an existing equivalent navigation frame strategy, namely the navigation frame coupled sliding mode controller (NFCSMC). The advantage of performing control in the body frame is due to the reduced complexity of the model represented in the body frame. Therefore, if the performance of a navigation frame based strategy is comparable to that of an equivalent body frame based strategy, the body frame based strategy has a

distinct advantage particularly in terms of reduced resources required for implementation.

Both the BFUSMC and the BFCSMC presented within this thesis are based on sliding mode control. There are several reasons as to why SMC was chosen over other control strategies. The most critical of these reasons is the fact that the mathematical model of an AUV is highly complex, nonlinear, and difficult to obtain. As such, dynamics that have not been accounted for in the control law, irrespective of the complexity of the model the controller is based on, will be excited during normal operation of the vehicle. Not only can SMC be applied directly to a nonlinear system, and therefore avoid the need to linearise a nonlinear system, SMC is also robust to modelling uncertainty [74, 75]. Hence, a control law based on SMC is able to account for unmodelled dynamics due to modelling uncertainty. Another reason for choosing SMC is its relatively simple architecture, which implies a lower computational resource requirement for implementation. AUVs are quite restricted with the amount of processing power that can be dedicated to a system such as the controller, and hence a control architecture that provides good performance from a relatively low computational load is extremely attractive. For these reasons, SMC is chosen as the algorithm to base both novel controllers on, as well as the algorithm in which to compare these novel controllers.

3.3. Sliding Mode Control Concepts

Sliding mode control is a nonlinear control algorithm that can be directly applied to nonlinear plant models. The essence of SMC is to restrict the motion of a system to a defined surface within the state space. The design of this surface is such that the system exhibits the desired reduced-order dynamics while on this surface.

The behaviour of SMC can be thought of as two phases. The initial phase, also known as the reaching phase, corresponds to driving the system from an arbitrary starting point to the defined surface, or sliding surface, within the state space. The final phase corresponds to the behaviour associated with keeping the system on this sliding surface. Under ideal conditions, this latter behaviour is known as the ideal sliding motion.

The design of a sliding mode controller consists of two parts. Firstly, a sliding surface is defined such that the system is stable and exhibits the desired reduced-order dynamics while on this surface. Secondly, a control law is designed such that the system is forced towards this sliding surface from an arbitrary starting point and, once the surface is reached within finite time, the system remains on this surface.

To assist in the second step, it is common to utilise a nonlinear switching function in the form of the signum function [74], which is defined as:

$$\operatorname{sgn}(x) = \begin{cases} -1 \text{ if } x < 0 \\ 0 \text{ if } x = 0 \\ 1 \text{ if } x > 0 \end{cases} \tag{3.1}$$

By using this function, the trajectory of the system can always be oriented towards the sliding surface. Based on the position of the system in the state space, under the condition that the system is not on the sliding surface, the signum function will possess a value of either +1 or -1, which will correspond to driving the system towards the surface. Due to the discontinuous nature of the signum function, when the system reaches, and subsequently crosses over, the surface, the signum function will switch values, and therefore continue to drive the system towards the surface, now from the other side of the surface. Hence, irrespective of the position of the system in the state space, it will always be driven towards the sliding surface.

The compensators presented within this thesis are required to track a reference trajectory. Therefore, it is typical to formulate the sliding surface in terms of the tracking error, which is the difference between the current state of the vehicle determined by the navigation system and the desired state of the vehicle determined by the guidance system. Therefore, once the system has reached the sliding surface, driving the system towards the origin will result in the tracking error being driven to zero. All that remains then is to design the control law such that the system is forced onto the sliding surface and remains on it.

By using the signum function defined by Equation (3.1), a significant limitation within SMC is exposed. Under nonideal conditions, due to, for example, delays or hysteresis, the application of the switched control can lag the time at which it should

be applied. This will lead to the system constantly moving from one side of the sliding surface to the other without actually remaining on it. This phenomenon is called chattering, and will be discussed in the following section.

3.3.1. Chattering

Due to the discontinuous nature of the signum function in the switching term of a sliding mode controller, a high frequency oscillation can be induced in the control signal that is applied to the plant. This oscillation is called chattering, and is usually undesirable as it can cause premature wear of actuators [74] as well as excessive power consumption. For this reason, alternatives to the signum function have been used to prevent chattering from occurring. These alternatives approximate the signum function while avoiding the sharp discontinuity at $x = 0$. Two simple alternatives are the saturation function [2, 3, 53], expressed as:

$$\text{sat}\left(\tfrac{x}{\phi}\right) = \begin{cases} \text{sgn}(x) \text{ if } \left|\tfrac{x}{\phi}\right| > 1 \\ \tfrac{x}{\phi} \text{ otherwise} \end{cases} \tag{3.2}$$

and the hyperbolic tangent function [76, 77], expressed as:

$$\tanh\left(\tfrac{x}{\phi}\right) \tag{3.3}$$

Both of these alternatives utilise a factor, ϕ, known as the boundary layer thickness to remove chattering. This boundary layer has the effect of low-pass filtering the control signal, and therefore the high frequency oscillation is removed. However, the limitation is that ideal sliding motion is no longer attained.

Figure 3.1 compares the saturation function, Equation (3.2), against the signum function, Equation (3.1), while Figure 3.2 compares the hyperbolic tangent function, Equation (3.3), against the signum function. For demonstration purposes, both these figures have the boundary layer thickness, ϕ, set to values of 0.1 and 0.5. What can be observed from Figure 3.1 and Figure 3.2 is that, as ϕ approaches zero, both the saturation function and the hyperbolic tangent function approach the signum function. Therefore, as ϕ approaches zero, the performance of an ideal sliding mode

controller is realised, and so too is the presence of chattering. Hence, ϕ defines a trade-off between the desired transient performance of SMC and the undesired presence of chattering.

The saturation function contains discontinuities at $x = \pm\phi$, at which point the saturation function switches between the signum function and the value of $\frac{x}{\phi}$. Furthermore, the slope of both the saturation function and the hyperbolic tangent

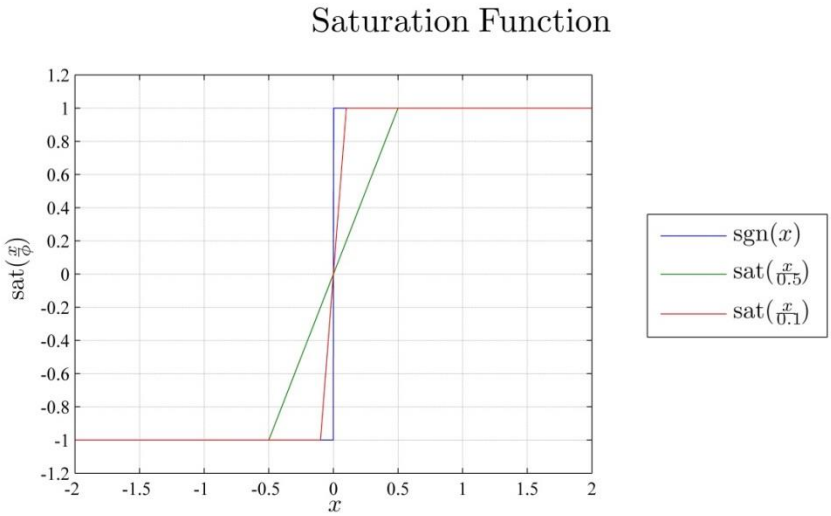

Figure 3.1: Saturation Function Compared to the Signum Function

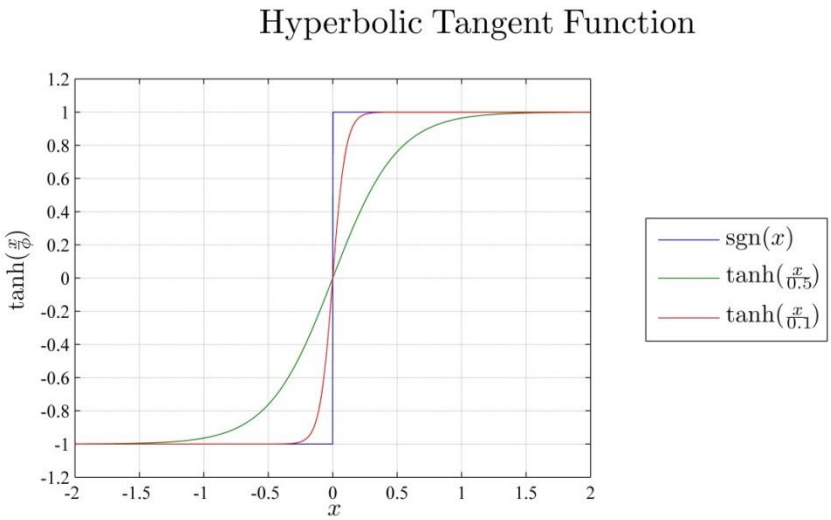

Figure 3.2: Hyperbolic Tangent Function Compared to the Signum Function

function are equal at $x = 0$, with this slope equalling $\frac{1}{\phi}$. Therefore, as $\tanh\left(\frac{x}{\phi}\right)$ is continuous for all *x*, this function is chosen for chatter removal within the simulation studies conducted in Chapter 4 and Chapter 6.

3.4. Existing AUV Control Strategies Utilising SMC

The two novel control strategies presented in this thesis are both based on SMC. This thesis presents a simulation study and therefore the performance of both the BFUSMC and the BFCSMC need to be compared against existing strategies of a similar nature. Fossen has developed and presented various control strategies for AUVs. In particular, a simple uncoupled sliding mode controller and a more complex coupled sliding mode controller have both been developed and implemented for AUVs [2, 53]. As these existing strategies are similar to the novel strategies being presented in this thesis, the development of these existing strategies will be presented here.

The same structure is adopted for presenting the design of each existing control strategy. This structure is defined as follows.

- Vehicle Model – The particular simplified model derived in Chapter 2 that is used within the controller design is identified.
- Controller Design – The derivation of the controller is presented, and the control law is defined.
- Stability Analysis – Using the stability analysis techniques introduced in Chapter 1, both the stability of the system is assessed and any conditions placed on control parameters are defined.

3.4.1. Uncoupled Sliding Mode Controller

Here, the steps taken by Fossen in designing a simple uncoupled sliding mode controller (USMC) for an underwater vehicle are followed [2]. The resultant controller is uncoupled because, when simplifying the vehicle model, each DoF is

treated independently of all others. Therefore, the resultant compensator can be considered as six individual sliding mode controllers, one implemented for each DoF.

1. Vehicle Model

The derivation of the USMC begins with the use of Simplified Model 4 of Section 2.3.4. The basis of this vehicle model is Equation (2.79), and is shown again here for convenience.

$$\mathbf{M}\dot{\mathbf{v}}_{\mathbf{b}}(t)+\mathbf{D}\left(\mathbf{v}_{\mathbf{b}}(t)\right)\mathbf{v}_{\mathbf{b}}(t)=\mathbf{M}\ddot{\boldsymbol{\eta}}_{\mathbf{n}}(t)+\mathbf{D}\left(\dot{\boldsymbol{\eta}}_{\mathbf{n}}(t)\right)\dot{\boldsymbol{\eta}}_{\mathbf{n}}(t)=\boldsymbol{\tau}(t) \tag{2.79}$$

As seen in Section 2.3.4, water currents are ignored and the hydrodynamic damping matrix, $\mathbf{D}\left(\mathbf{v}_{\mathbf{b}}(t)\right)$, only considers nonlinear effects, i.e., $\mathbf{D}\left(\mathbf{v}_{\mathbf{b}}(t)\right)=\mathbf{D}_{\mathbf{n}}\left(\mathbf{v}_{\mathbf{b}}(t)\right)$. Furthermore, all cross-coupling in the model is ignored such that the system inertia matrix, $\mathbf{M}$, as well as the hydrodynamic damping matrix, $\mathbf{D}\left(\mathbf{v}_{\mathbf{b}}(t)\right)$, are both diagonal matrices. The system inertia matrix is expressed as:

$$\mathbf{M}=\begin{bmatrix} m-X_{\dot{u}} & 0 & 0 & 0 & 0 & 0 \\ 0 & m-Y_{\dot{v}} & 0 & 0 & 0 & 0 \\ 0 & 0 & m-Z_{\dot{w}} & 0 & 0 & 0 \\ 0 & 0 & 0 & I_x-K_{\dot{p}} & 0 & 0 \\ 0 & 0 & 0 & 0 & I_y-M_{\dot{q}} & 0 \\ 0 & 0 & 0 & 0 & 0 & I_z-N_{\dot{r}} \end{bmatrix} \tag{3.4}$$

while the hydrodynamic damping matrix is expressed as:

$$\mathbf{D}\left(\mathbf{v}_{\mathbf{b}}(t)\right)=\begin{bmatrix} |u_b(t)|X_{|u|u} & 0 & 0 & 0 & 0 & 0 \\ 0 & |v_b(t)|Y_{|v|v} & 0 & 0 & 0 & 0 \\ 0 & 0 & |w_b(t)|Z_{|w|w} & 0 & 0 & 0 \\ 0 & 0 & 0 & |p_b(t)|K_{|p|p} & 0 & 0 \\ 0 & 0 & 0 & 0 & |q_b(t)|M_{|q|q} & 0 \\ 0 & 0 & 0 & 0 & 0 & |r_b(t)|N_{|r|r} \end{bmatrix} \tag{3.5}$$

By making the further assumption of the body frame being oriented such that it is parallel to the navigation frame, as seen in Section 2.3.4, $\dot{\boldsymbol{\eta}}_{\mathbf{n}}(t)=\mathbf{v}_{\mathbf{b}}(t)$ and hence Equation (2.79) can be rewritten as:

$$m_{ii}\ddot{x}_i(t) + d_{ii}\left|\dot{x}_i(t)\right|\dot{x}_i(t) = \tau_i(t) \tag{3.6}$$

where

$$\begin{aligned} i &= 1...6 \\ m_{ii} &= \left\{\mathbf{M}_{ii}\right\} \\ d_{ii}\left|\dot{x}_i(t)\right| &= \left\{\mathbf{D}_{ii}\left(\mathbf{v}_{\mathbf{b}_i}(t)\right)\right\} \\ x_i(t) &= \left\{\boldsymbol{\eta}_{\mathbf{n}_i}(t)\right\} \\ \tau_i(t) &= \left\{\boldsymbol{\tau}_i(t)\right\} \end{aligned}$$

Within Equation (3.6):

$$m_{ii} > 0 \forall i = 1...6 \tag{3.7}$$

$$d_{ii} > 0 \forall i = 1...6 \tag{3.8}$$

This allows the vehicle model to be represented using six individual equations, one for each DoF, in a completely uncoupled fashion.

2. Controller Design

In order to apply an uncoupled SMC scheme to an AUV, all six DoFs would require separate uncoupled SMCs. Hence, the design of six compensators is required. However, as the design process is identical for all six controllers, the design of a single DoF SMC for one DoF of the vehicle is presented here.

A scalar measure of the tracking performance of the sliding mode controller, $s_i(t)$, is defined by:

$$s_i(t) = \dot{\tilde{x}}_i(t) + \lambda_i \tilde{x}_i(t) \tag{3.9}$$

where $\tilde{x}_i(t) = x_i(t) - x_{d_i}(t)$ is the position or attitude error, $x_i(t)$ is the current vehicle position or attitude, and $x_{d_i}(t)$ is the desired vehicle position or attitude.

Within Equation (3.9), $\lambda_i > 0$ is the control bandwidth that relates the amount of tracking error, $\tilde{x}_i(t)$, and the time derivative of the tracking error, $\dot{\tilde{x}}_i(t)$, to the overall tracking performance, $s_i(t)$.

For $s_i(t) = 0$, this describes a sliding surface with exponential dynamics described by:

$$\tilde{x}_i(t) = e^{-\lambda_i(t-t_0)}\tilde{x}_i(t_0) \tag{3.10}$$

Under the condition of $s_i(t) = 0$, the tracking error, $\tilde{x}_i(t)$, is guaranteed to converge to zero in finite time. Hence, the control objective is now a matter of finding a nonlinear control law such that the following equation holds:

$$\lim_{t\to\infty} s_i(t) = 0 \tag{3.11}$$

In the design of the sliding control law, it is convenient to define a virtual reference $x_{r_i}(t)$ satisfying:

$$\dot{x}_{r_i}(t) = \dot{x}_{d_i}(t) - \lambda_i \tilde{x}_i(t) \tag{3.12}$$

and

$$\therefore s_i(t) = \dot{x}_i(t) - \dot{x}_{r_i}(t) \tag{3.13}$$

Therefore, by taking the time derivative of Equation (3.13) and multiplying by m_{ii}, the following equation exists for $m_{ii}\dot{s}_i(t)$:

$$m_{ii}\dot{s}_i(t) = m_{ii}\ddot{x}_i(t) - m_{ii}\ddot{x}_{r_i}(t) \tag{3.14}$$

Substitution of the vehicle model of Equation (3.6) into Equation (3.14) yields:

$$m_{ii}\dot{s}_i(t) = \left(\tau_i(t) - d_{ii}\left|\dot{x}_i(t)\right|\dot{x}_i(t)\right) - m_{ii}\ddot{x}_{r_i}(t)$$

Hence, the following equation is obtained for $m_{ii}\dot{s}_i(t)$.

$$\begin{aligned} m_{ii}\dot{s}_i(t) &= \left(\tau_i(t) - d_{ii}\left|\dot{x}_i(t)\right|\dot{x}_i(t)\right) - m_{ii}\ddot{x}_{r_i}(t) + d_{ii}\left|\dot{x}_i(t)\right|\dot{x}_{r_i}(t) - d_{ii}\left|\dot{x}_i(t)\right|\dot{x}_{r_i}(t) \\ &= d_{ii}\left|\dot{x}_i(t)\right|\dot{x}_{r_i}(t) - d_{ii}\left|\dot{x}_i(t)\right|\dot{x}_i(t) + \tau_i(t) - m_{ii}\ddot{x}_{r_i}(t) - d_{ii}\left|\dot{x}_i(t)\right|\dot{x}_{r_i}(t) \\ &= d_{ii}\left|\dot{x}_i(t)\right|\left(\dot{x}_{r_i}(t) - \dot{x}_i(t)\right) + \tau_i(t) - m_{ii}\ddot{x}_{r_i}(t) - d_{ii}\left|\dot{x}_i(t)\right|\dot{x}_{r_i}(t) \end{aligned}$$

$$\therefore m_{ii}\dot{s}_i(t) = -d_{ii}\left|\dot{x}_i(t)\right|s_i(t) + \left(\tau_i(t) - m_{ii}\ddot{x}_{r_i}(t) - d_{ii}\left|\dot{x}_i(t)\right|\dot{x}_{r_i}(t)\right) \tag{3.15}$$

Consider the scalar Lyapunov-like function candidate expressed as:

$$V(t) = \tfrac{1}{2} m_{ii} s_i^{\,2}(t) \tag{3.16}$$

From Equation (3.16), $V(t) \geq 0$ due to $m_{ii} > 0$ as seen in Equation (3.7). Differentiating Equation (3.16) with respect to time, under the assumption of $\dot{m}_{ii}(t) = 0$, yields:

$$\dot{V}(t) = m_{ii}\dot{s}_i(t)s_i(t) \tag{3.17}$$

Hence,

$$\dot{V}(t) = -d_{ii}\left|\dot{x}_i(t)\right|s_i^{\,2}(t) + s_i(t)\left(\tau_i(t) - m_{ii}\ddot{x}_{r_i}(t) - d_{ii}\left|\dot{x}_i(t)\right|\dot{x}_{r_i}(t)\right) \tag{3.18}$$

Taking the control law to be:

$$\tau_{d_i}(t) = \hat{m}_{ii}\ddot{x}_{r_i}(t) + \hat{d}_{ii}\left|\dot{x}_i(t)\right|\dot{x}_{r_i}(t) - K_{\mathrm{T}_{\mathrm{U}_i}} s_i(t) - K_{\mathrm{S}_{\mathrm{U}_i}} \operatorname{sgn}\left(s_i(t)\right) \tag{3.19}$$

where $\hat{m}_{ii}$ and $\hat{d}_{ii}$ are the estimates of m_{ii} and d_{ii} respectively,

$$K_{\mathrm{T}_{\mathrm{U}_i}} > 0 \tag{3.20}$$

is the tracking error gain, $K_{\mathrm{S}_{\mathrm{U}_i}}$ is the switching gain, and $\operatorname{sgn}(\bullet)$ is the signum function described in Equation (3.1), yields:

$$\begin{aligned} \dot{V}(t) = &-\left(K_{\mathrm{T}_{\mathrm{U}_i}} + d_{ii}\left|\dot{x}_i(t)\right|\right)s_i^{\,2}(t) + \left(\tilde{m}_{ii}\ddot{x}_{r_i}(t) + \tilde{d}_{ii}\left|\dot{x}_i(t)\right|\dot{x}_{r_i}(t)\right)s_i(t) \\ &- K_{\mathrm{S}_{\mathrm{U}_i}}\left|s_i(t)\right| \end{aligned} \tag{3.21}$$

Equation (3.21) contains the system inertia error, $\tilde{m}_{ii} = \hat{m}_{ii} - m_{ii}$, and the hydrodynamic damping error, $\tilde{d}_{ii} = \hat{d}_{ii} - d_{ii}$.

3. Stability Analysis

Using Lyapunov stability analysis, the condition on $K_{S_{U_i}}$ is found by requiring that $\dot{V}(t) < 0$. The particular choice, expressed as:

$$K_{S_{U_i}} \geq \left| \tilde{m}_{ii} \ddot{x}_{r_i}(t) + \tilde{d}_{ii} \left| \dot{x}_i(t) \right| \dot{x}_{r_i}(t) \right| + \alpha_i \tag{3.22}$$

with

$$\alpha_i > 0 \tag{3.23}$$

accomplishes this, as seen in:

$$\dot{V}(t) < -\left(K_{T_{U_i}} + d_{ii} \left| \dot{x}_i(t) \right| \right) s_i^2(t) - \alpha_i \left| s_i(t) \right| \leq 0 \tag{3.24}$$

This is due to $K_{T_{U_i}} > 0$ from Equation (3.20), $d_{ii} > 0$ from Equation (3.8) and $\alpha_i > 0$ from Equation (3.23).

As $\dot{V}(t) \leq 0$, this implies that $V(t) \leq V(t_0)$ and that $s_i(t)$ is bounded. This in turn implies that $\ddot{V}(t)$ is bounded and hence $\dot{V}(t)$ is uniformly continuous. From the definition of $V(t)$ in Equation (3.16), $V(t) \geq 0$ and hence $V(t) \to 0$ as $t \to \infty$. Barbălat's lemma then shows that as $V(t) \to 0$, $s_i(t) \to 0$ and hence $\tilde{x}_i(t) \to 0$ as $t \to \infty$. Hence, as the tracking error, $\tilde{x}_i(t)$, is shown to converge to zero, the system is shown to be stable.

In summary, an uncoupled sliding mode controller that has been developed by Fossen [2] was presented, and the system has been proven to be stable as the tracking error of the system is shown to converge to zero.

3.4.2. Navigation Frame Coupled Sliding Mode Controller

Fossen [53] has proposed the design of a navigation frame coupled sliding mode controller (NFCSMC). The design of the NFCSMC utilises properties of the vehicle model in both the navigation frame and the body frame. As it is typical to conduct

guidance in the navigation frame, the sliding surface for this controller is also defined in the navigation frame. The NFCSMC is an extension of the USMC presented in Section 3.4.1 as it has the capacity to include coupling that is present in the vehicle model.

1. Vehicle Model

The derivation of the NFCSMC begins with the use of Simplified Model 1 of Section 2.3.1. The basis of this vehicle model is Equation (2.66), and is shown again here for convenience.

$$\begin{aligned}\mathbf{M}_{\boldsymbol{\eta}}\left(\boldsymbol{\eta}_{\mathbf{n}}(t)\right)\ddot{\boldsymbol{\eta}}_{\mathbf{n}}(t)+\mathbf{C}_{\boldsymbol{\eta}}\left(\mathbf{v}_{\mathbf{b}}(t),\boldsymbol{\eta}_{\mathbf{n}}(t)\right)\dot{\boldsymbol{\eta}}_{\mathbf{n}}(t)\\ +\mathbf{D}_{\boldsymbol{\eta}}\left(\mathbf{v}_{\mathbf{b}}(t),\boldsymbol{\eta}_{\mathbf{n}}(t)\right)\dot{\boldsymbol{\eta}}_{\mathbf{n}}(t)+\mathbf{g}_{\boldsymbol{\eta}}\left(\boldsymbol{\eta}_{\mathbf{n}}(t)\right)=\boldsymbol{\tau}_{\boldsymbol{\eta}}\left(\boldsymbol{\eta}_{\mathbf{n}}(t)\right)\end{aligned} \tag{2.66}$$

2. Controller Design

A vector measure of the tracking performance of the sliding mode controller, $\mathbf{s}(t)$, is defined as:

$$\mathbf{s}(t)=\dot{\tilde{\boldsymbol{\eta}}}(t)+\boldsymbol{\lambda}\tilde{\boldsymbol{\eta}}(t) \tag{3.25}$$

where $\tilde{\boldsymbol{\eta}}(t)=\boldsymbol{\eta}_{\mathbf{n}}(t)-\boldsymbol{\eta}_{\mathbf{d}}(t)$ is the position and attitude error vector, $\boldsymbol{\eta}_{\mathbf{n}}(t)$ is the current vehicle position and attitude vector, and $\boldsymbol{\eta}_{\mathbf{d}}(t)$ is the desired vehicle position and attitude vector.

Within Equation (3.25), $\boldsymbol{\lambda}>0$ is the control bandwidth that relates the amount of tracking error, $\tilde{\boldsymbol{\eta}}(t)$, and the time derivative of the tracking error, $\dot{\tilde{\boldsymbol{\eta}}}(t)$, to the overall tracking performance, $\mathbf{s}(t)$.

For $\mathbf{s}(t)=\mathbf{0}$, this describes a sliding surface with exponential dynamics described by:

$$\tilde{\boldsymbol{\eta}}(t)=e^{-\boldsymbol{\lambda}(t-t_0)}\tilde{\boldsymbol{\eta}}(t_0) \tag{3.26}$$

Under the condition of $\mathbf{s}(t)=\mathbf{0}$, the tracking error, $\tilde{\boldsymbol{\eta}}(t)$, is guaranteed to converge to zero in finite time. Hence, the control objective is now a matter of finding a nonlinear control law such that the following equation holds.

$$\lim_{t\to\infty}\mathbf{s}(t)=\mathbf{0} \tag{3.27}$$

In the design of the sliding control law, it is convenient to define a virtual reference vector, $\mathbf{x}_{\mathbf{r}}(t)$, satisfying:

$$\dot{\mathbf{x}}_{\mathbf{r}}(t)=\dot{\boldsymbol{\eta}}_{\mathbf{d}}(t)-\boldsymbol{\lambda}\tilde{\boldsymbol{\eta}}(t) \tag{3.28}$$

and

$$\therefore \mathbf{s}(t)=\dot{\boldsymbol{\eta}}_{\mathbf{n}}(t)-\dot{\mathbf{x}}_{\mathbf{r}}(t) \tag{3.29}$$

Differentiating Equation (3.29) with respect to time yields:

$$\dot{\mathbf{s}}(t)=\ddot{\boldsymbol{\eta}}_{\mathbf{n}}(t)-\ddot{\mathbf{x}}_{\mathbf{r}}(t) \tag{3.30}$$

Consider the scalar Lyapunov-like function candidate expressed as:

$$V(t)=\tfrac{1}{2}\mathbf{s}^{T}(t)\mathbf{M}_{\boldsymbol{\eta}}\left(\boldsymbol{\eta}_{\mathbf{n}}(t)\right)\mathbf{s}(t) \tag{3.31}$$

From Equation (3.31), $V(t)\geq 0$ due to $\mathbf{M}_{\boldsymbol{\eta}}\left(\boldsymbol{\eta}_{\mathbf{n}}(t)\right)>\mathbf{0}$ as seen in Equation (2.68) of Section 2.3.1. Differentiating Equation (3.31) with respect to time yields:

$$\begin{aligned}\dot{V}(t)=&\tfrac{1}{2}\dot{\mathbf{s}}^{T}(t)\mathbf{M}_{\boldsymbol{\eta}}\left(\boldsymbol{\eta}_{\mathbf{n}}(t)\right)\mathbf{s}(t)+\tfrac{1}{2}\mathbf{s}^{T}(t)\mathbf{M}_{\boldsymbol{\eta}}\left(\boldsymbol{\eta}_{\mathbf{n}}(t)\right)\dot{\mathbf{s}}(t)\\&+\tfrac{1}{2}\mathbf{s}^{T}(t)\dot{\mathbf{M}}_{\boldsymbol{\eta}}\left(\boldsymbol{\eta}_{\mathbf{n}}(t)\right)\mathbf{s}(t)\end{aligned} \tag{3.32}$$

$\mathbf{M}_{\boldsymbol{\eta}}\left(\boldsymbol{\eta}_{\mathbf{n}}(t)\right)$ is positive definite, as seen in Equation (2.68) of Section 2.3.1, and hence:

$$\dot{\mathbf{s}}^{T}(t)\mathbf{M}_{\boldsymbol{\eta}}\left(\boldsymbol{\eta}_{\mathbf{n}}(t)\right)\mathbf{s}(t)=\mathbf{s}^{T}(t)\mathbf{M}_{\boldsymbol{\eta}}\left(\boldsymbol{\eta}_{\mathbf{n}}(t)\right)\dot{\mathbf{s}}(t).$$

Therefore, the following equation is obtained from Equation (3.32).

$$\dot{V}(t)=\mathbf{s}^{T}(t)\mathbf{M}_{\boldsymbol{\eta}}\left(\boldsymbol{\eta}_{\mathbf{n}}(t)\right)\dot{\mathbf{s}}(t)+\tfrac{1}{2}\mathbf{s}^{T}(t)\dot{\mathbf{M}}_{\boldsymbol{\eta}}\left(\boldsymbol{\eta}_{\mathbf{n}}(t)\right)\mathbf{s}(t) \tag{3.33}$$

Adding and subtracting $\mathbf{s}^T(t)\mathbf{C}_{\boldsymbol{\eta}}\left(\boldsymbol{\nu}_{\mathbf{b}}(t),\boldsymbol{\eta}_{\mathbf{n}}(t)\right)\mathbf{s}(t)$ to $\dot{V}(t)$ in Equation (3.33) yields:

$$\begin{aligned}\dot{V}(t) &= \mathbf{s}^T(t)\mathbf{M}_{\boldsymbol{\eta}}\left(\boldsymbol{\eta}_{\mathbf{n}}(t)\right)\dot{\mathbf{s}}(t) + \tfrac{1}{2}\mathbf{s}^T(t)\dot{\mathbf{M}}_{\boldsymbol{\eta}}\left(\boldsymbol{\eta}_{\mathbf{n}}(t)\right)\mathbf{s}(t) \\ &\quad - \mathbf{s}^T(t)\mathbf{C}_{\boldsymbol{\eta}}\left(\boldsymbol{\nu}_{\mathbf{b}}(t),\boldsymbol{\eta}_{\mathbf{n}}(t)\right)\mathbf{s}(t) + \mathbf{s}^T(t)\mathbf{C}_{\boldsymbol{\eta}}\left(\boldsymbol{\nu}_{\mathbf{b}}(t),\boldsymbol{\eta}_{\mathbf{n}}(t)\right)\mathbf{s}(t)\end{aligned}$$

$$\begin{aligned}\therefore \dot{V}(t) &= \mathbf{s}^T(t)\mathbf{M}_{\boldsymbol{\eta}}\left(\boldsymbol{\eta}_{\mathbf{n}}(t)\right)\dot{\mathbf{s}}(t) + \mathbf{s}^T(t)\mathbf{C}_{\boldsymbol{\eta}}\left(\boldsymbol{\nu}_{\mathbf{b}}(t),\boldsymbol{\eta}_{\mathbf{n}}(t)\right)\mathbf{s}(t) \\ &\quad + \tfrac{1}{2}\mathbf{s}^T(t)\left[\dot{\mathbf{M}}_{\boldsymbol{\eta}}\left(\boldsymbol{\eta}_{\mathbf{n}}(t)\right) - 2\mathbf{C}_{\boldsymbol{\eta}}\left(\boldsymbol{\nu}_{\mathbf{b}}(t),\boldsymbol{\eta}_{\mathbf{n}}(t)\right)\right]\mathbf{s}(t)\end{aligned} \tag{3.34}$$

$\left[\dot{\mathbf{M}}_{\boldsymbol{\eta}}\left(\boldsymbol{\eta}_{\mathbf{n}}(t)\right) - 2\mathbf{C}_{\boldsymbol{\eta}}\left(\boldsymbol{\nu}_{\mathbf{b}}(t),\boldsymbol{\eta}_{\mathbf{n}}(t)\right)\right]$ is skew-symmetric, as seen in Equation (2.69) of Section 2.3.1, and hence Equation (3.34) simplifies to:

$$\dot{V}(t) = \mathbf{s}^T(t)\mathbf{M}_{\boldsymbol{\eta}}\left(\boldsymbol{\eta}_{\mathbf{n}}(t)\right)\dot{\mathbf{s}}(t) + \mathbf{s}^T(t)\mathbf{C}_{\boldsymbol{\eta}}\left(\boldsymbol{\nu}_{\mathbf{b}}(t),\boldsymbol{\eta}_{\mathbf{n}}(t)\right)\mathbf{s}(t) \tag{3.35}$$

Substituting Equation (3.29) and Equation (3.30) into Equation (3.35) yields:

$$\begin{aligned}\dot{V}(t) &= \mathbf{s}^T(t)\mathbf{M}_{\boldsymbol{\eta}}\left(\boldsymbol{\eta}_{\mathbf{n}}(t)\right)\left[\ddot{\boldsymbol{\eta}}_{\mathbf{n}}(t) - \ddot{\mathbf{x}}_{\mathbf{r}}(t)\right] \\ &\quad + \mathbf{s}^T(t)\mathbf{C}_{\boldsymbol{\eta}}\left(\boldsymbol{\nu}_{\mathbf{b}}(t),\boldsymbol{\eta}_{\mathbf{n}}(t)\right)\left[\dot{\boldsymbol{\eta}}_{\mathbf{n}}(t) - \dot{\mathbf{x}}_{\mathbf{r}}(t)\right] \\ &= \mathbf{s}^T(t)\left[\mathbf{M}_{\boldsymbol{\eta}}\left(\boldsymbol{\eta}_{\mathbf{n}}(t)\right)\ddot{\boldsymbol{\eta}}_{\mathbf{n}}(t) - \mathbf{M}_{\boldsymbol{\eta}}\left(\boldsymbol{\eta}_{\mathbf{n}}(t)\right)\ddot{\mathbf{x}}_{\mathbf{r}}(t)\right] \\ &\quad + \mathbf{s}^T(t)\left[\mathbf{C}_{\boldsymbol{\eta}}\left(\boldsymbol{\nu}_{\mathbf{b}}(t),\boldsymbol{\eta}_{\mathbf{n}}(t)\right)\dot{\boldsymbol{\eta}}_{\mathbf{n}}(t) - \mathbf{C}_{\boldsymbol{\eta}}\left(\boldsymbol{\nu}_{\mathbf{b}}(t),\boldsymbol{\eta}_{\mathbf{n}}(t)\right)\dot{\mathbf{x}}_{\mathbf{r}}(t)\right]\end{aligned}$$

$$\begin{aligned}\therefore \dot{V}(t) &= \mathbf{s}^T(t)\left[\mathbf{M}_{\boldsymbol{\eta}}\left(\boldsymbol{\eta}_{\mathbf{n}}(t)\right)\ddot{\boldsymbol{\eta}}_{\mathbf{n}}(t) + \mathbf{C}_{\boldsymbol{\eta}}\left(\boldsymbol{\nu}_{\mathbf{b}}(t),\boldsymbol{\eta}_{\mathbf{n}}(t)\right)\dot{\boldsymbol{\eta}}_{\mathbf{n}}(t)\right] \\ &\quad - \mathbf{s}^T(t)\left[\mathbf{M}_{\boldsymbol{\eta}}\left(\boldsymbol{\eta}_{\mathbf{n}}(t)\right)\ddot{\mathbf{x}}_{\mathbf{r}}(t) + \mathbf{C}_{\boldsymbol{\eta}}\left(\boldsymbol{\nu}_{\mathbf{b}}(t),\boldsymbol{\eta}_{\mathbf{n}}(t)\right)\dot{\mathbf{x}}_{\mathbf{r}}(t)\right]\end{aligned} \tag{3.36}$$

Substituting Simplified Model 1, Equation (2.66) of Section 2.3.1, into Equation (3.36) yields:

$$\begin{aligned}\dot{V}(t) &= \mathbf{s}^T(t)\left[\boldsymbol{\tau}_{\boldsymbol{\eta}}\left(\boldsymbol{\eta}_{\mathbf{n}}(t)\right) - \mathbf{D}_{\boldsymbol{\eta}}\left(\boldsymbol{\nu}_{\mathbf{b}}(t),\boldsymbol{\eta}_{\mathbf{n}}(t)\right)\dot{\boldsymbol{\eta}}_{\mathbf{n}}(t) - \mathbf{g}_{\boldsymbol{\eta}}\left(\boldsymbol{\eta}_{\mathbf{n}}(t)\right)\right] \\ &\quad - \mathbf{s}^T(t)\left[\mathbf{M}_{\boldsymbol{\eta}}\left(\boldsymbol{\eta}_{\mathbf{n}}(t)\right)\ddot{\mathbf{x}}_{\mathbf{r}}(t) + \mathbf{C}_{\boldsymbol{\eta}}\left(\boldsymbol{\nu}_{\mathbf{b}}(t),\boldsymbol{\eta}_{\mathbf{n}}(t)\right)\dot{\mathbf{x}}_{\mathbf{r}}(t)\right] \\ &= \mathbf{s}^T(t)\left[\boldsymbol{\tau}_{\boldsymbol{\eta}}\left(\boldsymbol{\eta}_{\mathbf{n}}(t)\right) - \mathbf{M}_{\boldsymbol{\eta}}\left(\boldsymbol{\eta}_{\mathbf{n}}(t)\right)\ddot{\mathbf{x}}_{\mathbf{r}}(t) - \mathbf{C}_{\boldsymbol{\eta}}\left(\boldsymbol{\nu}_{\mathbf{b}}(t),\boldsymbol{\eta}_{\mathbf{n}}(t)\right)\dot{\mathbf{x}}_{\mathbf{r}}(t) - \mathbf{g}_{\boldsymbol{\eta}}\left(\boldsymbol{\eta}_{\mathbf{n}}(t)\right)\right] \\ &\quad - \mathbf{s}^T(t)\mathbf{D}_{\boldsymbol{\eta}}\left(\boldsymbol{\nu}_{\mathbf{b}}(t),\boldsymbol{\eta}_{\mathbf{n}}(t)\right)\left[\mathbf{s}(t) + \dot{\mathbf{x}}_{\mathbf{r}}(t)\right] \\ &= \mathbf{s}^T(t)\left[\boldsymbol{\tau}_{\boldsymbol{\eta}}\left(\boldsymbol{\eta}_{\mathbf{n}}(t)\right) - \mathbf{M}_{\boldsymbol{\eta}}\left(\boldsymbol{\eta}_{\mathbf{n}}(t)\right)\ddot{\mathbf{x}}_{\mathbf{r}}(t) - \mathbf{C}_{\boldsymbol{\eta}}\left(\boldsymbol{\nu}_{\mathbf{b}}(t),\boldsymbol{\eta}_{\mathbf{n}}(t)\right)\dot{\mathbf{x}}_{\mathbf{r}}(t) - \mathbf{g}_{\boldsymbol{\eta}}\left(\boldsymbol{\eta}_{\mathbf{n}}(t)\right)\right] \\ &\quad - \mathbf{s}^T(t)\left[\mathbf{D}_{\boldsymbol{\eta}}\left(\boldsymbol{\nu}_{\mathbf{b}}(t),\boldsymbol{\eta}_{\mathbf{n}}(t)\right)\dot{\mathbf{x}}_{\mathbf{r}}(t) - \mathbf{D}_{\boldsymbol{\eta}}\left(\boldsymbol{\nu}_{\mathbf{b}}(t),\boldsymbol{\eta}_{\mathbf{n}}(t)\right)\mathbf{s}(t)\right]\end{aligned}$$

$$\begin{aligned}\dot{V}(t) = \mathbf{s}^T(t)\Big[\boldsymbol{\tau}_{\eta}\left(\boldsymbol{\eta}_{\mathbf{n}}(t)\right) - \mathbf{M}_{\eta}\left(\boldsymbol{\eta}_{\mathbf{n}}(t)\right)\ddot{\mathbf{x}}_{\mathbf{r}}(t) - \mathbf{C}_{\eta}\left(\mathbf{v}_{\mathbf{b}}(t), \boldsymbol{\eta}_{\mathbf{n}}(t)\right)\dot{\mathbf{x}}_{\mathbf{r}}(t) \\ -\mathbf{D}_{\eta}\left(\mathbf{v}_{\mathbf{b}}(t), \boldsymbol{\eta}_{\mathbf{n}}(t)\right)\dot{\mathbf{x}}_{\mathbf{r}}(t) - \mathbf{g}_{\eta}\left(\boldsymbol{\eta}_{\mathbf{n}}(t)\right)\Big] - \mathbf{s}^T(t)\mathbf{D}_{\eta}\left(\mathbf{v}_{\mathbf{b}}(t), \boldsymbol{\eta}_{\mathbf{n}}(t)\right)\mathbf{s}(t)\end{aligned} \tag{3.37}$$

Fossen and Sagatun [78] show that the representation of the control law of Slotine and Di Benedetto [79] can be simplified by defining a virtual reference vector $\mathbf{q}_{\mathbf{r}}(t)$ satisfying the following transformation:

$$\dot{\mathbf{x}}_{\mathbf{r}}(t) = \mathbf{J}\left(\boldsymbol{\eta}_{\mathbf{n}}(t)\right)\dot{\mathbf{q}}_{\mathbf{r}}(t) \tag{3.38}$$

Rearranging Equation (3.38) yields:

$$\dot{\mathbf{q}}_{\mathbf{r}}(t) = \mathbf{J}^{-1}\left(\boldsymbol{\eta}_{\mathbf{n}}(t)\right)\dot{\mathbf{x}}_{\mathbf{r}}(t) \tag{3.39}$$

and taking the time derivative of Equation (3.39) yields:

$$\ddot{\mathbf{q}}_{\mathbf{r}}(t) = \mathbf{J}^{-1}\left(\boldsymbol{\eta}_{\mathbf{n}}(t)\right)\Big[\ddot{\mathbf{x}}_{\mathbf{r}}(t) - \dot{\mathbf{J}}\left(\boldsymbol{\eta}_{\mathbf{n}}(t)\right)\mathbf{J}^{-1}\left(\boldsymbol{\eta}_{\mathbf{n}}(t)\right)\dot{\mathbf{x}}_{\mathbf{r}}(t)\Big] \tag{3.40}$$

Hence, Equation (3.37) can be expressed as:

$$\begin{aligned}\dot{V}(t) = -\mathbf{s}^T(t)\mathbf{D}_{\eta}\left(\mathbf{v}_{\mathbf{b}}(t), \boldsymbol{\eta}_{\mathbf{n}}(t)\right)\mathbf{s}(t) + \left(\mathbf{J}^{-1}\left(\boldsymbol{\eta}_{\mathbf{n}}(t)\right)\mathbf{s}(t)\right)^T\Big[\boldsymbol{\tau}(t) \\ -\mathbf{M}\ddot{\mathbf{q}}_{\mathbf{r}}(t) - \mathbf{C}\left(\dot{\mathbf{q}}_{\mathbf{r}}(t)\right)\dot{\mathbf{q}}_{\mathbf{r}}(t) - \mathbf{D}\left(\dot{\mathbf{q}}_{\mathbf{r}}(t)\right)\dot{\mathbf{q}}_{\mathbf{r}}(t) - \mathbf{g}\left(\boldsymbol{\eta}_{\mathbf{n}}(t)\right)\Big]\end{aligned} \tag{3.41}$$

Taking the control law to be:

$$\begin{aligned}\boldsymbol{\tau}_{\mathbf{d}}(t) = \hat{\mathbf{M}}\ddot{\mathbf{q}}_{\mathbf{r}}(t) + \hat{\mathbf{C}}\left(\dot{\mathbf{q}}_{\mathbf{r}}(t)\right)\dot{\mathbf{q}}_{\mathbf{r}}(t) + \hat{\mathbf{D}}\left(\dot{\mathbf{q}}_{\mathbf{r}}(t)\right)\dot{\mathbf{q}}_{\mathbf{r}}(t) + \hat{\mathbf{g}}\left(\boldsymbol{\eta}_{\mathbf{n}}(t)\right) \\ -\mathbf{J}^T\left(\boldsymbol{\eta}_{\mathbf{n}}(t)\right)\mathbf{K}_{\mathbf{T_{NC}}}\mathbf{s}(t) - \mathbf{K}_{\mathbf{S_{NC}}}.\times\operatorname{sgn}\left(\mathbf{J}^{-1}\left(\boldsymbol{\eta}_{\mathbf{n}}(t)\right)\mathbf{s}(t)\right)\end{aligned} \tag{3.42}$$

where $\hat{\mathbf{M}}$, $\hat{\mathbf{C}}\left(\dot{\mathbf{q}}_{\mathbf{r}}(t)\right)$, $\hat{\mathbf{D}}\left(\dot{\mathbf{q}}_{\mathbf{r}}(t)\right)$ and $\hat{\mathbf{g}}\left(\boldsymbol{\eta}_{\mathbf{n}}(t)\right)$ are the estimates of $\mathbf{M}$, $\mathbf{C}\left(\dot{\mathbf{q}}_{\mathbf{r}}(t)\right)$, $\mathbf{D}\left(\dot{\mathbf{q}}_{\mathbf{r}}(t)\right)$ and $\mathbf{g}\left(\boldsymbol{\eta}_{\mathbf{n}}(t)\right)$ respectively,

$$\mathbf{K}_{\mathbf{T_{NC}}} \geq \mathbf{0} \tag{3.43}$$

is the 6×6 tracking error gain matrix, $\mathbf{K}_{\mathbf{S_{NC}}}$ is the 6×1 switching gain vector, $\operatorname{sgn}(\bullet)$ is the signum function described in Equation (3.1), and $.\times$ is used to denote element-by-element multiplication, yields:

$$\begin{aligned}\dot{V}(t) = -\mathbf{s}^T(t)\left[\mathbf{D}_{\boldsymbol{\eta}}\left(\mathbf{v}_{\mathbf{b}}(t),\boldsymbol{\eta}_{\mathbf{n}}(t)\right)+\mathbf{K}_{\mathbf{T_{NC}}}\right]\mathbf{s}(t)-\mathbf{K}_{\mathbf{S_{NC}}}^T\left|\mathbf{J}^{-1}\left(\boldsymbol{\eta}_{\mathbf{n}}(t)\right)\mathbf{s}(t)\right| \\ +\left(\mathbf{J}^{-1}\left(\boldsymbol{\eta}_{\mathbf{n}}(t)\right)\mathbf{s}(t)\right)^T\left[\tilde{\mathbf{M}}\ddot{\mathbf{q}}_{\mathbf{r}}(t)+\tilde{\mathbf{C}}\left(\dot{\mathbf{q}}_{\mathbf{r}}(t)\right)\dot{\mathbf{q}}_{\mathbf{r}}(t)\right. \\ \left.+\tilde{\mathbf{D}}\left(\dot{\mathbf{q}}_{\mathbf{r}}(t)\right)\dot{\mathbf{q}}_{\mathbf{r}}(t)+\tilde{\mathbf{g}}\left(\boldsymbol{\eta}_{\mathbf{n}}(t)\right)\right]\end{aligned} \tag{3.44}$$

Equation (3.44) contains the system inertia error, $\tilde{\mathbf{M}}=\hat{\mathbf{M}}-\mathbf{M}$, the Coriolis and centripetal forces error, $\tilde{\mathbf{C}}\left(\dot{\mathbf{q}}_{\mathbf{r}}(t)\right)=\hat{\mathbf{C}}\left(\dot{\mathbf{q}}_{\mathbf{r}}(t)\right)-\mathbf{C}\left(\dot{\mathbf{q}}_{\mathbf{r}}(t)\right)$, the hydrodynamic damping error, $\tilde{\mathbf{D}}\left(\dot{\mathbf{q}}_{\mathbf{r}}(t)\right)=\hat{\mathbf{D}}\left(\dot{\mathbf{q}}_{\mathbf{r}}(t)\right)-\mathbf{D}\left(\dot{\mathbf{q}}_{\mathbf{r}}(t)\right)$, and the gravitational and buoyancy error, $\tilde{\mathbf{g}}\left(\boldsymbol{\eta}_{\mathbf{n}}(t)\right)=\hat{\mathbf{g}}\left(\boldsymbol{\eta}_{\mathbf{n}}(t)\right)-\mathbf{g}\left(\boldsymbol{\eta}_{\mathbf{n}}(t)\right)$.

It must be noted that, as the sliding surface, $\mathbf{s}(t)$, is defined in the navigation frame from Equation (3.25), there is the requirement to transform this surface to the body frame as seen by the terms $\mathbf{J}^T\left(\boldsymbol{\eta}_{\mathbf{n}}(t)\right)\mathbf{K}_{\mathbf{T_{NC}}}\mathbf{s}(t)$ and $\mathbf{K}_{\mathbf{S_{NC}}}.\times\operatorname{sgn}\left(\mathbf{J}^{-1}\left(\boldsymbol{\eta}_{\mathbf{n}}(t)\right)\mathbf{s}(t)\right)$ within the control law of Equation (3.42). Furthermore, $\dot{\mathbf{q}}_{\mathbf{r}}(t)$ of Equation (3.39) is defined as transforming the virtual reference vector, $\dot{\mathbf{x}}_{\mathbf{r}}(t)$, from the navigation frame to the body frame. Therefore, at each time step, the control law must transform both the sliding surface, $\mathbf{s}(t)$, and the virtual reference vector, $\dot{\mathbf{x}}_{\mathbf{r}}(t)$, from the navigation frame to the body frame. These continual rotations will lead to high computational requirements when the NFCSMC is implemented within an AUV as these transformations are required for control action.

3. Stability Analysis

Using Lyapunov stability analysis, the condition on $K_{S_{NC_i}}$, the *i*th elements of $\mathbf{K}_{\mathbf{S_{NC}}}$, is found by requiring that $\dot{V}(t)\le 0$. The particular choice as given in:

$$K_{S_{NC_i}} \ge \left|\tilde{\mathbf{M}}\ddot{\mathbf{q}}_{\mathbf{r}}(t)+\tilde{\mathbf{C}}\left(\dot{\mathbf{q}}(t)\right)\dot{\mathbf{q}}_{\mathbf{r}}(t)+\tilde{\mathbf{D}}\left(\dot{\mathbf{q}}(t)\right)\dot{\mathbf{q}}_{\mathbf{r}}(t)+\tilde{\mathbf{g}}\left(\boldsymbol{\eta}_{\mathbf{n}}(t)\right)\right|_i+\alpha_{NC_i},(i=1...6) \tag{3.45}$$

with

$$\alpha_{NC_i} > 0 \tag{3.46}$$

accomplishes this, as seen in:

$$\dot{V}(t) < -\mathbf{s}^T(t)\left[\mathbf{D}_{\boldsymbol{\eta}}\left(\mathbf{v}_{\mathbf{b}}(t), \boldsymbol{\eta}_{\mathbf{n}}(t)\right) + \mathbf{K}_{\mathbf{T_{NC}}}\right]\mathbf{s}(t) - \boldsymbol{\alpha}_{\mathbf{NC}}^T\left|\mathbf{J}^{-1}\left(\boldsymbol{\eta}_{\mathbf{n}}(t)\right)\mathbf{s}(t)\right| \leq 0 \quad (3.47)$$

where

$$\boldsymbol{\alpha}_{\mathbf{NC}} = \begin{bmatrix} \alpha_{NC_1} & \alpha_{NC_2} & \cdots & \alpha_{NC_6} \end{bmatrix}^T \quad (3.48)$$

This is due to $\mathbf{D}_{\boldsymbol{\eta}}\left(\mathbf{v}_{\mathbf{b}}(t), \boldsymbol{\eta}_{\mathbf{n}}(t)\right) > \mathbf{0}$ from Equation (2.70) of Section 2.3.1 and $\mathbf{K}_{\mathbf{T_{NC}}} \geq \mathbf{0}$ from Equation (3.43) and hence $\mathbf{D}_{\boldsymbol{\eta}}\left(\mathbf{v}_{\mathbf{b}}(t), \boldsymbol{\eta}_{\mathbf{n}}(t)\right) + \mathbf{K}_{\mathbf{T_{NC}}} > \mathbf{0}$.

As $\dot{V}(t) \leq 0$, this implies that $V(t) \leq V(t_0)$ and that $\mathbf{s}(t)$ is bounded. This in turn implies that $\ddot{V}(t)$ is bounded and hence $\dot{V}(t)$ is uniformly continuous. From the definition of $V(t)$ in Equation (3.31), $V(t) \geq 0$ and hence $V(t) \to 0$ as $t \to \infty$. Barbălat's lemma then shows that as $V(t) \to 0$, $\mathbf{s}(t) \to \mathbf{0}$, and hence $\tilde{\boldsymbol{\eta}}(t) \to \mathbf{0}$ as $t \to \infty$. Hence, as the tracking error, $\tilde{\boldsymbol{\eta}}(t)$, is shown to converge to zero, the system is shown to be stable.

In summary, a navigation frame coupled sliding mode controller that has been developed by Fossen [53] was presented, and the system has been proven to be stable as the tracking error of the system is shown to converge to zero.

3.5. Body Frame Uncoupled Sliding Mode Controller

In this section, a new body frame uncoupled sliding mode controller (BFUSMC) is proposed. The BFUSMC is proposed as part of the algorithm development to be used to demonstrate the importance of including any coupling of the vehicle model within the control law. By comparing the performance of the BFUSMC with any coupled strategies, the importance and benefit of including coupling will be clearly demonstrated. The development of the BFUSMC follows similar principles to that of the USMC in Section 3.4.1, yet the key difference is the removal of the limitation requiring $\dot{\boldsymbol{\eta}}_{\mathbf{n}}(t) = \mathbf{v}_{\mathbf{b}}(t)$.

The structure in which the BFUSMC will be developed is as follows.

- Justification – The rationale for developing the BFUSMC will be presented.
- Vehicle Model – Simplified Model 3 derived in Chapter 2 forms the basis of this controller. A brief overview of this model will be provided.
- Controller Design – The derivation of the controller is presented, and the control law is defined.
- Stability Analysis – Using the stability analysis techniques introduced in Chapter 1, both the stability of the system is assessed and any conditions placed on control parameters are defined.

3.5.1. Justification

One critical requirement of the USMC as developed in Section 3.4.1 which severely limits its use for underwater vehicles is the necessity of $\dot{\boldsymbol{\eta}}_{\mathbf{n}}(t) = \mathbf{v}_{\mathbf{b}}(t)$. For a typical AUV, this requirement dictates that the attitude of the vehicle remains constant throughout the entire mission, i.e., the vehicle never turns. Imposing this restriction will severely limit the manoeuvring capabilities of the vehicle. The following derives the BFUSMC where this severe limitation is relaxed.

3.5.2. Vehicle Model

The derivation of the BFUSMC begins with the use of Simplified Model 3 of Section 2.3.3. The basis of this vehicle model is Equation (2.76), and is shown again here for convenience.

$$\mathbf{M}\dot{\mathbf{v}}_{\mathbf{b}}(t) + \mathbf{D}\left(\mathbf{v}_{\mathbf{b}}(t)\right)\mathbf{v}_{\mathbf{b}}(t) = \boldsymbol{\tau}(t) \tag{2.76}$$

It must be noted that the system inertia matrix, $\mathbf{M}$, and the hydrodynamic damping matrix, $\mathbf{D}\left(\mathbf{v}_{\mathbf{b}}(t)\right)$, are both diagonal matrices. Hence, the model can be represented as a system of six fully uncoupled equations. However, the following analysis utilises Simplified Model 3 in matrix form as seen in Equation (2.76) of Section 2.3.3.

3.5.3. Controller Design

To make the analysis easier, firstly define $\mathbf{x}(t)$ as the integral of the vehicle velocity, $\mathbf{v_b}(t)$, decomposed in the body frame, expressed as:

$$\mathbf{x}(t) = \int_0^t \mathbf{v_b}(\gamma)\, d\gamma \tag{3.49}$$

and $\mathbf{x_d}(t)$ as the integral of the desired vehicle velocity, $\mathbf{v_d}(t)$, decomposed in the body frame, expressed as:

$$\mathbf{x_d}(t) = \int_0^t \mathbf{v_d}(\gamma)\, d\gamma \tag{3.50}$$

A vector measure of the tracking performance of the sliding mode controller, $\mathbf{s}(t)$, is defined as:

$$\mathbf{s}(t) = \tilde{\mathbf{v}}(t) + \boldsymbol{\lambda}\tilde{\mathbf{x}}(t) \tag{3.51}$$

where $\tilde{\mathbf{x}}(t) = \mathbf{x}(t) - \mathbf{x_d}(t)$ is the tracking error in the body frame.

Within Equation (3.51), $\boldsymbol{\lambda} > \mathbf{0}$ is the control bandwidth that relates the amount of tracking error, $\tilde{\mathbf{x}}(t)$, and the velocity error, $\tilde{\mathbf{v}}(t) = \mathbf{v_b}(t) - \mathbf{v_d}(t)$, to the overall tracking performance, $\mathbf{s}(t)$.

For $\mathbf{s}(t) = \mathbf{0}$, this describes a sliding surface with exponential dynamics described by:

$$\tilde{\mathbf{x}}(t) = e^{-\boldsymbol{\lambda}(t-t_0)}\tilde{\mathbf{x}}(t_0) \tag{3.52}$$

Under the condition of $\mathbf{s}(t) = \mathbf{0}$, the tracking error, $\tilde{\mathbf{x}}(t)$, is guaranteed to converge to zero in finite time. Hence, the control objective is now a matter of finding a nonlinear control law such that the following equation holds.

$$\lim_{t\to\infty} \mathbf{s}(t) = \mathbf{0} \tag{3.53}$$

In the design of the sliding control law, it is convenient to define a virtual reference vector, $\mathbf{x_r}(t)$, satisfying:

$$\mathbf{x}_\mathbf{r}(t) = \mathbf{v}_\mathbf{d}(t) - \boldsymbol{\lambda}\tilde{\mathbf{x}}(t) \tag{3.54}$$

and

$$\therefore \mathbf{s}(t) = \mathbf{v}_\mathbf{b}(t) - \mathbf{x}_\mathbf{r}(t) \tag{3.55}$$

Differentiating Equation (3.55) with respect to time yields:

$$\dot{\mathbf{s}}(t) = \dot{\mathbf{v}}_\mathbf{b}(t) - \dot{\mathbf{x}}_\mathbf{r}(t) \tag{3.56}$$

Consider the scalar Lyapunov-like function candidate expressed as:

$$V(t) = \tfrac{1}{2}\mathbf{s}^T(t)\mathbf{M}\mathbf{s}(t) \tag{3.57}$$

From Equation (3.57), $V(t) \geq 0$ due to $\mathbf{M} > \mathbf{0}$ as seen in Equation (2.77) of Section 2.3.3. Differentiating Equation (3.57) with respect to time yields:

$$\dot{V}(t) = \tfrac{1}{2}\dot{\mathbf{s}}^T(t)\mathbf{M}\mathbf{s}(t) + \tfrac{1}{2}\mathbf{s}^T(t)\dot{\mathbf{M}}\mathbf{s}(t) + \tfrac{1}{2}\mathbf{s}^T(t)\mathbf{M}\dot{\mathbf{s}}(t) \tag{3.58}$$

By assuming $\dot{\mathbf{M}} = \mathbf{0}$, Equation (3.58) becomes:

$$\dot{V}(t) = \tfrac{1}{2}\dot{\mathbf{s}}^T(t)\mathbf{M}\mathbf{s}(t) + \tfrac{1}{2}\mathbf{s}^T(t)\mathbf{M}\dot{\mathbf{s}}(t) \tag{3.59}$$

$\mathbf{M}$ is positive definite, as seen in Equation (2.77) of Section 2.3.3, and hence:

$$\dot{\mathbf{s}}^T(t)\mathbf{M}\mathbf{s}(t) = \mathbf{s}^T(t)\mathbf{M}\dot{\mathbf{s}}(t)$$

Therefore, the following equation is obtained from Equation (3.59).

$$\dot{V}(t) = \mathbf{s}^T(t)\mathbf{M}\dot{\mathbf{s}}(t) \tag{3.60}$$

Substituting Equation (3.56) into Equation (3.60) yields:

$$\begin{aligned}\dot{V}(t) &= \mathbf{s}^T(t)\mathbf{M}\left[\dot{\mathbf{v}}_\mathbf{b}(t) - \dot{\mathbf{x}}_\mathbf{r}(t)\right] \\ &= \mathbf{s}^T(t)\mathbf{M}\dot{\mathbf{v}}_\mathbf{b}(t) - \mathbf{s}^T(t)\mathbf{M}\dot{\mathbf{x}}_\mathbf{r}(t) \\ &= \mathbf{s}^T(t)\left[\boldsymbol{\tau}(t) - \mathbf{D}\left(\mathbf{v}_\mathbf{b}(t)\right)\mathbf{v}_\mathbf{b}(t)\right] - \mathbf{s}^T(t)\mathbf{M}\dot{\mathbf{x}}_\mathbf{r}(t)\end{aligned}$$

$$\therefore \dot{V}(t) = -\mathbf{s}^T(t)\mathbf{D}\left(\mathbf{v}_\mathbf{b}(t)\right)\mathbf{v}_\mathbf{b}(t) + \mathbf{s}^T(t)\boldsymbol{\tau}(t) - \mathbf{s}^T(t)\mathbf{M}\dot{\mathbf{x}}_\mathbf{r}(t) \tag{3.61}$$

Adding and subtracting $\mathbf{s}^T(t)\mathbf{D}\left(\mathbf{v}_\mathbf{b}(t)\right)\mathbf{x}_\mathbf{r}(t)$ to $\dot{V}(t)$ in Equation (3.61) yields:

$$\begin{aligned}\dot{V}(t) &= -\mathbf{s}^T(t)\mathbf{D}(\mathbf{v_b}(t))\mathbf{v_b}(t) + \mathbf{s}^T(t)\mathbf{D}(\mathbf{v_b}(t))\mathbf{x_r}(t) - \mathbf{s}^T(t)\mathbf{D}(\mathbf{v_b}(t))\mathbf{x_r}(t) \\ &\quad + \mathbf{s}^T(t)\boldsymbol{\tau}(t) - \mathbf{s}^T(t)\mathbf{M}\dot{\mathbf{x}}_\mathbf{r}(t) \\ &= \mathbf{s}^T(t)\boldsymbol{\tau}(t) + \mathbf{s}^T(t)\mathbf{D}(\mathbf{v_b}(t))\left[\mathbf{x_r}(t) - \mathbf{v_b}(t)\right] - \mathbf{s}^T(t)\mathbf{D}(\mathbf{v_b}(t))\mathbf{x_r}(t) - \mathbf{s}^T(t)\mathbf{M}\dot{\mathbf{x}}_\mathbf{r}(t) \\ &= \mathbf{s}^T(t)\boldsymbol{\tau}(t) - \mathbf{s}^T(t)\mathbf{D}(\mathbf{v_b}(t))\mathbf{s}(t) - \mathbf{s}^T(t)\mathbf{D}(\mathbf{v_b}(t))\mathbf{x_r}(t) - \mathbf{s}^T(t)\mathbf{M}\dot{\mathbf{x}}_\mathbf{r}(t) \\ &= -\mathbf{s}^T(t)\mathbf{D}(\mathbf{v_b}(t))\mathbf{s}(t) + \mathbf{s}^T(t)\boldsymbol{\tau}(t) - \mathbf{s}^T(t)\mathbf{M}\dot{\mathbf{x}}_\mathbf{r}(t) - \mathbf{s}^T(t)\mathbf{D}(\mathbf{v_b}(t))\mathbf{x_r}(t)\end{aligned}$$

$$\therefore \dot{V}(t) = -\mathbf{s}^T(t)\mathbf{D}(\mathbf{v_b}(t))\mathbf{s}(t) + \mathbf{s}^T(t)\left[\boldsymbol{\tau}(t) - \mathbf{M}\dot{\mathbf{x}}_\mathbf{r}(t) - \mathbf{D}(\mathbf{v_b}(t))\mathbf{x_r}(t)\right] \quad (3.62)$$

Taking the control law to be:

$$\boldsymbol{\tau}_\mathbf{d}(t) = \hat{\mathbf{M}}\dot{\mathbf{x}}_\mathbf{r}(t) + \hat{\mathbf{D}}(\mathbf{v_b}(t))\mathbf{x_r}(t) - \mathbf{K}_{\mathbf{T_{BU}}}\mathbf{s}(t) - \mathbf{K}_{\mathbf{S_{BU}}}\mathrm{sgn}(\mathbf{s}(t)) \quad (3.63)$$

where $\hat{\mathbf{M}}$ and $\hat{\mathbf{D}}(\mathbf{v_b}(t))$ are the estimates of $\mathbf{M}$ and $\mathbf{D}(\mathbf{v_b}(t))$ respectively,

$$\mathbf{K}_{\mathbf{T_{BU}}} \geq \mathbf{0} \quad (3.64)$$

is the 6×6 tracking error gain matrix, $\mathbf{K}_{\mathbf{S_{BU}}}$ is the 6×6 switching gain matrix, and $\mathrm{sgn}(\bullet)$ is the signum function described in Equation (3.1), yields:

$$\begin{aligned}\dot{V}(t) = &-\mathbf{s}^T(t)\left[\mathbf{K}_{\mathbf{T_{BU}}} + \mathbf{D}(\mathbf{v_b}(t))\right]\mathbf{s}(t) - \mathbf{s}^T(t)\mathbf{K}_{\mathbf{S_{BU}}}\mathrm{sgn}(\mathbf{s}(t)) \\ &+ \mathbf{s}^T(t)\left[\tilde{\mathbf{M}}\dot{\mathbf{x}}_\mathbf{r}(t) + \tilde{\mathbf{D}}(\mathbf{v_b}(t))\mathbf{x_r}(t)\right]\end{aligned} \quad (3.65)$$

Equation (3.65) contains the system inertia error, $\tilde{\mathbf{M}} = \hat{\mathbf{M}} - \mathbf{M}$ and the hydrodynamic damping error, $\tilde{\mathbf{D}}(\mathbf{v_b}(t)) = \hat{\mathbf{D}}(\mathbf{v_b}(t)) - \mathbf{D}(\mathbf{v_b}(t))$.

It must be noted that, as the sliding surface, $\mathbf{s}(t)$, is defined in the body frame from Equation (3.51), there is no requirement of transforming this surface between the navigation frame and the body frame as is required for the NFCSMC of Section 3.4.2. Therefore, the BFUSMC is a more computationally efficient design compared to the NFCSMC.

3.5.4. Stability Analysis

In a similar fashion to the existing SMCs presented in Section 3.4, the conditions on $\mathbf{K}_{\mathbf{S_{BU}}}$ can be found using Lyapunov stability analysis. As $V(t) \geq 0$ from Equation (3.57), it is required that $\dot{V}(t) \leq 0$.

If a nonlinear function, $\mathbf{F}(t)$, is defined as:

$$\mathbf{F}(t) = \tilde{\mathbf{M}}\dot{\mathbf{x}}_{\mathbf{r}}(t) + \tilde{\mathbf{D}}\left(\mathbf{v}_{\mathbf{b}}(t)\right)\mathbf{x}_{\mathbf{r}}(t) \tag{3.66}$$

$\dot{V}(t) \leq 0$ will be true if the following inequality is also true.

$$\mathbf{K}_{\mathbf{S_{BU}}}\operatorname{sgn}\left(\mathbf{s}(t)\right) > \mathbf{F}(t) \tag{3.67}$$

If $\mathbf{K}_{\mathbf{S_{BU}}}$ is a diagonal matrix where the elements on the main diagonal are determined by:

$$K_{S_{BU_{ii}}} \geq \left|F_i(t)\right| + \alpha_{BU_i}, (i = 1...6) \tag{3.68}$$

setting

$$\alpha_{BU_i} > 0 \tag{3.69}$$

implies that the following inequality is true.

$$\mathbf{s}^T(t)\mathbf{K}_{\mathbf{S_{BU}}}\operatorname{sgn}\left(\mathbf{s}(t)\right) > \mathbf{s}^T(t)\left|\mathbf{F}(t)\right| \tag{3.70}$$

Therefore, $\dot{V}(t) \leq 0$ as seen in:

$$\begin{aligned}
\dot{V}(t) &= -\mathbf{s}^T(t)\left[\mathbf{D}\left(\mathbf{v}_{\mathbf{b}}(t)\right) + \mathbf{K}_{\mathbf{T_{BU}}}\right]\mathbf{s}(t) \\
&\quad + \mathbf{s}^T(t)\mathbf{F}(t) - \mathbf{s}^T(t)\mathbf{K}_{\mathbf{S_{BU}}}\operatorname{sgn}\left(\mathbf{s}(t)\right) \\
&= -\mathbf{s}^T(t)\mathbf{D}\left(\mathbf{v}_{\mathbf{b}}(t)\right)\mathbf{s}(t) - \mathbf{s}^T(t)\mathbf{K}_{\mathbf{T_{BU}}}\mathbf{s}(t) \\
&\quad + \mathbf{s}^T(t)\mathbf{F}(t) - \mathbf{s}^T(t)\mathbf{K}_{\mathbf{S_{BU}}}\operatorname{sgn}\left(\mathbf{s}(t)\right)
\end{aligned}$$

$$\begin{aligned}
\therefore \dot{V}(t) &\leq -\mathbf{s}^T(t)\mathbf{D}\left(\mathbf{v}_{\mathbf{b}}(t)\right)\mathbf{s}(t) - \mathbf{s}^T(t)\mathbf{K}_{\mathbf{T_{BU}}}\mathbf{s}(t) - \mathbf{s}^T(t)\boldsymbol{\alpha}_{\mathbf{BU}}\operatorname{sgn}\left(\mathbf{s}(t)\right) \\
&\leq 0
\end{aligned} \tag{3.71}$$

where

$$\boldsymbol{\alpha}_{\mathbf{BU}_{ij}} = \begin{cases} \alpha_{BU_i} \text{ for } i = j \\ 0 \text{ otherwise} \end{cases} \tag{3.72}$$

This is due to $\mathbf{D}\left(\mathbf{v_b}\left(t\right)\right) > \mathbf{0}$ from Equation (2.78) of Section 2.3.3, and $\mathbf{K}_{\mathbf{T}_{\mathbf{BU}}} \geq \mathbf{0}$ from Equation (3.64).

As $\dot{V}\left(t\right) \leq 0$, this implies that $V\left(t\right) \leq V\left(t_0\right)$ and that $\mathbf{s}\left(t\right)$ is bounded. This in turn implies that $\ddot{V}\left(t\right)$ is bounded and hence $\dot{V}\left(t\right)$ is uniformly continuous. From the definition of $V\left(t\right)$ in Equation (3.57), $V\left(t\right) \geq 0$ and hence $V\left(t\right) \to 0$ as $t \to \infty$. Barbălat's lemma then shows that as $V\left(t\right) \to 0$, $\mathbf{s}\left(t\right) \to \mathbf{0}$, and hence $\tilde{\mathbf{x}}\left(t\right) \to \mathbf{0}$ as $t \to \infty$. Hence, as the tracking error, $\tilde{\mathbf{x}}\left(t\right)$, is shown to converge to zero, the system is shown to be stable.

The derivation here has used the matrix representation of Simplified Model 3 throughout the design process. As this model is uncoupled, due to all off diagonal elements of the matrices being zero, the control law is also uncoupled as all the off diagonal elements of the matrices are zero. Hence, the BFUSMC can be implemented as six single SMCs, one controlling each DoF.

3.6. Body Frame Coupled Sliding Mode Controller

In this section, a novel body frame coupled sliding mode controller (BFCSMC) is proposed such that control is conducted in the body frame as opposed to the navigation frame as seen in the NFCSMC of Section 3.4.2. This structure is proposed to take advantage of the benefits that conducting control in the body frame offers, similar to that of the BFUSMC, yet the BFCSMC allows for any coupling identified in the model to be included in the control law.

The structure in which the BFCSMC will be developed is as follows.

- Justification – The rationale for developing the BFCSMC will be presented.

- Vehicle Model – Simplified Model 2 derived in Chapter 2 forms the basis of this controller. A brief overview of this model will be provided.
- Controller Design – The derivation of the controller is presented, and the control law is defined.
- Stability Analysis – Using the stability analysis techniques introduced in Chapter 1, both the stability of the system is assessed and any conditions placed on control parameters are defined.

3.6.1. Justification

As explained in Section 3.5.1, the USMC places severe restrictions on the manoeuvring capabilities of the vehicle it is controlling. The purpose of this thesis is to control highly manoeuvrable underwater vehicles, and therefore placing such severe restrictions on the manoeuvrability of the vehicle is infeasible. Hence, the USMC is excluded from the simulation studies presented in the following chapters.

The most significant limitation that exists for the BFUSMC is the lack of coupling within the model that the controller is based on. By not including coupling within the controller, an algorithm that is simple to implement is derived and this algorithm can be used for controlling underwater vehicles. However, when conducting complex manoeuvring where, for example, multiple DoFs are excited concurrently or when a single DoF is excited that is coupled through the plant model with another DoF, the resulting motion of the plant can be different to what is expected by the controller model. This unexpected motion is due to unmodelled dynamics within the controller and, even though SMC is robust to unmodelled dynamics, improved performance is obtained by minimising these unmodelled dynamics.

The NFCSMC, as proposed by Fossen [53], extends the capabilities of the USMC by relaxing the restriction of keeping the navigation frame parallel with the body frame. The NFCSMC also improves on both the USMC and the BFUSMC by including coupling within the controller model. However, there is a significant increase in computational requirements primarily due to the sliding surface being defined in the navigation frame. This is due to a more complex representation of the vehicle model

existing in the navigation frame compared to the body frame, and therefore the need to transform information from the body frame to the navigation frame and vice versa. Furthermore, in order to transform information between the body frame and the navigation frame, knowledge of the orientation of the vehicle within the navigation frame is required. This requires the navigation system to provide an estimate of the orientation of the vehicle.

The overall goal of this thesis is to propose controllers for implementation in highly manoeuvrable underwater vehicles. Due to the severe restrictions imposed on the available hardware and payload capabilities of particularly small and inexpensive AUVs, the control algorithm needs to be as computationally efficient as possible while still providing adequate compensation. Therefore, a novel control algorithm, namely the BFCSMC, is proposed.

The BFCSMC possesses the ability to retain coupling within the controller model in a similar fashion to the NFCSMC, and therefore should perform better than the BFUSMC. The BFCSMC also possesses the advantage of defining the sliding surface in the body frame as opposed to the navigation frame for the NFCSMC. The benefit of defining the sliding surface in the body frame is the significant reduction in computational requirements. This is due to there being no need to transform information between the body frame and the navigation frame, which the NFCSMC requires, and therefore no need to utilise an estimate of the attitude of the vehicle for transformation purposes. Furthermore, the model the BFCSMC is based on does not require an estimate of the position or attitude of the vehicle, and hence this control algorithm does not require the position or attitude to be estimated at all.

The remainder of this section presents the design and analysis of the BFCSMC.

3.6.2. Vehicle Model

The derivation of the BFCSMC begins with the use of Simplified Model 2 of Section 2.3.2. The basis of this vehicle model is Equation (2.71), and is shown again here for convenience.

$$\mathbf{M}\dot{\mathbf{v}}_{\mathbf{b}}(t)+\mathbf{C}\left(\mathbf{v}_{\mathbf{b}}(t)\right)\mathbf{v}_{\mathbf{b}}(t)+\mathbf{D}\left(\mathbf{v}_{\mathbf{b}}(t)\right)\mathbf{v}_{\mathbf{b}}(t)=\boldsymbol{\tau}(t) \tag{2.71}$$

As previously stated in Section 2.3.2, the gravitational and buoyancy forces vector, $\mathbf{g}(t)$, is ignored. This is a valid assumption for a highly manoeuvrable vehicle with neutral buoyancy and the centre of gravity coincides with the centre of buoyancy. One important note is that this model does not contain $\boldsymbol{\eta}_{\mathbf{n}}(t)$, and hence does not require any position or attitude information.

3.6.3. Controller Design

To make the analysis easier, firstly define $\mathbf{x}(t)$ as the integral of the vehicle velocity, $\mathbf{v}_{\mathbf{b}}(t)$, decomposed in the body frame, expressed as:

$$\mathbf{x}(t) = \int_0^t \mathbf{v}_{\mathbf{b}}(\gamma)\, d\gamma \tag{3.73}$$

and $\mathbf{x}_{\mathbf{d}}(t)$ as the integral of the desired vehicle velocity, $\mathbf{v}_{\mathbf{d}}(t)$, decomposed in the body frame, expressed as:

$$\mathbf{x}_{\mathbf{d}}(t) = \int_0^t \mathbf{v}_{\mathbf{d}}(\gamma)\, d\gamma \tag{3.74}$$

A vector measure of the tracking performance of the sliding mode controller, $\mathbf{s}(t)$, is defined as:

$$\mathbf{s}(t) = \tilde{\mathbf{v}}(t) + \boldsymbol{\lambda}\tilde{\mathbf{x}}(t) \tag{3.75}$$

where $\tilde{\mathbf{x}}(t) = \mathbf{x}(t) - \mathbf{x}_{\mathbf{d}}(t)$ is the tracking error in the body frame.

Within Equation (3.75), $\boldsymbol{\lambda} > \mathbf{0}$ is the control bandwidth that relates the amount of tracking error, $\tilde{\mathbf{x}}(t)$, and the velocity error, $\tilde{\mathbf{v}}(t) = \mathbf{v}_{\mathbf{b}}(t) - \mathbf{v}_{\mathbf{d}}(t)$, to the overall tracking performance, $\mathbf{s}(t)$.

For $\mathbf{s}(t) = \mathbf{0}$, this describes a sliding surface with exponential dynamics described by:

$$\tilde{\mathbf{x}}(t) = e^{-\boldsymbol{\lambda}(t-t_0)}\tilde{\mathbf{x}}(t_0) \tag{3.76}$$

Under the condition of $\mathbf{s}(t)=\mathbf{0}$, the tracking error, $\tilde{\mathbf{x}}(t)$, is guaranteed to converge to zero in finite time. Hence, the control objective is now a matter of finding a nonlinear control law such that the following equation holds.

$$\lim_{t\to\infty}\mathbf{s}(t)=\mathbf{0} \tag{3.77}$$

In the design of the sliding control law, it is convenient to define a virtual reference vector, $\mathbf{x}_\mathbf{r}(t)$, satisfying:

$$\mathbf{x}_\mathbf{r}(t)=\mathbf{v}_\mathbf{d}(t)-\boldsymbol{\lambda}\tilde{\mathbf{x}}(t) \tag{3.78}$$

and

$$\therefore \mathbf{s}(t)=\mathbf{v}_\mathbf{b}(t)-\mathbf{x}_\mathbf{r}(t) \tag{3.79}$$

Differentiating Equation (3.79) with respect to time yields:

$$\dot{\mathbf{s}}(t)=\dot{\mathbf{v}}_\mathbf{b}(t)-\dot{\mathbf{x}}_\mathbf{r}(t) \tag{3.80}$$

Consider the scalar Lyapunov-like function candidate expressed as:

$$V(t)=\tfrac{1}{2}\mathbf{s}^T(t)\mathbf{M}\mathbf{s}(t) \tag{3.81}$$

From Equation (3.81), $V(t)\geq 0$ due to $\mathbf{M}>\mathbf{0}$ as seen in Equation (2.73) of Section 2.3.2. Differentiating Equation (3.81) with respect to time yields:

$$\dot{V}(t)=\tfrac{1}{2}\dot{\mathbf{s}}^T(t)\mathbf{M}\mathbf{s}(t)+\tfrac{1}{2}\mathbf{s}^T(t)\dot{\mathbf{M}}\mathbf{s}(t)+\tfrac{1}{2}\mathbf{s}^T(t)\mathbf{M}\dot{\mathbf{s}}(t) \tag{3.82}$$

By assuming $\dot{\mathbf{M}}=\mathbf{0}$, Equation (3.82) becomes:

$$\dot{V}(t)=\tfrac{1}{2}\dot{\mathbf{s}}^T(t)\mathbf{M}\mathbf{s}(t)+\tfrac{1}{2}\mathbf{s}^T(t)\mathbf{M}\dot{\mathbf{s}}(t) \tag{3.83}$$

$\mathbf{M}$ is positive definite, as seen in Equation (2.73) of Section 2.3.2, and hence:

$$\dot{\mathbf{s}}^T(t)\mathbf{M}\mathbf{s}(t)=\mathbf{s}^T(t)\mathbf{M}\dot{\mathbf{s}}(t)$$

Therefore, the following equation is obtained from Equation (3.83).

$$\dot{V}(t)=\mathbf{s}^T(t)\mathbf{M}\dot{\mathbf{s}}(t) \tag{3.84}$$

Substituting Equation (3.80) into Equation (3.84) yields:

$$\begin{aligned}\dot{V}(t) &= \mathbf{s}^T(t)\mathbf{M}\left[\dot{\mathbf{v}}_\mathbf{b}(t) - \dot{\mathbf{x}}_\mathbf{r}(t)\right] \\ &= \mathbf{s}^T(t)\mathbf{M}\dot{\mathbf{v}}_\mathbf{b}(t) - \mathbf{s}^T(t)\mathbf{M}\dot{\mathbf{x}}_\mathbf{r}(t) \\ &= \mathbf{s}^T(t)\left[\boldsymbol{\tau}(t) - \mathbf{C}\left(\mathbf{v}_\mathbf{b}(t)\right)\mathbf{v}_\mathbf{b}(t) - \mathbf{D}\left(\mathbf{v}_\mathbf{b}(t)\right)\mathbf{v}_\mathbf{b}(t)\right] - \mathbf{s}^T(t)\mathbf{M}\dot{\mathbf{x}}_\mathbf{r}(t)\end{aligned}$$

$$\begin{aligned}\therefore \dot{V}(t) = &-\mathbf{s}^T(t)\mathbf{C}\left(\mathbf{v}_\mathbf{b}(t)\right)\mathbf{v}_\mathbf{b}(t) - \mathbf{s}^T(t)\mathbf{D}\left(\mathbf{v}_\mathbf{b}(t)\right)\mathbf{v}_\mathbf{b}(t) \\ &+ \mathbf{s}^T(t)\boldsymbol{\tau}(t) - \mathbf{s}^T(t)\mathbf{M}\dot{\mathbf{x}}_\mathbf{r}(t)\end{aligned} \tag{3.85}$$

Adding and subtracting $\mathbf{s}^T(t)\mathbf{C}\left(\mathbf{v}_\mathbf{b}(t)\right)\mathbf{x}_\mathbf{r}$ and $\mathbf{s}^T(t)\mathbf{D}\left(\mathbf{v}_\mathbf{b}(t)\right)\mathbf{x}_\mathbf{r}(t)$ to $\dot{V}(t)$ in Equation (3.85) yields:

$$\begin{aligned}\dot{V}(t) = &-\mathbf{s}^T(t)\mathbf{C}\left(\mathbf{v}_\mathbf{b}(t)\right)\mathbf{v}_\mathbf{b}(t) + \mathbf{s}^T(t)\mathbf{C}\left(\mathbf{v}_\mathbf{b}(t)\right)\mathbf{x}_\mathbf{r}(t) - \mathbf{s}^T(t)\mathbf{C}\left(\mathbf{v}_\mathbf{b}(t)\right)\mathbf{x}_\mathbf{r}(t) \\ &- \mathbf{s}^T(t)\mathbf{D}\left(\mathbf{v}_\mathbf{b}(t)\right)\mathbf{v}_\mathbf{b}(t) + \mathbf{s}^T(t)\mathbf{D}\left(\mathbf{v}_\mathbf{b}(t)\right)\mathbf{x}_\mathbf{r}(t) - \mathbf{s}^T(t)\mathbf{D}\left(\mathbf{v}_\mathbf{b}(t)\right)\mathbf{x}_\mathbf{r}(t) \\ &+ \mathbf{s}^T(t)\boldsymbol{\tau}(t) - \mathbf{s}^T(t)\mathbf{M}\dot{\mathbf{x}}_\mathbf{r}(t) \\ = &\,\mathbf{s}^T(t)\boldsymbol{\tau}(t) + \mathbf{s}^T(t)\mathbf{C}\left(\mathbf{v}_\mathbf{b}(t)\right)\left[\mathbf{x}_\mathbf{r}(t) - \mathbf{v}_\mathbf{b}(t)\right] - \mathbf{s}^T(t)\mathbf{C}\left(\mathbf{v}_\mathbf{b}(t)\right)\mathbf{x}_\mathbf{r}(t) \\ &+ \mathbf{s}^T(t)\mathbf{D}\left(\mathbf{v}_\mathbf{b}(t)\right)\left[\mathbf{x}_\mathbf{r}(t) - \mathbf{v}_\mathbf{b}(t)\right] - \mathbf{s}^T(t)\mathbf{D}\left(\mathbf{v}_\mathbf{b}(t)\right)\mathbf{x}_\mathbf{r}(t) - \mathbf{s}^T(t)\mathbf{M}\dot{\mathbf{x}}_\mathbf{r}(t) \\ = &\,\mathbf{s}^T(t)\boldsymbol{\tau}(t) - \mathbf{s}^T(t)\mathbf{C}\left(\mathbf{v}_\mathbf{b}(t)\right)\mathbf{s}(t) - \mathbf{s}^T(t)\mathbf{C}\left(\mathbf{v}_\mathbf{b}(t)\right)\mathbf{x}_\mathbf{r}(t) \\ &- \mathbf{s}^T(t)\mathbf{D}\left(\mathbf{v}_\mathbf{b}(t)\right)\mathbf{s}(t) - \mathbf{s}^T(t)\mathbf{D}\left(\mathbf{v}_\mathbf{b}(t)\right)\mathbf{x}_\mathbf{r}(t) - \mathbf{s}^T(t)\mathbf{M}\dot{\mathbf{x}}_\mathbf{r}(t) \\ = &-\mathbf{s}^T(t)\mathbf{C}\left(\mathbf{v}_\mathbf{b}(t)\right)\mathbf{s}(t) - \mathbf{s}^T(t)\mathbf{D}\left(\mathbf{v}_\mathbf{b}(t)\right)\mathbf{s}(t) \\ &+ \mathbf{s}^T(t)\boldsymbol{\tau}(t) - \mathbf{s}^T(t)\mathbf{M}\dot{\mathbf{x}}_\mathbf{r}(t) - \mathbf{s}^T(t)\mathbf{C}\left(\mathbf{v}_\mathbf{b}(t)\right)\mathbf{x}_\mathbf{r}(t) - \mathbf{s}^T(t)\mathbf{D}\left(\mathbf{v}_\mathbf{b}(t)\right)\mathbf{x}_\mathbf{r}(t)\end{aligned}$$

$$\begin{aligned}\therefore \dot{V}(t) = &-\mathbf{s}^T(t)\left[\mathbf{C}\left(\mathbf{v}_\mathbf{b}(t)\right) + \mathbf{D}\left(\mathbf{v}_\mathbf{b}(t)\right)\right]\mathbf{s}(t) \\ &+ \mathbf{s}^T(t)\left[\boldsymbol{\tau}(t) - \mathbf{M}\dot{\mathbf{x}}_\mathbf{r}(t) - \mathbf{C}\left(\mathbf{v}_\mathbf{b}(t)\right)\mathbf{x}_\mathbf{r}(t) - \mathbf{D}\left(\mathbf{v}_\mathbf{b}(t)\right)\mathbf{x}_\mathbf{r}(t)\right]\end{aligned} \tag{3.86}$$

Taking the control law to be:

$$\begin{aligned}\boldsymbol{\tau}_\mathbf{d}(t) = &\,\hat{\mathbf{M}}\dot{\mathbf{x}}_\mathbf{r}(t) + \hat{\mathbf{C}}\left(\mathbf{v}_\mathbf{b}(t)\right)\mathbf{x}_\mathbf{r}(t) \\ &+ \hat{\mathbf{D}}\left(\mathbf{v}_\mathbf{b}(t)\right)\mathbf{x}_\mathbf{r}(t) - \mathbf{K}_{\mathbf{T}_{\mathbf{BC}}}\mathbf{s}(t) - \mathbf{K}_{\mathbf{S}_{\mathbf{BC}}}\operatorname{sgn}\left(\mathbf{s}(t)\right)\end{aligned} \tag{3.87}$$

where $\hat{\mathbf{M}}$, $\hat{\mathbf{C}}\left(\mathbf{v}_\mathbf{b}(t)\right)$ and $\hat{\mathbf{D}}\left(\mathbf{v}_\mathbf{b}(t)\right)$ are the estimates of $\mathbf{M}$, $\mathbf{C}\left(\mathbf{v}_\mathbf{b}(t)\right)$ and $\mathbf{D}\left(\mathbf{v}_\mathbf{b}(t)\right)$ respectively,

$$\mathbf{K}_{\mathbf{T}_{\mathbf{BC}}} \geq \mathbf{0} \tag{3.88}$$

is the 6×6 tracking error gain matrix, $\mathbf{K}_{\mathbf{S}_{\mathbf{BC}}}$ is the 6×6 switching gain matrix, and $\mathrm{sgn}(\bullet)$ is the signum function described in Equation (3.1), yields:

$$\begin{aligned}\dot{V}(t) = -\mathbf{s}^T(t)\left[\mathbf{K}_{\mathbf{T}_{\mathbf{BC}}} + \mathbf{C}\left(\mathbf{v}_\mathbf{b}(t)\right) + \mathbf{D}\left(\mathbf{v}_\mathbf{b}(t)\right)\right]\mathbf{s}(t) - \mathbf{s}^T(t)\mathbf{K}_{\mathbf{S}_{\mathbf{BC}}}\mathrm{sgn}\left(\mathbf{s}(t)\right) \\ + \mathbf{s}^T(t)\left[\tilde{\mathbf{M}}\dot{\mathbf{x}}_\mathbf{r}(t) + \tilde{\mathbf{C}}\left(\mathbf{v}_\mathbf{b}(t)\right)\mathbf{x}_\mathbf{r}(t) + \tilde{\mathbf{D}}\left(\mathbf{v}_\mathbf{b}(t)\right)\mathbf{x}_\mathbf{r}(t)\right]\end{aligned} \tag{3.89}$$

This control law is illustrated in Figure 3.3.

Equation (3.89) contains the system inertia error, $\tilde{\mathbf{M}} = \hat{\mathbf{M}} - \mathbf{M}$, the Coriolis and centripetal forces error, $\tilde{\mathbf{C}}\left(\mathbf{v}_\mathbf{b}(t)\right) = \hat{\mathbf{C}}\left(\mathbf{v}_\mathbf{b}(t)\right) - \mathbf{C}\left(\mathbf{v}_\mathbf{b}(t)\right)$, and the hydrodynamic damping error, $\tilde{\mathbf{D}}\left(\mathbf{v}_\mathbf{b}(t)\right) = \hat{\mathbf{D}}\left(\mathbf{v}_\mathbf{b}(t)\right) - \mathbf{D}\left(\mathbf{v}_\mathbf{b}(t)\right)$.

It must be noted that, in the same context as the BFUSMC of Section 3.5, the BFCSMC also has the sliding surface, $\mathbf{s}(t)$, defined in the body frame from Equation (3.75). Again, there is no requirement of transforming this surface between the navigation frame and the body frame as is required for the NFCSMC of Section 3.4.2. Therefore, the BFCSMC is a more computationally efficient design compared to the NFCSMC.

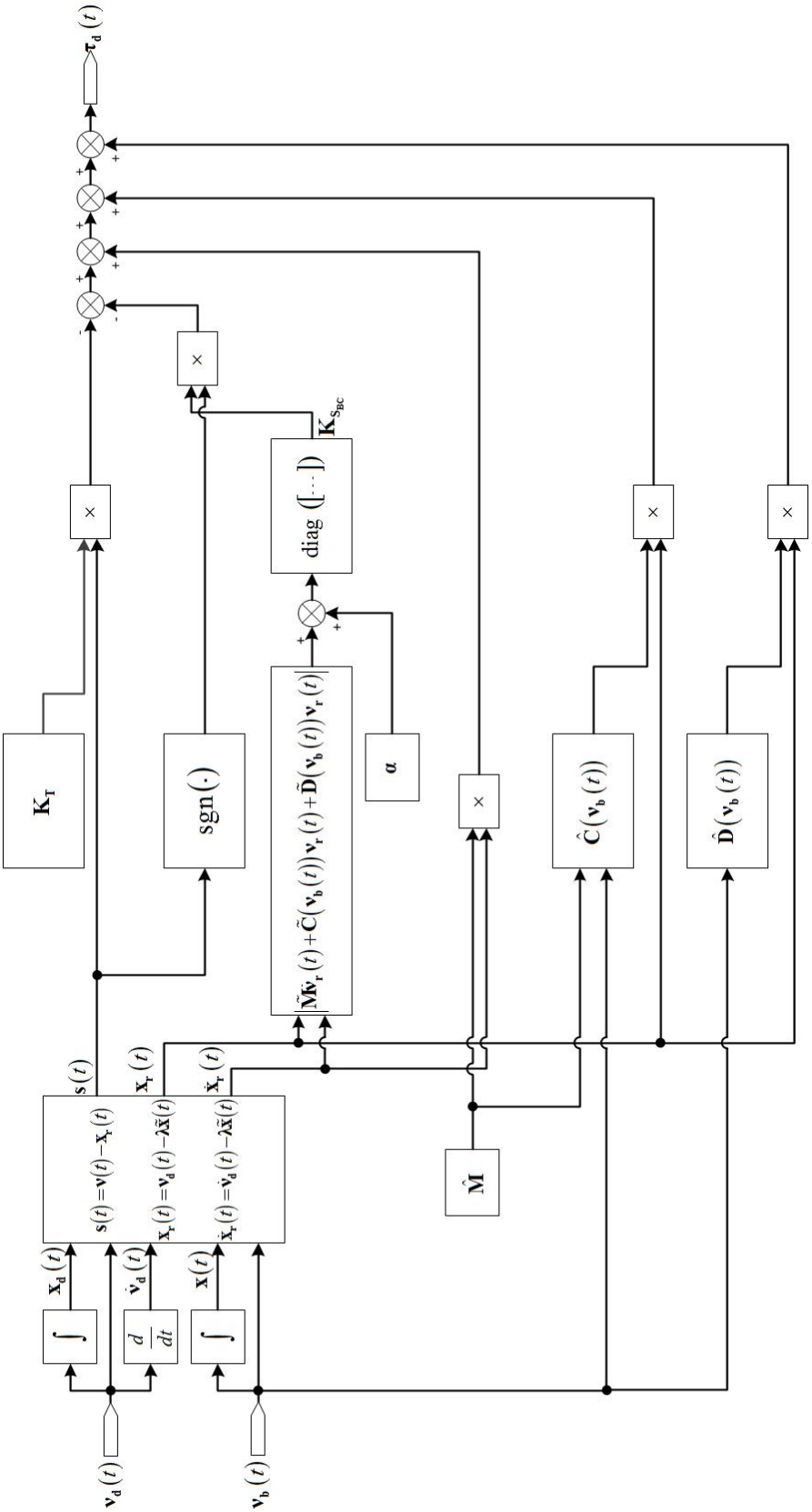

Figure 3.3: Body Frame Coupled Sliding Mode Controller

3.6.4. Stability Analysis

In a similar fashion to the existing SMCs presented in Section 3.4, the conditions on $\mathbf{K}_{\mathbf{S_{BC}}}$ can be found using Lyapunov stability analysis. As $V(t) \geq 0$ from Equation (3.81), it is required that $\dot{V}(t) \leq 0$.

If a nonlinear function, $\mathbf{F}(t)$, is defined as:

$$\mathbf{F}(t) = \tilde{\mathbf{M}}\dot{\mathbf{x}}_{\mathbf{r}}(t) + \tilde{\mathbf{C}}(\mathbf{v}_{\mathbf{b}}(t))\mathbf{x}_{\mathbf{r}}(t) + \tilde{\mathbf{D}}(\mathbf{v}_{\mathbf{b}}(t))\mathbf{x}_{\mathbf{r}}(t) \tag{3.90}$$

$\dot{V}(t) \leq 0$ will be true if the following inequality is true.

$$\mathbf{K}_{\mathbf{S_{BC}}}\operatorname{sgn}(\mathbf{s}(t)) > \mathbf{F}(t) \tag{3.91}$$

If $\mathbf{K}_{\mathbf{S_{BC}}}$ is a diagonal matrix where the elements on the main diagonal are determined by:

$$K_{S_{BC_{ii}}} \geq |F_i(t)| + \alpha_{BC_i}, (i = 1...6) \tag{3.92}$$

setting

$$\alpha_{BC_i} > 0 \tag{3.93}$$

implies that the following inequality is true.

$$\mathbf{s}^T(t)\mathbf{K}_{\mathbf{S_{BC}}}\operatorname{sgn}(\mathbf{s}(t)) > \mathbf{s}^T(t)|\mathbf{F}(t)| \tag{3.94}$$

Therefore, $\dot{V}(t) \leq 0$ as seen in:

$$\begin{aligned}
\dot{V}(t) &= -\mathbf{s}^T(t)\left[\mathbf{C}(\mathbf{v}_{\mathbf{b}}(t)) + \mathbf{D}(\mathbf{v}_{\mathbf{b}}(t)) + \mathbf{K}_{\mathbf{T_{BC}}}\right]\mathbf{s}(t) \\
&\quad + \mathbf{s}^T(t)\mathbf{F}(t) - \mathbf{s}^T(t)\mathbf{K}_{\mathbf{S_{BC}}}\operatorname{sgn}(\mathbf{s}(t)) \\
&= -\mathbf{s}^T(t)\left[\mathbf{C}(\mathbf{v}_{\mathbf{b}}(t)) + \mathbf{D}(\mathbf{v}_{\mathbf{b}}(t))\right]\mathbf{s}(t) - \mathbf{s}^T(t)\mathbf{K}_{\mathbf{T_{BC}}}\mathbf{s}(t) \\
&\quad + \mathbf{s}^T(t)\mathbf{F}(t) - \mathbf{s}^T(t)\mathbf{K}_{\mathbf{S_{BC}}}\operatorname{sgn}(\mathbf{s}(t))
\end{aligned}$$

$$\begin{aligned}
\therefore \dot{V}(t) &\leq -\mathbf{s}^T(t)\left[\mathbf{C}(\mathbf{v}_{\mathbf{b}}(t)) + \mathbf{D}(\mathbf{v}_{\mathbf{b}}(t))\right]\mathbf{s}(t) \\
&\quad - \mathbf{s}^T(t)\mathbf{K}_{\mathbf{T_{BC}}}\mathbf{s}(t) - \mathbf{s}^T(t)\boldsymbol{\alpha}_{\mathbf{BC}}\operatorname{sgn}(\mathbf{s}(t)) \\
&\leq 0
\end{aligned} \tag{3.95}$$

where

$$\boldsymbol{\alpha}_{\mathbf{BC}_{ij}} = \begin{cases} \alpha_{BC_i} \text{ for } i = j \\ 0 \text{ otherwise} \end{cases} \tag{3.96}$$

This is due to $\mathbf{C}\left(\mathbf{v_b}\left(t\right)\right)$ being skew-symmetric from Equation (2.74) Section 2.3.2, and hence:

$$\mathbf{s}^T\left(t\right)\mathbf{C}\left(\mathbf{v_b}\left(t\right)\right)\mathbf{s}\left(t\right) = 0 \forall \mathbf{s}\left(t\right) \in \mathbb{R}^6, \mathbf{v_b}\left(t\right) \in \mathbb{R}^6 \tag{3.97}$$

holds, $\mathbf{D}\left(\mathbf{v_b}\left(t\right)\right) > \mathbf{0}$ from Equation (2.75) of Section 2.3.2, and $\mathbf{K}_{\mathbf{T_{BC}}} \geq \mathbf{0}$ from Equation (3.88).

As $\dot{V}\left(t\right) \leq 0$, this implies that $V\left(t\right) \leq V\left(t_0\right)$ and that $\mathbf{s}\left(t\right)$ is bounded. This in turn implies that $\ddot{V}\left(t\right)$ is bounded and hence $\dot{V}\left(t\right)$ is uniformly continuous. From the definition of $V\left(t\right)$ in Equation (3.81), $V\left(t\right) \geq 0$ and hence $V\left(t\right) \to 0$ as $t \to \infty$. Barbălat's lemma then shows that as $V\left(t\right) \to 0$, $\mathbf{s}\left(t\right) \to \mathbf{0}$, and hence $\tilde{\mathbf{x}}\left(t\right) \to \mathbf{0}$ as $t \to \infty$. Hence, as the tracking error, $\tilde{\mathbf{x}}\left(t\right)$, is shown to converge to zero, the system is shown to be stable.

3.7. Chapter Summary

In this chapter, various control algorithms for use on underwater vehicles were discussed and presented. A comparison of the various ways a controller can be categorised based on decisions made during the design process was presented in Section 3.2. This comparison focussed on the advantages and limitations that were associated with each decision made. These advantages and limitations were then carried forward into the design of the specific controllers that followed.

Following in Section 3.3 was a general introduction to the concepts of SMC. This included a description of the essence of how sliding mode control works, as well as the basic methodology used when designing a SMC controller. A discussion of the key limitation of SMC, namely chattering, was also conducted. This discussion started with the typical cause and overall effect chattering will have on the system.

Following was a presentation of methods that have previously been implemented to minimise the effect of chattering.

Two existing sliding mode controllers for underwater vehicles were then presented in Section 3.4. Firstly, the uncoupled sliding mode controller (USMC), as presented by Fossen [2], was examined. The USMC utilises a highly simplified model within the control structure, and is therefore very efficient to implement. However, the limitation of requiring the navigation frame and the body frame remain parallel is infeasible, especially for a highly manoeuvrable vehicle. Therefore, the USMC is omitted from the simulation studies of Chapter 4 amd Chapter 6. Secondly, the navigation frame coupled sliding mode controller (NFCSMC), also as presented by Fossen [53], was examined. Not only did this strategy remove the limitation of parallel frames that exists for the USMC, it also utilises coupling of the model within the control law. These reasons make the NFCSMC a much better choice for implementation compared to the USMC. However, due to defining the sliding surface in the navigation frame, the NFCSMC requires information to be constantly rotated from the navigation frame to the body frame. This can impose large computational requirements when implementing the NFCSMC on such a constrained and restricted system as an AUV.

From limitations identified within the framework of the USMC, a new sliding mode controller, the body frame uncoupled sliding mode controller (BFUSMC) was proposed in Section 3.5. This algorithm removes the limitation of requiring the body frame and navigation frame to be parallel. An advantage of the BFUSMC is its simplicity of implementation, as there is no coupling within the model used for control design. Therefore, the BFUSMC has considerably less computational demand compared to a strategy that employs coupling within the control strategy. However, this lack of coupling can lead to unmodelled dynamics within the control algorithm and therefore a limited level of performance, depending on the overall requirements of the system. Acknowledging this limitation, the BFUSMC is still included in the simulation studies of this thesis, as it will be used as a benchmark for examining the performance gain of including coupling within the control structure.

From limitations identified within the framework of the NFCSMC, a novel sliding mode controller, the body frame coupled sliding mode controller (BFCSMC), was proposed in Section 3.6. This algorithm moves the formulation of the sliding surface from the navigation frame, as seen with the NFCSMC, to the body frame, as seen with the BFUSMC. This has a distinct advantage over the NFCSMC, as the model that the control law is based on is much simpler in the body frame and there is no need to transform information between the body frame and the navigation frame, as is seen with the NFCSMC. Hence, similar to the BFUSMC, the BFCSMC possesses the advantages of performing control in the body frame, and similar to the NFCSMC, the BFCSMC possesses the advantages of utilising a coupled model when designing the compensator. Furthermore, as the vehicle is designed to be highly manoeuvrable, there is no need to either sense or estimate position or attitude information, and therefore the BFCSMC reduces both computational and physical load compared to the NFCSMC. Therefore, the BFCSMC has distinct advantages over the USMC, the BFUSMC, and the NFCSMC.

Overall, this chapter presented the derivation of several controllers for use in controlling a highly manoeuvrable AUV. Based on the vehicle to be controlled, three control strategies will be used within the simulation studies of the following chapter. They are the BFUSMC, the NFCSMC and the BFCSMC.

Chapter 4

Control Simulation Study

4.1. Introduction

This chapter presents the simulation study results and analysis of the various control strategies presented in Chapter 3. This simulation study covers three case studies, where each case study utilises a different set of conditions to observe different behaviours.

Why a Simulation Study?

There are many reasons why a simulation study is one of the first steps taken in the design and implementation of any autonomous vehicle.

- Experimental analysis can proceed in the absence of a physical vehicle.

  A simulation environment implements the equations of motion that govern how an underwater vehicle interacts with the environment around it. Various algorithms can therefore be implemented and evaluated when a physical vehicle is unavailable.

- Easily assess the influence of individual parameters of the overall system.

  As a simulation study implements all systems within the environment as a set of equations, it is simple and straightforward to view the influence of individual parameters on the overall system. This information is useful, as it

allows insight into how the different components of the dynamics of the system interact with each other to produce the behaviour observed in a real life scenario. This is extremely difficult, if not impossible, to achieve within a physical experiment. The ease of observing this behaviour in a simulation environment indicates that a simulation environment can also assist in the design of the physical systems.

- No risk of damage to expensive equipment in the event of a failure.

  Underwater vehicles, even in their standard form without any extra sensor payload, are very expensive pieces of equipment. Especially in the development phase, there is the real possibility of catastrophic collisions with either stationary or moving objects. Each of these collisions has the potential to damage external equipment, or even rupture the hull causing complete destruction of the vehicle. As the simulation environment does not expose any equipment to a physical environment, there is no risk of this equipment being damaged.

- Fast turn-around time for algorithm re-configuration.

  Within a software environment, the easiest method for building up a large system is to break the system down into smaller logical subsystems with each subsystem implementing a singular task. If there are strict rules regarding how these subsystems interface with each other, then it becomes a trivial task to replace a particular algorithm with another for performance evaluation.

- Unbiased comparisons can be made between algorithms.

  Leading on from the previous point, a simulation environment provides a mechanism for viewing fair and unbiased comparisons between algorithms implemented for the same purpose. This is because the user has complete control over external disturbances such as water currents and conditions, as well as any variability in actuator performance. Hence, a simulation environment provides an environment where all conditions are repeatable. This allows for algorithm evaluation with the confidence that it is only a

change in algorithm that has affected the results, and not an external disturbance biasing the results.

- Simulations can potentially run faster than real-time.

  By utilising an appropriate program for conducting the underwater vehicle simulations, there is the potential for running simulations at much faster than real-time. What this means is that an experiment that would normally take several days to complete in open-water can potentially take hours, or even minutes, when conducted as a computer simulation. This allows for the rapid collection of results, and therefore fast analysis and evaluation of performance.

- Simulations can test the extreme conditions of the system.

  A simulation environment can programmatically introduce extreme operating conditions for the system to handle. These conditions can potentially mimic an environment beyond which can be created in a real-world experimental study. This can enable a much more thorough evaluation of the system performance over an extremely wide range of operating conditions.

- Used for performance evaluation of the real system.

  An accurate plant model combined with an accurate simulation environment can be used to obtain reliable results concerning the behaviour of the vehicle. This observed behaviour could act as a benchmark in evaluating the performance of the real system. In this sense, an accurate simulation environment can act as a crosscheck to ensure the real vehicle matches the design specifications.

There are, however, limitations of a simulation study. The primary drawback is that a simulation environment and a plant model can only ever approach, and never meet, the behaviour observed of a physical vehicle operating in a physical environment. The reliability of the results is directly related to the accuracy of both the plant model and the simulation environment. Nevertheless, careful design and implementation

will ensure that both the plant model and the simulation environment possess adequate levels of reliability and accuracy.

For the previously stated reasons, this chapter will present results gathered from a set of three carefully designed case studies of an underwater vehicle. The results of these three case studies are useful for real system design and vehicle synthesis.

Outline

This chapter is outlined as follows:

- Section 4.2 presents an overview of modelling error as it applies to underwater vehicles and summarises the error assumed within this simulation study.
- Section 4.3 presents the parameters of the compensators used within this simulation study.
- Section 4.4 presents the three case studies in their entirety, including results and observations obtained from these case studies, and conclusions that can be drawn from the observed behaviour.

4.2. Modelling Error

As discussed in Section 3.2.4, one particular property that makes sliding mode control extremely attractive to control engineers is its acknowledged robustness to modelling uncertainty [46, 80, 81]. As the process of obtaining the mathematical model of an underwater vehicle is both complex and prone to error, Ross, Fossen and Johansen [69] proposed an offline method for identifying the hydrodynamic coefficients of an underwater vehicle using free decay tests. The simulated results obtained from these tests were compared to the actual values, with varying degrees of error. The levels of error ranged from 0.2% for added mass coefficients to almost 100% for linear drag coefficients. In contrast, Kim *et al* [82] proposed several online methods for estimating hydrodynamic coefficients through the use of nonlinear observers. It was seen that, depending on the type of observer used and the states of the vehicle being observed, average error across all coefficients estimated ranged

from 1.18% to 12.6%. Furthermore, the methods that could realistically be implemented on a physical AUV ranged from 3.61% for an extended Kalman filter to 12.6% for a sliding mode observer.

Each sliding mode controller previously designed in Chapter 3 requires an estimate of the modelling error within the calculation of the switching gain vector or matrix. For the three compensators implemented within this simulation study, the estimate of the modelling error is seen for the calculation of $\mathbf{K}_{\mathbf{S}_{\mathbf{NC}}}$ in Equation (3.45) for the NFCSMC, the calculation of $\mathbf{K}_{\mathbf{S}_{\mathbf{BU}}}$ in Equation (3.68) for the BFUSMC, and the calculation of $\mathbf{K}_{\mathbf{S}_{\mathbf{BC}}}$ in Equation (3.92) for the BFCSMC. Acknowledging the best average coefficient error obtained by Kim *et al* [82] that could realistically be implemented on a physical AUV was 3.61%, it was decided that the assumed modelling error to be used within this simulation study was 5%. Furthermore, as the rigid body mass matrix, $\mathbf{M}_{\mathbf{RB}}$, is obtained based on the physical properties of the vehicle that can be easily and accurately measured, it is assumed that the rigid body mass matrix error, $\tilde{\mathbf{M}}_{\mathbf{RB}}$, is zero. Hence, the following error matrices are utilised within each sliding mode controller implemented within this simulation study, where $\tilde{\mathbf{M}}$ is the system inertia error matrix, $\tilde{\mathbf{C}}\left(\mathbf{v}_{\mathbf{b}}\left(t\right)\right)$ is the Coriolis and centripetal forces error matrix, $\tilde{\mathbf{D}}\left(\mathbf{v}_{\mathbf{b}}\left(t\right)\right)$ is the hydrodynamic damping error matrix, and, as $\mathbf{g}\left(\boldsymbol{\eta}_{\mathbf{n}}\left(t\right)\right)=\mathbf{0}$, the gravitational and buoyancy forces and moments error vector, $\tilde{\mathbf{g}}\left(\boldsymbol{\eta}_{\mathbf{n}}\left(t\right)\right)$, is also assumed to be zero.

$$\tilde{\mathbf{M}}=\tilde{\mathbf{M}}_{\mathbf{RB}}+\tilde{\mathbf{M}}_{\mathbf{A}}$$

$$=\begin{bmatrix} 0.0465 & 0 & 0 & 0 & 0 & 0 \\ 0 & 1.775 & 0 & 0 & 0 & 0 \\ 0 & 0 & 1.775 & 0 & 0 & 0 \\ 0 & 0 & 0 & 0.00352 & 0 & 0 \\ 0 & 0 & 0 & 0 & 0.244 & 0 \\ 0 & 0 & 0 & 0 & 0 & 0.244 \end{bmatrix}$$

$$\tilde{\mathbf{C}}\left(\mathbf{v_b}\left(t\right)\right)=\tilde{\mathbf{C}}_{\mathbf{RB}}\left(\mathbf{v_b}\left(t\right)\right)+\tilde{\mathbf{C}}_{\mathbf{A}}\left(\mathbf{v_b}\left(t\right)\right)$$

$$=\begin{bmatrix} 0 & 0 & 0 \\ 0 & 0 & 0 \\ 0 & 0 & 0 \\ 0 & 1.775w_b\left(t\right) & -1.775v_b\left(t\right) \\ -1.775w_b\left(t\right) & 0 & 0.0465u_b\left(t\right) \\ 1.775v_b\left(t\right) & -0.0465u_b\left(t\right) & 0 \end{bmatrix}$$

$$\begin{bmatrix} 0 & 1.775w_b\left(t\right) & -1.775v_b\left(t\right) \\ -1.775w_b\left(t\right) & 0 & 0.0465u_b\left(t\right) \\ 1.775v_b\left(t\right) & -0.0465u_b\left(t\right) & 0 \\ 0 & 0.244r_b\left(t\right) & -0.244q_b\left(t\right) \\ -0.244r_b\left(t\right) & 0 & 0.00352p_b\left(t\right) \\ 0.244q_b\left(t\right) & -0.00352p_b\left(t\right) & 0 \end{bmatrix}$$

$$\tilde{\mathbf{D}}\left(\mathbf{v_b}\left(t\right)\right)=\begin{bmatrix} 0.195\left|u_b\left(t\right)\right| & 0 & 0 \\ 0 & 65.5\left|v_b\left(t\right)\right| & 0 \\ 0 & 0 & 6.55\left|w_b\left(t\right)\right| \\ 0 & 0 & 0 \\ 0 & 0 & -0.159\left|w_b\left(t\right)\right| \\ 0 & 0.159\left|v_b\left(t\right)\right| & 0 \end{bmatrix}$$

$$\begin{bmatrix} 0 & 0 & 0 \\ 0 & 0 & -0.0316\left|r_b\left(t\right)\right| \\ 0 & 0.0316\left|q_b\left(t\right)\right| & 0 \\ 0.0065\left|p_b\left(t\right)\right| & 0 & 0 \\ 0 & 9.4\left|q_b\left(t\right)\right| & 0 \\ 0 & 0 & 4.7\left|r_b\left(t\right)\right| \end{bmatrix}$$

$$\tilde{\mathbf{g}}\left(\boldsymbol{\eta}_{\mathbf{n}}\left(t\right)\right)=\begin{bmatrix} 0 \\ 0 \\ 0 \\ 0 \\ 0 \\ 0 \end{bmatrix}$$

4.3. Compensator Parameters

Through the use of a nonlinear optimisation technique utilising a genetic algorithm, similar to that conducted by Alfardo-Cid *et al* [83], the tracking error gain matrix, $\mathbf{K}_{\mathbf{T_{BU}}}$ presented in Equation (3.64), for the BFUSMC is defined as:

$$\mathbf{K}_{\mathbf{T_{BU}}} = \begin{bmatrix} 0 & 0 & 0 & 0 & 0 & 0 \\ 0 & 6678.93 & 0 & 0 & 0 & 0 \\ 0 & 0 & 5515.70 & 0 & 0 & 0 \\ 0 & 0 & 0 & 3.71817 & 0 & 0 \\ 0 & 0 & 0 & 0 & 236.360 & 0 \\ 0 & 0 & 0 & 0 & 0 & 260.065 \end{bmatrix} \tag{4.1}$$

the tracking error gain matrix, $\mathbf{K}_{\mathbf{T_{NC}}}$ presented in Equation (3.43), for the NFCSMC is defined as:

$$\mathbf{K}_{\mathbf{T_{NC}}} = \begin{bmatrix} 4.30537\times10^{-3} & 0 & 0 & 0 & 0 & 0 \\ 0 & 9.75344\times10^{-4} & 0 & 0 & 0 & 0 \\ 0 & 0 & 22.0373 & 0 & 0 & 0 \\ 0 & 0 & 0 & 1.54634 & 0 & 0 \\ 0 & 0 & 0 & 0 & 29.8793 & 0 \\ 0 & 0 & 0 & 0 & 0 & 196.244 \end{bmatrix} \tag{4.2}$$

and the tracking error gain matrix, $\mathbf{K}_{\mathbf{T_{BC}}}$ presented in Equation (3.88), for the BFCSMC is defined as:

$$\mathbf{K}_{\mathbf{T_{BC}}} = \begin{bmatrix} 3.00502\times10^{-8} & 0 & 0 & 0 & 0 & 0 \\ 0 & 440.496 & 0 & 0 & 0 & 0 \\ 0 & 0 & 30.2090 & 0 & 0 & 0 \\ 0 & 0 & 0 & 0.333828 & 0 & 0 \\ 0 & 0 & 0 & 0 & 0.31283 & 0 \\ 0 & 0 & 0 & 0 & 0 & 205.466 \end{bmatrix} \tag{4.3}$$

In the design of the BFUSMC in Section 3.5, the NFCSMC in Section 3.4.2, and the BFCSMC in Section 3.6, all the compensators are stable if $\alpha_i > 0, (i = 1...6)$. For all

cases simulated here, $\alpha_i = 0.1, (i = 1...6)$ and hence the switching gain constant matrix, $\boldsymbol{\alpha}_{\mathbf{BU}}$ presented in Equation (3.72), for the BFUSMC is defined as:

$$\boldsymbol{\alpha}_{\mathbf{BU}} = \begin{bmatrix} 0.1 & 0 & 0 & 0 & 0 & 0 \\ 0 & 0.1 & 0 & 0 & 0 & 0 \\ 0 & 0 & 0.1 & 0 & 0 & 0 \\ 0 & 0 & 0 & 0.1 & 0 & 0 \\ 0 & 0 & 0 & 0 & 0.1 & 0 \\ 0 & 0 & 0 & 0 & 0 & 0.1 \end{bmatrix} \tag{4.4}$$

the switching gain constant vector, $\boldsymbol{\alpha}_{\mathbf{NC}}$ presented in Equation (3.48), for the NFCSMC is defined as:

$$\boldsymbol{\alpha}_{\mathbf{NC}} = \begin{bmatrix} 0.1 \\ 0.1 \\ 0.1 \\ 0.1 \\ 0.1 \\ 0.1 \end{bmatrix} \tag{4.5}$$

and the switching gain constant matrix, $\boldsymbol{\alpha}_{\mathbf{BC}}$ presented in Equation (3.96), for the BFCSMC is defined as:

$$\boldsymbol{\alpha}_{\mathbf{BC}} = \begin{bmatrix} 0.1 & 0 & 0 & 0 & 0 & 0 \\ 0 & 0.1 & 0 & 0 & 0 & 0 \\ 0 & 0 & 0.1 & 0 & 0 & 0 \\ 0 & 0 & 0 & 0.1 & 0 & 0 \\ 0 & 0 & 0 & 0 & 0.1 & 0 \\ 0 & 0 & 0 & 0 & 0 & 0.1 \end{bmatrix} \tag{4.6}$$

Finally, in order to reduce the effects of chattering, the BFUSMC, the NFCSMC and the BFCSMC were all implemented using the hyperbolic tangent function seen in Figure 3.1 instead of the signum function. In all cases, the boundary layer thickness, ϕ, was set to a value of 0.1, i.e.,

$$\operatorname{sgn}\left(\mathbf{s}(t)\right) \cong \tanh\left(\tfrac{\mathbf{s}(t)}{0.1}\right).$$

The hyperbolic tangent function was chosen such that the discontinuities were removed, while the value of ϕ, which can be selected as being arbitrarily small [74], was selected such that a good approximation of the signum function was obtained while still reducing the effect of chattering.

4.4. Case Studies

The aim of this simulation study is to assess the performance of compensators used for trajectory tracking of AUVs. In order to appraise these compensators appropriately, a reference trajectory is needed for the vehicle to follow. For the purposes of evaluating the performance of the designed compensators, three different case studies, each containing different trajectories aimed at revealing different properties of the compensators, are considered. The three trajectories are ordered in increasing levels of complexity, where the final trajectory closely matches that of a vehicle performing an underwater survey mission. These scenarios are summarised in Table 4.1 and are outlined as follows.

- The first case study, Case 1 of Section 4.4.1, is a relatively simple scenario where excitation of a single DoF at a time is required. This scenario is based on the simple demonstration of the uncoupled sliding mode controller (USMC) by Fossen [2] and demonstrates the speed of response as these inputs approximate step inputs. The input to the simulation is in the form of a series of desired position/attitude, velocity, and acceleration values at each time step.
- The second case study, Case 2 of Section 4.4.2, is more complex as it contains manoeuvring where multiple DoFs are excited at the same time. The input for this scenario is in the form of a series of waypoints that the vehicle must follow in succession. A line-of-sight (LOS) guidance system provides the desired trajectory data at each time step. A summary of LOS guidance is contained in Appendix B. The initial phase of the trajectory implements zigzag and spiral manoeuvres used by Kim *et al* [82] for the purposes of estimating hydrodynamic coefficients. In this scenario, the use of these

manoeuvres aid in demonstrating the ability of the compensator to follow a trajectory where multiple DoFs are being excited at the same time. The latter phase implements a series of straight lines to demonstrate the steady state behaviour of the vehicle.

- The third and final case study, Case 3 of Section 4.4.3, extends Case 2 not only by resembling a trajectory that a real-world AUV could follow; it also contains a time-varying water current disturbance. The input for this scenario is similar to that of Case 2, i.e., a set of waypoints, as it uses the same LOS guidance system. Again, the initial phase of this trajectory implements the zigzag and spiral manoeuvres seen in the Case 2 of Section 4.4.2. The latter phase consists of a raster scan covering an area of 250,000 m^2.

Across all case studies presented, the architecture of the plant model remains constant, and is as outlined in Section 2.2.3 and Appendix A.1.1. This plant model is used to mimic the real AUV under control for all case studies. This consistency ensures a fair and unbiased comparison across all controllers and scenarios.

The results presented here are in the form of error plots for $\boldsymbol{\eta}_{\mathbf{n}}(t)$, the position and attitude of the vehicle decomposed in the navigation frame, and $\boldsymbol{\nu}_{\mathbf{b}}(t)$, the

Table 4.1: Control Case Studies

Case	Input	Initial Conditions	System	Output
1	Single DoF Excitation	$\boldsymbol{\eta}_{\mathbf{n}}(t)=[0 \quad 0 \quad 0 \quad 0 \quad 0 \quad 0]^T$ $\boldsymbol{\nu}_{\mathbf{b}}(t)=[0 \quad 0 \quad 0 \quad 0 \quad 0 \quad 0]^T$	AUV Plant, No Disturbance	$\tilde{\boldsymbol{\eta}}_{\mathbf{n}}(t)$ and $\tilde{\boldsymbol{\nu}}_{\mathbf{b}}(t)$
2	Multiple DoF Excitation	$\boldsymbol{\eta}_{\mathbf{n}}(t)=[0 \quad 0 \quad 10 \quad 0 \quad 0 \quad 0]^T$ $\boldsymbol{\nu}_{\mathbf{b}}(t)=[1 \quad 0 \quad 0 \quad 0 \quad 0 \quad 0]^T$	AUV Plant, No Disturbance	$\tilde{\boldsymbol{\eta}}_{\mathbf{n}}(t)$ and $\tilde{\boldsymbol{\nu}}_{\mathbf{b}}(t)$
3	Multiple DoF Excitation	$\boldsymbol{\eta}_{\mathbf{n}}(t)=[0 \quad 0 \quad 10 \quad 0 \quad 0 \quad 0]^T$ $\boldsymbol{\nu}_{\mathbf{b}}(t)=[1 \quad 0 \quad 0 \quad 0 \quad 0 \quad 0]^T$	AUV Plant, Current Disturbance	$\tilde{\boldsymbol{\eta}}_{\mathbf{n}}(t)$ and $\tilde{\boldsymbol{\nu}}_{\mathbf{b}}(t)$

translational and angular velocity of the vehicle decomposed in the body frame. Therefore, the outputs for each simulation scenario are $\tilde{\boldsymbol{\eta}}_{\mathbf{n}}(t)$ and $\tilde{\mathbf{v}}_{\mathbf{b}}(t)$ as defined by

$$\tilde{\boldsymbol{\eta}}_{\mathbf{n}}(t) = \boldsymbol{\eta}_{\mathbf{d}}(t) - \boldsymbol{\eta}_{\mathbf{n}}(t) = \begin{bmatrix} \tilde{x}_n(t) \\ \tilde{y}_n(t) \\ \tilde{z}_n(t) \\ \tilde{\phi}_n(t) \\ \tilde{\theta}_n(t) \\ \tilde{\psi}_n(t) \end{bmatrix} \tag{4.7}$$

and

$$\tilde{\mathbf{v}}_{\mathbf{b}}(t) = \mathbf{v}_{\mathbf{d}}(t) - \mathbf{v}_{\mathbf{b}}(t) = \begin{bmatrix} \tilde{u}_b(t) \\ \tilde{v}_b(t) \\ \tilde{w}_b(t) \\ \tilde{p}_b(t) \\ \tilde{q}_b(t) \\ \tilde{r}_b(t) \end{bmatrix} \tag{4.8}$$

respectively.

Figure 4.1 provides a block diagram of the overall simulation environment. The inputs to the simulation environment are a water current disturbance, for Case 3 only, and the trajectory data consisting of the desired position/attitude, velocity and acceleration of the vehicle. The outputs are $\tilde{\boldsymbol{\eta}}_{\mathbf{n}}(t)$ defined by Equation (4.7) and $\tilde{\mathbf{v}}_{\mathbf{b}}(t)$ defined by Equation (4.8). The Control System block implements one of three controllers, namely the BFUSMC, the NFCSMC, or the BFCSMC. Therefore, there are three control systems to be studied and compared here, each having its distinct control law defined in Equation (3.63) for the BFUSMC, Equation (3.42) for the NFCSMC, and Equation (3.87) for the BFCSMC. As $\tilde{\boldsymbol{\eta}}_{\mathbf{n}}(t)$ and $\tilde{\mathbf{v}}_{\mathbf{b}}(t)$ are both 6×1 vectors, there are 12 error plots for each case study. Furthermore, the integrated absolute error (IAE) of these error plots is also included to gain further insight into

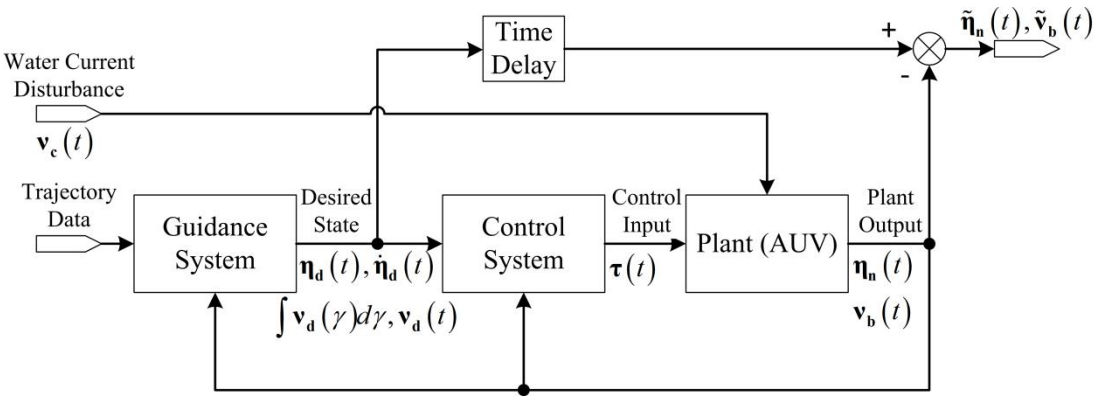

Figure 4.1: Simulation Block Diagram

the behaviour of these systems. This provides a sufficient basis for comparing and discussing the performance of the control methodologies presented.

Position/attitude and velocity errors are chosen as the outputs of the system due to the desire to observe the tracking performance of the system. The inputs to the system are time-varying trajectory data, which makes traditional performance measures such as settling time, overshoot, and steady-state error difficult to observe. By observing error plots, the tracking performance of the system can easily be observed in the presence of the time-varying input.

As the desired state of the vehicle, namely $\boldsymbol{\eta}_d(t)$ and $\mathbf{v}_d(t)$, vary with time, the error is calculated as the difference between the current state of the vehicle and the desired state of the vehicle which is delayed by a single time-step. This is required as the output of the LOS guidance system is the desired state of the vehicle at the next sampling time.

For each of the case studies, the following presentation structure is adopted:

- Aim: Stating the purpose of using the particular input trajectory for this case study;
- System Conditions: Describing the conditions specific to this case study such as inputs, initial conditions, disturbances, etc.;
- Flow Chart: Illustrating the flow chart describing the behaviour of this case study;

- Observations: Describing the position/attitude and velocity error plots of this case study;
- Simulation Results: Discussing observed behaviours seen in the position/attitude and velocity error plots of this case study;
- Conclusions: Drawing concluding remarks based on the results and discussion of the error plots of this case study.

4.4.1. Case 1

The first trajectory considered is restricted to exciting a single DoF at a time. This limits the amount of excitation of cross-coupling terms within the vehicle model. This limit is further enforced by assuming no external water currents are present for this particular scenario.

Aim

The aim of this case study is to demonstrate the basic functionality of the system being able to follow a relatively simple trajectory. This is achieved by exciting each DoF individually. As the desired trajectory approximates step inputs, this case study will demonstrate the speed of the system.

System Conditions

Figure 4.2 shows the basic element that forms the trajectory within this case study. As can be seen, the position or attitude is first perturbed +1 unit from the starting point in the first 10 s, then to -1 unit from the starting point in the following 10 s, and then returns to the starting point for the following 20 s. This excitation is then reversed, i.e., perturbed to -1 unit, then to +1 unit, then back to starting point, to give a total excitation time of 80 s. An additional 80 s of no excitation is included to observe the steady-state behaviour of the system. In the simulation where the DoF being excited is translational, the units are in metres, and if rotational, the units are in radians. Velocity and acceleration are simply the first and second derivatives respectively, of position or attitude with respect to time, with appropriate units.

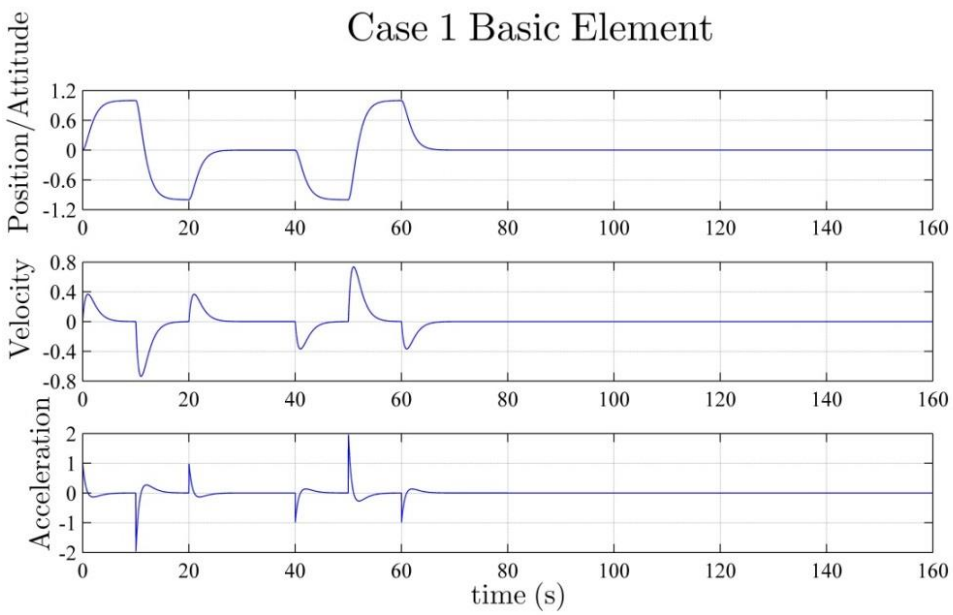

Figure 4.2: Basic Element for Case 1

In order to observe motion purely due to the controller tracking the desired trajectory, this particular case study does not contain any external disturbances.

Utilising the basic trajectory as seen in Figure 4.2, the respective trajectories covering all DoFs are constructed. Figure 4.3 shows the position information, Figure 4.4 shows the attitude information, Figure 4.5 shows the translational velocity information, and Figure 4.6 shows the angular velocity information. It must be noted that for Case 1, there are six individual simulations. Each simulation involves the excitation of a single DoF, and the resultant output is the position/attitude and velocity error of that same DoF. For example, the first simulation involves the excitation of the surge DoF only, and hence the only output observed for this first simulation is the north position error, $\tilde{x}_n(t)$, and the surge translational velocity error, $\tilde{u}_b(t)$. The second simulation involves the excitation of the sway DoF only, and hence the only output observed for this second simulation is the east position error, $\tilde{y}_n(t)$, and the sway translational velocity error, $\tilde{v}_b(t)$. The excitation and observation of the remaining four DoFs follows a similar process.

Figure 4.3 and Figure 4.4 contain the desired position information and the desired attitude information for Case 1.

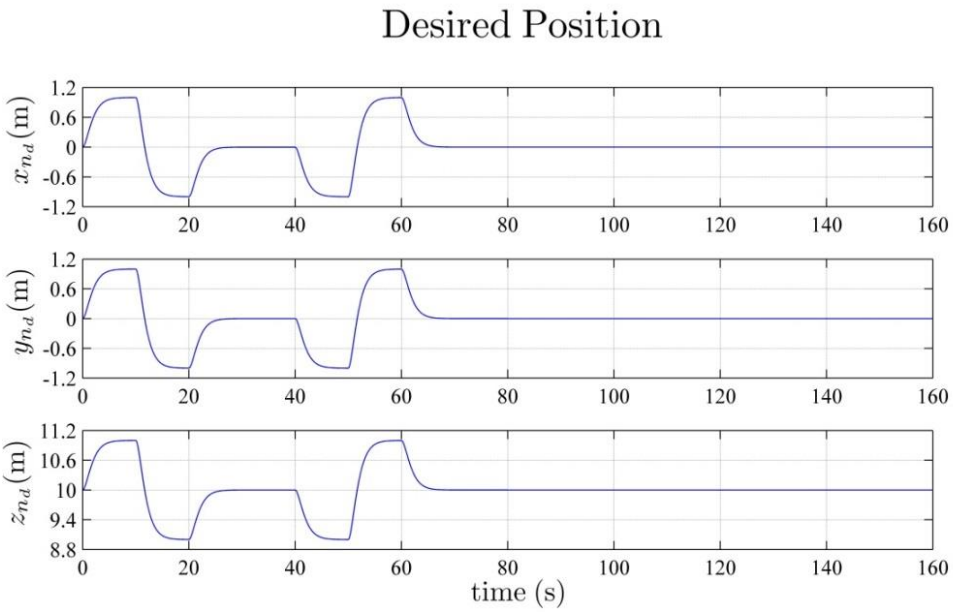

Figure 4.3: Desired Position for Case 1 (NED Frame)

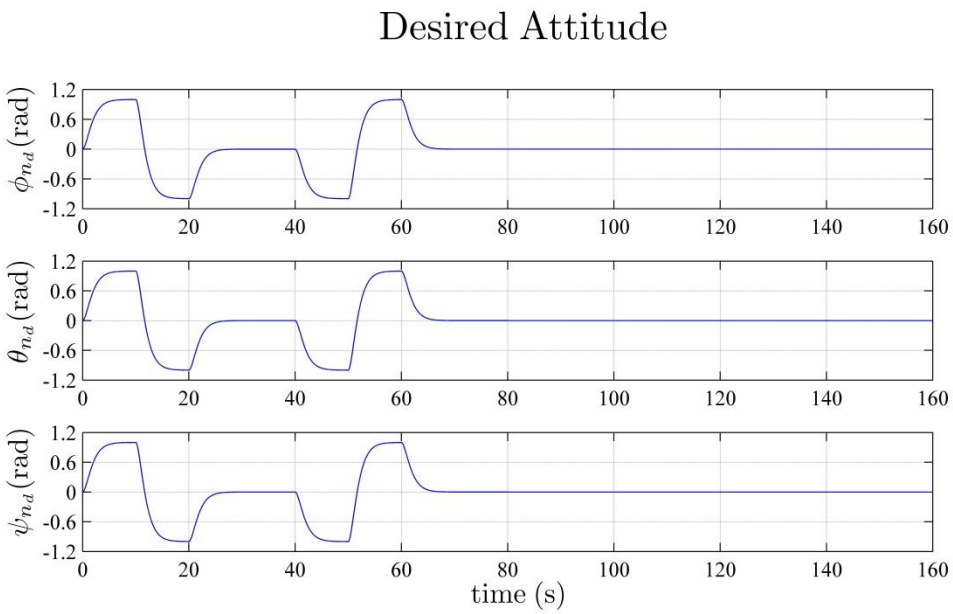

Figure 4.4: Desired Attitude for Case 1 (NED Frame)

Figure 4.5 and Figure 4.6 contain the desired translational velocity information and the desired angular velocity information for Case 1.

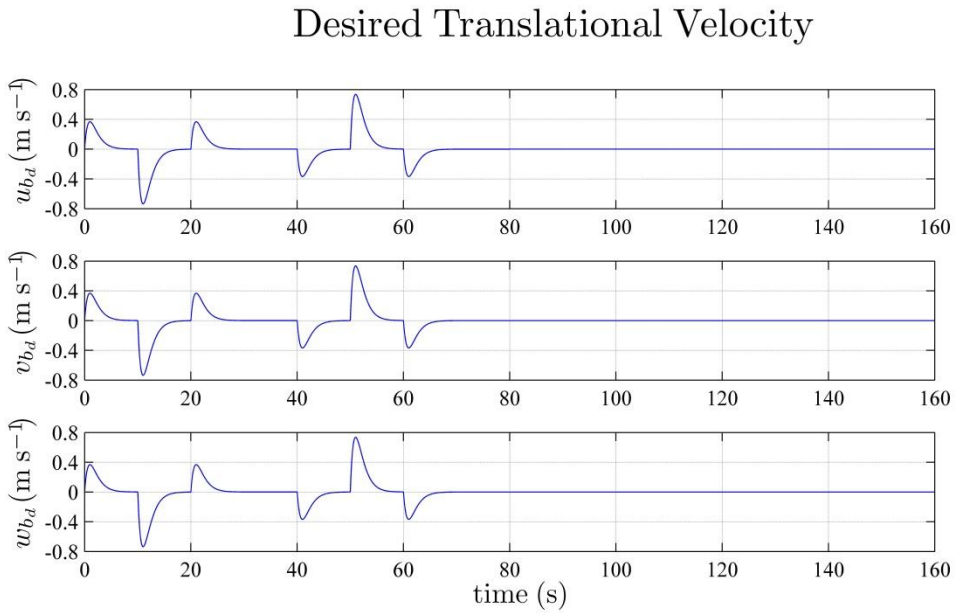

Figure 4.5: Desired Translational Velocity for Case 1 (Body Frame)

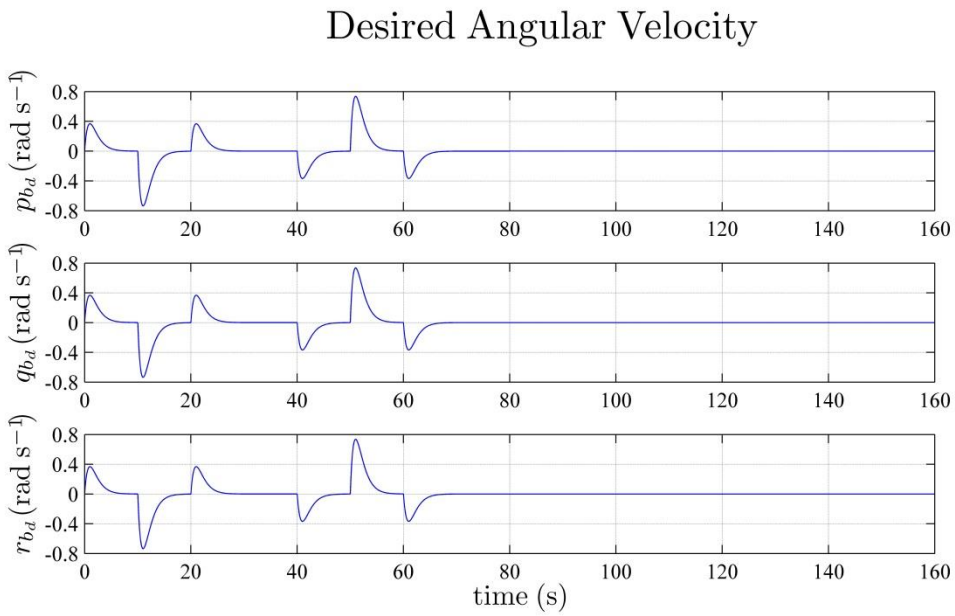

Figure 4.6: Desired Angular Velocity for Case 1 (Body Frame)

Flow Chart

The following flow chart illustrates the behaviour of Case 1.

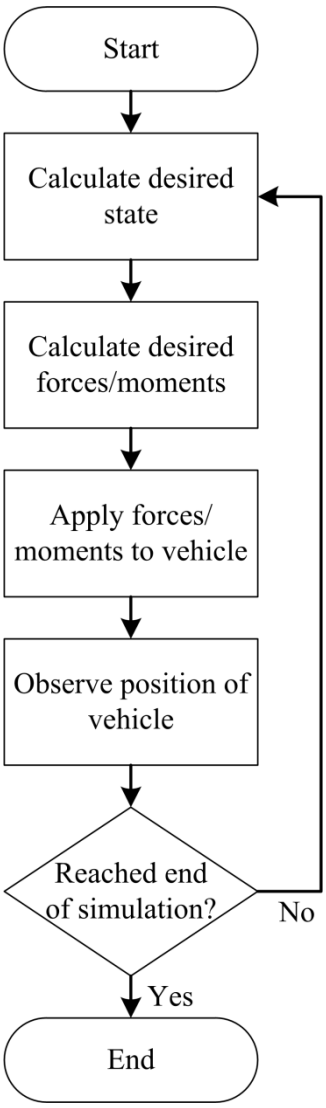

Figure 4.7: Flow Chart for Case 1

Simulation Results

The simulation results are divided into two sections. Firstly, the results of all three compensators, namely the BFUSMC, the NFCSMC, and the BFCSMC, will all be presented together. Secondly, only the compensators that are based on coupled simplified models, namely the NFCSMC and the BFCSMC, will be presented.

1. All Compensators

The following four figures contain the error plots for the BFUSMC, the NFCSMC and the BFCSMC for the input trajectory of Case 1 as outlined in Figure 4.3 through to Figure 4.6. Figure 4.8 shows the position error and position IAE for all compensators. Figure 4.9 shows the attitude error and attitude IAE for all compensators. Figure 4.10 shows the translational velocity error and translational velocity IAE for all compensators. Figure 4.11 shows the angular velocity error and angular velocity IAE for all compensators.

It is anticipated that, due to the limitation of not including coupling in the control law, the BFUSMC will not perform as well as both the NFCSMC and the BFCSMC.

(a) Simulation of Position Errors

Subject to the inputs outlined in Figure 4.3 through to Figure 4.6, the position error for the three compensated systems is given Figure 4.8.

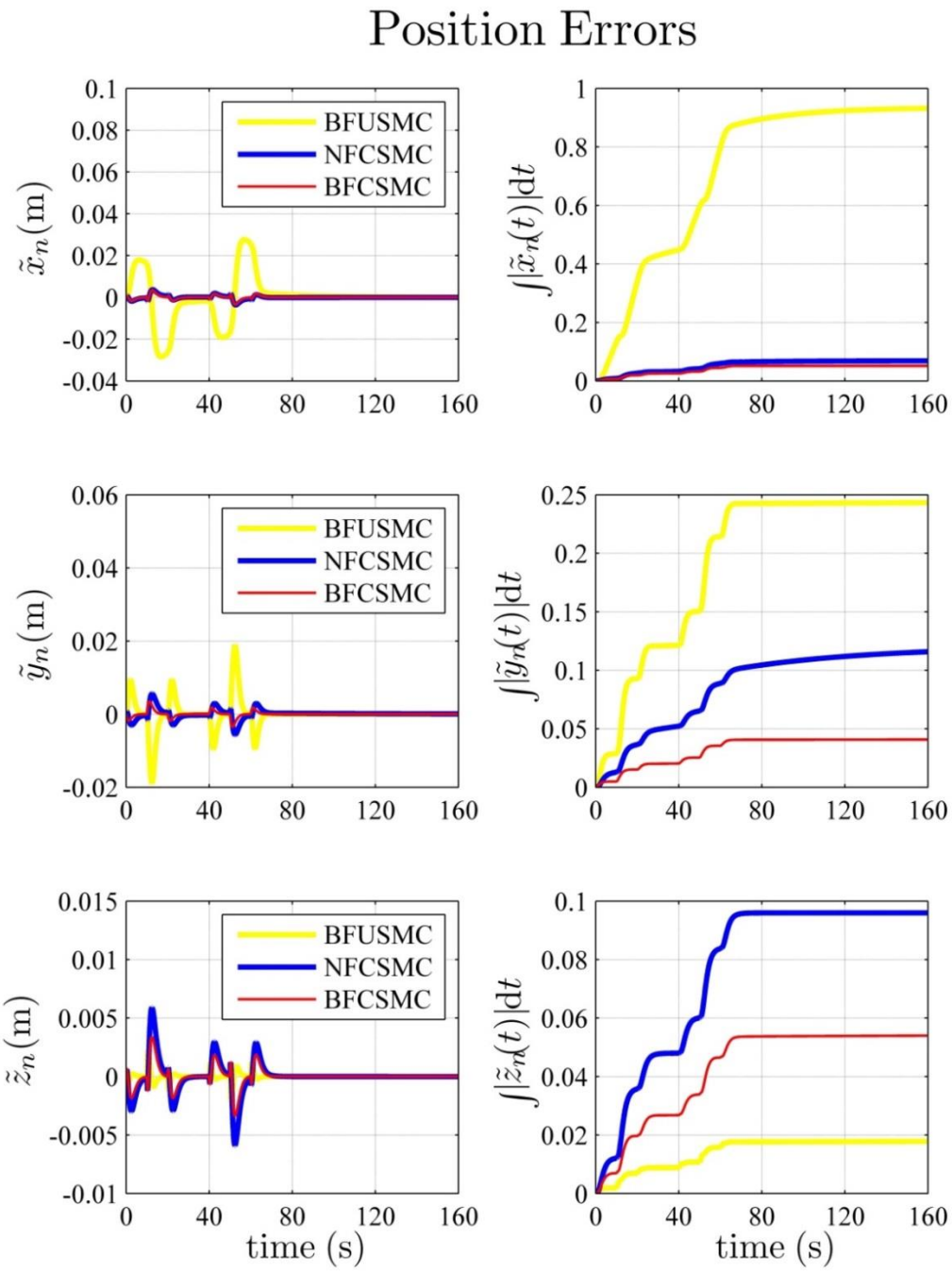

Figure 4.8: Position Errors for Case 1

It is observed from the north position error and east position error, $\tilde{x}_n$ and $\tilde{y}_n$ respectively, and the corresponding IAE plots that the BFUSMC has a much larger dynamic error and IAE compared to both the NFCSMC and the BFCSMC.

It is observed from the down position error, $\tilde{z}_n$, and its corresponding IAE plot that the NFCSMC has the largest dynamic error and IAE, followed by the BFCSMC, and the BFUSMC has both the smallest dynamic error and IAE.

(b) Simulation of Attitude Errors

Subject to the inputs outlined in Figure 4.3 through to Figure 4.6, the attitude error for the three compensated systems is given in Figure 4.9.

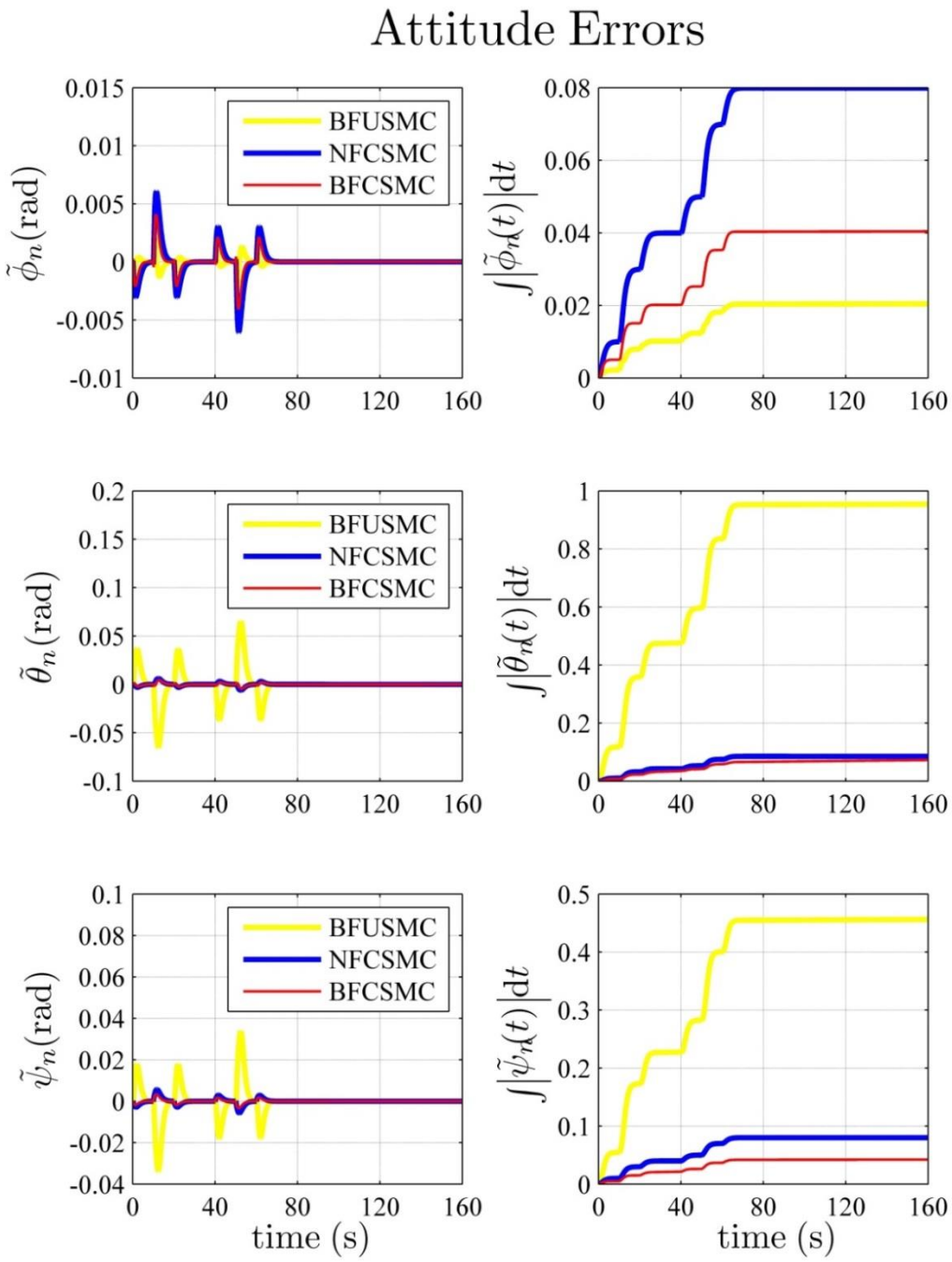

Figure 4.9: Attitude Errors for Case 1

It is observed from the roll attitude error, $\tilde{\phi}_n$, and its corresponding IAE plot that the NFCSMC has both the largest dynamic error and IAE, followed by the BFCSMC, with the BFUSMC has both the smallest dynamic error and IAE.

It is observed from the pitch attitude error and the yaw attitude error, $\tilde{\theta}_n$ and $\tilde{\psi}_n$ respectively, and the corresponding IAE plots that the BFUSMC has a much larger dynamic error and IAE compared to both the NFCSMC and the BFCSMC.

(c) Simulation of Translational Velocity Errors

Subject to the inputs outlined in Figure 4.3 through to Figure 4.6, the translational velocity error for the three compensated systems is given in Figure 4.10.

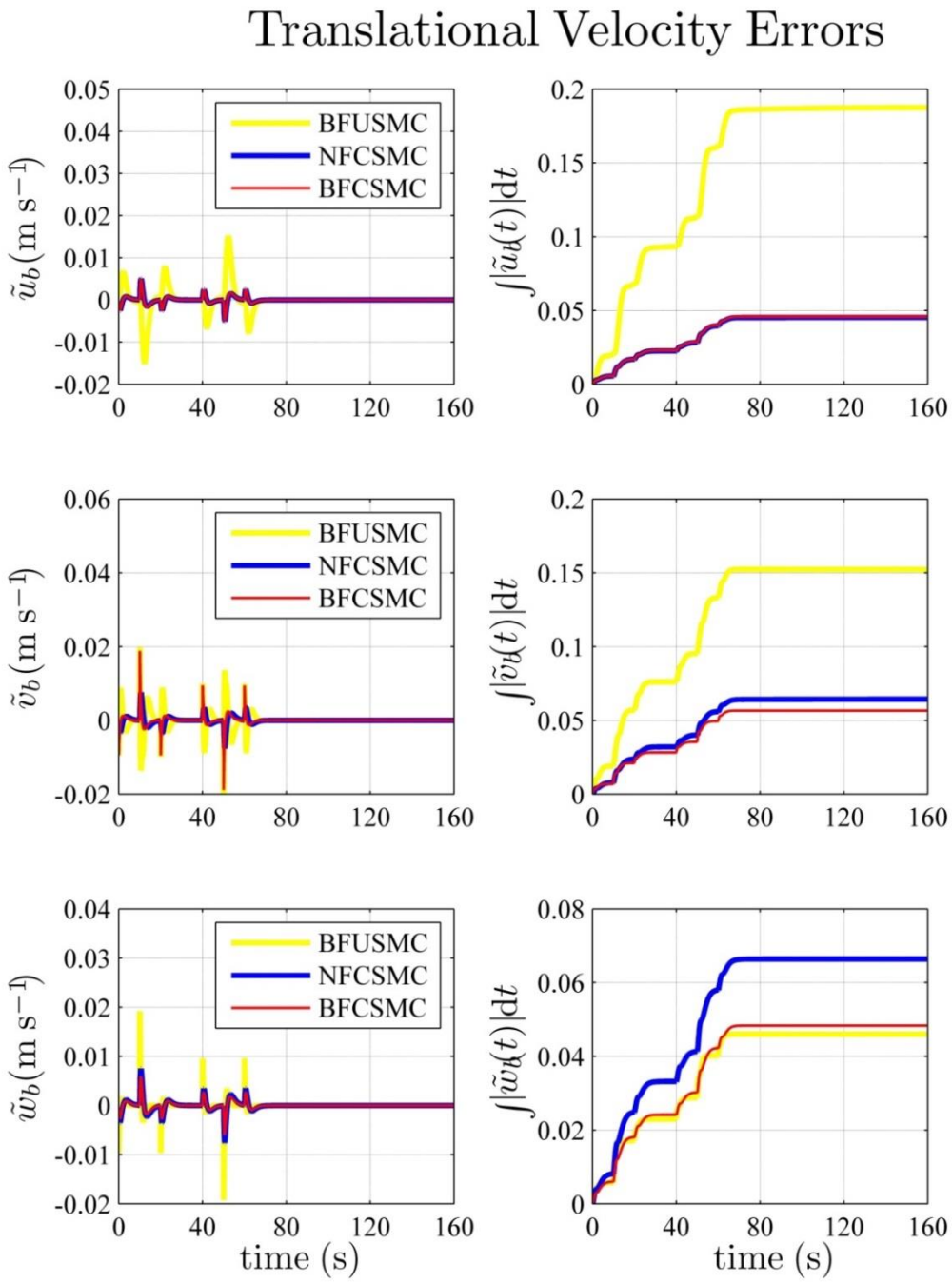

Figure 4.10: Translational Velocity Errors for Case 1

It is observed from the surge translational velocity error, $\tilde{u}_b$, and its corresponding IAE plot that the BFUSMC has a much larger dynamic error and IAE compared to both the NFCSMC and the BFCSMC.

It is observed from the sway translational velocity error, $\tilde{v}_b$, that the NFCSMC has the smallest dynamic error across the entire simulation time. It is also observed that the BFUSMC and the BFCSMC have similar maximum magnitude errors; however, the BFCSMC has considerably less overshoot. By observing the corresponding IAE plot, it is observed that the BFUSMC has a considerably larger IAE, while the NFCSMC and the BFCSMC have very similar IAE plots.

It is observed from the heave translational velocity error, $\tilde{w}_b$, that the BFUSMC has the largest dynamic error, followed by the NFCSMC, with the BFCSMC having the smallest dynamic error. By observing the corresponding IAE plot, it is seen that the NFCSMC has the largest IAE, while the BFUSMC and the BFCSMC have very similar IAE plots.

(d) Simulation of Angular Velocity Errors

Subject to the inputs outlined in Figure 4.3 through to Figure 4.6, the angular velocity error for the three compensated systems is given in Figure 4.11.

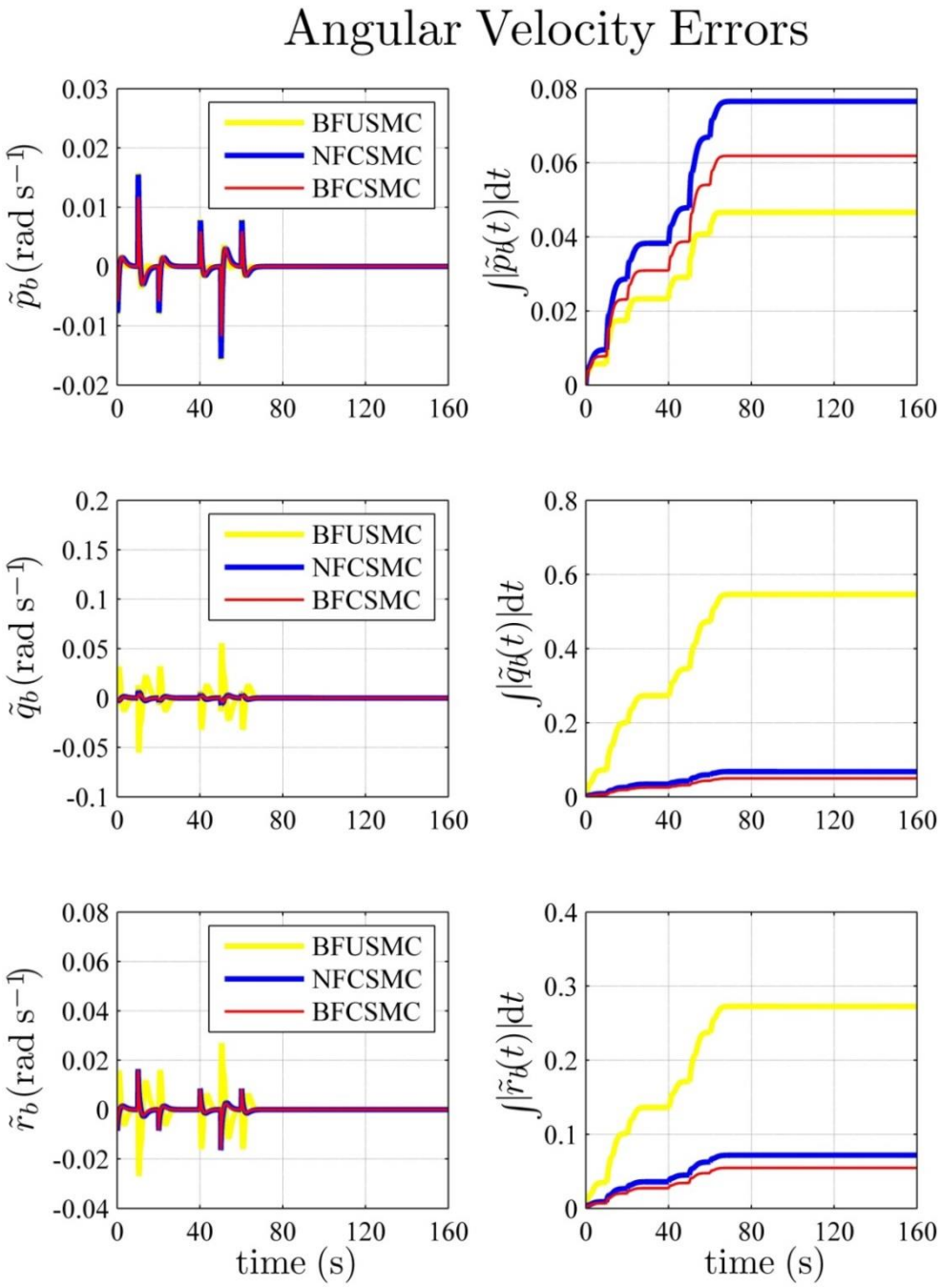

Figure 4.11: Angular Velocity Errors for Case 1

It is observed from the roll angular velocity error, $\tilde{p}_b$, that the BFUSMC and the NFCSMC have the largest dynamic error, with the BFCSMC having the smallest dynamic error. By observing the corresponding IAE plot, it is seen that the NFCSMC has the largest IAE, followed by the BFCSMC, with the BFUSMC having the smallest IAE.

It is observed from the pitch angular velocity error and the yaw angular velocity error, $\tilde{q}_b$ and $\tilde{r}_b$ respectively, and the corresponding IAE plots that the BFUSMC has a much larger dynamic error and IAE compared to both the NFCSMC and the BFCSMC.

(e) Concluding Remarks

Figure 4.8 through to Figure 4.11 compares the behaviour of the BFUSMC, the NFCSMC, and the BFCSMC when the input trajectory is that of Case 1. Based on the behaviours observed, the following remarks can be drawn.

Remark 1.1 – The BFUSMC demonstrates a limited performance compared to both the NFCSMC and the BFCSMC.

> The most apparent observation that can be made from Figure 4.8 through to Figure 4.11 is the limited performance of the BFUSMC compared to both the NFCSMC and the BFUSMC in the majority of plots. This is observed with respect to the north and east position errors, $\tilde{x}_n$ and $\tilde{y}_n$ respectively, of Figure 4.8, the pitch and yaw attitude errors, $\tilde{\theta}_n$ and $\tilde{\psi}_n$ respectively, of Figure 4.9, the surge and sway translational velocity errors, $\tilde{u}_b$ and $\tilde{v}_b$ respectively, of Figure 4.10, and the pitch and yaw angular velocity errors, $\tilde{q}_b$ and $\tilde{r}_b$ respectively, of Figure 4.11. As the BFUSMC does not include coupling within the control law, this behaviour demonstrates the importance of including this coupling when designing a control algorithm for an AUV.

The magnitude of the error seen for the BFUSMC is considerably larger than the error seen for both the NFCSMC and the BFCSMC within some of the figures presented in this case study. Hence, it is difficult to observe the behaviour of the

NFCSMC or the BFCSMC in these instances. Therefore, to gain a better insight into the performance of the two coupled control schemes, the same simulation is conducted, except that the behaviour of the BFUSMC is omitted.

2. Coupled Compensators

The following four figures contain the error plots for the NFCSMC and the BFCSMC for the input trajectory of Case 1 as outlined in Figure 4.3 through to Figure 4.6. Figure 4.12 shows the position error and position IAE for the NFCSMC and BFCSMC only. Figure 4.13 shows the attitude error and attitude IAE for the NFCSMC and BFCSMC only. Figure 4.14 shows the translational velocity error and translational velocity IAE for the NFCSMC and BFCSMC only. Figure 4.15 shows the angular velocity error and angular velocity IAE for the NFCSMC and BFCSMC only.

(a) Simulation of Position Errors

Subject to the inputs outlined in Figure 4.3 through to Figure 4.6, the position error for the two compensated systems is given in Figure 4.12.

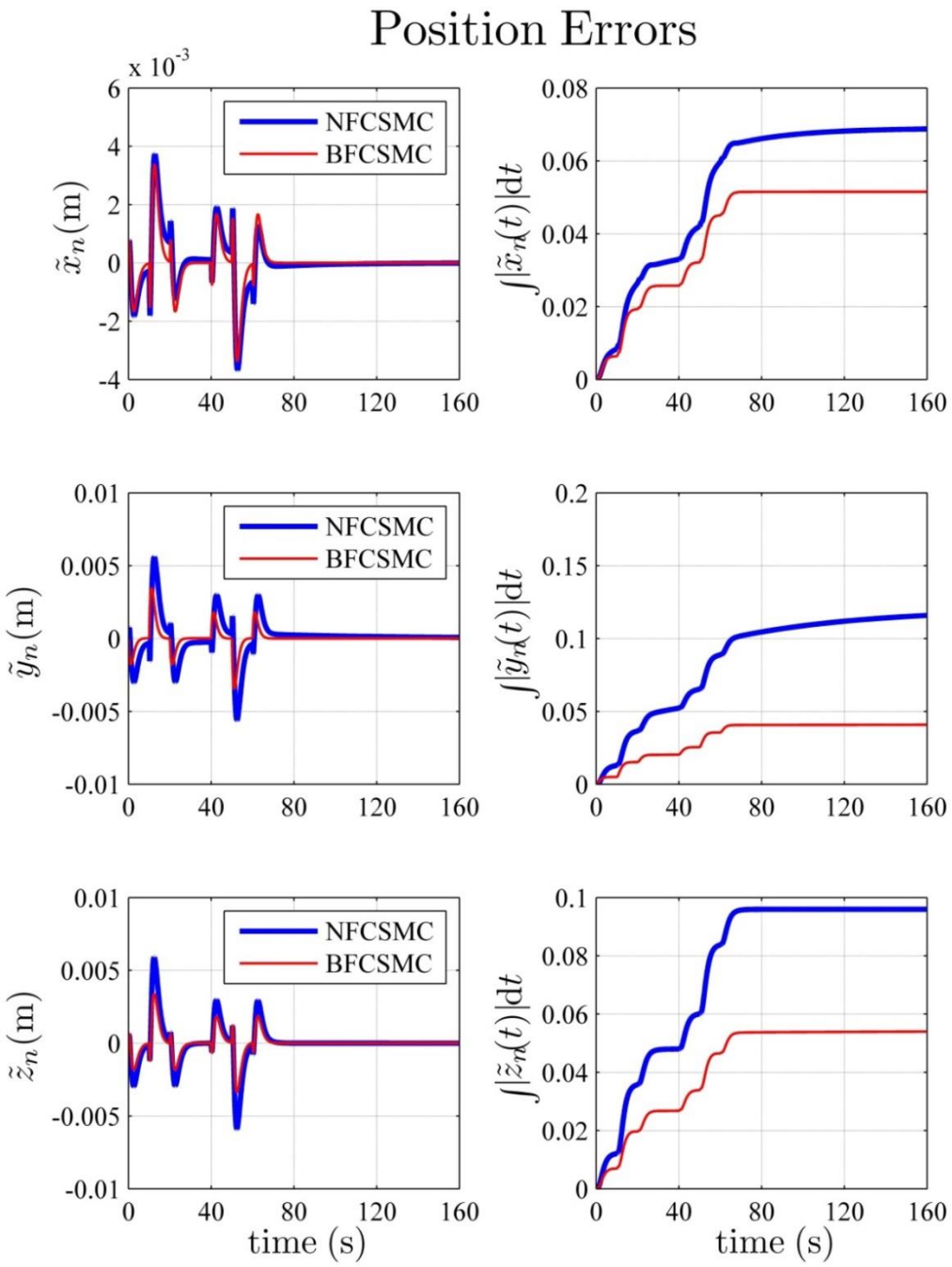

Figure 4.12: Position Error for Case 1 without BFUSMC

It is observed from the north position error, east position error, and down position error, $\tilde{x}_n$, $\tilde{y}_n$, and $\tilde{z}_n$ respectively, and the corresponding IAE plots that the NFCSMC has a larger dynamic error and IAE compared to the BFCSMC. It is also observed from the north and east position errors, $\tilde{x}_n$ and $\tilde{y}_n$ respectively, that the NFCSMC takes much longer to reach steady-state compared to the BFCSMC.

(b) Simulation of Attitude Errors

Subject to the inputs outlined in Figure 4.3 through to Figure 4.6, the attitude error for the two compensated systems is given in Figure 4.13.

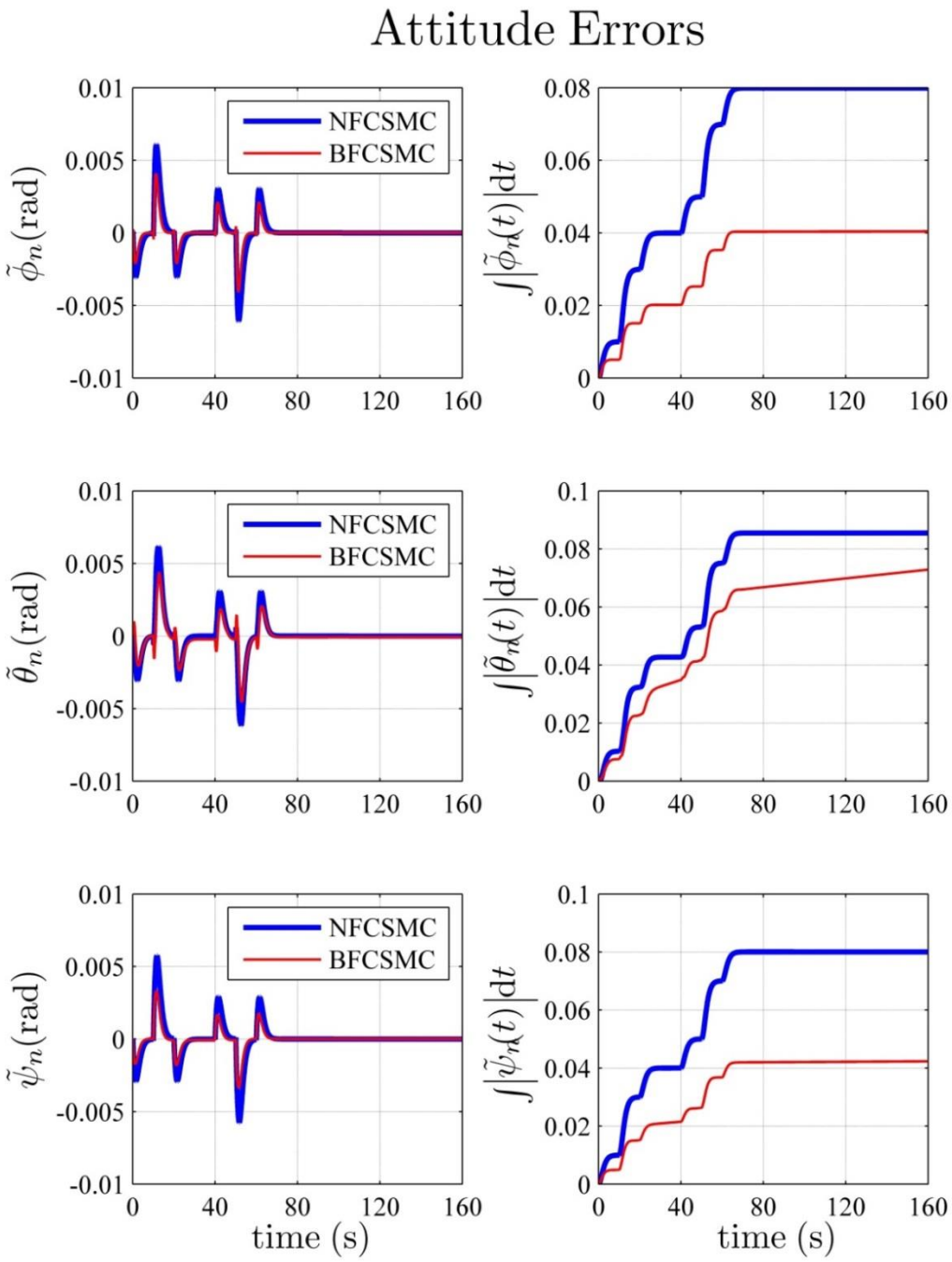

Figure 4.13: Attitude Errors for Case 1 without BFUSMC

It is observed from the roll attitude error, pitch attitude error, and yaw attitude error, $\tilde{\phi}_n$, $\tilde{\theta}_n$, and $\tilde{\psi}_n$ respectively, and the corresponding IAE plots that the NFCSMC has a larger dynamic error and IAE compared to the BFCSMC. It is also observed from the pitch attitude error, $\tilde{\theta}_n$, that the BFCSMC has a non-zero steady-state error.

(c) Simulation of Translational Velocity Errors

Subject to the inputs outlined in Figure 4.3 through to Figure 4.6, the translational velocity error for the two compensated systems is given in Figure 4.14.

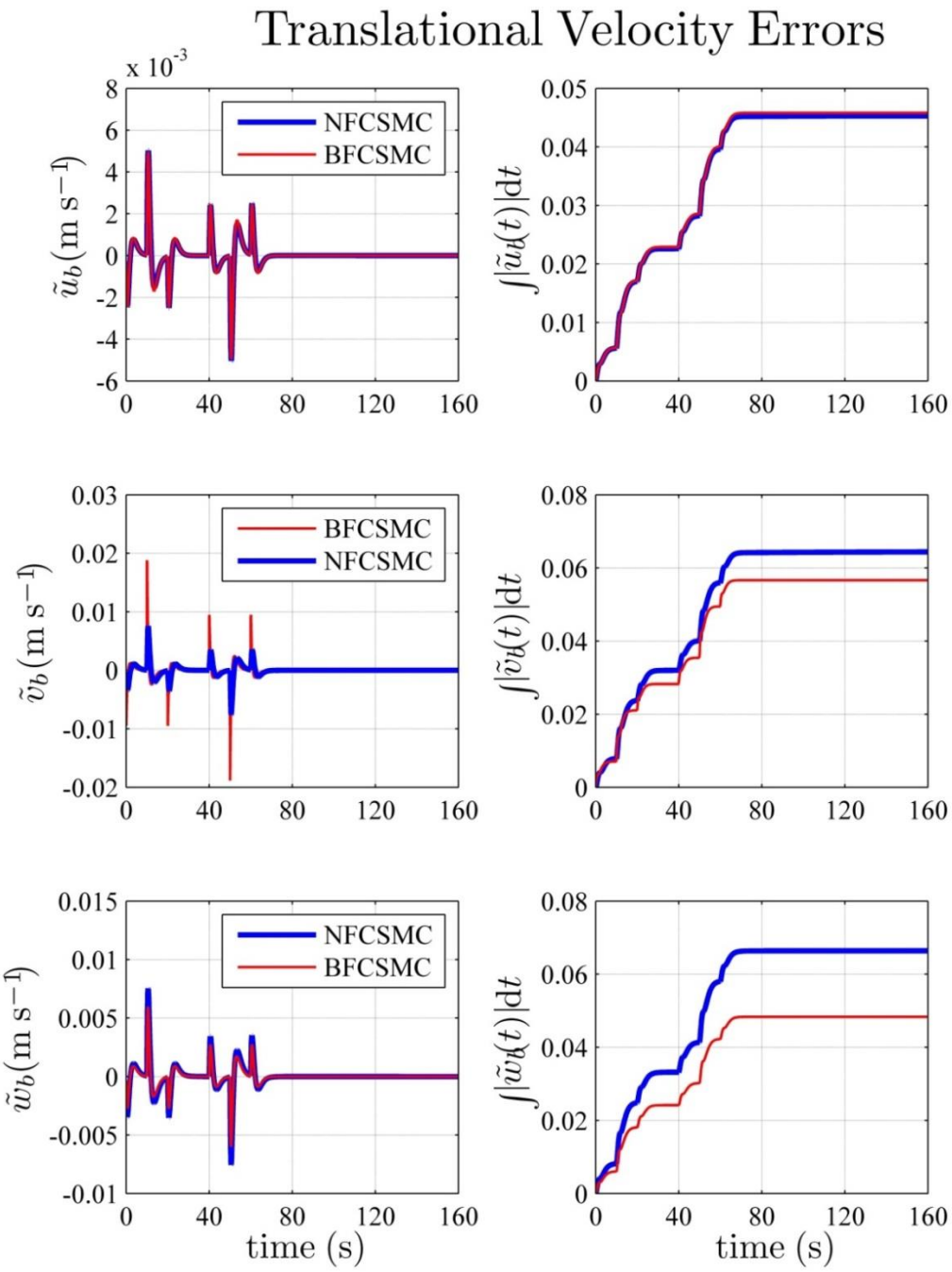

Figure 4.14: Translational Velocity Errors for Case 1 without BFUSMC

It is observed from the surge translational velocity error, $\tilde{u}_b$, and the corresponding IAE plot that both the NFCSMC and the BFUSMC behave similarly.

It is observed from the sway translational velocity error, $\tilde{v}_b$, that even though the BFCSMC has a larger dynamic error compared to the NFCSMC, it has a smaller corresponding IAE.

It is observed from the heave translational velocity error, $\tilde{w}_b$, and the corresponding IAE plot that the NFCSMC has a larger dynamic error and IAE compared to the BFCSMC.

(d) Simulation of Angular Velocity Errors

Subject to the inputs outlined in Figure 4.3 through to Figure 4.6, the angular velocity error for the two compensated systems is given in Figure 4.15.

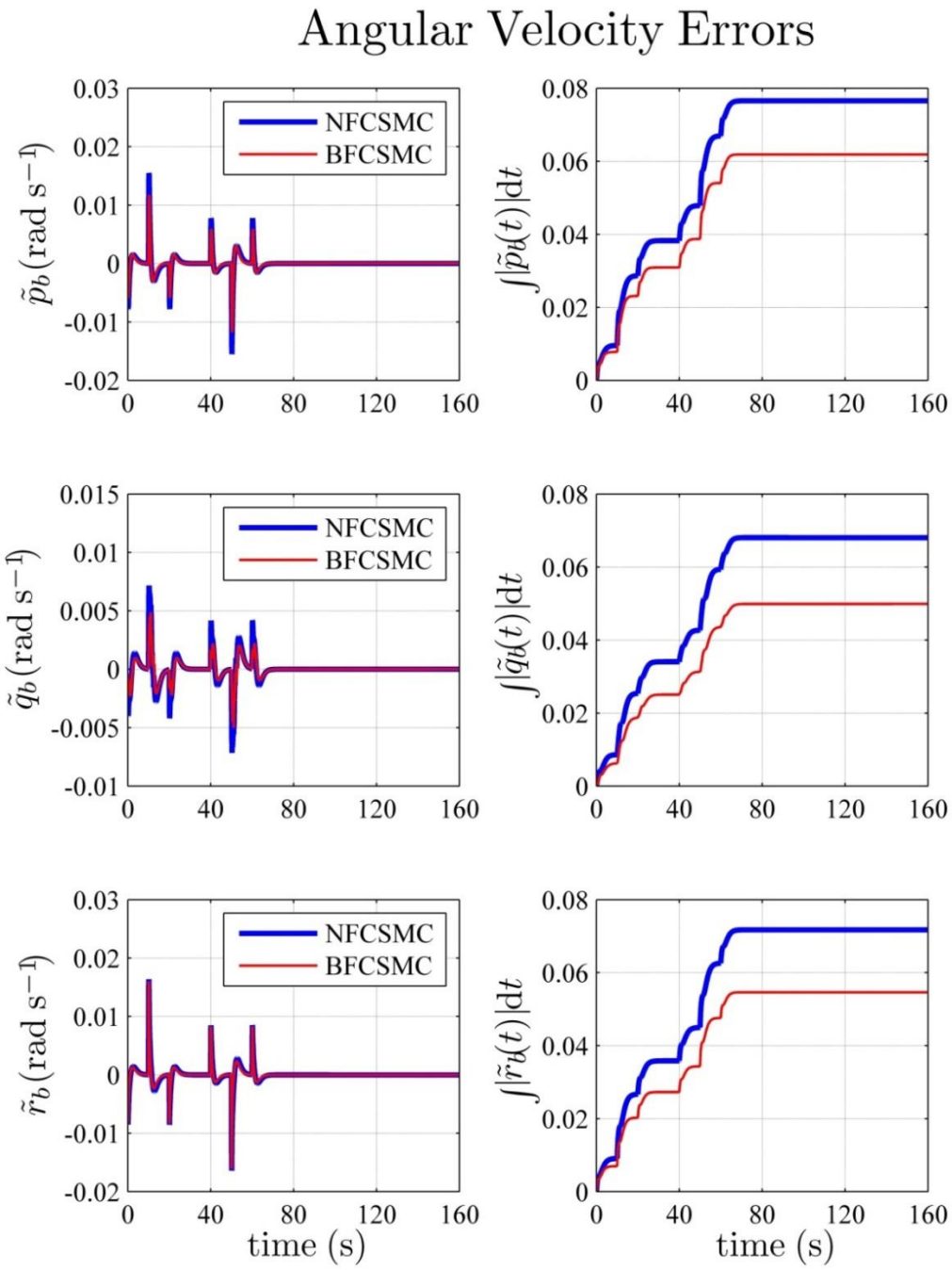

Figure 4.15: Angular Velocity Errors for Case 1 without BFUSMC

It is observed from the roll angular velocity error, the pitch angular velocity error, and the yaw angular velocity error, $\tilde{p}_b$, $\tilde{q}_b$ and $\tilde{r}_b$ respectively, and the corresponding IAE plots that the NFCSMC has a larger dynamic error and IAE compared to the BFCSMC.

(e) Concluding Remarks

Figure 4.12 through to Figure 4.15 compares the behaviour of the NFCSMC and the BFCSMC when the input trajectory is that of Case 1. Based on the behaviours observed, the following remarks can be drawn.

Remark 2.1 – The BFCSMC generally performs as good as, if not better than, the NFCSMC with respect to the maximum magnitude of errors.

> With respect to the maximum magnitude of the error plots, it can be observed that the simulation of the BFCSMC produces smaller maximum magnitudes compared to the NFCSMC in all cases except for the sway translational velocity error, $\tilde{v}_b$, in Figure 4.14. Here, the maximum magnitude of the BFCSMC is approximately $0.02\ \text{m s}^{-1}$ whereas the equivalent for the NFCSMC is approximately $0.008\ \text{m s}^{-1}$. This indicates the BFCSMC produces a larger initial overshoot when the desired velocity changes. However, by close observation of this same error plot, the convergence to zero error occurs faster for the BFCSMC compared to the NFCSMC.

Remark 2.2 – The BFCSMC generally performs as good as, if not better than, the NFCSMC with respect to integrated absolute error.

> By observing the respective IAE plots corresponding to all the error plots, again the BFCSMC is superior to the NFCSMC in the majority of the situations observed.
>
> The position errors of Figure 4.12 show that the BFCSMC obtains a significantly smaller IAE compared to the NFCSMC. Furthermore, it can be observed that there must be a long convergence time for the NFCSMC with respect to the north position error, $\tilde{x}_n$, and the east position error, $\tilde{y}_n$, as it takes a long time for the corresponding IAE plots to converge to a steady-

state value. Figure 4.16 and Figure 4.17 show only the last 80 s of $\tilde{x}_n$ and $\tilde{y}_n$ respectively. Here, it can be observed that neither $\tilde{x}_n$ or $\tilde{y}_n$ for the NFCSMC have converged to steady-state within the timeframe of the simulation. Hence, the positioning ability of the BFCSMC is superior that of the NFCSMC.

Figure 4.13 shows the plots of the attitude errors for the NFCSMC and the BFCSMC. What can be observed is that, particularly from the IAE plots, a much smaller dynamic error is observed for the BFCSMC.

The translational and angular velocity error plots of Figure 4.14 and Figure 4.15 respectively again show that the BFCSMC performs better than the NFCSMC in all but surge translational velocity error, $\tilde{u}_b$, where both systems perform equally well. The smaller IAE for the remaining velocities indicate that the BFCSMC is superior to the NFCSMC with respect to velocity tracking. When observing the sway translational velocity error, $\tilde{v}_b$ of Figure 4.15, the BFCSMC experiences a larger overshoot compared to the NFCSMC. Combining this observation with the fact that the IAE for this particular velocity is smaller indicates that the larger overshoots produce a

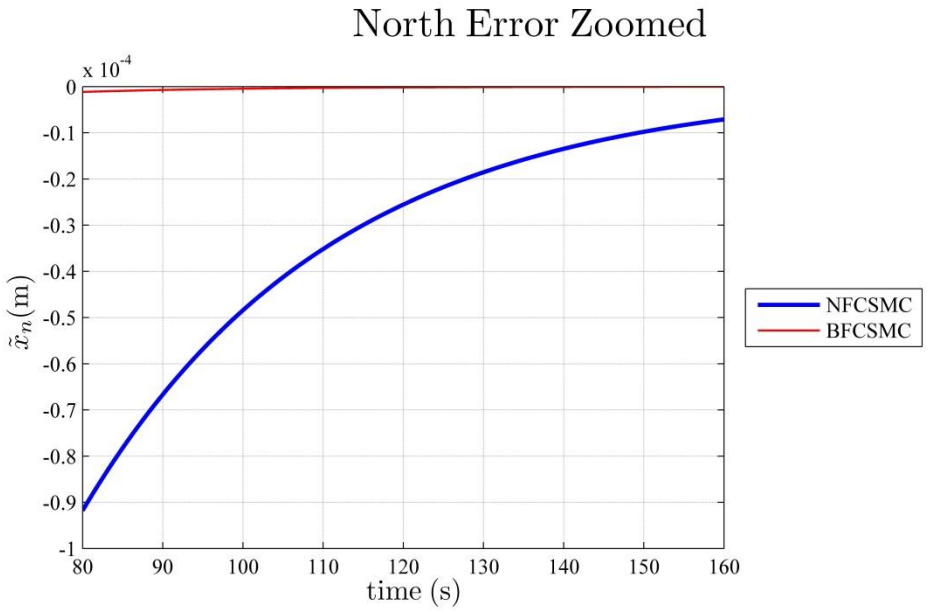

Figure 4.16: North Error Zoomed for Case 1

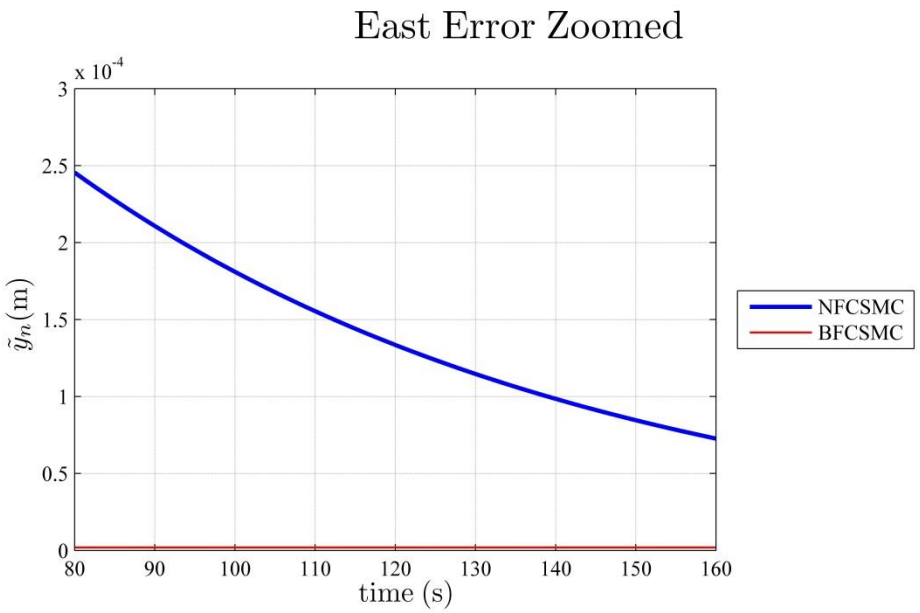

Figure 4.17: East Error Zoomed for Case 1

faster convergence. Observation of the remaining translational velocity, and all angular velocities, further enforces the fact that the BFCSMC is superior to the NFCSMC for velocity tracking.

Remark 2.3 – A small steady-state error is observed for the BFCSMC with respect to pitch attitude angle.

Observation of Figure 4.13 shows a small steady-state error for the pitch attitude error, $\tilde{\theta}_n$, for the BFCSMC. This can be deduced from the IAE plot not converging to a steady-state value. By zooming in on the final 80 s of the pitch attitude error plot, $\tilde{\theta}_n$, as seen in Figure 4.18, this steady-state error is easily observed. The BFCSMC converges to a steady-state error of approximately 7.5×10^{-5} rad. The implication of this result is the potential for a vehicle controlled by the BFCSMC to be unable to obtain the desired pitch angle.

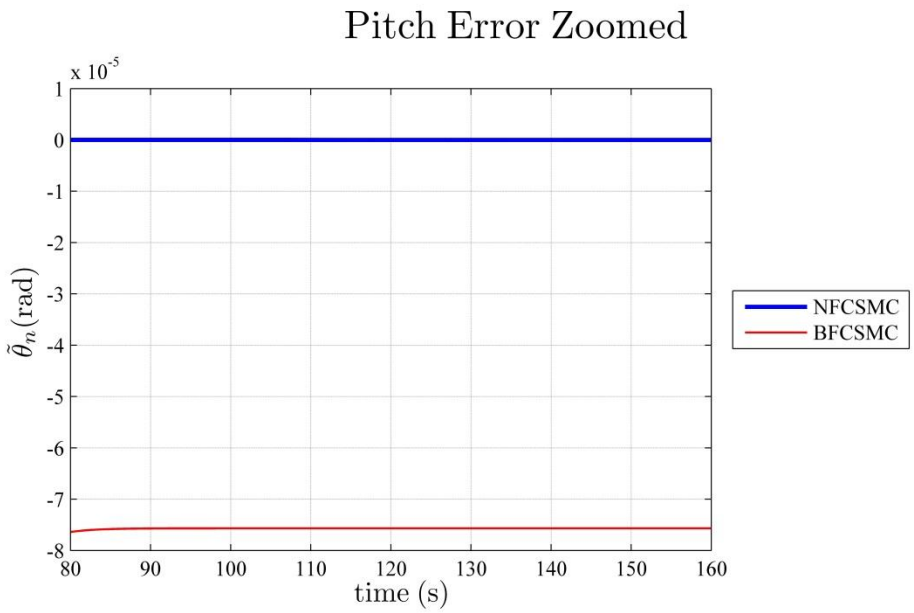

Figure 4.18: Pitch Error Zoomed for Case 1

Case 1 Conclusions

Overall, this case study demonstrates the ability of all three systems to track a simple and uncoupled set of manoeuvres. Only a single DoF is excited at a time, and therefore the performance of each compensator for each DoF can be observed independently of other DoFs.

In terms of tracking a change in desired position or attitude, with the corresponding changes in translational or rotational velocity, the BFUSMC performed in a limited capacity, as indicated in Remark 1.1, compared to both the NFCSMC and the BFCSMC. This clearly demonstrates the performance gained by including the inherent coupling of the model within the control law.

With respect to the NFCSMC and the BFCSMC only, the BFCSMC demonstrated a better performance compared to the NFCSMC as indicated by Remark 2.1 and Remark 2.2. Furthermore, Remark 2.2 also revealed the slower convergence for the north position error and the east position error of the NFCSMC compared to the BFCSMC. However, Remark 2.3 revealed a steady-state error was observed for the pitch attitude angle of the BFCSMC, which was not present for the NFCSMC.

Overall, with respect to this case study, the BFCSMC is the superior compensator as it generally performed better compared to both the NFCSMC and the BFUSMC when tracking this desired trajectory. As expected, the performance of the BFUSMC clearly showed the importance of including the inherent coupling of the vehicle model in the control law. Furthermore, the argument for selecting BFCSMC over the NFCSMC is further strengthened when the increased computational efficiency of the BFCSMC is acknowledged.

4.4.2. Case 2

The second case study used for analysis purposes contains a much more complex trajectory as seen in Figure 4.19, where multiple DoFs are excited at the same time. The reason for choosing this trajectory, as opposed to the trajectory in Case 1 of Section 4.4.1, is that a wider range of manoeuvring can be observed here through multi-DoF excitation. This style of trajectory is more akin to a real-world mission that an AUV would be asked to complete.

Aim

The aim of this case study is to demonstrate the performance of the system when multiple DoFs are excited at the same time. The intention here is to not only evaluate performance, but also observe any coupling effects induced by exciting multiple DoFs concurrently. A LOS guidance system, with a set of waypoints as input, provides the trajectory information to the control system. The LOS guidance system produces the desired states for the vehicle at each time-step such that the vehicle follows the desired trajectory.

System Conditions

The following plots outline the trajectory for the vehicle to follow. They have been produced using a LOS guidance system. This system takes the current state of the vehicle and a series of waypoints as input and produces an output of the desired state for the vehicle to reach at the next time step. Setting both the acceptance radius at each waypoint and the sight radius around the vehicle to a distance of 3 m, a constant translational speed of 1 m s^{-1} and a constant sampling rate of 100 Hz, the LOS

guidance system produces the desired trajectory for the vehicle to follow as seen in Figure 4.19 through to Figure 4.23.

Figure 4.19 shows a three dimensional (3D) plot of this desired trajectory. As can be observed, this case study requires the vehicle to follow a trajectory where multiple DoFs are excited at the same time. To remove any effects due to the vehicle being only partially submerged, the closest the desired trajectory gets to the surface is 10 m. The mission both starts and ends at this depth.

Figure 4.20 and Figure 4.21 break down this trajectory into the desired position and attitude components in the navigation frame assuming a constant translational speed of 1 m s^{-1}.

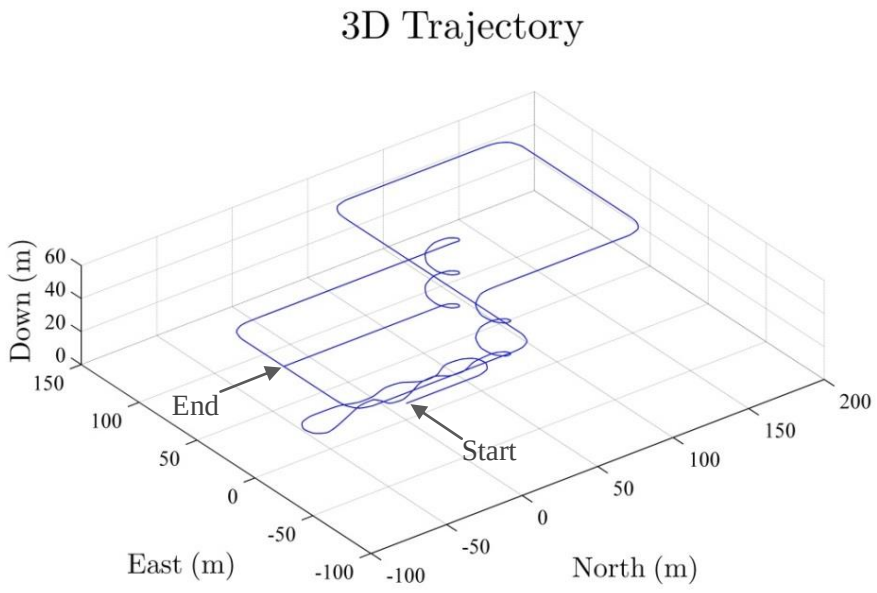

Figure 4.19: 3D Trajectory for Case 2

Figure 4.20 shows the desired position information and Figure 4.21 shows the desired attitude information.

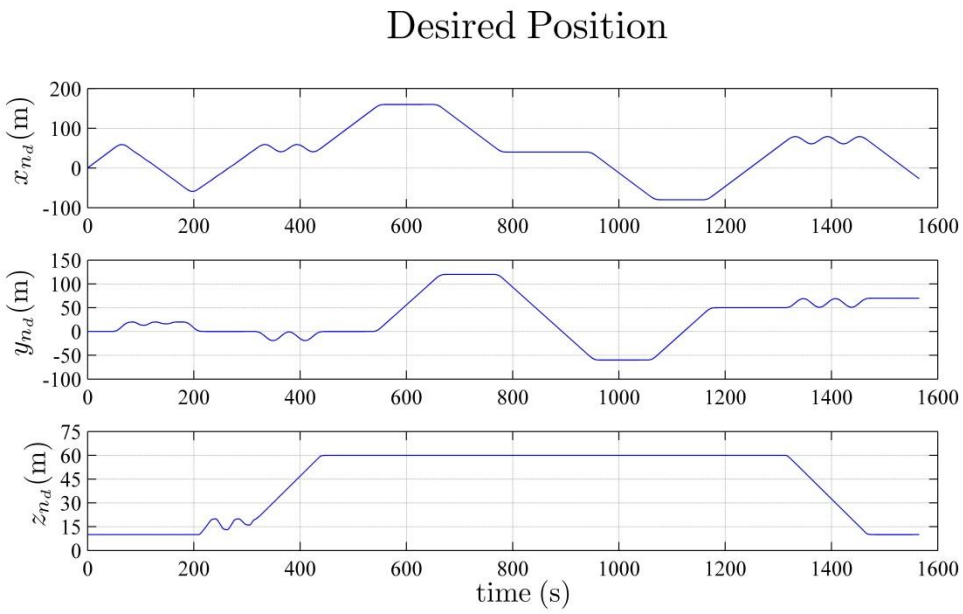

Figure 4.20: Desired Position for Case 2 (NED Frame)

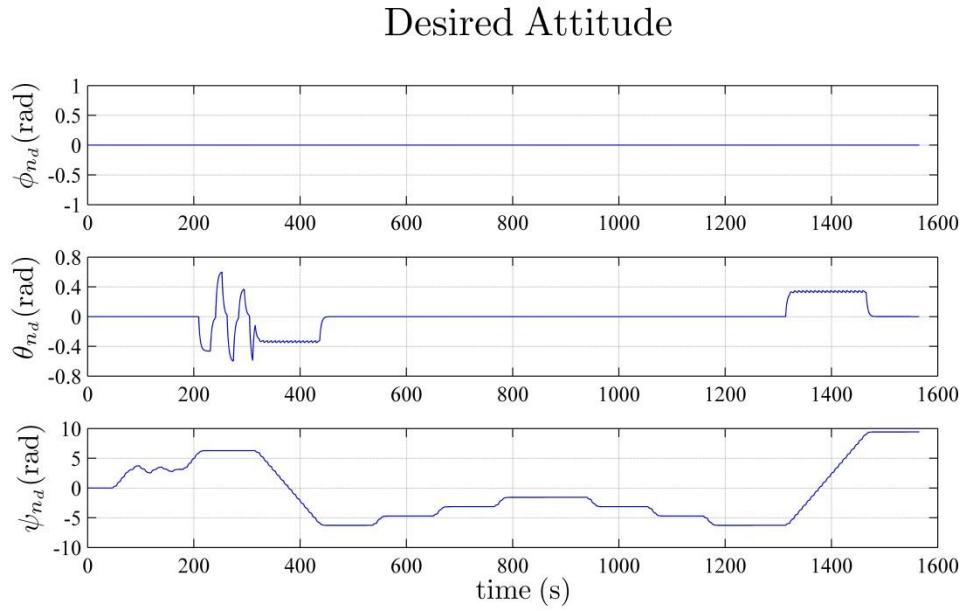

Figure 4.21: Desired Attitude for Case 2 (NED Frame)

By using the inverse of the kinematic equation, Equation (2.11), the desired translational and angular velocity information corresponding to this same trajectory is obtained. These velocities are decomposed in the body frame, with Figure 4.22 showing the translational velocities and Figure 4.23 showing the angular velocities.

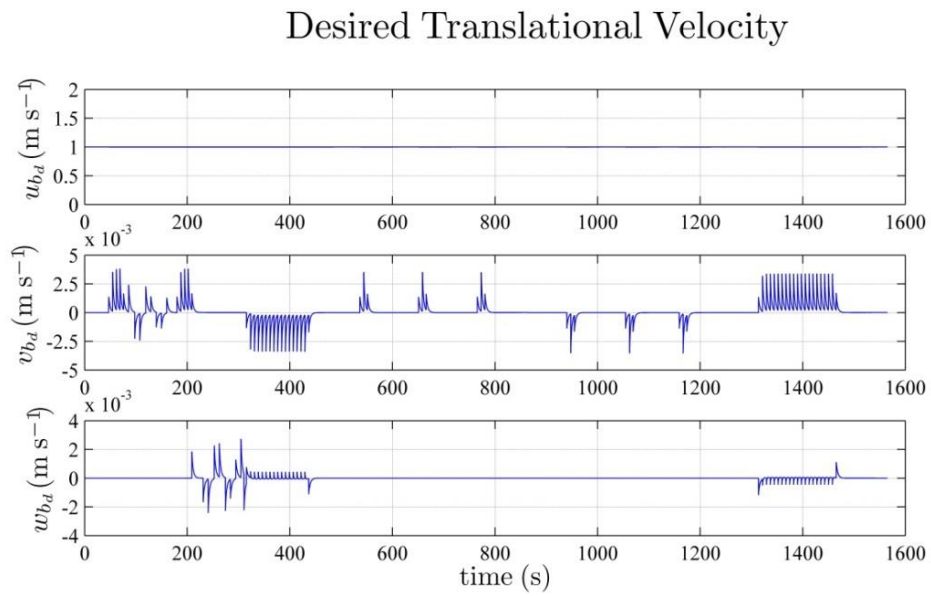

Figure 4.22: Desired Translational Velocity for Case 2 (Body Frame)

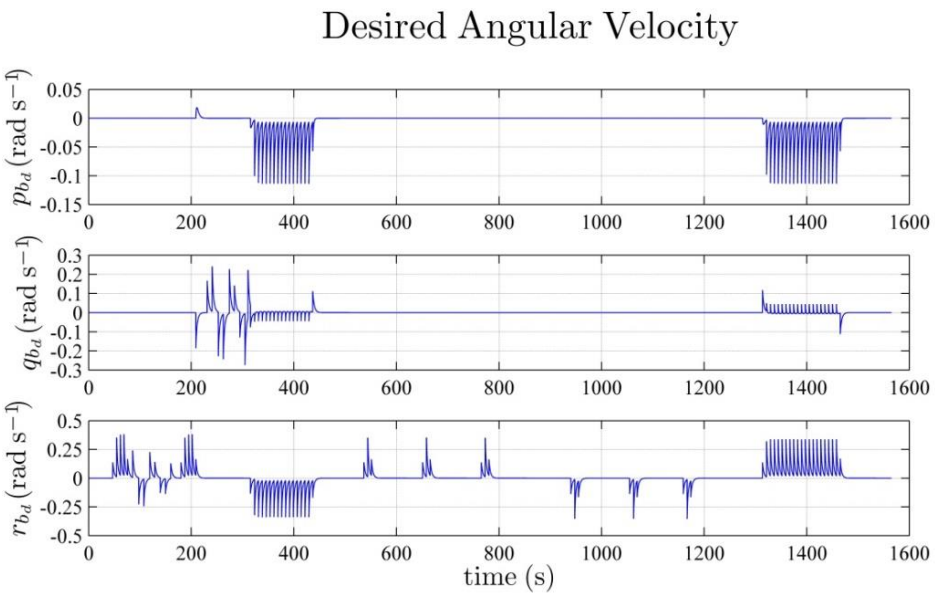

Figure 4.23: Desired Angular Velocity for Case 2 (Body Frame)

Flow Chart

The following flow chart illustrates the behaviour of Case 2.

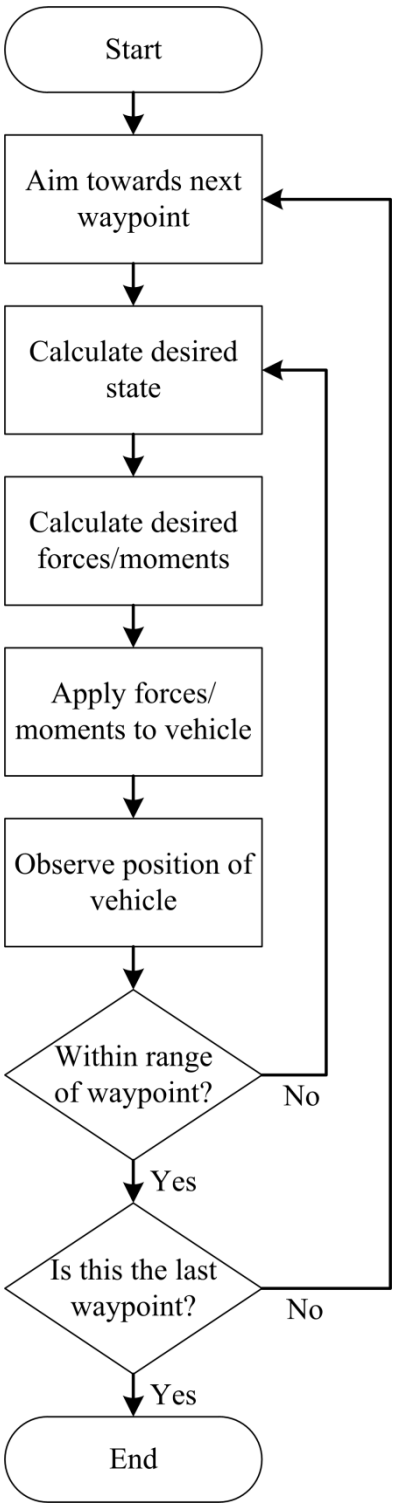

Figure 4.24: Flow Chart for Case 2

Simulation Results

The simulation results are divided into two sections. Firstly, the results of all three compensators, namely the BFUSMC, the NFCSMC, and the BFCSMC, will all be presented together. Secondly, only the compensators that are based on coupled simplified models, namely the NFCSMC and the BFCSMC, will be presented.

1. All Compensators

The following four figures contain the error plots for the BFUSMC, the NFCSMC and the BFCSMC for the input trajectory of Case 2 as outlined in Figure 4.19 through to Figure 4.23. Figure 4.25 shows the position error and position IAE for all compensators. Figure 4.26 shows the attitude error and attitude IAE for all compensators. Figure 4.27 shows the translational velocity error and translational velocity IAE for all compensators. Figure 4.28 shows the angular velocity error and angular velocity IAE for all compensators.

It is anticipated that, due to the limitation of not including coupling in the control law, the BFUSMC will not perform as well as both the NFCSMC and the BFCSMC. It is further anticipated that this difference in performance between the BFUSMC and both the NFCSMC and the BFCSMC will be larger than what was observed for Case 1 of Section 4.4.1 due to the increased complexity of manoeuvring required.

(a) Simulation of Position Errors

Subject to the inputs outlined in Figure 4.19 through to Figure 4.23, the position error for the three compensated systems is given in Figure 4.25.

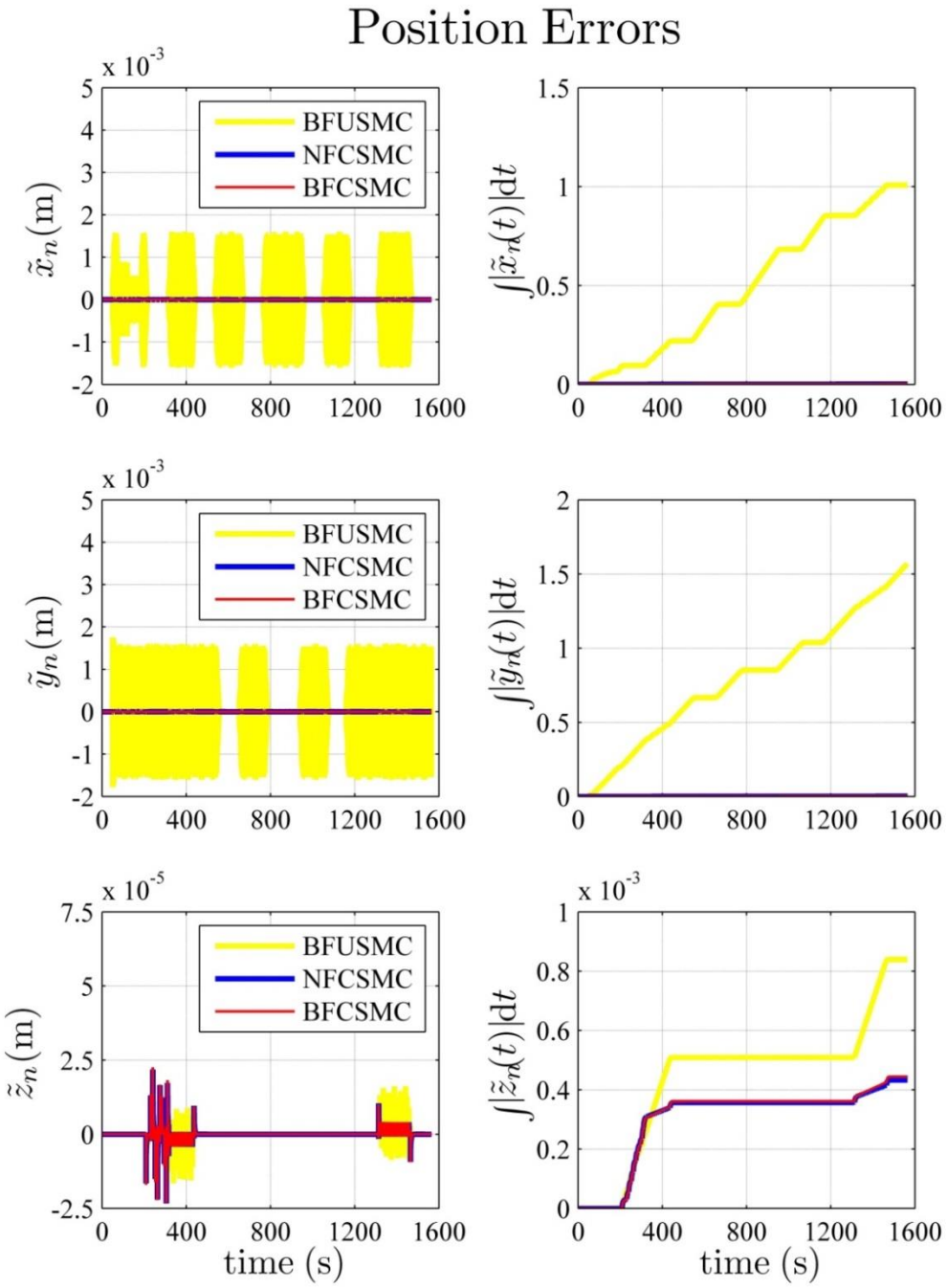

Figure 4.25: Position Errors for Case 2

It is observed from the north position error and east position error, $\tilde{x}_n$ and $\tilde{y}_n$ respectively, and the corresponding IAE plots that the BFUSMC has a much larger dynamic error and IAE compared to both the NFCSMC and the BFCSMC.

It is observed from the down position error, $\tilde{z}_n$, and the corresponding IAE plot that the BFUSMC has a larger dynamic error and IAE, particularly around 400 s and 1400 s, compared to both the NFCSMC and the BFCSMC. Both these times correspond to the vehicle performing the spiral manoeuvre. The NFCSMC and the BFCSMC perform similarly with respect to the down position error.

(b) Simulation of Attitude Errors

Subject to the inputs outlined in Figure 4.19 through to Figure 4.23, the attitude error for the three compensated systems is given in Figure 4.26.

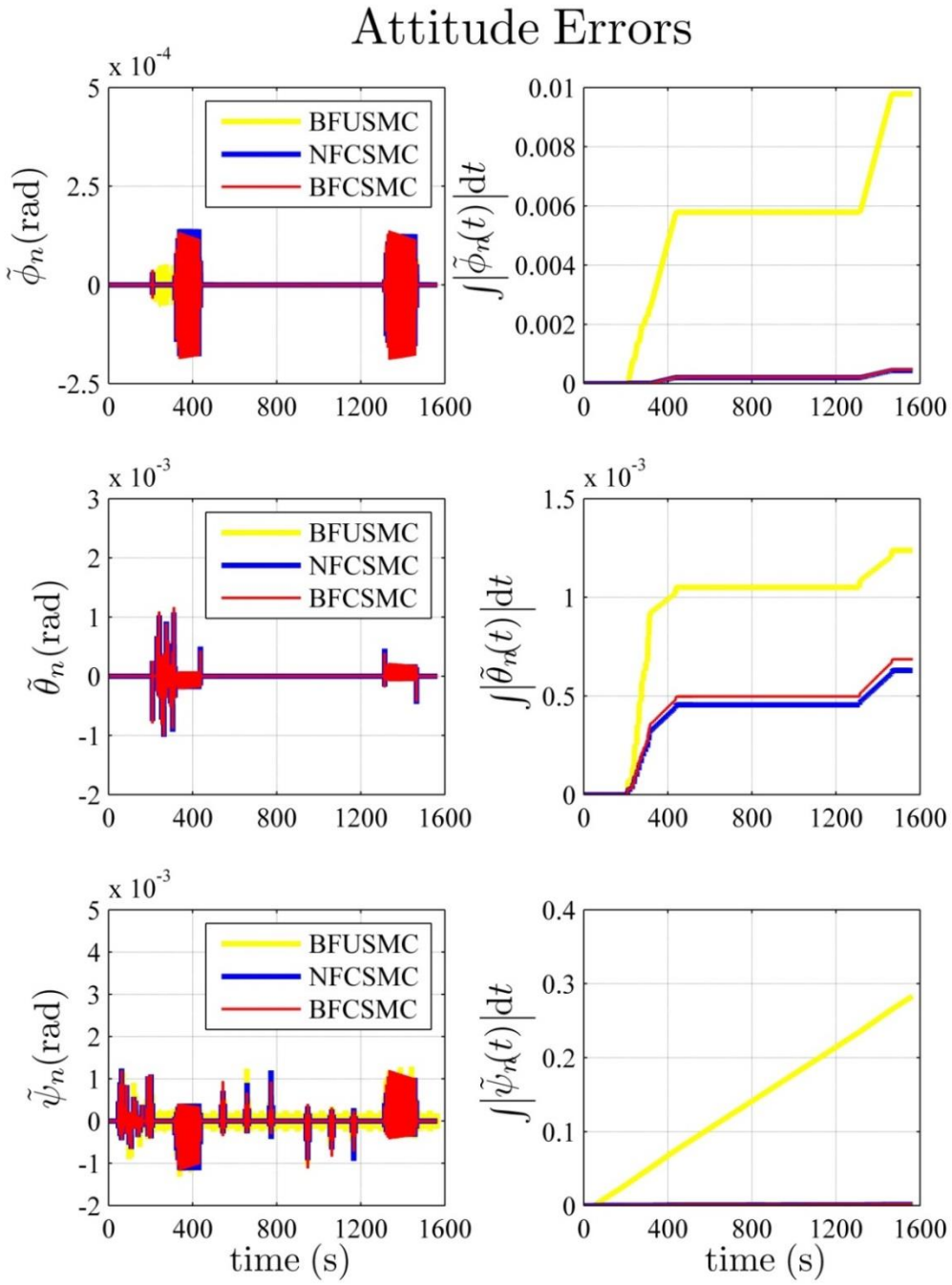

Figure 4.26: Attitude Errors for Case 2

It is observed from the roll attitude error and the pitch attitude error, $\tilde{\phi}_n$ and $\tilde{\theta}_n$ respectively, that all three compensators perform similarly except for the roll attitude error around 300 s. Here, the BFUSMC performs significantly worse compared to the NFCSMC and the BFCSMC. By observing the corresponding IAE plots, it is seen that the BFUSMC has a much larger IAE compared to both the NFCSMC and the BFCSMC.

It is observed from the yaw attitude error, $\tilde{\psi}_n$, and the corresponding IAE plot that the BFUSMC has a much larger dynamic error and IAE across the entire simulation compared to both the NFCSMC and the BFCSMC.

(c) Simulation of Translational Velocity Errors

Subject to the inputs outlined in Figure 4.19 through to Figure 4.23, the translational velocity error for the three compensated systems is given in Figure 4.27.

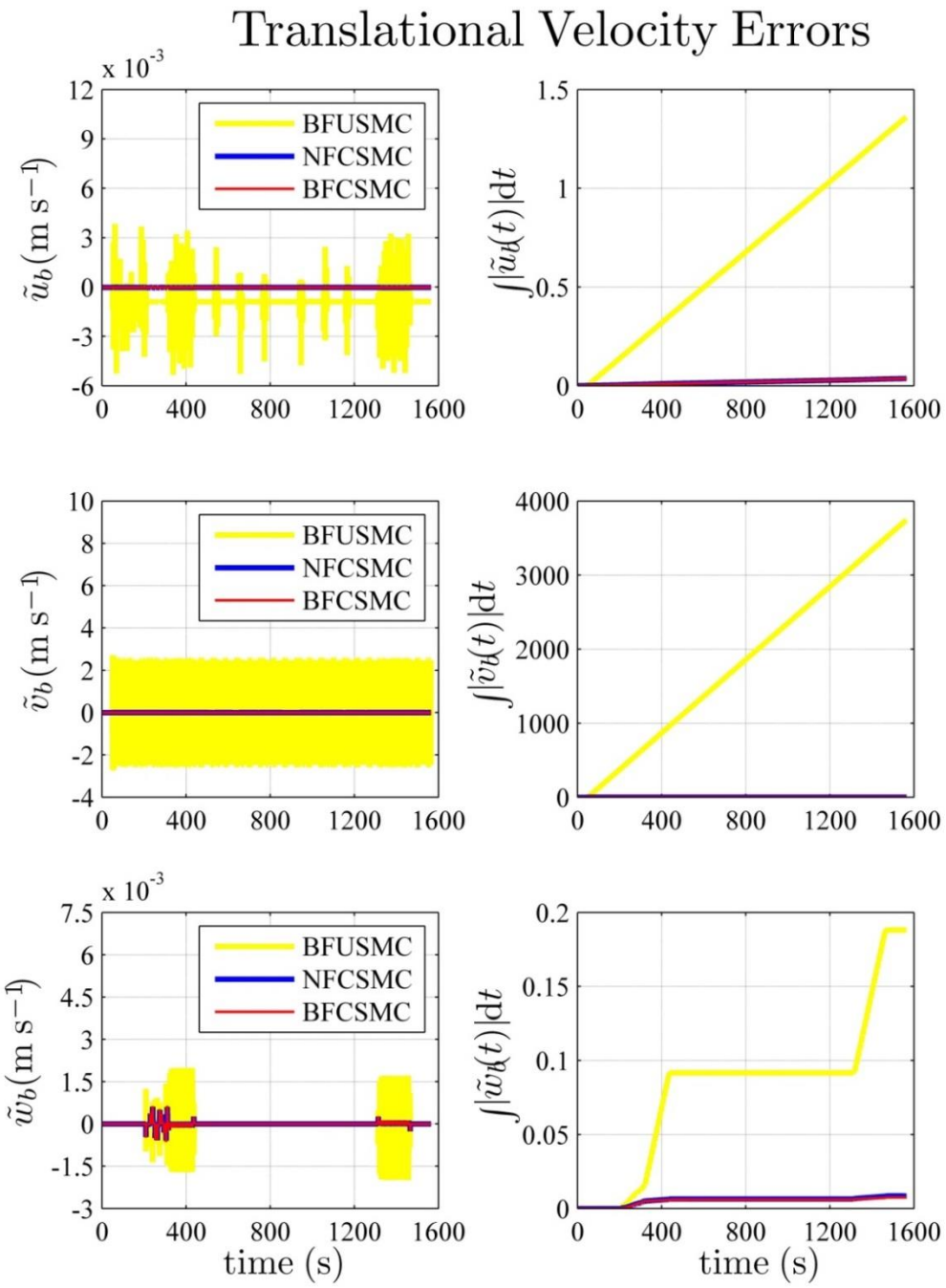

Figure 4.27: Translational Velocity Errors for Case 2

It is observed from the surge translational velocity error, the sway translational velocity error, and the heave translational velocity error, $\tilde{u}_b$, $\tilde{v}_b$, and $\tilde{w}_b$ respectively, and the corresponding IAE plots that the BFUSMC has a much larger dynamic error and IAE compared to both the NFCSMC and the BFCSMC. Furthermore, a consistent steady-state error is observed for the BFUSMC when observing the surge translational velocity error, $\tilde{u}_b$.

(d) Simulation of Angular Velocity Errors

Subject to the inputs outlined in Figure 4.19 through to Figure 4.23, the angular velocity error for the three compensated systems is given in Figure 4.28.

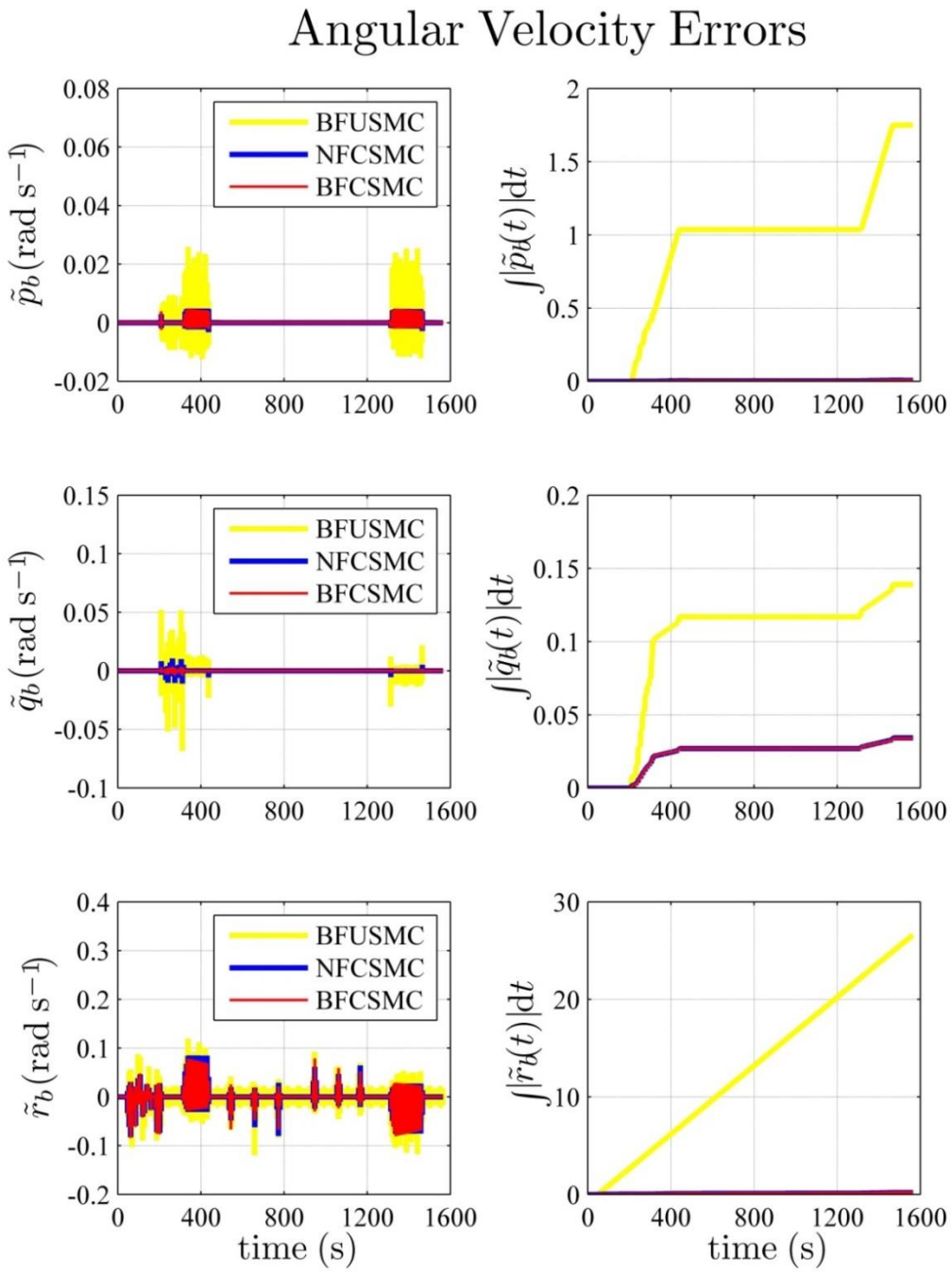

Figure 4.28: Angular Velocity Errors for Case 2

It is observed from the roll angular velocity error, the pitch angular velocity error, and the yaw angular velocity error, $\tilde{p}_b$, $\tilde{q}_b$, and $\tilde{r}_b$ respectively, and the corresponding IAE plots that the BFUSMC has a much larger dynamic error and IAE compared to both the NFCSMC and the BFCSMC.

(e) Concluding Remarks

Figure 4.25 through to Figure 4.28 compares the behaviour of the BFUSMC, the NFCSMC, and the BFCSMC when the input trajectory is that of Case 2. Based on the behaviours observed, the following remarks can be drawn.

Remark 1.1 – The BFUSMC demonstrates a limited performance compared to both the NFCSMC and the BFCSMC.

> The most general observation from Figure 4.25 through to Figure 4.28 is that again the BFUSMC demonstrates limited performance compared to both the NFCSMC and the BFCSMC. Paying particular attention to the north position error, $\tilde{x}_n$, and the east position error, $\tilde{y}_n$, of Figure 4.25, and all the translational and angular velocities of Figure 4.27 and Figure 4.28 respectively, significant errors are observed for the BFUSMC compared to both the BFCSMC and the NFCSMC. This is particularly evident during the highly coupled manoeuvres such as the spiral manoeuvres. Furthermore, observation of all IAE plots from Figure 4.25 through to Figure 4.28 illustrates the limited performance of the BFUSMC under the conditions outlined for this case study. This case study again highlights the need to include coupling within the control algorithm.

The magnitude of the error seen for the BFUSMC is considerably larger than the error seen for both the NFCSMC and the BFCSMC within some of the figures presented in this case study. Hence, it is difficult to observe the behaviour of the NFCSMC or the BFCSMC in these instances. Therefore, to gain a better insight into the performance of the two coupled control schemes, the same simulation is conducted, except that the behaviour of the BFUSMC is omitted.

2. Coupled Compensators

The following four figures contain the error plots for the NFCSMC and the BFCSMC for the input trajectory of Case 2 as outlined in Figure 4.19 through to Figure 4.23. Figure 4.29 shows the position error and position IAE for the NFCSMC and BFCSMC only. Figure 4.30 shows the attitude error and attitude IAE for the NFCSMC and BFCSMC only. Figure 4.31 shows the translational velocity error and translational velocity IAE for the NFCSMC and BFCSMC only. Figure 4.32 shows the angular velocity error and angular velocity IAE for the NFCSMC and BFCSMC only.

It is anticipated that both the NFCSMC and the BFCSMC will perform similarly for this trajectory, due to the similar nature of the controllers and the fact that both the NFCSMC and the BFCSMC include the inherent coupling of the vehicle model in the control law.

(a) Simulation of Position Errors

Subject to the inputs outlined in Figure 4.19 through to Figure 4.23, the position error for the two compensated systems is given in Figure 4.29.

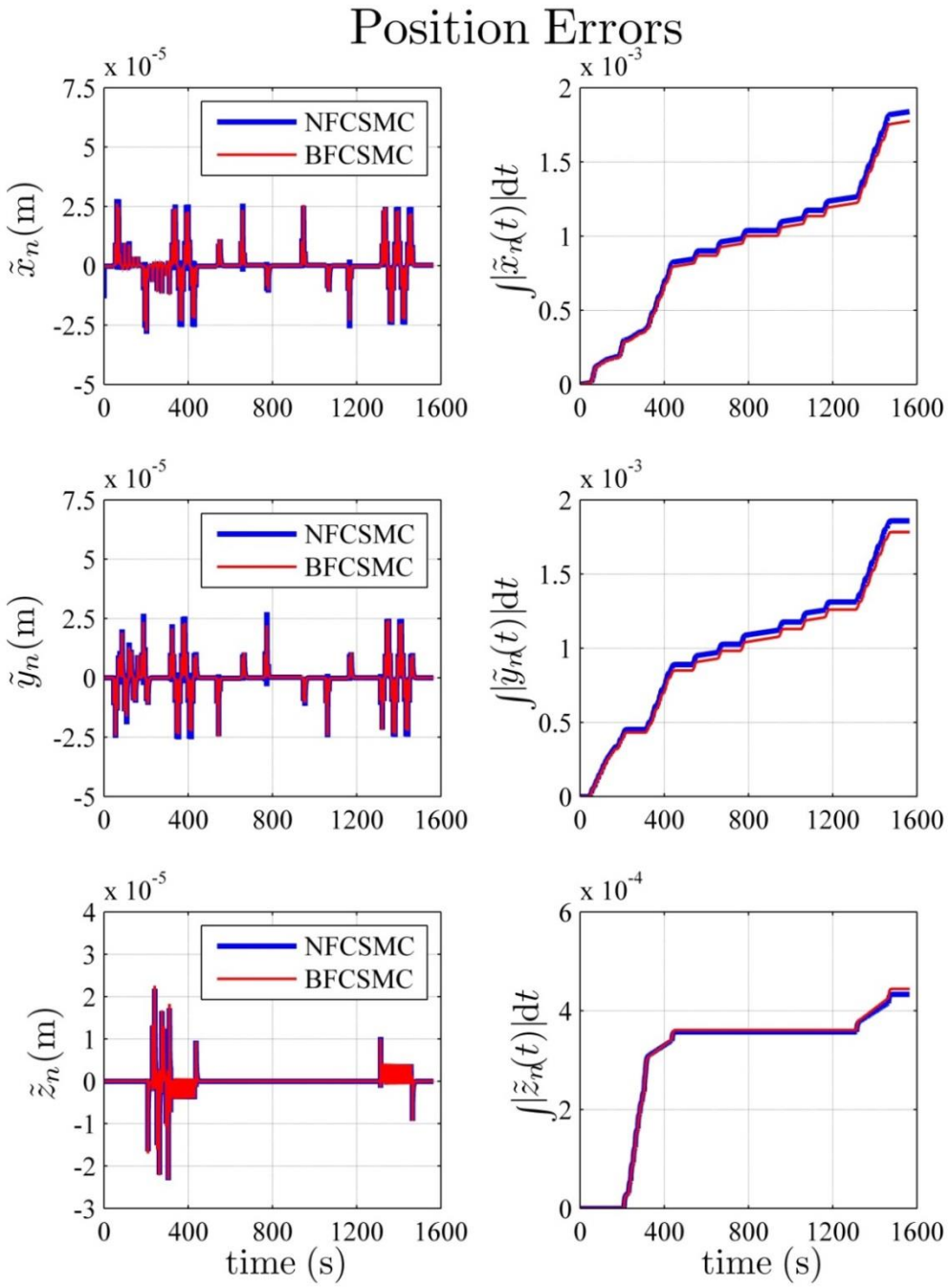

Figure 4.29: Position Errors for Case 2 without BFUSMC

It is observed from the north position error, the east position error, and the down position error, $\tilde{x}_n$, $\tilde{y}_n$, and $\tilde{z}_n$ respectively, and the corresponding IAE plots that both the NFCSMC and the BFCSMC perform very similarly.

(b) Simulation of Attitude Errors

Subject to the inputs outlined in Figure 4.19 through to Figure 4.23, the attitude error for the two compensated systems is given in Figure 4.30.

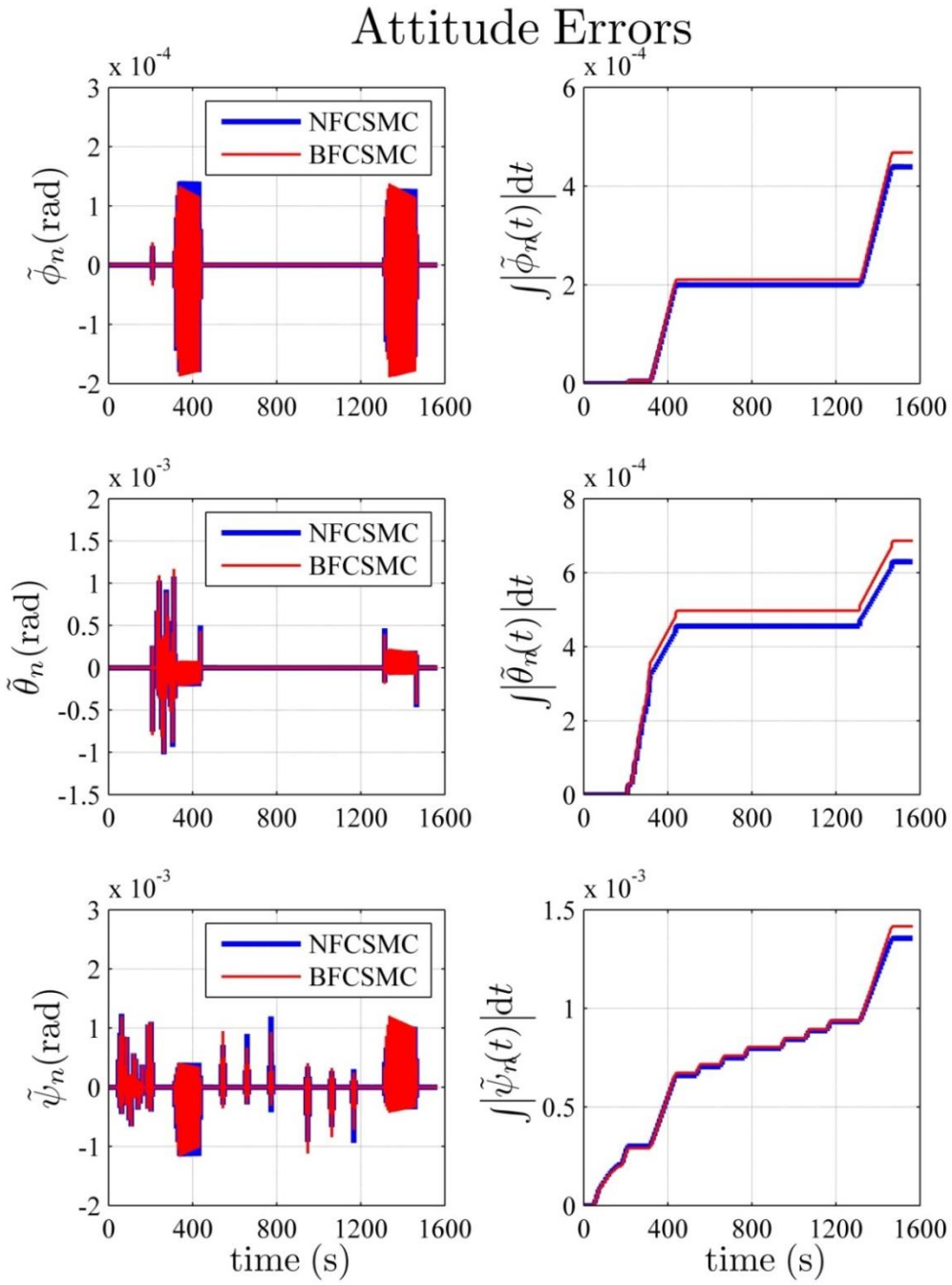

Figure 4.30: Attitude Errors for Case 2 without BFUSMC

It is observed from the roll attitude error, the pitch attitude error, and the yaw attitude error, $\tilde{\phi}_n$, $\tilde{\theta}_n$, and $\tilde{\psi}_n$ respectively, and the corresponding IAE plots that both the NFCSMC and the BFCSMC perform very similarly.

(c) Simulation of Translational Velocity Errors

Subject to the inputs outlined in Figure 4.19 through to Figure 4.23, the translational velocity error for the two compensated systems is given in Figure 4.31.

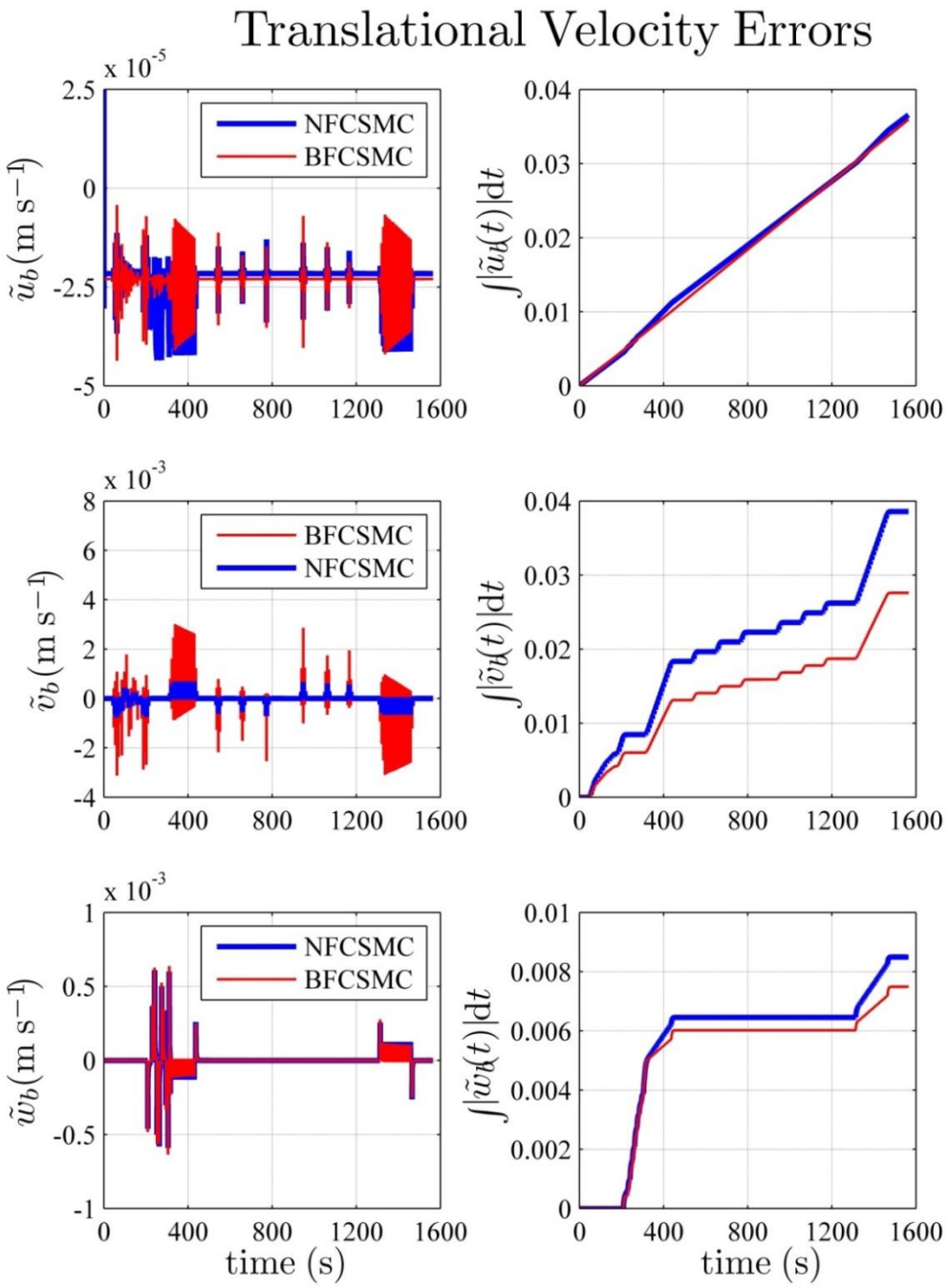

Figure 4.31: Translational Velocity Errors for Case 2 without BFUSMC

It is observed from the surge translational velocity error, $\tilde{u}_b$, that the NFCSMC has a larger dynamic error compared to the BFCSMC, particularly at around 300 s. Furthermore, both the NFCSMC and the BFCSMC have a non-zero steady-state error. The corresponding IAE plot shows that both the NFCSMC and the BFCSMC perform similarly in this respect.

It is observed from the sway translational velocity error, $\tilde{v}_b$, that the NFCSMC has a much smaller dynamic error compared to the BFCSMC. However, the corresponding IAE plot shows that the NFCSMC has a larger IAE compared to the BFCSMC.

It is observed from the heave translational velocity error, $\tilde{w}_b$, and the corresponding IAE plot that both the NFCSMC and the BFCSMC perform very similarly.

(d) Simulation of Angular Velocity Errors

Subject to the inputs outlined in Figure 4.19 through to Figure 4.23, the angular velocity error for the two compensated systems is given in Figure 4.32.

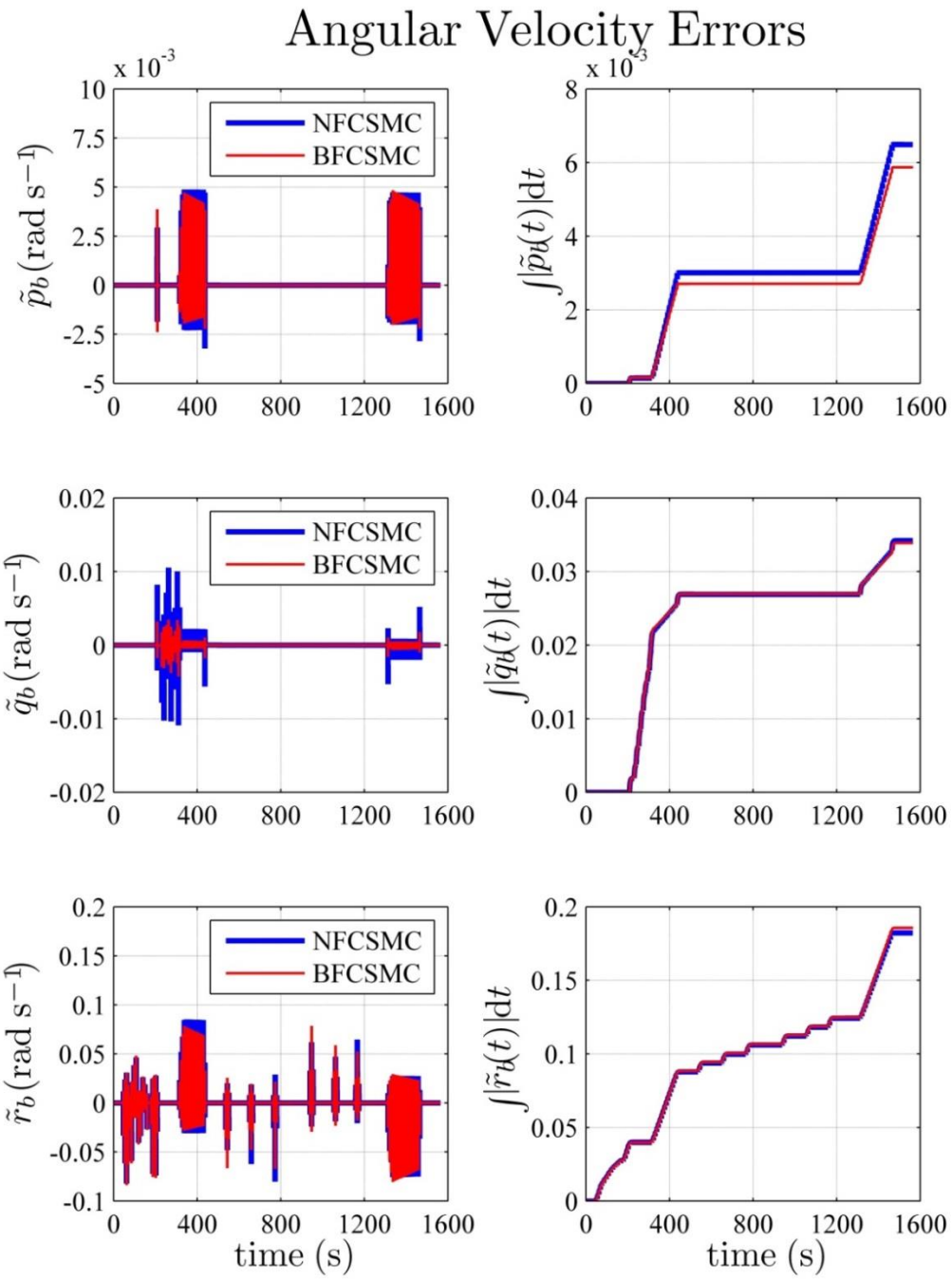

Figure 4.32: Angular Velocity Errors for Case 2 without BFUSMC

It is observed from the roll angular velocity error and the yaw angular velocity error, $\tilde{p}_b$ and $\tilde{r}_b$ respectively, and the corresponding IAE plots that both the NFCSMC and the BFCSMC perform very similarly.

It is observed from the pitch angular velocity error, $\tilde{q}_b$, that the NFCSMC has a much larger dynamic error compared to the BFCSMC. However, the corresponding IAE plot shows that both the NFCSMC and the BFCSMC perform very similarly in this respect.

(e) Concluding Remarks

Figure 4.29 through to Figure 4.32 compares the behaviour of the NFCSMC and the BFCSMC when the input trajectory is that of Case 2. Based on the behaviours observed, the following remarks can be drawn.

Remark 2.1 – Generally, similar behaviour is observed for both the NFCSMC and the BFCSMC with respect to position and attitude.

> Figure 4.29 and Figure 4.30 show that both the BFCSMC and the NFCSMC behave similarly within this case study. The position error plots and the corresponding IAE plots seen in Figure 4.29 show that there is near identical behaviour for both the BFCSMC and the NFCSMC. Figure 4.30 also shows similar behaviour between the two systems, here with respect to attitude errors.

Remark 2.2 – A small steady-state error is observed in the surge velocity for both the NFCSMC and the BFCSMC.

> With respect to the translational velocity errors of Figure 4.31, a small steady-state error is observed in the surge velocity, u_b, for both the BFCSMC and the NFCSMC. The BFCSMC has a steady-state error of approximately $2.30\text{x}10^{-5}$ m s^{-1} while the NFCSMC has a steady-state error of approximately $2.16\text{x}10^{-5}$ m s^{-1}. These steady-state errors are easily observed when zooming in on the surge translational velocity error, as seen in Figure 4.33.

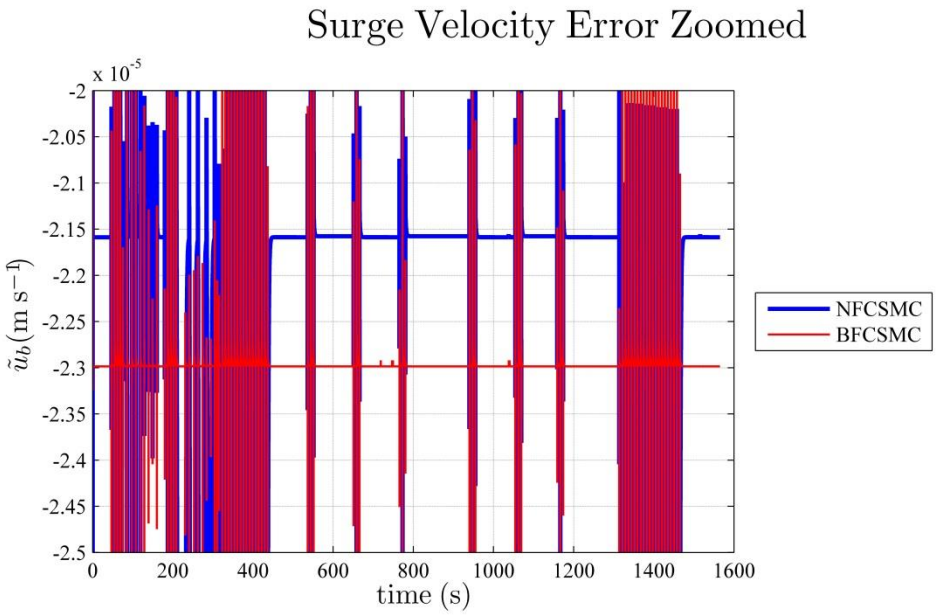

Figure 4.33: Surge Translational Velocity Error Zoomed for Case 2

Remark 2.3 – The BFCSMC demonstrates better performance when executing a vertical zigzag manoeuvre.

It is observed from the surge translational velocity error, $\tilde{u}_b$, of Figure 4.31 and the pitch angular velocity error, $\tilde{q}_b$, of Figure 4.32 that the NFCSMC has larger errors compared to the BFCSMC between approximately 200 s and 300 s. This corresponds to the vehicle executing a vertical zigzag manoeuvre, which requires control of both the surge DoF and the pitch DoF. Hence, the NFCSMC is less capable of controlling the surge and pitch DoFs concurrently. This manoeuvre is similar to the type of manoeuvre that a vehicle would execute when profiling the water depth over a large area, and therefore the BFCSMC is better suited to this task.

Remark 2.4 – Larger overshoot yet smaller IAE for BFCSMC when looking at the sway translational velocity error, $\tilde{v}_b$, of Figure 4.31.

The sway translational velocity error, $\tilde{v}_b$, of Figure 4.31 is where a significant difference is observed between the behaviours of the BFCSMC and the NFCSMC across the entire simulation. Similar to the observation for this DoF in Case 1 of Section 4.4.1, the BFCSMC experiences a larger magnitude

of dynamic error while also having a smaller IAE. Again, this is due to the BFCSMC having a larger overshoot while at the same time having a faster convergence.

Remark 2.5 – Larger overshoot yet similar IAE for NFCSMC when looking at the pitch angular velocity error, $\tilde{q}_b$, of Figure 4.32.

Observation of the pitch angular velocity error, $\tilde{q}_b$, of Figure 4.32 shows that the NFCSMC experiences a much larger dynamic error compared to the BFCSMC. However, the corresponding IAE plot shows very similar behaviour.

Case 2 Conclusions

The aim of this case study was to observe the performance of the BFUSMC, the NFCSMC, and the BFCSMC under complex manoeuvring conditions where multiple DoFs are excited simultaneously. This aim was accomplished using a LOS guidance system that interpreted a series of waypoints and generated a complex path for the vehicle to follow. The error plots presented here indicated that all three systems were able to follow the desired trajectory such that all waypoints were traversed in succession; however, there were varying degrees of performance.

As indicated in Remark 1.1, Figure 4.25 through to Figure 4.28 clearly showed the limited performance of the BFUSMC compared to both the NFCSMC and the BFCSMC under the conditions presented in this case study. This clearly demonstrates the performance gained by including the inherent coupling of the model within the control law.

Quite similar behaviour was observed for the NFCSMC and the BFCSMC with respect to position errors of Figure 4.29 and attitude errors of Figure 4.30, as indicated by Remark 2.1. Both the error plots and the corresponding IAE plots show this behaviour. As the BFCSMC is much simpler to implement compared to the NFCSMC, as there is no need to transform information between the navigation frame and the body frame for the BFCSMC, this similar behaviour demonstrates that the BFCSMC is a better choice under the circumstances presented in this case study.

Significant differences were observed for the translational velocity errors of Figure 4.31 and the angular velocity errors of Figure 4.32. Of particular note are the sway translational velocity error, $\tilde{v}_b$, of Figure 4.31, as indicated in Remark 2.4, and the pitch angular velocity error, $\tilde{q}_b$, of Figure 4.32, as indicated by Remark 2.5. By observing the sway translational velocity error, the NFCSMC has a smaller dynamic error while the BFCSMC has a smaller IAE. With respect to the pitch angular velocity error, the BFCSMC has the smaller dynamic error while both systems exhibit similar performance with respect to the IAE.

It was also seen that the NFCSMC produced larger surge translational velocity errors when executing the vertical zigzag manoeuvre compared to the BFCSMC as indicated by Remark 2.3. As this is similar to a manoeuvre that a vehicle would perform when conducting water column profiling over a large area, this indicates that the BFCSMC is better suited to this task than the NFCSMC. Furthermore, as the BFCSMC is simpler and more computationally efficient to implement, a vehicle controlled by the BFCSMC for water column profiling would be more accurate and, as the computational efficiency will lead to increased energy efficiency, the vehicle will have a longer range.

Overall, both the BFCSMC and the NFCSMC performed quite similarly for this particular case study, while the performance of the BFUSMC was limited in comparison. This was expected as the trajectory for this case study contained manoeuvres where multiple DoFs were excited concurrently, which would excite the inherent coupling within the plant model. The limited performance of the BFUSMC was expected, as it does not include this coupling within its control law. Therefore, this case study has highlighted the importance of including coupling within the control law. Furthermore, as approximately similar behaviour was observed between the NFCSMC and the BFCSMC, the BFCSMC is the superior choice due to its reduced computational requirements.

4.4.3. Case 3

The final case study considered here is a mission that an AUV would be very well suited. The trajectory here consists of a raster scan covering an area of approximately 250,000 m^2, with each scan being 20 m apart. Depending on the sensor payload, this mission could be used for collecting salinity levels, temperature readings, or water density levels. Furthermore, this type of mission is also well suited to sea floor survey missions if the vehicle is equipped with some sort of imaging sensor, such as a video camera or a side-scan sonar. This case study includes similar manoeuvres to those seen in Case 2 of Section 4.4.2. To increase the realism of this case study, a time-varying water current disturbance is also included in the simulation environment.

Aim

The aim of this case study is to demonstrate the performance of system under realistic conditions, i.e., exciting multiple DoFs while under the influence of a water current disturbance. Case 1 of Section 4.4.1 and Case 2 of Section 4.4.2 have provided information in regards to performance under ideal conditions, yet this case study adds an extra level of authenticity by introducing a random, time-varying disturbance in the form of an unknown water current.

System Conditions

The following plots have been produced in the same way as the desired plots for the trajectory of Case 2 of Section 4.4.2. As noted previously, the depth is restricted to a minimum of 10 m to avoid any effects due to partial submergence, and the desired translational speed is kept constant at 1 m s^{-1}.

The same LOS guidance system utilised in Case 2 of Section 4.4.2 is utilised here with the same operating parameters such as acceptance and sight radius set to 3 m and sampling rate of 100 Hz, to produce the 3D trajectory as seen in Figure 4.34. Figure 4.35 shows the corresponding position information, Figure 4.36 shows the attitude information, Figure 4.37 shows the translational velocity information, and Figure 4.38 shows the angular velocity information. Again, position/attitude data is

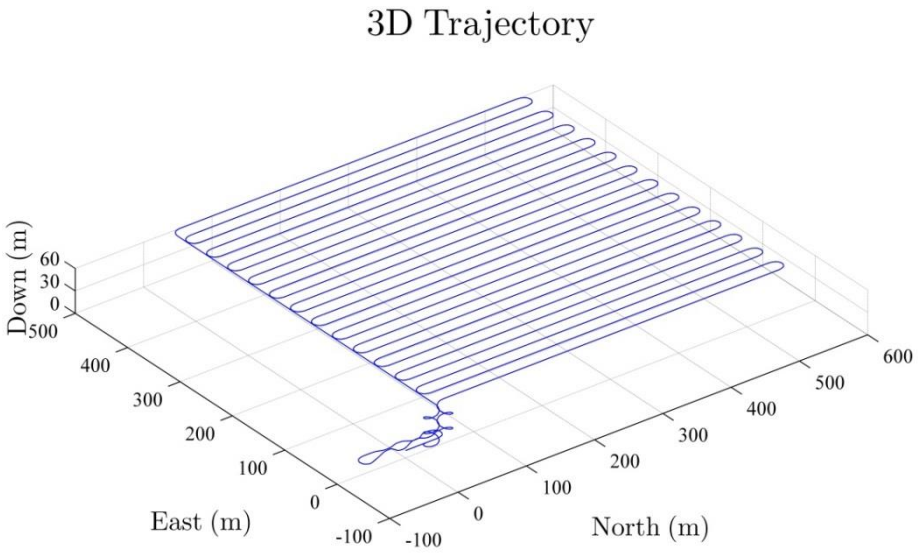

Figure 4.34: 3D Trajectory for Case 3

decomposed in the navigation frame and velocity data is decomposed in the body frame.

The corresponding position and attitude data, decomposed in the NED frame, given in Figure 4.35 and Figure 4.36 respectively.

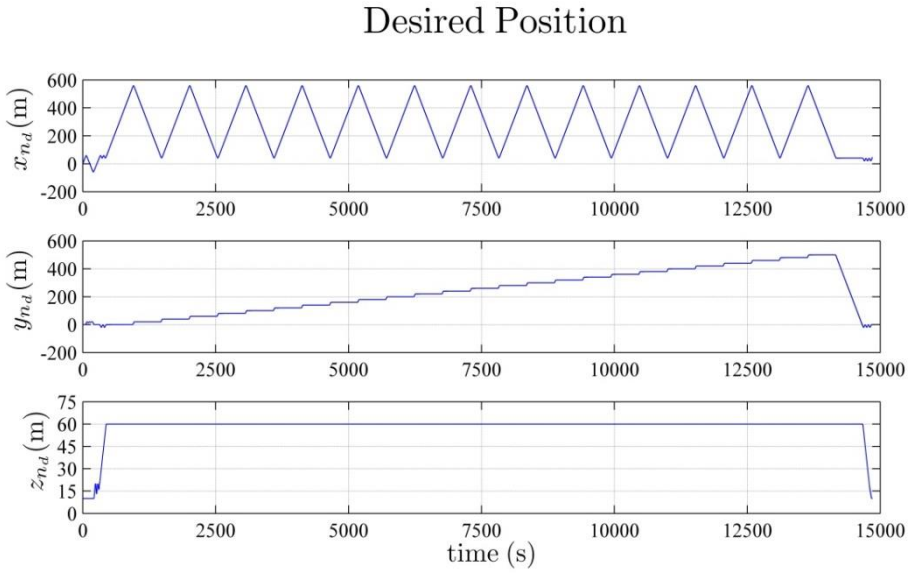

Figure 4.35: Desired Position for Case 3 (NED Frame)

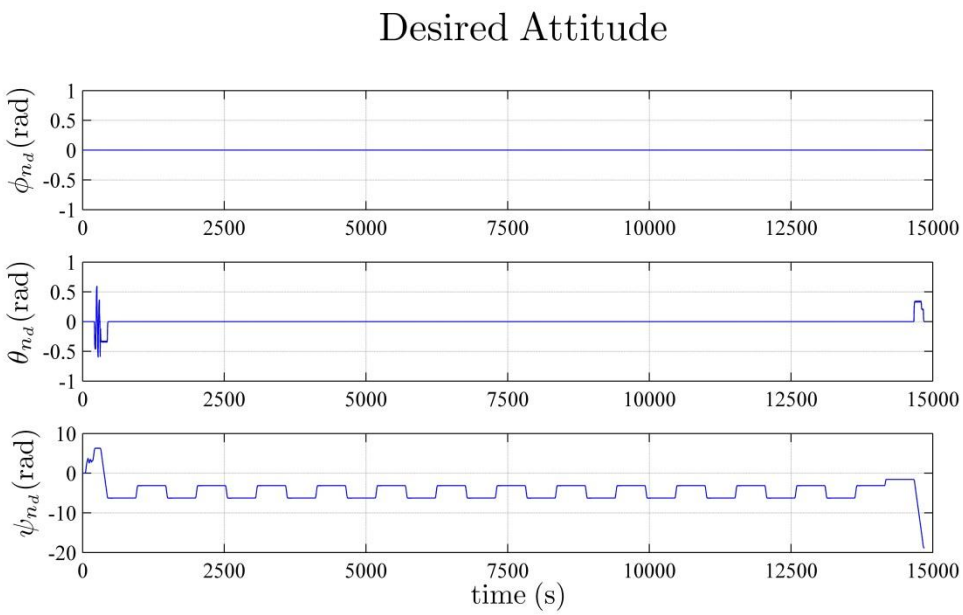

Figure 4.36: Desired Attitude for Case 3 (NED Frame)

Figure 4.37 shows the corresponding translational velocity information, and Figure 4.38 shows the angular velocity information, both decomposed in the body frame.

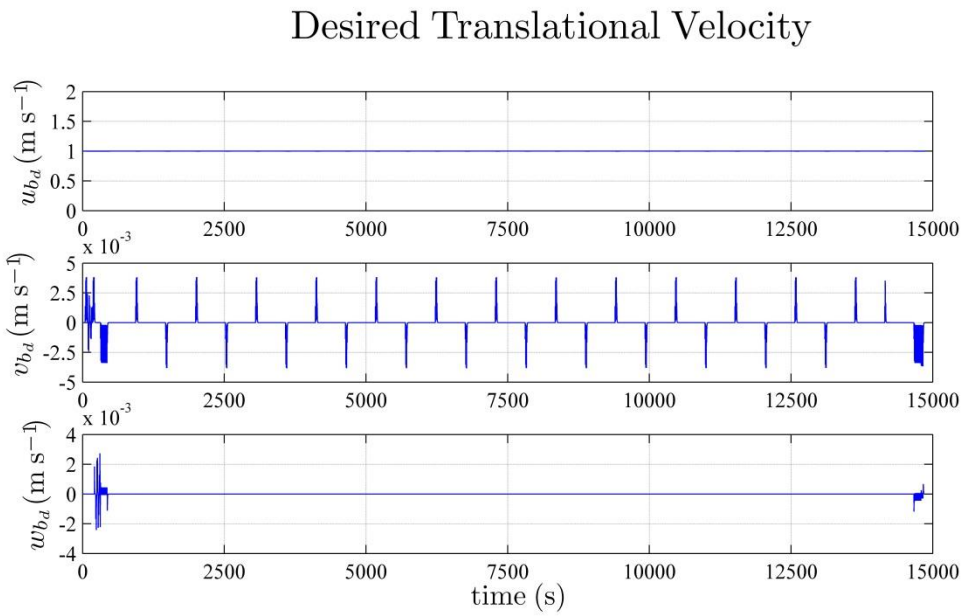

Figure 4.37: Desired Translational Velocity for Case 3 (Body Frame)

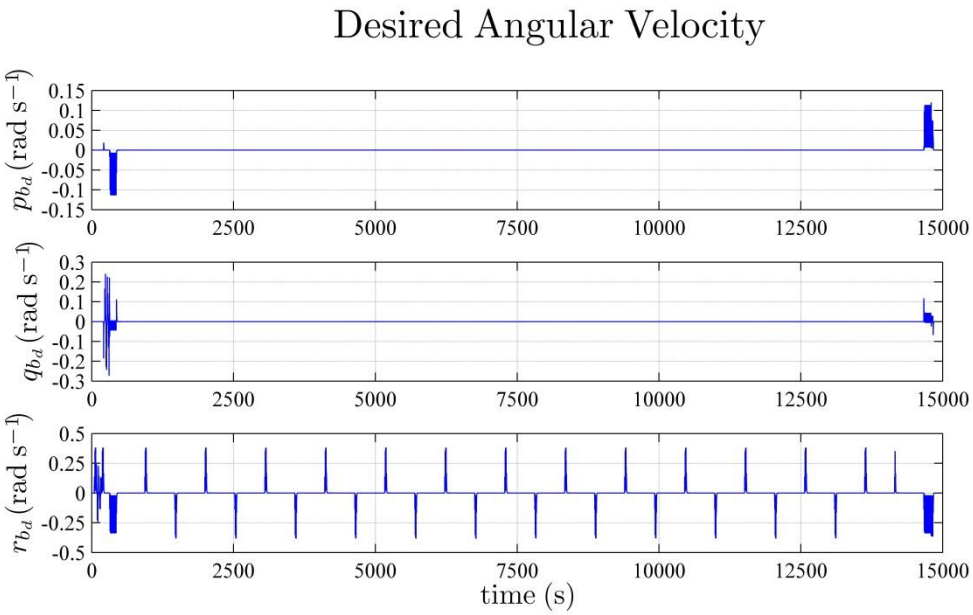

Figure 4.38: Desired Angular Velocity for Case 3 (Body Frame)

An extra component that is present in this case study is a disturbance in the form of a time-varying water current. It is assumed here that the water current is irrotational, and hence only has influence on the translational velocities of the vehicle. Even though this current is irrotational, it still induces rotational motion on the vehicle due to coupling between translational and rotational DoFs within the vehicle model.

This time-varying current is implemented using a 1st-order Gauss-Markov Process [3], with the translational components, decomposed in the NED frame, shown in Figure 4.39. As the current is irrotational, the rotational components of the current are all zero, as shown in Figure 4.40. Figure 4.41 shows the overall magnitude of the simulated water current.

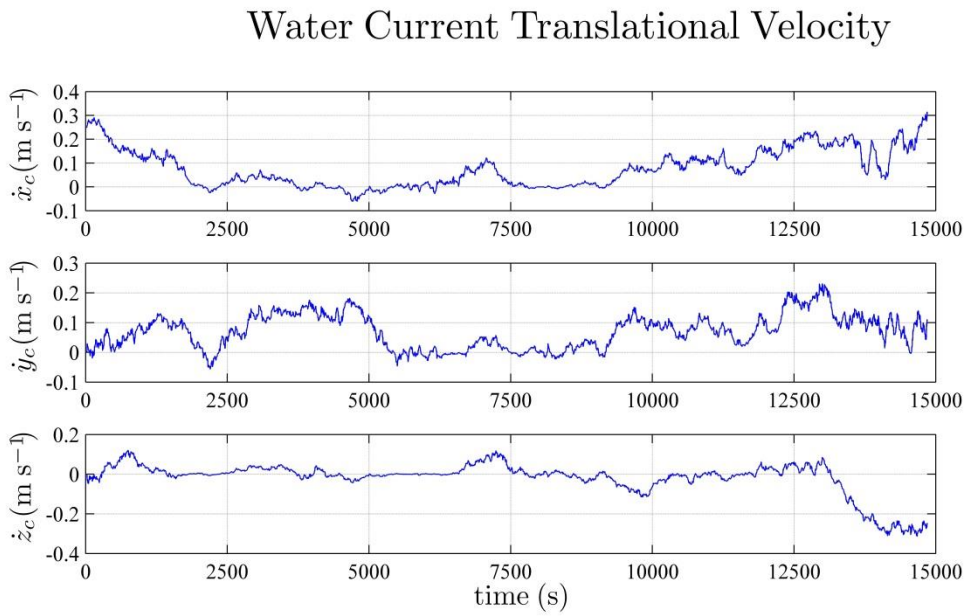

Figure 4.39: Water Current Translational Velocity for Case 3 (NED Frame)

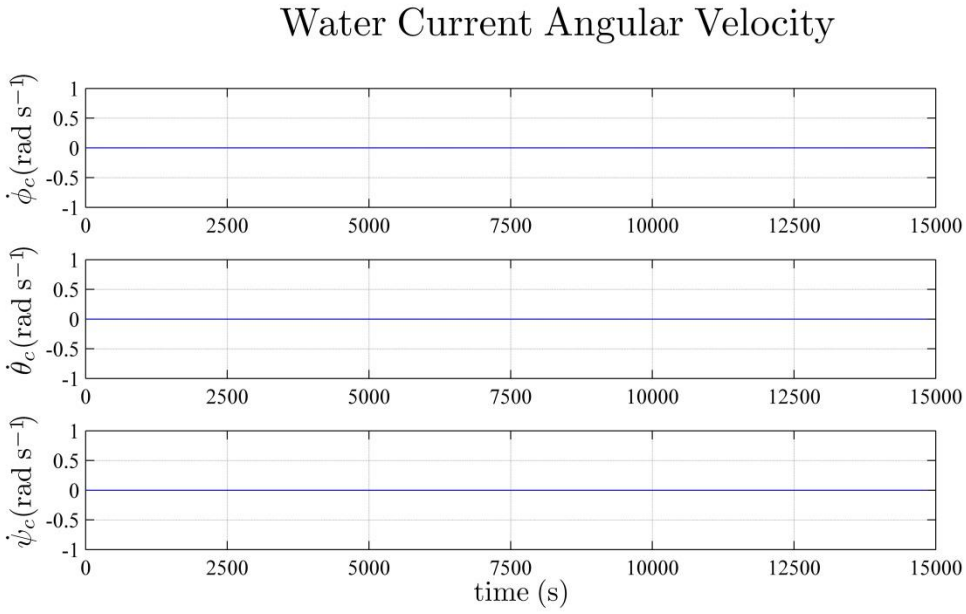

Figure 4.40: Water Current Angular Velocity for Case 3 (NED Frame)

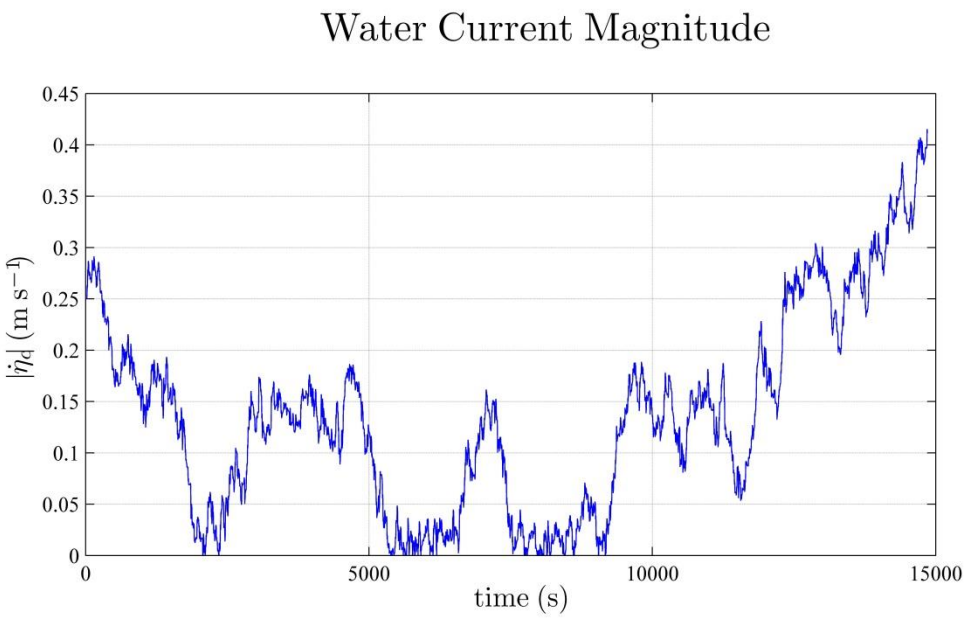

Figure 4.41: Water Current Magnitude for Case 3

Flow Chart

The following flow chart illustrates the behaviour of Case 3.

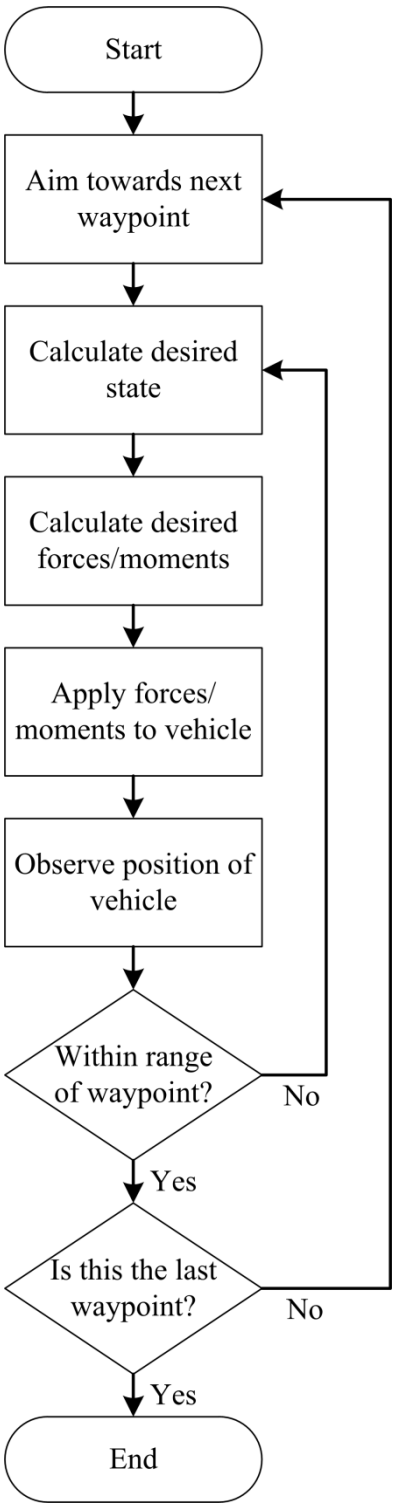

Figure 4.42: Flow Chart for Case 3

Simulation Results

The simulation results are divided into two sections. Firstly, the results of all three compensators, namely the BFUSMC, the NFCSMC, and the BFCSMC, will all be presented together. Secondly, only the compensators that are based on coupled simplified models, namely the NFCSMC and the BFCSMC, will be presented.

1. All Compensators

The following four figures contain the error plots for the BFUSMC, the NFCSMC and the BFCSMC for the input trajectory of Case 3 as outlined in Figure 4.34 through to Figure 4.41. Figure 4.43 shows the position error and position IAE for all compensators. Figure 4.44 shows the attitude error and attitude IAE for all compensators. Figure 4.45 shows the translational velocity error and translational velocity IAE for all compensators. Figure 4.46 shows the angular velocity error and angular velocity IAE for all compensators.

It is anticipated that, due to the limitation of not including coupling in the control law, the BFUSMC will not perform as well as both the NFCSMC and the BFCSMC, as has been observed in Case 1 and Case 2 of this simulation study.

(a) Simulation of Position Errors

Subject to the inputs outlined in Figure 4.34 through to Figure 4.41, the position error for the three compensated systems is given in Figure 4.43.

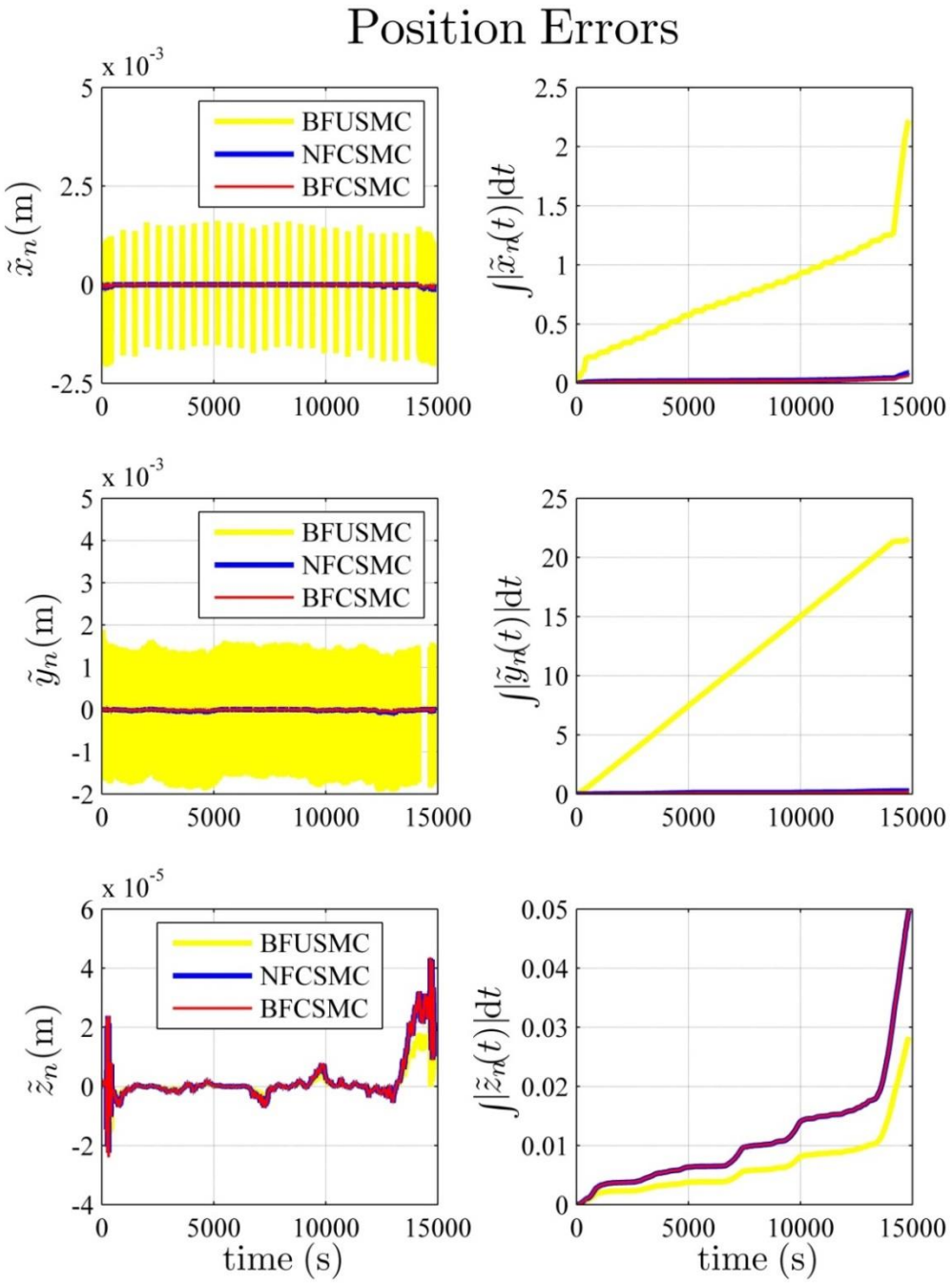

Figure 4.43: Position Errors for Case 3

It is observed from the north position error and the east position error, $\tilde{x}_n$ and $\tilde{y}_n$ respectively, and the corresponding IAE plots that the BFUSMC has a significantly larger dynamic error and IAE compared to both the NFCSMC and the BFCSMC.

It is observed from the down position error, $\tilde{z}_n$, and the corresponding IAE plot that both the NFCSMC and the BFCSMC perform very similarly. It is also observed that the BFUSMC performs similarly with respect to the dynamic error except for the last 2000 s where it performs slightly better. Furthermore, it is observed that the BFUSMC performs slightly better than both the NFCSMC and the BFCSMC with respect to the IAE plot.

(b) Simulation of Attitude Errors

Subject to the inputs outlined in Figure 4.34 through to Figure 4.41, the attitude error for the three compensated systems is given in Figure 4.44.

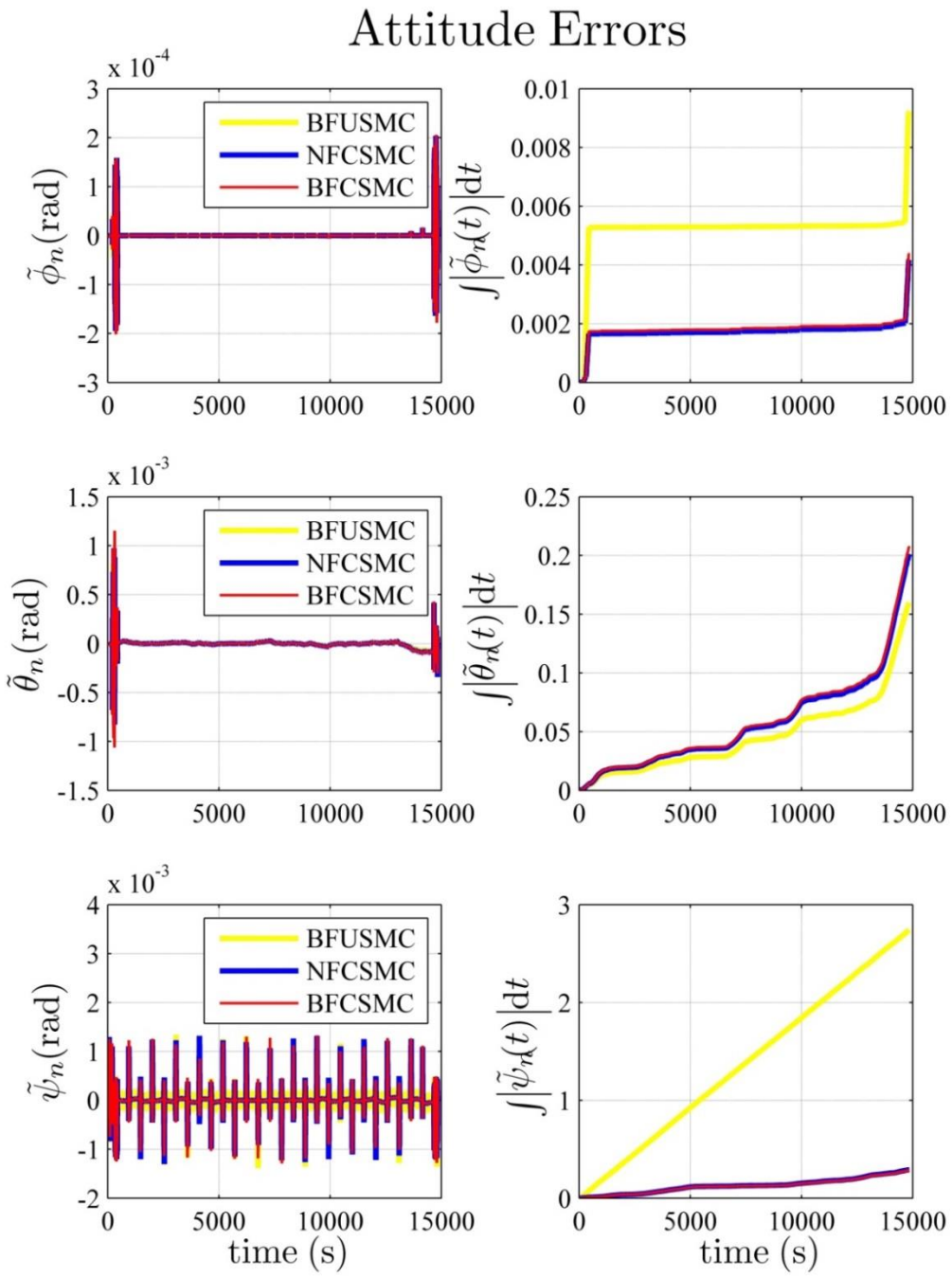

Figure 4.44: Attitude Errors for Case 3

It is observed from the roll attitude error and the yaw attitude error, $\tilde{\phi}_n$ and $\tilde{\psi}_n$ respectively, that all three systems perform quite similarly. However, the corresponding IAE plot shows that the NFCSMC and the BFCSMC perform quite similarly, whereas the BFUSMC possesses limited performance in comparison.

It is observed from the pitch attitude error, $\tilde{\theta}_n$, and the corresponding IAE plot that all three systems perform quite similarly, with the BFUSMC performing slightly better with respect to the IAE plot.

(c) Simulation of Translational Velocity Errors

Subject to the inputs outlined in Figure 4.34 through to Figure 4.41, the translational velocity error for the three compensated systems is given in Figure 4.45.

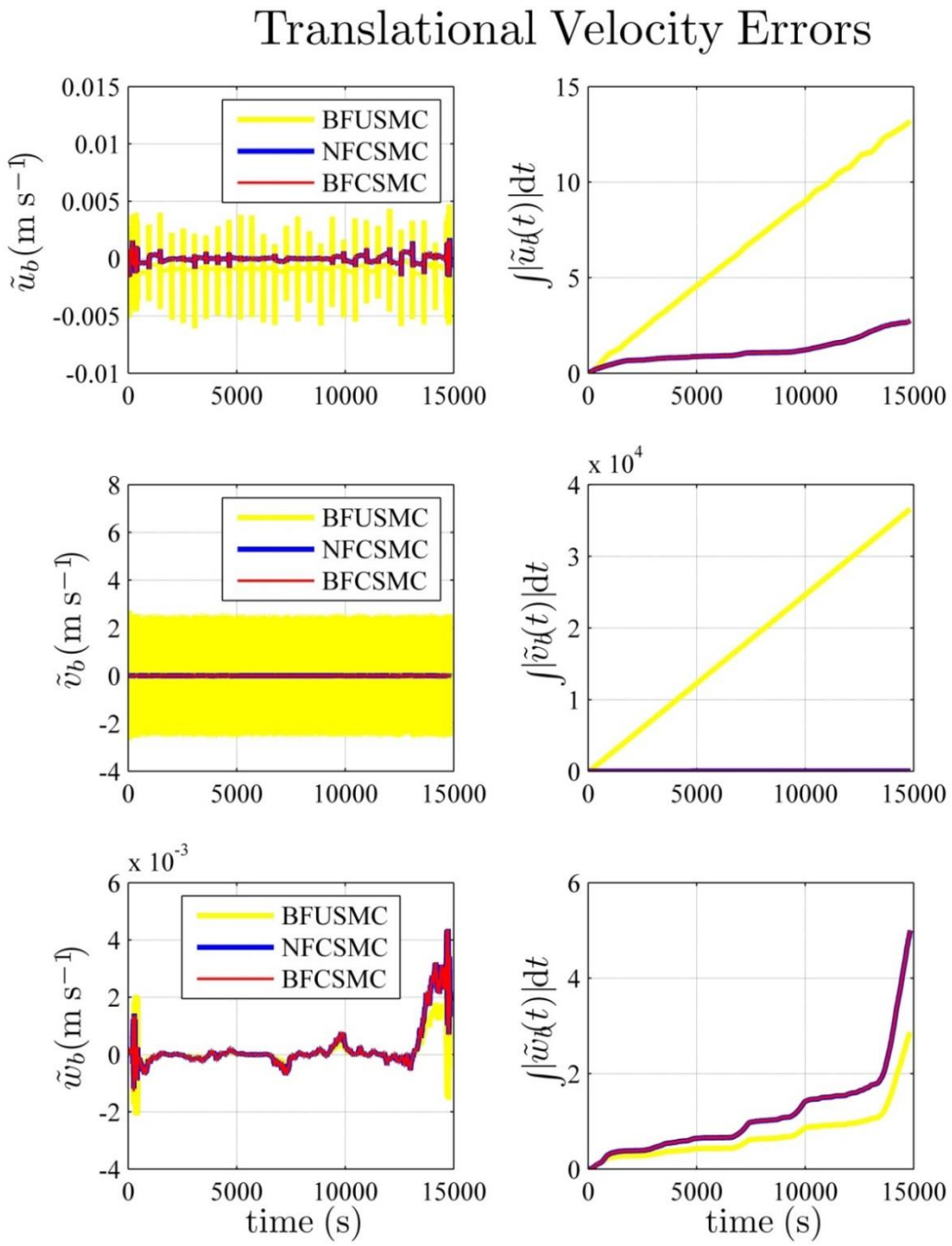

Figure 4.45: Translational Velocity Errors for Case 3

It is observed from the surge translational velocity error and the sway translational velocity error, $\tilde{u}_b$ and $\tilde{v}_b$ respectively, and the corresponding IAE plots that the BFUSMC has a much larger dynamic error and IAE compared to both the NFCSMC and the BFCSMC.

It is observed from the heave translational velocity error, $\tilde{w}_b$, that all three systems perform quite similarly with respect to dynamic error, with the BFUSMC performing slightly worse in the initial 1000 s and slightly better in the final 2000 s. With respect to the corresponding IAE plot, both the NFCSMC and the BFCSMC perform quite similarly while the BFUSMC performs slightly better than both the NFCSMC and the BFCSMC.

(d) Simulation of Angular Velocity Errors

Subject to the inputs outlined in Figure 4.34 through to Figure 4.41, the angular velocity error for the three compensated systems is given in Figure 4.46.

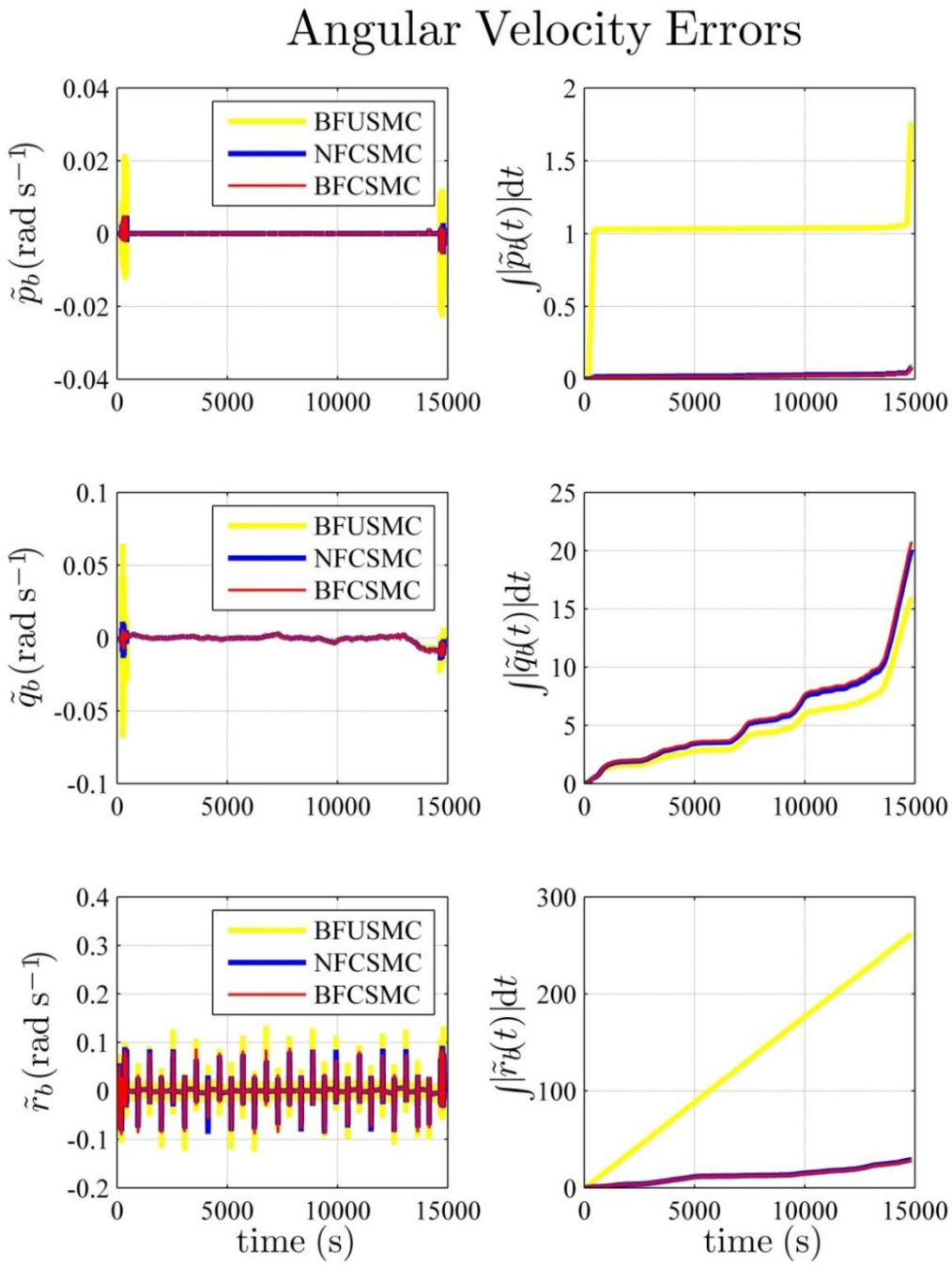

Figure 4.46: Angular Velocity Errors for Case 3

It is observed from the roll angular velocity error and the yaw angular velocity error, $\tilde{p}_b$ and $\tilde{r}_b$ respectively, and the corresponding IAE plots that the BFUSMC has a larger dynamic error and a significantly larger IAE compared to both the NFCSMC and the BFCSMC.

It is observed from the pitch angular velocity error, $\tilde{q}_b$, that the BFUSMC has a much larger dynamic error compared to both the NFCSMC and the BFCSMC, particularly during the initial and final 1000 s. The corresponding IAE plot shows that all three systems perform very similarly, with the BFUSMC performing slightly better in this respect.

(e) Concluding Remarks

Figure 4.43 through to Figure 4.46 compares the behaviour of the BFUSMC, the NFCSMC, and the BFCSMC when the input trajectory is that of Case 3. Based on the behaviours observed, the following remarks can be drawn.

Remark 1.1 – The BFUSMC demonstrates a limited performance compared to both the NFCSMC and the BFCSMC.

> The most apparent observation, especially from Figure 4.43 and Figure 4.45, is that again the BFUSMC performs in a limited capacity compared to the NFCSMC and the BFCSMC. This is easily seen with respect to the north position error, $\tilde{x}_n$, and the east position error, $\tilde{y}_n$, of Figure 4.43 and the surge translational velocity error, $\tilde{u}_b$, and the sway translational velocity error, $\tilde{v}_b$, of Figure 4.45. This clearly demonstrates the importance of including coupling within the control law.

The magnitude of the error seen for the BFUSMC is considerably larger than the error seen for both the NFCSMC and the BFCSMC within some of the figures presented in this case study. Hence, it is difficult to observe the behaviour of the NFCSMC or the BFCSMC in these instances. Therefore, to gain a better insight into the performance of the two coupled control schemes, the same simulation is conducted, except that the behaviour of the BFUSMC is omitted.

2. Coupled Compensators

The following four figures contain the error plots for the NFCSMC and the BFCSMC for the input trajectory of Case 3 as outlined in Figure 4.34 through to Figure 4.41. Figure 4.47 shows the position error and position IAE for the NFCSMC and BFCSMC only. Figure 4.48 shows the attitude error and attitude IAE for the NFCSMC and BFCSMC only. Figure 4.49 shows the translational velocity error and translational velocity IAE for the NFCSMC and BFCSMC only. Figure 4.50 shows the angular velocity error and angular velocity IAE for the NFCSMC and BFCSMC only.

(a) Simulation of Position Errors

Subject to the inputs outlined in Figure 4.34 through to Figure 4.41, the position error for the two compensated systems is given in Figure 4.47.

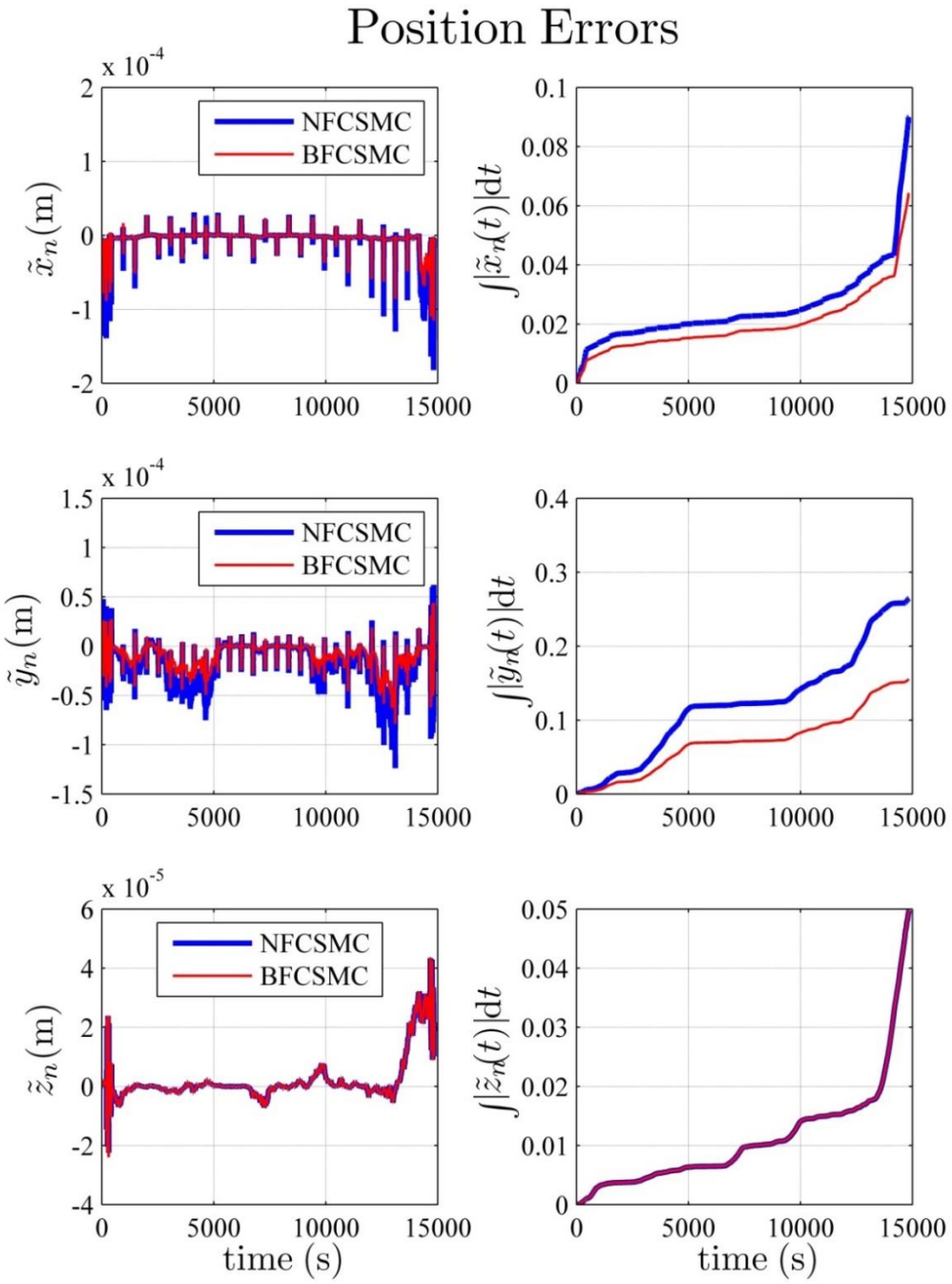

Figure 4.47: Position Errors for Case 3 without BFUSMC

It is observed from the north position error and the east position error, $\tilde{x}_n$ and $\tilde{y}_n$ respectively, and the corresponding IAE plots that the NFCSMC has a larger dynamic error and IAE compared to the BFCSMC.

It is observed from the down position error, $\tilde{z}_n$, and the corresponding IAE plot that both the NFCSMC and the BFCSMC perform very similarly.

(b) Simulation of Attitude Errors

Subject to the inputs outlined in Figure 4.34 through to Figure 4.41, the attitude error for the two compensated systems is given in Figure 4.48.

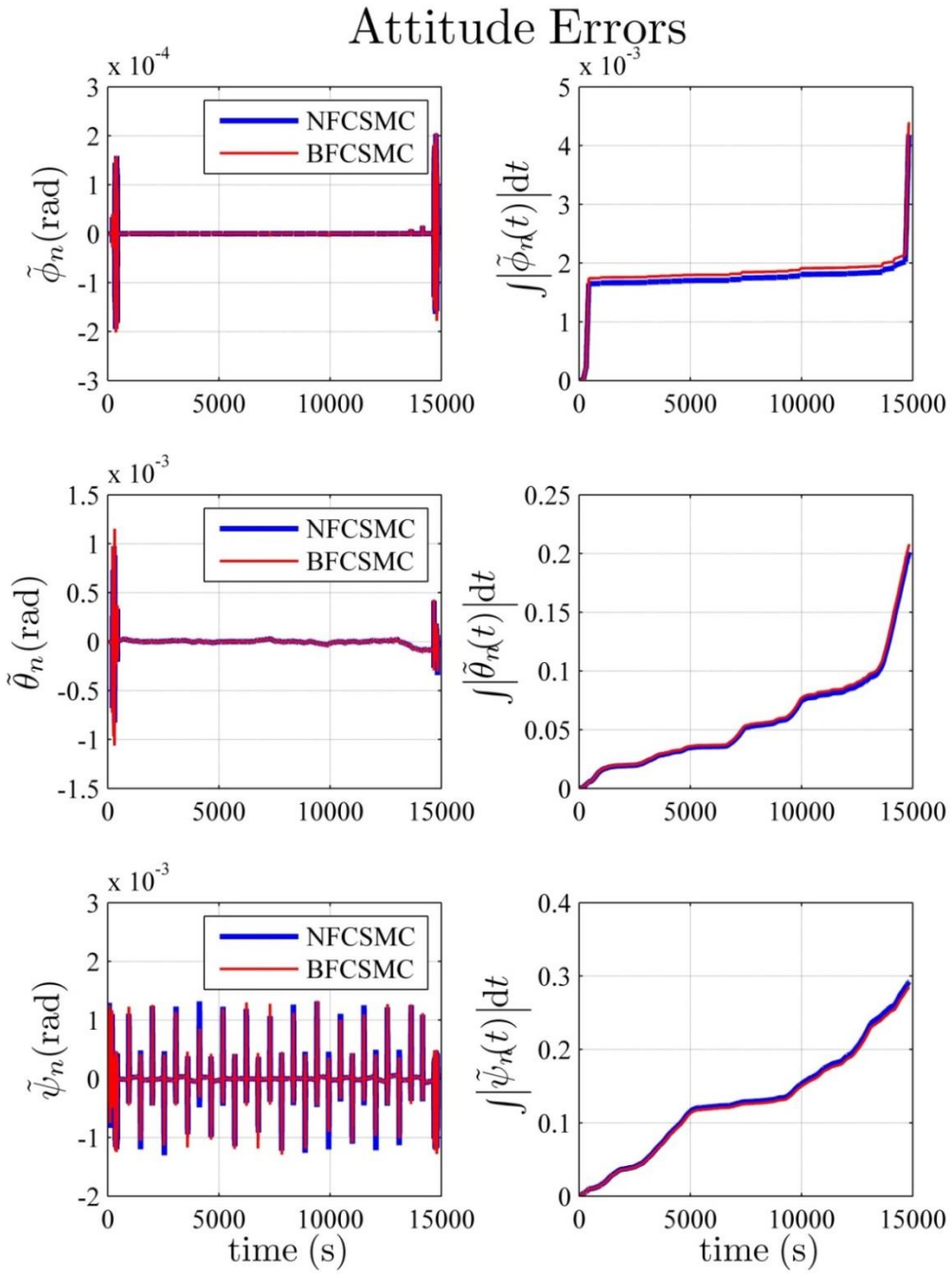

Figure 4.48: Attitude Errors for Case 3 without BFUSMC

It is observed from the roll attitude error, the pitch attitude error, and the yaw attitude error, $\tilde{\phi}_n$, $\tilde{\theta}_n$ and $\tilde{\psi}_n$ respectively, and the corresponding IAE plots that both the NFCSMC and the BFCSMC perform very similarly.

(c) Simulation of Translational Velocity Errors

Subject to the inputs outlined in Figure 4.34 through to Figure 4.41, the translational velocity error for the two compensated systems is given in Figure 4.49.

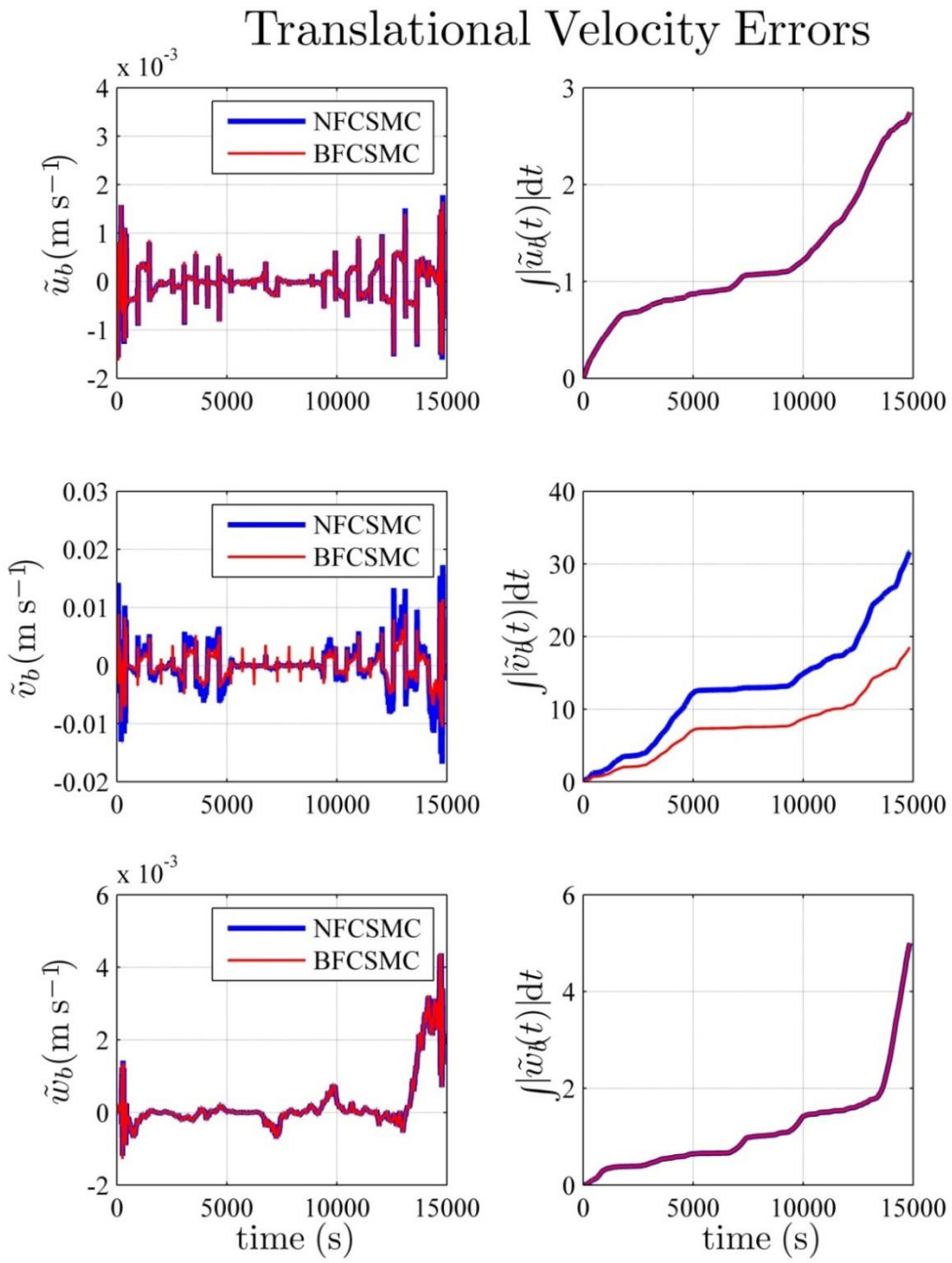

Figure 4.49: Translational Velocity Errors for Case 3 without BFUSMC

It is observed from the surge translational velocity error and the heave translational velocity error, $\tilde{u}_b$ and $\tilde{w}_b$ respectively, and the corresponding IAE plots that both the NFCSMC and the BFCSMC perform very similarly.

It is observed from the sway translational velocity error, $\tilde{v}_b$, and the corresponding IAE plot that the NFCSMC has a much larger dynamic error and IAE compared to the BFCSMC.

(d) Simulation of Angular Velocity Errors

Subject to the inputs outlined in Figure 4.34 through to Figure 4.41, the angular velocity error for the two compensated systems is given in Figure 4.50.

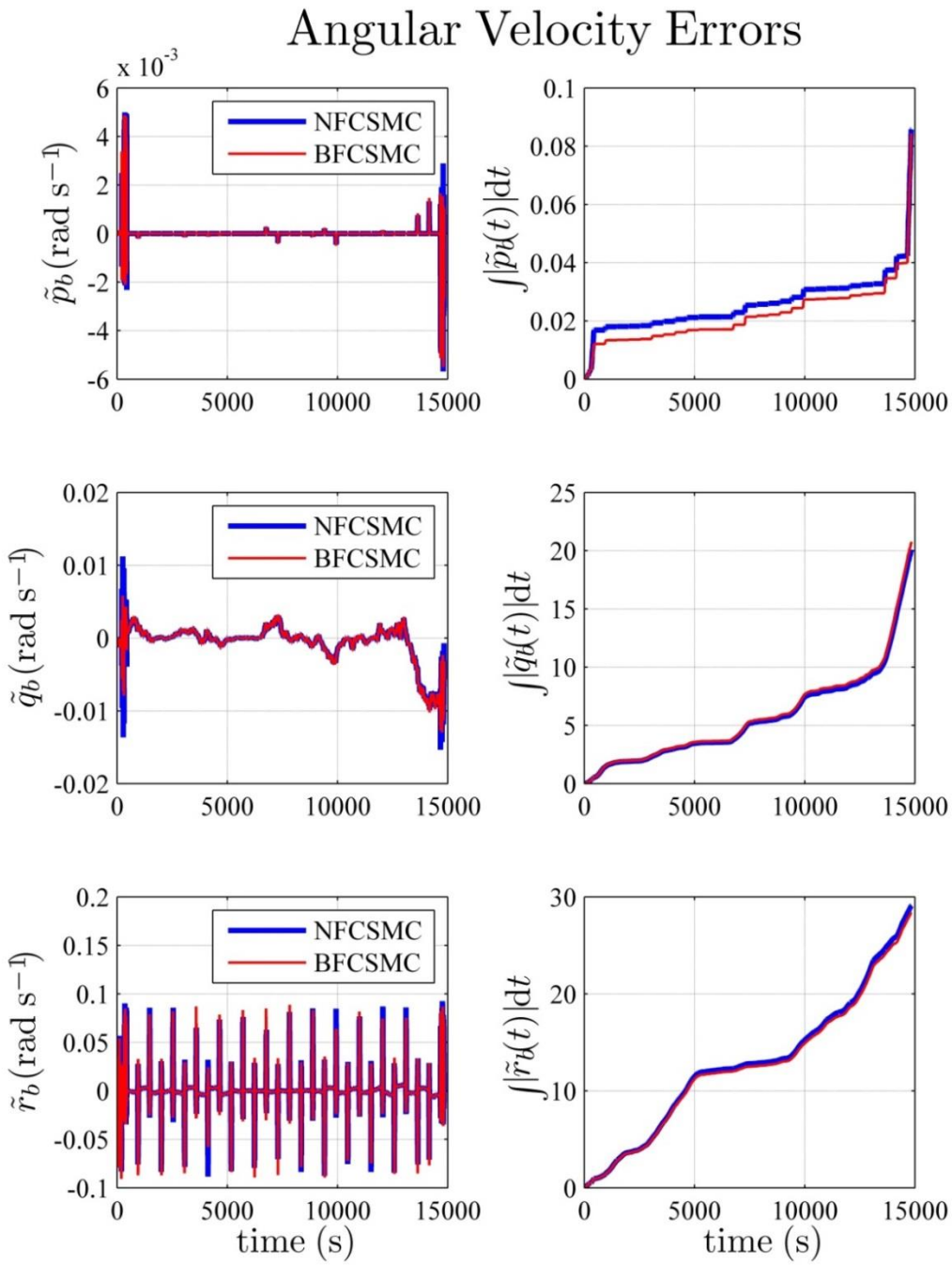

Figure 4.50: Angular Velocity Errors for Case 3 without BFUSMC

It is observed from the roll angular velocity error and the yaw angular velocity error, $\tilde{p}_b$ and $\tilde{r}_b$ respectively, and the corresponding IAE plots that both the NFCSMC and the BFCSMC perform very similarly.

It is observed from the pitch angular velocity error, $\tilde{q}_b$, that the NFCSMC has a larger dynamic error compared to the BFCSMC. However, the corresponding IAE plot shows that both the NFCSMC and the BFCSMC perform very similarly.

(e) Concluding Remarks

Figure 4.47 through to Figure 4.50 compares the behaviour of the NFCSMC and the BFCSMC when the input trajectory is that of Case 3. Based on the behaviours observed, the following remarks can be drawn.

Remark 2.1 – Generally, the BFCSMC performs equal to, or better than, the NFCSMC.

By comparing the NFCSMC to the BFCSMC, Figure 4.47 through to Figure 4.50 show that the BFCSMC performs equal to, or better than, the NFCSMC across all error plots. By looking at the position error plots of Figure 4.47, it can be seen that for the north position error, $\tilde{x}_n$, and the east position error, $\tilde{y}_n$, the BFCSMC performs better than the NFCSMC in terms of both dynamic error and IAE. From observation of the down error plot, $\tilde{z}_n$, it is seen that both systems perform equally well.

The attitude errors of Figure 4.48 show that both systems behave in much the same way for all attitude errors.

With reference to the translational velocity errors of Figure 4.49, it is particularly evident from the sway translational velocity error, $\tilde{v}_b$, that the BFCSMC performs better than the NFCSMC. This is seen with respect to both the dynamic error and the IAE, particularly when the water current is having a significant influence on the vehicle.

The angular velocity errors of Figure 4.50 show that there is little difference between the performances of the BFCMSC compared to the NFCSMC. The

general observation is that there is a slight decrease in dynamic error for the BFCSMC, but this is only marginal. All the IAE plots are quite similar, which indicates that the overall performance for the two systems to be quite similar.

Remark 2.2 – The BFCSMC performs significantly better compared to the NFCSMC when observing the east position error, $\tilde{y}_b$, of Figure 4.47 and the sway translational velocity error, $\tilde{v}_b$, of Figure 4.49.

Figure 4.51 shows only the east position error and the corresponding easterly component of the water current. By directly comparing these signals, it is

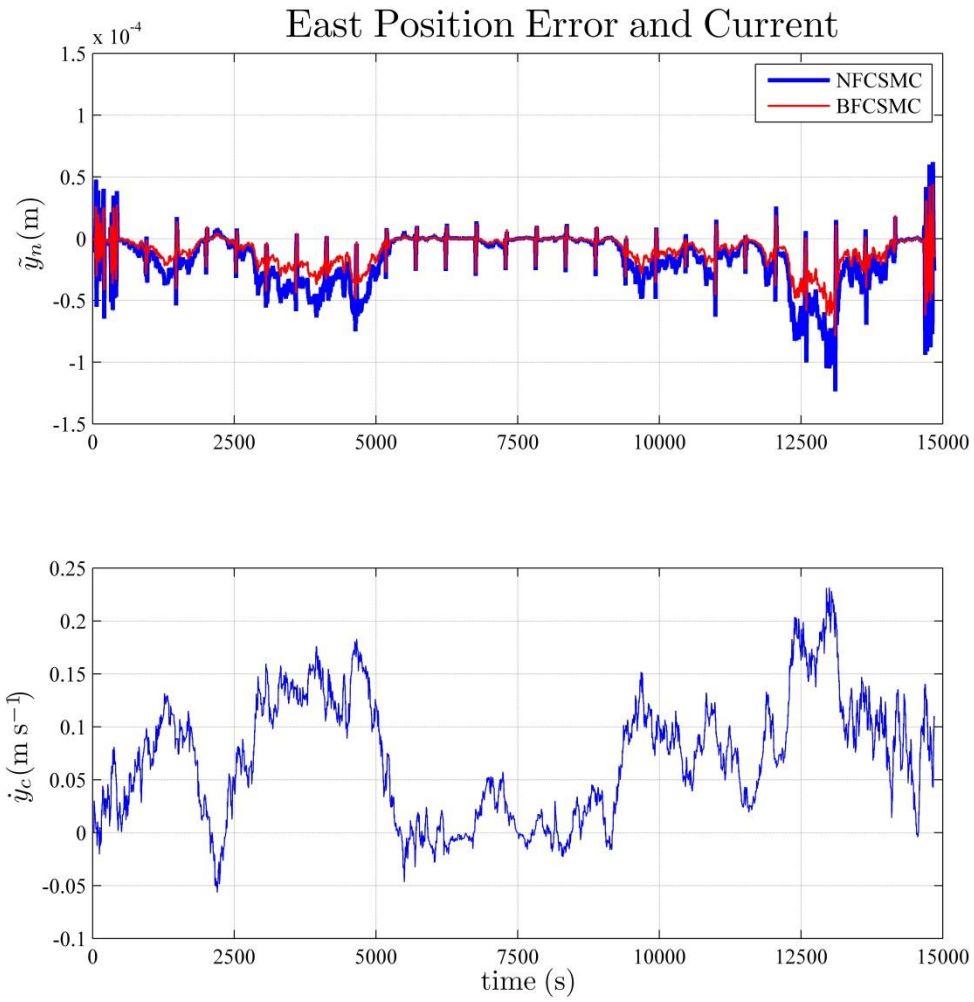

Figure 4.51: East Position Error and Current

obvious that the easterly component of the water current has a direct influence on the east position error of the vehicle irrespective of the compensator used. It can also be seen that the magnitude of the error is directly proportional to the strength of the water current. Furthermore, it is also quite evident that the BFCSMC is better at providing compensation under these conditions, particularly when the water current magnitude is above 0.1 m s^{-1}.

Figure 4.52 shows the sway translational velocity error for the NFCSMC and the BFCSMC, as well as the sway component of the water current for both

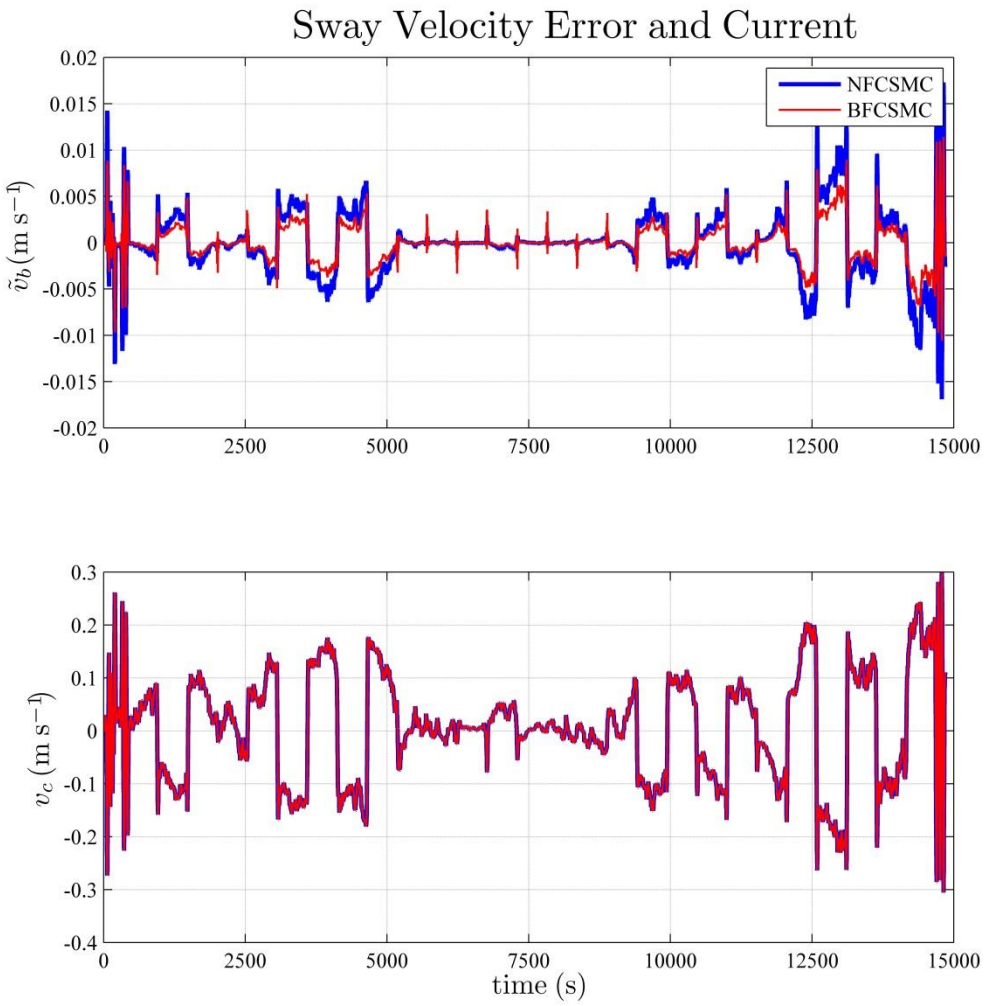

Figure 4.52: Sway Translational Velocity Error and Current

systems. As the attitude errors are very similar for both systems, the water current, decomposed in the body frame, is also very similar for both systems. What is evident from this figure is that the BFCSMC is much better at compensating for the water current disturbance than the NFCSMC. This is seen by observing the fact that the NFCSMC experiences a larger error compared to the BFCSMC when the sway component of the water current is also large. In a similar fashion to what was observed for the east position error, the larger errors are particularly evident when the magnitude of the current is above 0.1 m s^{-1}.

By looking at Figure 4.47 through to Figure 4.50, it is evident that the larger errors occur in the east position and the sway velocity, and in conjunction with Figure 4.51 and Figure 4.52, it is clear that the corresponding water current is responsible for these errors. This is most easily seen when the vehicle is performing the raster scan portion of the mission, between approximately 450 s and 14500 s. During this raster scan, the vehicle is primarily moving in a north-south direction, and therefore the direction of the sway velocity is usually in either an easterly or a westerly direction. Hence, the same water current component is influencing both the east position error and the sway translational velocity error. Moreover, by looking at the vehicle model, particularly the drag component that influences the sway hydrodynamic force due to a sway velocity, $Y_{|v|v}$ as seen in Table A.2, this coefficient has by far the largest magnitude and therefore will have the greatest influence on the hydrodynamic forces applied to the vehicle. This is why the effect of the water current is most evident in these two plots; the unmodelled water current disturbance is producing a larger hydrodynamic force in the sway direction due to the large drag coefficient for this DoF.

Case 3 Conclusions

The use of this final case study was to evaluate the performance of all three compensators, namely the BFUSMC, the NFCSMC, and the BFCSMC, under realistic conditions. This included a trajectory that simulated the raster scan of a

250,000 m^2 area of ocean while a time-varying water current disturbance was present.

By the inclusion of a time-varying water current disturbance into the simulation, both the NFCSMC and the BFCSMC systems performed similarly under these conditions while still being able to complete the desired mission. As indicated in Remark 1.1, the BFUSMC performed in a limited capacity compared to the NFCSMC and the BFUSMC. This was anticipated as the combination of a time-varying water current and a desired trajectory where multiple DoFs are excited concurrently was expected to expose the lack of coupling within the control law of the BFUSMC. This again clearly demonstrated the need to include the inherent coupling of the vehicle model in the control law.

Concerning the coupled controllers, namely the NFCSMC and the BFCSMC, as noted in Remark 2.1, both these control systems performed quite similarly.

What was particularly evident, as noted in Remark 2.2, the error plots presented show that the water current had a large influence on the east position error and the sway translational velocity error. Observation of the vehicle model reveals that much larger hydrodynamic drag coefficients are present for the sway DoF compared to other DoFs. Hence, any unmodelled disturbance in the direction of the sway DoF will induce a large hydrodynamic force in this same direction relative to unmodelled disturbances in the direction of any other DoF. Hence, the larger errors seen in the east position and sway translational velocity are due to hydrodynamic drag forces applied to the vehicle by the water current.

Overall, the aim of this case study was to observe the performance of the compensators under realistic conditions. This included a trajectory that could be used for a survey mission while also applying an unmodelled disturbance in the form of a time-varying water current to the vehicle. Upon observation of the resulting error plots, it can be concluded that the BFCSMC performs better than the NFCSMC, which in turn performs better than the BFUSMC. Therefore, owing to its computational efficiency, the BFUSMC is the superior choice for this case study.

4.5. Chapter Summary

In this chapter, a simulation study was conducted with the BFUSMC, the NFCSMC and the BFCSMC all controlling an identical high fidelity AUV model. Section 2.2.3 presented a high fidelity model of the vehicle for use as the plant model, while Section 2.4 presented a comparison of the different models utilised for the control design in Chapter 3.

One of the desirable properties of sliding mode control is its robustness to modelling uncertainty. Hence, Section 4.2 introduced modelling error as it applies to underwater vehicles. Based on results presented by Kim *et al* [82] for the online estimation of hydrodynamic coefficients, an error of 5% was assumed for the hydrodynamic coefficients within this simulation study. This same modelling error was included in the control law of each compensator used within this simulation study.

Section 4.3 presented the parameters of the compensators used in the simulation studies presented in this chapter.

Section 4.4 presented the three case studies conducted in this chapter. The first case study, Case 1 presented in Section 4.4.1, consisted of perturbations of individual DoFs. This study revealed that all systems were able to track the desired trajectories, with the BFCSMC performing the best overall, particularly with respect to the IAE plots.

The second case study, Case 2 presented in Section 4.4.2, expanded on the trajectory used in Case 1 by introducing coupled manoeuvring. A LOS guidance system, in conjunction with a series of waypoints, produced the desired trajectory for the vehicle to follow. The guidance system updated the desired trajectory at every time sample based on the current state of the vehicle. This simulation revealed the limited capability of the BFUSMC to track a trajectory containing coupled manoeuvring compared to the other control algorithms. This clearly demonstrates the need to include coupling within the control algorithm, as results that are more desirable were observed for both the NFCSMC and the BFCSMC. With respect to the NFCSMC and the BFCSMC, both systems performed similarly with respect to position and

attitude errors, while differences occurred with respect to translational and angular velocity errors. Considering all behaviours, it was concluded that for this particular case study, the BFCSMC performed slightly better than the NFCSMC and considerably better than the BFUSMC.

The final case study, Case 3, was a more realistic scenario as presented in Section 4.4.3. This case study retained the same waypoint and LOS guidance mechanisms used in Case 2 of Section 4.4.2, but here an unknown, time-varying water current disturbance was also included. This trajectory was designed to mimic a raster scan mission that could be used to survey a 250,000 m^2 area of ocean. This scenario demonstrated that again the BFUSMC possessed a limited capability when asked to execute coupled manoeuvring, which furthermore highlighted the importance of including coupling within the control law. With respect to the remaining two compensators, namely the NFCSMC and the BFCSMC, it was evident that the unmodelled water current disturbance induced errors in both position and velocity. This was due to the water current applying significant forces to the vehicle due to the hydrodynamics of the vehicle model. In terms of controller performance, it was observed that the BFCSMC performed equally well, if not better, than the NFCSMC across all position/attitude and velocity error plots.

Overall, this simulation study covered a range of manoeuvring situations that an underwater vehicle could face. Over the wide range of trajectories in the three case studies considered here, the BFCSMC system performed as well or better than the NFCSMC system, with the BFUSMC performing in a limited capacity in comparison. The demonstrated performance of the BFUSMC is attributed to the fact that the model this control law is based on is uncoupled. As identified in all case studies presented here, this simulation study demonstrates the need to include coupling within the control law in order to obtain an accurate controller. Combining this fact with the reduced cost of implementation, the BFCSMC is superior to both the BFUSMC and the NFCSMC as seen in these simulation studies.

It must be noted, however, that under certain circumstances, the BFUSMC could be a viable option. The simulation study conducted here generally dealt with the vehicle following a trajectory, and hence was continually moving. This continual movement

can potentially excite the parameters within the vehicle model responsible for coupled motion, and for this reason, the BFUSMC did not perform as well as the algorithms that did include coupling. If instead the vehicle were required to hold position, these coupling terms within the vehicle model would not have as significant an impact on the overall behaviour of the vehicle. Hence, for positioning and slow moving applications, the BFUSMC could be suitable. As the BFUSMC is more computationally efficient compared to the BFCSMC, a further extension could be to implement a process where the better performance of the BFCSMC provides compensation during high speed manoeuvring, while the efficiency of the BFUSMC is used for low speed manoeuvring and positioning applications.

Chapter 5

Actuation and Allocation

5.1. Introduction

This chapter presents an overview of the common actuators used on underwater vehicles, and introduces the process of control allocation. This chapter includes the presentation of a novel control allocation scheme.

This chapter is organised as follows:

- Section 5.2 presents an overview of common actuators available to underwater vehicle designers, highlighting both their useful characteristics, and any possible limitations to be considered when implemented within such a constrained system.
- Section 5.3 presents an overview of control allocation, and a novel control allocation scheme is proposed.

Figure 5.1 illustrates the general structure of how actuation and allocation fit into the overall control structure of an underwater vehicle. As discussed throughout Chapter 3, the control law is responsible for generating the desired forces, $\boldsymbol{\tau}_{\mathbf{d}}(t)$, to apply to the vehicle such that the required motion is achieved. The role of control allocation is to take the desired force generated by the control law and distribute these forces amongst all the actuators of the vehicle by generating the appropriate control signals,

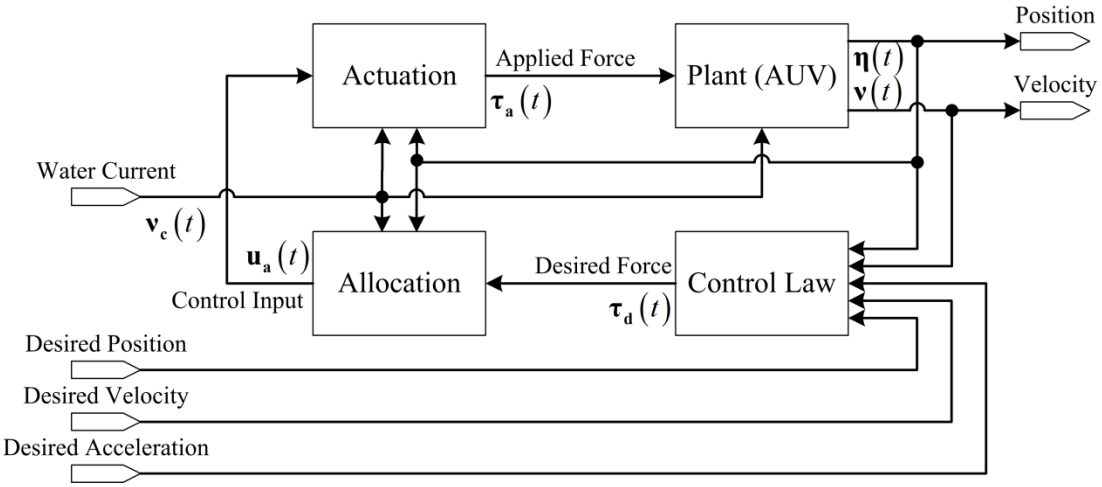

Figure 5.1: Plant and Control Structure (Including Allocation and Actuation)

$\mathbf{u}_a(t)$, to apply to the actuators. The actuators then provide the applied force, $\boldsymbol{\tau}_a(t)$, which is then applied to the vehicle. Ideally, the force applied to the vehicle will be equal to the desired force generated by the control law.

There are numerous types of actuators available to underwater vehicle designers, and the fundamental law that governs how all these actuators works is the same, which is Newton's Third Law of Motion. This law enforces the fact that as the vehicle applies a force to the environment surrounding it, so too must the environment apply an equal but opposite force to the vehicle. The actuators examined here, namely thrusters and control surfaces, are typically used on underwater vehicles for motion control, and all manoeuvre the vehicle based on Newton's Third Law.

Allocation is the process of determining how each actuator will be used such that the desired force generated by the control law will be applied to the vehicle by the actuators. Overactuated vehicles are vehicles whose actuator configuration ensures that there are more actuators than controllable DoFs. This is a common configuration for highly manoeuvrable AUVs as it ensures the vehicle possesses the maximum manoeuvring capabilities. As this thesis is addressing the control of highly manoeuvrable AUVs, it will be assumed that the vehicle is overactuated.

5.2. Actuation

Actuators are the physical devices that give a vehicle the ability to manoeuvre. The total force applied to an underwater vehicle, $\boldsymbol{\tau}_{\mathbf{a}}(t)$, due to all actuators, can be expressed as:

$$\boldsymbol{\tau}_{\mathbf{a}}(t) = \mathbf{T}\mathbf{K}\left(u_r(t)\right)\mathbf{u}_{\mathbf{a}}(t) \tag{5.1}$$

and can be represented by Figure 5.2. Equation (5.1) is a slight modification of a similar equation presented by Fossen [3] where the key difference is the force coefficient matrix of $\mathbf{K}\left(u_r(t)\right)$ being dependent on $u_r(t)$ as seen here. The remainder of this section will discuss each term within Equation (5.1), and how this equation relates to Figure 5.2.

If there are *n* actuators acting on the vehicle, $\mathbf{T}$ is the actuator configuration matrix of size $6\times n$ that determines the distribution of the generalised force amongst all actuators. $\mathbf{K}\left(u_r(t)\right)$ is the force coefficient matrix, which is diagonal and of size $n\times n$, that contains the total force produced by each actuator. $\mathbf{u}_{\mathbf{a}}(t)$ is the control input vector of size $n\times 1$ that contains the control signals that are applied to each individual actuator.

For each actuator, there exists a column of $\mathbf{T}$ and an element on the main diagonal of $\mathbf{K}\left(u_r(t)\right)$ that determines how each actuator applies a force to each DoF. The contents of the column of $\mathbf{T}$ is determined by the placement of the actuator compared to the centre of gravity of the vehicle, while the element of $\mathbf{K}\left(u_r(t)\right)$ is the maximum amount of force the actuator is capable of applying to the vehicle. As

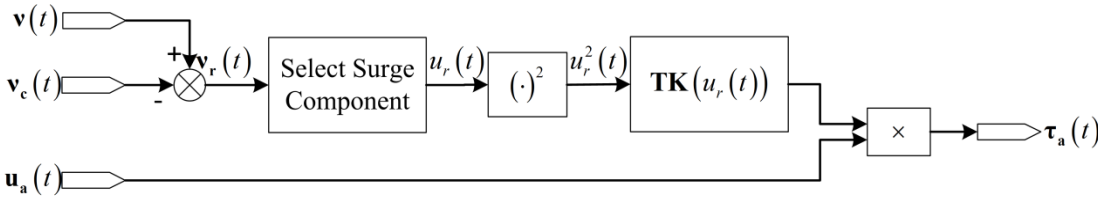

Figure 5.2: Actuation

will be seen in Section 5.2.2, the elements of $\mathbf{K}(u_r(t))$ that are associated with control surfaces are dependent on the velocity of the water flowing over them.

Each column of $\mathbf{T}$, in combination with the corresponding elements of $\mathbf{K}(u_r(t))$ and $\mathbf{u_a}(t)$, determine how much force is applied to each DoF due to each actuator. Furthermore, the parameters contained within $\mathbf{T}$ are highly dependent on the placement of the actuator with respect to the centre of gravity. Hence, each column of $\mathbf{T}$, corresponding to a different actuator, is of the form:

$$\mathbf{T}_i = \begin{bmatrix} t_1 \\ t_2 \\ t_3 \\ t_4 \\ t_5 \\ t_6 \end{bmatrix} \tag{5.2}$$

where the elements t_1, t_2, and t_3 in conjunction with the corresponding element of $\mathbf{K}(u_r(t))$ determine the forces to be applied to the surge DoF, the sway DoF, and the heave DoF of the vehicle respectively, while the elements t_4, t_5, and t_6 in conjunction with $\mathbf{K}(u_r(t))$ determine the moments to be applied to the roll DoF, the pitch DoF, and the yaw DoF of the vehicle respectively. The force elements, t_1, t_2, and t_3, are generally determined by the direction the actuator applies a force on the vehicle relative to the body axes of the vehicle, while the moment elements, t_4, t_5, and t_6, are generally determined by the distance the actuator is from the centre of gravity, i.e., the distance at which the force is being applied.

Throughout the examination of the different actuators in the following sections, l_x denotes the displacement of the actuator along the *x*-axis of the vehicle, l_y denotes the displacement of the actuator along the *y*-axis of the vehicle, and l_z denotes the displacement of the actuator along the *z*-axis of the vehicle.

Within the context of underwater vehicles, the main actuators used are thrusters and control surfaces. Depending on the configuration and position of a thruster on a vehicle, it can produce forward motion, heave and pitching motion, or sway and yawing motion, or a combination of all of these motions.

5.2.1. Main Thruster

The main thruster is the primary mechanism used for control of the surge motion of underwater vehicles. For torpedo shaped vehicles, this thruster is typically located at the stern of the vehicle, and applies a force along the longitudinal axis of the vehicle. Of all the thrusters that an underwater vehicle can employ, this generally has the highest rated power and is utilised the most. Propeller diameters for these thrusters generally approach that of the vehicle hull. Furthermore, a nozzle of some form surrounding the propeller can be used to improve manoeuvring efficiency.

The structure of the column of the actuator configuration matrix associated with the main thruster is expressed as [3]:

$$\mathbf{T}_i = \begin{bmatrix} 1 \\ 0 \\ 0 \\ 0 \\ l_z \\ -l_y \end{bmatrix} \tag{5.3}$$

It is seen from Equation (5.3) that not only can this thruster apply a surge force; it can also apply both a pitching and yawing moment, depending on its placement with respect to the centre of gravity. It is for this reason that main thrusters are generally placed such that both l_y and l_z are zero, and therefore no pitch or yaw moment applied.

By Newton's Third Law of Motion, the main thruster applies a torque reaction to the vehicle in the opposite direction to which it is rotating. Figure 5.3 demonstrates this effect, where the propeller of an aircraft is applying a torque reaction to the body of the aircraft. This torque reaction will then apply a rolling moment to the body of the aircraft. Underwater vehicles experience this same effect.

Considering this effect, the column of the actuator configuration matrix is now given by:

$$\mathbf{T}_i = \begin{bmatrix} 1 \\ 0 \\ 0 \\ K_{MT} \\ l_z \\ -l_y \end{bmatrix} \tag{5.4}$$

where K_{MT} is the torque reaction coefficient for the main thruster.

5.2.2. Control Surfaces

Along with the main thruster, control surfaces, also known as control fins, are the most common actuator used on underwater vehicles. They can be located either fore or aft of the centre of gravity, and provide forces and moments by deflecting the fluid that is flowing around it. In general, the tail section of the vehicle contains four control surfaces, two mounted horizontally and two mounted vertically, to provide manoeuvring capability to the vehicle.

Figure 5.3: Torque Reaction [84]

The columns of the actuator configuration matrix for horizontally and vertically mounted control surfaces are given by:

$$\mathbf{T}_i = \begin{bmatrix} 0 \\ 0 \\ 1 \\ l_y \\ -l_x \\ 0 \end{bmatrix} \tag{5.5}$$

for horizontally mounted control surfaces [3], and:

$$\mathbf{T}_i = \begin{bmatrix} 0 \\ 1 \\ 0 \\ -l_z \\ 0 \\ l_x \end{bmatrix} \tag{5.6}$$

for vertically mounted control surfaces [3].

Here, it can be seen that horizontal surfaces provide a heave force in combination with roll and pitch moments, and vertical surfaces provide a sway force in combination with a roll and yaw moment. Even though these actuators consume very little power to move and hold position, they require fluid to be moving around them in order to apply any force or moment to the vehicle. Hence, the elements of $\mathbf{K}\left(u_r\left(t\right)\right)$ that are associated with control surfaces typically depend on the square of the surge velocity of the vehicle relative to the water current, $u_r^2\left(t\right)$.

5.2.3. Tunnel Thrusters

Tunnel thrusters are typically smaller and have a lower power output compared to the main thruster of an underwater vehicle. The primary use of these devices is to increase the low-speed manoeuvrability of the vehicle. These thrusters are generally mounted inside tunnels that are transverse to the longitudinal axis of the vehicle.

These tunnels usually run either horizontally or vertically through the body of the vehicle, with the thruster itself centrally located within the tunnel.

The columns of the actuator configuration matrix for horizontally and vertically oriented tunnel thrusters are given by:

$$\mathbf{T}_i = \begin{bmatrix} 0 \\ 1 \\ 0 \\ -l_z \\ 0 \\ l_x \end{bmatrix} \tag{5.7}$$

for horizontally oriented tunnel thrusters [3], and:

$$\mathbf{T}_i = \begin{bmatrix} 0 \\ 0 \\ 1 \\ l_y \\ -l_x \\ 0 \end{bmatrix} \tag{5.8}$$

for vertically oriented tunnel thrusters [3].

As can be seen from Equation (5.7), a horizontal tunnel thruster provides a sway force in combination with a roll and yaw moment, while from Equation (5.8), a vertical thruster provides a heave force in combination with a roll and pitch moment. Typically, these thrusters are oriented such that there is no roll moment.

In a similar fashion to the main thruster applying a torque reaction to the vehicle, so to do tunnel thrusters apply torque reactions to the vehicle. The columns of the actuator configuration matrix for horizontally and vertically oriented tunnel thrusters, considering torque reactions, are given by:

$$\mathbf{T}_i = \begin{bmatrix} 0 \\ 1 \\ 0 \\ -l_z \\ M_{HT} \\ l_x \end{bmatrix} \tag{5.9}$$

for horizontally oriented tunnel thrusters considering torque reaction, and:

$$\mathbf{T}_i = \begin{bmatrix} 0 \\ 0 \\ 1 \\ l_y \\ -l_x \\ N_{VT} \end{bmatrix} \tag{5.10}$$

for vertically oriented tunnel thrusters considering torque reaction. Here, M_{HT} is the torque reaction coefficient due to the horizontal thruster, which will apply a pitching moment to the vehicle, and N_{VT} is the torque reaction coefficient due to the vertical thruster, which will apply a yawing moment to the vehicle.

These actuators are very effective at increasing the manoeuvrability of an underwater vehicle, yet there are limitations associated with these devices. Firstly, these devices require power to function. Particularly on small autonomous vehicles where space and hence energy capacity is limited, over-utilisation of these actuators can dramatically reduce the time and/or range of a particular mission. Secondly, the openings of the tunnels on the hull of the vehicle can increase drag and therefore reduce the efficiency of the vehicle moving through the water, particularly at high speeds. Furthermore, studies have shown that the efficiency of tunnel thrusters themselves are reduced as forward vehicle velocity is increased [85].

5.2.4. Typical Configuration and Usage

All of the aforementioned actuators have advantages and disadvantages, and therefore must be utilised appropriately to maximise these advantages whilst minimising the disadvantages.

A typical actuator configuration for a torpedo shaped AUV is to have a single main thruster and a set of four independent control surfaces, two horizontal and two vertical, arranged at the stern of the vehicle. This configuration allows for the actuation of all six DoFs provided the vehicle is moving with respect to the water. If manoeuvrability is required when there is little or no relative water velocity, tunnel thrusters are required. For maximum manoeuvrability from these thrusters, a pair of horizontal thrusters are implemented equidistant fore and aft of the centre of gravity to provide a sway force and yaw moment, while a pair of vertical thrusters are also implemented equidistant fore and aft of the centre of gravity to provide a heave force and pitch moment. One such implementation of this configuration is the thruster based AUV developed at the Indian Institute of Technology [86].

The arrangement described previously takes advantage of the benefits of these actuators, yet careful selection on how and when these actuators are used will help to minimise their disadvantages. For example, if the vehicle is moving forward through the water, fluid will be flowing over the control surfaces, and therefore these actuators will be very efficient at manoeuvring the vehicle while the tunnel thrusters will not be. Conversely, if the vehicle is stationary, control surfaces are unusable yet the tunnel thrusters are available. Therefore, if the vehicle is moving relative to the water, control surfaces offer efficient manoeuvring capabilities. If the vehicle is either stationary or moving at low speed, tunnel thrusters can provide manoeuvring control. This usage will retain the maximum manoeuvrability of the vehicle while also minimising power consumption.

5.3. Control Allocation

This section will introduce control allocation with respect to overactuated underwater vehicles. The focus of this section will be on the allocation of control with the actuators mentioned in Section 5.2 where the vehicle contains a single main thruster and four independent control surfaces at the rear of the vehicle arranged in a crucifix form, as well as two horizontal tunnel thrusters and two vertical tunnel thrusters.

5.3.1. Direct Inverse Allocation

The simplest method for performing control allocation is to invert Equation (5.1), as seen in:

$$\mathbf{u_a}(t) = \left[\mathbf{TK}\left(u_r(t)\right)\right]^{+} \boldsymbol{\tau}_\mathbf{a}(t) \tag{5.11}$$

where $[\cdot]^{+}$ is the generalised inverse, or pseudoinverse, operator. The simplicity of this scheme makes it relatively easy to implement within an AUV. However, there are some limitations.

Firstly, assuming it exists, directly calculating the generalised inverse of a matrix can be both time consuming and inaccurate, depending on the size and structure of the matrix. In this particular case, nine actuators on the vehicle and control required for all six DoFs means the matrix $\mathbf{TK}\left(u_r(t)\right)$ will be of size 6×9. Hence, the generalised inverse of a 6×9 matrix is required each time control is applied to the vehicle.

Secondly, there is no means to bias allocation towards particular actuator based on the current state of the vehicle. If, for example, the vehicle is moving at maximum forward velocity, both tunnel thrusters and control surfaces will be utilised for manoeuvring, which is inefficient as the tunnel thrusters lose their effectiveness as forward speed increases. Conversely, if the vehicle is attempting to hold position, control surfaces are ineffective and only tunnel thrusters can apply forces and moments to the vehicle.

5.3.2. 2-Stage Scheme

AUVs are extremely restricted in the payloads they can carry. This restriction includes the amount of energy storage that is contained within a vehicle and therefore the efficient use of the energy that is available is of utmost importance. Applying forces to obtain the desired movement of the vehicle is a major source of power consumption. Therefore, efficiently using the actuators to obtain the desired movement is critical in extending the range and usability of such a vehicle. The allocation scheme proposed here aims to increase the efficiency of vehicle movement

by utilising the most power efficient actuators, i.e., control surfaces to their fullest before introducing other less efficient actuators, i.e., tunnel thrusters. A conceptual overview of this scheme is illustrated in Figure 5.4. Hence, this scheme will only call upon the less power efficient actuators when absolutely needed.

The control allocation scheme proposed here can fundamentally be viewed as a cascade of two direct inverse allocation stages as presented in Section 5.3.1. As the main thruster is required for forward motion, and the control surfaces are the most efficient actuators for manoeuvring, the first stage tries to realise $\boldsymbol{\tau}_{\mathbf{d}}(t)$ using only these actuators. Using Equation (5.11), an attempt to realise $\boldsymbol{\tau}_{\mathbf{d}}(t)$ using only the main thruster and the control surfaces, is seen in:

$$\mathbf{u}_{\mathbf{1}}(t) = \left[\hat{\mathbf{T}}_{\mathbf{1}}\hat{\mathbf{K}}_{\mathbf{1}}\left(u_r(t)\right)\right]^{+}\boldsymbol{\tau}_{\mathbf{d}}(t) = \begin{bmatrix} u_{\mathrm{MT}}(t) \\ \mathbf{u}_{\mathbf{CS}}(t) \end{bmatrix} \tag{5.12}$$

where the matrix $\hat{\mathbf{T}}_{\mathbf{1}}\hat{\mathbf{K}}_{\mathbf{1}}\left(u_r(t)\right)$ contains estimates of the parameters associated with the main thruster and control surfaces only. $u_{\mathrm{MT}}(t)$ and $\mathbf{u}_{\mathbf{CS}}(t)$ are the vectors of control signals for the main thruster and control surfaces respectively.

Using Equation (5.1), an estimate of how much force will be applied to the vehicle due to the main thruster and control surfaces only, denoted by $\hat{\boldsymbol{\tau}}_{\mathbf{1}}(t)$, is expressed as:

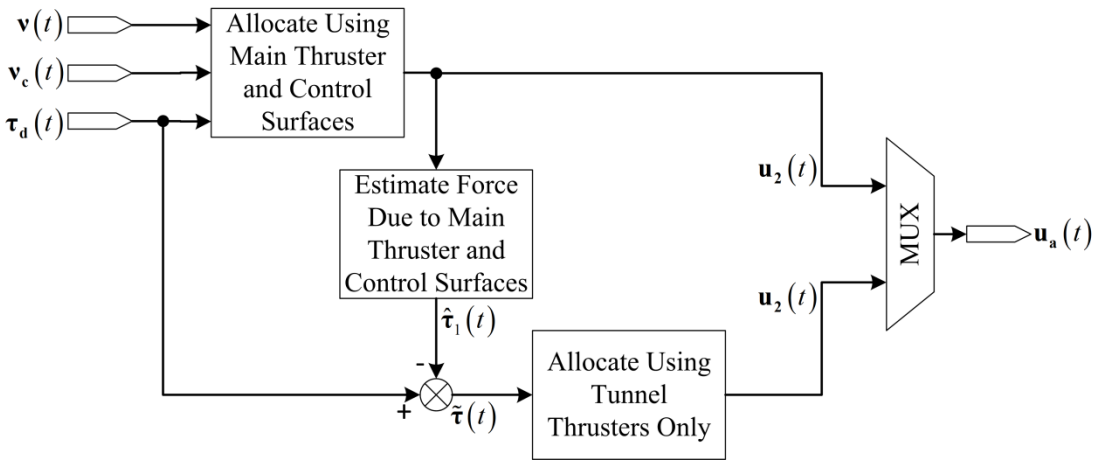

Figure 5.4: Conceptual Overview of 2-Stage Control Allocation Scheme

$$\hat{\boldsymbol{\tau}}_{\mathbf{1}}(t) = \hat{\mathbf{T}}_{\mathbf{1}}\hat{\mathbf{K}}_{\mathbf{1}}\left(u_r(t)\right)\mathbf{u}_{\mathbf{1}}(t) \tag{5.13}$$

The second stage then calculates the forces and moments, if any, that have not been realised by the main thruster and control surfaces, and attempts to allocate any remaining force to the tunnel thrusters. A second separate direct inverse allocation scheme achieves this goal.

The difference between the force provided by the main thruster and control surfaces, and the total desired force, $\tilde{\boldsymbol{\tau}}(t)$, is calculated using:

$$\tilde{\boldsymbol{\tau}}(t) = \boldsymbol{\tau}_{\mathbf{d}}(t) - \hat{\boldsymbol{\tau}}_{\mathbf{1}}(t) \tag{5.14}$$

An attempt to realise any remaining force using the tunnel thrusters is achieved by again using Equation (5.11), this time in the form of:

$$\mathbf{u}_{\mathbf{2}}(t) = \left[\hat{\mathbf{T}}_{\mathbf{2}}\hat{\mathbf{K}}_{\mathbf{2}}\right]^{+}\tilde{\boldsymbol{\tau}}(t) = \mathbf{u}_{\mathbf{TT}}(t) \tag{5.15}$$

where the matrix $\hat{\mathbf{T}}_{\mathbf{2}}\hat{\mathbf{K}}_{\mathbf{2}}$ contains estimates of the parameters associated with the tunnel thrusters only. $\mathbf{u}_{\mathbf{TT}}(t)$ is the vector of control signals for the tunnel thrusters.

The overall vector of control signals for all actuators is expressed as:

$$\mathbf{u}_{\mathbf{a}}(t) = \begin{bmatrix}\mathbf{u}_{\mathbf{1}}(t)\\ \mathbf{u}_{\mathbf{2}}(t)\end{bmatrix} = \begin{bmatrix}u_{\mathrm{MT}}(t)\\ \mathbf{u}_{\mathbf{CS}}(t)\\ \mathbf{u}_{\mathbf{TT}}(t)\end{bmatrix} \tag{5.16}$$

where $u_{\mathrm{MT}}(t)$ and $\mathbf{u}_{\mathbf{CS}}(t)$ are obtained from Equation (5.12) and $\mathbf{u}_{\mathbf{TT}}(t)$ is obtained from Equation (5.15).

Figure 5.5 illustrates the overall 2-stage control allocation scheme.

There are several advantages to using this method compared to the direct inverse allocation method.

1. This method is simpler and more efficient to implement, as the one large generalised inverse is not required. Instead, two smaller generalised inverses replace the large generalised inverse, which is computationally more efficient. As it is common to compute the generalised inverse of a matrix

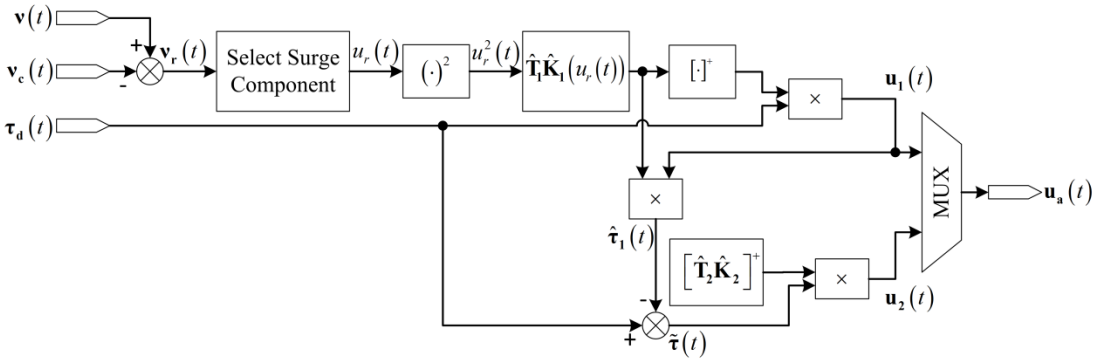

Figure 5.5: 2-Stage Control Allocation Scheme

using the singular value decomposition (SVD), and the number of operations required to compute the SVD is $O\left(mn^2\right)$ [87], where m and n are the dimensions of the matrix and $m \geq n$, smaller matrices will require less operations when computing the generalised inverse.

2. The control surfaces are utilised fully before the tunnel thrusters are considered. In the case that the control surfaces can completely realise the desired generalised force, the tunnel thrusters will not be utilised at all. This can lead to significant power savings, particularly if the majority of the vehicle's mission is trajectory tracking as opposed to station keeping.

3. In the event that the vehicle is simply cruising from one location to another without any regard for following a set path, the allocation scheme can easily disable the tunnel thrusters to conserve power.

There is, however, one limitation introduced to the overall simulation environment by the inclusion of actuation and allocation. Additional nonlinearities are introduced through each actuator only being able to provide a limited force and/or moment. Hence, nonlinearities in the form of saturations are introduced to the system. As the control algorithms of Chapter 3 all assume these nonlinearities do not exist, a process is required to ensure these nonlinearities do not affect the overall system.

Acceleration, be it translational or rotational, is the reaction of the vehicle due to the application of a force or moment. Therefore, the desired acceleration generated by the guidance system is directly related to the force or moment to be applied to the

vehicle. By limiting this desired acceleration, the nonlinear effects of actuators reaching saturation can be avoided. The following section presents a process for limiting this desired acceleration. This acceleration limiting process is used in partnership with the 2-stage scheme presented here to form the overall novel control allocation scheme.

Acceleration Limiting

By the introduction of actuation and allocation, a limit is placed on the magnitudes of forces and moments being applied to the vehicle. This is due to each actuator only being able to apply a limited force to the vehicle, i.e., each actuator has a limited saturation level. This behaviour can lead to large errors experienced by the vehicle if these saturation nonlinearities are not taken into consideration.

By Newton's 2nd Law of Motion,

$$\text{Force} = \text{mass} \times \text{acceleration},$$

the desired force generated by the control law is related to the desired acceleration asked by the guidance system. By limiting the desired acceleration from the guidance system, the force generated by the control law will also be limited. Appropriate limitations placed on the desired acceleration will therefore avoid the saturation levels of the actuators, and therefore the controllers as designed in Chapter 3 can still be applied to a system where actuation and allocation are included.

In the context of real-time optimal guidance, Yakimenko and Kragelund [88] discuss methods whereby the dynamics of the vehicle are used to ensure that a proposed trajectory is achievable based on vehicle manoeuvrability limitations. A similar method will be used here to ensure that limitations are placed on the desired accelerations asked by the guidance system. This will be based on both the actuators being used and the dynamics of the vehicle. An outline of how this is achieved is illustrated in Figure 5.6.

The desired acceleration asked by the guidance system is transformed to desired forces and moments based on the inverse of the plant dynamics of the vehicle. The

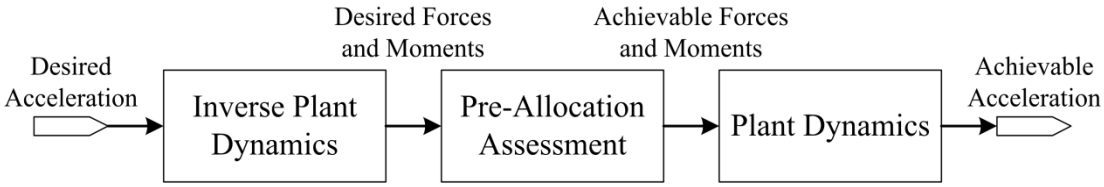

Figure 5.6: Acceleration Limiting

inverse plant dynamics, based on Simplified Model 2 of Equation (2.71), can be expressed as:

$$\dot{\mathbf{v}}_{\mathbf{b}}(t) = \mathbf{M}^{-1}\left[\boldsymbol{\tau}(t) - \mathbf{C}\left(\mathbf{v}_{\mathbf{b}}(t)\right)\mathbf{v}_{\mathbf{b}}(t) - \mathbf{D}\left(\mathbf{v}_{\mathbf{b}}(t)\right)\mathbf{v}_{\mathbf{b}}(t)\right] \tag{5.17}$$

These desired forces and moments are then passed through a pre-allocation assessment to ascertain an estimate of how much of the desired forces and moments can be realised by the actuators. This is achieved by firstly obtaining the desired control inputs using a control allocation scheme, and secondly using models of the actuators to estimate the achievable forces and moments that will be applied to the vehicle. These achievable forces and moments are then transformed to achievable accelerations by using the plant dynamics. The resulting accelerations are therefore limited based on the dynamics of both the vehicle and the actuators. This ensures that the nonlinearities introduced due to actuator saturation are avoided, and therefore the control algorithms developed in Chapter 3 are still applicable.

A demonstration of the impact acceleration limiting can have on a system is illustrated in Figure 5.7. This example was created using a standard 2nd order linear system purely for illustration purposes. In this case, the acceleration limiting scheme has a sampling frequency of 1 Hz and the desired acceleration command is a step input of size 1 m s^{-1}. Without acceleration limiting, the desired output converges within approximately 1 s. However, if acceleration limiting is introduced, in this case the maximum acceleration step size is 0.2 m s^{-1}, the system takes five steps to reach the desired 1 m s^{-1} and therefore the output now converges within approximately 6 s. Therefore, it can easily be seen that the introduction of acceleration limiting will limit the acceleration step size in order to avoid reaching the saturation limits of the actuators, yet it will also expand the time period over which the change in acceleration occurs.

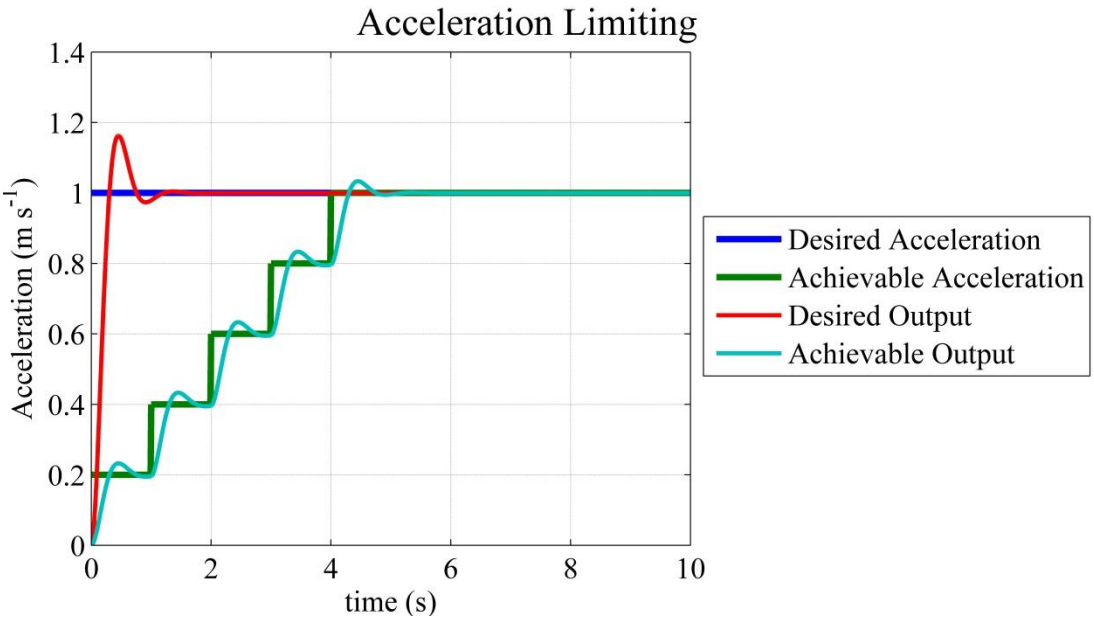

Figure 5.7: Effect of Acceleration Limiting

5.4. Chapter Summary

This aim of this chapter was to present a discussion of commonly used actuators and allocation techniques used in underwater vehicles. Section 5.2 focussed on actuation, and presented a mathematical overview of thrusters, both for primary propulsion and for controlled manoeuvring, as well as control surfaces. This overview discussed both the advantages and disadvantages associated with each actuator, such as power consumption, efficiency, and limitations of use based on the state of the vehicle.

Section 5.3 then introduced allocation and the role it plays in the overall closed-loop control of an underwater vehicle. Here, a novel control allocation scheme was presented in Section 5.3.2 that aims to take advantage of all the positive aspects of certain actuators implemented on a vehicle, while at the same time minimising their drawbacks. Based on the analysis of the actuators conducted in Section 5.2, this novel 2-stage control allocation scheme attempts to realise the generalised forces and moments demanded by the control system using only the main thruster and the highly efficient control surfaces. In the event that the forces and moments produced by these actuators are lacking, only then does the allocation scheme call upon the less efficient tunnel thrusters to generate the remainder of the desired forces and

moments. Hence, this scheme prioritises the most efficient actuators over the less efficient actuators when realising the overall generalised force asked of by the control system. Furthermore, as the introduction of actuators can potentially introduce nonlinearities in the form of force saturation, a process that limits the desired acceleration, and therefore desired force, was also introduced as part of the novel control allocation scheme. Under these conditions, the compensators as designed in Chapter 3 will be applicable as the introduced nonlinearities due to actuator saturation should be avoided. Overall, the aim of this novel control allocation scheme is to improve the power efficiency of the vehicle without affecting the manoeuvring efficiency of the vehicle.

Chapter 6

Actuation and Allocation Simulation Study

6.1. Introduction

The simulation study of Chapter 4 assumed the demanded generalised force from the control system is directly applied to the vehicle. Actuation and allocation were introduced in Chapter 5. This chapter also demonstrated how actuation and allocation could be applied to underwater vehicles. The aim of the simulation study presented in this chapter is to extend the simulation study of Chapter 4 by implementing actuation and allocation, in the form of the 2-stage scheme presented in Section 5.3.2, into the simulation environment. Based on the specific features of the BFUSMC as seen in Chapter 4, particularly with respect to coupled manoeuvring, it is not implemented within this simulation study. Instead, as the NFCSMC and the BFCSMC offer a similar level of performance as seen in Chapter 4, they will be examined here from the angle of including actuation and allocation.

Section 6.2 details the simulation model used here, including the parameters of the actuators used to apply forces and moments to the vehicle. To conduct a fair comparison, the same plant model is used here as used in Chapter 4; hence any differences observed in the simulation study will be due to the addition of actuation and allocation to the simulator.

Two of the three case studies presented in Chapter 4 are used here for simulation purposes. These cases, Case 2 of Section 4.4.2 and Case 3 of Section 4.4.3, are simulated and analysed here in Section 6.3. The results obtained here are compared to the equivalent case studies seen in Chapter 4. Case 1 of Section 4.4.1 is not simulated here due to the roll DoF being uncontrollable when both the relative surge velocity of the vehicle, $u_r(t)$, is zero and actuation is implemented. Therefore, a fair and unbiased comparison of the BFCSMC and the NFCSMC will be made by examining the responses of these systems both with actuation and allocation, and without actuation or allocation.

6.2. System Model

The plant model used within this simulation study is the same model as used in the simulation study of Chapter 4. The structure of this plant model is outlined in Section 2.2.3 and the parameters of the matrices within the model are detailed in Appendix A.1.1. This same model is used to ensure a fair comparison is made in terms of performance of the overall system with and without actuation and allocation.

In terms of the actuation that is simulated in this study, the details of these actuators are contained in Table A.5 of Appendix A, with the actuator configuration matrix, $\mathbf{T}$, and the force coefficient matrix, $\mathbf{K}(u_r(t))$, detailed in Section A.1.2.

All simulations are conducted with the use of the 2-stage allocation scheme presented in Section 5.3.2, including the process outlined for limiting the desired acceleration to attainable levels.

6.3. Case Studies

As seen in the simulation study of Chapter 4, two of the three case studies seen previously will be simulated here with the key difference being the inclusion of actuation and allocation in the simulation environment. The two case studies are Case 2 outlined in Section 4.4.2 and Case 3 outlined in Section 4.4.3. The case studies simulated here are summarised in Table 6.1 and outlined as follows.

Table 6.1: Actuation and Allocation Case Studies

Case	Input	Initial Conditions	System	Output
2	Multiple DoF Excitation	$\boldsymbol{\eta}_{\mathbf{n}}(t) = [0 \quad 0 \quad 10 \quad 0 \quad 0 \quad 0]^T$ $\mathbf{v}_{\mathbf{b}}(t) = [1 \quad 0 \quad 0 \quad 0 \quad 0 \quad 0]^T$	AUV Plant with Actuation and Allocation, No Disturbance	$\tilde{\boldsymbol{\eta}}_{\mathbf{n}}(t)$ and $\tilde{\mathbf{v}}_{\mathbf{b}}(t)$
3	Multiple DoF Excitation	$\boldsymbol{\eta}_{\mathbf{n}}(t) = [0 \quad 0 \quad 10 \quad 0 \quad 0 \quad 0]^T$ $\mathbf{v}_{\mathbf{b}}(t) = [1 \quad 0 \quad 0 \quad 0 \quad 0 \quad 0]^T$	AUV Plant with Actuation and Allocation, Current Disturbance	$\tilde{\boldsymbol{\eta}}_{\mathbf{n}}(t)$ and $\tilde{\mathbf{v}}_{\mathbf{b}}(t)$

- The first case study of Section 6.3.1 is identical to Case 2 of Section 4.4.2. Multi-DoF excitation is provided by a line-of-sight (LOS) guidance system that takes a set of waypoints as input and outputs the desired state of the vehicle at each time step. The initial phase of the trajectory contains the zigzag and spiral manoeuvres used by Kim *et al* [82] for the purposes of hydrodynamic coefficient estimation and the latter phase implements a series of straight lines such that steady-state behaviour is observed.
- The second and final case study of Section 6.3.2 is equivalent to Case 3 of Section 4.4.3. The same time-varying water current disturbance is included to demonstrate the ability of the system to handle an unknown dynamic disturbance, and the same set of waypoints is provided as input to a LOS guidance system such that the trajectory of Section 4.4.3 is duplicated.

The results presented here are in the same form as those presented in Section 4.4, i.e., error plots for both $\boldsymbol{\eta}_{\mathbf{n}}(t)$, the position and attitude of the vehicle decomposed in the navigation frame, and $\mathbf{v}_{\mathbf{b}}(t)$, the translational and angular velocity of the vehicle decomposed in the body frame. In a similar fashion to Section 4.4, error plots were chosen for presenting the results due to the desire to observe the tracking

performance of the system with a time-varying input. Hence, the overall output of this simulation study is $\tilde{\boldsymbol{\eta}}_{\mathbf{n}}(t)$ and $\tilde{\mathbf{v}}_{\mathbf{b}}(t)$ as defined by

$$\tilde{\boldsymbol{\eta}}_{\mathbf{n}}(t) = \boldsymbol{\eta}_{\mathbf{d}}(t) - \boldsymbol{\eta}_{\mathbf{n}}(t) = \begin{bmatrix} \tilde{x}_n(t) \\ \tilde{y}_n(t) \\ \tilde{z}_n(t) \\ \tilde{\phi}_n(t) \\ \tilde{\theta}_n(t) \\ \tilde{\psi}_n(t) \end{bmatrix} \tag{6.1}$$

and

$$\tilde{\mathbf{v}}_{\mathbf{b}}(t) = \mathbf{v}_{\mathbf{d}}(t) - \mathbf{v}_{\mathbf{b}}(t) = \begin{bmatrix} \tilde{u}_b(t) \\ \tilde{v}_b(t) \\ \tilde{w}_b(t) \\ \tilde{p}_b(t) \\ \tilde{q}_b(t) \\ \tilde{r}_b(t) \end{bmatrix} \tag{6.2}$$

respectively.

The same method for determining error at each time step is used, as outlined in Section 4.4. This error is determined by taking the difference between the current output of the plant, and the previous output from the guidance system. This is required as the guidance system will always output the desired state of the plant for the following time-step. A block diagram detailing this simulation study is contained in Figure 6.1.

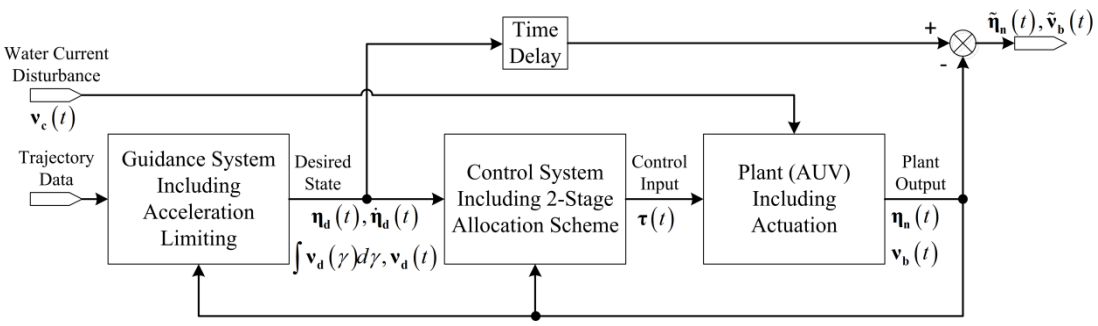

Figure 6.1: Simulation Block Diagram with Actuation and Allocation

For each of the simulation studies, the following structure is adopted.

- Aim: Stating the purpose of using the particular input trajectory for this case study;
- System Conditions: Describing the conditions specific to this case study such as inputs, initial conditions, disturbances, etc.;
- Flow Chart: Illustrating the flow chart describing the behaviour of this case study;
- Observations: Describing the position/attitude and velocity error plots of this case study;
- Simulation Results: Discussing observed behaviours seen in the position/attitude and velocity error plots of this case study;
- Conclusions: Drawing concluding remarks based on the results and discussion of the error plots of this case study.

6.3.1. Case 2

As mentioned previously, the trajectory simulated here is the same as that seen in Case 2 of Section 4.4.2. The difference here being that in this case study, actuation and allocation is included in the simulation where allocation is performed using the proposed 2-stage scheme of Section 5.3.2.

Aim

The aim of this case study is to observe the performance of both the BFCSMC and the NFCSMC when actuation and allocation are both included in the simulation and complex, multi-DoF manoeuvring is requested from the guidance system.

System Conditions

The desired trajectory that the vehicle is to follow is contained in the following plots. A 3D plot is provided in Figure 6.2 and the desired position and attitude plots are given in and Figure 6.4 respectively.

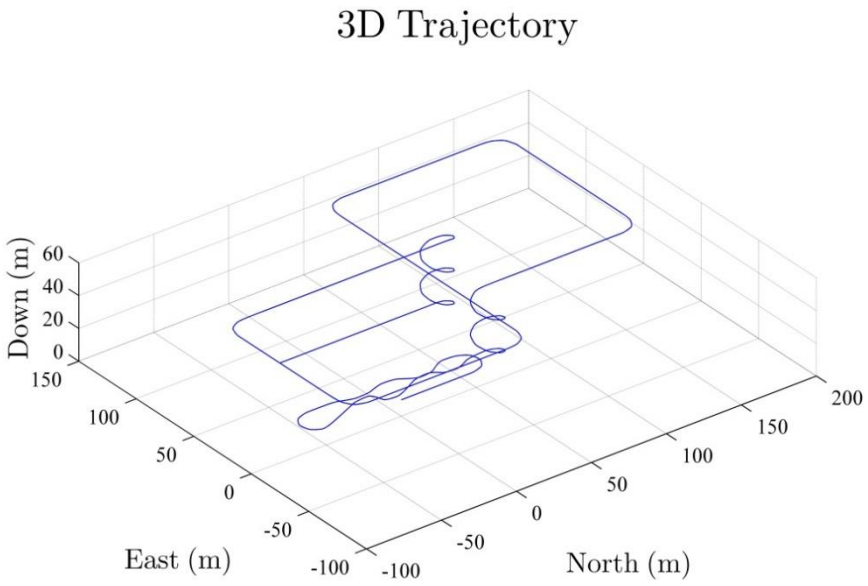

Figure 6.2: 3D Trajectory for Case 2 with Actuation and Allocation

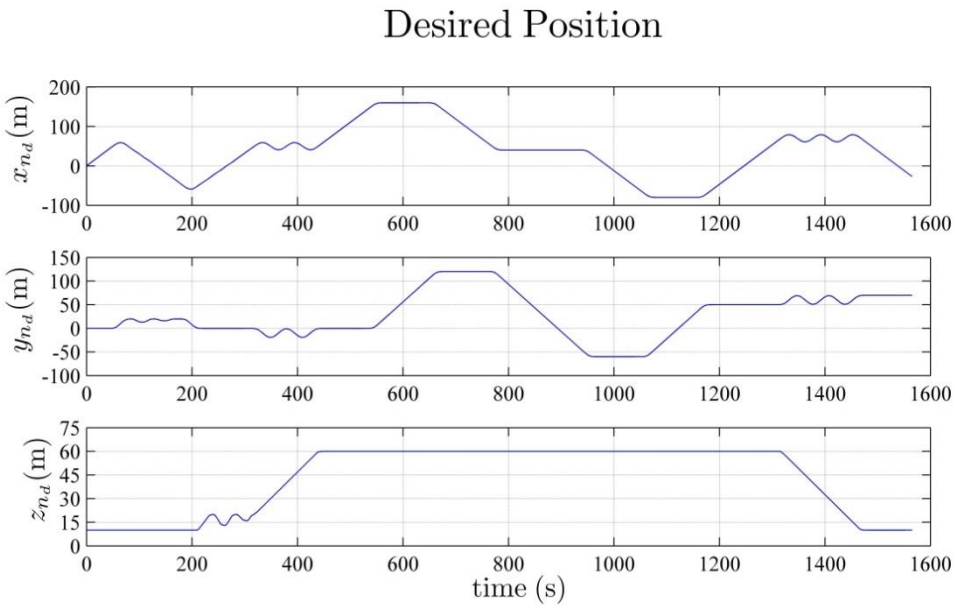

Figure 6.3: Desired Position for Case 2 with Actuation and Allocation (NED Frame)

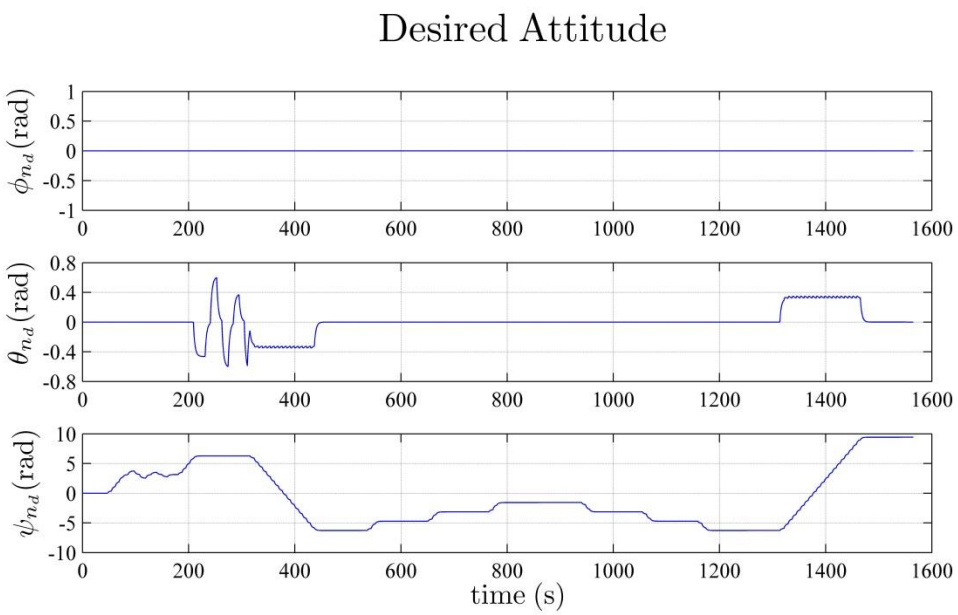

Figure 6.4: Desired Attitude for Case 2 with Actuation and Allocation (NED Frame)

The same conditions are placed on the trajectory generated by the LOS guidance system as seen in Section 4.4.2, such as a constant 1 m s^{-1} translational speed. Figure 6.5 and Figure 6.6 provide the respective translational and angular velocities that correspond to the position and attitude of and Figure 6.4.

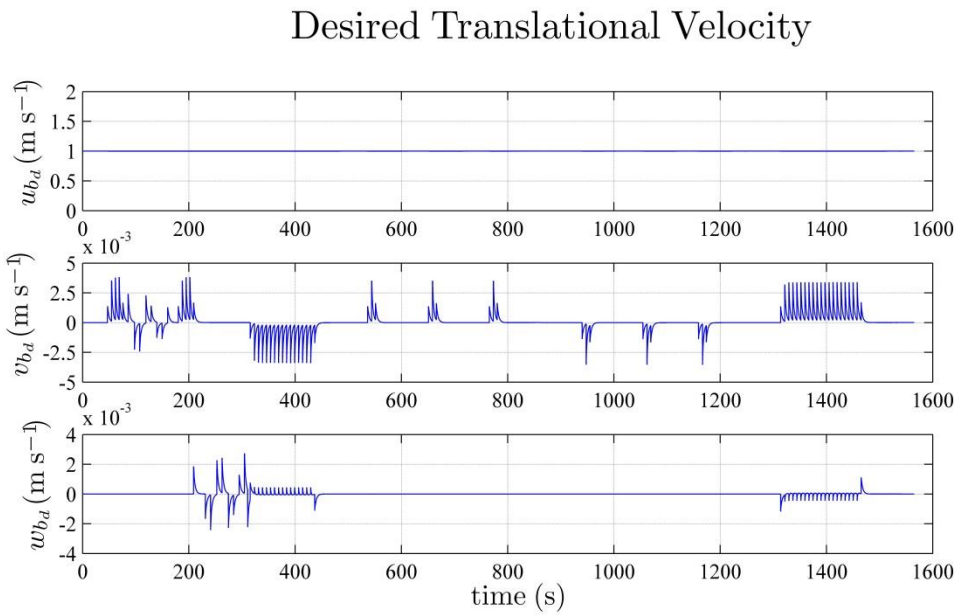

Figure 6.5: Desired Translational Velocity for Case 2 with Actuation and Allocation (Body Frame)

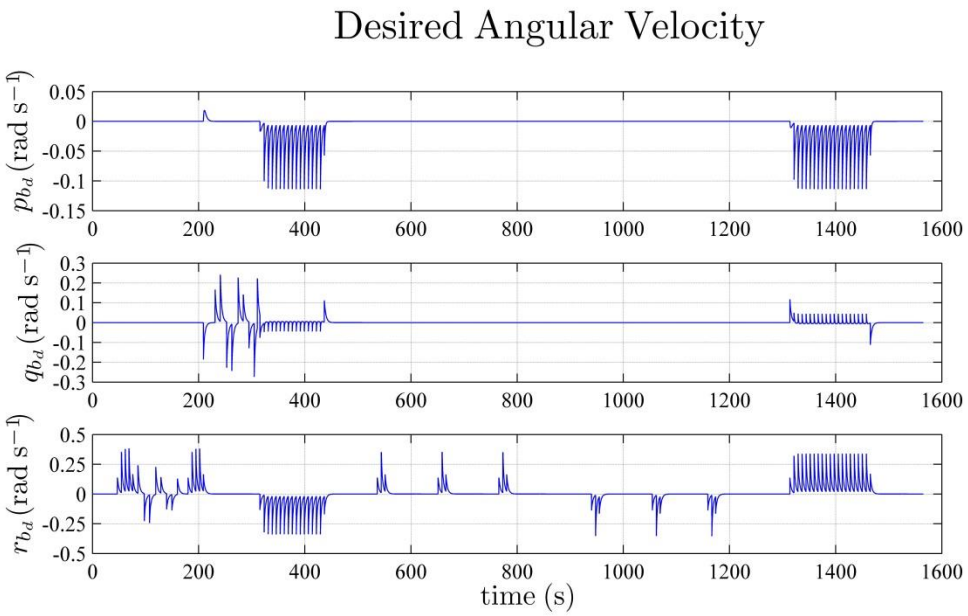

Figure 6.6: Desired Angular Velocity for Case 2 with Actuation and Allocation (Body Frame)

Flow Chart

The following flow chart illustrates the behaviour of Case 2 with actuation and allocation.

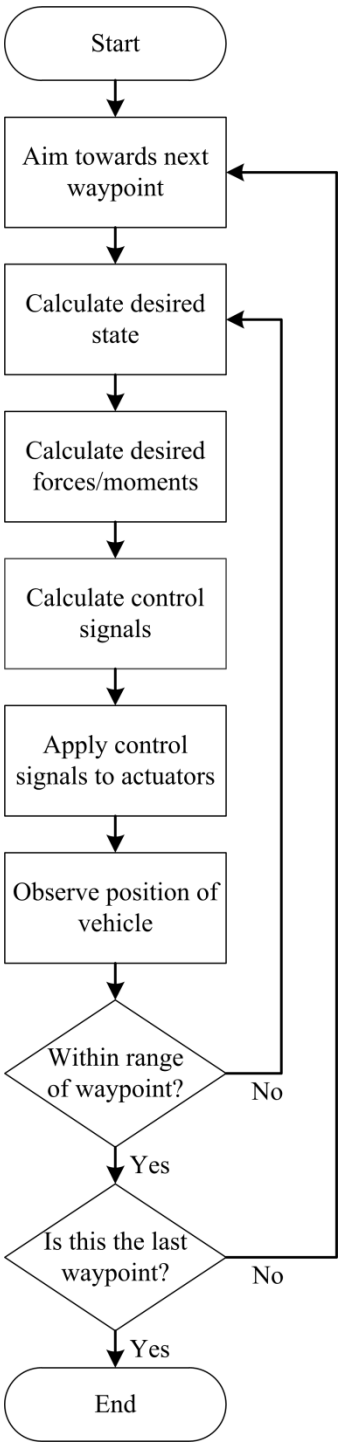

Figure 6.7: Flow Chart for Case 2 with Actuation and Allocation

Simulation Results

The simulation results are divided into two sections. Firstly, the results of the two coupled compensators, namely the NFCSMC and the BFCSMC, with actuation and the 2-stage control allocation scheme will be presented. Secondly, only the results of the BFCSMC system will be presented, comparing the performance observed in this simulation study, where actuation and allocation are included, with the performance observed in the simulation study of Chapter 4, where no actuation or allocation was included.

1. All with Allocation

The following four figures contain the error plots for both the BFCSMC and the NFCSMC for the input trajectory of Case 2, as outlined in through to Figure 6.6, and the 2-stage control allocation scheme is used. Figure 6.8 shows the position error and position IAE for the NFCSMC and the BFCSMC compensated systems, both with actuation and allocation. Figure 6.9 shows the attitude error and attitude IAE for the NFCSMC and the BFCSMC compensated systems, both with actuation and allocation. Figure 6.10 shows the translational velocity error and translational velocity IAE for the NFCSMC and the BFCSMC compensated systems, both with actuation and allocation. Figure 6.11 shows the angular velocity error and angular velocity IAE for the NFCSMC and the BFCSMC compensated systems, both with actuation and allocation.

(a) Simulation of Position Error

Subject to the inputs outlined in through to Figure 6.6, the position error for the NFCSMC and BFCSMC compensated systems with actuation and allocation is given in Figure 6.8.

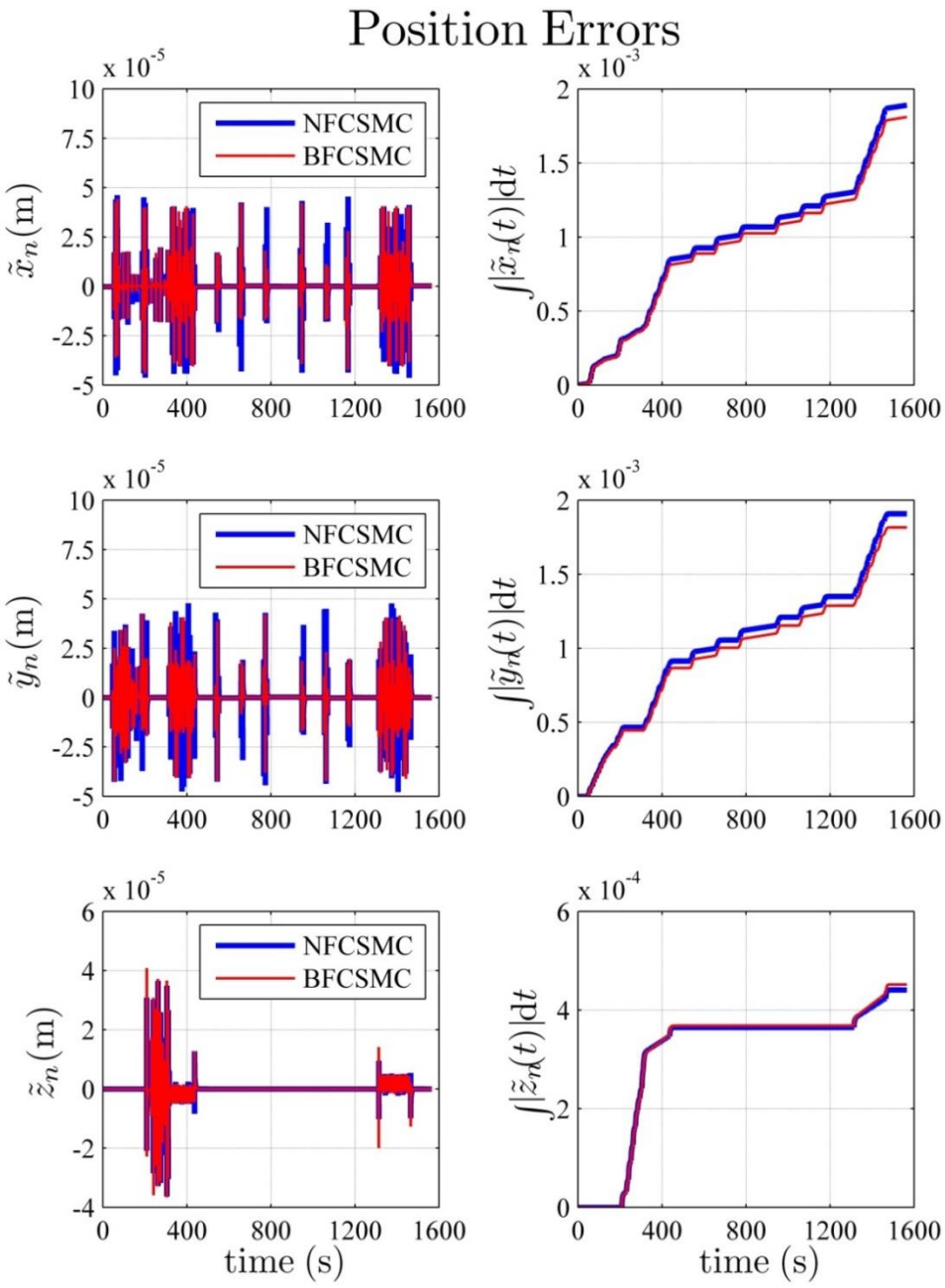

Figure 6.8: Position Errors for Case 2 with Actuation and Allocation

It is observed from the north position error and the east position error, $\tilde{x}_n$ and $\tilde{y}_n$ respectively, that the NFCSMC has a larger dynamic error compared to the BFCSMC. However, the corresponding IAE plots show that both the NFCSMC and the BFCSMC perform very similarly.

It is observed from the down position error, $\tilde{z}_n$, and the corresponding IAE plot that both the NFCSMC and the BFCSMC perform very similarly.

(b) Simulation of Attitude Error

Subject to the inputs outlined in through to Figure 6.6, the attitude error for the NFCSMC and BFCSMC compensated systems with actuation and allocation is given in Figure 6.9.

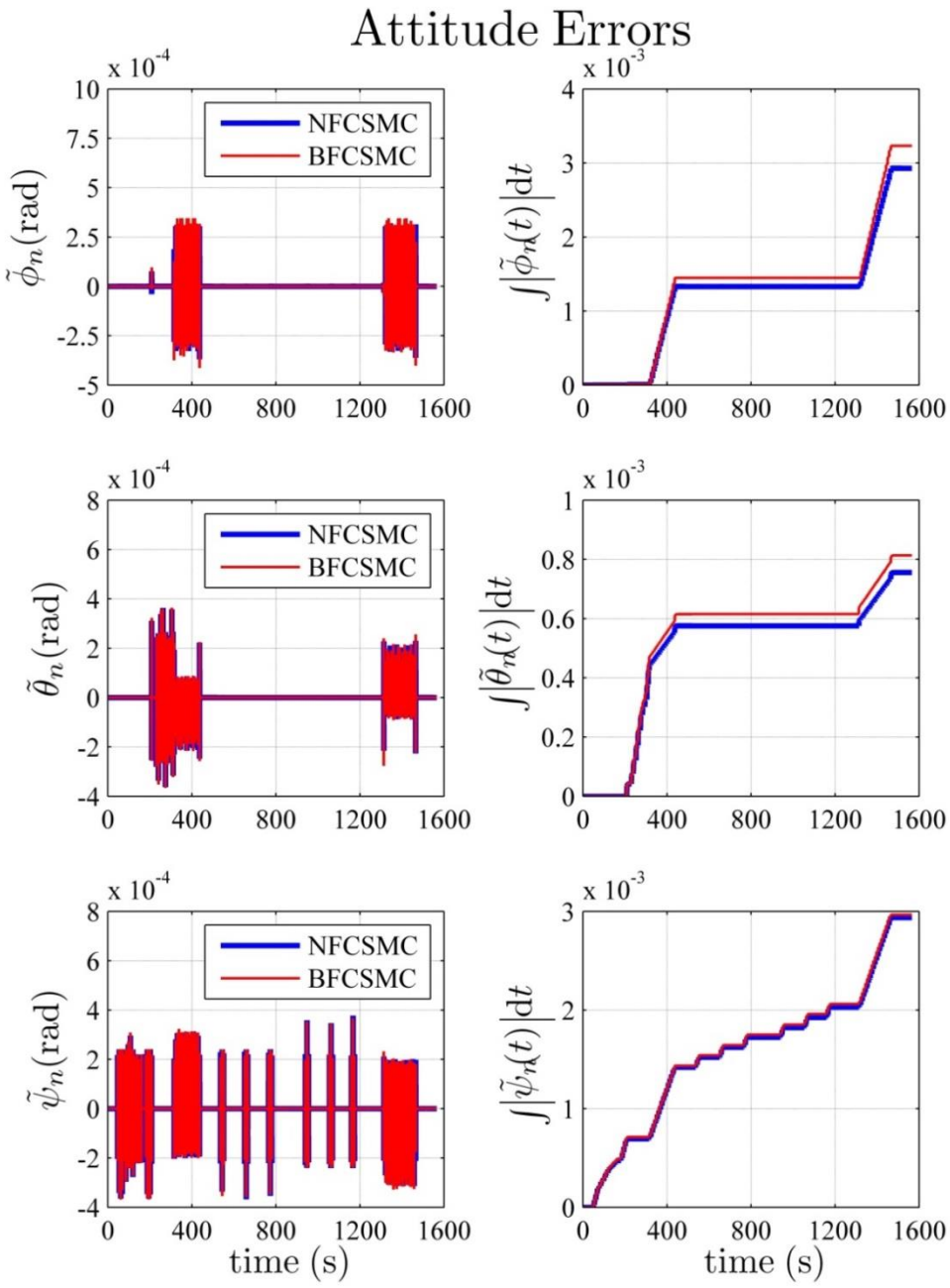

Figure 6.9: Attitude Errors for Case 2 with Actuation and Allocation

It is observed from the roll attitude error, the pitch attitude error, and the yaw attitude error, $\tilde{\phi}_n$, $\tilde{\theta}_n$, and $\tilde{\psi}_n$ respectively, and the corresponding IAE plots that both the NFCSMC and the BFCSMC perform very similarly.

(c) Simulation of Translational Velocity Error

Subject to the inputs outlined in through to Figure 6.6, the translational velocity error for the NFCSMC and BFCSMC compensated systems with actuation and allocation is given in Figure 6.10.

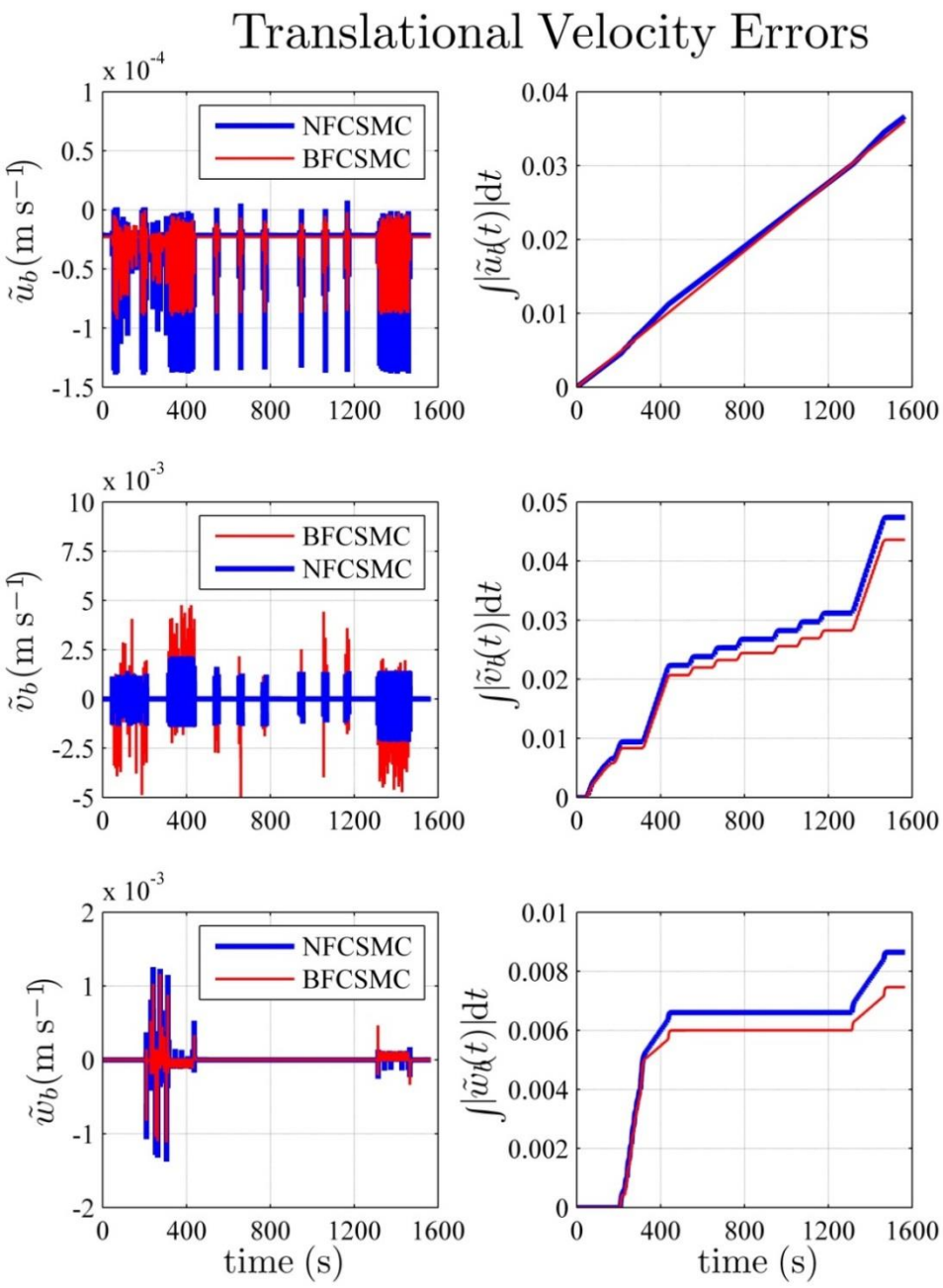

Figure 6.10: Translational Velocity Errors for Case 2 with Actuation and Allocation

It is observed from the surge translational velocity error, $\tilde{u}_b$, that the NFCSMC has a much larger dynamic error compared to the BFUSMC. Furthermore, it is observed that both systems have a non-zero steady-state error. The corresponding IAE plot shows that both systems perform very similarly in this respect.

It is observed from the sway translational velocity error, $\tilde{v}_b$, that the NFCSMC has a smaller dynamic error compared to the BFCSMC. However, observation of the corresponding IAE plot shows that both the NFCSMC and the BFCSMC perform very similarly in this respect.

It is observed from the heave translational velocity error, $\tilde{w}_b$, and the corresponding IAE plot that the NFCSMC has a slightly larger dynamic error and IAE compared to the BFCSMC.

(d) Simulation of Angular Velocity Error

Subject to the inputs outlined in through to Figure 6.6, the angular velocity error for the NFCSMC and BFCSMC compensated systems with actuation and allocation is given in Figure 6.11.

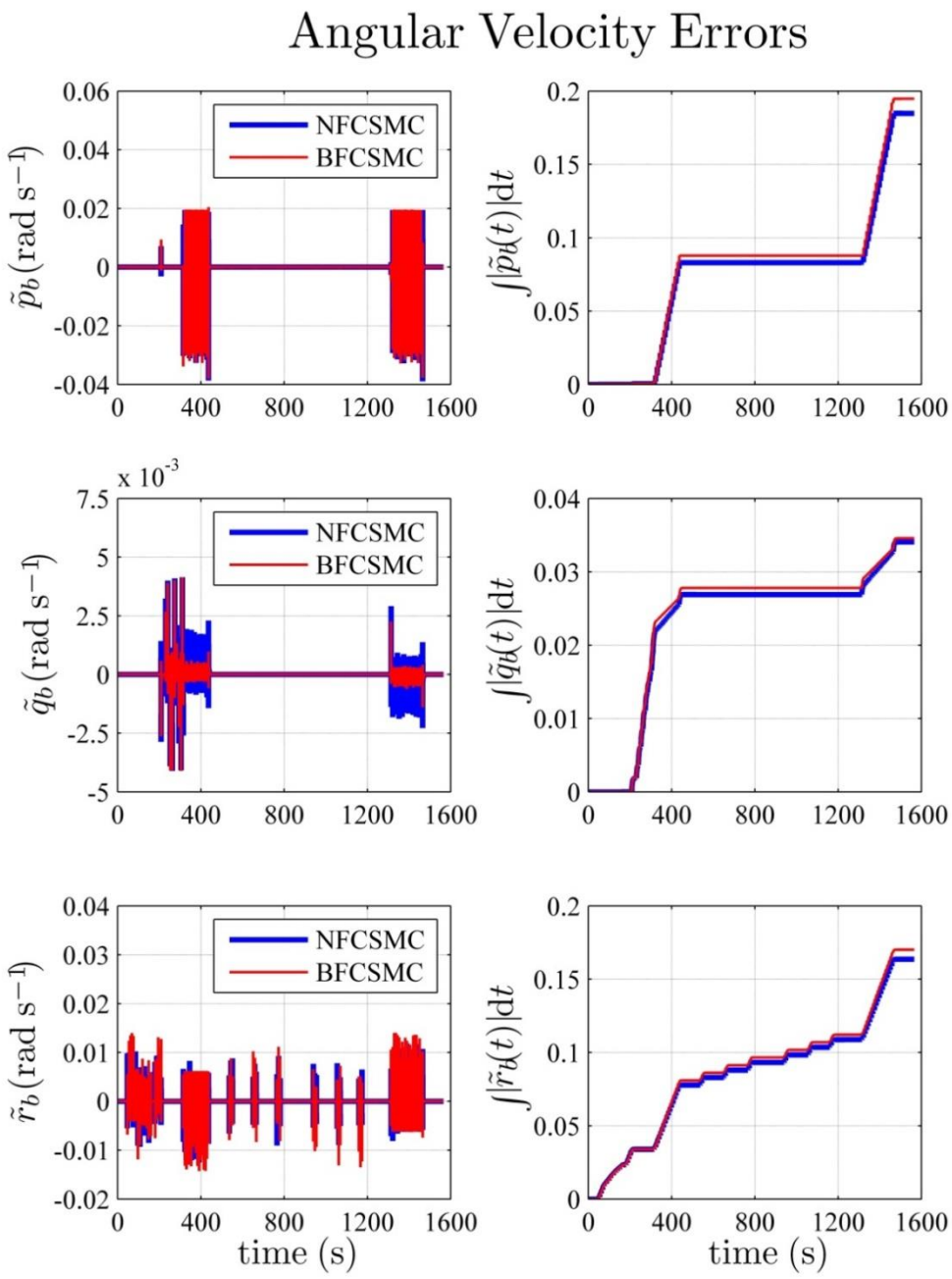

Figure 6.11: Angular Velocity Errors for Case 2 with Actuation and Allocation

It is observed from the roll angular velocity error and the yaw angular velocity error, $\tilde{p}_b$ and $\tilde{r}_b$ respectively, and the corresponding IAE plots that both the NFCSMC and the BFCSMC perform very similarly.

It is observed from the pitch angular velocity error, $\tilde{q}_b$, that the NFCSMC has a larger dynamic error, particularly around 400 s and 1400 s. However, the corresponding IAE plot shows that both the NFCSMC and the BFUSMC perform very similarly in this respect.

(e) Concluding Remarks

Figure 6.8 through to Figure 6.11 compares the behaviour of the NFCSMC and the BFCSMC when the input trajectory is that of Case 2 and both actuation and allocation are implemented in the simulation environment. Based on the behaviours observed, the following remarks can be drawn.

Remark 1.1 – Similar relative behaviour between the BFCSMC and the NFCSMC is observed in this case study as compared to Case 2 of Section 4.4.2.

> Figure 6.8 through to Figure 6.11 compares the behaviour of the NFCSMC with the BFCSMC when the trajectory to be tracked is that of Case 2 and both actuation and allocation are introduced to the simulation. What can be observed here is that both the NFCSMC and the BFCSMC behave in a very similar fashion across most error plots. This was also observed in Section 4.4.2 where the same input trajectory was supplied yet there was no actuation or allocation in the simulation environment. Therefore, it can be concluded that the inclusion of actuation and allocation to the simulation environment has a very similar effect on both the NFCSMC and the BFCSMC.

The simulation presented thus far compares the performance of the NFCSMC and the BFCSMC when both actuation and allocation are included. What it does not achieve is a comparison of a system with actuation and allocation against a system without actuation or allocation. Based on the superior performance of the BFCSMC as observed in Chapter 4, the following section presents the simulation of the

BFCSMC with actuation and allocation, as presented in this chapter, and the BFCSMC without actuation or allocation, as presented in Chapter 4.

2. BFCSMC Only

To assess the behaviour due to the inclusion of actuation and allocation, the following four figures, Figure 6.12 through to Figure 6.15, compare the performance of the BFCSMC as seen here with actuation and allocation, against the performance of the BFCSMC as seen in Section 4.4.2, without actuation or allocation. Figure 6.12 shows the position error and position IAE for the BFCSMC compensated system, both with and without actuation and allocation. Figure 6.13 shows the attitude error and attitude IAE for the BFCSMC compensated system, both with and without actuation and allocation. Figure 6.14 shows the translational velocity error and translational velocity IAE for the BFCSMC compensated system, both with and without actuation and allocation. Figure 6.15 shows the angular velocity error and angular velocity IAE for the BFCSMC compensated system, both with and without actuation and allocation.

(a) Simulation of Position Error

Subject to the inputs outlined in through to Figure 6.6, the position error for the BFCSMC compensated system, both with and without actuation and allocation, is given in Figure 6.12.

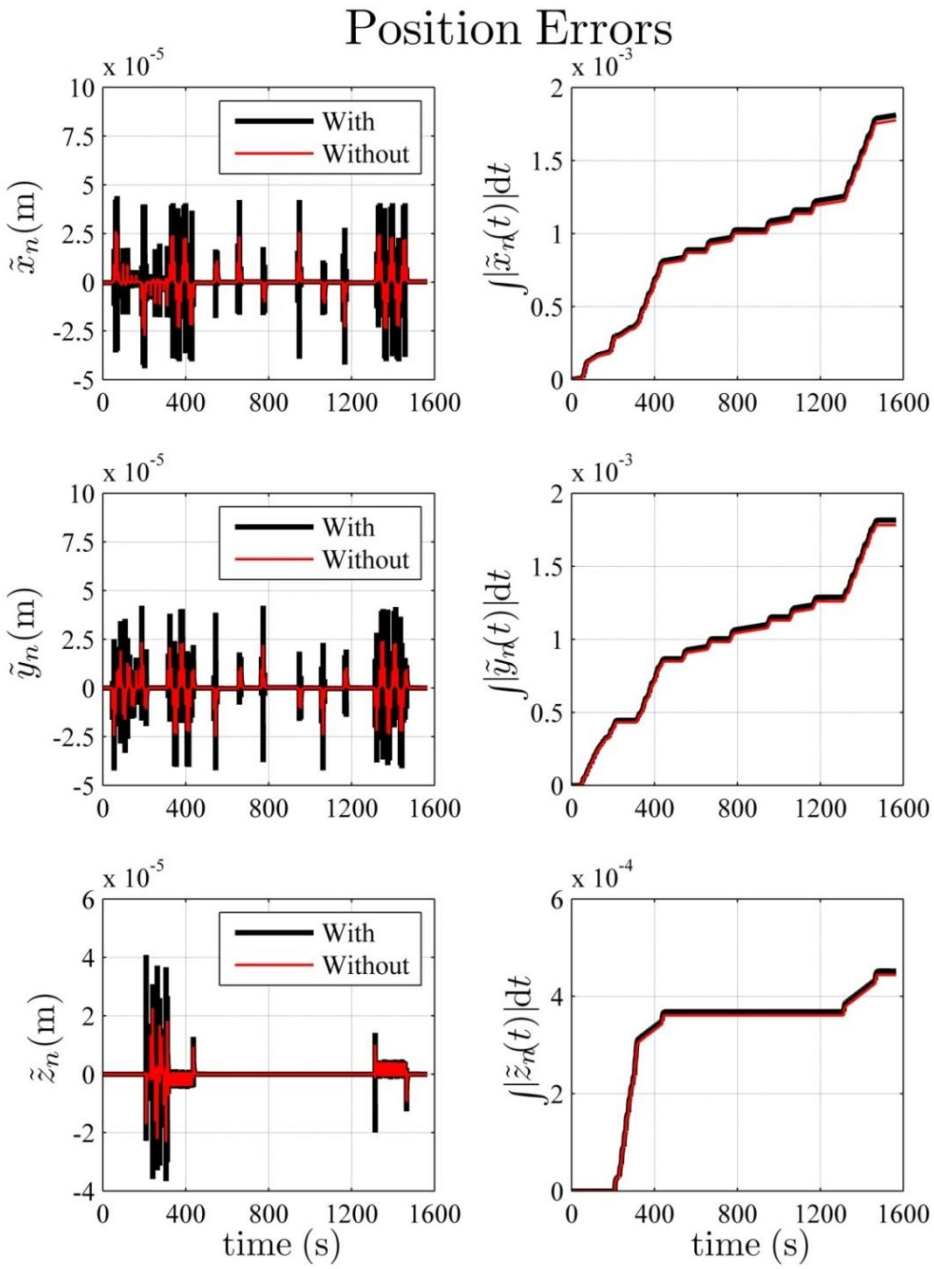

Figure 6.12: Position Errors for BFCSMC With and Without Actuation and Allocation for Case 2

It is observed from the north position error, the east position error, and the down position error, $\tilde{x}_n$, $\tilde{y}_n$, and $\tilde{z}_n$ respectively, that the system with actuation and allocation has a slightly larger dynamic error compared to the system without actuation or allocation. However, the corresponding IAE plots show that both systems perform very similarly in this respect.

(b) Simulation of Attitude Error

Subject to the inputs outlined in through to Figure 6.6, the attitude error for the BFCSMC compensated system, both with and without actuation and allocation, is given in Figure 6.13.

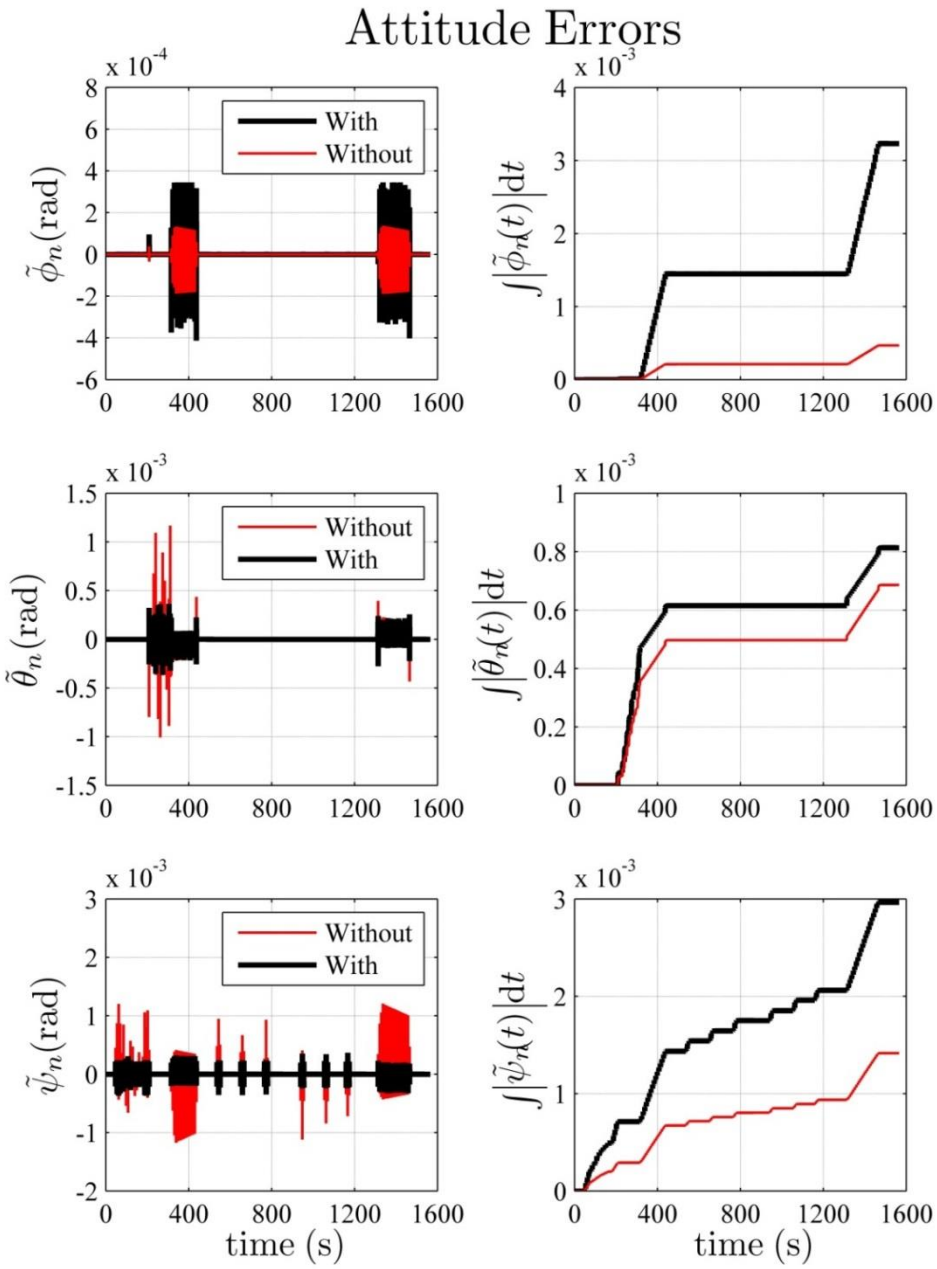

Figure 6.13: Attitude Errors for BFCSMC With and Without Actuation and Allocation for Case 2

It is observed from the roll attitude error, $\tilde{\phi}_n$, and the corresponding IAE plot that the system with actuation and allocation has a larger dynamic error and IAE compared to the system without actuation or allocation.

It is observed from the pitch attitude error and the yaw attitude error, $\tilde{\theta}_n$ and $\tilde{\psi}_n$ respectively, that the system with actuation and allocation has a smaller dynamic error compared to the system without actuation or allocation. However, it is observed that the system with actuation and allocation has a larger IAE compared to the system without actuation or allocation.

(c) Simulation of Translational Velocity Error

Subject to the inputs outlined in through to Figure 6.6, the translational velocity error for the BFCSMC compensated system, both with and without actuation and allocation, is given in Figure 6.14.

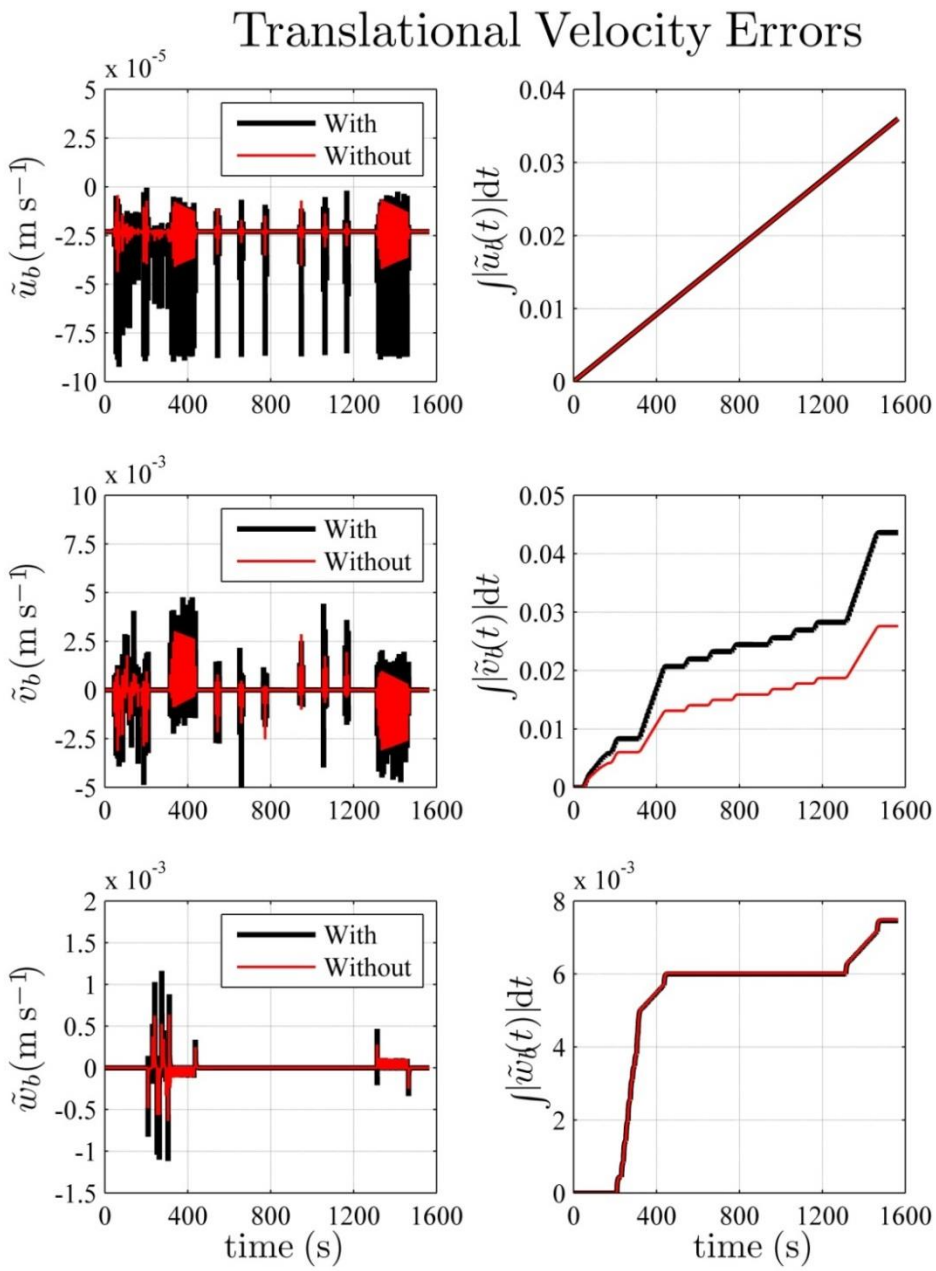

Figure 6.14: Translational Velocity Errors for BFCSMC With and Without Actuation and Allocation for Case 2

It is observed from the surge translational velocity error, $\tilde{u}_b$, that the system with actuation and allocation has a larger dynamic error compared to the system without actuation or allocation. Furthermore, it is observed that both systems have a similar non-zero steady-state error. It is also observed that both systems have a very similar IAE.

It is observed from the sway translational velocity error, $\tilde{v}_b$, and the corresponding IAE plot that the system with actuation and allocation has a larger dynamic error and IAE compared to the system without actuation or allocation.

It is observed from the heave translational velocity error, $\tilde{w}_b$, that the system with actuation and allocation has a larger dynamic error compared to the system without actuation or allocation. However, the corresponding IAE plot shows that both systems perform similarly in this respect.

(d) Simulation of Angular Velocity Error

Subject to the inputs outlined in through to Figure 6.6, the angular velocity error for the BFCSMC compensated system, both with and without actuation and allocation, is given in Figure 6.15.

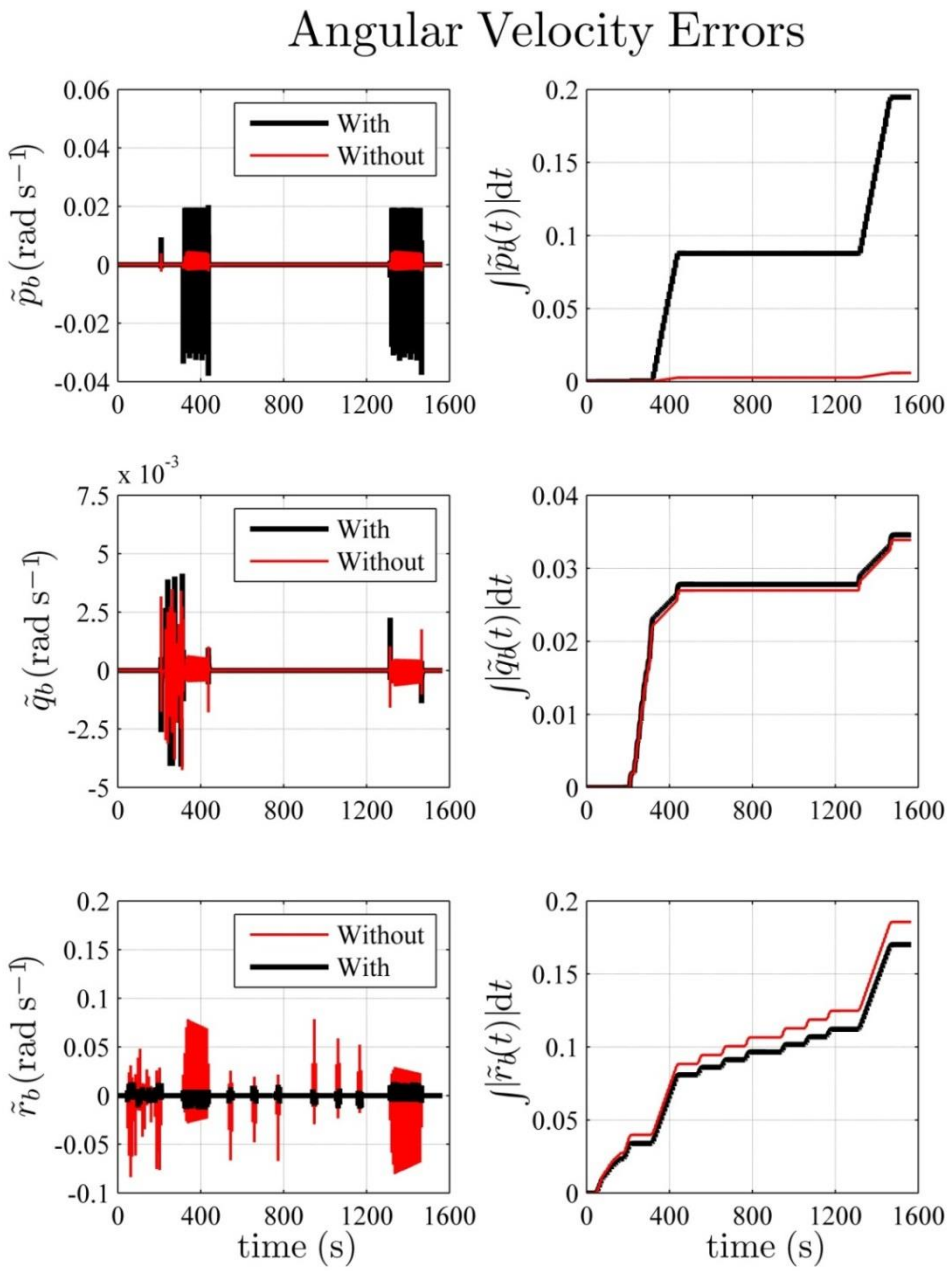

Figure 6.15: Angular Velocity Errors for BFCSMC With and Without Actuation and Allocation for Case 2

It is observed from the roll angular velocity error, $\tilde{p}_b$, that the system with actuation and allocation has a significantly larger dynamic error and IAE compared to the system without actuation or allocation.

It is observed from the pitch angular velocity error, $\tilde{q}_b$, and the corresponding IAE plot that both systems perform very similarly.

It is observed from the yaw angular velocity error, $\tilde{r}_b$, that the system with actuation and allocation has a smaller dynamic error compared to the system without actuation or allocation. However, the corresponding IAE plot shows that both systems perform very similarly in this respect

(e) Concluding Remarks

Figure 6.12 through to Figure 6.15 compares the behaviour of the BFCSMC as seen here with the behaviour of the BFCSMC as seen in Section 4.4.2. As the only difference between the simulation environment here and that of Section 4.4.2 is the inclusion of actuation and allocation, any differences observed in Figure 6.12 through to Figure 6.15 are purely due to actuation and allocation. Based on the behaviours observed in Figure 6.12 through to Figure 6.15, the following remarks can be drawn.

Remark 2.1 – Generally, the inclusion of actuation and allocation causes an increase in the size of the dynamic error for position and translational velocity DoFs while the IAE remains relatively unchanged.

> Observation of the position error plots of Figure 6.12 shows that the inclusion of actuation and allocation causes an increase in the size of dynamic error. This is observed in all three position error plots. It is also observed that the IAE for all three position errors is very similar for both the system with actuation and allocation, and the system without actuation or allocation.
>
> The translational velocity errors of Figure 6.14 show that the system with actuation and allocation has larger dynamic errors in all three instances. As seen in Section 4.4.2, the same steady-state error is observed for the surge

translational velocity error, $\tilde{u}_b$. Observation of the translational velocity IAE plots show that for the surge and heave DoFs, both systems perform very similarly, while for the sway DoF, the system without actuation or allocation performs better with respect to the IAE.

Remark 2.2 – Generally, the inclusion of actuation and allocation causes an increase in the size of the IAE for both the attitude and angular velocity DoFs regardless of the impact on the dynamic error.

Observation of the attitude errors of Figure 6.13 show that different behaviour is seen for different attitude DoFs with respect to the size of the dynamic error. The dynamic error for the roll attitude error, $\tilde{\phi}_n$, is larger for the system with actuation and allocation, whereas the dynamic error for the pitch attitude error and yaw attitude error, $\tilde{\theta}_n$ and $\tilde{\psi}_n$ respectively, is larger for the system without actuation or allocation. With respect to the corresponding attitude IAE plots, larger errors were observed for all three DoFs when actuation and allocation was included in the simulation.

Observation of the angular velocity errors of Figure 6.15 shows again that different behaviour is seen for different DoFs with respect to the size of the dynamic error. The system with actuation and allocation has a larger dynamic error with regards to the roll and pitch angular velocity errors, $\tilde{p}_b$ and $\tilde{q}_b$ respectively, while the opposite is true for the yaw angular velocity error, $\tilde{r}_b$, where the system with actuation and allocation has a larger dynamic error. With respect to the corresponding IAE plots, a significantly larger error is observed for the roll angular velocity DoF of the system with actuation and allocation, while both systems perform quite similarly with respect to the IAE plots of the pitch and yaw angular velocities.

Case 2 Conclusions

This case study presented the effect that the incorporation of actuation and allocation had on the previously studied trajectory presented in Case 2 of Section 4.4.2. It was observed that the performance of the NFCSMC relative to the BFCSMC seen here

was very similar to the performance of the NFCSMC relative to the BFCSMC seen in Section 4.4.2, as noted in Remark 1.1. Therefore, it can be concluded that the inclusion of actuation and allocation has a similar effect on both systems. Furthermore, as the relative behaviour between the two systems is still very similar, the previous conclusion of the BFCSMC performing better than the NFCSMC still stands.

Case 2 of Section 4.4.2 did not include actuation or allocation. Hence, any differences observed here can be attributed to the inclusion of actuation and allocation. In terms of steady-state response, very similar behaviour was observed here compared to Case 2 of Section 4.4.2. Steady-state error was again observed for the surge translational velocity, as noted in Remark 2.1, with the same error value obtained here as seen in Case 2 of Section 4.4.2. This result indicates that the inclusion of actuation and allocation has very little effect on steady-state error.

With respect to dynamic error, this is where the effect of including actuation and allocation was observed. The general effect was that a larger dynamic error was observed here compared to Case 2 of Section 4.4.2. Some error plots did indicate an improvement of dynamic error with the inclusion of actuation and allocation. However, this improvement was not reflected in the corresponding IAE plots. By direct comparison of the IAE plots for the BFCSMC with actuation and allocation and the BFCSMC without actuation or allocation, it can be seen that the BFCSMC without actuation or allocation performed as well as, if not better than, the BFCSMC with actuation and allocation, as noted in Remark 2.1 and Remark 2.2. This is most evident in all the attitude errors seen in Figure 6.13 and the roll angular velocity error, $\tilde{p}_b$, seen in Figure 6.15.

It was anticipated that the inclusion of actuation into the simulation would have a detrimental effect on the performance especially if the nonlinearities due to actuator saturation were reached. To avert this situation, a process was implemented where the desired acceleration was limited in such a way that the nonlinearities of actuator saturation were avoided. This resulted in a smaller magnitude in the input signal to the controller, yet a change in this input signal now occurred over a longer time

period. Hence, the error was also experienced over a longer time period and therefore the error observed in the figures of this case study show an increase in magnitude when actuation and allocation are implemented. This was especially evident when the vehicle was to undergo a change in attitude, such as a change in yaw or a change in pitch.

Overall, there was an observed deterioration in the performance of the system with the inclusion of actuation and allocation. However, this was expected. Both the NFCSMC and the BFCSMC were able to follow the desired trajectory where multiple DoFs were excited that the same time with the inclusion of actuation and allocation into the simulation environment, and hence the vehicle was able to maintain manoeuvrability with the inclusion of the 2-stage allocation scheme proposed in Section 5.3.2. The BFCSMC was able to perform this task slightly better than the NFCSMC and therefore, owing to its simpler implementation, the BFCSMC is a better choice for this application.

6.3.2. Case 3

The final case study conducted here is similar to that seen in Case 3 of Section 4.4.3. This case study asks the vehicle to conduct a raster scan mission covering an area of approximately 250,000 m^2 while under the influence of a time-varying external water current disturbance. The difference presented here is that both actuation and allocation are included in the simulation.

Aim

The aim of this case study is to observe the performance of an AUV system under realistic conditions in terms of both the trajectory to follow and the external disturbance encountered. This simulation expands on Case 3 of Section 4.4.3 by including both actuation and allocation in the system model.

System Conditions

The desired trajectory seen here is the same as seen in Section 4.4.3. A 3D trajectory plot is shown in Figure 6.16 while the associated desired position and attitude plots are shown in Figure 6.17 and Figure 6.18 respectively.

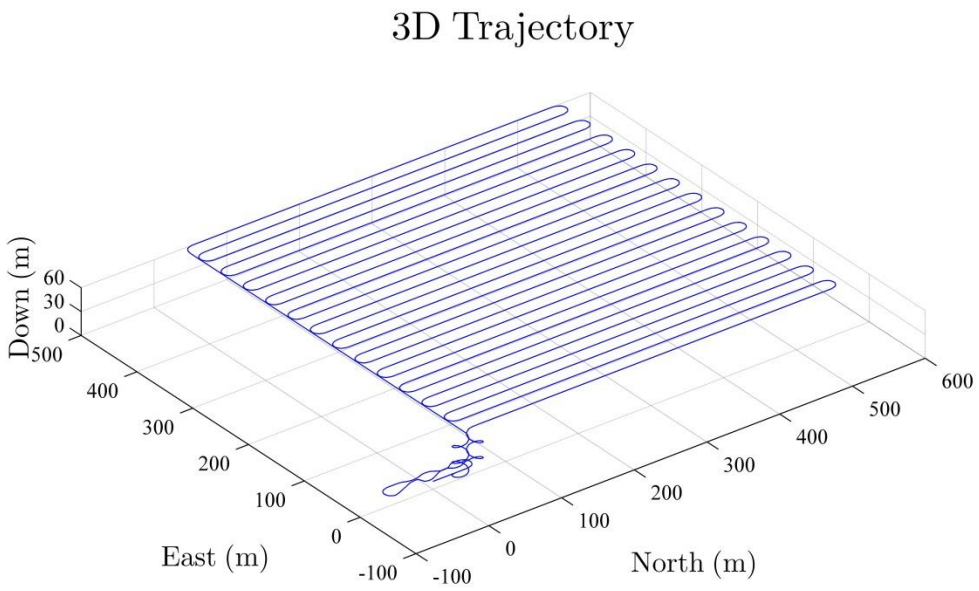

Figure 6.16: 3D Trajectory for Case 3 with Actuation and Allocation

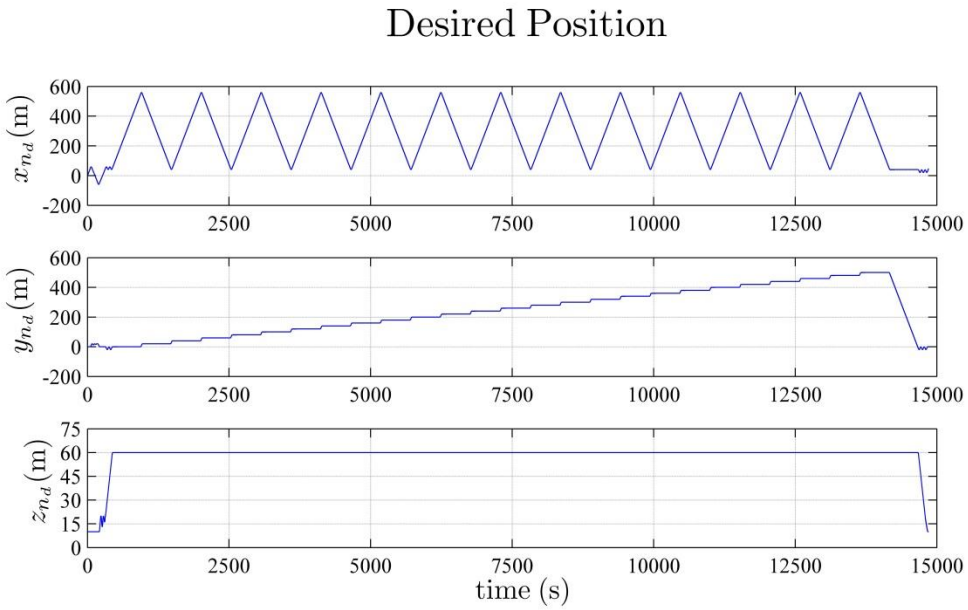

Figure 6.17: Desired Position for Case 3 with Actuation and Allocation (NED Frame)

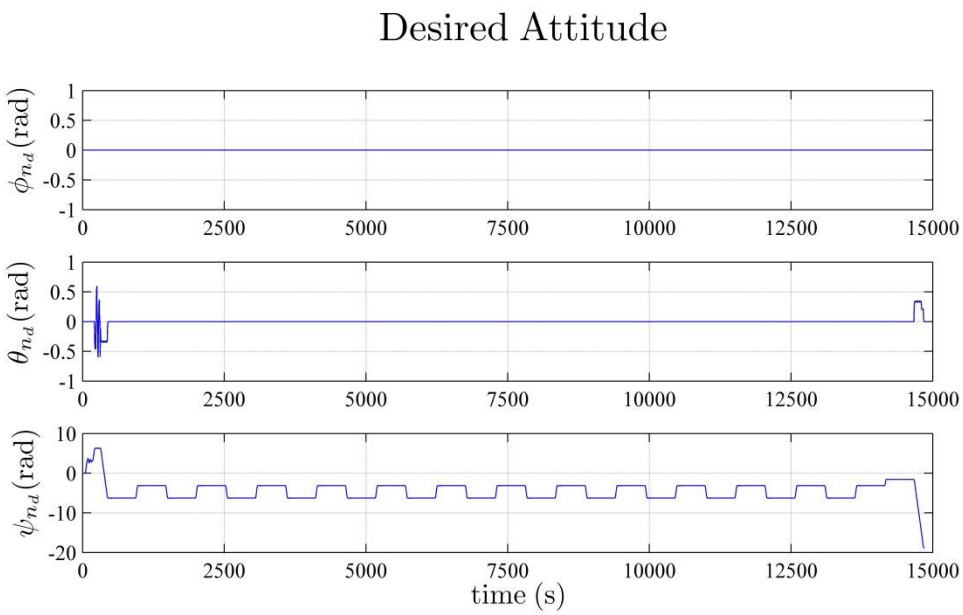

Figure 6.18: Desired Attitude for Case 3 with Actuation and Allocation (NED Frame)

Again, the same LOS guidance system is used and, under the same conditions as previously mentioned in Section 6.3.1, Figure 6.19 and Figure 6.20 are produced for desired translational and angular velocities respectively.

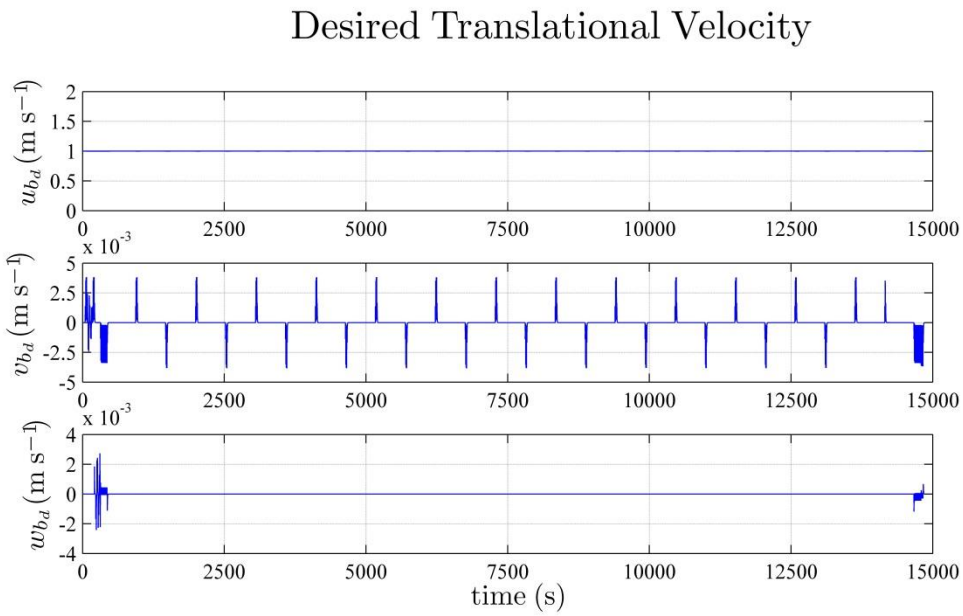

Figure 6.19: Desired Translational Velocity for Case 3 with Actuation and Allocation (Body Frame)

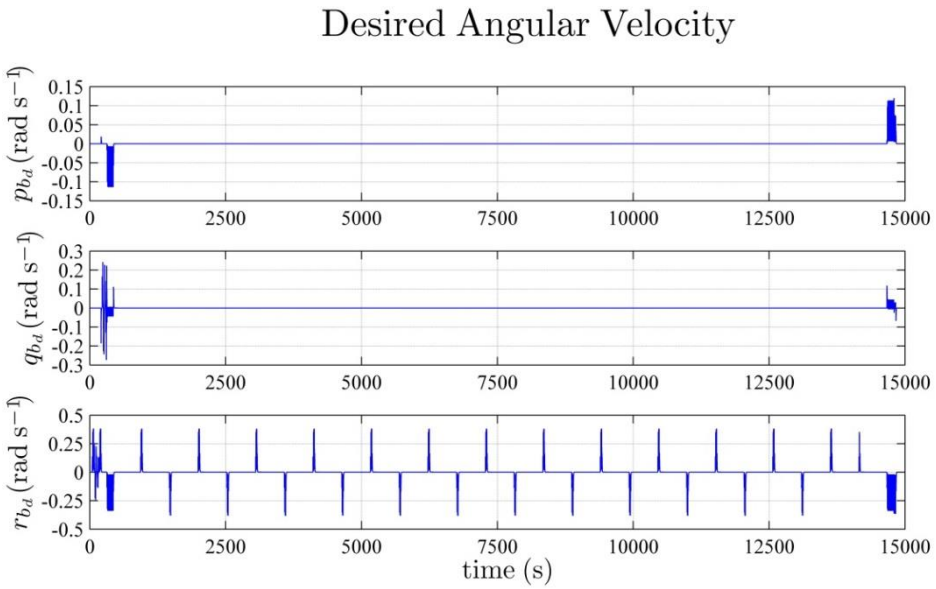

Figure 6.20: Desired Angular Velocity for Case 3 with Actuation and Allocation (Body Frame)

Water currents are present in this simulation study, and again are implemented using a 1st-order Gauss-Markov Process [3]. The water current translational and rotational velocities are shown in Figure 6.21 and Figure 6.22 respectively, while the overall magnitude of this water current is shown in Figure 6.23. Again, this water current is

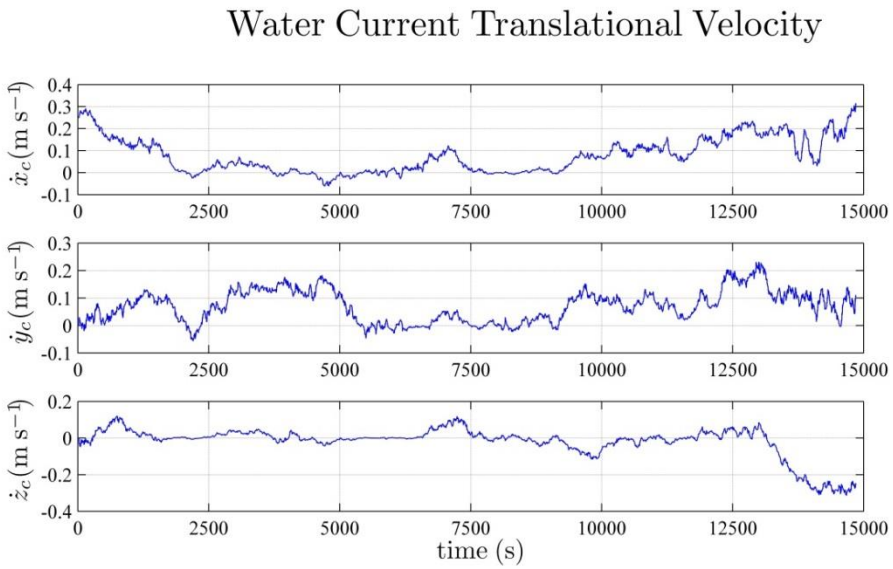

Figure 6.21: Water Current Translational Velocity for Case 3 with Actuation and Allocation (NED Frame)

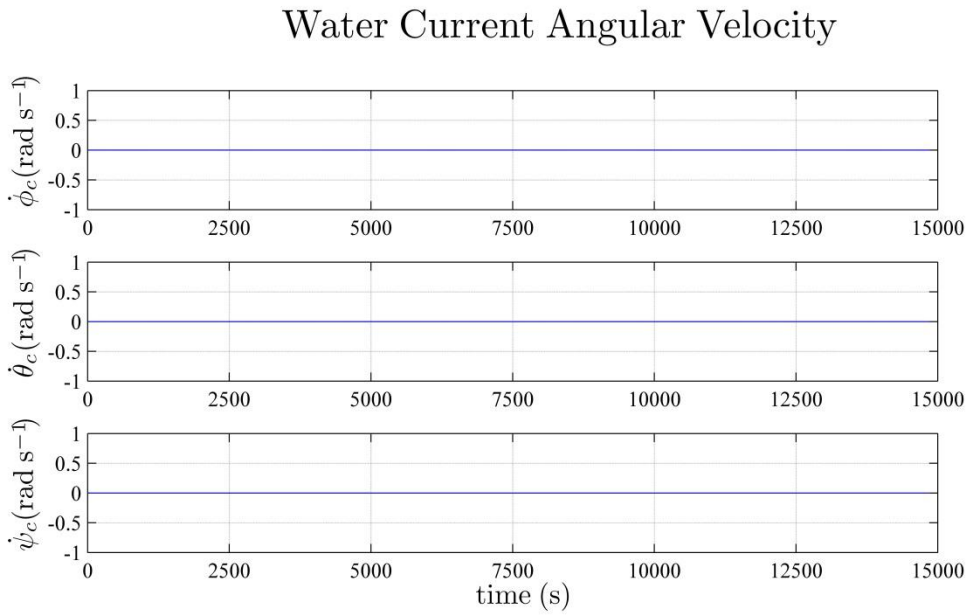

Figure 6.22: Water Current Angular Velocity for Case 3 with Actuation and Allocation (NED Frame)

assumed irrotational, hence the behaviour seen in Figure 6.22.

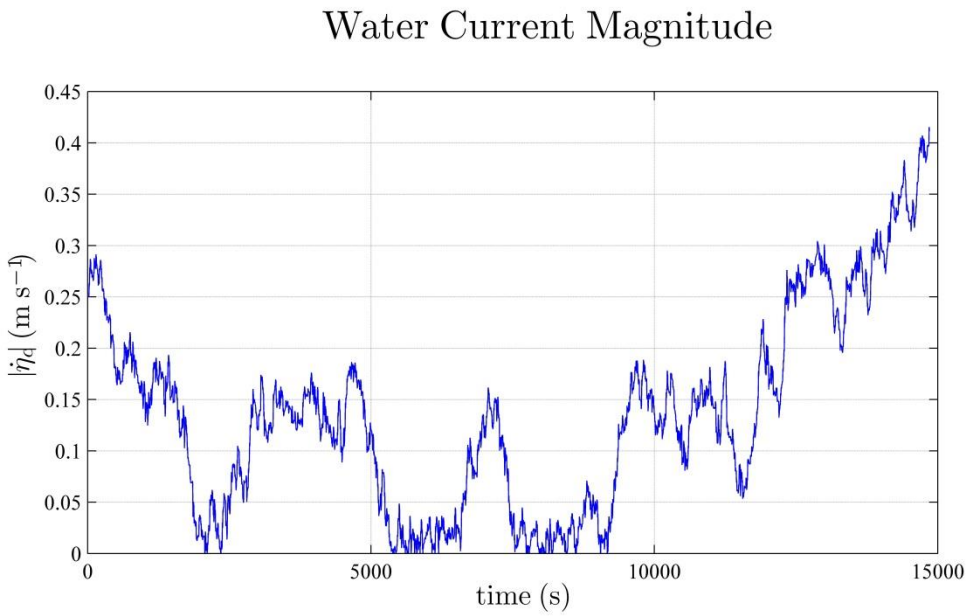

Figure 6.23: Water Current Magnitude for Case 3 with Actuation and Allocation

Flow Chart

The following flow chart illustrates the behaviour of Case 3 with actuation and allocation.

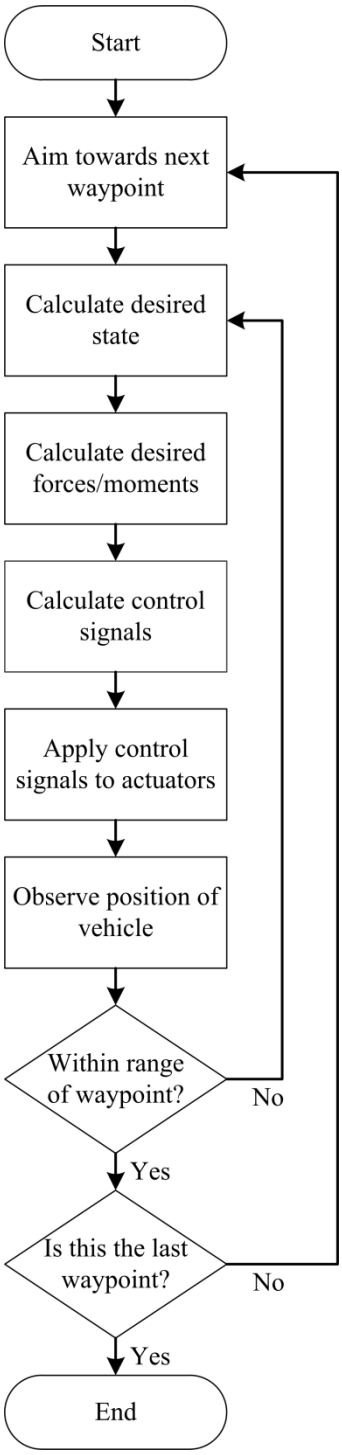

Figure 6.24: Flow Chart for Case 3 with Actuation and Allocation

Simulation Results

The simulation results are divided into two sections. Firstly, the results of the two coupled compensators, namely the NFCSMC and the BFCSMC, with actuation and the 2-stage control allocation scheme will be presented. Secondly, only the results of the BFCSMC system will be presented, comparing the performance observed in this simulation study, where actuation and allocation are included, with the performance observed in the simulation study of Chapter 4, where no actuation or allocation was included.

1. All with Allocation

The following four figures contain the error plots for both the BFCSMC and the NFCSMC for the input trajectory of Case 3, as outlined in Figure 6.16 through to Figure 6.23, and the 2-stage control allocation scheme is used. Figure 6.25 shows the position error and position IAE for the NFCSMC and the BFCSMC compensated systems, both with actuation and allocation. Figure 6.26 shows the attitude error and attitude IAE for the NFCSMC and the BFCSMC compensated systems, both with actuation and allocation. Figure 6.27 shows the translational velocity error and translational velocity IAE for the NFCSMC and the BFCSMC compensated systems, both with actuation and allocation. Figure 6.28 shows the angular velocity error and angular velocity IAE for the NFCSMC and the BFCSMC compensated systems, both with actuation and allocation.

(a) Simulation of Position Error

Subject to the inputs outlined in Figure 6.16 through to Figure 6.23, the position error for the NFCSMC and BFCSMC compensated systems with actuation and allocation is given in Figure 6.25.

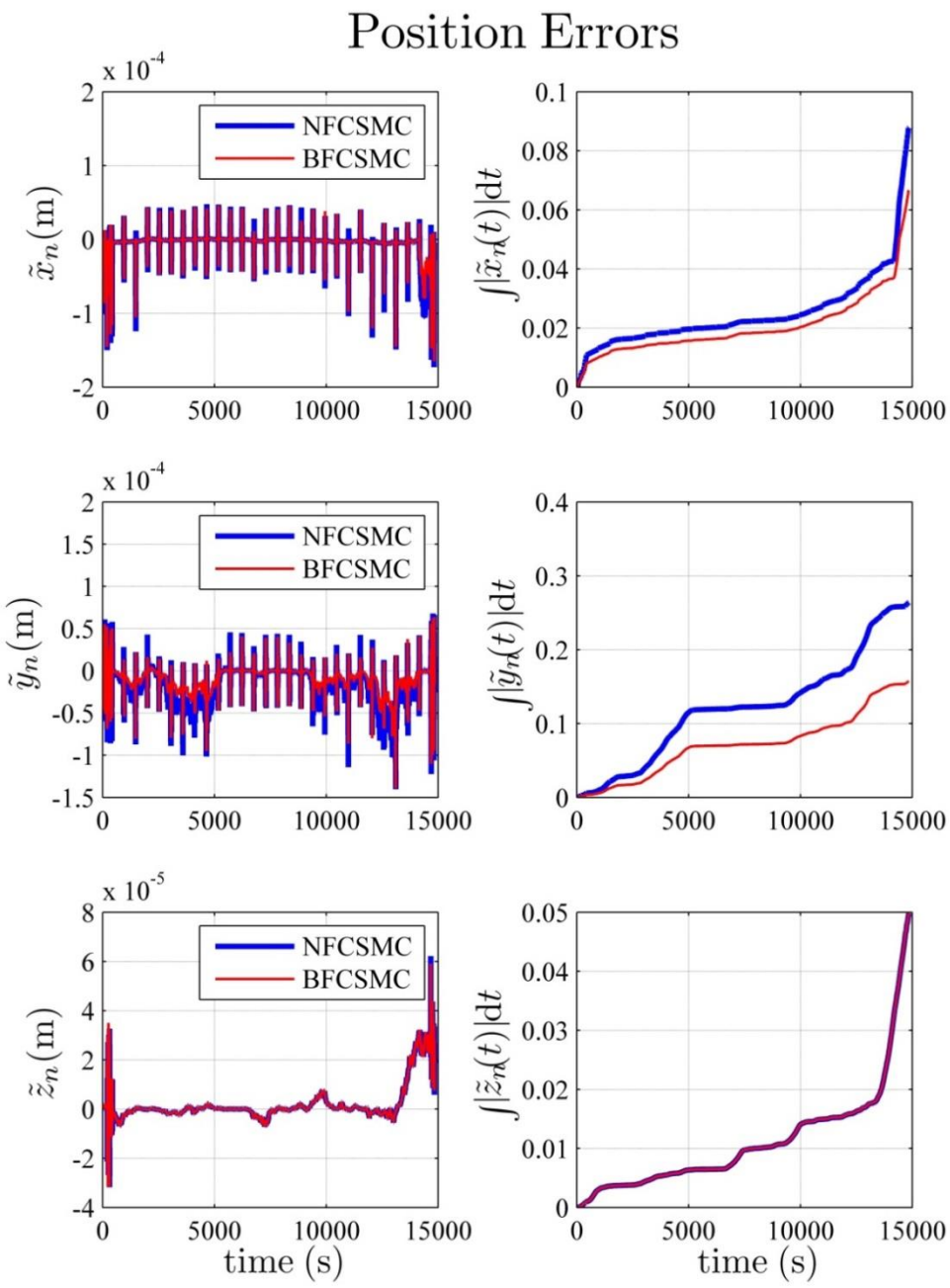

Figure 6.25: Position Errors for Case 3 with Actuation and Allocation

It is observed from the north position error and the down position error, $\tilde{x}_n$ and $\tilde{z}_n$ respectively, and the corresponding IAE plots that both the NFCSMC and the BFCSMC perform very similarly.

It is observed from the east position error, $\tilde{y}_n$, and the corresponding IAE plot that the NFCSMC has a larger dynamic error and IAE compared to the BFCSMC.

(b) Simulation of Attitude Error

Subject to the inputs outlined in Figure 6.16 through to Figure 6.23, the attitude error for the NFCSMC and BFCSMC compensated systems with actuation and allocation is given in Figure 6.26.

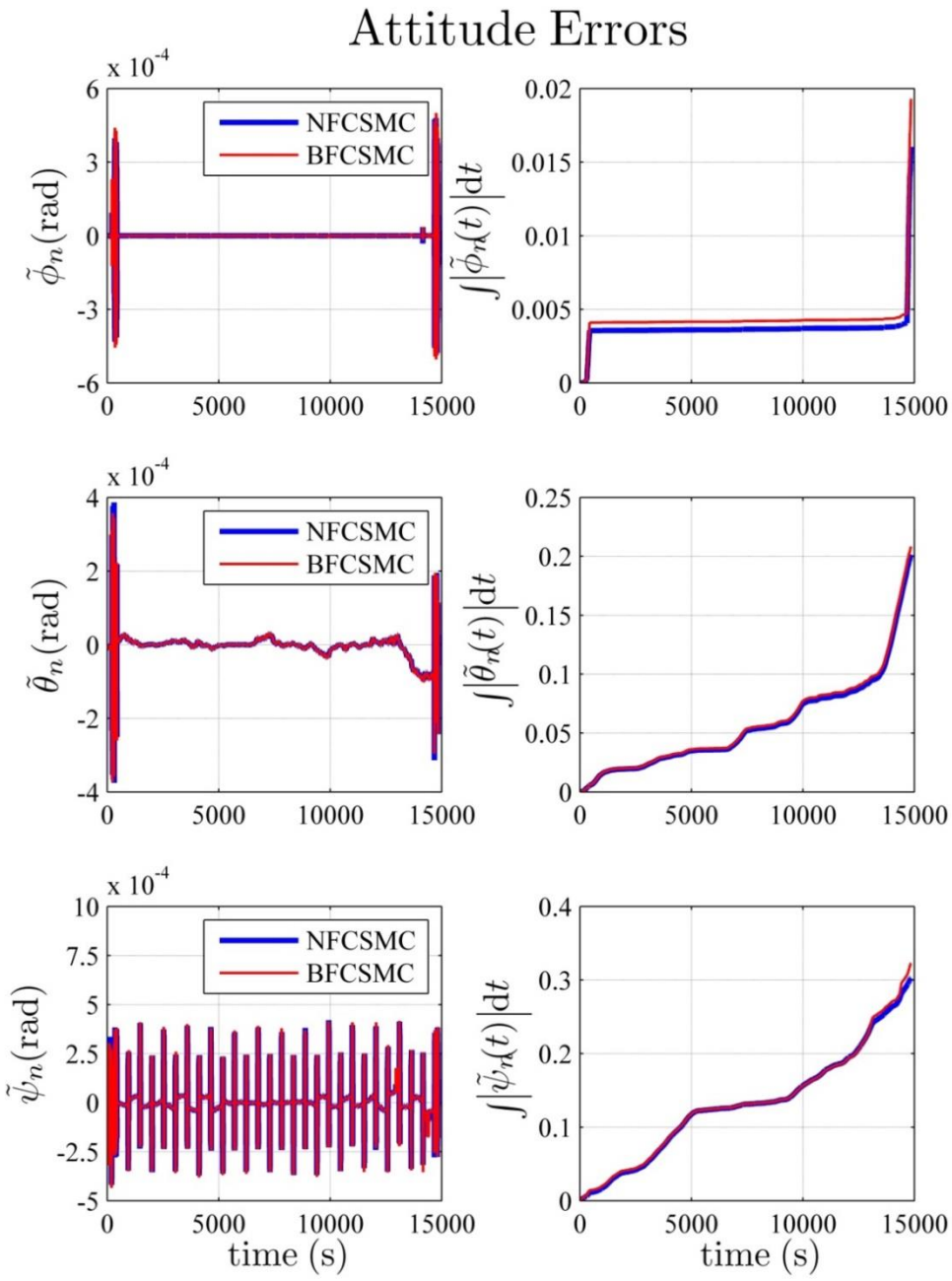

Figure 6.26: Attitude Errors for Case 3 with Actuation and Allocation

It is observed from the roll attitude error, the pitch attitude error, and the yaw attitude error, $\tilde{\phi}_n$, $\tilde{\theta}_n$, and $\tilde{\psi}_n$ respectively, and the corresponding IAE plots that both the NFCSMC and the BFCSMC perform very similarly.

(c) Simulation of Translational Velocity Error

Subject to the inputs outlined in Figure 6.16 through to Figure 6.23, the translational velocity error for the NFCSMC and BFCSMC compensated systems with actuation and allocation is given in Figure 6.27.

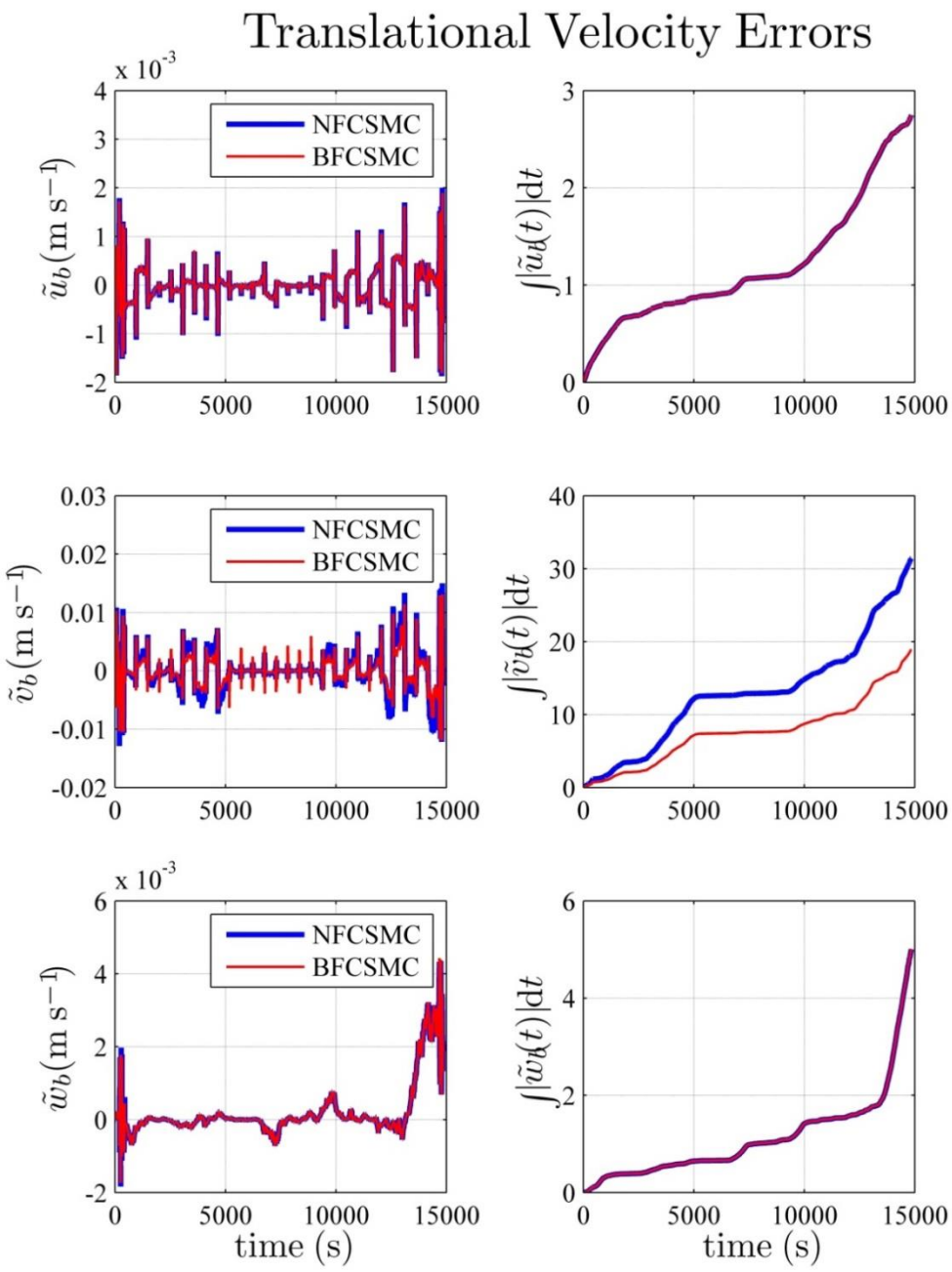

Figure 6.27: Translational Velocity Errors for Case 3 with Actuation and Allocation

It is observed from the surge translational velocity error and the heave translational velocity error, $\tilde{u}_b$ and $\tilde{w}_b$ respectively, and the corresponding IAE plots that both the NFCSMC and the BFCSMC perform very similarly.

It is observed from the sway translational velocity error, $\tilde{v}_b$, and the corresponding IAE plot that the NFCSMC has a larger dynamic error and IAE compared to the BFCSMC.

(d) Simulation of Angular Velocity Error

Subject to the inputs outlined in Figure 6.16 through to Figure 6.23, the angular velocity error for the NFCSMC and BFCSMC compensated systems with actuation and allocation is given in Figure 6.28.

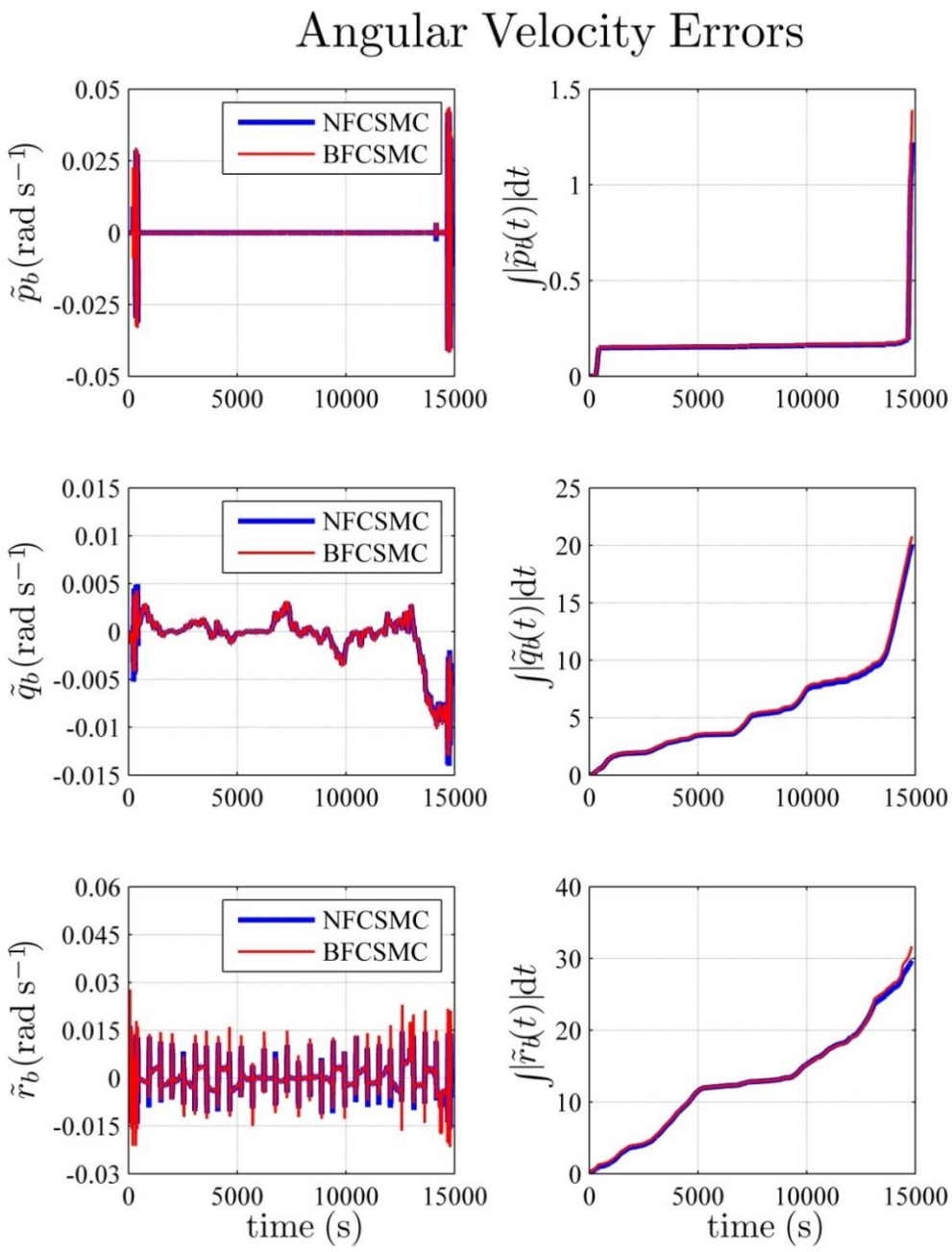

Figure 6.28: Angular Velocity Errors for Case 3 with Actuation and Allocation

It is observed from the roll angular velocity error, the pitch angular velocity error, and the yaw angular velocity error, $\tilde{p}_b$, $\tilde{q}_b$, and $\tilde{r}_b$ respectively, and the corresponding IAE plots that both the NFCSMC and the BFCSMC perform very similarly

(e) Concluding Remarks

Figure 6.25 through to Figure 6.28 compares the behaviour of the NFCSMC and the BFCSMC when the input trajectory is that of Case 3 and both actuation and allocation are implemented in the simulation environment. Based on the behaviours observed, the following remarks can be drawn.

Remark 1.1 – Similar relative behaviour between the BFCSMC and the NFCSMC is observed in this case study as compared to Case 3 of Section 4.4.3.

Akin to what was observed for the trajectory of Case 2 with actuation and allocation of Section 6.3.1 and without actuation or allocation of Section 4.4.2, similar behaviour is seen when comparing the results presented here for Case 3 with actuation and allocation and the results presented in Section 4.4.3 for Case 3 without actuation or allocation.

The performance of the NFCSMC relative to the BFCSMC as seen here is very similar to the performance of the NFCSMC relative to the BFCSMC as seen in Section 4.4.3. Therefore, the effect due to the inclusion of actuation and allocation is very similar for both systems, and hence any differences seen here compared to the results presented in Section 4.4.3 are purely due to the inclusion of actuation and allocation.

Remark 1.2 – The unknown water current disturbance has a significant impact on the east positon error and sway translational velocity error.

For the same reasons as discussed in Section 4.4.3, the large errors are observed for the east position and the sway translational velocity. Again, the large errors in these plots are due to the unknown water current disturbance having a significant effect on the sway motion of the vehicle due to the dominating drag coefficient within this DoF. It is also observed here that the

BFCSMC performs better than the NFCSMC with respect to these two error plots. Considering these observations, the conclusion that the BFCSMC performs better than the NFCSMC as seen in Section 4.4.3 also stands with respect to the results presented here.

The simulation presented thus far compares the performance of the NFCSMC and the BFCSMC when both actuation and allocation are included. What it does not achieve is a comparison of a system with actuation and allocation against a system without actuation or allocation. Based on the superior performance of the BFCSMC as observed in Chapter 4, the following section presents the simulation of the BFCSMC with actuation and allocation, as presented in this chapter, and the BFCSMC without actuation or allocation, as presented in Chapter 4.

2. BFCSMC Only

To assess the behaviour due to the inclusion of actuation and allocation, the following four figures, Figure 6.29 through to Figure 6.32, compare the performance of the BFCSMC as seen here, with actuation and allocation, against the performance of the BFCSMC as seen in Section 4.4.3, without actuation or allocation. Figure 6.29 shows the position error and position IAE for the BFCSMC compensated system, both with and without actuation and allocation. Figure 6.30 shows the attitude error and attitude IAE for the BFCSMC compensated system, both with and without actuation and allocation. Figure 6.31 shows the translational velocity error and translational velocity IAE for the BFCSMC compensated system, both with and without actuation and allocation. Figure 6.32 shows the angular velocity error and angular velocity IAE for the BFCSMC compensated system, both with and without actuation and allocation.

(a) Simulation of Position Error

Subject to the inputs outlined in Figure 6.29 through to Figure 6.32, the position error for the BFCSMC compensated system, both with and without actuation and allocation, is given in Figure 6.29.

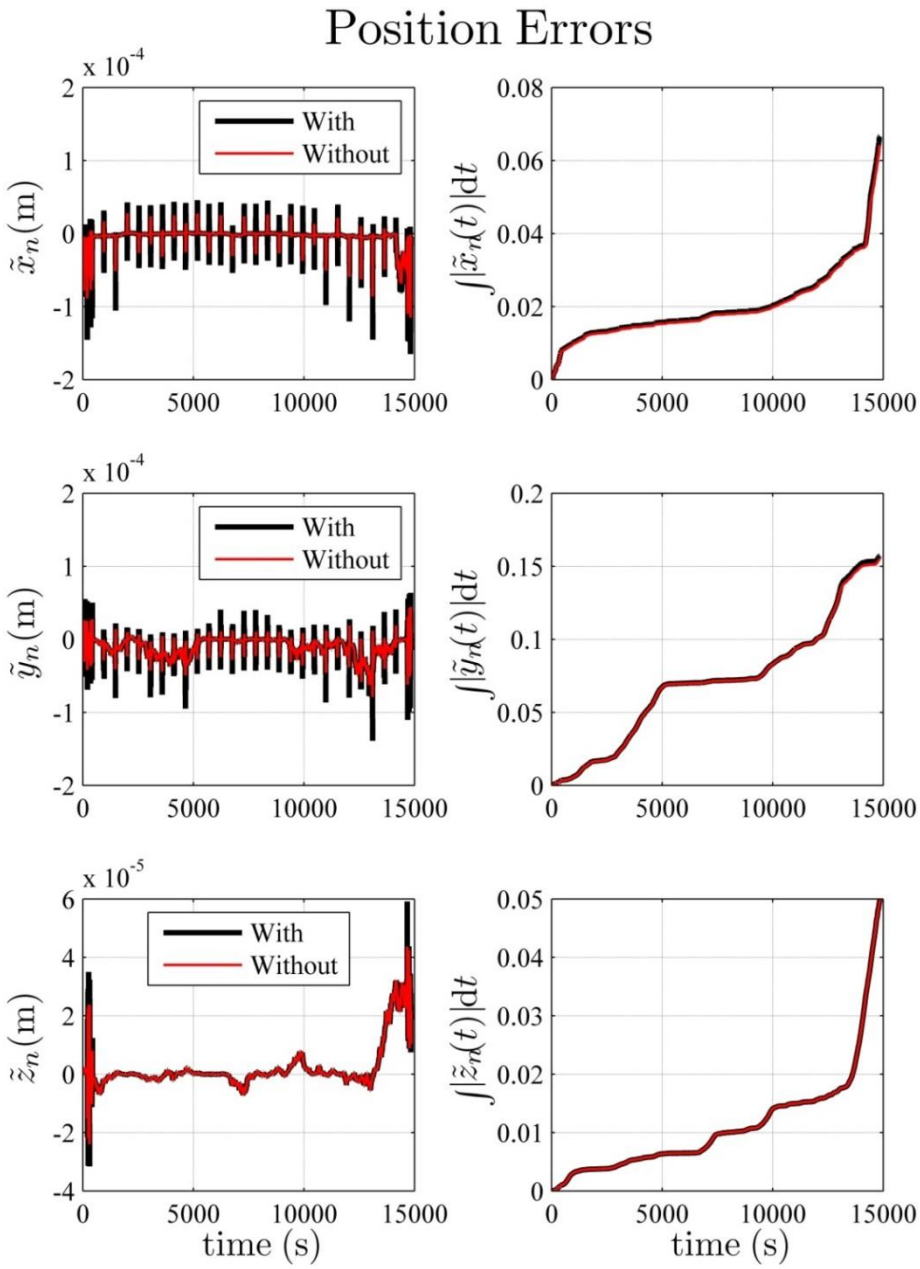

Figure 6.29: Position Errors for BFCSMC With and Without Actuation and Allocation for Case 3

It is observed from the north position error, the east position error, and the down position error, $\tilde{x}_n$, $\tilde{y}_n$, and $\tilde{z}_n$ respectively, that the system with actuation and allocation has a slightly larger dynamic error compared to the system without actuation or allocation. However, the corresponding IAE plots show that both systems perform very similarly in this respect.

(b) Simulation of Attitude Error

Subject to the inputs outlined in Figure 6.29 through to Figure 6.32, the attitude error for the BFCSMC compensated system, both with and without actuation and allocation, is given in Figure 6.30.

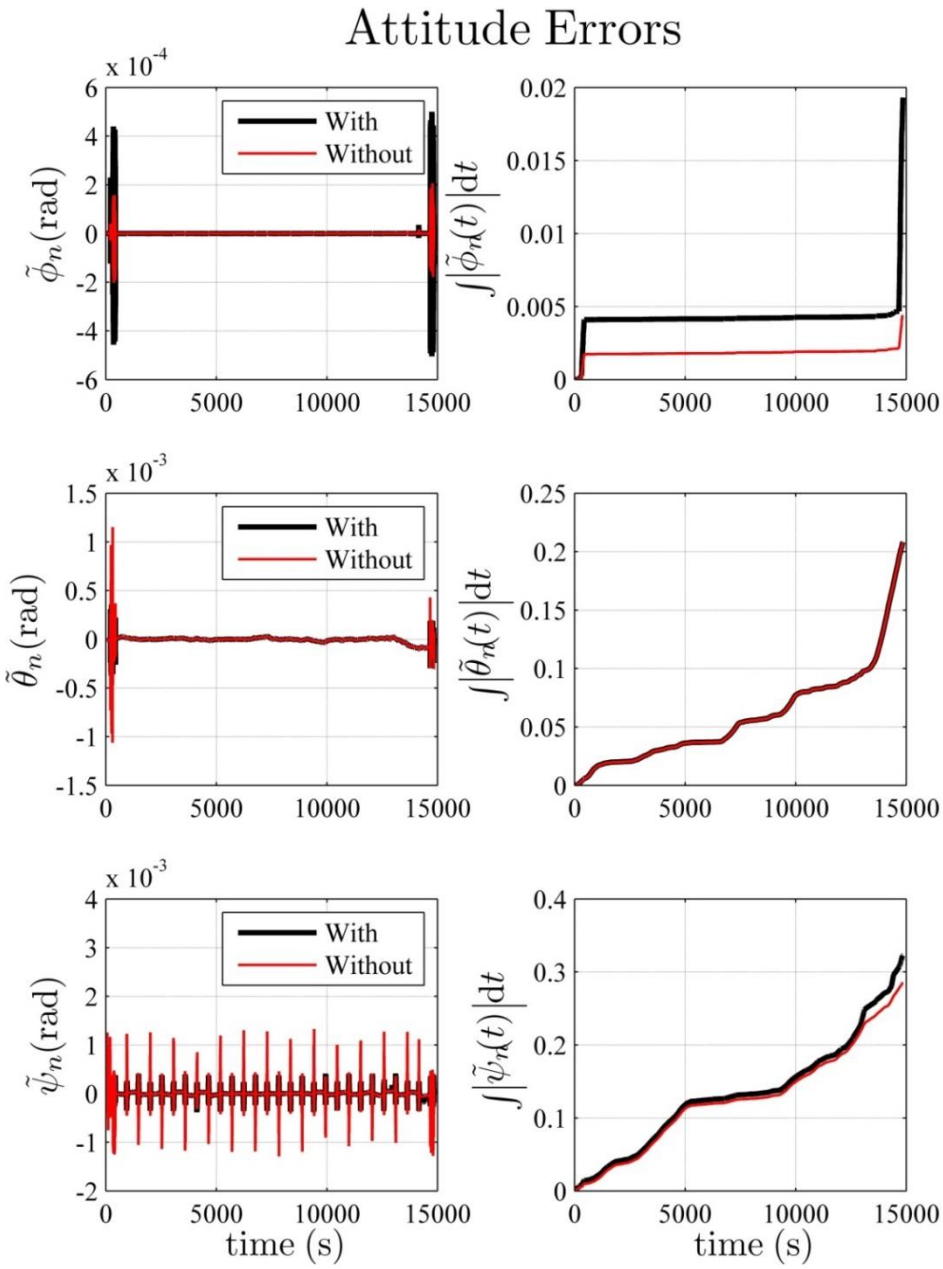

Figure 6.30: Attitude Errors for BFCSMC With and Without Actuation and Allocation for Case 3

It is observed from the roll attitude error, $\tilde{\phi}_n$, and the corresponding IAE plot that the system with actuation and allocation has a larger dynamic error and IAE compared to the system without actuation or allocation.

It is observed for the pitch attitude error and the yaw attitude error, $\tilde{\theta}_n$ and $\tilde{\psi}_n$ respectively, that the system with actuation and allocation has a smaller dynamic error compared to the system without actuation or allocation. However, the corresponding IAE plots show that both systems perform very similarly in this respect.

(c) Simulation of Translational Velocity Error

Subject to the inputs outlined in Figure 6.29 through to Figure 6.32, the translational velocity error for the BFCSMC compensated system, both with and without actuation and allocation, is given in Figure 6.31.

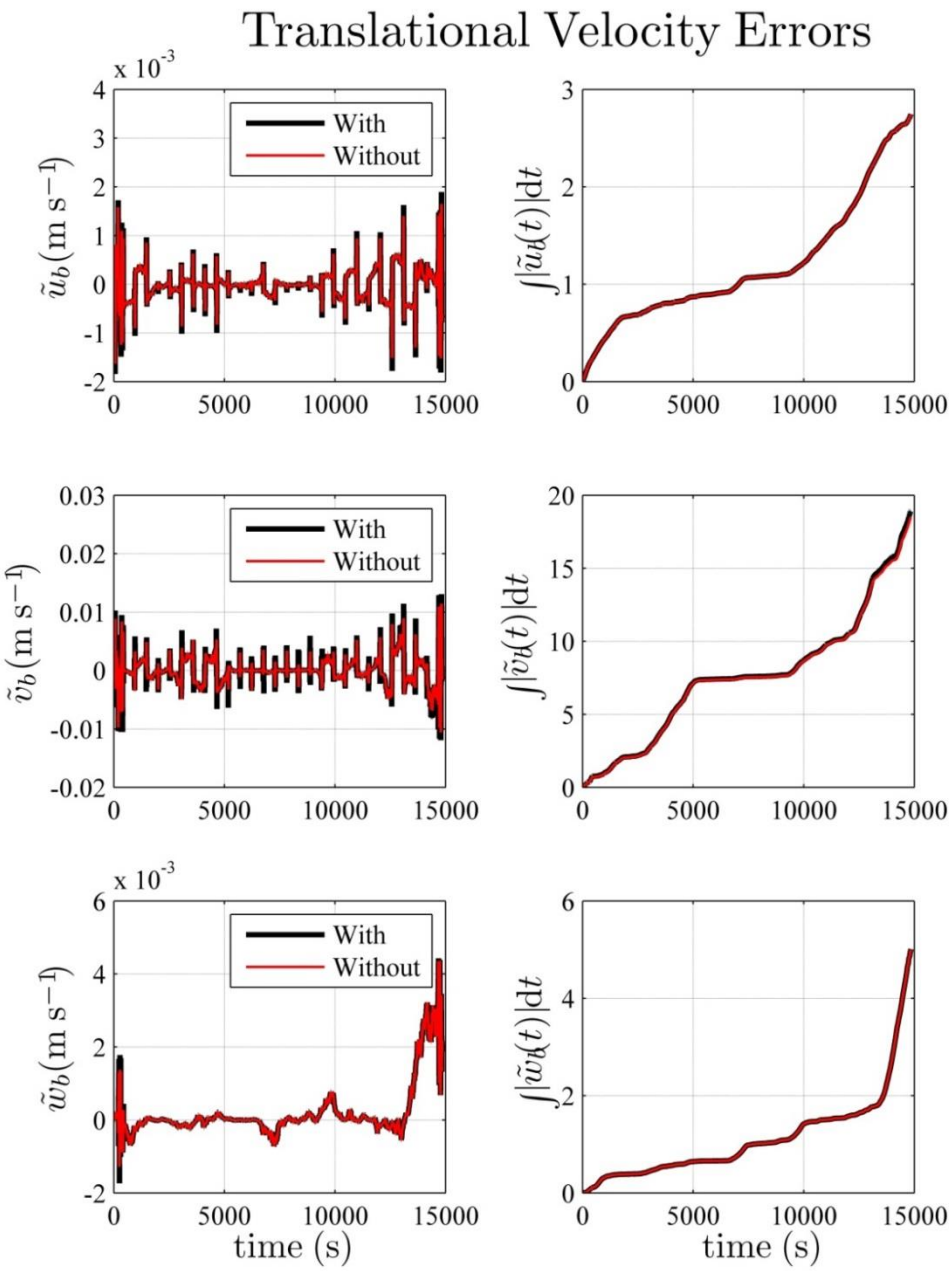

Figure 6.31: Translational Velocity Errors for BFCSMC With and Without Actuation and Allocation for Case 3

It is observed from the surge translational velocity error, the sway translational velocity error, and the heave translational velocity error, $\tilde{u}_b$, $\tilde{v}_b$ and $\tilde{w}_b$ respectively, and the corresponding IAE plots that both systems perform very similarly.

(d) Simulation of Angular Velocity Error

Subject to the inputs outlined in Figure 6.29 through to Figure 6.32, the angular velocity error for the BFCSMC compensated system, both with and without actuation and allocation, is given in Figure 6.32.

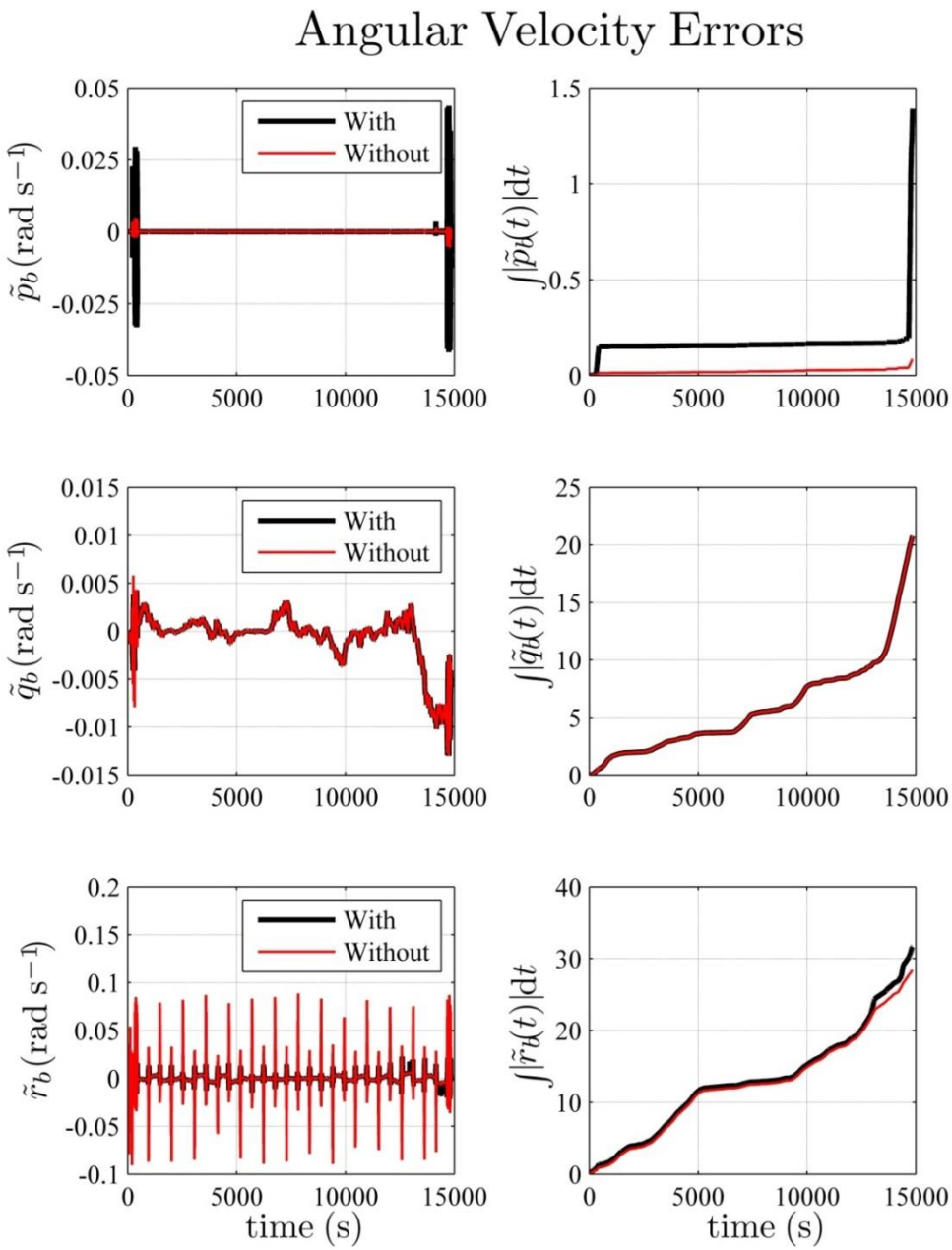

Figure 6.32: Angular Velocity Errors for BFCSMC With and Without Actuation and Allocation for Case 3

It is observed from the roll angular velocity error, $\tilde{p}_b$, and the corresponding IAE plot that the system with actuation and allocation has a larger dynamic error and IAE compared to the system without actuation or allocation.

It is observed from the pitch angular velocity error, $\tilde{q}_b$, and the corresponding IAE plot that both systems perform very similarly.

It is observed from the yaw angular velocity error, $\tilde{r}_b$, that the system with actuation and allocation has a smaller dynamic error compared to the system without actuation or allocation. However, it is observed from the corresponding IAE plot that both systems perform very similarly in this respect.

(e) Concluding Remarks

Figure 6.29 through to Figure 6.32 compares the behaviour of the BFCSMC as seen here with the behaviour of the BFCSMC as seen in Section 4.4.3. As the only difference between the simulation environment here and that of Section 4.4.3 is the inclusion of actuation and allocation, any differences observed in Figure 6.29 through to Figure 6.32 are purely due to actuation and allocation. Based on the behaviours observed in Figure 6.29 through to Figure 6.32, the following remarks can be drawn.

Remark 2.1 – Generally, the inclusion of actuation and allocation causes an increase in the size of the dynamic error for position and translational velocity DoFs while the IAE remains relatively unchanged.

> By looking at the position errors of Figure 6.29, it can be seen that the introduction of actuation and allocation into the simulation environment has an effect on the dynamic error of the system. In all three positions, the system without actuation or allocation experienced a smaller dynamic error compared to the system with actuation and allocation. When looking at the associated IAE plots, it is seen that there is very little difference between the two systems. This indicates that the duration of these larger spikes in the error plots are insignificant compared to the overall behaviour of the system.

The translational velocity errors of Figure 6.31 display similar trends to those of the position errors of Figure 6.29. The system with actuation and allocation experiences a larger dynamic error, while the corresponding IAE plots are very similar for both systems.

Remark 2.2 – The inclusion of actuation and allocation causes an increase in the size of the dynamic error and the IAE of the roll attitude error and the roll angular velocity error.

With respect to the roll attitude error, $\tilde{\phi}_n$, of Figure 6.30 and the roll angular velocity error, $\tilde{p}_b$, of Figure 6.32, the inclusion of actuation and allocation has a significant impact on both the dynamic error and the IAE. This is particularly evident at the start and end of the mission where the vehicle is performing the spiral manoeuvre.

Remark 2.3 – The inclusion of actuation and allocation causes a decrease in the size of the dynamic error for the pitch attitude error, yaw attitude error, pitch angular velocity error, and yaw angular velocity error, while the IAE remains relatively unchanged.

With respect to the pitch and yaw attitude error, $\tilde{\phi}_n$ and $\tilde{\psi}_n$ respectively, of Figure 6.30 and the pitch and yaw angular velocity error, $\tilde{q}_b$ and $\tilde{r}_b$ respectively, of Figure 6.32, it is observed that the system without actuation or allocation has a larger dynamic error compared to the system with actuation and allocation while the IAE is predominately unaffected.

Case 3 Conclusions

The aim of this case study was to examine the performance of the NFCSMC and the BFCSMC under realistic conditions with the incorporation of actuation and allocation into the simulation environment. This scenario required the vehicle to follow a trajectory similar to that which an AUV would be required to follow during a survey mission. Furthermore, a time-varying water current is introduced to the system such that the influence of an unknown disturbance can be observed. Even though the plots presented clearly show the effect the current had on the vehicle, as

noted in Remark 1.2, both compensators were still able to control the vehicle such that the entire trajectory was followed.

By comparison of the results presented here with those presented in Section 4.4.3, where there was no actuation or allocation, it was observed that the performance of the NFCSMC relative to the BFCSMC seen here was very similar to the performance of the NFCSMC relative to the BFCSMC as seen in Section 4.4.3, as noted in Remark 1.1. Therefore, the differences observed here were purely attributed to the inclusion of actuation and allocation into the simulation environment. Furthermore, the observation of the BFCSMC being superior to the NFCSMC still stands. As the BFCSMC is more computationally efficient to implement compared to the NFCSMC, the BFCSMC is well suited to the task of controlling an AUV.

Similar to what was observed in Section 6.3.1, the majority of error plots presented here experienced a larger dynamic error with the inclusion of actuation and allocation, as noted in Remark 2.1 for the position error and translational velocity errors and Remark 2.2 for the roll attitude and angular velocity error. However, there were some error plots where the dynamic error seen here was smaller, as noted in Remark 2.3 for both the pitch and yaw attitude error and angular velocity error. Even though this was observed, the corresponding IAE plot for each of the error plots, be it position/attitude or translational/angular velocity, indicated that the system without actuation or allocation performed equally well or better than the system with actuation and allocation. This is expected as the inclusion of actuation and allocation limits the magnitude of force and torque that is applied to the vehicle. In terms of actuation, these limits are due to physical characteristics of the actuators themselves. If these limits are reached, nonlinearities will be introduced into the system. The acceleration limiting scheme is introduced to avoid reaching these nonlinearities, however this scheme now extends the time period of which the change in acceleration is applied. This in turn extends the time period of the error and hence leads to the increase in the IAE as observed particularly for the roll attitude error and the roll angular velocity error.

Overall, the incorporation of actuation and allocation into the simulation environment that simulated a realistic AUV mission was successful. Even though the

inclusion of actuation and allocation lead to degradation of performance, it was still seen that both the BFCSMC and the NFCSMC were able to track the desired trajectory. Furthermore, it was observed that the BFCSMC was superior to the NFCSMC when viewing the entire duration of the case study. This indicates that the BFCSMC is the superior choice for this type of mission, not only due to the superior performance, but also owing to the fact that it is more computationally efficient to implement in comparison to the NFCSMC.

6.4. Chapter Summary

This chapter presented the simulation study results for the situation when actuation and allocation are included in the simulation environment. Two of the three controllers seen in the simulation studies of Chapter 4 were again used here, namely the NFCSMC and the BFCSMC. The BFUSMC was not implemented here, as it is less suited to the trajectories presented within this simulation study. The addition of actuation and allocation here is what sets this simulation study apart from the simulation study presented in Chapter 4. For consistency, the same plant model as used in Chapter 4 was used here as outlined in Section 2.2.3 and the parameters of the matrices within the model are detailed in Appendix A.1.1. Actuation was implemented in the form of a single high-powered main thruster, four independent control surfaces at the stern of the vehicle mounted in a cruciform shape, and four independent tunnel thrusters, two fore of the centre of the vehicle and two aft of the centre of the vehicle. Allocation was implemented in the form of the novel 2-stage scheme presented in Section 5.3.2, including the process outlined for limiting the desired acceleration to attainable levels.

To allow for an unbiased comparison of the results presented here to those of Chapter 4, two case studies that were previously presented were also used here, namely Case 2 of Section 4.4.2 and Case 3 of Section 4.4.3. Only these two case studies were chosen as Case 1 of Section 4.4.1 was impractical as roll is uncontrollable when the relative surge velocity of the vehicle is zero and the previously mentioned actuator configuration is implemented.

What was observed from both case studies conducted here was that, even though effects due to the introduction of actuation and allocation were apparent, the impact was not severe enough to cause instabilities in either system. Both the BFCSMC and the NFCSMC were able to track the desired trajectories, even while under the influence of an unknown, time-varying water current disturbance. The impact of actuation and allocation on the steady-state errors observed in the simulation study of the Case 2 of Section 4.4.2 were undetectable. The steady-state error seen in Section 4.4.2 was also seen here, indicating that actuation and allocation had no impact on steady-state error.

By looking at the dynamic error of the error plots, and the corresponding IAE plots, this is where the impact of actuation and allocation was seen. The vast majority of cases produced larger dynamic errors when actuation and allocation was implemented, while the IAE plots for the systems implemented here were either quite comparable to, or worse than, those of Chapter 4. This is as expected due to the required inclusion of an acceleration limiting process in order to avoid exciting nonlinearities due to actuator saturation.

In terms of actuation, the magnitude of force/torque provided by an individual actuator is limited and as such, the demand of an unrealistic force/torque will lead to actuator saturation and hence an unmodelled nonlinearity will be excited. To avoid this nonlinearity, and therefore justify the use of an unaltered control law, the desired acceleration from the guidance system was limited such that the desired force would also be limited. Hence, the nonlinearity is avoided. The compromise this imposes on the system is an extension to the time period the change in desired acceleration is applied, and therefore the time period of the error is also extended. This will then lead to the observed increase in IAE.

Even though this expected behaviour was observed, the vehicle was still able to track the desired trajectory satisfactorily, and therefore manoeuvrability was maintained. Furthermore, the superior performance of the BFCSMC over the NFCSMC observed in Chapter 4 was again seen here. With the inclusion of actuation and allocation into the simulation environment, the BFCSMC still outperforms the NFCSMC concerning trajectory tracking ability, as demonstrated through this simulation study.

Hence, owing to its simpler implementation costs in terms of computational efficiency, the BFCSMC is the superior choice for controlling an AUV compared to the NFCSMC.

Chapter 7

Summary, Conclusion and Future Work

7.1. Summary

This chapter will summarise the entire thesis, including the various controllers compared, the control allocation scheme presented, results from simulating these systems, and a brief discussion of these results.

As underwater vehicles, in particular AUVs, are becoming more and more prevalent as both research platforms and commercial equipment, the demands placed on the reliable operation of these tools are also increasing. The control system is just one component in the entire autonomy architecture of an AUV, yet is one of the most important. This thesis proposed two novel control systems that can be applied to underwater vehicles such that accuracy and robustness to both modelling uncertainty and external unknown disturbances are obtained. Furthermore, a novel control allocation scheme was also proposed that aims to maintain the high level of manoeuvrability that AUVs possess while increasing power efficiency by using the available actuators in an intelligent fashion.

In Chapter 2, an overview of vehicle modelling was conducted. Based on the work of Fossen [2, 3, 53], the various matrices that form the mathematical model of an underwater vehicle were examined. This was conducted such that a clear

understanding of the properties of each of these matrices was obtained. There were several reasons for conducting this thorough investigation. Firstly, a model was derived to represent the true plant model to be used within the simulation studies. This model was based on the REMUS 100 AUV with minor variations such that the manoeuvrability of the vehicle was increased. Secondly, a rigid and systematic mathematical approach was used to apply common assumptions to the complete model in order to derive several simplified models for control design purposes. The behaviour of these models was then validated against the behaviour of the plant model to verify the integrity of each simplified model. From the comparative study conducted, it was observed that the linearised model, Simplified Model 5, was unstable when excited by the particular set of inputs used. Based on this observation, Simplified Model 5 was omitted from the simulation study, and the four remaining nonlinear simplified models were deemed suitable for control design purposes.

Chapter 3 covered the core component of this thesis, namely the design of compensators for underwater vehicles. This chapter started with a review of different strategies employed for AUV control, looking at both advantages and disadvantages. Sliding mode control (SMC) is a control algorithm that has several advantages that makes it attractive to control engineers. These advantages include simplicity of implementation, robustness to modelling uncertainty, and the ability to design the controller without the need to linearise a nonlinear plant model. Considering these advantages, SMC was selected as the algorithm for the base of the novel strategies proposed in this thesis. An overview of SMC was conducted, covering both the concepts and the methodology for designing a sliding mode controller. This included a discussion of the undesired behaviour of chattering and common techniques for removing this behaviour from the system. Two existing control strategies utilising SMC implemented by Fossen, namely the uncoupled sliding mode controller (USMC) and the navigation frame coupled sliding mode controller (NFCSMC), were selected as possible candidates for comparing the novel strategies against, and hence the design of both the USMC and the NFCSMC was presented. The USMC and the NFCSMC both utilised simplified models that were derived and verified in Chapter 2. However, as the USMC was impractical to implement for highly manoeuvrable

AUVs, this controller was excluded from the simulation studies. This chapter concluded with the proposal of two novel strategies for controlling AUVs. The first novel strategy, namely the body frame uncoupled sliding mode controller (BFUSMC), utilised an uncoupled simplified model from Chapter 2. The BFUSMC was proposed as part of the algorithm development to demonstrate the importance of including coupling in the design of the control law. The second novel strategy, namely the body frame coupled sliding mode controller (BFCSMC), utilised a coupled simplified model from Chapter 2.

Based on the vehicle modelling of Chapter 2 in combination with the experimental work conducted by Prestero [54, 89], Chapter 4 presented a simulation study of the BFUSMC and the BFCSMC in comparison with the NFCSMC which was also presented in Chapter 3. This simulation study, which utilised an identical high fidelity model as the plant across all compensators and all cases, was used to assess the performance of these compensators under various operating conditions by observing the respective compensators trajectory tracking abilities through the simulation of three scenarios.

1. A simple trajectory where a single DoF was excited at a time was applied as input to the system. This revealed several attributes of both systems.
    - Firstly, all three systems have the ability to track such a trajectory.
    - Secondly, all systems exhibit similar behaviours, as all systems produced similar error plots.
    - Overall, it was observed that the BFCSMC performed the best in this situation, followed by the NFCSMC. The BFUSMC was less competitive due to the omission of the inherent coupling within the control law.
2. The tracking ability of a more complex trajectory comprising of coupled manoeuvring was examined. This trajectory was implemented by a line-of-sight (LOS) guidance system that took several waypoints as input and produced a set of desired states at each time step for the compensator to

follow. The observations from this simulation study can be summarised as follows.

- Uncoupled schemes are no longer good enough in these cases due to the omission of the inherent coupling within the control law.
- Steady-state errors were observed for both the BFCSMC and the NFCSMC when viewing the surge translational velocity error. The steady-state error experienced by the NFCSMC was slightly smaller compared to the BFCSMC.
- Dynamic errors were observed for both systems and these errors converged to steady-state quite quickly. As a general observation, the majority of the error plots presented showed that both systems had very similar characteristics with respect to dynamic error.
- The BFCSMC was able to better track the vertical zigzag manoeuvre conducted near the start of the simulation.

3. The final simulation scenario introduced an unknown time-varying water current disturbance into the simulation environment. As the demanded trajectory was similar to that of a raster scan mission used for oceanographic surveying, this mimicked a realistic scenario that a physical AUV could be commanded to execute. The following observations were made from this simulation study.
    - The effect of the current disturbance is evident, yet all systems are able to track the desired trajectory under these conditions.
    - In terms of performance, again uncoupled schemes are no longer good enough in these cases due to the omission of the inherent coupling within the control law.
    - Even though the performance of the remaining systems was similar, the BFCMSC performed better than the NFCSMC with respect to east position error and sway translational velocity error, particularly when a larger effect due to the current disturbance was observed.

Chapter 5 presented an overview of both actuation and control allocation as applied to underwater vehicles. This chapter started with an overview of the most common actuators employed for controlling underwater vehicles, including high power thrusters for forward propulsion and smaller tunnel thrusters for increased manoeuvrability, as well as control surfaces or control fins. This overview focussed on the advantages and disadvantages of each type of actuator. Following this was an introduction to control allocation, and a novel 2-stage control allocation scheme was proposed. This scheme was proposed to make full use of the power efficient control surfaces to realise as much of the generalised force asked of by the control system before employing assistance from the less efficient tunnel thrusters. This scheme therefore aimed to increase the power efficiency of the vehicle by only calling on the tunnel thrusters when absolutely needed. As the introduction of actuators will also introduce nonlinearities to the system through actuator saturation, a mechanism to alter the desired state from the guidance system such that no actuator reaches saturation was also included within this novel allocation scheme.

Finally, Chapter 6 extended the previous simulation study of Chapter 4 by including actuation and the novel 2-stage control allocation scheme proposed in Chapter 5. For consistency, two of the three cases used in Chapter 4 were also used in the simulation study presented in this chapter. These were the trajectory of Case 2 that utilised the LOS guidance system, and the trajectory of Case 3 that conducted a raster scan mission while under the influence of a water current disturbance. Due to the previously discussed limitations of the BFUSMC, specifically the omission of the inherent coupling within the control law, only the NFCSMC and the BFCSMC were included in the simulation studies of this chapter. The simulation studies of Case 2 and Case 3 within this chapter showed similar behaviour to those observed in Chapter 4 without actuation or allocation concerning convergence and steady-state error. The difference observed was associated with dynamic error, more specifically the magnitudes of these errors. In general, the systems simulated in Chapter 6 showed larger dynamic errors compared to the equivalent simulations of Chapter 4. This was expected behaviour, as the altering of the desired state to avoid the actuator saturation will have an impact on the overall performance of the system. Even with

these relatively pronounced dynamic errors, both systems were able to track the desired trajectories, and furthermore, the BFCSMC still outperformed the NFCSMC as was previously seen in Chapter 4.

7.2. Conclusions

Based on the results and discussions of Chapter 4 and Chapter 6, several conclusions can be drawn based on the findings from the simulation studies. These conclusions are related to the performance of the control systems concerning dynamic error, steady-state error and the handling of unknown disturbances. The effect of introducing actuation and allocation into the simulation environment was also investigated.

In all the cases examined within this simulation study, it was seen that all the compensators simulated were able to track the desired trajectory. Most notably was the fact that the BFUSMC could only perform in a limited capacity compared to the BFCSMC and the NFCSMC. For simple, low speed manoeuvring where the inherent coupling within the model is not excited, an uncoupled control scheme should perform adequately. However, as this simulation study demonstrated, a scheme that accommodates for this inherent coupling achieves a higher level of performance particularly for manoeuvring where this coupling is excited. Focusing only on the BFCSMC and the NFCSMC, the general observation was that the BFCSMC performed better than the NFCSMC. This was observed for the majority of the error plots, particularly with respect to dynamic error, as well as the IAE plots.

Concerning steady-state error, nearly all simulation studies not containing a disturbance demonstrated a steady-state error convergence to zero. The notable exception was the surge translational velocity for both the BFCSMC and the NFCSMC when Case 2 was observed. For both of these compensators, a small steady-state error was observed. However, the magnitude of this steady-state error was quite small.

Finally, by looking at both simulation studies conducted with a time-varying water current disturbance, it is seen that both systems react very similarly to this situation.

The effect of the current pushing the vehicle off course is evident, especially when the vehicle is attempting to travel in a straight line at constant speed. This is due to the compensator having no knowledge or ability to utilise any information regarding this water current or the effect this water current has on the hydrodynamics of the vehicle. These compensators function by observing the after-effect of the water current, via a change in position/attitude and velocity error, and then attempt to reduce this effect in the following control step. As previously noted, the behaviour of both compensators was very similar, yet it was observed that for the east position error and sway translational velocity error, the BFCSMC performed better than the NFCSMC, particularly when the magnitude of the corresponding water current was at its largest. Hence, from this simulation study, the better choice here is the BFCSMC.

By the introduction of actuation and allocation into the simulation environment, no impact was observed on steady-state error, yet a significant impact was observed on dynamic error. This lack of impact on steady-state error is due to the actuators being capable of delivering the required force/moment under steady-state conditions. However, when the vehicle is manoeuvring, different behaviour occurs. Each actuator is only able to deliver a limited amount of force. If too much force is asked of an actuator, it will saturate and therefore introduce an undesirable nonlinearity into the system. A process of limiting the desired acceleration to achievable levels, by use of vehicle and actuator dynamics, was introduced to avoid the system exciting these nonlinearities. The constraint imposed by this acceleration limiting scheme is that the commanded control action is now smaller, and hence the error is expanded out over a longer time period. This lead to the larger error observed. A clear observation made from this simulation study was that, even though the observed dynamic error was larger for the situations where actuation and allocation were included, the manoeuvrability of the vehicle was still maintained, as the system was still able to track the desired trajectory. Furthermore, the relative performances of the two overall control systems were retained, i.e., the BFCSMC was still superior to the NFCSMC.

Overall, it was observed that, from the simulation studies presented in this thesis, the BFCSMC is preferable to both the NFCSMC and the BFUSMC as the BFCSMC

performed equally well or better. Furthermore, as noted throughout Chapter 3, the computational load required for implementation of the BFCSMC is also significantly less compared to the NFCSMC, as there is no requirement of constantly transforming information from the navigation frame to the body frame. This leads to increased computational efficiency, and therefore an increase in the overall power efficiency of the vehicle. The BFUSMC performed in a limited capacity compared to both the NFCSMC and the BFCSMC, and therefore the BFCSMC is the most desired compensator of the three simulated here. If this compensator was also implemented along with an intelligent allocation scheme, such as the 2-stage scheme presented here, the overall power efficiency of the vehicle can further be increased which can lead to, for example, longer mission durations.

7.3. Recommendations for Future Work

Based on the research conducted here and the observation of the results obtained, the following recommendations for future work are made.

1. Improvement of simulation environment by including more accurate actuator models.

   The controllers designed in Chapter 3 assumed the generalised force determined by the control system was directly applied to the vehicle, i.e., perfect actuation. This is a valid assumption under the condition that the time constant of the vehicle is significantly larger compared to the time constants of the actuators [25], e.g., 10 times larger depending on both the vehicle and the actuator. To improve the accuracy of the simulation environment, dynamics due to, for example, inertia, slippage, and drag can be incorporated into these actuator models. This improved simulation environment would provide a mechanism for easily comparing the manoeuvrability performance of underactuated vehicles with overactuated vehicles as well as examining the effect the actuators have on the hydrodynamic coefficients of the vehicle mathematical model.

Research has been conducted into accurate thruster models across a wide range of operating points [90-92], and the incorporation of these dynamics into the simulation environment will result in an improvement of accuracy in the simulation environment.

The trade-off with this added accuracy is computational load. As the complexity of the models increase, so too does the processing power required to evaluate the model at each time-step. Depending on the extent of actuator modelling incorporated, a large increase in computational load could have the potential to yield a marginal increase in accuracy. In this particular case, it would therefore be impractical to include actuator dynamics.

2. Incorporation of water current estimates directly into controller.

   As can be seen in the models that all the compensators presented here are based on, there is no allowance for any knowledge of water current disturbances. The consequence of this can be seen in Case 3 presented in both Chapter 4 and Chapter 6.

   If knowledge of the water current can be introduced into the control law, then the potential exists to reduce the impact of this disturbance based on the accuracy of the water current estimate. Even though different control laws are proposed based on much simpler models, both Moreira and Soares [26] and Levedahl and Silverberg [67] incorporate fluid motion, through water current estimation or wave motion estimation, into the control law. Hence, a worthwhile exercise would be to investigate whether similar techniques could be incorporated into these control laws such that active water current compensation could be achieved. This would lead to knowledge of the hydrodynamic effect this water current has on the vehicle, and therefore actively compensate for it rather than observing the reaction to this disturbance before applying compensation.

3. Incorporation of navigation system to provide a navigation estimate.

   The simulation studies presented here assume that a perfect navigation solution exists, and is applied to both the guidance system and the control

system. With the introduction of a navigation system providing an estimate of the state of the vehicle, a more realistic simulation environment will be implemented. Therefore, the results generated will better represent the actual response of a vehicle when estimation error is incorporated.

4. Real-world testing and evaluation with a physical model.

   The results presented in this thesis were obtained from a high fidelity simulation environment. As such, this is only an approximation of the performance that would be observed with these compensators if a physical vehicle were to be released into open water and attempt to follow the same trajectories. As more accurately modelled real world effects are introduced to the simulator, the accuracy of the result will increase and so will the computational power required for running the simulator.

   Therefore, to obtain a truly reliable result, the only option is to implement the designed controllers on a physical vehicle and then observe the performance of the vehicle. In terms of implementing any of the compensators presented here on a physical vehicle, the following steps would need to be taken.

   a. Obtain a model of the physical vehicle that the controller is to be implemented on, including estimates of the accuracy of the parameters within this model.

   b. Conduct simple experimentation in a constrained environment under controlled conditions and observe the behaviour of the vehicle.

   c. Progress to sea trials where the vehicle can be observed under less constrained and controlled conditions.

7.4. Final Remark

Even though underwater vehicles have been in existence in one form or another for centuries, the potential of small, low cost, highly manoeuvrable autonomous underwater vehicles is only just beginning to be realised. Hence, it is the author's hope that this area of maritime engineering continues to grow as the technology becomes available to build these vehicles and implement the various algorithms

required to make an underwater vehicle truly autonomous. The world's oceans are largely unexplored, it is hoped that this research brings us one step closer to discovering what is really down there.

Appendix A

Vehicle Simulation Model

This appendix details the vehicle model used in the simulation studies.

A.1. Vehicle Parameters

The model is based on the REMUS 100 AUV, and the following parameters were obtained using experimental validation and verification by Prestero [54, 89].

Table A.1: REMUS 100 Kinematic and Hydrostatic Parameters (at Centre of Buoyancy)

Name	Symbol	Value	Unit
Mass	m	30.48	kg
Inertia	I_x	0.177	kg m^2
	I_y	3.45	kg m^2
	I_z	3.45	kg m^2
Centre of Gravity	x_g	0	m
	y_g	0	m
	z_g	0.0196	m
Weight	W	299.0088	N
Buoyancy	B	306	N
Centre of Buoyancy	x_b	0	m
	y_b	0	m
	z_b	0	m

Table A.2: REMUS 100 Added Mass and Nonlinear Damping Parameters

DOF	Added Mass			Nonlinear Damping		
	Name	**Value**	**Unit**	**Name**	**Value**	**Unit**
Surge	$X_{\dot{u}}$	0.93	kg	$X_{\|u\|u}$	3.9	kg/m
Sway	$Y_{\dot{v}}$	35.5	kg	$Y_{\|v\|v}$ $Y_{\|r\|r}$	1310 −0.632	kg/m kg m/rad^2
Heave	$Z_{\dot{w}}$	35.5	kg	$Z_{\|w\|w}$ $Z_{\|q\|q}$	131 0.632	kg/m kg m/rad^2
Roll	$K_{\dot{p}}$	0.0704	kg m^2/rad	$K_{\|p\|p}$	0.13	kg m^2/rad^2
Pitch	$M_{\dot{q}}$	4.88	kg m^2/rad	$M_{\|w\|w}$ $M_{\|q\|q}$	−3.18 188	kg kg m^2/rad^2
Yaw	$N_{\dot{r}}$	4.88	kg m^2/rad	$N_{\|v\|v}$ $N_{\|r\|r}$	3.18 94	kg kg m^2/rad^2

Table A.3: REMUS 100 Lift and Actuation Parameters

DOF	Lift			Actuation		
	Name	**Value**	**Unit**	**Name**	**Value**	**Unit**
Surge				X_{prop}	9.25	N
Sway	Y_{uv} Y_{ur}	28.6 −6.15	kg/m kg/rad	$Y_{uu\delta_r}$	9.64	kg/(m rad)
Heave	Z_{uw} Z_{uq}	28.6 6.15	kg/m kg/rad	$Z_{uu\delta_s}$	9.64	kg/(m rad)
Roll				K_{prop}	−0.543	Nm
Pitch	M_{uw} M_{uq}	10.6 3.93	kg/m kg/rad	$M_{uu\delta_s}$	−6.15	kg/rad
Yaw	N_{uv} N_{ur}	−10.6 3.93	kg/m kg/rad	$N_{uu\delta_r}$	−6.15	kg/rad

This thesis is aimed at controlling highly manoeuvrable AUVs. Therefore, the following modifications were made to the above vehicle model parameters in order

to realise a more manoeuvrable vehicle model. The main differences are due to the following:

1. Neutral buoyancy, i.e., both weight and buoyancy equal at 299.0088 N.
2. Centre of buoyancy coincident with the centre of gravity.
3. Increasing main thruster power from 9.25 N to 93.2 N based on a Tecnadyne Model 540 thruster that could easily be substituted onto the vehicle.
4. Four independent control surfaces instead of two pairs of conjoined control surfaces.
5. Introduction of four tunnel thrusters, each producing 42 N of force, based on the 70 mm IntegratedThruster produced by TSL Technology Ltd.

Table A.4: REMUS 100 Modified Parameters

Name	Parameter	Actual Value	Modified Value	Units
Buoyancy	B	306	299.0088	N
Centre of Gravity	x_g y_g z_g	0 0 0.0196	0 0 0	m m m
Main Propeller Force	X_{prop}	9.25	93.2	N
Top Rudder	$Y_{uu\delta_{tr}}$ $K_{uu\delta_{tr}}$ $N_{uu\delta_{tr}}$	Single Rudder: $Y_{uu\delta_r} = 9.64$ kg/(m rad) $N_{uu\delta_r} = -6.15$ kg/rad	4.82 0.241 −3.07	kg/(m rad) kg/rad kg/rad
Bottom Rudder	$Y_{uu\delta_{br}}$ $K_{uu\delta_{br}}$ $N_{uu\delta_{br}}$		4.82 −0.241 −3.07	kg/(m rad) kg/rad kg/rad
Left Stabiliser	$Z_{uu\delta_{ls}}$ $K_{uu\delta_{ls}}$ $M_{uu\delta_{ls}}$	Single Stabiliser: $Z_{uu\delta_s} = 9.64$ kg/(m rad) $M_{uu\delta_s} = -6.15$ kg/rad	4.82 −0.241 3.07	kg/(m rad) kg/rad kg/rad
Right Stabiliser	$Z_{uu\delta_{rs}}$ $K_{uu\delta_{rs}}$ $M_{uu\delta_{rs}}$		4.82 0.241 3.07	kg/(m rad) kg/rad kg/rad
Fore Horizontal Thruster	Y_{fh} N_{fh}	N/A	42 16.8	N Nm
Aft Horizontal Thruster	Y_{ah} N_{ah}	N/A	42 −16.8	N Nm
Fore Vertical Thruster	Z_{fv} M_{fv}	N/A	42 −18.9	N Nm
Aft Vertical Thruster	Z_{av} M_{av}	N/A	42 18.9	N Nm

A.1.1. Kinetic Equation

Combining the information contained in the above tables, the following matrices form the mathematical model of the vehicle used in the simulation environment.

$$\mathbf{M}_{\mathbf{RB}} = \begin{bmatrix} 30.48 & 0 & 0 & 0 & 0 & 0 \\ 0 & 30.48 & 0 & 0 & 0 & 0 \\ 0 & 0 & 30.48 & 0 & 0 & 0 \\ 0 & 0 & 0 & 0.177 & 0 & 0 \\ 0 & 0 & 0 & 0 & 3.45 & 0 \\ 0 & 0 & 0 & 0 & 0 & 3.45 \end{bmatrix}$$

$$\mathbf{M}_{\mathbf{A}} = \begin{bmatrix} 0.93 & 0 & 0 & 0 & 0 & 0 \\ 0 & 35.5 & 0 & 0 & 0 & 0 \\ 0 & 0 & 35.5 & 0 & 0 & 0 \\ 0 & 0 & 0 & 0.0704 & 0 & 0 \\ 0 & 0 & 0 & 0 & 4.88 & 0 \\ 0 & 0 & 0 & 0 & 0 & 4.88 \end{bmatrix}$$

$$\mathbf{C}_{\mathbf{RB}}\left(\mathbf{v}(t)\right) = \begin{bmatrix} 0 & 0 & 0 \\ 0 & 0 & 0 \\ 0 & 0 & 0 \\ 0 & 30.48w_b(t) & -30.48v_b(t) \\ -30.48w_b(t) & 0 & 30.48u_b(t) \\ 30.48v_b(t) & -30.48u_b(t) & 0 \end{bmatrix}$$

$$\begin{bmatrix} 0 & 30.48w_b(t) & -30.48v_b(t) \\ -30.48w_b(t) & 0 & 30.48u_b(t) \\ 30.48v_b(t) & -30.48u_b(t) & 0 \\ 0 & 3.45r_b(t) & -3.45q_b(t) \\ -3.45r_b(t) & 0 & 0.177p_b(t) \\ 3.45q_b(t) & -0.177p_b(t) & 0 \end{bmatrix}$$

$$\mathbf{C_A}\left(\mathbf{v_r}(t)\right)=\begin{bmatrix} 0 & 0 & 0 & 0 & 0 & 0 \\ 0 & 0 & 0 & 0 & 0 & 0 \\ 0 & 0 & 0 & 0 & 0 & 0 \\ 0 & 35.5w_r(t) & -35.5v_r(t) & 0 & 4.88r_r(t) & -4.88q_r(t) \\ -35.5w_r(t) & 0 & 0.93u_r(t) & -4.88r_r(t) & 0 & 0.0704p_r(t) \\ 35.5v_r(t) & -0.93u_r(t) & 0 & 4.88q_r(t) & -0.0704p_r(t) & 0 \end{bmatrix}$$

$$\mathbf{D}\left(\mathbf{v_r}(t)\right)=\begin{bmatrix} 3.9|u_r(t)| & 0 & 0 & 0 & 0 & 0 \\ 0 & 1310|v_r(t)| & 0 & 0 & 0 & -0.632|r_r(t)| \\ 0 & 0 & 131|w_r(t)| & 0 & 0.632|q_r(t)| & 0 \\ 0 & 0 & 0 & 0.13|p_r(t)| & 0 & 0 \\ 0 & 0 & -3.18|w_r(t)| & 0 & 188|q_r(t)| & 0 \\ 0 & 3.18|v_r(t)| & 0 & 0 & 0 & 94|r_r(t)| \end{bmatrix}$$

$$\mathbf{L}\left(\mathbf{v_r}(t)\right)=\begin{bmatrix} 0 & 0 & 0 & 0 & 0 & 0 \\ 0 & 28.6u_r(t) & 0 & 0 & 0 & -6.15u_r(t) \\ 0 & 0 & 28.6u_r(t) & 0 & 6.15u_r(t) & 0 \\ 0 & 0 & 0 & 0 & 0 & 0 \\ 0 & 0 & 10.6u_r(t) & 0 & 3.93u_r(t) & 0 \\ 0 & -10.6u_r(t) & 0 & 0 & 0 & 3.93u_r(t) \end{bmatrix}$$

$$\mathbf{g}\left(\boldsymbol{\eta}_\mathbf{n}(t)\right)=\begin{bmatrix} 0 & 0 & 0 & 0 & 0 & 0 \end{bmatrix}^T$$

The method for linearising the nonlinear vehicle model was shown in Section 2.3.5. This method requires the selection of a linearisation point at which to obtain the linearised model. The following matrices correspond to an operating point of the vehicle being 10 m below the surface of the water and travelling in a straight line at a constant surge velocity of 1 m s^{-1}.

$$\boldsymbol{\eta}_{\mathbf{n}}^{0} = \begin{bmatrix} 0 & 0 & 10 & 0 & 0 & 0 \end{bmatrix}^{T}$$

$$\mathbf{v}_{\mathbf{b}}^{0} = \begin{bmatrix} 1 & 0 & 0 & 0 & 0 & 0 \end{bmatrix}^{T}$$

$$\boldsymbol{\tau}^{0} = \begin{bmatrix} 3.9 & 0 & 0 & 0 & 0 & 0 \end{bmatrix}^{T}$$

Linearising the plant model about this linearisation point yields the following matrices of the state-space representation:

$$\mathbf{A} = \begin{bmatrix}
0 & 0 & 0 & 0 & 0 & 0 & 1 & 0 & 0 & 0 & 0 & 0 \\
0 & 0 & 0 & 0 & 0 & 1 & 0 & 1 & 0 & 0 & 0 & 0 \\
0 & 0 & 0 & 0 & -1 & 0 & 0 & 0 & 1 & 0 & 0 & 0 \\
0 & 0 & 0 & 0 & 0 & 0 & 0 & 0 & 0 & 1 & 0 & 0 \\
0 & 0 & 0 & 0 & 0 & 0 & 0 & 0 & 0 & 0 & 1 & 0 \\
0 & 0 & 0 & 0 & 0 & 0 & 0 & 0 & 0 & 0 & 0 & 1 \\
0 & 0 & 0 & 0 & 0 & 0 & -0.25591 & 0 & 0 & 0 & 0 & 0 \\
0 & 0 & 0 & 0 & 0 & 0 & 0 & -0.93832 & 0 & 0 & 0 & -0.82874 \\
0 & 0 & 0 & 0 & 0 & 0 & 0 & 0 & -0.93832 & 0 & 0.82874 & 0 \\
0 & 0 & 0 & 0 & 0 & 0 & 0 & 0 & 0 & 0 & 0 & 0 \\
0 & 0 & 0 & 0 & 0 & 0 & 0 & 0 & 6.9478 & 0 & -1.1391 & 0 \\
0 & 0 & 0 & 0 & 0 & 0 & 0 & -6.9478 & 0 & 0 & 0 & -1.1391
\end{bmatrix}$$

$$\mathbf{B} = \begin{bmatrix}
0 & 0 & 0 & 0 & 0 & 0 \\
0 & 0 & 0 & 0 & 0 & 0 \\
0 & 0 & 0 & 0 & 0 & 0 \\
0 & 0 & 0 & 0 & 0 & 0 \\
0 & 0 & 0 & 0 & 0 & 0 \\
0 & 0 & 0 & 0 & 0 & 0 \\
0.032808 & 0 & 0 & 0 & 0 & 0 \\
0 & 0.032808 & 0 & 0 & 0 & 0 \\
0 & 0 & 0.032808 & 0 & 0 & 0 \\
0 & 0 & 0 & 5.6497 & 0 & 0 \\
0 & 0 & 0 & 0 & 0.28986 & 0 \\
0 & 0 & 0 & 0 & 0 & 0.28986
\end{bmatrix}$$

$$\mathbf{C} = \mathbf{I}_{12\times 12}$$

$$\mathbf{D} = \mathbf{0}_{12\times 6}$$

A.1.2. Actuator Forces and Moments

When constructing the actuator configuration matrix and the force coefficient matrix for the actuators as seen in Table A.4, the following table details the position of the actuator with respect to the origin of the body frame and force coefficient for each actuator.

Table A.5: REMUS 100 Modified Actuators

Actuator	**Position (m)**	**Force Coefficient (N)**
Main Thruster	$[-0.727 \quad 0 \quad 0]^T$	93.2
Bottom Rudder	$[-0.637 \quad 0 \quad 0.05]^T$	4.82
Right Stabiliser	$[-0.637 \quad 0.05 \quad 0]^T$	4.82
Top Rudder	$[-0.637 \quad 0 \quad -0.05]^T$	4.82
Left Stabiliser	$[-0.637 \quad -0.05 \quad 0]^T$	4.82
Fore Horizontal Thruster	$[0.4 \quad 0 \quad 0]^T$	42
Aft Vertical Thruster	$[-0.45 \quad 0 \quad 0]^T$	42
Aft Horizontal Thruster	$[-0.4 \quad 0 \quad 0]^T$	42
Fore Vertical Thruster	$[0.45 \quad 0 \quad 0]^T$	42

For the simple control allocation method as presented in Section 5.3.1, the actuator configuration matrix and force coefficient matrix are as seen below.

$$\mathbf{T} = \begin{bmatrix} 1 & 0 & 0 & 0 & 0 & 0 & 0 & 0 & 0 \\ 0 & 1 & 0 & 1 & 0 & 1 & 0 & 1 & 0 \\ 0 & 0 & 1 & 0 & 1 & 0 & 1 & 0 & 1 \\ 0 & -0.05 & 0.05 & 0.05 & -0.05 & 0 & 0 & 0 & 0 \\ 0 & 0 & 0.637 & 0 & 0.637 & 0 & 0.45 & 0 & -0.45 \\ 0 & -0.637 & 0 & -0.637 & 0 & 0.4 & 0 & -0.4 & 0 \end{bmatrix}$$

$$\mathbf{K}\left(u_r(t)\right)=\begin{bmatrix} 93.2 & 0 & 0 & 0 & 0 & 0 & 0 & 0 & 0 \\ 0 & 4.82u_r^2(t) & 0 & 0 & 0 & 0 & 0 & 0 & 0 \\ 0 & 0 & 4.82u_r^2(t) & 0 & 0 & 0 & 0 & 0 & 0 \\ 0 & 0 & 0 & 4.82u_r^2(t) & 0 & 0 & 0 & 0 & 0 \\ 0 & 0 & 0 & 0 & 4.82u_r^2(t) & 0 & 0 & 0 & 0 \\ 0 & 0 & 0 & 0 & 0 & 42 & 0 & 0 & 0 \\ 0 & 0 & 0 & 0 & 0 & 0 & 42 & 0 & 0 \\ 0 & 0 & 0 & 0 & 0 & 0 & 0 & 42 & 0 \\ 0 & 0 & 0 & 0 & 0 & 0 & 0 & 0 & 42 \end{bmatrix}$$

For the 2-stage allocation method as presented in Section 5.3.2, the actuator configuration matrices and force coefficient matrices are as seen below.

$$\mathbf{T_1}=\begin{bmatrix} 1 & 0 & 0 & 0 & 0 \\ 0 & 1 & 0 & 1 & 0 \\ 0 & 0 & 1 & 0 & 1 \\ 0 & -0.05 & 0.05 & 0.05 & -0.05 \\ 0 & 0 & 0.637 & 0 & 0.637 \\ 0 & -0.637 & 0 & -0.637 & 0 \end{bmatrix}$$

$$\mathbf{T_2}=\begin{bmatrix} 0 & 0 & 0 & 0 \\ 1 & 0 & 1 & 0 \\ 0 & 1 & 0 & 1 \\ 0 & 0 & 0 & 0 \\ 0 & 0.45 & 0 & -0.45 \\ 0.4 & 0 & -0.4 & 0 \end{bmatrix}$$

$$\mathbf{K_1}\left(u_r(t)\right)=\begin{bmatrix} 93.2 & 0 & 0 & 0 & 0 \\ 0 & 4.82u_r^2(t) & 0 & 0 & 0 \\ 0 & 0 & 4.82u_r^2(t) & 0 & 0 \\ 0 & 0 & 0 & 4.82u_r^2(t) & 0 \\ 0 & 0 & 0 & 0 & 4.82u_r^2(t) \end{bmatrix}$$

$$\mathbf{K_2}=\begin{bmatrix} 42 & 0 & 0 & 0 \\ 0 & 42 & 0 & 0 \\ 0 & 0 & 42 & 0 \\ 0 & 0 & 0 & 42 \end{bmatrix}$$

Appendix B

Line-of-Sight Guidance

The role of guidance within the autonomy structure of an AUV is to determine the desired state of the vehicle, based on the current state of the vehicle, such that the vehicle successfully completes its mission. Due to the limited computing power and sensory abilities of small AUVs, the guidance system within such a vehicle is usually quite rudimentary, requiring an *a priori* knowledge of the desired path to follow.

B.1. Waypoint Guidance

One very simple method of performing 2D guidance is for the vehicle to aim at and head towards the next waypoint. In this case, the next waypoint is the target location, and the guidance system calculates the desired heading based on the vehicle location and this target location [3]. Under the condition that the magnitude of the water current disturbance is less than the maximum speed of the vehicle, the vehicle will always move towards the next waypoint. Once the vehicle lies within a predetermined distance from the target location, known as the acceptance radius, the guidance system shifts its attention to the following waypoint.

This method works well under the condition of little or no water current disturbance. However, if the water current does not meet this condition, the vehicle can severely diverge from the desired path, especially if the target location is a large distance from the vehicle and the water current is inducing a sway motion on the vehicle.

B.2. Line-of-Sight Guidance

The limitation of the previously described waypoint guidance is due to the vehicle always targeting the next waypoint. An improvement over this system is for the vehicle to target a location somewhere along the line formed between the previous and next waypoints [3]. Therefore, the vehicle will remain within a predetermined distance, known as the sight radius, of the trajectory formed from linking all the waypoints together. By further incorporating the desired translational velocity, the guidance system can calculate the next position, and hence next desired state, of the vehicle for the next time step. This is the method used for guidance within this thesis.

For ease of visualisation, a 2D example of this LOS guidance is seen in Figure B.1. The initial position of the vehicle is the coordinates (0,0). Here, the black line defines the trajectory formed by linking the desired waypoints together, while the grey circle defines the acceptance radius. Once the vehicle lies within this acceptance radius, the guidance system shifts its attention to the following waypoint.

The blue circle forms the sight radius, which defines how far away the guidance system looks when deciding what location to face. The guidance system determines the target location by where the desired trajectory, the black line, intersects the sight

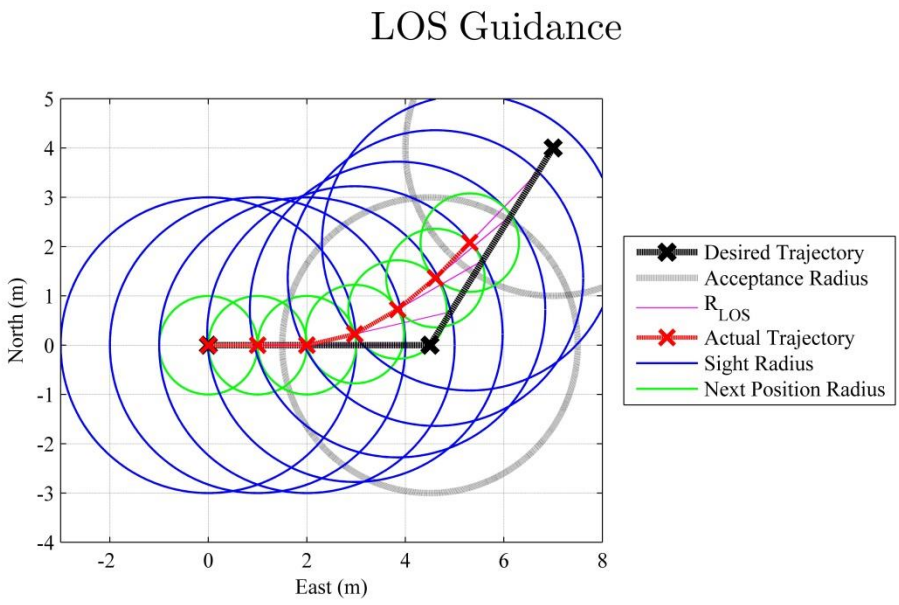

Figure B.1: LOS Guidance

radius, the blue circle.

The magenta line represents the vector from the vehicle to the target location, labelled here as R_{LOS}. By using the desired translational velocity of the vehicle and the sampling period of the guidance system, the next position radius can be determined. The green circles represent the next position radius in Figure B.. The guidance system determines the next position of the vehicle by where R_{LOS}, the magenta line, intersects the next position radius, the green circle.

Overall, the red line represents the actual trajectory travelled by the vehicle. It is obvious from Figure B. that the vehicle does not actually pass through each waypoint. This is because the acceptance radius determines the upper limit on how close the vehicle is required to get to each waypoint before the guidance system shifts its attention to the following waypoint. However, the vehicle can get closer to the waypoint than this acceptance radius, depending on where the following waypoint is located. This is evident from Figure B. when the vehicle starts following the second part of the desired trajectory.

In this example, a very simple case of 2D guidance is seen. The basic operation of this guidance system consists of solving a series of line circle intersect problems to determine the actual trajectory for the vehicle to follow. To extend this example into 3D space is relatively straightforward. Instead of solving line circle intersects, it is now a matter of solving line sphere intersect problems to determine the actual trajectory for the vehicle to follow.

Bibliography

[1] NOAA, *How much of the ocean have we explored?* [Accessed: 28th November, 2012]. Available: http://oceanservice.noaa.gov/facts/exploration.html

[2] T. I. Fossen, *Guidance and Control of Ocean Vehicles*. 1994, Chichester, England: John Wiley & Sons, Inc. 494 p.

[3] T. I. Fossen, *Marine Control Systems: Guidance, Navigation and Control of Ships, Rigs and Underwater Vehicles*. 1st ed. 2002, Trondheim, Norway: Marine Cybernetics. 570 p.

[4] WHOI, *Remotely Operated Vehicle Jason/Medea*. [Accessed: 26th November, 2012]. Available: http://www.whoi.edu/ndsfVehicles/Jason/

[5] M. Watanabe, S. Tashiro, and H. Momma, *Loss of the Full Ocean Depth ROV Kaiko - Part 3: The Cause of Secondary Cable Fracture*. Presented at *14th International Offshore and Polar Engineering Conference*. 2004. Toulon, France.

[6] AUVAC, *Mary Ann and Ginger - AUVAC*. [Accessed: 30th November, 2012]. Available: http://auvac.org/configurations/view/115

[7] Teledyne Gavia, *GAVIA | Autonomous Underwater Vehicles | Technical Specifications*. [Accessed: 1st December, 2012]. Available: http://www.gavia.is/Products/Gavia-Technology/Technical-Specifications/

[8] P. B. Boyle and J. J. Cech Jr., *Fishes : An Introduction to Ichthyology*. 5th ed. 2004, Upper Saddle River, NJ: Prentice Hall, Inc.

[9] Subsea World News, *Subsea World News - Iceland Underwater Robots to Join Russian Navy Fleet*. [Accessed: 1st December, 2012]. Available: http://subseaworldnews.com/2012/02/28/iceland-underwater-robots-to-join-russian-navy-fleet/

[10] Teledyne Gavia, *GAVIA | Autonomous Underwater Vehicles | Gavia Technology*. [Accessed: 26th November, 2012]. Available: http://www.gavia.is/Products/Gavia-Technology/

[11] Teledyne Gavis, *GAVIA | Autonomous Underwater Vehicles | Payloads*. [Accessed: 1st December, 2012]. Available: http://www.gavia.is/Products/Gavia-Technology/Payloads/

[12] L. R. Fodrea, *Obstacle Avoidance Control for the REMUS Autonomous Underwater Vehicle*. Master of Science in Mechanical Engineering, Naval Postgraduate School, Monterey: 2002. 77 p.

[13] E. W. McGookin, D. J. Murray-Smith, Y. Li, and T. I. Fossen, *Ship Steering Control System Optimisation Using Genetic Algorithms*. Control Engineering Practice, 2000, **8**: p. 429-443.

[14] T. I. Fossen, M. Breivik, and R. Skjetne, *Line-of-Sight Path Following of Underactuated Marine Craft*. Presented at *2003 IFAC Conference on Maneuvering and Control of Marine Craft*. 2003. Girona, Spain.

[15] J. E. Refsnes and A. J. Sørensen, *Design of Control System of Torpedo Shaped ROV with Experimental Results*. Presented at *MTS/IEEE Oceans*. 2004. Kobe, Japan.

[16] Encylcopedia Britannica Inc., *dead reckoning (navigation) -- Britannica Online Encyclopedia*. [Accessed: 25th February, 2013]. Available: http://www.britannica.com/EBchecked/topic/154249/dead-reckoning

[17] A. J. Kapaldo, *Gyroscope Calibration and Dead Reckoning for an Autonomous Underwater Vehicle*. Master of Science in Electrical Engineering, Virginia Polytechnic Institute and State University, Blacksburg: 2005. 63 p.

[18] G. Welch and G. Bishop, *An Introduction to the Kalman Filter*. 2004. University of North Carolina: Chapel Hill. 16 p.

[19] A. J. Healey, E. P. An, and D. B. Marco, *On Line Compensation of Heading Sensor Bias for Low Cost AUVs*. Presented at *IEEE Workshop on Autonomous Underwater Vehicles*. 1998. Cambridge, MA, USA.

[20] A. Lammas, K. Sammut, and F. He, *Improving Navigational Accuracy for AUVs using the MAPR Particle Filter*. Presented at *MTS/IEEE Oceans*. 2008. Quebec City, QC, Canada.

[21] A. Lammas, K. Sammut, and F. He, *6-DoF Navigation Systems for Autonomous Underwater Vehicles*, in *Mobile Robots Navigation*. A. Barrera, Editor. 2010. InTech: Vukovar, Croatia. p. 457-483.

[22] C. L. Phillips and R. D. Harbor, *Feedback Control Systems*. 4th ed. 2000, Upper Saddle River, NJ: Prentice Hall, Inc.

[23] M. Santhakumar and T. Asokan, *Coupled, Non-Linear Control System Design for Autonomous Underwater Vehicle (AUV)*. Presented at *10th International Conference on Control, Automation, Robotics and Vision*. 2008. Hanoi, Vietnam.

[24] G. Xia, L. Tang, F. Guo, Q. Chen, and J. Leng, *Design of a Hybrid Controller for Heading Control of an Autonomous Underwater Vehicle*. Presented at *IEEE International Conference on Industrial Technology*. 2009. Gippsland, Australia.

[25] B. Ferreira, M. Pinto, A. Matos, and N. Cruz, *Control of the MARES Autonomous Underwater Vehicle*. Presented at *MTS/IEEE Oceans*. 2009. Biloxi, MS, USA.

[26] L. Moreira and C. G. Soares, *H_2 and H_∞ Designs For Diving And Course Control Of An Autonomous Underwater Vehicle In Presence Of Waves*. IEEE Journal of Oceanic Engineering, 2008, **33**(2): p. 69-88.

[27] J.-H. Li and P.-M. Lee, *Design of an Adaptive Nonlinear Controller for Depth Control of an Autonomous Underwater Vehicle*. Ocean Engineering, 2005, **32**: p. 2165-2181.

[28] J. Guo, F. C. Chiu, and C.-C. Wang, *Adaptive Control of an Autonomous Underwater Vehicle Testbed Using Neural Networks*. Presented at *MTS/IEEE Oceans*. 1995. San Diego, CA, USA.

[29] P.-H. Nguyen and Y.-C. Jung, *Control of Autonomous Underwater Vehicles using Adaptive Neural Network*. Presented at *IEEE International Conference on Advanced Technologies for Communications*. 2009. Haiphong, Vietnam.

[30] H.-N. Yu, J.-M. Zhao, and Y.-R. Xu, *Tuning of Neuro-Fuzzy Controller by Real-Coded Genetic Algorithm with Application to an Autonomous Underwater Vehicle Control System*. Presented at *IEEE International Conference on Machine Learning and Cybernetics*. 2002. Beijing, China.

[31] B. Sun, D. Zhu, and W. Li, *An Integrated Backstepping and Sliding Mode Tracking Control Algorithm for Unmanned Underwater Vehicles*. Presented at *International Conference on Control*. 2012. Cardiff, UK.

[32] P. A. DeBitetto, *Fuzzy Logic for Depth Control of Unmanned Undersea Vehicles*. IEEE Journal of Oceanic Engineering, 1995, **20**(3): p. 242-248.

[33] S. M. Smith, G. J. S. Rae, D. T. Anderson, and A. M. Shein, *Fuzzy Logic Control of an Autonomous Underwater Vehicle*. Control Engineering Practice, 1994, **2**(2): p. 321-331.

[34] A. Faruq, S. S. Abdullah, M. Fauzi, and S. Nor, *Optimization of Depth Control for Unmanned Underwater Vehicle Using Surrogate Modeling Technique*. Presented at *4th International Conference on Modeling, Simulation and Applied Optimization*. 2011. Kuala Lumpur, Malaysia.

[35] J.-S. Wang and C. S. G. Lee, *Efficient Neuro-Fuzzy Control Systems for Autonomous Underwater Vehicle Control*. Presented at *IEEE International Conference on Robotics and Automation*. 2001. Seoul, Republic of Korea.

[36] J.-S. Wang, C. S. G. Lee, and J. Yuh, *Self-Adaptive Neuro-Fuzzy Systems with Fast Parameter Learning for Autonomous Underwater Vehicle Control*. Presented at *IEEE International Conference on Robotics and Automation*. 2000. San Francisco, CA, USA.

[37] J. Vieira, F. Morgado Dias, and A. Mota, *Neuro-Fuzzy Systems: A Survey*. Presented at *5th WSEAS International Conference on Neural Networks and Applications*. 2004. Udine, Italy.

[38] J. Xu and M. Zhang, *Neural Network Modeling and Generalized Predictive Control for an Autonomous Underwater Vehicle*. Presented at *6th IEEE International Conference on Industrial Informatics*. 2008. Daejeon, Republic of Korea.

[39] L. Medagoda and S. B. Williams, *Model Predictive Control of an Autonomous Underwater Vehicle in an in situ Estimated Water Current Profile*. Presented at *IEEE Oceans*. 2012. Yeosu, Republic of Korea.

[40] E. Y. Hong, H. G. Soon, and M. Chitre, *Depth control of an autonomous underwater vehicle, STARFISH*. Presented at *IEEE Oceans*. 2010. Sydney, Australia.

[41] A. Lebedev and V. Filaretov, *Multi-Channel Variable Structure System for the Control of Autonomous Underwater Vehicle*. Presented at *International Conference on Mechatronics and Automation*. 2007. Harbin, China.

[42] D. B. Marco and A. J. Healey, *Command, Control, and Navigation Experimental Results with the NPS ARIES AUV*. IEEE Journal of Oceanic Engineering, 2001, **26**(4): p. 466-476.

[43] M. E. Jackson and Y. B. Shtessel, *Sliding Mode Thermal Control for Space Station Furnace Facility*. IEEE Transactions on Control Systems Technology, 1998, **6**(5): p. 612-622.

[44] S. Jezernik, P. Inderbitzin, T. Keller, and R. Riener, *Sliding Mode Control of Functional Electrical Stimulation for Knee Joint Angle Tracking*. Presented at *7th International Workshop on Functional Electrical Stimulation*. 2001. Vienna, Austria.

[45] N. Yagiz and I. Yuksek, *Sliding Mode Control of Active Suspensions for a Full Vehicle Model*. International Journal of Vehicle Design, 2001, **23**(2/3): p. 264-276.

[46] H. Bang, C.-K. Ha, and J. H. Kim, *Flexible Spacecraft Attitude Maneuver by Application of Sliding Mode Control*. Acta Astronautica, 2005, **57**: p. 841-850.

[47] V. Utkin, J. Guldner, and J. Shi, *Sliding Mode Control in Electromechanical Systems*. 1st ed. 1999, London, England: Taylor & Francis. 325 p.

[48] J. S. Riedel and A. J. Healey, *Shallow Water Station Keeping of AUVs Using Multi-sensor Fusion for Wave Disturbance Prediction and Compensation*. Presented at *IEEE Oceans*. 1998. Nice, France.

[49] T. I. Fossen, T. A. Johansen, and T. Perez, *A Survey of Control Allocation Methods for Underwater Vehicles*, in *Underwater Vehicles*. A. V. Inzartsev, Editor. 2009. InTech: Vienna, Austria. p. 109-128.

[50] A. M. Lyapunov, *Obshchaya Zadacha ob Ustoychivosti Dvizheniya (in Russian)*. Mathematical Society of Kharkov, 1892: p.

[51] I. Barbălat, *Systèmes d'Équations Différentielles d'Oscillations Non Linéaires*. Revue Roumaine de Mathématiques Pures et Appliquées, 1959, **4**(2): p. 267-270.

[52] J.-J. E. Slotine and W. Li, *Applied Nonlinear Control*. 1991, Englewood Cliffs, NJ: Prentice Hall. 473 p.

[53] T. I. Fossen, *Nonlinear Modelling and Control of Underwater Vehicles*. Doctor of Philosophy in Engineering Cybernetics, Norwegian Institute of Technology, Trondheim: 1991. 185 p.

[54] T. Prestero, *Verification of a Six-Degree of Freedom Simulation Model for the REMUS Autonomous Underwater Vehicle*. Master of Science in Ocean Engineering and Master of Science in Mechanical Engineering, Massachusetts Institute of Technology and the Woods Hole Oceanographic Institution, Cambridge and Woods Hole: 2001. 128 p.

[55] B.-H. Jun, J.-Y. Park, F.-Y. Lee, P.-M. Lee, C.-M. Lee, K. Kim, Y.-K. Lim, and J.-H. Oh, *Development of the AUV 'ISiMI' and a Free Running Test in an Ocean Engineering Basin*. Ocean Engineering, 2009, **36**: p. 13.

[56] J. Yuh, M. E. West, and P. M. Lee, *An Autonomous Underwater Vehicle Control with a Non-Regressor Based Algorithm*. Presented at *IEEE International Conference on Robotics and Automation*. 2001. Seoul, Republic of Korea.

[57] G. Evers, J. H. A. M. Vervoort, R. C. Engelaar, H. Nijmeijer, A. G. de Jager, X. Q. Chen, and W. H. Wang, *Modeling and Simulated Control of an Under Actuated Autonomous Underwater Vehicle*. Presented at *IEEE International Conference on Control and Automation*. 2009. Christchurch, New Zealand.

[58] A. Lammas, *Improving Navigation Estimates for Underwater Vehicles Using the MAPR Particle Filter*. Doctor of Philosophy (Engineering), Flinders University of South Australia, Adelaide, Australia: 2012. 307 p.

[59] H. Bø, *Hydrodynamic Estimation and Identification*. Master of Science, Norwegian University of Science and Technology, Trondheim: 2004. 164 p.

[60] H. Pan and M. Xin, *Depth Control of Autonomous Underwater Vehicles Using Indirect Robust Control Method*. Presented at *American Control Conference*. 2012. Montréal, QC, Canada.

[61] A. Lammas, K. Sammut, and F. He, *MAPR Particle Filter for AUV Sensor Fusion*. Presented at *Society of Underwater Technology Annual Conference*. 2009. Perth, Australia.

[62] B.-H. Jeon, P.-M. Lee, J.-H. Li, S.-W. Hong, Y.-G. Kim, and J. Lee, *Multivariable Optimal Control of an Autonomous Underwater Vehicle for Steering and Diving Control in Variable Speed*. Presented at *IEEE Oceans*. 2003. San Diego, CA, USA.

[63] S. M. Zanoli and G. Conte, *Remotely Operated Vehicle Depth Control*. Control Engineering Practice, 2003, **11**: p. 453-459.

[64] X. Bian, Y. Qu, Z. Yan, and W. Zhang, *Nonlinear Feedback Control for Trajectory Tracking of an Unmanned Underwater Vehicle*. Presented at *IEEE International Conference on Information and Automation*. 2010. Harbin, China.

[65] J. Che, J. Cernio, J. Prainito, M. Zuba, C. Cao, J.-H. Cui, and K. Kazerounian, *An Advanced Autonomous Underwater Vehicle Design and Control Strategy*. Presented at *IEEE Oceans*. 2012. Hampton Road, VA , USA.

[66] U. D. Gül and K. Leblebicioğlu, *Autonomous Underwater Vehicle Modelling, Control, Motion and Mission Planning Design*. Presented at *20th Signal Processing and Communications Applications Converence*. 2012. Muğla, Turkey.

[67] B. E. Levedahl and L. Silverberg, *Control of Underwater Vehicles in Full Unsteady Flow*. IEEE Journal of Oceanic Engineering, 2009, **34**(4): p. 656-668.

[68] F. T. Mrad and A. S. Majdalani, *Adequate Six Degree of Freedom Control of Astable Unmanned Underwater Vehicles*. Presented at *IEEE International Symposium on Industrial Electronics*. 2002. L'Aquila, Italy.

[69] A. Ross, T. I. Fossen, and T. A. Johansen, *Identification of Underwater Vehicle Hydrodynamic Coefficients Using Free Decay Tests*. Presented at *IFAC Conference on Control Applications in Marine Systems*. 2004. Ancona, Italy.

[70] F. T. Mrad and A. S. Majdalani, *Composite Adaptive Control of Astable UUVs*. IEEE Journal of Oceanic Engineering, 2003, **28**(2): p. 303-307.

[71] B. Jalving, *The NDRE-AUV Flight Control System*. IEEE Journal of Oceanic Engineering, 1994, **19**(4): p. 497-501.

[72] S. Miyamoto, T. Aoki, T. Maeda, K. Hirokawa, T. Ichikawa, T. Saitou, H. Kobayashi, E. Kobayashi, and S. Iwasaki, *Maneuvering Control System Design for Autonomous Underwater Vehicle*. Presented at *MTS/IEEE Oceans*. 2001. Honolulu, HI, USA.

[73] G. Bartolini and A. Ferrara, *Multi-Input Sliding Mode Control of a Class of Uncertain Nonlinear Systems*. IEEE Transactions on Automatic Control, 1996, **41**(11): p. 1662-1665.

[74] C. Edwards and S. K. Spurgeon, *Sliding Mode Control: Theory and Applications*. 1998, London, England: Taylor & Francis Ltd. 237 p.

[75] H. K. Khalil, *Nonlinear Systems*. 3rd ed. 2002, Upper Saddle River, NJ: Prentice Hall, Inc. 750 p.

[76] G. Song, Y. Wang, L. Cai, and R. W. Longman, *A Sliding-Mode Based Smooth Adaptive Robust Controller for Friction Compensation*. Presented at *American Control Conference*. 1995. Seattle, WA, USA.

[77] G. Song, L. Cai, Y. Wang, and R. W. Longman, *A Sliding-Mode Based Smooth Adaptive Robust Controller for Friction Compensation*. International Journal of Robust and Nonlinear Control, 1998, **8**: p. 725-739.

[78] T. I. Fossen and S. I. Sagatun, *Adaptive Control of Nonlinear Underwater Robotic Systems*. Presented at *International Conference on Robotics and Automation*. 1991. Sacramento, CA, USA.

[79] J.-J. E. Slotine and M. D. Di Benedetto, *Hamiltonian Adaptive Control of Spacecraft*. IEEE Transactions on Automatic Control, 1990, **35**(7): p. 848-852.

[80] H. H. Choi, *LMI-Based Sliding Surface Design for Integral Sliding Mode Control of Mismatched Uncertain Systems*. IEEE Transactions on Automatic Control, 2007, **52**(4): p. 736-742.

[81] M.-C. Fang and J.-H. Luo, *The Nonlinear Hydrodynamic Model for Simulating a Ship Steering in Waves with Autopilot System*. Ocean Engineering, 2005, **32**: p. 1486-1502.

[82] J. Kim, K. Kim, H. S. Choi, W. Seong, and K.-Y. Lee, *Estimation of Hydrodynamic Coefficients for an AUV Using Nonlinear Observers*. IEEE Journal of Oceanic Engineering, 2002, **27**(4): p. 830-840.

[83] E. Alfardo-Cid, E. W. McGookin, D. J. Murray-Smith, and T. I. Fossen, *Genetic Algorithms Optimisation of Decoupled Sliding Mode Controllers: Simulated and Real Results*. Control Engineering Practice, 2005, **13**: p. 739-748.

[84] Talk Aviation, *Talk Aviation - Basic Propeller Principles*. [Accessed: 4th December, 2012]. Available: http://talkaviation.com/content/basic-propeller-principles-223/

[85] A. Palmer, G. E. Hearn, and P. Stevenson, *Experimental Testing of an Autonomous Underwater Vehicle with Tunnel Thrusters*. Presented at *First International Symposium on Marine Propulsors*. 2009. Trondheim, Norway.

[86] R. Prasnath Kumar, S. Sarath Babu, Y. Srilekha, C. S. Kumar, D. Sen, and A. Dasgupta, *Test-Bed for Navigation and Control of a Thruster Based AUV*. Presented at *IEEE Oceans*. 2006. Singapore, Republic of Singapore.

[87] L. N. Trefethen and D. Bau III, *Numerical Linear Algebra*. 1997, Philadelphia, PA, USA: Society for Industrial and Applied Mathematics. 361 p.

[88] O. A. Yakimenko and S. P. Kragelund, *Real-Time Optimal Guidance and Obstacle Avoidance for UMVs*, in *Autonomous Underwater Vehicles*. N. Cruz, Editor. 2011. InTech: Rijeka, Croatia. p. 67-98.

[89] T. Prestero, *Development of a Six-Degree of Freedom Simulation Model for the REMUS Autonomous Underwater Vehicle*. Presented at *12th International Symposium on Unmanned Untethered Submersible Technology*. 2001. Durham, NH, USA.

[90] R. Bachmayer, L. L. Whitcomb, and M. Grossenbaugh, *An Accurate Four-Quadrant Nonlinear Dynamical Model for Marine Thrusters: Theory and Experimental Validation*. IEEE Journal of Oceanic Engineering, 2000, **25**(1): p. 146-159.

[91] J. Kim and W. K. Chung, *Accurate and Practical Thruster Modeling for Underwater Vehicles*. Ocean Engineering, 2006, (33): p. 566-586.

[92] L. L. Whitcomb and D. R. Yoerger, *Development, Comparison, and Preliminary Experimental Validation of Nonlinear Dynamic Thruster Models*. IEEE Journal of Oceanic Engineering, 1999, **24**(4): p. 481-494.